



UNIVERSITY OF  
BIRMINGHAM

THE DEVELOPMENT OF NOVEL ADHESION PROMOTERS  
FOR WATERBORNE COATINGS AND POLYPROPYLENE CAR  
BUMPERS

by

HELEN LOUISE BRANNON

A thesis submitted to  
The University of Birmingham  
for the degree of  
DOCTOR OF ENGINEERING

School of Chemical Engineering  
College of Engineering and Physical Sciences  
The University of Birmingham

March 2014

UNIVERSITY OF  
BIRMINGHAM

**University of Birmingham Research Archive**

**e-theses repository**

This unpublished thesis/dissertation is copyright of the author and/or third parties. The intellectual property rights of the author or third parties in respect of this work are as defined by The Copyright Designs and Patents Act 1988 or as modified by any successor legislation.

Any use made of information contained in this thesis/dissertation must be in accordance with that legislation and must be properly acknowledged. Further distribution or reproduction in any format is prohibited without the permission of the copyright holder.

## ACKNOWLEDGEMENTS

First of all, I wish to greatly acknowledge all of my supervisors: Dr. Audrée Andersen, Dr. Christina Haaf-Kleinhubbert, Dr. Björn Heinz, Dr. Phil Cox, Dr. Richard Greenwood and Professor Jon Preece, of whom without, this project would not have been such a success. I have learnt so much from you over the last four years, and have vastly developed as a person. I was extremely lucky to have such expertise behind me. I very much enjoyed working with you, and it has been an unforgettable experience which I will forever treasure. I hope that we will stay in contact in the future. I will for sure miss our meetings at the Casino!

I would also like to acknowledge Dr. Markus Hickl, who provided great encouragement and believed in my work, organising presentations of my work within the company.

A special big thank you also goes to my mum, dad and brother, for being so supportive over the years and believing in me. Also my friends I met in Birmingham: Cerise, Jenni, Isa, Tony, James and Dan who made my first year in Birmingham so enjoyable and remained good friends throughout my time in Germany. My friends I met in Germany: Marce, Juli, Thomas, Véro, Bo and Kristina, for being such wonderful friends and making my time living in Germany unforgettable.

Moving to Germany and a new company was a very daunting experience at first. However, working daily with such brilliant people made it a great experience I will remember forever. I am very grateful of Herman Hecky and Thomas Rosenkranz who made me feel

so welcome on my first days at BASF. Ralf Häuselmann, Michael Vetter, Peter Thuery, Claudia Goebel and Stefan Wahl for making my time in B1 so much fun, as well as the two jokers, Ralf Horn and Frank Voellinger, who made every day so funny! An extra thank you also goes to Michael for so kindly offering to teach me how to scuba dive in his club, which is now a new favourite past time of mine. From working in J550, I would like to thank Dr. Herve Dietsch for all his words of wisdom, and allowing me to work in his lab with the great people Thomas Sturm and Siegfried Muth, as well as Nicole Lichterfeld and Pia Muehlbeier-Entzminger who always brightened up the day.

Furthermore, I was very fortunate to travel to Münster during my time at BASF, which I thoroughly enjoyed. I would look forward to working with the fantastic people: Frederik Foelling, Markus Saedler and Fatmir Raka. I thank them all for providing my initial training and giving me such a great experience visiting Münster. I also say an extra thank you to Frederik who assisted me with the spray gun application and to Markus and his family for allowing me to stay with them during one of my visits.

Meeting fellow post-graduate students was also a key part of my great experience at BASF. I would like to thank Viet Nguyen-Kim for all the fun we had sitting together in the same office, and for all the help he provided me for finding somewhere to live, as well as the fun we had organising the intern get-togethers. Furthermore, Simon Aben: without the Raclette evenings, the crêpes, French wine and my new favourite cheese, Comté, life would not have been the same! I also enjoyed all the social events he organised, through which I met some other lifelong friends.

I would also like to thank the English crew at BASF: Andrew, Mark, Nick, Neil, Kay and Suzanne, who kept the English spirit alive on our regular lunch breaks and gatherings!

I am particularly grateful for the knowledge I gained during my research project from the following people: Dr. Bernhard Von Vacano and Dr. Sabine Hirth, who guided me and taught me the two surface sensitive techniques used in this study: ToF-SIMS and XPS. Dr. Karl-Heinz Gunzelmann for all the help with GC/MS. Dr. Imke Mueller for conducting the computational studies within this project. Dr. Walter Maier for his help with NMR studies. Dr. Svetlana Guriyanova for her advice with mechanical testing and allowing me to work in her lab. Dr. Thomas Frechen for his expertise on polymer staining and microscopy. Dr. Joseph Sharples from the EPR research facility at University of Manchester for running the EPR samples (and the EPSRC for funding this).

My special thanks are also extended to all the analytical technicians at BASF who have taught me so much and vastly extended my scientific knowledge: Guido Lupa, Peter Boeshans and Marion Wagner.

Another special acknowledgement is for my German teacher and new friend, Caroline Ebert, who was very patient with me and made learning German a fun hobby.

I would like to express my very great appreciation to the EPSRC and BASF for their funding of this project.

Lastly, but not least, I would like to thank Professor Ian Norton for all of his support during the writing stage of my thesis.

A special thank you is also for the L<sup>A</sup>T<sub>E</sub>X community, for creating such a wonderful free typesetting system which was used to write this thesis.

*Als allererstes möchte ich mich bei meinen Betreuern für die Unterstützung und Aufmunterung bedanken. Ich habe die Zusammenarbeit sehr genossen.*

*Meine Familie, welche mich in allen Situationen sehr unterstützt hat.*

*In Ludwigshafen möchte ich mich für eine tolle Zeit mit viel Spaß in B1 bei Ralf (x2), Michael, Peter, Claudia, Frank und Stefan bedanken.*

*Auch allen meinen Kollegen im J550 Labor möchte ich Danke sagen: Thomas, Siegfried, Nicole and Pia.*

*Ebenfalls für eine sehr schöne Zeit möchte ich mich in Münster bei Frederik, Markus und Fatmir bedanken.*

*Danke auch an meine Deutschlehrerin, Caroline, welche mir Deutsch beigebracht hat.*

*Ich hoffe, ich habe niemanden vergessen.*

*Und vielen vielen Dank an alle Freunde und Bekannte in Deutschland. Es war eine super-tolle Zeit in Deutschland, die ich niemals vergessen werde :)*

*Liebe Helen*

## ABSTRACT

The ability of waterborne coatings to adhere to polypropylene-based substrates is a challenge in the automotive industry. This thesis seeks to explore novel methods to improve the adhesion and provide coated substrates of an industrial standard. Two methods are explored, whereby a physical entanglement method is found to be unsuccessful but a chemical bonding method is found to give patentable results. It is found that the UV curing of carbene precursors as candidate adhesion promoters, gives an adhesive force which is comparable to the industrial state of the art method, flaming. Initially, the UV energy initiates CH insertion reactions, which covalently graft the adhesion promoter to the polypropylene surface. Secondly, the hydrophilic functional groups of the adhesion promoter adhere to the waterborne basecoat, thus optimal adhesion is achieved. Statistical modelling of the results reveals that the adhesive strength depends on the UV intensity, the adhesion promoter concentration and functional group type. To explore the industrial applicability, the safety and stability during storage and the aesthetics of the adhesion promoters were investigated. This research is the first step to developing a formulation that is able to replace the current flaming method.

# Contents

|  |             |
|--|-------------|
| <b>List of Figures</b>   | <b>xii</b>  |
| <b>List of Tables</b>  | <b>xxxv</b> |
| <b>Terms and Abbreviations</b>   | <b>xl</b>   |
| <b>I Introduction</b>  | <b>1</b>    |
| <b>1 Business Case</b>   | <b>2</b>    |
| 1.1 Adhesion Challenge: Coating Plastic . . . . .                              | 4           |
| 1.2 Project Goal . . . . .   | 4           |
| <b>2 Literature Review</b>   | <b>7</b>    |
| 2.1 The Phenomena of Adhesion . . . . .  | 7           |
| 2.1.1 Definition . . . . .   | 8           |
| 2.1.2 Wettability . . . . .  | 9           |
| 2.1.3 Adhesion Mechanisms . . . . .  | 9           |
| 2.2 Why Replace Steel with Plastic? . . . . .                                  | 10          |
| 2.2.1 Thermoplastic Polyolefins (TPO) . . . . .                                | 11          |
| 2.3 The State of the Art . . . . .   | 12          |
| 2.3.1 Flaming Pre-treatment . . . . .  | 12          |
| 2.3.2 Chlorinated Polyolefin Adhesion Promoters . . . . .                      | 13          |
| 2.4 Influence of the Substrate Microstructure on Adhesion Mechanisms . . . . . | 14          |



|         |  |    |
|---------|--|----|
| 2.4.1   | Microstructure of Injection Moulded TPO . . . . .                          | 14 |
| 2.4.2   | Influence of TPO Microstructure on Adhesion . . . . .                      | 17 |
| 2.5     | Characterisation of Adhesion . . . . .                                     | 18 |
| 2.5.1   | Peel Tests . . . . .   | 18 |
| 2.5.2   | Cross-Hatch Test . . . . .   | 19 |
| 2.5.3   | Steam Jet Test . . . . .   | 20 |
| 2.5.4   | Surface Characterisation . . . . .   | 20 |
| 2.5.5   | Substrate Characterisation . . . . .                                       | 22 |
| 2.6     | Other Adhesion Improvement Methods . . . . .                               | 23 |
| 2.6.1   | Oxidative Methods . . . . .  | 23 |
| 2.6.2   | Block Copolymers as Adhesion Promoters . . . . .                           | 24 |
| 2.6.3   | Grafting . . . . .   | 25 |
| 2.6.3.1 | Maleic Anhydride (MA) . . . . .  | 25 |
| 2.6.3.2 | Poly(Acrylic Acid) . . . . .   | 26 |
| 2.6.4   | Chemical Etching . . . . .   | 27 |
| 2.6.5   | Novel Surface Treatment . . . . .  | 27 |
| 2.7     | Unsuccessful Adhesion Techniques . . . . .                                 | 28 |
| 2.7.1   | Chemical Bonding by Catalytic Oxidation of Inactivated C-H Bonds . . . . . | 28 |
| 2.7.2   | C-H insertion of Nitrene . . . . .   | 28 |
| 2.8     | Current Patents based on Adhesion Promoters for Plastics . . . . .         | 28 |
| 2.9     | Diazirines as Potential Adhesion Promoters . . . . .                       | 29 |
| 2.10    | Conclusions . . . . .  | 30 |

## **II Materials and Methods 31**

### **3 Materials 32**

|       |  |    |
|-------|--|----|
| 3.1   | Substrates . . . . .                           | 32 |
| 3.1.1 | Polypropylene-based Substrates . . . . .       | 32 |
| 3.1.2 | Grafting Proof-of-Concept Substrates . . . . . | 33 |

|          |   |           |
|----------|---|-----------|
| 3.2      | Chlorinated Polyolefin (CPO) Adhesion Promoter . . . . .  | 33        |
| 3.3      | Candidate Adhesion Promoters for Physical Entanglement . . . . .  | 35        |
| 3.4      | Candidate Adhesion Promoters for Covalent Bonding (Grafting) . . . . .  | 35        |
| 3.5      | Waterborne Basecoat and Topcoat . . . . .   | 35        |
| 3.6      | Solvents . . . . .  | 37        |
| 3.7      | Alkane thiols . . . . .   | 37        |
| 3.8      | Reaction between Trimeric Isocyanate and TPDOH . . . . .  | 38        |
| <b>4</b> | <b>Methods</b>  | <b>39</b> |
| 4.1      | Scanning Electron Microscopy (SEM) and Transmission Electron Microscopy<br>(TEM) with a Ruthenium Tetraoxide ( $\text{RuO}_4$ ) Staining Technique, and En-<br>ergy Dispersive X-ray Spectroscopy (EDX) . . . . . | 39        |
| 4.2      | ImageJ SEM Image Analysis . . . . .   | 40        |
| 4.3      | White Light Interferometry . . . . .  | 41        |
| 4.4      | Nanoindentation . . . . .   | 43        |
| 4.5      | Surface Free Energy Determination . . . . .   | 44        |
| 4.5.1    | Owens-Wendt Method . . . . .  | 44        |
| 4.5.2    | Owens-Wendt Theory . . . . .  | 46        |
| 4.5.3    | Surface Free Energy of the Basecoat (Wet): Wu Method . . . . .  | 47        |
| 4.6      | Wettability: Contact Angle Measurements . . . . .   | 48        |
| 4.7      | Automated Flaming Station . . . . .   | 49        |
| 4.8      | Substrate Cleaning . . . . .  | 49        |
| 4.8.1    | Cleaning TPO Substrates . . . . .   | 49        |
| 4.8.2    | Cleaning Gold Surfaces . . . . .  | 50        |
| 4.9      | Self-Assembled Monolayer (SAM) Formation . . . . .  | 50        |
| 4.10     | Adhesion Promoter (AP) Deposition for Grafting Experiments . . . . .  | 51        |
| 4.11     | Doctor Blade Coating Application . . . . .  | 51        |
| 4.11.1   | CPO . . . . .   | 51        |
| 4.11.2   | Candidate APs . . . . .   | 51        |

|        |   |    |
|--------|---|----|
| 4.12   | Spray Gun Coating Application . . . . .   | 52 |
| 4.13   | Thermal Cure . . . . .  | 52 |
| 4.14   | UV Cure . . . . .   | 53 |
| 4.15   | Cross Hatch Test (CHT) . . . . .  | 53 |
| 4.16   | Steam Jet Test (SJT) . . . . .  | 54 |
| 4.17   | Hansen Solubility Parameters: Solvent Selection for Swelling Substrates . .                                     | 54 |
| 4.18   | Solvent Swelling: Milligram Balance . . . . .   | 60 |
| 4.19   | Time of Flight Secondary Mass Spectrometry (ToF-SIMS) . . . . .   | 61 |
| 4.19.1 | Surface Composition Analysis . . . . .  | 61 |
| 4.19.2 | High Lateral Resolution Images . . . . .  | 62 |
| 4.19.3 | Mode of Failure Analysis . . . . .  | 62 |
| 4.20   | X-ray Photoelectron Spectroscopy (XPS) . . . . .  | 62 |
| 4.21   | Computational Methods . . . . .   | 63 |
| 4.21.1 | Predicted 3D Structures of APs for the Prediction of the Concen-<br>tration Required for a Monolayer . . . . .  | 63 |
| 4.21.2 | Predicted Infrared (IR) Spectrum of TPD . . . . .   | 64 |
| 4.21.3 | Predicted Singlet/Triplet States of Carbenes . . . . .  | 64 |
| 4.22   | Temperature Measurement during UV Curing . . . . .  | 65 |
| 4.23   | Ultraviolet-Visible (UV-Vis) Spectroscopy . . . . .   | 66 |
| 4.23.1 | Thermal Degradation . . . . .   | 66 |
| 4.23.2 | UV Degradation . . . . .  | 67 |
| 4.24   | Nuclear Magnetic Resonance (NMR) Spectroscopy . . . . .   | 67 |
| 4.25   | Electron Paramagnetic Resonance Spectroscopy (EPR) . . . . .  | 67 |
| 4.25.1 | UV Degradation . . . . .  | 68 |
| 4.25.2 | Thermal Degradation . . . . .   | 68 |
| 4.26   | Mass Spectrometry Techniques used for Solution Analysis . . . . .   | 68 |
| 4.26.1 | Gas Chromatography / Mass Spectrometry (GC/MS), Field Ioni-<br>sation (FI) (Cool-on-Column Technique) . . . . . | 69 |

|          |  |    |
|----------|--|----|
| 4.26.1.1 | Gas Chromatography . . . . .   | 69 |
| 4.26.1.2 | Field Ionisation (FI) . . . . .  | 69 |
| 4.26.1.3 | Time-of-Flight (ToF) Mass Spectrometry . . . . .   | 70 |
| 4.26.1.4 | Mass Scale Calibration . . . . .   | 70 |
| 4.26.2   | Positive Ionisation Mass Spetrometry (MS), (LIFDI) . . . . .   | 70 |
| 4.26.2.1 | Liquid Injection Field Desorption Ionisation (LIFDI) . . . . .   | 70 |
| 4.26.2.2 | Time-of-Flight Mass Spectrometry . . . . .   | 71 |
| 4.26.2.3 | Mass scale Calibration . . . . .   | 71 |
| 4.27     | Infrared Spectroscopy (IR) . . . . .   | 71 |
| 4.27.1   | Transmission Infrared Spectroscopy (IR) . . . . .  | 71 |
| 4.27.2   | Attenuated Total Reflection Infrared Spectroscopy (ATR-IR) . . . . .                                       | 72 |
| 4.28     | Raman Spectroscopy . . . . .   | 72 |
| 4.29     | Colorimetry . . . . .  | 72 |
| 4.30     | Differential Scanning Calorimetry (DSC) . . . . .  | 72 |
| 4.31     | Simultaneous Differential Scanning Calorimetry - Thermogravimetric Analysis (DSC - TGA) . . . . .          | 73 |
| 4.32     | Impact Sensitivity Drop-Weight Test . . . . .  | 74 |
| 4.33     | Synthesis of 3-phenyl-3-(trifluoromethyl)-3H- diazirine ( <i>or</i> TPD) . . . . .                         | 74 |
| 4.34     | Reaction of Trimeric Isocyanate and TPDOH . . . . .  | 74 |
| 4.35     | Exploratory Data Analysis . . . . .  | 74 |
| 4.35.1   | Pearson and Spearman correlation analysis . . . . .  | 75 |
| 4.35.2   | ANOVA and Kruskal-Wallis . . . . .   | 75 |
| 4.35.3   | Rigorous Empirical Model Building using Stepwise Ordinary Least Squares (stepOLS) $y_j=g_j(x_i)$ . . . . . | 78 |

### **III Results and Discussions 81**

#### **5 Substrate Characterisation 82**

|     |                    |    |
|-----|--------------------|----|
| 5.1 | Overview . . . . . | 82 |
|-----|--------------------|----|

|          |   |            |
|----------|---|------------|
| 5.2      | Introduction . . . . .  | 82         |
| 5.3      | Substrate Morphology . . . . .  | 83         |
| 5.3.1    | EPDM Mapping . . . . .  | 83         |
| 5.3.1.1  | Untreated Substrates . . . . .  | 83         |
| 5.4      | Physical Properties of Substrates . . . . .   | 93         |
| 5.5      | Thermodynamics: Surface Energy . . . . .  | 94         |
| 5.6      | The State of the Art: Adhesion of Polar Coatings to Hydrophobic PP/EPDM<br>(TPO) Substrates . . . . . | 96         |
| 5.6.1    | Flaming Pre-treatment . . . . .   | 96         |
| 5.6.2    | CPO Adhesion Promoters . . . . .  | 101        |
| 5.7      | Conclusions . . . . .   | 105        |
| <b>6</b> | <b>Physical Adhesion: Surface Swelling and Interfacial Polymer Chain En-<br/>tangement</b>            | <b>107</b> |
| 6.1      | Overview . . . . .  | 107        |
| 6.2      | Introduction . . . . .  | 107        |
| 6.3      | Substrate Swelling . . . . .  | 109        |
| 6.3.1    | Selecting Appropriate Solvent: Mass Change . . . . .  | 110        |
| 6.3.2    | Mechanical Properties: Substrate Hardness and Young's Modulus . . . . .                               | 113        |
| 6.3.3    | Surface Roughness . . . . .   | 119        |
| 6.4      | Candidate Adhesion Promoter Selection . . . . .   | 124        |
| 6.4.1    | Interaction of APs with PP . . . . .  | 126        |
| 6.4.2    | Adhesion Tests . . . . .  | 127        |
| 6.5      | Future Work . . . . .   | 129        |
| 6.6      | Conclusions . . . . .   | 130        |
| <b>7</b> | <b>Chemical Adhesion: A Proof- Of-Concept Grafting Study</b>  | <b>131</b> |
| 7.1      | Overview . . . . .  | 131        |
| 7.2      | Introduction . . . . .  | 131        |

|          |  |            |
|----------|--|------------|
| 7.3      | Identifying and Characterising Adhesion Promoters (AP's)   | 132        |
| 7.3.1    | CH Insertion Proof-of-Concept  | 133        |
| 7.4      | Grafting to Substrates   | 139        |
| 7.4.1    | Surface Grafting of TPD to the Model Self Assembled Monolayer (SAM) Surface  | 141        |
| 7.4.2    | Surface Grafting of TPD to Polypropylene Substrates Containing No Additives  | 146        |
| 7.4.3    | Surface Grafting of TPD to Industrial TPO/0 Substrates, Containing No EPDM   | 149        |
| 7.4.4    | Surface Grafting of TPD to Industrial TPO/2 Substrates, Containing EPDM  | 149        |
| 7.5      | Modification of TPD, Tailoring for the Adhesion at the AP/Basecoat Interface   | 152        |
| 7.5.1    | Surface Grafting of TPDOH to Industrial TPO/0 Substrates at 80 °C  | 152        |
| 7.5.2    | Surface Grafting of TPDCOOH to Industrial TPO/0 Substrates at 80 °C  | 156        |
| 7.5.3    | Surface Grafting of TPDOH to Industrial TPO/0 Substrates at 100 °C   | 158        |
| 7.5.4    | Surface Grafting of TPDCOOH to Industrial TPO/0 Substrates at 100 °C   | 159        |
| 7.5.5    | Prediction of TPD Solution Concentration to Create a Monolayer   | 160        |
| 7.5.6    | Surface Grafting of TPDOH and TPDCOOH to Industrial TPO/0 Substrates with UV Curing at a Radiance Exposure of 1900 mJ cm <sup>-2</sup> | 161        |
| 7.6      | Summary  | 163        |
| 7.7      | Conclusions  | 164        |
| <b>8</b> | <b>Chemical Adhesion: Cross-Hatch and Steam Jet Adhesion Tests</b>   | <b>166</b> |
| 8.1      | Overview   | 166        |
| 8.2      | Introduction   | 166        |
| 8.3      | Doctor Blade Application of Coatings   | 171        |

|       |  |     |
|-------|--|-----|
| 8.3.1 | Thermal Curing . . . . .   | 171 |
| 8.3.2 | UV Curing . . . . .  | 180 |
| 8.3.3 | Wet-on-Wet . . . . .   | 186 |
| 8.4   | Spray Gun Application of Coatings . . . . .  | 188 |
| 8.4.1 | Thermal Curing . . . . .   | 188 |
| 8.4.2 | UV Curing . . . . .  | 192 |
|       | 8.4.2.1 Dependence of the Substrate Type and UV Radiant Ex-<br>posure on the Adhesion . . . . .                      | 192 |
|       | 8.4.2.2 Dependence of the TPDCOOH Concentration, Substrate<br>Type and UV Radiant Exposure on the Adhesion . . . . . | 196 |
| 8.4.3 | UV Curing vs. Thermal Curing . . . . .   | 199 |
|       | 8.4.3.1 Surface Elemental Composition . . . . .  | 199 |
|       | 8.4.3.2 UV-Vis Kinetics Study . . . . .  | 201 |
|       | 8.4.3.3 EPR Spectrometry Study . . . . .   | 206 |
| 8.4.4 | Chemical Mapping of Coated Cross-Sections . . . . .  | 209 |
|       | 8.4.4.1 Basecoat and Clearcoat on an Untreated Substrate . . . . .   | 210 |
|       | 8.4.4.2 Comparing TPDOH and TPDCOOH . . . . .  | 211 |
|       | 8.4.4.3 Comparing the Doctor Blade and Spray Methods of Ap-<br>plication . . . . .                                   | 211 |
|       | 8.4.4.4 Comparing Substrate Type . . . . .   | 213 |
|       | 8.4.4.5 Comparing Number of Primer Layers . . . . .  | 214 |
|       | 8.4.4.6 Comparing the TPDCOOH Solution Concentration . . . . .   | 215 |
| 8.5   | Industrial Applicability . . . . .   | 216 |
| 8.5.1 | Stability of TPD's . . . . .   | 216 |
|       | 8.5.1.1 Storage Stability . . . . .  | 216 |
|       | 8.5.1.2 Ageing Effect . . . . .  | 218 |
| 8.5.2 | Evaluation of Synthesis . . . . .  | 218 |
| 8.5.3 | Colour of APs after CH Insertion . . . . .   | 219 |

|           |   |            |
|-----------|---|------------|
| 8.5.4     | Differential Scanning Calorimetry (DSC) and Simultaneous Differential Scanning Calorimetry-Thermogravimetry (DSC-TG) . . . . .  | 220        |
| 8.5.4.1   | Reaction Processes Occurring . . . . .  | 222        |
| 8.5.4.2   | Safety of Substances . . . . .  | 223        |
| 8.5.5     | Impact Sensitivity . . . . .  | 225        |
| 8.5.6     | Formulation into Coatings . . . . .   | 225        |
| 8.6       | Conclusions . . . . .   | 228        |
| <b>9</b>  | <b>Modelling Adhesion Results</b>   | <b>230</b> |
| 9.1       | Overview . . . . .  | 230        |
| 9.2       | Introduction . . . . .  | 230        |
| 9.3       | Exploratory Data Analysis . . . . .   | 230        |
| 9.3.1     | Pearson and Spearman Correlation Analysis . . . . .   | 231        |
| 9.3.2     | Boxplots: Understanding and Exploring the Relationship between Lead Responses and Potential Categorical Factors $X_i$ . . . . . | 237        |
| 9.4       | Stepwise Ordinary Least Squares (stepOLS) . . . . .   | 240        |
| 9.4.1     | CHT . . . . .   | 241        |
| 9.4.2     | SJT . . . . .   | 242        |
| 9.5       | Conclusions . . . . .   | 244        |
| <b>IV</b> | <b>Final Conclusions and Future Work</b>  | <b>247</b> |
| <b>V</b>  | <b>Appendices</b>   | <b>252</b> |
| <b>10</b> | <b>Supplementary Material</b>   | <b>253</b> |
|           | Appendix 10.A Standard Used for Nanoindentation . . . . .   | 254        |
|           | Appendix 10.B Data Interpolation . . . . .  | 255        |
|           | Appendix 10.C Surface Roughness of Swollen TPO/0 . . . . .  | 256        |
|           | Appendix 10.D Surface Roughness of Swollen R/0 . . . . .  | 258        |



|   |     |
|---|-----|
| Appendix 10.E Surface Roughness of Swollen R/25 . . . . .   | 259 |
| Appendix 10.F Substrate Characterisation . . . . .  | 260 |
| 10.F.1 Surface Roughness . . . . .  | 260 |
| 10.F.2 Chemical Composition . . . . .   | 261 |
| 10.F.2.1 Microscopy . . . . .   | 261 |
| 10.F.2.2 Time of Flight Secondary Ion Mass Spectrometry (ToF-SIMS) . . . . .                                    | 268 |
| 10.F.3 Mechanical Properties: Substrate and Young's Modulus . . . . .   | 272 |
| 10.F.3.1 Substrate Hardness . . . . .   | 272 |
| 10.F.3.2 Substrate Young's Modulus . . . . .  | 278 |
| 10.F.4 Effect of Solvent Cleaning on the Substrate Morphology . . . . .   | 279 |
| 10.F.4.1 Surface Roughness . . . . .  | 279 |
| Appendix 10.G Candidate Adhesion Promoter   |     |
| Characterisation . . . . .  | 286 |
| 10.G.1 Carbene Precursors . . . . .   | 286 |
| Appendix 10.H Self Assembled Monolayers (SAMs) on Gold Surfaces as Model  |     |
| Systems . . . . .   | 293 |
| Appendix 10.I Lowest Energy Conformers of Diaziridine and Diazirine (TPD) . . . . .                             | 298 |
| Appendix 10.J Predicted IR Spectra of Diaziridine . . . . .   | 299 |
| Appendix 10.K Predicted IR Spectra of Diazirine (TPD) . . . . .   | 300 |
| Appendix 10.L Predicted Excited States of TPD, TPDOH and TPDCOOH . . . . .                                      | 301 |
| Appendix 10.M Adhesion Promoter Synthesis . . . . .   | 302 |
| 10.M.1 Synthesis of 3-phenyl-3-(trifluoromethyl)-3H-diazirine ( <i>or</i> TPD) . . . . .                        | 302 |
| 10.M.1.1 Step 1: 2,2,2-trifluoro-1-phenylethanone oxime (2) from 2,2,2-trifluoro-1-phenylethanone (1) . . . . . | 302 |
| 10.M.1.2 Step 2: 2,2,2-trifluoro-1-phenylethanone O-tosyl oxime (3) from (2) . . . . .                          | 303 |

|  |     |
|--|-----|
| 10.M.1.3 Step 3: 3-phenyl-3-(trifluoromethyl)diaziridine (4) from (3)                        | 303 |
| 10.M.1.4 AB System . . . . .   | 305 |
| 10.M.1.5 Step 4: 3-phenyl-3-(trifluoromethyl)-3H-diazirine (or TPD)(5)<br>from (4) . . . . . | 306 |
| Appendix 10.N Statistical Modelling Data . . . . .   | 308 |
| Appendix 10.O Stepwise Ordinary Least Squares Analysis . . . . .                             | 310 |
| Appendix 10.P Patent Search . . . . .  | 313 |

|                   |            |
|-------------------|------------|
| <b>References</b> | <b>321</b> |
|-------------------|------------|

## List of Figures

|     |  |    |
|-----|--|----|
| 1.1 | The different divisions of BASF. Adapted from a public presentation from BASF Investor Day Automotive, September 2012. <sup>2</sup> . . . . .  | 3  |
| 1.2 | A diagram highlighting the reduction of VOC by using waterborne coatings. Adapted from a public presentation from BASF Investor Day Automotive, September 2012. <sup>2</sup> . . . . .   | 3  |
| 1.3 | Top: Schematic diagram representing the mis-match in surface energy of a waterborne basecoat (blue circles) and a PP substrate (grey triangles). Bottom, left: Photograph showing a coating that has delaminated from a car bumper. Bottom, right: Polar and dispersion (van der Waals forces) energy components of a wet and dry waterborne basecoat, a flame treated substrate and an untreated PP substrate, in order of decreasing polar components. . . . . | 5  |
| 1.4 | A schematic diagram representing (1.) the production line used in industry today and (2.) the overall goal / vision of the paint formulators. Brackets indicate that a primer is not always used. BC = basecoat, CC= clearcoat or topcoat. . . . .   | 6  |
| 1.5 | The overall objective of the project. . . . .  | 6  |
| 2.1 | Types of adhesive interactions. . . . .  | 7  |
| 2.2 | An example of an application process of a CPO primer. <sup>29</sup> . . . . .  | 14 |
| 2.3 | Proposed chemical mechanism for adhesion between a TPO (with EPDM), CPO and a topcoat. <sup>63,65</sup> . . . . .  | 15 |

|     |  |    |
|-----|--|----|
| 2.4 | Three-dimensional schematic (generalised) representation of the TPO microstructure and surface morphology. Adapted from Ryntz <i>et al.</i> <sup>29,30,45,64,66-68</sup>   | 16 |
| 2.5 | A photograph of substrates after (a) a CHT test (100 % adhesion) and (b) a SJT (40 % adhesion). . . . .  | 20 |
| 2.6 | A schematic diagram showing a block copolymer adhering a hydrophobic and hydrophilic polymer together. . . . .   | 24 |
| 2.7 | The polymers tested for improved adhesion on PP, adapted by Overbeek. <sup>124</sup> . . . . .   | 25 |
| 2.8 | The reaction mechanism of MA grafting to PP. <sup>40</sup> . . . . .   | 26 |
| 2.9 | Methylene in its (a) triplet and (b) singlet excited state. Diagram composed from information in the book: Modern Physical Organic Chemistry. <sup>136</sup> . . . . .   | 29 |
| 3.1 | Molecular structures of (a) TPD, (b) TPDOH and (c) TPDCOOH . . .   | 35 |
| 3.2 | A pie chart showing the percentage of the different components in the waterborne basecoat formulation. . . . .   | 37 |
| 4.1 | Schematic profile of a surface, showing the roughness parameters Ra and Rq, for the peaks and valleys in the Z direction. An adaptation from Bellitto <i>et al.</i> <sup>140</sup> . . . . .   | 42 |
| 4.2 | A schematic representation of nano-indentation in Continuous Stiffness Mode (CSM) from Agilent technologies. (a) A sinusoidal oscillation is used in permanent superposition to the force signal. The oscillation is applied directly to the shaft with the tip and produced by the coil (shown schematically on right hand side). For elastic materials, there is no phase shift (b) but measurement of viscoelastic materials result in a phase shift between force and displacement signal (c). . . . . | 45 |

|      |  |    |
|------|--|----|
| 4.3  | Schematic diagram demonstrating the basic principle behind linear interpolation: the line of best fit between two data points, $x_1$ and $x_2$ , from which $x$ can be calculated. . . . .   | 45 |
| 4.4  | A schematic diagram showing cases where liquid drops are non-wetting or wetting on a substrate surface. . . . .  | 48 |
| 4.5  | Schematic diagram of a laboratory flame treatment station . . . . .  | 49 |
| 4.6  | Top: a summary of the coating and curing steps. Bottom: the dried thicknesses of the coatings. . . . .   | 52 |
| 4.7  | The UV emission spectrum from the IST UV curing system. . . . .  | 53 |
| 4.8  | Cross-Hatch Test. Setup : 1 = tape, 2 = coatings, 3 = grid, 4 = substrate; Test details: a = length of grid is 10 mm, b = length of grid and guidelines is 16 mm, c = the guide blades and cutting blades are on the same plane, d = the tape is applied and smoothed/ flattened, e = pull of direction and angle of the tape. . . . . | 55 |
| 4.9  | Steam Jet Test . . . . .   | 56 |
| 4.10 | The Hansen Solubility Parameters of the selected solvents and a PP polymer, and the ratio of the distance of the selected solvent to the radius of the PP sphere (RED number). A perfect solvent has an RED of 0. A solvent with an RED value $< 1$ should swell the polymer. . . . .  | 59 |
| 4.11 | The Hansen Solubility Parameters of the selected solvents and an EPDM polymer, and the ratio of the distance of the selected solvent to the radius of the PP sphere (RED number). A perfect solvent has an RED of 0. A solvent with an RED value $< 1$ should swell the polymer. . . . .   | 59 |
| 4.12 | The Hansen Solubility Parameters, and sphere of the chosen solvents and PP, and the ratio of the distance of the chosen solvents to the radius of the PP sphere (RED number). . . . .  | 60 |
| 4.13 | Molecular structures of the carbenes generated from (a) TPD, (b) TPDOH and (c) TPDCOOH, with the loss of $N_2$ . . . . .   | 65 |

|      |  |    |
|------|--|----|
| 4.14 | Hierarchical schematic diagram demonstrating the responses, factors and levels tested for categorical data. . . . .  | 79 |
| 4.15 | The stepwise Ordinary Least Squares (stepOLS) modelling process. . . . .   | 80 |
| 5.1  | A summary of the substrate characterisation chapter. . . . .   | 83 |
| 5.2  | The oxidation reaction between osmium tetroxide and alkene double bonds, forming a five-membered ring: a cyclic osmate ester <sup>160</sup> . . . . .  | 84 |
| 5.3  | SEM micrographs of the top cross-section of ruthenium tetroxide (RuO <sub>4</sub> ) stained industrial substrates, schematically represented in (a), for (b) TPO/0, (c) TPO/2 and (d) TPO/20 (insert shows backscattered electrons on RHS) substrates. . . . .   | 85 |
| 5.4  | SEM micrographs (left) taken from the cross -section of a TPO/2 substrate and images showing the traced EPDM domains and % area coverage calculated (right). . . . .   | 87 |
| 5.5  | SEM micrographs of ruthenium tetroxide (RuO <sub>4</sub> ) stained research PP substrates containing (a) R/0, (b) R/5, (c) R/10, (d) R/15, (e) R/20, (f) R/25, taken from the top part of the substrate cross section as shown in the schematic diagram. . . . .   | 89 |
| 5.6  | SEM micrographs of ruthenium tetroxide (RuO <sub>4</sub> ) stained research PP substrates taken from the top cross-section, containing: (a) R/5, (b) R/10, (c) R/15, (d) R/20, (e) R/25 (top) and images of the subsequent traced EPDM domains (bottom). Table: % area coverage of EPDM for the top, middle and bottom cross-sectional areas as shown in the schematic diagram (top, right). . . . . | 90 |
| 5.7  | SEM micrographs of ruthenium tetroxide stained research PP substrates taken from the surface, containing (a) R/5, (b) R/10, (c) R/15, (d) R/20, (e) R/25 (top) and images of the subsequent traced EPDM domains (bottom). Table: % area coverage of EPDM for the substrate surface, as shown in the schematic diagram (top, right). . . . .  | 91 |

|      |   |     |
|------|---|-----|
| 5.8  | SEM micrographs of the surface of TPO/20 (a) before treatment and (b) after heat treatment at 80 °C for 1 hour. Inset: area of EPDM magnified. The EDX graph shows the chemical composition at point 4. The atomic % is displayed in the table (bottom) showing the presence of Ru (staining) on the areas appearing whiter in contrast, due to EPDM.   | 93  |
| 5.9  | A bar graph representing the surface energy values of the labelled substrates and a waterborne basecoat before and after drying. All surface energy calculations were measured using the Owens-Wendt method, with the exception of the wet basecoat which was calculated using the Wu method. . . . .   | 94  |
| 5.10 | Steps of the coating application and curing process. . . . .  | 97  |
| 5.11 | Photographs displaying the cross-hatch test (adhesion test) procedure. Reproduced with permission from BASF Coatings GmbH. . . . .  | 98  |
| 5.12 | A bar graph representing the surface energy values of the labelled substrates before and after flaming and a waterborne basecoat before and after drying. All surface energy calculations were measured using the Owens-Wendt method, with the exception of the wet basecoat which was calculated using the Wu method. . . . .  | 100 |
| 5.13 | Normalised negative ToF-SIMS data taken from a R/15 research substrate before and after flaming, and 6 hours after the flaming treatment.   | 101 |
| 5.14 | Left: Negative, high lateral resolution mode ToF-SIMS image of a 200 $\mu\text{m}^2$ area taken from a cross section of TPO/CPO/basecoat/topcoat/epoxy-glue substrate, cut with a cryo-microtome; Graph overlay: Line graph showing the chloride ( $\text{Cl}^-$ ) ion distribution across the coatings; Image overlay: Magnified cross-section showing the $\text{Cl}^-$ diffusion into the TPO and basecoat. Right: Schematic diagram showing the positioning of the layered coatings. ToF-SIMS data were normalised to the total ion count. Image resolution is 1.6 $\mu\text{m}/\text{pixel}$ . . . . . | 103 |

|     |  |     |
|-----|--|-----|
| 6.1 | A summary of the physical adhesion chapter. . . . .  | 108 |
| 6.2 | The mass change with the square root of time, after TPO/2 substrates were firstly (a) exposed to the four solvent types selected by HSP parameters for 1 hour, and (b) left to air dry for 1 hour. Presented data are averaged values taken from 3 different substrates. Lines of best fit are shown for deviations from Fick's Law. . . . .   | 112 |
| 6.3 | Surface hardness profile of a (a) TPO/0, (b) R/0 and a (c) R/25 substrate, before and after swelling for 1 hour, 10 minutes, and 1 minute. Top right: schematic diagram showing solvent migration into the surface of a substrate, with the solvent molecules (orange spheres) pushing apart the substrate polymer chains, increasing their mobility. . . . .  | 114 |
| 6.4 | Surface hardness profile of a (a) R/0 and (b) R/25 substrate, before and after swelling for 1 minute, and drying for 6 hours and for 3 days. . . .   | 116 |
| 6.5 | Summary of surface hardness profiles of a (a) TPO/0, (b) R/0 and (c) R/25 substrate, before and after swelling for 1 minute, and drying for 6 hours. Bottom: Average hardness change of TPO/0, R/0 and R/25 substrates before and after swelling for 1 minute and drying for 6 hours.  | 118 |
| 6.6 | Top: 2D and 3D images of surface roughness and x and y profiles of R/0 after (a) 10 minute swelling time, (b) after it was left to dry for 5 hours and (c) R/25 after 1 minute swelling time, (d) after it was left to dry for 5 hours. Bottom: Average root mean square roughness (Rq) of the TPO/0, R/0 and R/25 substrates before and after swelling for 10 minutes and drying for 5 hours, and after swelling for 1 minute and drying for 5 hours. . . . . | 120 |



|     |  |     |
|-----|--|-----|
| 6.7 | Schematic diagram demonstrating the hypothesis that the regions of EPDM found at the surface of a substrate could swell at a greater rate than the surrounding PP matrix, causing a greater deviation in peaks and valleys at the surface as demonstrated by the orange area (different parts of the surface will swell at different rates). . . . . | 123 |
| 6.8 | Schematic diagram demonstrating the hypothesis of achieving improved adhesion between a hydrophilic waterborne basecoat and a hydrophobic PP-based substrate, via molecular chain entanglement with a candidate AP and subsequent interactions between function groups of the AP and the basecoat. . . . .   | 125 |
| 6.9 | A scatter graph showing the surface tension (x-axis) and wettability (y-axis) of the candidate APs on a TPO/2 substrate. The polymers chosen for adhesion tests are highlighted with blue dashed circles. . . . .  | 126 |
| 7.1 | A summary of the chemical adhesion, a proof-of-concept chapter. . . . .  | 132 |
| 7.2 | The mass spectrum of the reaction products after a highly concentrated solution of TPD in cyclohexane (1.3 M) was refluxed for 8h. Cyclohexane was in excess to TPD by 7:1. . . . .  | 134 |
| 7.3 | <sup>19</sup> F NMR spectra of thermally reacted (80 °C, 8h) 3 mM TPD solutions in (a) cyclohexane and (b) D <sub>12</sub> -cyclohexane. Inserts show magnified doublet peaks, labelled with chemical shift (ppm) and coupling constant, <i>J</i> (Hz). Chemical shifts were calculated relative to 100 % CF <sub>3</sub> COOH. . . . .              | 136 |
| 7.4 | <sup>19</sup> F NMR spectra of UV reacted (2.2 mW, 8h) 3 mM TPD solutions in (a) cyclohexane and (b) D <sub>12</sub> -cyclohexane. Inserts show magnified doublet peaks, labelled with chemical shift (ppm) and coupling constant, <i>J</i> (Hz). Chemical shifts were calculated relative to 100 % CF <sub>3</sub> COOH . . . . .                   | 137 |

|     |   |     |
|-----|---|-----|
| 7.5 | A systematic approach to testing the grafting ability of TPD to solid surfaces: (a) model alkane-thiol-gold self-assembled monolayer surface of differing chain lengths, (b) polypropylene sheet containing no pigment, (c) industrial TPO polypropylene substrate containing all additives including pigment. . . . .  | 140 |
| 7.6 | Experimental protocol for the grafting proof-of-concept experiment. . .   | 140 |
| 7.7 | Thermal grafting of TPD at 80 °C on the model SAM surface. ToF-SIMS results show normalised F <sup>-</sup> intensity found at the surface and XPS results show F wt.% found at the surface: (a) normalised F <sup>-</sup> intensity, 24 h cure; (b) *F wt.% , 24 h cure; (c) normalised F <sup>-</sup> intensity , 30 min cure; (d) *F wt.%, 30 min cure: for surfaces A-F as represented in Figure 7.6 (substrate C was not measured in XPS (d) to avoid contamination). *A1 represents the gold surface before plasma cleaning and SAM formation and A2 after plasma cleaning and SAM formation.          | 142 |
| 7.8 | XPS peaks taken from the survey spectrum of a TPD-grafted SAM surface (80 °C, 24h) showing the F 1s peak (LHS), and the C1s peak (RHS), and the subsequent modelling highlighting the binding energies due to the C-F <sub>3</sub> bonding at 687.9 eV and 292.3 eV. This shows strong evidence that the TPD moiety can be distinguished from inorganic C-F surface contamination and other C bonding from the surface. For comparing the different surfaces, the F wt.% was taken from the F 1s peak (spectra were fitted by assuming a Gaussian/Lorentzian-Sum-Shape (90/10) for all components). . . . . | 144 |
| 7.9 | Top: the mechanism of carbene generation via thermal activation and the subsequent C-H insertion into the substrate surface, highlighting the fragmentation; bottom: negative ToF-SIMS peak at m/z = 173 due to the fragmentation of the C-H insertion product past the newly formed C-C bond, proving a covalent bond is formed during the grafting process.   | 145 |

|      |  |     |
|------|--|-----|
| 7.10 | Thermal grafting of TPD at 80 °C on PP sheets containing no pigment. ToF-SIMS results show normalised F <sup>-</sup> intensity found at the surface and XPS results show F wt.% found at the surface: (a) normalised F <sup>-</sup> intensity , 24 h cure; (b) F wt.% , 24 h cure; (c) normalised F <sup>-</sup> intensity , 30 min cure; (d) F wt.%, 30 min cure: for surfaces A-F as represented in Figure 7.6 (substrate C was not measured in XPS to avoid contamination). . . . .                     | 147 |
| 7.11 | Thermal grafting of TPD at 80 °C on the industrial TPO/0 substrate. ToF-SIMS results show normalised F <sup>-</sup> intensity found at the surface and XPS results show F wt.% found at the surface: (a) normalised F <sup>-</sup> intensity , 24 h cure; (b) XPS , 24 h cure; (c) normalised F <sup>-</sup> intensity , 30 min cure; (d) F wt.%, 30 min cure: for surfaces A-F as represented in Figure 7.6 (substrate C was not measured in XPS to avoid contamination).                                 | 150 |
| 7.12 | Thermal grafting of TPD at 80 °C on the industrial TPO/2 substrate (containing 2 % EPDM). ToF-SIMS results show normalised F <sup>-</sup> intensity found at the surface and XPS results show F wt.% found at the surface: (a) normalised F <sup>-</sup> intensity , 24 h cure; (b) F wt.%, 24 h cure; (c) normalised F <sup>-</sup> intensity , 30 min cure; (d) F wt.%, 30 min cure: for surfaces A-F as represented in Figure 7.6 (substrate C was not measured in XPS to avoid contamination). . . . . | 151 |
| 7.13 | Modifying TPD with hydrophilic functional groups to allow for adhesion with the applied waterborne basecoat via hydrogen bonding, as shown schematically for (a) TPDCOOH and (b) TPDOH. . . . .  | 152 |

|      |   |     |
|------|---|-----|
| 7.14 | Thermal grafting of TPDOH at 80 °C for 30 min on the industrial TPO/0 substrate. ToF-SIMS results show normalised F <sup>-</sup> intensity found at the surface and XPS results show F wt.% found at the surface: (a) normalised F <sup>-</sup> intensity, TPDOH pure; (b) F wt.%, TPDOH pure; (c) normalised F <sup>-</sup> intensity, 0.5 M TPDOH; (d) F wt.%, 0.5 M TPDOH: for surfaces A-F as represented in Figure 7.6 (substrate C was not measured in XPS to avoid contamination). Due to the lower volatility of TPDOH compared to TPD, the intensity of substrate C for TPDOH is larger. . . . . | 155 |
| 7.15 | XPS narrow region scans of (a) F 1s peak and (b) C 1s peak, before and after TPDCOOH grafting, and ToF-SIMS spectra of (c) the TPO/0 substrate before and (d) after TPDCOOH grafting. The spectra show that F and O containing species are unique to TPDCOOH, (the C 1s spectrum shows a peak at 285 eV characteristic of C—C/C—H present in both TPO/0 and TPDCOOH.) . . . . .   | 157 |
| 7.16 | Thermal grafting of TPDCOOH at 80 °C for 30 min on the industrial TPO/0 substrate. ToF-SIMS results show normalised F <sup>-</sup> intensity found at the surface and XPS results show F wt.% found at the surface: (a) normalised F <sup>-</sup> intensity, 0.5 M TPDCOOH; (b) F wt.%, 0.5 M TPDCOOH: for surfaces A-F as represented in Figure 7.6 (substrate C was not measured in XPS to avoid contamination). . . . .  | 158 |
| 7.17 | Thermal grafting of TPDOH at 100 °C for 30 min on the industrial TPO/0 substrate. ToF-SIMS results show normalised F <sup>-</sup> intensity found at the surface and XPS results show F wt.% found at the surface: (a) normalised F <sup>-</sup> intensity, TPDOH pure; (b) F wt.%, TPDOH pure; (c) normalised F <sup>-</sup> intensity, 0.5 M TPDOH; (d) F wt.%, 0.5 M TPDOH: for surfaces A-F as represented in Figure 7.6 (substrate C was not measured in XPS to avoid contamination). . . . .  | 159 |

|      |   |     |
|------|---|-----|
| 7.18 | Thermal grafting of TPDCOOH at 100 °C for 30 min on the industrial TPO/0 substrate. ToF-SIMS results show normalised F <sup>-</sup> intensity found at the surface and XPS results show F wt.% found at the surface: (a) normalised F <sup>-</sup> intensity, 0.5 M TPDCOOH; (b) F wt.%, 0.5 M TPDCOOH: for surfaces A-F as represented in Figure 7.6 (substrate C was not measured in XPS to avoid contamination). . . . .   | 160 |
| 7.19 | Theoretical calculations for the concentration required of each AP for one monolayer on the surface, the concentration % excess of the 0.5 M solutions used, and the number of layers that would be present in a 5 μm thickness. Calculations of the molecule diameter were calculated using Cosmo, assuming an energetically lower conformer is favoured in the gas phase. The volume occupied by one molecule of AP was modelled as a cube and rigidity of the AP molecules was assumed, so that layers of cubes stack on top of each other without collapsing. Calculations were based on a 5 μm layer thickness, and an area of 8 x 8 cm. . . . . | 161 |
| 7.20 | UV grafting of TPDOH and TPDCOOH at 1900 mJ cm <sup>-2</sup> radiant exposure on the industrial TPO/0 substrate. ToF-SIMS results show normalised F <sup>-</sup> intensity found at the surface and XPS results show F wt.% found at the surface: (a) normalised F <sup>-</sup> intensity, 0.5 M TPDOH; (b) F wt.%, 0.5 M TPDOH; (c) normalised F <sup>-</sup> intensity, 0.5 M TPDCOOH; (d) F wt.%, 0.5 M TPDCOOH: for surfaces A-F as represented in Figure 7.6 (substrate C was not measured in XPS to avoid contamination). . .   | 163 |
| 8.1  | A summary of the chemical adhesion tests chapter. . . . .   | 167 |
| 8.2  | A schematic diagram showing the cross-section of a finished coated substrate, and the thicknesses of the wet coatings. . . . .  | 168 |
| 8.3  | A flow diagram showing the progression of application methods and adhesion tests performed. . . . .   | 170 |

|     |  |     |
|-----|--|-----|
| 8.4 | A bar graph showing the dispersion and polar components of the surface energy (together making the total surface energy) of a TPO/0 substrate surface after various AP's were applied with a doctor blade and cured at (a) 80 °C for 30 min (b) 80 °C for 24h (c) 100 °C for 30 min and (d) 100 °C for 24h. The results of each chart are displayed in descending order of AP polar contribution from the left-hand side of the chart, with the two state-of-arts displayed at the right-hand side of the chart. . . . .       | 172 |
| 8.5 | Schematic diagram demonstrating (a) good adhesion, (b) cohesive failure, and adhesive failure at the (c) AP/basecoat interface and (d) substrate/AP interface. . . . .   | 175 |
| 8.6 | The F <sup>-</sup> intensities measured from the delaminated surfaces of the substrate and basecoat after the AP primer layer was cured thermally at (a) 80 °C for 30 mins, (b) 80 °C for 24h, (c) 100 °C for 30 minutes and (d) 100 °C for 24h, before the baseocat and clearcoat were applied, cured and left for a 7 day post-cure. . . . .   | 176 |
| 8.7 | 2D chemical maps showing the normalised F <sup>-</sup> intensity measured from the delaminated side of the basecoat from the samples: (a) 0.5 M TPDOH cured at 80 °C for 24 h, (b) 0.5 M TPDCOOH cured at 80 °C for 24 h, (c) 0.5 M TPDOH cured at 80 °C for 30 min and (d) 5 mM TPDCOOH cured at 80 °C for 30 min. The line scans represent a sum of the line scans in the x-direction (pixel by pixel). . . . .  | 179 |
| 8.8 | A bar graph showing the dispersion and polar components of the surface energy (together making the total surface energy) of a TPO/0 substrate surface after various AP's were applied with a doctor blade and cured at (a) 1900 mJ cm <sup>-2</sup> (b) 630 mJ cm <sup>-2</sup> and (c) 122 mJ cm <sup>-2</sup> . The results of each chart are displayed in descending order of AP polar contribution from the left-hand side of the chart, with the two state-of-arts displayed at the right-hand side of the chart. . . . . | 180 |

|      |  |     |
|------|--|-----|
| 8.9  | The $F^-$ intensities measured from the delaminated surfaces of the substrate and basecoat after the AP primer layer was UV cured at (a) 1900 $\text{mJ cm}^{-2}$ , (b) 630 $\text{mJ cm}^{-2}$ and (c) 122 $\text{mJ cm}^{-2}$ , before the basecoat and clearcoat were applied, cured thermally and left for a 7 day post-cure.  | 183 |
| 8.10 | The temperature generated during UV curing at the various radiant exposures measured. The cure at 2300 $\text{mJ cm}^{-2}$ took $\sim 2$ seconds. . . . .  | 185 |
| 8.11 | 2D chemical maps showing the normalised $F^-$ intensity measured from the delaminated side of the substrate from (a) 5 mM TPDCOOH cured at 1900 $\text{mJ cm}^{-2}$ and (b) 5 mM TPDOH cured at 1900 $\text{mJ cm}^{-2}$ , and from the delaminated side of the basecoat from the samples:(c) 5 mM TPDOH cured at 1900 $\text{mJ cm}^{-2}$ and (d) 0.5 M TPDOH cured at 1900 $\text{mJ cm}^{-2}$ . The line scans represent a sum of the line scans in the x-direction (pixel by pixel). . . . . | 186 |
| 8.12 | The $F^-$ intensities measured from the delaminated surfaces of the substrate and basecoat after the AP primer layer was applied wet-on-wet with basecoat and cured before the application and curing of the clearcoat, which was left for a 7 day post-cure. . . . .  | 187 |
| 8.13 | A bar graph showing the dispersion and polar components of the surface energy (together making the total surface energy) of a TPO/0 substrate surface after (a) 5 mM TPDCOOH and (b) 5 mM TPDOH was applied with a spray gun and cured at 80 °C, and (c) 5 mM TPDCOOH and (d) 5 mM TPDOH was applied with a spray gun and cured at 100 °C. The two state-of-arts are displayed at the right-hand side of the chart. .  | 189 |

|      |   |     |
|------|---|-----|
| 8.14 | The $F^-$ intensities measured from the delaminated surfaces of the substrate and basecoat after (a) 5 mM TPDCOOH was cured thermally at 80 °C for 10 and 30 mins, (b) 5 mM TPDOH was cured thermally at 80 °C for 10 and 30 mins, (c) 5 mM TPDCOOH was cured thermally at 100 °C for 10 and 30 mins and (d) 5 mM TPDOH was cured thermally at 100 °C for 10 and 30 mins, before the basecoat and clearcoat were applied, cured and left for a 7 day post-cure. . . . . | 191 |
| 8.15 | A bar graph comparing the dispersion and polar components of the surface energy (together making the total surface energy) of a TPO/0 substrate after 5 mM TPDCOOH and 5 mM TPDOH were applied with a spray gun and UV cured at different radiance exposures. The two state-of-arts are displayed at the right-hand side of the chart. . . .  | 192 |
| 8.16 | The $F^-$ intensities measured from the delaminated surfaces of the substrate and basecoat after 5 mM TPDOH was applied as a primer and UV cured, before the basecoat and clearcoat were applied, cured thermally and left for a 7 day post-cure. . . . .   | 194 |
| 8.17 | A bar graph comparing the dispersion and polar components of the surface energy (together making the total surface energy) of a TPO/0 substrate after 5 mM TPDCOOH was applied at different concentrations with a spray gun and UV cured at different radiant exposures. The two state-of-arts are displayed at the right-hand side of the chart. . .   | 197 |
| 8.18 | Bar graphs displaying the $F^-$ intensity on a TPO/0 substrate from (a) thermally cured substrates and (b) UV cured substrates, and the $F$ wt.% on a TPO/0 substrate from (c) thermally cured substrates and (d) UV cured substrates. Both 5 mM TPDOH and 5 mM TPDCOOH AP primers were tested. . . . .   | 199 |



|      |  |     |
|------|--|-----|
| 8.19 | Bar graphs displaying the (a) $F^-$ intensity and (b) F wt.% after a 5 mM TPDCOOH AP primer was applied at varying concentrations and cured with two different UV radiant exposures. . . . .   | 200 |
| 8.20 | Top: UV-Vis spectra taken at 80 °C of the -N=N- chromophore, from (a) TPD in Toluene, (b) TPDOH in Toluene, (c) TPDCOOH in Toluene. Bottom: Concentration vs. time curves at 80 °C for (d) TPD , (e) TPDOH and (f) TPDCOOH. All reactions are first order: rate of reaction is directly proportional to the concentration of TPD/OH/COOH. The decomposition of TPD is a unimolecular process. . . . .  | 202 |
| 8.21 | Top: UV-Vis spectra taken at 100 °C of the -N=N- chromophore, from (a) TPD in Toluene, (b) TPDOH in Toluene, (c) TPDCOOH in Toluene. Bottom: Concentration vs. time curves at 100 °C for (d) TPD , (e) TPDOH and (f) TPDCOOH. All reactions are first order: rate of reaction is directly proportional to the concentration of TPD/OH/COOH. The decomposition of TPD is a unimolecular process. . . . .  | 203 |
| 8.22 | Top: UV-Vis spectra of the -N=N- chromophore, taken at 2 mW $\text{cm}^{-2}$ from (a) TPD in Toluene, (b) TPDOH in Toluene, (c) TPDCOOH in Toluene. Bottom: Time for 99 % reaction completion vs. power of UV source in mW $\text{cm}^{-2}$ for (d) TPD , (e) TPDOH and (f) TPDCOOH. All reactions are first order: rate of reaction is directly proportional to the concentration of TPD/OH/COOH. The decomposition of TPD is a unimolecular process. . . . . | 204 |
| 8.23 | The UV reaction scheme for TPD showing the formation of the diazo isomer and subsequent indirect formation of the carbene. Adapted from Brunner <i>et al.</i> <sup>135</sup> . . . . .   | 205 |
| 8.24 | Structures of the products identified with GC-MS from the thermal and UV activated reactions of 3 mM solutions of TPD (a-c), TPDOH (d-e) and TPDCOOH (f-g) in toluene. . . . .   | 206 |

|      |   |     |
|------|---|-----|
| 8.25 | X-band EPR spectra recorded at 293 K (experimental conditions: frequency was 9.87 GHz; power was 20 mW) for a non-irradiated (red), irradiated with UV LED (black) and thermally activated at 80 °C (blue) sample. . . . .  | 208 |
| 8.26 | (a)ToF-SIMS image showing the clearcoat from the $\text{NCO}^-$ ion ( $m/z = 42$ ) and the basecoat from the $\text{C}_2\text{N}_3^-$ ion ( $m/z = 66$ ), normalised against total ion counts, (b) image: magnified area of basecoat/clearcoat; overlay: line graph of $\text{F}^-$ ( $m/z = 19$ ) normalised intensity, and (c) schematic diagram of basecoat/clearcoat with estimated coating thicknesses. . . . .  | 210 |
| 8.27 | ToF-SIMS images showing the clearcoat from the $\text{NCO}^-$ ion ( $m/z = 42$ ), the basecoat from the $\text{C}_2\text{N}_3^-$ ion ( $m/z = 66$ ), and the TPO substrate from the $\text{C}_{28}\text{H}_{42}\text{PO}_4^-$ ion ( $m/z = 473$ ), with an overlay of the $\text{F}^-$ ( $m/z = 19$ ) for a UV cured ( $1900 \text{ mJ cm}^{-2}$ ) (a) 5 mM TPDCOOH and (b) 0.5 M TPDOH primer layer, applied with a doctor blade. All intensities were normalised against total ion count. . . . .                                     | 211 |
| 8.28 | ToF-SIMS images showing the clearcoat from the $\text{NCO}^-$ ion ( $m/z = 42$ ), the basecoat from the $\text{C}_2\text{N}_3^-$ ion ( $m/z = 66$ ), and the TPO substrate from the $\text{C}_{28}\text{H}_{42}\text{PO}_4^-$ ion ( $m/z = 473$ ), with an overlay of the $\text{F}^-$ ( $m/z = 19$ ) for a primer of 5 mM TPDCOOH which was cured by UV at $1900 \text{ mJ cm}^{-2}$ and applied with a (a) doctor blade and (b) spray gun. All intensities were normalised against total ion count. . . . .                           | 212 |
| 8.29 | ToF-SIMS images showing the clearcoat from the $\text{NCO}^-$ ion ( $m/z = 42$ ), the basecoat from the $\text{C}_2\text{N}_3^-$ ion ( $m/z = 66$ ), and the TPO substrate from the $\text{C}_{28}\text{H}_{42}\text{PO}_4^-$ ion ( $m/z = 473$ ), with an overlay of the $\text{F}^-$ ( $m/z = 19$ ) for a primer of 5 mM TPDCOOH which was cured by UV at $1900 \text{ mJ cm}^{-2}$ and spray applied to the following substrates:(a)R/0, (b) R/10 and (c) R/20. All intensities were normalised against the total ion count. . . . . | 214 |

|      |  |     |
|------|--|-----|
| 8.30 | ToF-SIMS images showing the clearcoat from the $\text{NCO}^-$ ion ( $m/z = 42$ ), the basecoat from the $\text{C}_2\text{N}_3^-$ ion ( $m/z = 66$ ), and the TPO substrate from the $\text{C}_{28}\text{H}_{42}\text{PO}_4^-$ ion ( $m/z = 473$ ), with an overlay of the $\text{F}^-$ ( $m/z = 19$ ) for a primer of 5 mM TPDCOOH which was spray applied (a) 2 x, (b) 3 x, and (c) 5 x, to a TPO/0 substrate and cured by UV at $1900 \text{ mJ cm}^{-2}$ . All intensities were normalised against the total ion count. . . . . | 215 |
| 8.31 | ToF-SIMS images showing the clearcoat from the $\text{NCO}^-$ ion ( $m/z = 42$ ), the basecoat from the $\text{C}_2\text{N}_3^-$ ion ( $m/z = 66$ ), and the TPO substrate from the $\text{C}_{28}\text{H}_{42}\text{PO}_4^-$ ion ( $m/z = 473$ ), with an overlay of the $\text{F}^-$ ( $m/z = 19$ ) for a primer of (a) 5 mM TPDCOOH and (b) 10 mM TPDCOOH which was spray applied and UV cured at $1900 \text{ mJ cm}^{-2}$ . All intensities were normalised against the total ion count. . . . .                              | 216 |
| 8.32 | Stability study measuring UV-Vis spectra of 3 mM solutions in toluene, over a six month period, for solutions of (a) TPD, (b) TPDOH and (c) TPDCOOH stored in the refrigerator at $3^\circ\text{C}$ , and solutions of (d) TPD, (e) TPDOH and (f) TPDCOOH stored in transparent glass vials on a windowsill at room temperature. . . . .   | 217 |
| 8.33 | LHS: DSC results, RHS: simultaneous DSC-TGA for (a) TPD, (b) TPDOH and (c) TPDCOOH. . . . .  | 221 |
| 8.34 | The reaction of trimeric isocyanate with three equivalents of TPDOH. . . . .   | 226 |
| 8.35 | The reaction of HDI trimeric isocyanate with three equivalents of TPDOH, monitored by IR spectroscopy at 0h and after 96h of stirring at room temperature. . . . .   | 227 |
| 9.1  | A summary of the chemical adhesion tests chapter. . . . .  | 231 |
| 9.2  | Pearson correlation heat-map, $r = \pm 1$ is perfect correlation ; $r = 0$ is no correlation. . . . .  | 232 |
| 9.3  | Spearman correlation heat-map, $r = \pm 1$ is perfect correlation ; $r = 0$ is no correlation. . . . .   | 233 |

|      |  |     |
|------|--|-----|
| 9.4  | Radar graph showing greatest Spearman and Pearson correlation coefficients for the CHT, where $r = \pm 1$ is perfect correlation ; $r = 0$ is no correlation. . . . .  | 234 |
| 9.5  | Radar graph showing greatest Spearman and Pearson correlation coefficients for the SJT, where $r = \pm 1$ is perfect correlation ; $r = 0$ is no correlation. Note: Elastic Modulus and Hardness are negative correlation coefficients. . . . .  | 237 |
| 9.6  | Boxplots of (a) CHT vs Cure Method [ANOVA.F = 100.0835, p.kruskal = 0], (b) CHT vs AP Type [ANOVA.F = 83.7393, p.kruskal = 0], (c) CHT vs Substrate Type [ANOVA.F = 21.3075, p.kruskal = 0], (d) SJT vs Substrate Type [ANOVA.F = 7.0076, p.kruskal = 0.003] and (e) CHT vs AP Application Method [ANOVA.F = 3.9211, p.kruskal = 0.889]. . . | 239 |
| 9.7  | Schematic diagram highlighting the donor and acceptor sites for H-bonding for (a) carboxylic acids and (b) alcohols. . . . .   | 240 |
| 9.8  | StepOLS results on standardised data for $\text{CHT} = f(x_i)$ . $R^2 = 0.981$ . . . .   | 241 |
| 9.9  | Boxplot of CHT vs the combined interaction between the cure method and the AP type [ANOVA.F = 303.7315, p.kruskal = 0]. The combination of TPDCOOH and UV was unique at maximising the CHT result in accordance with stepOLS analysis. The red numbers display the number of results for each variable. . . . .                              | 242 |
| 9.10 | stepOLS results on standardised data for $\text{SJT} = f(x_i)$ . $R^2 = 0.34$ (non-linear). . . . .  | 243 |
| 9.11 | A trellis plot showing standardised correlation between the SJT results and the UV radiant exposure, number of primer sprays for varying concentration: (a) Low concentration, (b) middle concentration and (c) high concentration. . . . .  | 244 |
| 9.12 | A summary of the results chapters, highlighting the flow of the work and the interactions between the chapters. . . . .  | 248 |

|       |   |     |
|-------|---|-----|
| 9.13  | The overall objective of the project, highlighting the goals achieved during this study. The technology is patent pending. . . . .  | 250 |
| 10.1  | Graphs of (a) the Young's modulus profile and (b) the hardness profile of the reference material, polycarbonate, over a displacement of 5 $\mu\text{m}$ from the substrate surface. . . . .   | 254 |
| 10.2  | 2D and 3D images of surface roughness and x and y profiles of TPO/0 after (a) 10 minute swelling time and (b) after it was left to dry for 5 hours. . . . .   | 256 |
| 10.3  | 2D and 3D images of surface roughness and x and y profiles of TPO/0 after (a) 1 minute swelling time and (b) after it was left to dry for 5 hours. . . . .  | 257 |
| 10.4  | 2D and 3D images of surface roughness and x and y profiles of R/0 after (a) 1 minute swelling time and (b) after it was left to dry for 5 hours. . . . .  | 258 |
| 10.5  | 2D and 3D images of surface roughness and x and y profiles of R/25 after (a) 10 minute swelling time and (b) after it was left to dry for 5 hours. . . . .  | 259 |
| 10.6  | 2D and 3D images of the surface roughness and x and y profiles of (a) TPO/0, (b) TPO/2 and (c) TPO/20 substrates. . . . .   | 262 |
| 10.7  | 2D and 3D images of the surface roughness and x and y profiles of (d) R/0, (e) R/5 and (f) R/10 substrates. . . . .   | 263 |
| 10.8  | 2D and 3D images of the surface roughness and x and y profiles of (g) R/15, (h) R/20 and (i) R/25 substrates. . . . .   | 264 |
| 10.9  | Average root mean square roughness ( $R_q$ ) of the different polymer substrates . . . . .  | 265 |
| 10.10 | TEM micrographs taken from a stained $\text{RuO}_4$ ultra-thin section (cross-section) of a TPO/2 substrate, (a) showing talc (top) and carbon black (bottom), at 20,000 x magnification, (b) the same but 50,000 x magnification, (c) carbon black spherical particles, 50,000 x magnification . . . . . | 265 |

|       |   |     |
|-------|---|-----|
| 10.11 | Typical fillers found in TPO plastics: (a) Schematic representation of carbon black spherical particles, with hydrophilic functional groups at the surface, (b) a 3D lattice of CaCO <sub>3</sub> and (c) a 2D representation of talc and the different interactions between the layered structure <sup>171</sup> . . . | 268 |
| 10.12 | The positive ion ToF-SIMS spectrum of the TPO/0 substrate surface .   | 269 |
| 10.13 | The negative ion ToF-SIMS spectrum of the TPO/0 substrate surface .   | 270 |
| 10.14 | Irgafos 168 . . . . .   | 271 |
| 10.15 | Schematic diagram showing the generation of the $m/z = 69$ fragment characteristic of PP: (a) dimethylcyclopropylium ion or (b) and (c) allyl ion, which are stabilised through the inductive effective of the methyl groups or by resonance stabilisation. . . . .   | 273 |
| 10.16 | Top: (a) Surface hardness profile of all substrates and (b) Young's modulus profile of all substrates, measured using nano-indentation. Bottom: (c) Average hardness fo all substrates and (d) average Young's modulus for all substrates. . . . .  | 277 |
| 10.17 | 2D and 3D images of the surface roughness and x and y profiles of untreated (a) TPO/0, (b) R/0 and (c) R/25 substrates. . . . .   | 281 |
| 10.18 | 2D and 3D images of the surface roughness and x and y profiles of solvent wiped (c) TPO/0, (d) R/0 and (e) R/25 substrates. . . . .   | 282 |
| 10.19 | 2D and 3D images of the surface roughness and x and y profiles of non-abrasive solvent cleaned (c) TPO/0, (d) R/0 and (e) R/25 substrates. .  | 283 |
| 10.20 | The effect of substrate cleaning on the Rq surface roughness parameter.   | 284 |
| 10.21 | Plots of (a) <sup>1</sup> H NMR of TPD , (b) <sup>13</sup> C NMR of TPD, (c) <sup>1</sup> H NMR of TPDOH , (d) <sup>13</sup> C NMR of TPDOH, (e) <sup>1</sup> H NMR of TPDCOOH and (f) <sup>13</sup> C NMR of TPDCOOH. . . . .  | 287 |

|       |   |     |
|-------|---|-----|
| 10.22 | The IR spectra of (a) TPD, (b) TPDOH and (c) TPDCOOH. For TPD, the measured spectrum is shown in black, and the red overlay stick spectra shows the predicted IR spectrum. IR symbols: between 2 atoms: $\nu$ = stretch; between 3 atoms: $\delta$ = symmetric bending, $\alpha$ = anti-symmetric bending, $\omega$ = out of plane bending/wagging, $\rho$ = rocking; between 4 or more atoms: $\tau$ = torque, $\delta$ = in plane deformation and $\gamma$ = out of plane deformation. . . . .  | 288 |
| 10.23 | The UV-Vis spectra of 3 mM solutions of (a) TPD, (b) TPDOH and (c) TPDCOOH in toluene, measured at 25 °C. . . . .   | 290 |
| 10.24 | The mass spectra measured of (a) TPD, (b) TPDOH and (c) TPDCOOH.  | 292 |
| 10.25 | A schematic diagram showing a self assembled monolayer (SAM) covalently bonded to a gold surface (left). A mixture of alkyl thiols, C <sub>9</sub> and C <sub>18</sub> , in a ratio of 4:1 were used to form the SAM. After the TPD was thermally reacted with the SAM surface it was likely to graft to the exposed top part of the C <sub>18</sub> chain due to less steric hindrances (right). The fluorine atoms of the CF <sub>3</sub> group on the TPD moiety, chemically distinguished the TPD from the rest of the surface, and was used in ToF-SIMS and XPS to characterise the grafting efficiency. . . . . | 293 |
| 10.26 | A schematic diagram showing three ways in which mixed chain length SAMs can form: (a) ordered, highly packed domains of alike chain lengths, (b) highly packed ordered chains at the surface and lower ordering diffuse chains at the outer surface with mixing of the two chain lengths and (c) a less packed, disordered surface where longer chains fold.  | 294 |
| 10.27 | Regions of the negative ion ToF-SIMS spectrum of the mixed thiol (C <sub>9</sub> :C <sub>18</sub> → 4:1) SAM on a gold surface, after 24 hours of adsorption, highlighting the characteristic peaks. . . . .  | 296 |
| 10.28 | Optimised lowest energy conformers of diaziridine (top) and diazirine (=TPD) (bottom), used to calculate the predicted IR spectra. . . . .  | 298 |

|       |  |     |
|-------|--|-----|
| 10.29 | IR vibrational spectrum output from control file of Diaziridine . . . . .  | 299 |
| 10.30 | IR vibrational spectrum output from control file of Diazirine . . . . .  | 300 |
| 10.31 | Predicted electronic excited states of TPD, TPDOH and TPDCOOH.<br>The energy of the optimised states is given in atomic units (au). The<br>difference between the excited states was convert from the atomic unit<br>of energy, called Hartree: 1 Hartree = 2625.5 kJ/mol. Geometry opti-<br>misation method = BP86/def2-SV(P). . . . .  | 301 |
| 10.32 | Reaction scheme for synthesis of 3-phenyl-3-(trifluoromethyl)-3H-diazirine<br>(or TPD) . . . . .   | 302 |
| 10.33 | Reaction set-up for addition of liquid ammonia to reaction mixture: 1.<br>Gas release bottle containing acetic acid (50 % in water); 2. Empty<br>safety pressure release (in case acid jumps from other bottle under pres-<br>sure); 3. Over pressure release (containing metal balls to maintain pres-<br>sure); 4. Thermometer; 5. Mechanical stirrer; 6. Cold finger (containing<br>dry ice, $-78.5^{\circ}\text{C}$ ); 7. Ammonia gas cylinder; 8. 4-necked round bot-<br>tomed flask containing reaction dispersion; 9. Dish filled with dry ice &<br>acetone to maintain cold reaction dispersion and keep ammonia in its<br>liquid phase as long as possible. . . . . | 304 |
| 10.34 | Possible stereoisomers of 2,2,2-Trifluoromethyl-3-phenyldiaziridine. 3D<br>images: energy minimisation ran through chemBio3D version 12.0, us-<br>ing implemented MM2 energy minimise option (pink sphere = lone pair<br>of electrons, yellow = fluorine, blue = nitrogen, white = hydrogen, grey<br>= carbon). . . . .  | 305 |
| 10.35 | NMR spectra of diaziridine, 4: (a) $^1\text{H}$ NMR spectrum (insert of NH<br>protons, AB system), (b) $^1\text{H}$ NMR spectrum before and after $\text{D}_2\text{O}$ shake<br>up, (c) 2D COSY $^1\text{H}$ NMR spectrum and (d) 2D NOSEY spectrum. . .   | 307 |



|       |  |     |
|-------|--|-----|
| 10.36 | A list of the numerical, catagorical data. Red = lead responses $y_j$ . Blue = factors $x_i$ (that were controlled), potentially affecting $y_j$ . Black = variables measured. . . . . | 308 |
| 10.37 | The number of samples measured from the adhesion tests, demonstrating the slicing of data that occured. . . . .  | 309 |
| 10.38 | Rigorous empirical model building using stepwise Ordinary Least Squares (stepOLS) $Y_j = \text{CHT}(x_i)$ . . . . .  | 310 |
| 10.39 | Rigorous empirical model building using stepwise Ordinary Least Squares (stepOLS) $Y_j = \text{SJT}(x_i)$ . . . . .  | 311 |
| 10.40 | Top 10 variables that were found to have the greatest influence on the CHT and SJT results, based on standard linear regression. . . . .   | 312 |
| 10.41 | Patent search summary part 1. Available on CD for magnified view. . .  | 317 |
| 10.42 | Patent search summary part 2. Available on CD for magnified view. . .  | 318 |
| 10.43 | Patent search summary part 3. Available on CD for magnified view. . .  | 319 |
| 10.44 | Patent search summary part 4. Available on CD for magnified view. . .  | 320 |

## List of Tables

|     |  |    |
|-----|--|----|
| 3.1 | Summary of substrates, including predetermined properties of the industrial substrates available from the manufacturers. For the Daplen <sup>TM</sup> EE103AE and SABIC <sup>®</sup> PP 108MF10 substrates, the density was measured using ISO 1183 and the Vicat softening temperature was measured using ISO 306. For the SABIC <sup>®</sup> PP 95610 substrate, the density was measured using ASTM D792 and the Vicat softening temperature was measured using ASTM D1525. | 34 |
| 3.2 | A list of commercially available active polymers provided from BASF and their descriptions.  | 36 |
| 4.1 | Predetermined polar and dispersion components of the surface tension of the probe liquids used to determine the surface energy of the substrates.  | 46 |
| 4.2 | $y_j$ lead responses, for $y_j=mx_i + c$ .   | 76 |
| 4.3 | Numerical $x_i$ factors, for $y_j=mx_i + c$ .  | 76 |
| 4.4 | Other numerical responses (App = application.)   | 76 |
| 4.5 | Categorical $x_i$ factors  | 77 |
| 5.1 | Adhesion results before and after flaming pre-treatment. The basecoat and topcoat were dried at 80 °C for 10 minutes and 30 minutes respectively. All adhesion tests were performed after a 7 day post-cure period after the topcoat was applied.  | 99 |

|     |  |     |
|-----|--|-----|
| 5.2 | CHT adhesion results from before and after CPO (40 % solids in xylene) primer application. The CPO was applied with varying thickness's and dried at 80 °C for 10 minutes or applied wet-on-wet with the basecoat. The basecoat and topcoat were dried at 80 °C for 10 minutes and 30 minutes respectively. All CHT tests were performed after a 7 day post-cure period after the topcoat was applied. . . . . | 103 |
| 6.1 | CHT adhesion results after the candidate AP primer layer was applied to a dried substrate and to a substrate that was pre-swollen in cyclohexane for one minute. All adhesion tests were performed after a 7 day post-cure period after the topcoat was applied. No improvement in adhesion was observed for all variables tested. . . . .   | 128 |
| 7.1 | GC relative peak-to-TPD ratios of CH insertion products. [* indicates product in excess.] . . . . .  | 138 |
| 7.2 | Summary of the TPO/0 substrate surface after the grafting of TPD, TPDOH and TPDCOOH under the various conditions tested (thermal and UV exposure) and after washing with tetrahydrofuran (THF) (= step F in Figure 7.6). . . . .   | 164 |
| 8.1 | The variables of the AP type, concentration, thickness and application method that were tested to investigate their affect on adhesion. . . . .  | 169 |
| 8.2 | The variables of each curing method that were tested to investigate their affect on adhesion. . . . .  | 171 |
| 8.3 | CHT results after various AP's were applied with a doctor blade and thermally cured before the basecoat and clearcoat were applied, cured and left for a 7 day post-cure. . . . .  | 173 |

|     |  |     |
|-----|--|-----|
| 8.4 | Summary of the modes of failure observed for each tested sample, after the coated surface had delaminated from the substrate during the adhesion test. The AP primer was applied with a doctor blade and thermally cured before the basecoat and clearcoat were applied and cured, and left for a 7 day post-cure. . . . .         | 177 |
| 8.5 | CHT results after various AP's were applied with a doctor blade and cured with UV before the basecoat and clearcoat were applied, cured and left for a 7 day post-cure. . . . .  | 182 |
| 8.6 | Summary of the modes of failure observed for each tested sample after the coated surface had delaminated from the substrate during the adhesion test. The AP primer was applied with a doctor blade and UV cured before the basecoat and clearcoat were applied and cured, and left for a 7 day post-cure. . . . .                 | 184 |
| 8.7 | CHT results after various AP's were applied with a doctor blade wet-on-wet with the basecoat, which was cured before the clearcoat was applied, cured and left for a 7 day post-cure. . . . .  | 187 |
| 8.8 | Summary of the modes of failure observed for each tested sample after the coated surface had delaminated from the substrate during the adhesion test. The AP primer was applied with a doctor blade and applied wet-on-wet with the basecoat before applying the clearcoat which was cured and left for a 7 day post-cure. . . . . | 188 |
| 8.9 | CHT results after various AP's were applied with a spray gun and thermally cured before the basecoat and clearcoat were applied, cured and left for a 7 day post-cure. . . . .   | 190 |

|      |  |     |
|------|--|-----|
| 8.10 | CHT results after 5 mM TPDCOOH and 5 mM TPDOH were applied with a spray gun and cured with UV before the basecoat and clearcoat were applied, cured and left for a 7 day post-cure. These CHT results were obtained for all tested substrates: TPO/0, TPO/2, TPO/20, R/0, R/5, R/10, R/15, R/20, R/25 (no CHT variance occurred). . . . .  | 193 |
| 8.11 | SJT results after 5 mM TPDCOOH was applied with a spray gun to various types of substrates, and cured with UV before the basecoat and clearcoat were applied, cured and left for a 7 day post-cure. . . . .  | 195 |
| 8.12 | SJT results after 5 mM TPDCOOH was applied with a spray gun to various types of substrates, and cured with UV at 2837 mJ cm <sup>-2</sup> , before the basecoat and clearcoat were applied, cured and left for a 7 day post-cure. .  | 198 |
| 8.13 | SJT results after 5 mM TPDCOOH was applied with a spray gun to various types of substrates, and cured with UV at 1278 mJ cm <sup>-2</sup> , before the basecoat and clearcoat were applied, cured and left for a 7 day post-cure. .  | 198 |
| 8.14 | Summary of the kinetic study from thermal and UV reactions of TPD, TPDOH and TPDCOOH. . . . .  | 204 |
| 8.15 | (a) Working backwards, the 1:1 mole ratios for each step were used to calculate the mass required of each step for synthesising the 2.7 g TPD that was produced [*Assuming £1,870 per 1 kg (AnalR Normapur, VWR, as of January 2014), **Assuming £112.00 per 100 g (ALFA (AESAR), VWR, as of January 2014)], (b) Estimating the cost on the basis of the starting material (1) and the silver oxide required to generate TPD. It is assumed in mass production that the solvent costs and other chemicals used would be minimal. . . . . | 219 |
| 8.16 | Calorimeter results using Hazen-Farbzahl method (calibrated against H <sub>2</sub> O = 0) for 3 mM TPD, TPDOH, and TPDCOOH in toluene after 1h reflux and 1h UV (1 mW cm <sup>-2</sup> ). Scale = 1 – 1000. . . . .  | 220 |
| 8.17 | Expected mass losses from the APs . . . . .  | 223 |

|      |   |     |
|------|---|-----|
| 8.18 | Summary of DSC results. . . . .   | 224 |
| 8.19 | The impact sensitivity results from each AP. . . . .  | 225 |
| 9.1  | ANOVA.F and p.kruskal values sorted list in order of decreasing discrimination (=relevance of $x_i$ ) . . . . . | 238 |

## List of Terms and Abbreviations

|        |   |
|--------|---|
| AFM    | Atomic Force Microscopy                           |
| ANOVA  | Analysis of Variance                              |
| AP     | Adhesion Promoter                                 |
| ATR-IR | Attenuated Total Reflection Infrared Spectroscopy |
| CHT    | Cross Hatch Test                                  |
| COC    | Cool-on-Column                                    |
| CPO    | Chlorinated Polyolefin                            |
| DSC    | Differential Scanning Calorimetry                 |
| EDX    | Energy Dispersive X-ray Spectroscopy              |
| ehc    | Emitter Heating Current                           |
| EPDM   | Ethylene-Propylene-Diene-Monomer                  |
| FD     | Field Desorption                                  |
| FI     | Field Ionisation                                  |
| GC     | Gas Chromatography                                |
| GC/MS  | Gas Chromatography/ Mass Spectrometry             |
| HSP    | Hansen Solubility Parameters                      |
| ID     | Inside Diameter                                   |
| IR     | Infrared Spectroscopy                             |

|          |  |
|----------|--|
| LIFDI    | Liquid Injection Field Desorption                    |
| MEK      | Methyl Ethyl Ketone                                  |
| OD       | Outside Diameter                                     |
| OW       | Owens-Wendt  |
| PP       | Polypropylene  |
| R/0      | Polypropylene Research Substrate (0 % EPDM)          |
| R/10     | Polypropylene Research Substrate (10 % EPDM)         |
| R/15     | Polypropylene Research Substrate (15 % EPDM)         |
| R/20     | Polypropylene Research Substrate (20 % EPDM)         |
| R/25     | Polypropylene Research Substrate (25 % EPDM)         |
| R/5      | Polypropylene Research Substrate (5 % EPDM)          |
| Ra       | Average Roughness                                    |
| RED      | Relative Energy Difference                           |
| Rq       | Root Mean Square Roughness                           |
| SAM      | Self Assembled Monolayer                             |
| SEM      | Scanning Electron Microscopy                         |
| SJT      | Steam Jet Test                                       |
| STD      | Standard Deviation                                   |
| stepOLS  | stepwise Ordinary Least Squares                      |
| TEM      | Transmission Electron Microscopy                     |
| TGA      | Thermogravimetric Analysis                           |
| THF      | Tetrahydrofuran                                      |
| ToF      | Time of Flight                                       |
| ToF-SIMS | Time of Flight Secondary Ion Mass Spectrometry       |
| TPD      | 3-Phenyl-3-(trifluoromethyl)-3H-diazirine            |
| TPDCOOH  | 4-[3-(Trifluoromethyl)-3H-diazirin-3-yl]benzoic Acid |



|        |  |
|--------|--|
| TPDOH  | 4-[3-(Trifluoromethyl)-3H-diazirin-3-yl]benzyl Alcohol |
| TPO    | Thermoplastic Polyolefins                              |
| TPO/0  | Daplen EE103AE (0 % EPDM)                              |
| TPO/2  | Sabic PP 108MF10 (2 % EPDM)                            |
| TPO/20 | Sabic PP 95610 (20 % EPDM)                             |
| UV-Vis | Ultraviolet-Visible Spectroscopy                       |
| XPS    | X-ray Photoelectron Spectroscopy                       |

# Part I

## Introduction

# Chapter 1

## BUSINESS CASE

**The automotive market today.** A recent worldwide marketing study<sup>1</sup> claimed that in the year 2012, 11 - 14 % of a passenger vehicle was constructed from plastic. Replacing steel components of cars with plastic benefits both the consumer and the manufacturer with a lighter weight vehicle gaining a greater fuel economy and reduced carbon emissions (as required by EU regulations). According to this study, the global automotive plastics consumption is expected to grow at a compound annual growth rate of 8.5 % from 6.7 million tons in 2011 to 10.2 million tons in 2016.

The industrial sponsors of this EngD project were BASF SE and BASF Coatings GmbH. The BASF group is divided into different divisions, with coatings accounting for 4 % of the sales in 2012, as shown in Figure 1.1. BASF is a leading player in coatings, and due to the increasing volatile organic compound (VOC) regulations worldwide, they look to pioneer waterborne technology, which was used in this study. Figure 1.2 highlights the benefits of using waterborne coatings which is estimated to reduce the VOC content of conventional coatings by up to 66 %.<sup>2</sup>

This study combines the use of both waterborne coatings and plastic components of cars used in the industry today.

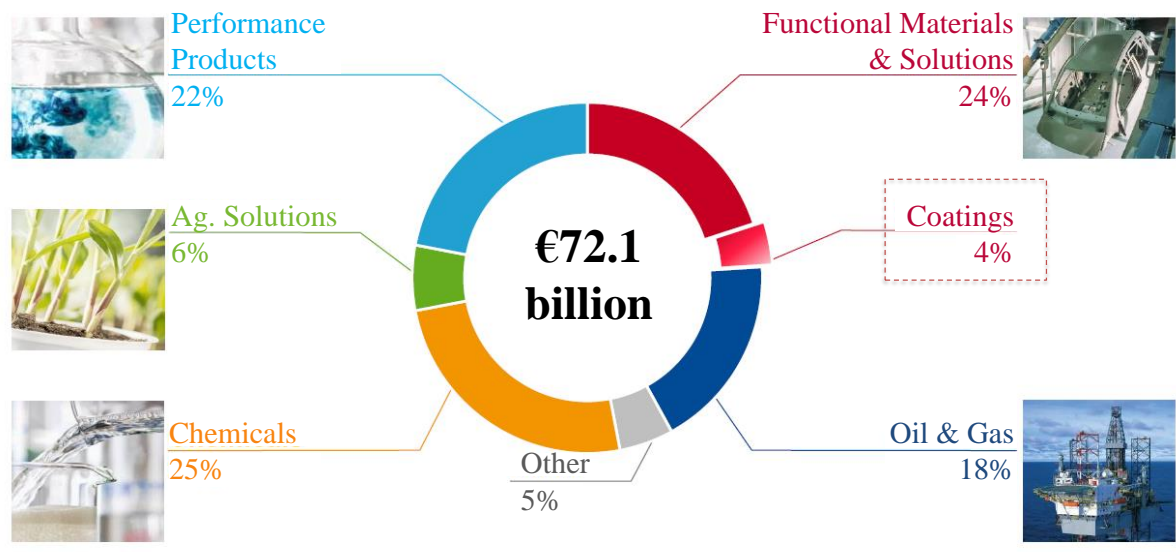


Figure 1.1: The different divisions of BASF. Adapted from a public presentation from BASF Investor Day Automotive, September 2012.<sup>2</sup>

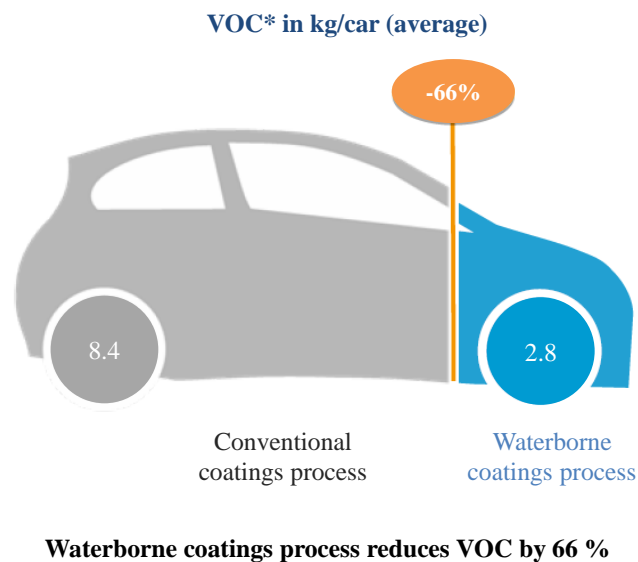


Figure 1.2: A diagram highlighting the reduction of VOC by using waterborne coatings. Adapted from a public presentation from BASF Investor Day Automotive, September 2012.<sup>2</sup>

## 1.1 Adhesion Challenge: Coating Plastic

The replacement of steel by plastic components of vehicles created a unique challenge for paint formulators.<sup>3</sup> Polypropylene (PP) is the most widely used plastic in the automotive industry, accounting for 37 % of the global consumption of automotive plastics in 2013.<sup>4</sup> PP is non-polar and has a low surface energy whereas a polar waterborne basecoat has a high surface energy, particularly of the polar component, as can be seen in Figure 1.3. The schematic diagram emphasises the mismatch in polar surface energy, which is one reason for the poor adhesion observed when a waterborne basecoat is applied and cured directly to an untreated PP substrate (as shown in the photograph).

One current state of art used in the industry today is the use of a flaming step. It partially oxidises the PP surface, increasing the polar surface energy as seen in Figure 1.3, which then more closely matches to the polar surface energy of the waterborne basecoat. This allows for good wetting of the surface by the basecoat, and good adhesion is achieved.<sup>5</sup> The disadvantage of the flame pre-treatment is the added costs to the production line. Other oxidative methods also exist, such as plasma treatments.

An alternative state of the art is the use of chlorinated polyolefin (CPO) adhesion promoters (APs), which adhere to both the PP-based substrate surface and to the applied basecoat. The disadvantage of the use of CPOs is the fact that both the chlorinated products and the organic solvents used are undesirable from an environmental point of view.<sup>6</sup> Therefore, alternative, cost effective APs are sought.

## 1.2 Project Goal

The goal of this study was to develop novel APs to improve the adhesion of waterborne basecoats and topcoat systems to plastic components of vehicles, such as car bumpers.

Rather than creating a new production process for the car components, it was in BASF's interest to develop an integrated process that utilised the current production

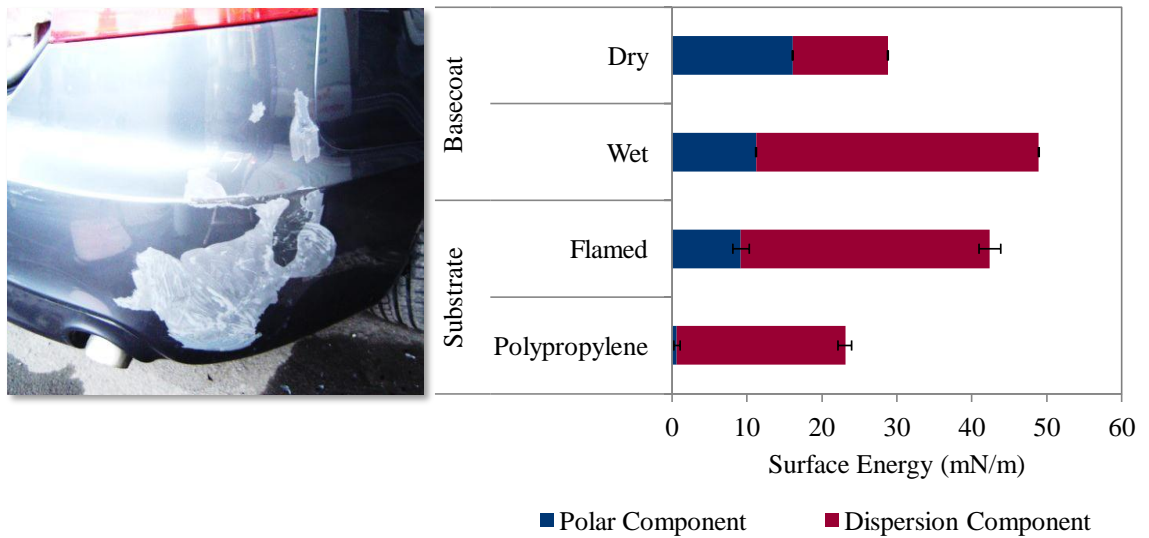
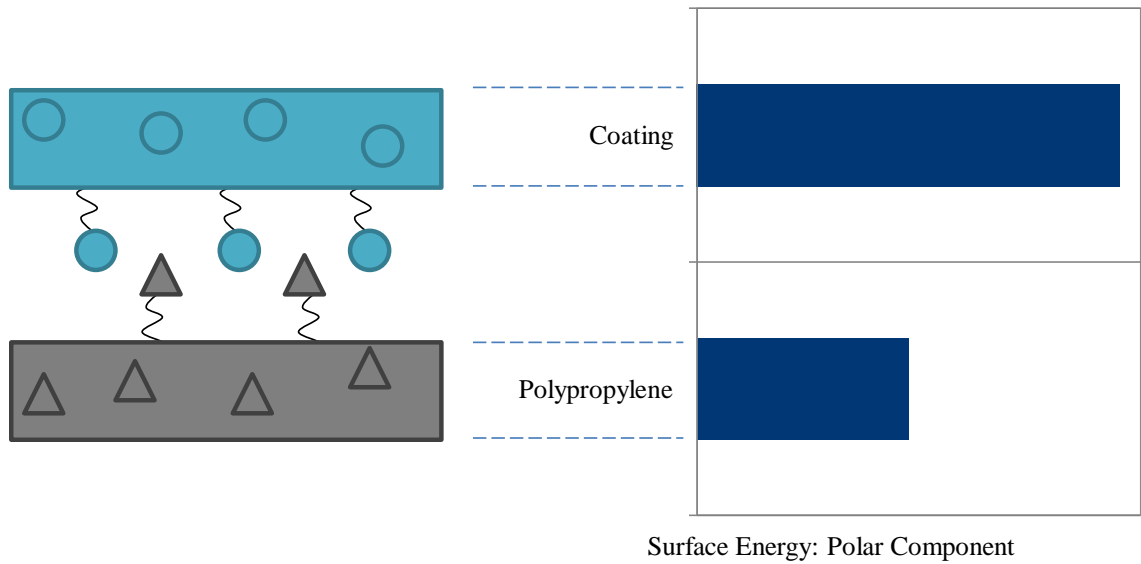


Figure 1.3: Top: Schematic diagram representing the mis-match in surface energy of a waterborne basecoat (blue circles) and a PP substrate (grey triangles). Bottom, left: Photograph showing a coating that has delaminated from a car bumper. Bottom, right: Polar and dispersion (van der Waals forces) energy components of a wet and dry waterborne basecoat, a flame treated substrate and an untreated PP substrate, in order of decreasing polar components.

line, as shown in Figure 1.4, where step 1 schematically represents the current production line implemented in industry and step 2 represents the overall goal: an integrated system to reduce the number of steps in the production line from three / four (depending if a primer is used) to just two. The coatings division is a leader in integrating processes which reduce the total energy consumption in car production. This saves the company time and money. It is estimated that an integrated process can save up to 17 % of the total energy required for car production.<sup>2</sup> Therefore, the APs were to be developed without altering the coatings process already implemented. Hence, the ultimate goal of this overall objective would be to formulate the AP into the existing basecoat. However, the practical goal of this study was to identify potential APs, before testing the adhesion of the AP to the substrate and to the basecoat, as shown in Figure 1.5. This meant the AP was applied as a primer for the initial adhesion and suitability tests.

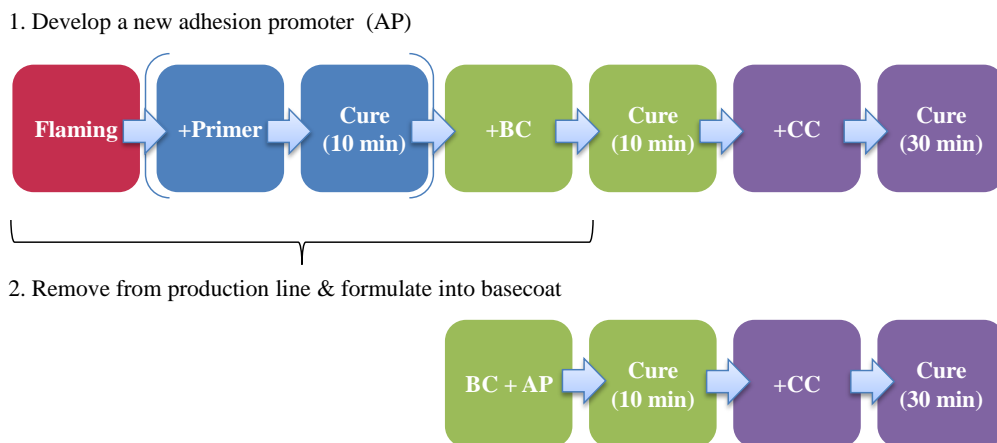


Figure 1.4: A schematic diagram representing (1.) the production line used in industry today and (2.) the overall goal / vision of the paint formulators. Brackets indicate that a primer is not always used. BC = basecoat, CC= clearcoat or topcoat.



Figure 1.5: The overall objective of the project.

# Chapter 2

## LITERATURE REVIEW

### 2.1 The Phenomena of Adhesion



Figure 2.1: Types of adhesive interactions.



### 2.1.1 Definition

Adhesion is a complex field.<sup>7-13</sup> The Academic Press Dictionary of Science and Technology defines adhesion as "the sticking together of two surfaces in contact".<sup>14</sup>

The thermodynamic definition of adhesion, shown in Equation 2.1<sup>15</sup> ( $W_A$  = work of adhesion,  $\gamma_{S1}$  = surface free energy of material 1 (e.g. substrate),  $\gamma_{S2}$  = surface free energy of material 2 (e.g. film),  $\gamma_{S1S2}$  = interfacial free energy) signifies the change in free energy when an interface is formed or separated to infinity. It is related to all of the interfacial intermolecular interactions between the contacting materials.<sup>16-18</sup>

Alternatively for liquid coatings,  $W_A$  can be determined by the Young-Dupré Equation 2.2<sup>19-21</sup> ( $\gamma_{LV}$  = surface free energy of the liquid,  $\theta$  = contact angle of liquid coating on the substrate).

However, in reality many factors influence adhesion (see Figure 2.1), which affect the value of  $W_A$ . Therefore, the definition of  $W_A$  cannot be used as described, because the calculation is difficult as the various parameters of the phenomena affecting the adhesion are not known.<sup>16-18,22</sup> Therefore, the different techniques used to measure adhesion, such as the cross hatch test (CHT) and the steam jet test (SJT), have been described by Mittal *et al.*<sup>16</sup> as measuring practical adhesion, which is a function of the work of adhesion plus the other influential factors (Equation 2.3).

$$W_A = \gamma_{S1} + \gamma_{S2} - \gamma_{S1S2} \quad (2.1)$$

$$W_A = \gamma_{LV} + (1 + \cos\theta) \quad (2.2)$$

$$\text{Practical Adhesion} = f(W_A, \text{other factors}) \quad (2.3)$$

### 2.1.2 Wettability

The wettability of a liquid on a substrate (described in Section 4.6) depends on the surface energy or surface tension difference. An assessment can be made using contact angle measurements.<sup>23</sup> Derived from the Young-Dupré equation,<sup>15</sup> an equilibrium of surface tensions can be described by Equation 2.4, where  $\Delta\gamma$  = wettability,  $\gamma_{SG}$  = surface tension at the solid / gas interface and  $\gamma_{SL}$  = surface tension at the solid / liquid interface. The wettability of a coating on a substrate surface is important to ensure the maximum interaction between the coating and the substrate (this is also affected by the coating viscosity which must be low enough for spreading), thus producing the best adhesion.<sup>24</sup>

$$\Delta\gamma = \gamma_{SG} - \gamma_{SL} \quad (2.4)$$

### 2.1.3 Adhesion Mechanisms

Several types of adhesion mechanisms are possible, as shown in Figure 2.1.<sup>25</sup>

Diffusive adhesion can occur when two polymers penetrate into one another so that polymer chain entanglement occurs, creating an interlocking mechanism.<sup>26</sup> An analogy of this is spaghetti, where the mixing of the strands improves the strength and increases the force to pull them apart due to the entanglement. This type of adhesion mechanism has been suggested for a CPO AP on a thermoplastic polyolefin (TPO) substrate (although it is a speculative topic in research<sup>27</sup>), when it was found that the diffusion of a CPO into the substrate lead to inter-chain entanglement which caused the improved adhesion without any chemical bonding.<sup>28-30</sup>

Mechanical adhesion is similar but on a larger scale, taking into account the surface porosity and roughness which can effect the adhesive properties.<sup>31</sup> An analogy to this mechanism is velcro, in which the small features significantly increase the surface roughness, and greater adhesion is obtained. This type of adhesion mechanism has been observed on a plasma treated PP surface. The impact of gaseous species with the PP

surface caused by the plasma etching increases the surface roughness which induces a greater surface wettability, thus adhesion is improved.<sup>32</sup>

Dispersive adhesion takes into account van der Waals forces, which is observed in nature on a gecko's foot. The foot has small features known as setae which are arranged in lamellae. Each small feature is hair-like, which creates a significantly large surface area. Therefore, the low attraction force of van der Waals is vastly multiplied, creating high adhesive forces, hence their ability to stand vertical on glass.<sup>33,34</sup> Many current research areas focus on bio-inspired adhesion mechanisms. The gecko is no exception, with the creation of surfaces based on a gecko's foot.<sup>35-37</sup> A group from The University of Massachusetts Amherst have developed an adhesive pad called Geckskin<sup>TM</sup>, which is claimed to hold up to 700 pounds.<sup>38</sup>

Chemical adhesion is achieved by interactions between two surfaces such as forming a covalent bond or hydrogen bonding. An example is epoxy resins which are often used in the food packaging industry.<sup>39</sup> They can form ester bond linkages with polymer substrates. Furthermore, grafting of a PP surface has also been studied, to create a new covalent bond between a functional molecule and the PP surface. For example, the grafting of maleic anhydride to PP significantly improves the adhesion and hydrophilicity of the substrate surface.<sup>40</sup>

Electrostatic adhesion is the final type of adhesion described. This is when charge transfer occurs between the mobile phase and the substrate surface, so that they are held together by the attractive opposite charges. Such adhesion mechanisms occur between surfaces and toner particles during electrophotography (a printing technique).<sup>41</sup>

## **2.2 Why Replace Steel with Plastic?**

Car bumpers are important in the protection of vehicles in low speed collisions. They can be aesthetically pleasing and offer advantages to both the designers and the drivers. Despite the low paintability, car bumpers made of plastic have many advantages over the

traditional steel.<sup>3,42</sup>

- Reduced costs
- Weight reduction (greater fuel economy)
- Improved vehicle safety
- Styling potential
- Reduced maintenance
- Corrosion resistance
- Recyclability

### **2.2.1 Thermoplastic Polyolefins (TPO)**

PP is a widely used semi-crystalline thermoplastic with excellent processability properties but poor impact strength.<sup>43</sup> To improve the impact strength and toughness of PP for industrial use, blends of PP are created known as TPO substrates in North America, or PP-ethylene-propylene-diene-monomer (EPDM) or ethylene propylene rubber (EPR) in Europe and Asia (it is referred to as TPO during this study). TPO substrates are a family of blends of isotactic PP containing elastomers such as EPDM rubber, as well as additional fillers and additives such as thermal and process stabilisers, ultraviolet (UV) stabilisers and pigments.<sup>44,45</sup> Also several fillers may be used such as glass fibres, lime, talc, carbon black and pigments. Different grades have different characteristic properties such as Young's modulus, Izod impact strength test (standard method) and density. For car bumpers, the main requirements are high flow (for injection moulding), good dimension stability (retain shape), high resistance to UV radiation (prevent degradation by sun light), high impact strength at low temperatures (important in the case of an accident) and good paintability (this being the most challenging property). Fiat and Citroen first started using TPO for flexible bumper covers in the mid 1970s.<sup>46</sup> Their

light weight, low cost, good mechanical properties, recyclability and ease of moulding into complex shapes means they have become an increasingly popular alternative to steel for automotive applications such as car bumpers. TPOs are commonly blended in a high-speed mixer or a twin-screw extruder, and the parts are fabricated by injection moulding.<sup>3,44,47</sup>

The adhesion of coatings to a TPO car bumper is not only important for the manufacturer who wants a reputation for good quality products, as well as lower production costs and various regulations to be met, but it is also important for the consumer who does not want a car bumper to be easily damaged during a light collision or due to environmental exposure. The consumer also wants a vehicle which is aesthetically pleasing. Therefore, state of the art techniques exist to improve the adhesion of coatings to TPO components of cars, such as the car bumper.<sup>3</sup>

## **2.3 The State of the Art**

### **2.3.1 Flaming Pre-treatment**

Flame treatment is the most widely used technique in the industry to accomplish paint adhesion to TPO parts in Europe. The process oxidises a thin layer of the surface of the PP substrate in a controlled manner, forming oxygen containing chemical groups on the surface which undergo cross-linking and chain scission.<sup>44</sup> Therefore, adhesion to a flamed substrate involves short-range interactions with the chemical groups found at the surface.<sup>48</sup> ESCA (Electron spectroscopy for chemical analysis, also known as X-ray photoelectron spectroscopy (XPS)) has shown that the depth of oxidation for typical flame treatments is 5 -10 nm,<sup>49</sup> although it depends on the flame parameters used.

The technique has many advantages over other oxidative techniques such as corona discharge: reliability, efficiency, ease of operation, energy consumption, equipment space requirements, the ability to achieve great wettability without a significant loss of treatment with ageing, and very importantly no generation of toxic, corrosive ozone.<sup>49</sup> It is also the

preferred method for treating three-dimensional shapes over corona treatment.<sup>50</sup>

However, flaming can be a very complex technique due to several different chemical groups forming on the surface during the treatment. Furthermore, it has been observed that other modified PP surfaces containing the same amount of oxygen exhibited different adhesive properties. This implies that the surface chemistry is a very important factor and that it is indeed the chemical nature of the functional groups found at the surface that is important for adhesion rather than the amount of oxygen on the surface.<sup>48</sup>

Several studies that have looked into the adhesion mechanism of functionalised substrates have found that hydrogen bonding occurring with OH groups at the surface is a key factor to the improvement of adhesion.<sup>48,51-56</sup> Sheng *et al.*<sup>57,58</sup> estimated that approximately ( $\sim$ ) 20 - 30 % of the oxygen added to a PP surface could be in the form of hydroxyl species. Furthermore, secondary ion mass spectrometry (SIMS) studies have shown that chemical bonds involving double bonds (for example in EPDM) are created by the flame treatment, thus EPDM may facilitate the adhesion.<sup>59,60</sup>

### **2.3.2 Chlorinated Polyolefin Adhesion Promoters**

Chlorinated polyolefins are an alternative treatment to a flame pre-treatment.<sup>61,62</sup> They are a type of AP that are used around the world, with the exception of Europe where EU regulations forbid their use.<sup>6,63</sup> They are most common in North America, where they are usually applied to the substrate surface as a primer before coating. The CPO thin film increases the surface free energy which promotes adhesion to the coatings.<sup>29</sup> Although there are many types of CPO APs available, it is believed anchoring into the TPO substrate surface is the dominant adhesion mechanism.<sup>45,64</sup> Although the use of a CPO requires an additional coating layer to be applied, it is the method of choice for North America because of its flexibility for diverse applications and types of TPOs and topcoats it can be used with.<sup>63</sup> Figure 2.2 shows the process of how a CPO can be applied to a TPO substrate and cured.

As well as a physical entanglement adhesion mechanism between the CPO and the

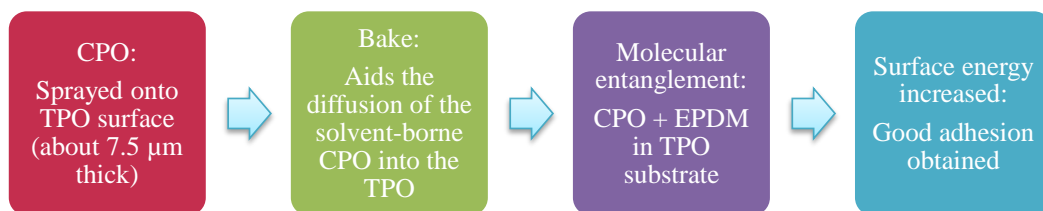


Figure 2.2: An example of an application process of a CPO primer.<sup>29</sup>

substrate, a chemical adhesion mechanism has also been proposed.<sup>63,65</sup> The mechanism in shown in Figure 2.3. It was proposed that the topcoat H-bonds to the CPO. Furthermore, non-polar interactions also occur at the CPO/TPO interface between the aliphatic parts of the two layers. The chlorides in the CPO are unstable when the system is heated to high temperatures during curing of the coatings, and a weak base from the topcoat diffuses into the CPO and catalyses the elimination of HCl from the CPO (dehydrohalogenation), resulting in the formation of alkenes in the CPO layer. Esters and carboxylic acids can also be formed in the CPO layer by the attack of the anhydride in the CPO from an OH in the topcoat. In the mechanism shown, the system lost one H-bond but gained a covalent ester linkage and at least two more H-bonds from the new carboxylic acid in the CPO. Other interactions include  $\pi - \pi$  interactions between EPDM in the TPO and alkenes in the CPO. All these interactions collectively result in better adhesion for the entire system.

## 2.4 Influence of the Substrate Microstructure on Adhesion Mechanisms

### 2.4.1 Microstructure of Injection Moulded TPO

Research by Ryntz *et al.*<sup>29,30,45,64,66-68</sup> in the last two decades has focused on understanding the relationship between the morphology of TPO and the adhesion performance by

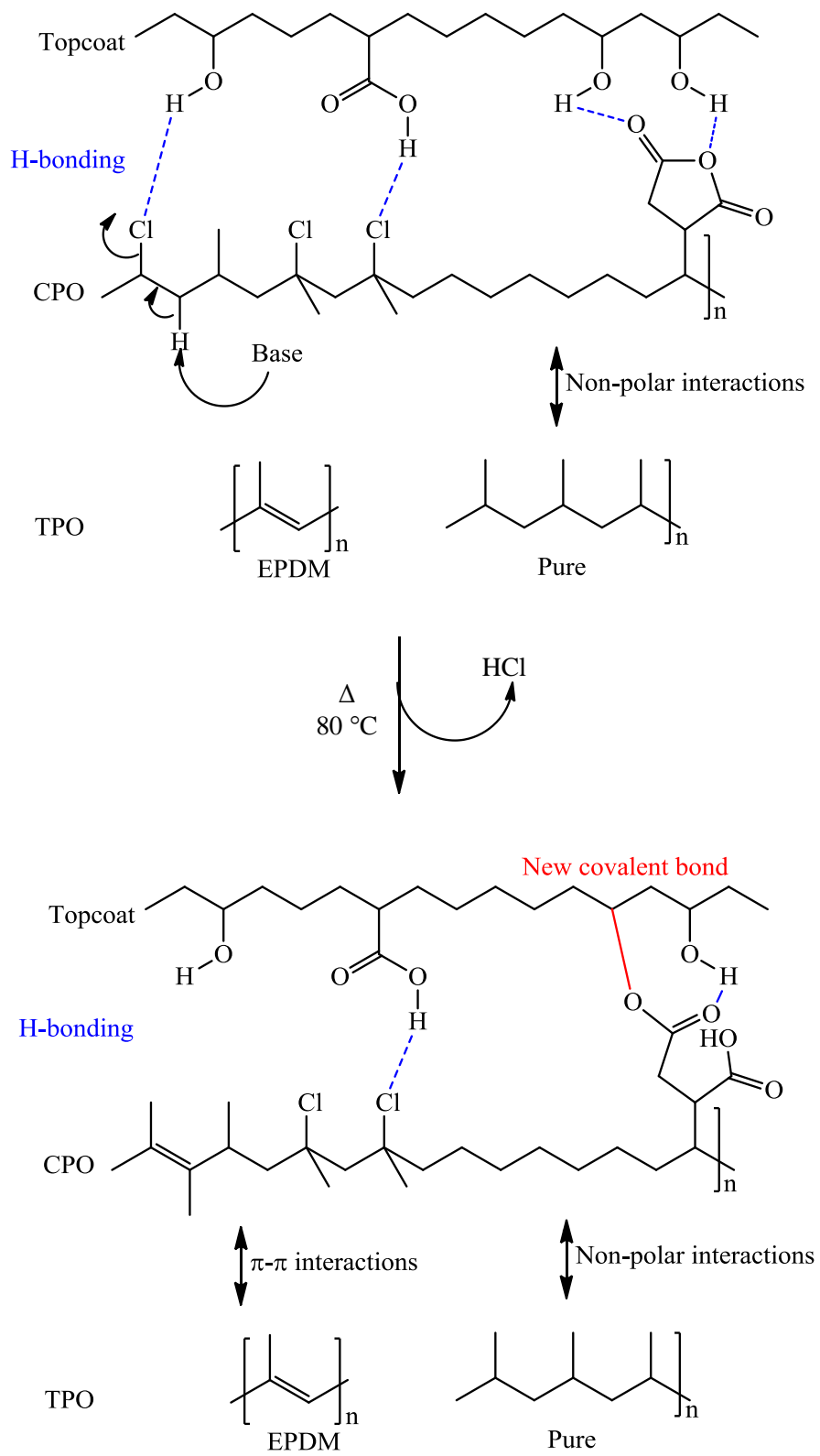


Figure 2.3: Proposed chemical mechanism for adhesion between a TPO (with EPDM), CPO and a topcoat.<sup>63,65</sup>



CPO APs. The microstructure and morphology of an injection moulded TPO is schematically represented in Figure 2.4. A series of techniques such as differential scanning calorimetry (DSC), X-ray microfocus fluoroscopy and differential interference contrast (DIC) microscopy were utilised by Ryntz *et al.*<sup>45,64</sup> to assess the TPO blend morphology. Due to the shearing forces and thermal gradients induced in the melt as a TPO is injected into a mould, the crystallinity of the PP varies at the surface relative to the bulk. Non-ideal nucleation of the PP occurs at the surface due to rapid cooling as it encounters the low temperature mould. This results in a thin trans-crystalline PP region at the surface which is phase separated by the elastomer. The PP nucleates in more ideal conditions under the trans-crystalline layer, resulting in a thick layer of large PP spherulite crystals. The next layer is elastomer-rich, containing EPDM domains. These domains are found to be elliptical nearer the surface, with the long axis of domains following the flow direction of the TPO melt. Below the elastomer-rich region, the bulk TPO dominates in which globular shaped EPDM domains are inter-dispersed in the bulk PP matrix. The TPO surface morphology is shown to be highly dependent on the manufacturing process parameters such as temperature, flow rate, injection pressure, mould geometry and mould temperature, which in turn, influence the adhesive properties of an AP applied to the surface.<sup>67,68</sup>

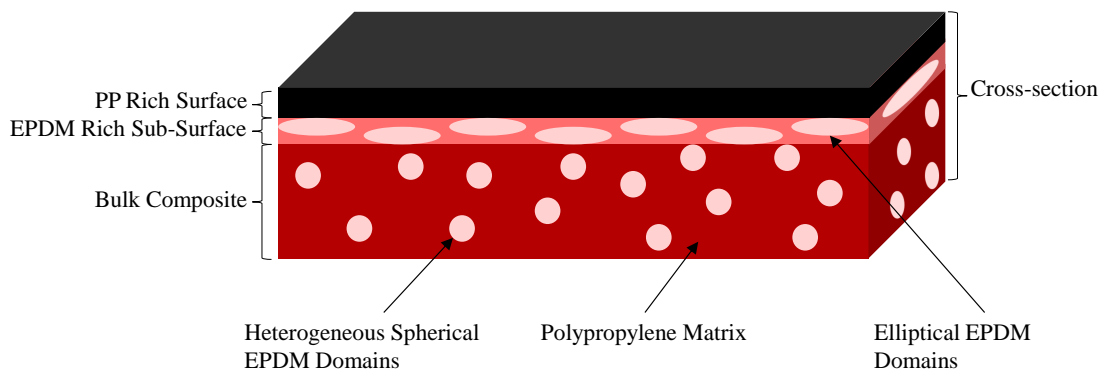


Figure 2.4: Three-dimensional schematic (generalised) representation of the TPO microstructure and surface morphology. Adapted from Ryntz *et al.*<sup>29,30,45,64,66–68</sup>

## 2.4.2 Influence of TPO Microstructure on Adhesion

Although the specific mechanism of how CPOs promote adhesion is unknown, it is often speculated in the literature that the presence of the EPDM elastomer not only improves the impact strength of the TPO substrates, but it also aids the improvement of the adhesion. It is therefore important that the EPDM-rich layers lay close to the surface, as it is believed that this sub-surface region accounts for the paintability of TPO when using CPO APs. When an AP is able to swell and diffuse into the PP surface to improve adhesion via molecular chain entanglement, the surface composition such as crystallinity, depth of the EPDM sub-surface layer and thickness of the different sub-surface regions, have a significant impact on the ability of the AP to improve the paintability of the surface.<sup>3,45,64</sup> For example, a highly crystalline layer of PP would tend to retard diffusion and therefore result in poor adhesion. In contrast, an amorphous PP layer would tend to permit swelling and aid diffusion of the AP and solvents into the EPDM-rich phase, thus improving adhesion by allowing for mechanical interlocking.

The distribution of the EPDM-rich sub-surface layer may also play a vital role in the cohesive strength of the painted TPO substrate. It is important to gain the correct balance between TPO swelling and cohesive integrity. Therefore, solvents which swell the TPO, but evaporate soon after application and allow the EPDM to de-swell, are likely to achieve better adhesion results.<sup>27,45,62,64,69-71</sup> Contrary to this hypothesis, Schuman *et al.* discovered that the ability of a solvent to swell the TPO substrate was not as well correlated to adhesion, as was the ability of the solvent to change the surface roughness of the substrate. The improvement in adhesion is likely to be due to the large surface area of the rougher surfaces, thus increasing the interfacial contact between the CPO and the TPO.<sup>27</sup>

It is difficult to predict the improvement of adhesion using a diffusion model of a CPO due to the heterogeneous nature of TPO substrates. As well as solvent swelling, it has been shown that baking the CPO on the TPO substrates above room temperature also

improved adhesion by promoting diffusion and mechanical interlocking of the CPO into the EPDM regions of the TPO.<sup>72,73</sup> However, the diffusion length scale was a function of the local TPO structure, CPO structure and solvent, thus not the temperature alone.<sup>3,73</sup> For added complication, significant correlations between the adhesion properties of a CPO, the solvent used and the top-coat toughness have also been demonstrated.<sup>74</sup> Adhesion is therefore a function of the total system attributes (the substrate characteristics, the CPO, the applied basecoat and top coat), rather than an individual factor.

Unpublished results from BASF Coatings have demonstrated an improvement of adhesion with the presence of EPDM in TPOs, when using a flaming pre-treatment.<sup>75</sup> It is thought that the oxidation effect of the flaming pretreatment reaches the depths of the EPDM-rich subsurface and is more easily able to break double bonds within the EPDM structure, increasing the number of oxygen containing species on the TPO surface. This increases the polar surface energy and thus, compatibility with a waterborne basecoat. Therefore, adhesion is greater on a TPO substrate compared to a pure PP substrate.

## 2.5 Characterisation of Adhesion

### 2.5.1 Peel Tests

Peel tests are a common industrially relevant method to assess the adhesion of a coating to a surface.<sup>76-82</sup> Adhesive tape is applied onto the surface of the substrate, pressure is applied, and either the force required to delaminate the coating from the surface is measured or the force is at a set value and the degree of delamination is assessed.

For example, Peel tests have been used to assess the adhesion strength of a plasma treated substrate, where it was found that a treatment of less than one minute resulted in a decrease of the adhesion but treatments of greater than one minute resulted in an increase of adhesion with time.<sup>79</sup>

Although peel tests are a popular method to measure adhesion, many problems exist and data analysis can be complex. Firstly, the test can cause cohesive failure within the

substrate, therefore, the force that is measured is not only the force required to delaminate the coating. Secondly, a significant amount of energy is dissipated during the bending of the peel tape, making the comparison of different measurements difficult (the energy dissipated would have to be the same each time). Lastly, the type of tape that is used can influence the adhesion results obtained.<sup>83,84</sup>

## 2.5.2 Cross-Hatch Test

In contrast to the peel test, the CHT<sup>85</sup> is a simple empirical test which can be used qualitatively to assess the adhesion of coated substrates.<sup>86</sup> According to the German standard ISO2409: a bladed knife is scored into the coated surface in one direction, and again in the perpendicular direction, as shown in Figure 2.5(a). An adhesive tape is then applied to the grid formed on the surface, and the tape is pulled with a standardised force. The number of squares delaminated is calculated to a percentage, and a grade is determined (0 = 100 % adhesion and 5 = 0 % adhesion).

The test has previously been used to assess the adhesion of coated substrates after they had been exposed to petroleum, depending on the topcoat type used and the location that the substrate sample had been released from the injection mould. The adhesion of the areas closer to the edge of the injection mould with topcoats of lower glass transition temperatures gave better adhesion due to the lower penetration of petroleum.<sup>67</sup>

The test has the advantage that it is quick to perform and acts as a good preliminary test to assess the adhesion with many samples. Furthermore, the forces applied are lower than that of the peel test, thus cohesive failure of the substrate is less likely to occur. However, this can be checked using surface sensitive techniques such as time-of-flight secondary ion mass spectrometry (ToF-SIMS) or XPS to measure the delaminated surfaces.<sup>70</sup>

### 2.5.3 Steam Jet Test

A steam jet test is often used in the automotive industry as a more vigorous, yet also qualitative, adhesion test. The parameters used for the test are chosen by the customer. In the cases when good adhesion is achieved with cross-hatch tests, further tests with the steam jet are often performed. The high temperature and high pressured steam is designed to mimic a car wash to assess how well the coatings would withstand the conditions.<sup>87</sup> To perform the test, a knife is used to score the surface in two diagonals (called Andreas Cross) on a rectangular substrate, as shown in Figure 2.5(b). The steam is then applied to the pre-damaged area, and the amount of delamination of the coating is assessed to give a grade (0 = 100 % adhesion and 5 = 0 % adhesion).<sup>87</sup>

A comparative steam jet test study of the adhesive performance of untreated and treated TPO substrates subjected to a flame and plasma pre-treatment showed that the treated substrates gave the better adhesion.<sup>88</sup>

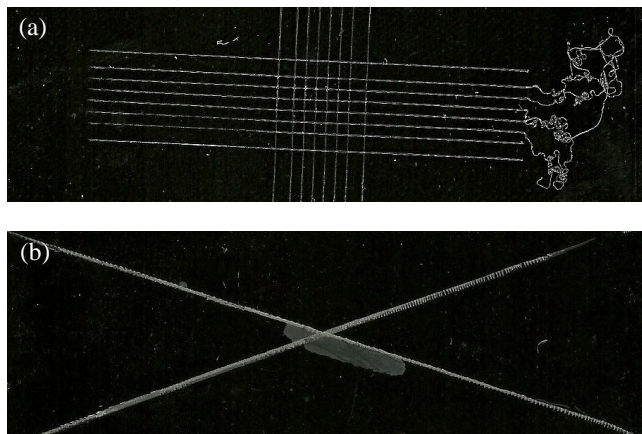


Figure 2.5: A photograph of substrates after (a) a CHT test (100 % adhesion) and (b) a SJT (40 % adhesion).

### 2.5.4 Surface Characterisation

Many surface sensitive techniques have been used to investigate the adhesive properties or mechanisms of coated substrates.<sup>7,10,48,89-93</sup> These include ToF-SIMS, XPS, atomic force

microscopy (AFM), scanning electron microscopy (SEM) and attenuated total reflection infrared spectroscopy (ATR-IR) to characterise polarity and chemical composition, as well as using contact angles to calculate the surface energy. Other mechanical property measurements include interferometry to measure the surface roughness and nano-indentation to measure a substrate's hardness or Young's modulus.

**ToF-SIMS and XPS** The techniques, ToF-SIMS and XPS, are often used together to complement one-another for the chemical characterisation of a surface. They both have advantages and disadvantages. ToF-SIMS is a technique that measures the mass of fragments from a sample surface, generated by an ion source. It is a qualitative technique due the so-called *matrix effect*, which is when the ionisation yield (shown in Equation 2.5 where  $I_m$  = secondary ion current of species  $m$ ,  $I_p$  = primary flux,  $Y_m$  = sputter yield,  $\alpha^+$  = ionisation probability to positive ions,  $\theta_m$  = fractional concentration of the chemistry  $m$  in the surface layer and  $\eta$  = transmission of the analysis system) is dependent on the chemical nature of the sample being analysed.<sup>94</sup> However, an advantage that ToF-SIMS has over XPS is that the sampling depth is much smaller, approximately the first 1 - 3 atomic layers ( $\sim 10$  Å) compared to  $\sim 30$  - 100 Å for XPS.<sup>95</sup> Therefore, ToF-SIMS is a true representation of the surface. However, this can be a disadvantage when contaminants are present at the surface. An advantage of XPS is that it is a quantitative technique. It involves the irradiation of a sample with X-rays of a characteristic energy and it measures the flux of ejected (secondary) electrons from the sample surface. Each element has a characteristic binding energy, therefore, the chemical composition of a surface can be determined, using Equation 2.6<sup>96</sup> (where  $E_{kinetic}$  = kinetic energy of the photoelectron,  $h$  = Planck's constant,  $\nu$  = frequency of the radiation ( $h\nu$  = energy of photon),  $E_{binding}$  = binding energy of the photoelectron,  $\Phi_{spectrometer}$  = work function of the spectrometer).

$$I_m = I_p Y_m \alpha^+ \theta_m \eta \quad (2.5)$$

$$E_{kinetic} = h\nu - E_{binding} - \Phi_{spectrometer} \quad (2.6)$$

Both techniques have been used to investigate adhesion mechanisms as well as investigating the location of the locus of failures when delamination occurs. Through extensively researching the capabilities of ToF-SIMS and XPS in adhesion research, Watts *et al.* have demonstrated the ability to investigate polymer interfaces buried below the surface of a substrate using a low angle tapered section,<sup>97</sup> the ability to look at adhesive failure between two surfaces at a joint,<sup>98</sup> and the ability to characterise the adhesion of various APs on aluminium surfaces.<sup>99–101</sup>

Furthermore, Garbassi *et al.*<sup>102</sup> have used ToF-SIMS and XPS to characterise the adhesive behaviour of a flame pre-treatment. It was found that the depth of oxidation increased as the number of flame treatments increased. They characterised the change by monitoring the formation of polar groups using XPS,<sup>103</sup> as well as the change in surface chemistry with depth using ToF-SIMS analysis.

Clemens *et al.* used ToF-SIMS and XPS to study the mode of failures that occurred between a coating and a substrate on which a CPO primer had been applied.<sup>70</sup> In all cases, the quantitative data acquired using XPS was complemented by the qualitative data acquired using ToF-SIMS.

### 2.5.5 Substrate Characterisation

One method that has previously been used to differentiate EPDM from the PP matrix is the use of OsO<sub>4</sub> and RuO<sub>4</sub> to stain the EPDM so that it is visible in SEM or transmission electron microscopy (TEM): techniques which show surface morphology.<sup>44,62,104–110</sup> Energy dispersive X-ray spectroscopy (EDX) is an analytical technique used for elemental analysis that can be used in conjunction with SEM and TEM, to verify which areas contain the heavy metals (Os or Ru),<sup>111</sup> and hence identify the EPDM domains.

ToF-SIMS can be used to identify additives present at the polymer surfaces such as

Irgafos 168 (BASF <sup>®</sup>) and Irganox 1010 (BASF <sup>®</sup>), which are often added to TPOs as antioxidants.<sup>112,113</sup>

Mechanical characterisation of the substrates has been previously achieved with nano-indentation to determine the Young's modulus and hardness.<sup>114</sup> As previously mentioned, the hardness of a substrate may determine if an AP is able to penetrate and mechanically interlock into the substrate surface.

For calculating surface energy, the Owens-Wendt theory is often used. For example, an increase in the polar contribution of flamed TPO substrates occurs after a flame pre-treatment. After the flaming, the TPO surface energy closer matches the surface energy of the basecoat, enabling improved wetting of the basecoat on the substrate surface, thus improving adhesion.<sup>115</sup>

The surface roughness of a TPO substrate also plays an important role in the adhesion of an applied coating, as previously mentioned.<sup>27</sup> Rougher surfaces enable a greater contact area between the basecoat and the substrate, which may increase any adhesion interactions or reactions occurring. White light interferometry was used in this study to investigate the surface roughness of the different substrates, link the results to the substrate composition, and predict any influences on adhesion.

## **2.6 Other Adhesion Improvement Methods**

### **2.6.1 Oxidative Methods**

As previously mentioned, plasma<sup>116</sup> treatment can be used as an alternative oxidation method to the state of the art flame pre-treatment. Other methods used to improve adhesion to non-polar polymer surfaces include, corona discharge,<sup>117,118</sup> UV radiation<sup>119</sup> and chemical oxidation.<sup>120,121</sup>

Plasma is created when an electric field is applied to a gas, and positively charged (ionised) atoms and detached electrons are generated, creating a charged gas that is able to conduct electricity due to the movement of the charges. Corona is a type of plasma



generated when a voltage is applied to two electrodes separated by air. The oxygen in the air generates ozone, therefore, this technique can be considered environmentally unfriendly. It is thought that the high energy of the charged electrical corona is able to break bonds at a substrate surface, which then recombine with free radicals from the corona creating polar groups at the surface. The surface energy and wettability of the surface is then increased which improves the adhesion to polar coatings. For plasma treatment, the gases are injected into the corona discharge to modify the chemical composition of the corona plasma which changes the reaction with the substrate.<sup>122</sup>

Another way to oxidise a PP surface is the use of UV treatment. It has been studied in air with and without the presence of ozone. The oxygen content at the surface was found to be the same as would be achieved by corona treatment, and the contact angle (see Section 4.6) decreased to near  $0^\circ$  (water was wetting the surface).<sup>123</sup>

A disadvantage of using oxidative methods to improve adhesion is the ageing effect, where the hydrophilicity at the surface decreases over time. Therefore, the coating must be applied soon after the treatment due to the short life time of the radical species generated. Furthermore, non-uniform coverage can sometime occur which often leads to cohesive failure near the surface of the TPO.<sup>70</sup>

## 2.6.2 Block Copolymers as Adhesion Promoters

Blockcopolymers are often used as adhesion promoters to join together hydrophobic and hydrophilic surfaces, as shown in Figure 2.6.

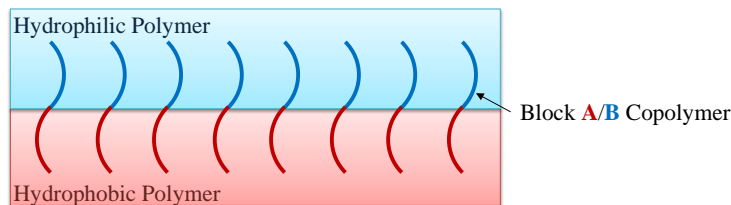


Figure 2.6: A schematic diagram showing a block copolymer adhering a hydrophobic and hydrophilic polymer together.

It has been shown that controlling polymer properties enables the achievement of good adhesion to untreated PP substrates.<sup>124, 125</sup> Figure 2.7 shows an example of three different types of polymer blend that were tested for their effect on the adhesion of waterborne coatings to untreated PP surfaces. Only the block copolymer of an acrylic acid (AA) and a block of isobornyl acrylate polymer (iBOA), with a butyl methacrylate (BMA) and butyl acrylate (BA) polymer, showed good adhesive properties, where a cross-hatch test of 0 (100 % adhesion) was achieved. The single phase or inverse phase shell morphologies shown were found to give poor adhesion. The first block copolymer showed the best adhesive properties because the first block polymer (AA and iBOA) which was the AP, was very brittle in nature and any mechanical forces resulted in the loss of the adhesion property of the polymer. By co-polymerising it with the second block polymer (BMA / BA), which had a much lower glass transition temperature, it allowed for flexibility which retained the adhesion property. It was thought that the kinetics of the reactions were another reason for the adhesion differences observed. In the first system, the hydrophobic adhering blocks were able to diffuse through the acid to the surface. For the other two structures, the adhering blocks were buried and not able to diffuse to the surface in time to create an improved adhesion. Thus, the kinetics and the tailoring of an AP system are important factors to consider when designing new adhesive systems.

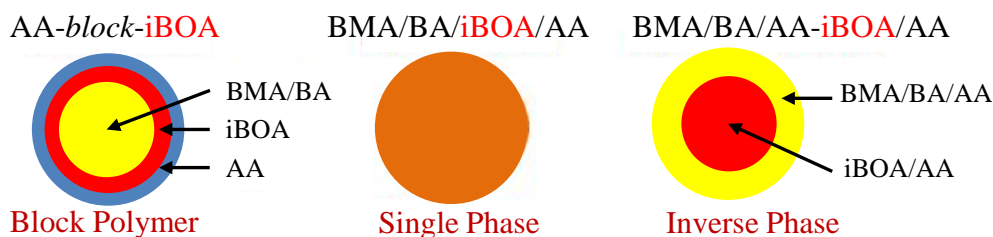


Figure 2.7: The polymers tested for improved adhesion on PP, adapted by Overbeek.<sup>124</sup>

## 2.6.3 Grafting

### 2.6.3.1 Maleic Anhydride (MA)

In this study, the term *graft* refers to the bonding of an AP to a substrate surface.

The grafting of maleic anhydride (MA) to PP has been shown to significantly improve the adhesion and wettability of the substrate.<sup>40,107</sup> The grafting proceeds by a free radical reaction as shown in Figure 2.8. An MA-grafted PP surface has shown good adhesive properties to steel surfaces.<sup>126</sup> Furthermore, CPO APs have been known to have MA components which facilitate the adhesion.<sup>70</sup> Using MA-grafted PP for the adhesion of automotive coatings for car components, such as a car bumper, is patented by Dow.<sup>127</sup>

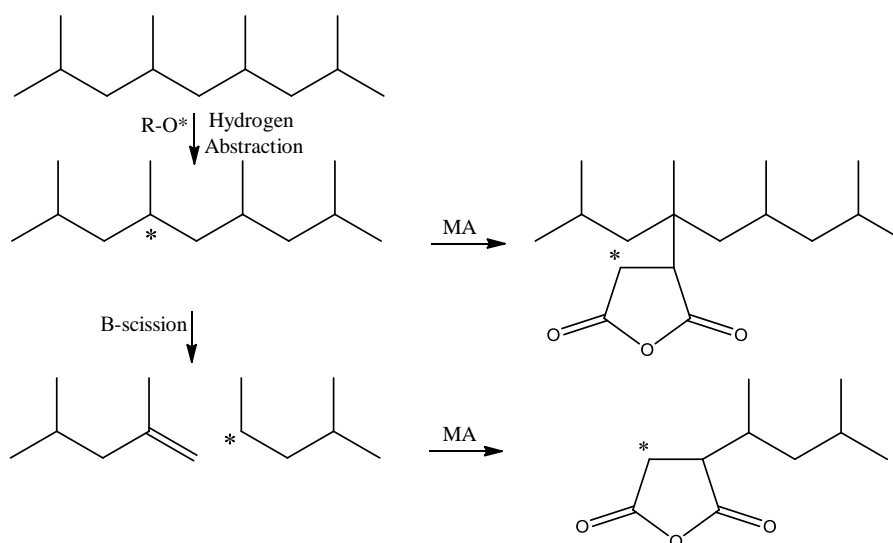


Figure 2.8: The reaction mechanism of MA grafting to PP.<sup>40</sup>

### 2.6.3.2 Poly(Acrylic Acid)

Grafting of poly(acrylic acid) has also been used to increase the hydrophilicity of a PP surface. The surface energy of the substrate surface was reported to increase from 2 mN m<sup>2</sup> to 29 mN m<sup>2</sup> for the modified surface.<sup>93</sup>

An AP formed by the graft copolymerisation of acrylic monomers onto isotactic PP has also been studied. When the AP was applied as a primer, the substrate showed excellent adhesive strengths via physical interactions at the interface rather than forming chemical bonds. However, the adhesion was found to depend on the substrate hardness. It was thought that the graft process generated degradation products which formed a weak boundary layer on the hard substrate and were not able to penetrate into the surface, thus

causing adhesive failure. In contrast, it was thought that the degradation products may have penetrated into the softer substrate so no boundary layer was present, thus leading to improved adhesion.<sup>107</sup>

#### **2.6.4 Chemical Etching**

Another technique which has previously been researched and patented is the technique of chemical etching with 1,1,1-trichloroethane (TCE).<sup>128-131</sup> It is believed that TCE has several roles during the adhesion improvement process: firstly it degrades the TPO car bumper which removes any weak boundary layers which could cause adhesive failure, secondly it etches the surface which extensively roughens the surface and thirdly it swells the TPO.

#### **2.6.5 Novel Surface Treatment**

A recent study revealed a new surface treatment called Accelerated Thermo-molecular adhesion Process (ATmaP). The technique grafts functional groups to the PP surface derived from an atomised and vaporised nitrogen-containing coupling agent. It is a modified flame treatment where nitrogen functional groups are generated by passing a stream of n-methylpyrrolidone solution through the burner with the gas mixture. The adhesion of the surface was found to significantly improve to a magnitude comparable to the conventional flame pre-treatment. ToF-SIMS and XPS analysis revealed the treatment resulted in chain scission, reactions with the air and the grafting of NO functional groups at the substrate surface.<sup>132</sup>

## **2.7 Unsuccessful Adhesion Techniques**

### **2.7.1 Chemical Bonding by Catalytic Oxidation of Inactivated C-H Bonds**

The functionalisation of TPO substrates by a catalyst medium comprising of pyridine, acetic acid, hydrogen peroxide with iron(III) chloride hexahydrate, did not significantly improve adhesion, despite a significant accumulation of OH groups at the surface (verified by XPS) and a significant increase in the surface roughness. It was thought the method degraded the surface which created a weak boundary layer and hindered the adhesion.<sup>107</sup>

### **2.7.2 C-H insertion of Nitrene**

An azido based organic solution was applied to a TPO substrate in its pure form and cured with UV. It was predicted that the decomposition of the azido group ( $R-N=N^+=N^-$ ) would afford a nitrene (analogous to a carbene) which could C-H insert into the PP surface. However, no improvement was observed. It was thought that the nitrene group had reacted with other components found at the surface, because it was not orientated towards the non-polar PP, and that the lifetime of the nitrenes was not long enough for reorientation to occur.<sup>107</sup>

## **2.8 Current Patents based on Adhesion Promoters for Plastics**

The most recent patents report waterborne coating compositions for promoting adhesion to plastic surfaces. Uses of functionalised homopolymers or copolymers having a single unsaturation, a terminal succinic anhydride moiety and additional succinic anhydride substitutions on the PP backbone have been reported.<sup>133</sup> A CPO-containing a thermally curable waterborne coating formulation has also been reported, containing one urethane

acrylic hybrid resin in a correct balance with water.<sup>134</sup>

## 2.9 Diazirines as Potential Adhesion Promoters

Diazirines are precursors of carbenes which are known to be capable of C-H insertion reactions. They have the advantage that they are stable to store and safer to work with compared to their analogous linear isomers, diazo compounds.<sup>135</sup> Upon excitation, carbenes can be formed in a singlet or triplet excited state, as shown by the example of the carbene methylene in Figure 2.9.

Many applications of carbenes generated from diazirines already exist. A patent search, of which the results can be found in Appendix 10.P, revealed their main application was in the field of photoaffinity labelling. Other applications included the use in biomedical devices such as contact lenses and implants, cosmetics, anti-fouling of ships, as well as modifying many types of surfaces.

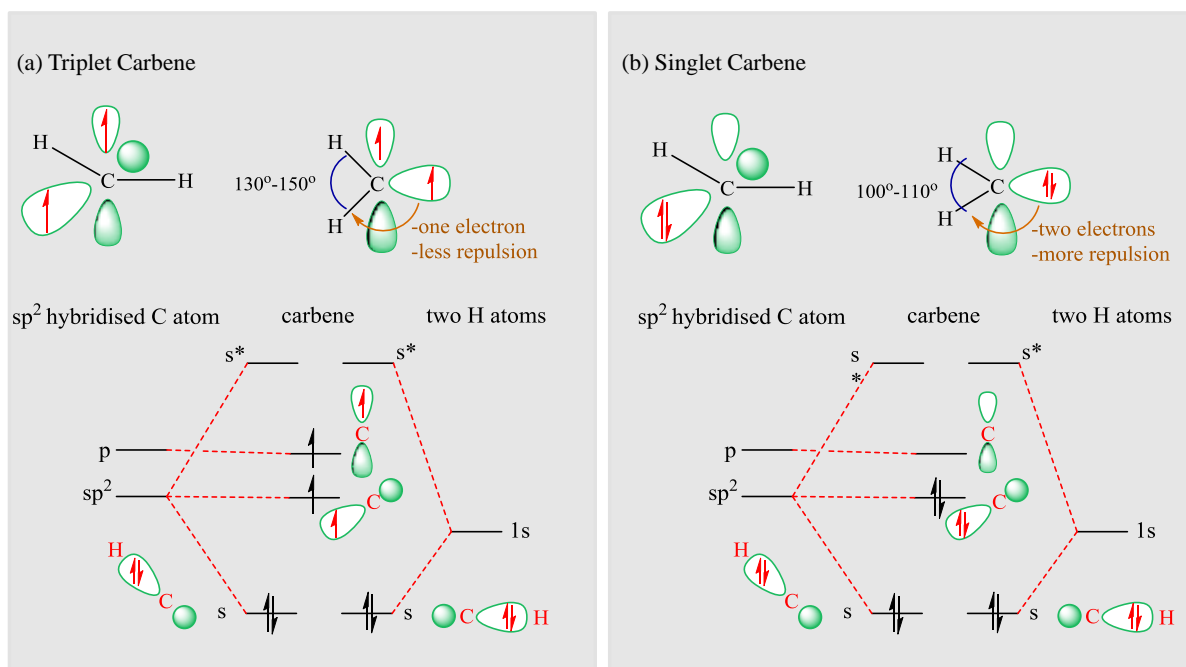


Figure 2.9: Methylene in its (a) triplet and (b) singlet excited state. Diagram composed from information in the book: Modern Physical Organic Chemistry.<sup>136</sup>

## 2.10 Conclusions

The literature review demonstrated that many methods had previously been tested to improve the adhesion of coatings to non-polar polymer substrates. Although some novel methods have been shown to be successful, it is often the cost of implementing the new technologies into the industry that is their main disadvantage. For a new method to replace a state of the art technique, it has to be cost-effective for the industry.

This study investigates the ability of two different methods to improve the adhesion of waterborne coatings to PP-based substrates: a physical entanglement method and a grafting method, utilising the knowledge gained from the literature review.

## Part II

# Materials and Methods



# Chapter 3

## MATERIALS

### 3.1 Substrates

#### 3.1.1 Polypropylene-based Substrates

All the substrates used in this research were supplied in the form of plaques. Two groups of substrates were examined.

The first group were industrial grade TPO substrates, commercially available and used for the manufacture of car bumpers and other exterior parts, used in Europe. They were created by injection moulding and were black in colour. TPO/0 refers to Daplen<sup>TM</sup>EE103AE, a 10 % mineral filled, 0 % EPDM modified PP compound, provided by Borealis. TPO/2 refers to SABIC<sup>®</sup> PP 108MF10, a high impact PP copolymer containing 2 % EPDM, provided by Sabic. TPO/20 refers to SABIC<sup>®</sup> PP 95610, a high impact PP copolymer containing 20 % EPDM, provided by Sabic. These plaques were supplied with the dimensions 118 x 122 x 3 mm.

The second group of substrates were created by injection moulding for research purposes, to assess the effect of EPDM elastomer content on the adhesion of coatings to the substrates (they are not used in industry). They were supplied by BASF Schweiz AG (in Basel) and produced to contain only PP, a mould release agent, and EPDM (when present). They are white in colour, but increase in opacity with increasing amounts of

EPDM. These plaques were supplied with the dimensions 118 x 118 x 3 mm. These substrates are referred to as R/x, where x = percentage of (%) EPDM, and x was 0, 5, 10, 15, 20 or 25.

The substrates are summarised in Table 3.1. The density and the Vicat softening point are shown for the industrial substrates (defined by the manufacturer). The Vicat softening point is the determination of the softening point for materials that have no definite melting point, such as plastics. It is taken as the temperature at which the specimen is penetrated to a depth of 1 mm under a specified load and heat rate, by a flat-ended needle with a 1 mm<sup>2</sup> circular cross-section.<sup>137</sup> It was important that no adhesion tests or curing of the coatings went above this temperature to avoid deformation of the substrates which would leave them unsuitable for industrial use.

### **3.1.2 Grafting Proof-of-Concept Substrates**

Gold coated silicon wafers were supplied by BASF SE. Chromium (1 nm) was applied to each silicon wafer to improve the adhesion of the 50 nm gold coating applied to the wafer.

A glass-cutting knife was used to create 1 x 1 cm squares for the grafting study.

PP sheets (2 mm thickness) containing no pigments were supplied by Direct Plastics (UK).

## **3.2 Chlorinated Polyolefin (CPO) Adhesion Promoter**

A CPO, 515-2 (40 % solids in xylene) was supplied by Eastman Chemical Company (USA). It contained approximately 30 wt.% chlorine. The best adhesion results were found when the CPO was applied as a primer, wet-on-wet, with the waterborne basecoat.

Table 3.1: Summary of substrates, including predetermined properties of the industrial substrates available from the manufacturers. For the Daplen<sup>TM</sup> EE103AE and SABIC<sup>®</sup> PP 108MF10 substrates, the density was measured using ISO 1183 and the Vicat softening temperature was measured using ISO 306. For the SABIC<sup>®</sup> PP 95610 substrate, the density was measured using ASTM D792 and the Vicat softening temperature was measured using ASTM D1525.

| Substrate | Commercial Name               | Industrial? | Density (kg m <sup>-3</sup> ) | Vicat Softening Temperature (10N) | % EPDM |
|-----------|-------------------------------|-------------|-------------------------------|-----------------------------------|--------|
| TPO/0     | Daplen <sup>TM</sup> EE103AE  | ✓           | 950                           | 120 °C                            | 0      |
| TPO/2     | SABIC <sup>®</sup> PP 108MF10 | ✓           | 900                           | 125 °C                            | 2      |
| TPO/20    | SABIC <sup>®</sup> PP 95610   | ✓           | 905                           | 145 °C                            | 20     |
| R/0       | -                             | ✗           | Not Known                     |                                   | 0      |
| R/5       | -                             | ✗           |                               |                                   | 5      |
| R/10      | -                             | ✗           |                               |                                   | 10     |
| R/15      | -                             | ✗           |                               |                                   | 15     |
| R/20      | -                             | ✗           |                               |                                   | 20     |
| R/25      | -                             | ✗           |                               |                                   | 25     |

### 3.3 Candidate Adhesion Promoters for Physical Entanglement

All the candidate APs listed in Table 3.2 were supplied by BASF SE (Ludwigshafen, Germany).

### 3.4 Candidate Adhesion Promoters for Covalent Bonding (Grafting)

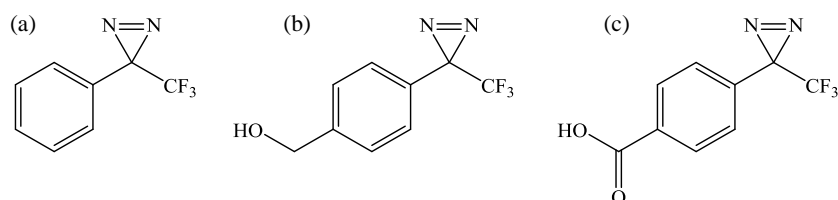


Figure 3.1: Molecular structures of (a) TPD, (b) TPDOH and (c) TPDCOOH

Denoted as **TPD** in this report, 3-Phenyl-3-(trifluoromethyl)-3H-diazirine,  $\geq 98.0$  % (LC), was supplied by TCI Chemicals.

Denoted as **TPDOH** in this report, 4-[3-(Trifluoromethyl)-3H-diazirin-3-yl]benzyl Alcohol,  $\geq 97.0$  % (LC), was supplied by TCI Chemicals.

Denoted as **TPDCOOH** in this report, 4-[3-(Trifluoromethyl)-3H-diazirin-3-yl]benzoic Acid,  $\geq 97.0$  % (LC), was supplied by TCI Chemicals.

### 3.5 Waterborne Basecoat and Topcoat

A non-pigmented (appeared white / milky in colour but dried transparent) waterborne basecoat, a black pigmented waterborne basecoat, and a clearcoat / hardener system to be applied as a topcoat, were supplied by BASF Coatings GmbH (Münster, Germany). The formulation of the waterborne basecoat is shown in Figure 3.2.

Table 3.2: A list of commercially available active polymers provided from BASF and their descriptions.

| <b>Commercial Name</b> | <b>Description</b>           |
|------------------------|------------------------------|
| EFKA 3580              | Polyacrylate                 |
| EFKA3570               | Polyethylene Imine           |
| Emulan EL              | Castor Oil Ethoxylate        |
| Emulan P               | Fatty Alcohol Alkoxyate      |
| Emulan TO2080          | Oxo Alcohol Ethoxylate       |
| Emulphor FAS30         | Fatty Alcohol Polyglycol     |
| Lupasol PO100          | Polyethylene Imine           |
| Lutensol AP9           | Alkyl Phenol Ethoxylate      |
| Lutensol ON70          | Alkyl Phenol Ethoxylate      |
| Plurafac LF1300        | Fatty Alcohol Alkoxyate      |
| Plurafac LF403         | Fatty Alcohol Alkoxyate      |
| Plurafac LF224         | Fatty Alcohol Alkoxyate      |
| Plurafac LF223         | Fatty Alcohol Alkoxyate      |
| Pluriol A10R           | Reactive Polyalkylene Glycol |
| Pluriol A1350P         | Reactive Polyalkylene Glycol |
| Pluriol A23R           | Reactive Polyalkylene Glycol |
| Pluriol A308R          | Reactive Polyalkylene Glycol |
| Pluriol A 520E         | Reactive Polyalkylene Glycol |
| Pluriol P900           | Polypropylene Glycol         |
| Pluronic PE 6200       | EO/PO Block Copolymer        |
| Pluronic RPE 3110      | EO/PO Block Copolymer        |
| Pluronic RPE2520       | EO/PO Block Copolymer        |

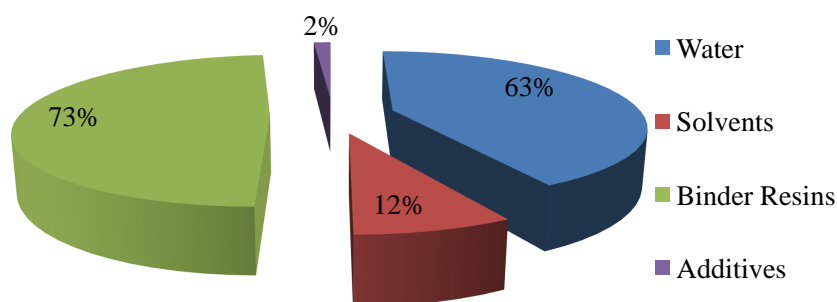


Figure 3.2: A pie chart showing the percentage of the different components in the water-borne basecoat formulation.

### 3.6 Solvents

Cyclohexane, puriss, purity (GC)  $\geq 99.5\%$ , was supplied by Sigma-Aldrich.

Toluene, anhydrous, 99.8 %, was supplied by Sigma-Aldrich.

Solvesso 150 and Solvesso 200 were provided by BASF SE, but supplied by ExxonMobil. (They are crude mixtures of aromatic hydrocarbons (aromatic content  $>99$  wt.%). Solvesso 150 has a distillation range of 182 – 207 °C and Solvesso 200 has a distillation range of 232 – 287 °C.)

Ethanol ACS reagent,  $\geq 99.5\%$ , (200 proof), absolute, was supplied by Sigma-Aldrich.

THF, anhydrous,  $\geq 99.9\%$ , inhibitor-free, was supplied by Sigma-Aldrich.

Acetone, Chromasolv<sup>®</sup> for HPLC,  $\geq 99.9\%$ , was supplied by Sigma-Aldrich.

Isopropanol, LC-MS Chromasolv<sup>®</sup> grade, was obtained from Sigma Aldrich.

Methyl ethyl ketone (MEK), ACS reagent,  $\geq 99.9\%$ , was supplied by Sigma-Aldrich.

### 3.7 Alkane thiols

1-Nonanethiol, 96 %, was supplied by Sigma Aldrich.

1-Octadecanethiol, 98 %, was supplied by Sigma Aldrich.

## 3.8 Reaction between Trimeric Isocyanate and TP-DOH

Basonat<sup>TM</sup>100, a solvent-free aliphatic polyisocyanate, was provided by BASF SE.

TPDOH was supplied by TCI chemicals.

# Chapter 4

## METHODS

### 4.1 Scanning Electron Microscopy (SEM) and Transmission Electron Microscopy (TEM) with a Ruthenium Tetraoxide ( $\text{RuO}_4$ ) Staining Technique, and Energy Dispersive X-ray Spectroscopy (EDX)

The morphologies of the TPO and research substrate blends were studied by SEM and TEM. The plane or face of the desired cross-section was cryogenically cut through the sample using Histo knives in a Leica cryomicrotome Ultracut S.

For SEM in the back-scattered mode, the contrast between the blend components of the cryo-sectioned face was achieved by staining the samples with ruthenium tetroxide ( $\text{RuO}_4$ ) vapour for 30 minutes at room temperature, where the  $\text{RuO}_4$  solution was prepared according to the procedure described by Montezinos *et al.*<sup>104</sup> The samples were then measured with an Zeiss Ultra 55 SEM operated at 20kV (in the back-scattered mode, areas of higher density, higher atomic number or smaller porosity appear brighter).

For TEM, ultrathin sections were cryo-microtomed with a Leica microtome Ultracut S, using a Diatome ultra diamond knife. During sectioning with the diamond knife, the samples floated on to the surface of the water / DMSO solution in a boat, and were



collected for analysis with TEM. The sections were put on a copper grid with a carbon support layer.

Contrast between the blend components was also achieved by exposing the samples to RuO<sub>4</sub> vapour. The staining procedure was applied after cutting the thin sections, rather than to a bulk substrate prior to cutting. The stained sections were examined in a TEM (Zeiss Libra 120) operated at 120 kV.

To confirm the presence of ruthenium (Ru) in the contrasted samples, elemental microanalysis, based on EDX, was conducted on the SEM Zeiss Ultra 55 operated at 20 keV, equipped with a Thermo Fisher EDX detector.

For heat treatment of the substrates, a conventional oven was heated to 80 °C and the substrates heated in the oven for one hour before analysis with the SEM. Ideally, measurements would be done on the substrates as soon as they had been heated, however, due to practical limitations, the SEM measurements were done within one week of heating.

## 4.2 ImageJ SEM Image Analysis

To assess the distribution of the EPDM domains on the substrate surface and on the cross-section relative to the position from the surface, ImageJ,<sup>138</sup> a Java-based public domain image processing and analysis program, developed at the National Institute of Health (NIH) (USA), was utilised. Each image to be processed was first loaded as a TIFF file, consisting of the image to be analysed and a scale bar (already created from the SEM / TEM software). The image dimensions were calibrated using the *Set Scale* tool in the software.

The newly scaled images were then used for analysis. It was found that enhancing the contrast of the coloured images gave the best results. The colour threshold was adjusted so that the particles of interest were adequately covered. The *Analyze Particles* command was selected from the *Analyze* menu, the size (pixel<sup>2</sup>) set to 0-Infinity (defining the size of the particles to be searched for and analysed; in this case covering all possibilities of sizes)

and the circularity range set to 0-1. Circularity =  $4\pi( [\text{Area}] / [\text{Perimeter}]^2)$ . A value of 1.0 indicates a perfect circle and as the value approaches 0.0, it indicates an increasingly elongated shape (software states values may not be valid for very small particles.) Other options selected were *Display Results* (measurements for each particle were displayed in the *Results Table*), *Clear results* (any previous measurements listed in the *Results Table* were cleared), and *Summarize* (particle count, total particle area, average particle size, area fraction and the mean of all parameters listed in the *Set Measurements* dialog box were displayed in a separate *Summary* table).

The option *Mask* for the image display was selected, generating an 8-bit image containing simple black-filled shapes of the measured particles (graylevels: *Outlines*: 0; *Background*: 255). The resolution of each image was 0.2  $\mu\text{m}/\text{pixel}$ . The *Set Measurements* window found on the *Analyze* menu enabled the measurement of *Area* to be selected, displaying the area of each particle in  $\mu\text{m}^2$ . The data from the *Results* window was exported to Microsoft Excel<sup>139</sup> for further statistical analysis. The particle areas were summed up and divided by the total area measured, to give the estimated % coverage area from the EPDM particles.

Due to the calculation of the % area of coverage from the EPDM particles depending on the image threshold set (to insure good contrast between the PP matrix and EPDM particles), the accuracy of the program (identifying the areas and making the calculations), and the resolution of the image itself, it was not possible to calculate the errors in the calculations. Therefore, the values calculated were used only as an approximation.

### 4.3 White Light Interferometry

Surface roughness measurements were carried out using a WYKO NT9300 surface profiler (Veeco Instruments, USA) in the vertical-scanning interferometry (VSI) mode. The back-scan and scanning distance were set at 5 and 15  $\mu\text{m}$ , respectively. A 120 x 90  $\mu\text{m}$  area was scanned by choosing a magnification of 50 x 1. The saturation value was chosen in a range

of 0.01 - 0.05 %. For the VSI mode, the vertical resolution was up to 3 nm for a single measurement and the largest vertical distance that could be measured was 500  $\mu\text{m}$ . Two parameters describing the surface roughness (or smoothness) are the average roughness (Ra) and the root mean square roughness (Rq). Ra is the mean height variation calculated over the whole measurement array, as shown in Equation 4.1. Rq is the root mean square average of the measured height deviations taken within the evaluation length or area, and measured from the mean linear surface, as shown in Equation 4.2. A schematic representation of these values is shown in Figure 4.1. Higher values of Ra or Rq indicate a rougher surface.

$$R_a = \frac{1}{L} \int_0^L |Z(x)| dx \quad (4.1)$$

$$R_q = \sqrt{\frac{1}{L} \int_0^L |Z^2(x)| dx} \quad (4.2)$$

For each sample, images were obtained from 10 different areas on the surface, and the surface roughness parameters were averaged and the standard deviations were calculated. Measurements were taken before and after solvent swelling. An advantage of the WYKO surface profiling system is that it allows surface roughness measurements to be taken without contact to the sample. Measurements were also tested in the phase-shift interferometry (PSI) mode, which is optimal for smoother surfaces.

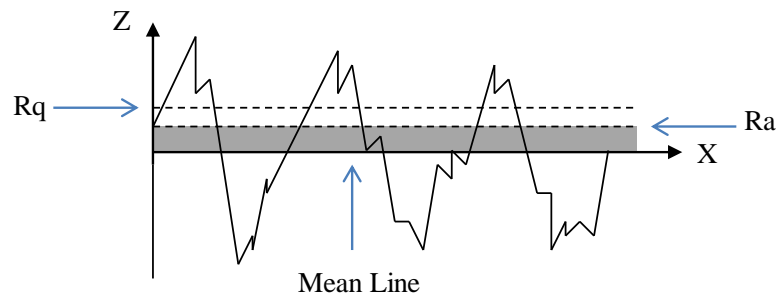


Figure 4.1: Schematic profile of a surface, showing the roughness parameters Ra and Rq, for the peaks and valleys in the Z direction. An adaptation from Bellitto *et al.*<sup>140</sup>

However, a greater surface roughness contrast could be seen in VSI mode (often more useful for rough surfaces and surfaces with steep steps), and was therefore the method of choice. In VSI mode, a white line beam passes through a microscope objective to the sample surface. A beam splitter reflects half of the incident beam to the reference surface. The beams reflected from the sample and from the reference surface recombine at the beam splitter to form interference fringes, where the best contrast fringe occurs at the best focus.

## 4.4 Nanoindentation

**Data Measurements** Nanoindentation measurements were carried out using an Agilent Nano indenter G200 (Agilent Technologies, USA) with a diamond indenter tip with Berkovich geometry.

The measurements were done in Continuous Stiffness Mode (CSM), which produced repeatable results compliant with ISO 14577 standards. The Young's modulus and hardness profiles were measured with a displacement range of 0.3 - 3  $\mu\text{m}$  from the substrate surface (with nano-depth resolution).

During the CSM measurement, the nano-indenter applied a load to the indenter tip, which forced the tip into the surface whilst simultaneously superimposing an oscillating force with a force amplitude, generally several orders of magnitude smaller than the nominal load, as shown in Figure 4.2. The CSM measuring method separates the in-phase and out-of-phase components of the load-displacement history. This separation provides an accurate measurement of the location of initial surface contact and continuous measurement of contact stiffness as a function of depth or frequency, thus eliminating the need for unloading cycles. Since the contact stiffness is determined directly, no assumptions (such as mechanical equilibrium) are required to correct for elasticity.<sup>141</sup>

Ten measurements were taken on each sample to generate hardness and moduli data.

Details of how the Young's modulus and hardness have been calculated from the

measurements can be found elsewhere.<sup>142,143</sup>

The measurements were calibrated against a polycarbonate reference material (see Appendix 10.A), which showed an average linear progression of Young's modulus and Hardness in the displacement range 300 - 5  $\mu\text{m}$ . The average Young's modulus measured corresponded exactly with the literature value of 2.4 GPa.

**Data interpolation for creating graphs of average values** The nanoindenter measured the force and displacement every 0.2 seconds; hence the Young's modulus and hardness calculations were time dependent and not displacement dependent. Therefore, different displacement depths were recorded for each measurement. To be able to average the data from each 10 measurements for each sample, an interpolation mathematical equation was utilised. Although interpolation could be a subject for speculation, the values and graphs created were verified against each individual measurement, and were found to be in the correct range, and so can be considered an accurate account. The basic principle behind the interpolation calculation is shown in Figure 4.3. When two known values are  $(x_1, y_1)$  and  $(x_2, y_2)$ , the values for  $(x, y)$  are calculated using Equation 4.3. Full details of how the interpolation was calculated can be found in Appendix 10.B.

$$y = y_1 + (x - x_1) \frac{y_2 - y_1}{x_2 - x_1} \quad (4.3)$$

## 4.5 Surface Free Energy Determination

### 4.5.1 Owens-Wendt Method

Contact angles were obtained using the sessile drop method with an OCAH 200 contact angle device from Dataphysics (Germany). Three liquids of known surface tension were used as a probe for the surface free energy calculations: diiodomethane (Merck, >96 %), ethylene glycol (Merck, >99.5 %) and distilled water (Table 4.1 shows the predetermined values used.)

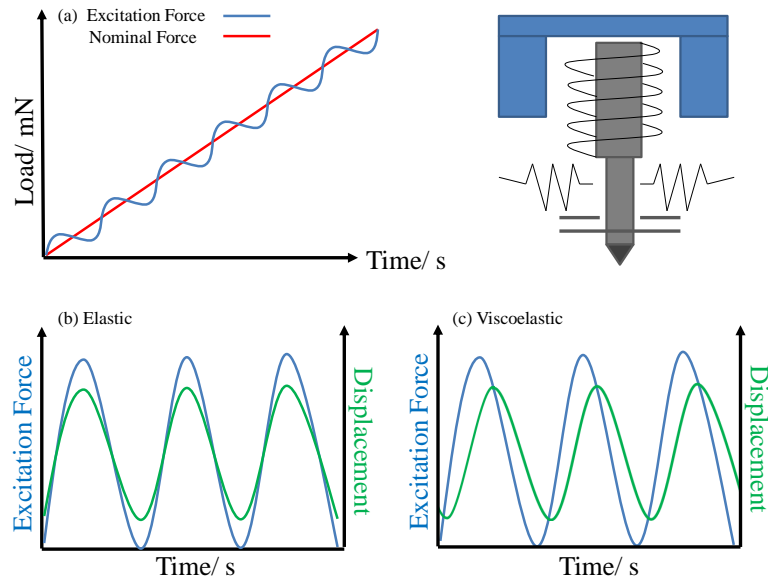


Figure 4.2: A schematic representation of nano-indentation in Continuous Stiffness Mode (CSM) from Agilent technologies. (a) A sinusoidal oscillation is used in permanent superposition to the force signal. The oscillation is applied directly to the shaft with the tip and produced by the coil (shown schematically on right hand side). For elastic materials, there is no phase shift (b) but measurement of viscoelastic materials result in a phase shift between force and displacement signal (c).

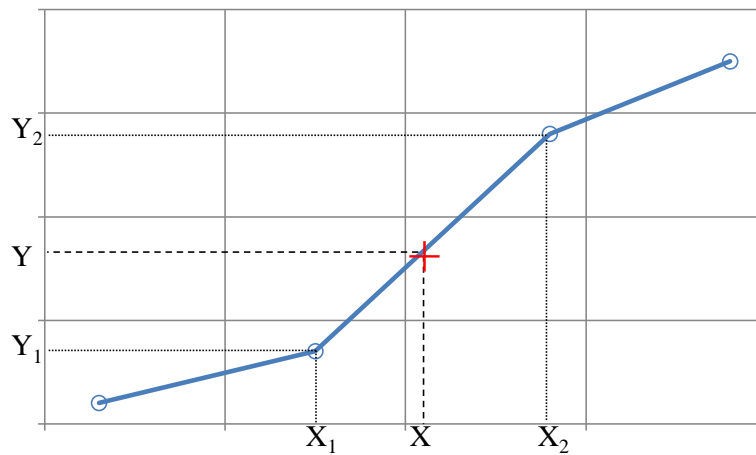


Figure 4.3: Schematic diagram demonstrating the basic principle behind linear interpolation: the line of best fit between two data points,  $x_1$  and  $x_2$ , from which  $x$  can be calculated.

Table 4.1: Predetermined polar and dispersion components of the surface tension of the probe liquids used to determine the surface energy of the substrates.

| Probe liquid           | Dispersion<br>$\gamma_{\text{d}}/\text{mJ m}^{-2}$ | Polar<br>$\gamma_{\text{p}}/\text{mJ m}^{-2}$ | Total<br>$\gamma_{\text{l}}/\text{mJ m}^{-2}$ |
|------------------------|--|---|---|
| <b>Diiodomethane</b>   | 50.80  | 0.00  | 50.80   |
| <b>Ethylene Glycol</b> | 29.30  | 18.20   | 47.50   |
| <b>Water</b>           | 21.80  | 51.00   | 72.80   |

For improved accuracy, ten drops were measured for each liquid probe on each surface (over 1000 contact angles), and the values were averaged. The drop image was stored by a video camera, which commenced recording upon an optical trigger, as soon as the drop was deposited. It recorded 360 images for 12 s for each drop. The contact angle (average of the left and the right) from the shape of the drop was calculated from the video after it was recorded, using an image analysis system in the equipment software. Contact angles could be measured over a short time scale by initially recording the video, to limit the influence of any reaction between the drop and the substrate. This method also limited the volume reduction of the drop due to evaporation, which could cause inaccurate results.<sup>144</sup> If the contact angle was  $<20^\circ$ , a circle fitting was used. For a contact angle between  $20 - 80^\circ$ , an ellipse fitting was used. For a contact angle  $>80^\circ$ , a tangent fitting was used. A 0.72 mm diameter syringe needle was used to create a drop of constant volume. All contact angles were measured at room temperature. The surface roughness values of the substrates (Ra) were  $<0.5 \mu\text{m}$ , a generally accepted value which is known not to significantly affect the accuracy of the results.<sup>144</sup>

## 4.5.2 Owens-Wendt Theory

The surface free energies of the different substrates were calculated using the theoretical model, Owens-Wendt (OW), shown in Equation 4.4.

The equation can be rearranged to give a linear equation, in the form of  $y = mx + c$ , as shown in Equation 4.5.

$$\gamma_l(1 + \cos\theta) = 2\sqrt{\gamma_{sp}\gamma_{lp}} + 2\sqrt{\gamma_{sd}\gamma_{ld}} \quad (4.4)$$

$$\frac{\gamma_l(1 + \cos\theta)}{2(\gamma_{ld})^{1/2}} = (\gamma_{sp})^{1/2} \cdot [(\gamma_{lp})^{1/2}/(\gamma_{ld})^{1/2}] + (\gamma_{sd})^{1/2} \quad (4.5)$$

The OW model gives the long-range dispersion,  $\gamma_{sd}$  (van der Waals) and the short-range polar,  $\gamma_{sp}$  (sum of polar, hydrogen, inductive and acid-base interactions) components of surface free energy. The total surface energy is the sum of the two components ( $\gamma_{sd} + \gamma_{sp} = \gamma_s$ ).

The average contact angle of each probe liquid and their known surface tensions were plotted, and the line of best fit was calculated. The gradient gave  $(\gamma_{sp})^{1/2}$ , from which  $\gamma_{sp}$  is calculated, and the intercept with the y-axis at  $x=0$  gave  $(\gamma_{sd})^{1/2}$ , from which  $\gamma_{sd}$  is calculated.

To assess the variation of surface energies by standard deviations in the calculations, a new method was created. Graphs and lines of best fit were plotted with the maximum and minimum contact angles measured for each probe liquid. Each possible surface energy component was then calculated, and the maximum and minimum values for  $\gamma_{sp}$  and  $\gamma_{sd}$  were recorded as the standard deviation in the surface free energy. These standard deviations gave a good impression of surface homogeneity or heterogeneity. However, it should be noted that other factors influencing accuracy, such as instrumental error, air humidity, and variation in room temperature,<sup>144</sup> were not taken into account.

### 4.5.3 Surface Free Energy of the Basecoat (Wet): Wu Method

An alternative to the Owens-Wendt method is the Wu method.<sup>145</sup> This was also used to calculate the surface energy and subsequent  $\gamma_{sp}$  and  $\gamma_{sd}$  components. In contrast to Owens-Wendt and others who used the geometric mean of the surface tensions in their calculations, Wu used the harmonic mean. The calculation behind this method is shown in Equation 4.6. This method provided improved accuracy in the results obtained for



the higher energy waterborne basecoat. The measurements were done by an analytical group in BASF Münster GmbH. A Krüss Tensiometer K12 (Germany), using the ring method, was used to determine the surface tension of the basecoat. The contact angle of the basecoat on a Teflon surface of known polar and dispersion components was then calculated, and the Wu method was used to calculate the polar and dispersive components of the surface energy of the basecoat.

$$\gamma_{(12)} = \sigma_l + \sigma_s - 4\left(\frac{\sigma_{ld} \cdot \sigma_{sd}}{\sigma_{ld} + \sigma_{sd}} + \frac{\sigma_{lp} \cdot \sigma_{sp}}{\sigma_{lp} + \sigma_{sp}}\right) \quad (4.6)$$

## 4.6 Wettability: Contact Angle Measurements

Contact angles were obtained using the sessile drop method with an OCAH (optical contact angle high speed) 200 instrument from Dataphysics (DataPhysics Instruments GmbH, Germany). Each candidate AP was placed into a syringe with 0.72 mm diameter (GLT, Nordson EFD, Germany), and deposited onto the surface of the substrate. The contact angles were measured by video, as described above for surface free energy measurements. Contact angles  $> 90^\circ$  were said to be non-wetting and contact angles  $< 90^\circ$  were said to be wetting, as shown in Figure 4.4.

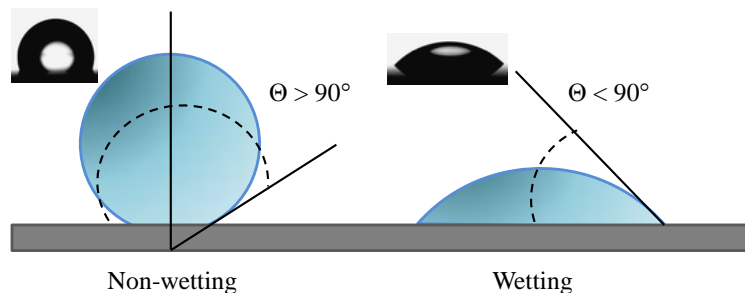


Figure 4.4: A schematic diagram showing cases where liquid drops are non-wetting or wetting on a substrate surface.

## 4.7 Automated Flaming Station

A flame pre-treatment of the substrates was performed using a flame station custom made by Gelsenkirchen (Germany), provided by BASF Coatings GmbH, Münster, Germany. A schematic diagram of the equipment is shown in Figure 4.5. The distance between the flame and the substrate was set to 20 cm, and the gas (propane): air ratio was 24: 1. The flame station was automated and set to 1200 mm/sec. Each substrate was subject to one flame cycle (forward and back).

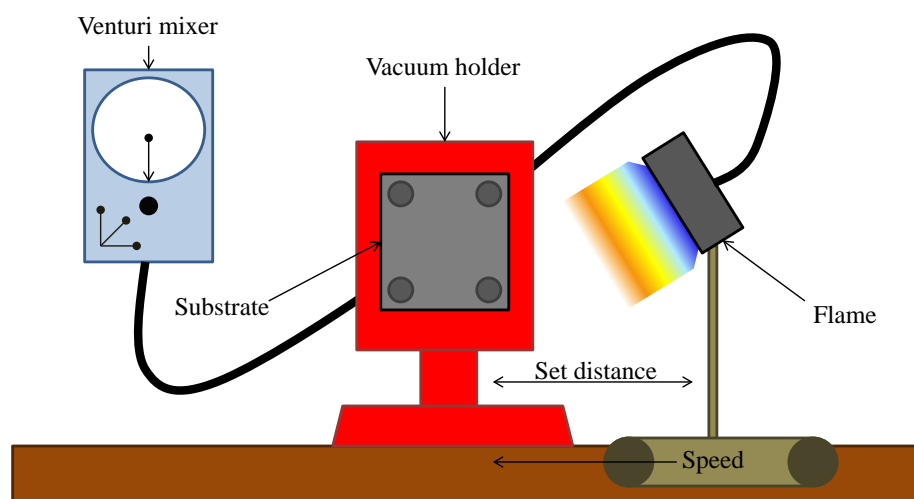


Figure 4.5: Schematic diagram of a laboratory flame treatment station

## 4.8 Substrate Cleaning

### 4.8.1 Cleaning TPO Substrates

For the investigation of the effect of cleaning substrates on the surface roughness, isopropanol was purchased from Sigma Aldrich (LC-MS Chromasolv<sup>®</sup> Grade).

Itex<sup>®</sup> Classic VP wipes (made in Germany), free of oil and silicone to avoid surface contamination, were soaked in isopropanol and used to wipe the substrates in a vertical direction. For non-abrasive cleaning, laboratory glass pipettes were used to dispense the isopropanol over the surface. The substrates were air dried.

### 4.8.2 Cleaning Gold Surfaces

The gold-coated silicon wafers (used for the grafting model system) were cleaned using a FEMTO plasma cleaner (Diener Electronic GmbH, Germany) directly before being submersed in the thiol solution to form a self assembled monolayer (SAM). A standard procedure was used where the chamber was evacuated to 0.2 mbar, rinsed with argon gas for one minute, plasma was generated at 20 % power (= 50 watts) for ten minutes at a controlled by-pressure of 0.3 mbar, before air was re-released into the chamber for 2 minutes.

## 4.9 Self-Assembled Monolayer (SAM) Formation

The standard procedure used to form the SAM on the gold surfaces can be found elsewhere.<sup>146</sup> The thiol solution was made so that the concentration of the C<sub>18</sub> and C<sub>9</sub> alkane thiols were in a ratio of 1:4.

The SAM thickness was measured using an alpha-SE<sup>®</sup>Ellipsometer ( J. A. Woollam Company Incorporated, USA). The amplitude change ( $\Delta\Psi$ ) and phase difference ( $\Delta\lambda$ ) between orthogonally polarised light from a white-light source was spectroscopically measured upon reflection at 70° from the surface. Using the Fresnel-Equations,<sup>147</sup> a physical model was fitted to the experimental data. Measurements were taken on the cleaned gold surface before and after SAM formation, and the difference in thicknesses were calculated to give the thickness of the SAM. Five measurements were taken on different areas of three samples, and an average thickness was calculated for each experiment. Details on the measurement and procedure are detailed elsewhere.<sup>148–150</sup>

## 4.10 Adhesion Promoter (AP) Deposition for Grafting Experiments

AP solutions were made with acetone at the desired concentrations. A glass syringe was used to deposit three 10  $\mu\text{L}$  droplets of the solution onto the substrate surface. The substrate was left to dry at room temperature for 15 minutes before the next stage.

## 4.11 Doctor Blade Coating Application

### 4.11.1 CPO

The coatings were applied using an R K303 multicoater by Erichsen (Hemer, Germany). The CPO primer was applied with a 4  $\mu\text{m}$  doctor blade and the waterborne basecoat was applied with a 50  $\mu\text{m}$  doctor blade, producing a dried thickness of 15 - 18  $\mu\text{m}$ . The CPO and basecoat were applied with a *wet-on-wet* method, where no curing step was implemented between coatings. The CPO and basecoat were then dried at 80 °C, for ten minutes. After ten minutes of drying, the topcoat was applied with a 100  $\mu\text{m}$  doctor blade, producing a dried thickness of 42 - 45  $\mu\text{m}$ . The topcoat was dried at 80 °C, for 30 minutes and left to cool. The substrate was stored at room temperature, in a ventilated atmosphere for 7 days post-curing, prior to the adhesion tests. The coating application process and dried thicknesses of the coatings are summarised in Figure 4.6.

### 4.11.2 Candidate APs

The coatings were applied using an R K303 multicoater by Erichsen (Hemer, Germany). The candidate AP primers were applied with a 4  $\mu\text{m}$  doctor blade. The primer was either applied *wet-on-wet* with the basecoat, or dried at 80 °C for ten minutes. The waterborne basecoat was applied with a 50  $\mu\text{m}$  doctor blade, and dried at 80 °C for ten minutes, producing a dried thickness of 15 - 18  $\mu\text{m}$ . After ten minutes of air drying / cooling, the

topcoat was applied with a 100  $\mu\text{m}$  doctor blade, producing a dried thickness of 42 - 45  $\mu\text{m}$ . The topcoat was dried at 80 °C for 30 minutes and left to cool. The substrate was stored at room temperature in a ventilated atmosphere for 7 days post-curing, prior to the adhesion tests. The coating application process and dried thicknesses of the coatings are summarised in Figure 4.6.

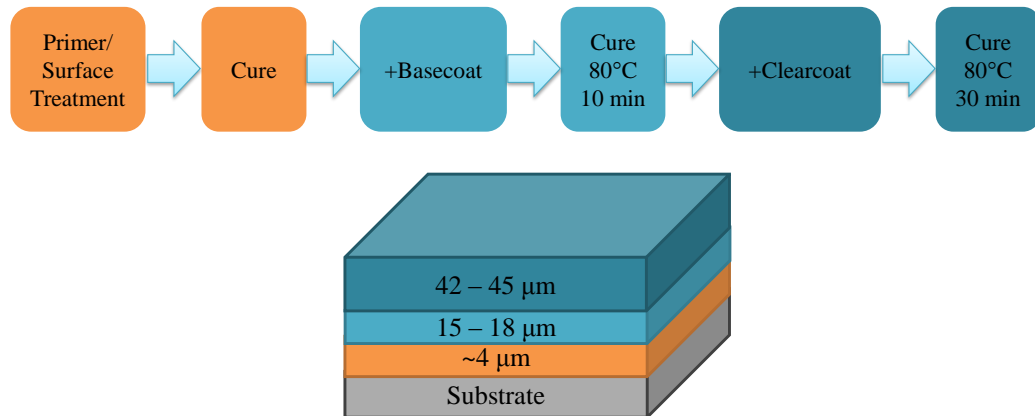


Figure 4.6: Top: a summary of the coating and curing steps. Bottom: the dried thicknesses of the coatings.

## 4.12 Spray Gun Coating Application

A hand-held Satajet 4000 B RP spray gun (SATA GmbH, Germany) with a 1.4 mm nozzle was used at 3 bar pressure for primer and coating application. The coatings were applied in a climate control room at 23 °C, 65 % humidity. The coating and curing process is summarised in Figure 4.6. The thickness of the coatings were measured by ultrasonic reflection according to ISO 2808 at BASF Coatings GmbH. Unless stated otherwise, the substrates were not cleaned prior to the application of the primer / coatings.

## 4.13 Thermal Cure

A conventional oven with a solvent extraction unit was used to thermally cure samples at the desired temperature for a set time. The substrates were protected from dirt using glass Petri dishes.

## 4.14 UV Cure

A large scale UV curing device was used from IST Strahlentechnik Metz GmbH (Germany), type: M-40-2\*1-R-Ir-SLC-So-inert, UV lamp type: M 400 U 2 H. The radiant exposure was measured using a UV Power Puck S/N 2245. The UV emission spectrum from the device is shown in Figure 4.7.

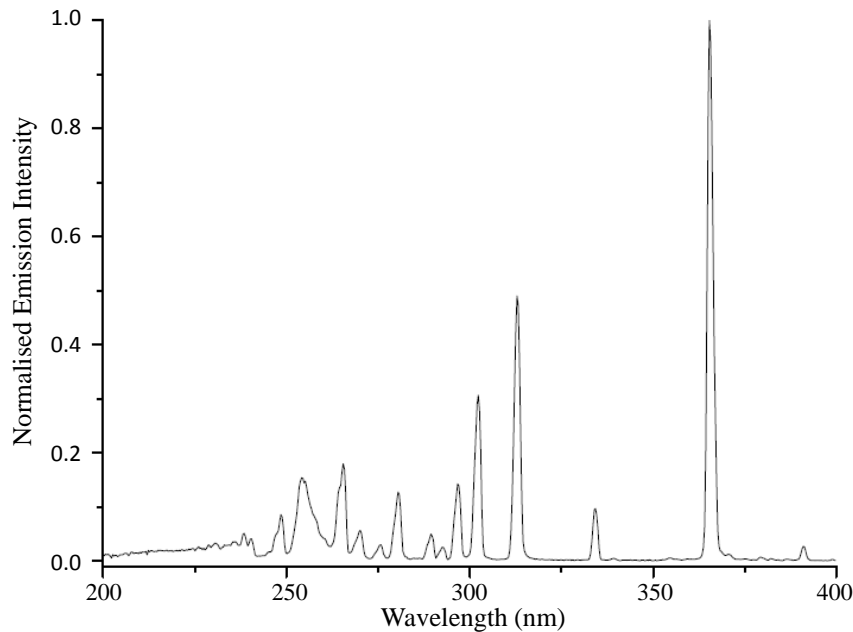


Figure 4.7: The UV emission spectrum from the IST UV curing system.

## 4.15 Cross Hatch Test (CHT)

As a first check of adhesion, a CHT was carried out according to the German standard ISO2409. The substrates were coated with all coatings, cured, and stored for post-curing for 7 days prior to the adhesion test. To perform the CHT, a grid was formed of six horizontal and six vertical cuts in the dried coated layers, using a multi-cross cutter (Model 295, Erichsen, Germany). The grid area was then covered with an adhesive tape (Tesa 4651, Germany) and manually removed. A grade was then assigned to each

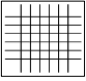
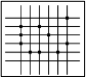
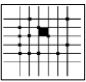
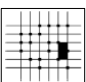
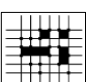
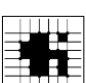
substrate which ranged between 5, the worst (more than 65 % of the grid squares were removed) and 0, the best (no square was removed), as shown in Figure 4.8.

## 4.16 Steam Jet Test (SJT)

In the cases when good adhesion was observed in the CHT's, further tests were performed with a steam jet. The adhesion of the coated system (primer, base coat, clear coat) was evaluated by a SJT according to Daimler-Chrysler specifications. The experiments were performed with paint test equipment provided by Walter Gertebau (Sachsenheim-Ochsenbach, Germany) using a power wash jet (Nr.  $\frac{1}{4}$ MEG2506, Spraying Systems, Remshalden, Germany). A cross (2 x 13 mm length at  $\sim 19^\circ\text{C}$ , creating a rectangle outline of 118 x 36 mm) was made in the coated layer using a graver (Sikkens graver, type 463, blade 1 mm; Sikkens, Stuttgart, Germany) prior to the test. The steam-jet (steam temperature =  $60^\circ\text{C}$ ; steam pressure = 67 bar, test period = 60 s, distance between jet and substrate = 100 mm) impinged on the substrate perpendicularly. When no delamination of the paint layer was visible, the paint adhesion was considered to meet industrial standards, according to the specification. The results were graded as shown in Figure 4.9.

## 4.17 Hansen Solubility Parameters: Solvent Selection for Swelling Substrates

The solvents used to swell the substrates were chosen based on their Hansen Solubility Parameters (HSPs).<sup>151</sup> Three HSP parameters are commonly described:  $\delta\text{D}$  (dispersion contribution),  $\delta\text{H}$  (hydrogen contribution) and  $\delta\text{P}$  (polar contribution). Together these parameters form a theory which can be used to predict the solubility of a polymer. All three parameters add up to the enthalpy of vaporisation of the material and the theory is based on the principle of two systems mixing at no enthalpy cost. For example, the evaporation of a proportion of a solvent A and replacing it with a proportion of a solvent

| Delamination            | Schematic Example   | CHT Grade |
|-------------------------|---|-----------|
| 0 %                     |    | 0         |
| $0 \% < x \leq 5 \%$    |    | 1         |
| $5 \% < x \leq 15 \%$   |    | 2         |
| $15 \% < x \leq 35 \%$  |    | 3         |
| $35 \% < x \leq 65 \%$  |    | 4         |
| $65 \% < x \leq 100 \%$ |  | 5         |

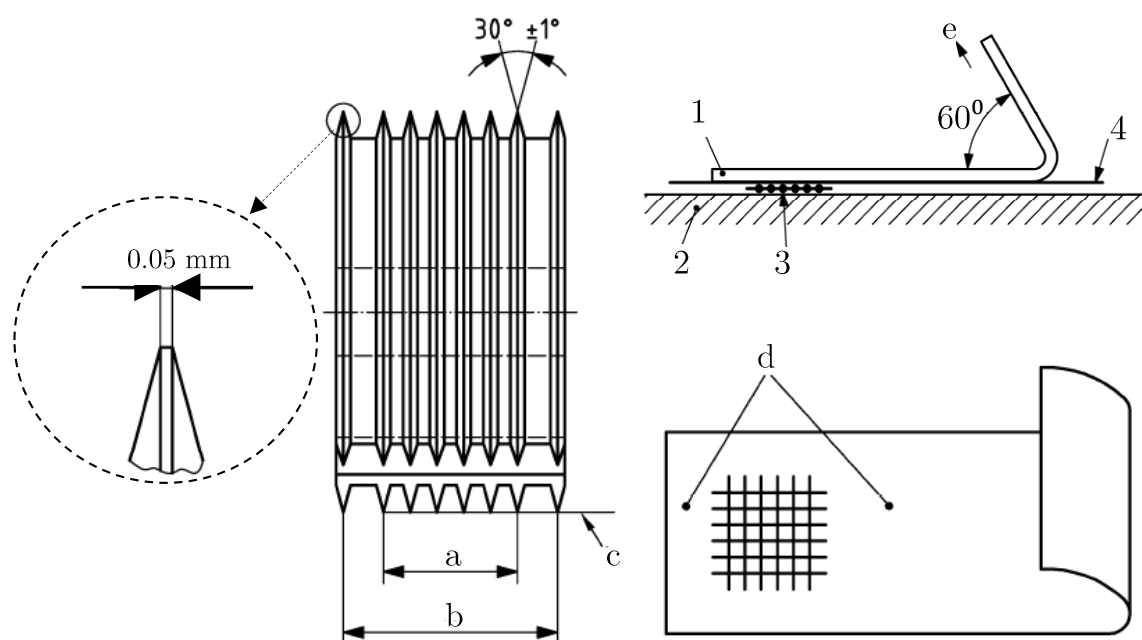


Figure 4.8: Cross-Hatch Test. Setup : 1 = tape, 2 = coatings, 3 = grid, 4 = substrate; Test details: a = length of grid is 10 mm, b = length of grid and guidelines is 16 mm, c = the guide blades and cutting blades are on the same plane, d = the tape is applied and smoothed/ flattened, e = pull of direction and angle of the tape.



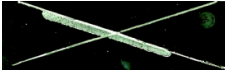





| Delamination                        |                                   | Photographic Example   | SJT Grade |
|-------------------------------------|-----------------------------------|--|-----------|
| Length (l)                          | Width (w)                         |  |           |
| $l > 40 \text{ mm}$                 | $6 \text{ mm} > w$                |    | 5         |
| $40 \text{ mm} > l > 25 \text{ mm}$ | $6 \text{ mm} > w > 3 \text{ mm}$ |    | 4         |
| $40 \text{ mm} > l > 25 \text{ mm}$ | $3 \text{ mm} > w > 0 \text{ mm}$ |    | 3         |
| $25 \text{ mm} > l > 10 \text{ mm}$ | $6 \text{ mm} > w > 3 \text{ mm}$ |  |           |
| $25 \text{ mm} > l > 10 \text{ mm}$ | $3 \text{ mm} > w > 0 \text{ mm}$ |  | 2         |
| $10 \text{ mm} > l > 0 \text{ mm}$  | $6 \text{ mm} > w > 3 \text{ mm}$ |  |           |
| $10 \text{ mm} > l > 0 \text{ mm}$  | $3 \text{ mm} > w > 0 \text{ mm}$ |  | 1         |
| 0 mm                                | 0 mm                              |  | 0         |



Figure 4.9: Steam Jet Test

B, leads to no enthalpy cost because the enthalpies of vaporisation of both solvents are the same; hence the so-called theory *like dissolves like*.

The most commonly cited and alternative theory for the prediction of the solubility of a polymer is the Hildebrand theory (defined as the square root of the internal energy of vaporisation divided by the molar volume *or* cohesive energy density).<sup>152,153</sup> However, this theory was not used because it only takes into account the dispersion properties of a molecule and does not account for the polar contribution. The advantage of the HSP parameters is that they do take into account the extra polar component and are not restricted to the behaviour of only hydrocarbon solvents. Although it was acknowledged that the HSPs are an approximation, they proved useful to select which solvents were suitable for swelling the PP-based substrates.

For visualisation, the HSPiP software (version 3.1.14, copyright 2008/11)<sup>151</sup> implements a green sphere with a set radius for a chosen polymer, the centre of which represents the optimum HSP for good solvency / swellability of the selected polymer. According to the theory, any solvents with HSP values inside the green sphere will swell the polymer. In this case, a PP polymer standard, implemented in the software ( $\delta D = 18$ ,  $\delta P = 0$ ,  $\delta H = 1$ ), was used as a model for the substrates. The results were also calculated for an EPDM substrate (also implemented in the software,  $\delta D = 18.6$ ,  $\delta P = 3.4$ ,  $\delta H = 4.4$ ), to predict what effect the EPDM content of the substrates would have on the solvent selection for swellability. The radius of the green sphere was set to 8 for the PP and 10.7 for the EPDM (predefined in the software). The HSP distance of the solvent from the optimum HSP value (centre of sphere) in 3D space was calculated using Equation 4.7.

A second parameter, known as the Relative Energy Difference (RED), was calculated for a list of solvents and a selected substrate. The value was used to characterise the swellability or solubility of the chosen substrate. The software was used to generate the RED values using Equation 4.8, by calculating the 3D distance between each solubility parameter of a list of selected solvents and the PP (or EPDM) substrate. It is the ratio of the distance of the solvent to the radius of the sphere, which gives an indication of how

good the solvent would be at swelling the PP or EPDM (an RED value of 0 indicates a perfect solvent, where a solvent at the edge of the sphere would have an RED value of 1). Any solvent with an RED value  $< 1$  indicated a solvent that should swell the PP or EPDM.

Figure 4.10 shows the HSPs for selected solvents (chosen on their availability and cost) and PP. The solid blue spheres represent the solvents inside the green sphere of the PP, that have RED  $< 1$  and therefore should swell the PP. The open blue spheres represent the solvents not inside the sphere (RED  $> 1$ ) that are predicted to have no swelling effect on PP. The top three solvents, toluene, cyclohexane and aromatic solvents, were chosen for further tests. To verify their compatibility with the EPDM component of the substrates, the RED values were also calculated for the same solvent list and EPDM, as shown in Figure 4.11. It can be seen that all three solvents also have RED  $< 1$  for EPDM, and so were expected to swell the EPDM component of the substrates as well as the PP. A summary of the chosen substrates is shown in Figure 4.12. The 'aromatic solvents' refer to Solvesso solvents (ExxonMobil) which were initially tested for swellability, having the advantage that they are mixed aromatic hydrocarbon products from the thermal cracking of crude oil, which are cost-effective and good for industrial products. However, due to their low volatility (could cause cohesive failure within substrate) and high pungency they were ruled out as possibilities.

$$\text{Distance}^2 = 4(\delta D_A - \delta D_B)^2 + (\delta P_A - \delta P_B)^2 + (\delta H_A - \delta H_B)^2 \quad (4.7)$$

$$\text{Relative Energy Difference} = \text{Distance}/\text{Radius} \quad (4.8)$$

| Solvent                | Hansen Solubility Parameters (MPa <sup>1/2</sup> ) |            |            | RED (MPa <sup>1/2</sup> ) |
|------------------------|--|------------|------------|---------------------------|
|                        | $\delta D$   | $\delta P$ | $\delta H$ |                           |
| Toluene                | 18   | 1.4        | 2          | 0.21                      |
| Cyclohexane            | 16.8   | 0          | 0.2        | 0.32                      |
| Aromatic Solvents      | 17.2   | 1          | 3.1        | 0.35                      |
| Chloroform             | 17.8   | 3.1        | 5.7        | 0.7                       |
| Hexane                 | 14.9   | 0          | 0          | 0.79                      |
| n-Butyl Acetate        | 15.8   | 3.7        | 6.3        | 0.97                      |
| Methyl Isobutyl Ketone | 15.3   | 6.1        | 4.1        | 1.09                      |
| Tetrahydrofuran        | 16.8   | 5.7        | 8          | 1.16                      |
| Ethyl Acetate          | 15.8   | 5.3        | 7.2        | 1.16                      |
| MEK                    | 16   | 9          | 5.1        | 1.33                      |
| Acetone                | 15.5   | 10.4       | 7          | 1.62                      |
| Cyclohexanol           | 17.4   | 4.1        | 13.5       | 1.65                      |
| 1-Butanol              | 16   | 5.7        | 15.8       | 2.04                      |
| Acetonitrile           | 15.3   | 18         | 6.1        | 2.43                      |
| Ethanol                | 15.8   | 8.8        | 19.4       | 2.6                       |
| Methanol               | 14.7   | 12.3       | 22.3       | 3.18                      |
| <b>Polypropylene</b>   | <b>18</b>  | <b>0</b>   | <b>1</b>   |                           |

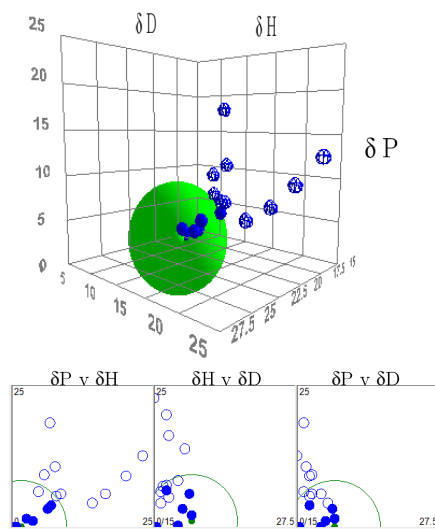


Figure 4.10: The Hansen Solubility Parameters of the selected solvents and a PP polymer, and the ratio of the distance of the selected solvent to the radius of the PP sphere (RED number). A perfect solvent has an RED of 0. A solvent with an RED value < 1 should swell the polymer.

| Solvent                | Hansen Solubility Parameter (MPa <sup>1/2</sup> ) |            |            | RED (MPa <sup>1/2</sup> ) |
|------------------------|---|------------|------------|---------------------------|
|                        | $\delta D$  | $\delta P$ | $\delta H$ |                           |
| Chloroform             | 17.8  | 3.1        | 5.7        | 0.25                      |
| Toluene                | 18  | 1.4        | 2          | 0.43                      |
| Aromatic Solvents      | 17.2  | 1          | 3.1        | 0.49                      |
| Tetrahydrofuran        | 16.8  | 5.7        | 8          | 0.69                      |
| n-Butyl Acetate        | 15.8  | 3.7        | 6.3        | 0.73                      |
| Ethyl Acetate          | 15.8  | 5.3        | 7.2        | 0.81                      |
| Cyclohexane            | 16.8  | 0          | 0.2        | 0.82                      |
| Methyl Isobutyl Ketone | 15.3  | 6.1        | 4.1        | 0.89                      |
| MEK                    | 16  | 9          | 5.1        | 0.96                      |
| Cyclohexanol           | 17.4  | 4.1        | 13.5       | 1.16                      |
| Hexane                 | 14.9  | 0          | 0          | 1.17                      |
| Acetone                | 15.5  | 10.4       | 7          | 1.21                      |
| 1-Butanol              | 16  | 5.7        | 15.8       | 1.58                      |
| Acetonitrile           | 15.3  | 18         | 6.1        | 2.01                      |
| Ethanol                | 15.8  | 8.8        | 19.4       | 2.1                       |
| Methanol               | 14.7  | 12.3       | 22.3       | 2.67                      |
| <b>EPDM</b>            | <b>18.6</b>                                       | <b>3.4</b> | <b>4.4</b> |                           |

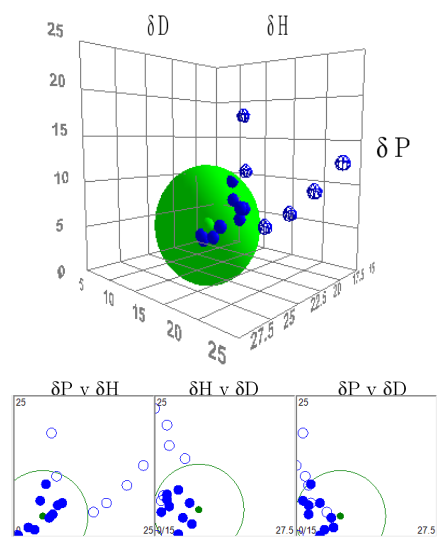


Figure 4.11: The Hansen Solubility Parameters of the selected solvents and an EPDM polymer, and the ratio of the distance of the selected solvent to the radius of the PP sphere (RED number). A perfect solvent has an RED of 0. A solvent with an RED value < 1 should swell the polymer.

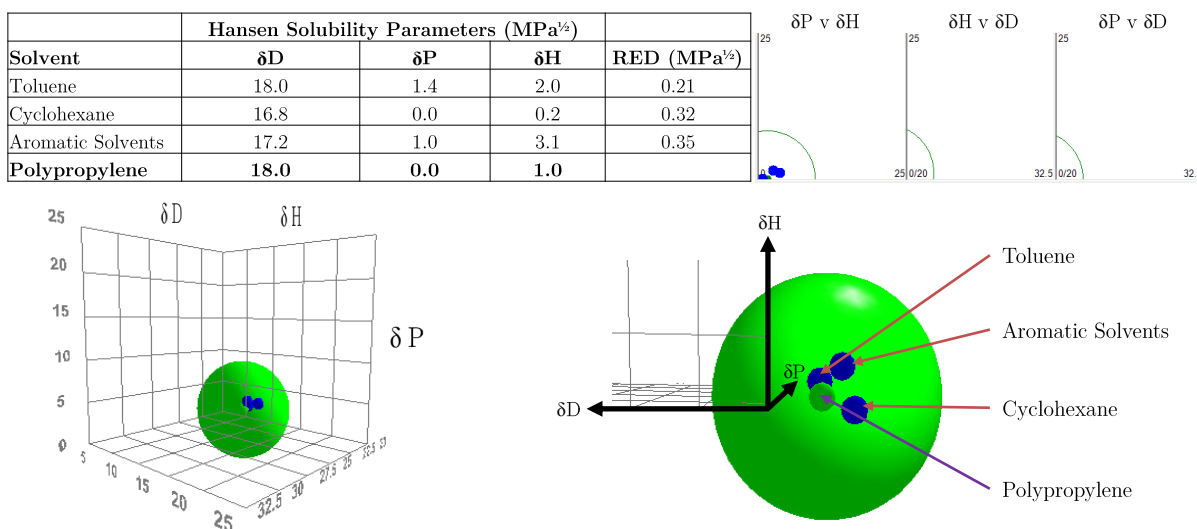


Figure 4.12: The Hansen Solubility Parameters, and sphere of the chosen solvents and PP, and the ratio of the distance of the chosen solvents to the radius of the PP sphere (RED number).

## 4.18 Solvent Swelling: Milligram Balance

For measuring the mass change of solvent penetration into the substrate over time, a standard laboratory milligram balance was used. A 50 mm diameter Petri dish was filled with solvent to the maximum, so that a convex meniscus formed at the top, and the substrate was placed on top of the dish. The volume of the solvent available to penetrate into the substrate surface, and the contact area with the surface remained constant for each measurement. Initially the mass of the substrates before swelling were measured. After fixed periods of times, the substrates were removed from contact with the solvent and the surface air dried with a cool air pump, before the mass was re-measured. For each time measured, a different substrate was used and each measurement was repeated three times. The relative mass increase was then calculated. The substrates that were swollen for one hour were left to air dry in a fume hood and their mass re-measured at fixed periods of time to measure the rate of solvent evaporation / substrate drying.

It was assumed that the increase in mass after the solvent had penetrated into the

substrate surface was due to polymer swelling. Other effects, such as immediate solvent evaporation out of the substrate may have occurred in a competing process. However, the interest was in the time dependence of the substrate mass change (irrespective of the competing processes) and subsequently the substrate swelling, which may have affected the adhesion of candidate APs to the substrate.

## 4.19 Time of Flight Secondary Mass Spectrometry (ToF-SIMS)

A TOF.SIMS-5 mass spectrometer (ION-TOF GmbH, Münster, Germany), was used in this study, equipped with a liquid metal ion gun (LMIG) generating  $\text{Bi}^+$  primary ions, operating at 25 kV. The average pulsed current was set to  $1.00 \mu\text{A}$  with a 25.0 ns pulse width. The analysis was performed under so-called *static conditions*<sup>94</sup> with an ion dose of the order of  $9 \times 10^{11}$  ions  $\text{cm}^{-2}$ . Sample charge up was compensated by low energy electron flooding provided by the built in flood gun.

### 4.19.1 Surface Composition Analysis

Three ToF-SIMS spectra were collected and analysed for areas of  $2.0 \times 2.0 \text{ mm}^2$  on each sample, in positive and negative modes. Each experiment was repeated three times. Values presented are mean values and standard deviations of the three spots, and three repeats. The ToF-SIMS data were analysed using ION-TOF software. Spectra  $m/z$  values were mass calibrated using  $\text{H}^+$ ,  $\text{C}^+$ ,  $\text{CH}_2^+$ ,  $\text{CH}_3^+$  and  $\text{C}_2\text{H}_3^+$  peaks in positive mode, and  $\text{C}^-$ ,  $\text{CH}^-$ ,  $\text{CH}_2^-$ ,  $\text{O}^-$  and  $\text{OH}^-$  peaks in negative mode. Although care was taken to work in clean conditions, it should be noted that inorganic peaks such as  $\text{Na}^+$  and  $^{37}\text{Cl}^-$ , as well as characteristic polydimethylsiloxane (PDMS) peaks such as  $\text{C}_5\text{H}_{15}\text{OSi}_2^+$  and  $\text{C}_5\text{H}_{15}\text{O}_4\text{Si}_3^-$ , were sometimes observed in the acquired spectra due to contamination. The standard deviation on all the detected peaks was  $<10$  milliatomic mass units. Data presented were normalised against the total ion count. Spectra were collected using high

mass resolution conditions (bunched beam mode,  $m/\Delta m > 6000$  for Si).

### 4.19.2 High Lateral Resolution Images

High-resolution images were obtained with the instrument in the so-called *burst alignment mode*, in which smaller focus of the primary ion beam is obtained (200 - 300 nm), however, at the expense of significantly lower mass resolution ( $m/\Delta m \sim 350$ ).<sup>154</sup> Secondary ion images were acquired using the  $\text{Bi}^{3+}$  primary ion gun. During acquisition, the primary ion beam was scanned in a raster pattern (128 x 128 pixels) over an analysis area of 200 x 200  $\mu\text{m}$ . Thus the image resolution was 1.6  $\mu\text{m}/\text{pixel}$ , unless otherwise stated. For some measurements, analysis areas varied, depending on the thickness of the coatings.

### 4.19.3 Mode of Failure Analysis

Surface composition analysis was performed as described above, with the exception of the  $\text{F}^-$  ion count being normalised against the  $\text{C}^-$  ion count. This was because the total ion count from the underside of a delaminated basecoat and the surface of a delaminated substrate was significantly different due to the so-called *matrix effect* (where the ion yield is dependent on the electronic state of the material being analysed).<sup>94</sup> Therefore, normalising against the total ion counts to compare both surfaces would not have given a good estimation of the mode of failure. The total  $\text{C}^-$  count from both surfaces was closer in value, so a better estimation of the mode of failure could be obtained.

## 4.20 X-ray Photoelectron Spectroscopy (XPS)

XPS analysis was carried out under ultra-high vacuum conditions ( $5 \times 10^{-8}$  Torr) using a Kratos Axis NOVA equipped with a hemispherical analyser and a monochromatised radiation source (Al K, 15.0 kV, 150 W). The analysed area was 800 x 300  $\mu\text{m}^2$ , allowing the acquisition of three spectra on each sample. Spectra were taken at a 90° take-off angle. Pass energies used for survey scans and high-resolution elemental scans were 160

eV and 40 eV, respectively. Spectra were referenced to C-C/C-H at 284.8 eV for PP in the C 1s spectrum. Sample charge up was compensated by the built in neutraliser leading to an average shift of the C 1s peak maximum of 4 eV from the reference value of 284.8 eV.

Data reduction was performed by applying Casa XPS software<sup>96</sup> version 2.3.16. Background subtraction in the survey spectra was performed using the implemented routine with a Shirley background, as implemented in the Casa XPS software. Elemental concentration was calculated from the peak areas by using the sensitivity factors provided by the instrument manufacturer.

Spectra were fitted by assuming a Gaussian/Lorentzian-Sum-Shape (90/10) for all components. A variation of the position of the peak maximum of  $\pm 0.5$  eV was allowed for the binding energy of the spectrum components as well as a full width at half-maximum (FWHM) variation of  $\pm 2$  eV around a mean of 1.0, 1.6 and 1.6 eV for C 1s, N 1s & F 1s. In the case of the PP C-C peak, the FWHM was in the range 0.8-1.1 eV.

## 4.21 Computational Methods

### 4.21.1 Predicted 3D Structures of APs for the Prediction of the Concentration Required for a Monolayer

To calculate an estimate of the solution concentration required for one monolayer of AP on a substrate surface, the 3D volume of each AP was modelled on a cube, using coordinates calculated with *COSMOconf* software by *COSMOlogic* GmbH & Co KG (Germany). The energetically favourable lower energy conformer (in the gas phase) was used for the model.

An area of 8 x 8 cm was used, a 1:1 reaction stoichiometry was assumed, where a molecule of area  $x$  would react to one polymer of area  $x$ . The thickness of the film applied was selected as 5  $\mu\text{m}$ , representing the area and thickness covered by a dried coating after a doctor blade application method (used in Chapter 8). The 3D area of a TPD, TPDOH



or TPDCOOH molecule was predicted by computational means, using Cosmo where the energetically favoured conformer was assumed and the molecule was modelled as a cube where  $x=y=z$ .

### 4.21.2 Predicted Infrared (IR) Spectrum of TPD

The infrared spectroscopy (IR) spectrum of TPD was predicted using gas phase calculations (BASF SE, Germany), performed by density functional theory. The first step was to optimise several conformations of TPD to find the lowest energy conformer to calculate the predicted IR spectrum. First, the geometry of the molecule was optimised on BP86/def2-SV(P) level of theory using the Turbomole program suite (TURBOMOLE GmbH, Germany) with standard geometry optimisation criteria: scf-enry  $10^{-6}$ , gradient norm  $10^{-3}$ , max. comp. gradient norm:  $10^{-3}$ , RMS of change in geometry  $10^{-1}$ , max. change in geometry  $10^{-1}$ . This was then refined with a finer geometry optimisation with criteria:  $10^{-8}|10^{-4}|10^{-4}|10^{-2}|10^{-2}$  for the same quantities. Next a frequency calculation was carried out for this geometry on BP86/def2-SV(P) level of theory. This gave the frequencies and intensities of the predicted spectrum.

The lowest energy conformers that were calculated for Diaziridine and Diazirine (TPD) (used to calculate the predicted IR spectra) can be found in Appendix 10.I. The predicted IR vibrational spectra output for Diaziridine and Diazirine (TPD) are shown in Appendices 10.J and 10.K.

### 4.21.3 Predicted Singlet/Triplet States of Carbenes

To predict the excited electronic states of the three AP molecules (molecular structures shown in Figure 4.13), computational analysis of geometry optimisation for the singlet and triplet state ( $-N_2$ ) was first performed using BP86/def2-SVP level of theory (quantum chemistry). The energy difference between the two states was in favour of the triplet carbene for all 3 APs.

Next, an alternative method, requiring greater computational power, was used to

calculate the ground electronic states. The method was based on a previous study of an unsubstituted diazirine.<sup>155</sup> Multi-configurational self-consistent field theory (MCSCF) numbers were used with a small reference space and def2-SV(P) basis set, with the BP86/def2-SV(P)-optimised geometries (the MCSCF program was implemented in Gaussian software). This calculation method has the advantage of analysing many different arrangements of electrons in the spin orbitals. The energy difference between the two states calculated with MCSCF was also in favour of the triplet carbene for all 3 APs, thus both calculations were in agreement. Further details on the MCSCF theory for excited states can be found elsewhere.<sup>156</sup>

The results are shown in Appendix 10.L. For the initial geometry optimisation: the triplet carbene was favoured for TPD, TPDOH, TPDCOOH by  $-38.2 \text{ kJ mol}^{-1}$ ,  $-32.2 \text{ kJ mol}^{-1}$  and  $-47.1 \text{ kJ mol}^{-1}$ , respectively. For the MCSCF-numbers and def2-SV(P) basis set, the triplet carbene was also favoured for TPD, TPDOH, TPDCOOH by  $-27.9 \text{ kJ mol}^{-1}$ ,  $-15.3 \text{ kJ mol}^{-1}$  and  $-32.4 \text{ kJ mol}^{-1}$ , respectively.

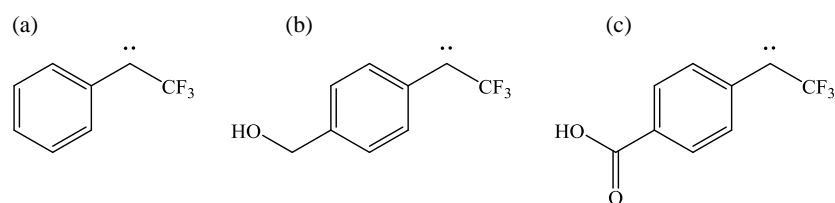


Figure 4.13: Molecular structures of the carbenes generated from (a) TPD, (b) TPDOH and (c) TPDCOOH, with the loss of  $\text{N}_2$ .

## 4.22 Temperature Measurement during UV Curing

The temperature change during UV curing was measured using a V-M.O.L.E Thermal Profiler by Electronic Controls Design Incorporated (USA).

## 4.23 Ultraviolet-Visible (UV-Vis) Spectroscopy

### 4.23.1 Thermal Degradation

Ultraviolet-visible spectroscopy (UV-Vis) was used to test the thermal degradation of AP solutions. A Varian Cary 5000 UV-Vis-NIR Spectrophotometer equipped with a temperature control was used. The temperature was controlled with the Varian software via an external temperature controller which drove a Peltier heat pump attached to the sample holder for both the sample and reference beams. Thermocouples in the sample holders were used to provide feedback to regulate the sample temperature.

AP solutions were prepared in toluene (b.p 110 – 111 °C) because a solvent with a higher boiling point than the experiment temperature (80/100 °C) was needed to avoid rapid evaporation of the solvent. To compensate for any pressure build up, a quartz cuvette closed with a septum sealed cap (Starna Scientific Limited, UK) was connected to a syringe and balloon, to which excess gas could escape.

The solutions were placed into the quartz cuvette and heated to the correct temperature. A blank measurement was taken at room temperature before the instrument measured the spectra over a set repeating period of time. The sample time was chosen depending on the measurement conditions. For example, less measurements were needed at 100 °C than 80 °C due to the higher rate of reaction. Sample measurement commenced once the required temperature was reached.

The same experiment was repeated at room temperature to test for any degradation in the room light and temperature. It was concluded no degradation of the solution occurred at room temperature in the time period of the experiment.

Calibration solutions were prepared and measured. Calibration curves were generated and the absorbance change with time was converted to the concentration change over time.

### 4.23.2 UV Degradation

To test the effect of UV power on the degradation of AP solutions over time, an external UV cabinet by MRC systems GmbH (Germany) was used. Samples were manually taken over time and the UV-Vis spectra were measured with an Ocean Optics (USA) UV-Vis USB 4000 detector. The UV cabinet was equipped with four Philips (Netherlands) Actinic TL 20W/10, G13 Lampholder, 590 mm length lamps with a  $\lambda_{max}$  at 370 nm and spectral output from  $\sim 340 - 400$  nm.

The power was varied from  $0.1 \text{ mW cm}^{-2}$  up to the maximum  $2 \text{ mW cm}^{-2}$ . The temperature was monitored and never exceeded  $30^\circ\text{C}$ .

The change in absorbance intensity was measured over time, and converted to a change in concentration over time using calibration curves. The relationship between the rate of reaction and the UV power was then investigated.

## 4.24 Nuclear Magnetic Resonance (NMR) Spectroscopy

Bruker NMR instruments (Bruker BioSpin GmbH, Germany) were used to record various types of nuclear magnetic resonance (NMR) spectroscopy:  $^1\text{H}$  NMR (500 MHz),  $^{13}\text{C}$  NMR (125 MHz),  $^{19}\text{F}$  NMR (376 MHz), 2D  $^1\text{H}$  COSY NMR (500 MHz) and 2D  $^1\text{H}$  NOESY NMR (500 MHz), respectively. The spectra were analysed using Mestrenova software, version 8.1 (Mestrelab Research, Spain).

## 4.25 Electron Paramagnetic Resonance Spectroscopy (EPR)

Electron paramagnetic resonance spectroscopy (EPR) was used to detect the formation of triplet carbenes (unpaired electron species) upon thermal or UV activation of TPDCOOH. The measurements were performed at the national EPR research facility at the University

of Manchester.

#### **4.25.1 UV Degradation**

The TPDCOOH sample was measured as provided (pure, white powder), being loaded into a 4 mm outside diameter (OD) quartz tube. Spectra were recorded using a Bruker (USA) EMX Micro spectrometer equipped with a Premium-X microwave bridge (9.87 GHz, X-band frequency) at room temperature (power 20 mW, 10 dB attenuation; 60 dB receiver gain, 4 G modulation amplitude). Two scans were recorded for each sample over the range 0 - 6800 G. The first sample was recorded with no irradiation, whereas the second sample was run after five minutes of irradiation using a 365 nm LED, guided by fibre-optic cable into the sample tube. This was maintained whilst running the spectrum.

#### **4.25.2 Thermal Degradation**

The sample was measured as provided, being loaded into a 4 mm OD quartz tube. Spectra were recorded using a Bruker (USA) EMX Micro spectrometer equipped with a Premium-X microwave bridge (9.87 GHz, X-band frequency). The power was varied between 2 mW and 20 mW; the attenuation varied between 10 dB and 20 dB; the receiver gain was tested between 10 dB and 60 dB; the modulation amplitude was set at 4 G. The temperature was set at 80 °C. Samples were also measured at 100 °C but no differences were observed.

### **4.26 Mass Spectrometry Techniques used for Solution Analysis**

**General** All experiments were carried out on a Micromass GCT instrument (Waters, USA) with an orthogonal acceleration time-of-flight (ToF) mass spectrometer, equipped with a HP6890 gas chromatograph and a Linden CMS (Germany) Liquid Injection Field Desorption (LIFDI) probe, respectively.

## **4.26.1 Gas Chromatography / Mass Spectrometry (GC/MS), Field Ionisation (FI) (Cool-on-Column Technique)**

### **4.26.1.1 Gas Chromatography**

The gas chromatography (GC) column used in this study was a 10-m ZB-1 HT (Zebron Inferno, Phenomenex USA) with 0.25  $\mu\text{m}$  film thickness and 0.25 mm inside diameter (ID) capillary (Zorbax), connected to a 0.53 mm x 10 cm guard column, which itself is connected to a cool-on-column (COC) injector. About 1  $\mu\text{m}$  of the sample was deposited via the COC injector directly into the guard column. The temperature of the GC-ToF interface was maintained at 250 °C. The initial GC oven temperature was typically controlled at 60 °C and ramped up to 250 °C at 80 °C/min to ensure the separation of low-boiling species and the elution of high-boiling molecules.

### **4.26.1.2 Field Ionisation (FI)**

Field ionisation (FI) is used to ionise molecules eluting from the GC. The FI emitter (CARBOTEC, Germany) consists of a 5  $\mu\text{m}$  tungsten wire onto which short carbon microneedles (length approx. 5  $\mu\text{m}$ ) have been grown. The FI emitter is carefully aligned with the end of the GC capillary column so that effluent molecules pass near the tips of the carbon dendrites. The emitter (at ground voltage) is approx. 2 mm away from a pair of extraction rods held at high potential (-12 kV), producing very high electric fields ( $10^7$ - $10^8$  V  $\text{cm}^{-1}$ ) around the tips of the carbon dendrites. It is generally believed that, under the influence of these fields an electron can be removed from the molecule via quantum tunneling effects, generating radical molecular ions with minimal fragmentation. The FI emitter current was typically set at 0 mA during the scan. The emitter is flashed by a current of 9 mA during an interscan cycle (0.3 s) to regenerate the emitter.

### 4.26.1.3 Time-of-Flight (ToF) Mass Spectrometry

Ions generated by FI are accelerated and focused into a pusher region of the ToF. A voltage pulse of 960 V is applied, ejecting ions orthogonal to the original ion path. The ion packet drift occurred through a ToF with a path length of approx. 0.45 m. A reflectron reflects ions back to a dual microchannel plate detector. Ion arrivals are recorded using a time-to-digital converter (TDC) with a sampling rate of 3.6 GHz. The voltage pulse is applied at a frequency of 30 kHz. A full spectrum is generated every 40  $\mu$ s. The mass range is normally set at 10-700 Da. The scan duration time / spectrum accumulation time is 1.2 s (*i.e.* every scan is an accumulation of 30,000 spectra).

### 4.26.1.4 Mass Scale Calibration

Perfluoro tributylamine (PFTBA, FC43) was used as a reference compound to calibrate a mass range from 50 to 614 Da. The calibrant was introduced into the ion source via a reference inlet and was pumped out after the calibration.

## 4.26.2 Positive Ionisation Mass Spectrometry (MS), (LIFDI)

### 4.26.2.1 Liquid Injection Field Desorption Ionisation (LIFDI)

LIFDI is used to ionise molecules which are dissolved in volatile solvents (in this work THF). The sample solution is introduced via a deactivated fused silica capillary (ID 50  $\mu$ m) and its droplets are deposited directly onto the carbon microneedles. After self-evaporation of the solvent (high vacuum,  $\sim 1^{-5}$  mbar), the analytes stay at the surface of the carbon dendrites. The field desorption (FD) emitter (Linden CMS GmbH, Germany) consists of a 13  $\mu$ m tungsten wire onto which long carbon microneedles (length approx. 60  $\mu$ m) have been grown. The FI emitter is carefully aligned to the extraction rods held at high potential (-12 kV), producing very high electric fields ( $10^7$ - $10^8$  V cm $^{-1}$ ) around the tips of the carbon dendrites. It is generally believed that, under the influence of these fields, an electron can be removed from the molecule via quantum tunneling effects,

followed by the desorption of the resulting radical molecular ions into the gas phase. An emitter heating current (ehc) can be applied to support the ionisation / desorption process. The ehc varies depending on the nature of the analytes, therefore, it was typically ramped from 0 - 100 mA during the data acquisition. The ramping rate was set manually and halted when higher currents of ion desorption occurred to avoid too much thermal influence. When an ehc ramp is applied, an emitter regeneration cycle is not possible. This was done at the end of the ramp at higher values of approx. 70-100 mA. Additional information about the LIFDI process can be found elsewhere.<sup>157</sup>

#### **4.26.2.2 Time-of-Flight Mass Spectrometry**

ToF mass spectrometry was performed as described in Section 4.26.1.3. The parameters were the same with the following exceptions. The voltage pulse is applied at a frequency of 16.7 kHz. A full spectrum is generated every 60  $\mu$ s. The mass range is normally set at 10 - 2000 Da. The scan duration time or spectrum accumulation time is 1.8 s (*i.e.* every scan is an accumulation of 30,000 spectra).

#### **4.26.2.3 Mass scale Calibration**

Mass scale calibration was performed as described in Section 4.26.1.4.

## **4.27 Infrared Spectroscopy (IR)**

### **4.27.1 Transmission Infrared Spectroscopy (IR)**

The IR spectra were recorded with 4  $\text{cm}^{-1}$  resolution, using a potassium bromide (KBr) window and Thermo Fischer Scientific (USA) 6700-2 Fourier Transform (FT) infrared spectrometer, equipped with a deuterated triglycine sulfate (DTGS) detector and a KBr beamsplitter.



#### **4.27.2 Attenuated Total Reflection Infrared Spectroscopy (ATR-IR)**

All ATR-IR spectra were recorded on a Nicolet Nexus FTIR spectrometer (ThermoScientific, USA) equipped with DTGS detector using a commercial Diamond-ATR unit (Smart Orbit, ThermoScientific, USA). Spectra were obtained by accumulating 32 scans at  $4\text{ cm}^{-1}$ . The angle of incidence and the active reflections were close to  $45^\circ$  and 1, respectively. The experiments were performed using unpolarized light. The ATR-IR measurements were carried out at room temperature.

#### **4.28 Raman Spectroscopy**

Raman spectra were obtained with a Witec alpha 300 R (Witec GmbH, Germany) spectrometer containing a green Nd:YAG (neodymium-doped yttrium aluminum garnet) laser (compass 315-50) of wavelength 532 nm, and power of  $\sim 25\text{ mW}$ .

#### **4.29 Colorimetry**

The yellowness of AP solutions was tested using a LICO 400 colorimeter (analisi, Belgium). The solutions were placed into 1 mm round cuvettes. The Hazen-Farbzahl method was selected (DIN ISO 6271, ASTM D 1209) and the measurements were calibrated against water (=0). The scale ranged from 0 - 1000.

#### **4.30 Differential Scanning Calorimetry (DSC)**

DSC is a technique in which the difference in energy inputs into a substance and a reference material is measured as a function of temperature, while the substance and reference material are subjected to a controlled temperature program.

The test method used complies with DIN 51007. A TA 800 heatflux DSC (Mettler,

USA) was used with a closed high-pressure glass cell. Liquid samples (TPD and TPDOH) were measured under a nitrogen atmosphere, whilst the white powder solid (TPDCOOH) was measured in air. An empty cell was used as a reference. The evaluated temperature range was 30 – 500 °C, the heating rate was 2.5 K min<sup>-1</sup> and the sensitivity was set at either 20 mW or 50 mW.

The *onset* temperature refers to the point at which a deflection from the established baseline is first observed.

The *peak temperature* corresponds to the maximum deflection of the DSC curve.

Peaks observed above the baseline refer to *exothermic* processes (chemical reactions accompanied by the evolution of heat).

## 4.31 Simultaneous Differential Scanning Calorimetry - Thermogravimetric Analysis (DSC - TGA)

The principles of DSC and thermogravimetric analysis (TGA) were combined by mounting the sample and the reference sensor system of a DSC instrument on either side of a TGA scale, thus enabling the simultaneous measurements of mass and enthalpy changes of a sample relative to an inert reference.

The test method complies with DIN 51006 and DIN 51007. A 449 C simultaneous thermal analyser (STA) (Netzch GmbH, Germany), which is a heat-flow differential scanning calorimeter combined with a compensating thermal balance, was used with an aluminium oxide (Al<sub>2</sub>O<sub>3</sub>) open crucible. An empty crucible was used as a reference. Liquid samples (TPD and TPDOH) were measured under a nitrogen atmosphere, whilst the white powder solid (TPDCOOH) was measured in air. A gas flow rate of 20.0 cm<sup>3</sup> min<sup>-1</sup> was used. The temperature range measured was 30 – 500 °C. The heating rate was 2.0 K min<sup>-1</sup>.

The principle behind DSC is described in Section 4.30. TGA is a technique in which the difference in mass change of a substance and reference material is measured as a function of temperature, while the substance and reference are subjected to a controlled

temperature program. The onset and peak temperatures were measured, as described above.

One disadvantage of the DSC-TGA measurement was that an open cell was required. Therefore, volatile substances such as TPD were likely to evaporate during the measurement, rendering the results inaccurate / unreliable.

### **4.32 Impact Sensitivity Drop-Weight Test**

Each AP was impacted by a drop-weight, falling from different given heights. It was observed whether the impact initiates explosive decomposition of the substance, as detected by a recognisable bang. This method is used in the chemical industry to determine the safety measures needed for different substances. The test method can be found in the EC Commission Directive 92/69/EEC, Annex A.14.

### **4.33 Synthesis of 3-phenyl-3-(trifluoromethyl)-3H- diazirine (*or* TPD)**

The details of the synthesis of TPD can be found in Appendix 10.M.

### **4.34 Reaction of Trimeric Isocyanate and TPDOH**

Basonat<sup>TM</sup>100, a solvent-free aliphatic polyisocyanate, was provided by BASF SE. TPDOH was supplied by TCI chemicals as described above. HI 100 (1.29 g, 15mmol) was mixed with 3 x TPDOH (0.5 g, 15mmol), and stirred in a bronze, foil-coated glass vial for 96 hours.

### **4.35 Exploratory Data Analysis**

A list of the data variable names that were tested can be found in Appendix 10.N.

### 4.35.1 Pearson and Spearman correlation analysis

The two lead responses tested were the CHT and the SJT, as shown in Table 4.2. The numerical ( $x_i$ ) factors (parameters controlled as part of the experimental design) are shown in Table 4.3 and the other numerical responses (parameters that were measured) are shown in Table 4.4.

The Pearson correlation coefficient was calculated using Equation 4.9. It was assumed that the data were linearly related and bivariate normally distributed.

$$r = \frac{n(\sum x_i y_j) - (\sum x_i)(\sum y_j)}{[n \sum x_i^2 - (\sum x_i)^2][n \sum y_j^2 - (\sum y_j)^2]} \quad (4.9)$$

The Spearman's rank-order correlation is the non-parametric version of the Pearson correlation. It was calculated using Equation 4.10, where  $d_i = x_i - y_i$  (the distance between two numbers in each pair of ranks) and  $n =$  the number of pairs of data. Spearman's correlation coefficient is a statistical measure of the strength of a monotonic relationship (no repeating data, *i.e.* no "ties") between paired data.

$$r = 1 - \left( \frac{6 \sum d_i^2}{n(n^2 - 1)} \right) \quad (4.10)$$

Both the Pearson and Spearman correlation coefficients were calculated and their values compared. Accordance between the Pearson and Spearman coefficient indicated "normality" of the data (a difference between the Pearson and Spearman coefficient would have indicated the presence of outliers / clusters, *i.e.* "non-normality").

The data were also checked visually by observing the bivariate scatter plots for  $y_j = mx_i + c$ , and the data were concluded reliable.

### 4.35.2 ANOVA and Kruskal-Wallis

Two lead responses were tested: the CHT and the SJT, as shown in Table 4.2. The categorical factors ( $x_i$ ) (parameters controlled as part of the experimental design) are

Table 4.2:  $y_j$  lead responses, for  $y_j=mx_i + c$ .

|                |                        |
|----------------|------------------------|
| Adhesion Tests | Cross-Hatch Test (CHT) |
|                | Steam Jet Test (SJT)   |

Table 4.3: Numerical  $x_i$  factors, for  $y_j=mx_i + c$ .

|   |  |
|---|--|
| Adhesion Promoter Application Variables | Concentration                            |
|   | Number of AP layers applied              |
|   | Temperature (in case of thermal cure)    |
|   | Time (in case of thermal cure)           |
|   | UV radiant exposure (in case of UV cure) |
| Substrate Variables                     | % EPDM                                   |

Table 4.4: Other numerical responses (App = application.)

|                             |   |
|-----------------------------|---|
| Adhesion Promoter Variables | F- Intensity (ToF-SIMS)                 |
|                             | F wt. % (XPS)                           |
|                             | Surface roughness Ra (after primer App) |
|                             | Surface Roughness Rq (after primer App) |
|                             | Polar S.E. (after primer App)           |
|                             | Dispersion S.E. (after primer App)      |
|                             | Total S.E. (after primer App)           |
| Substrate Variables         | Surface Roughness Ra                    |
|                             | Surface Roughness Rq                    |
|                             | Hardness                                |
|                             | Elastic Modulus                         |
|                             | Polar S.E. (untreated substrate)        |
|                             | Dispersion S.E. (untreated substrate)   |
|                             | Total S.E. (untreated substrate)        |

shown in Table 4.5. A summary of how the categorical data was split into lead responses, factors and levels, is shown in Figure 4.14.

Table 4.5: Categorical  $x_i$  factors

|   |  |
|---|--|
| Adhesion Promoter Application Variables | Adhesion Promoter Type                       |
|   | Application Method                           |
|   | Curing Method                                |
|   | Wash step (only performed on one experiment) |
| Substrate Variables                     | Substrate Type                               |
|   | Industrial or Research Substrate             |

Two principle statistical models were used to understand and explore the relationship between lead responses and potential categorical (text) factors ( $x_i$ ): analysis of variance (ANOVA) and Kruskal-Wallis. For visual representation of the data, boxplots were created.

The difference between the two methods is that ANOVA is a parametric test and Kruskal-Wallis is a non-parametric test. In simpler terms, non-parametric statistics do not assume the data / population follows a Gaussian (normal) distribution whereas parametric statistics do assume a Gaussian distribution. For example, if a school class took an exam under a time limit, non-parametric statistics could be used for assessing the order in which pupils completed the exam (1st, 2nd, 3rd etc.) and parametric statistics could be used for looking at the scores of the exams. Hence the order (or rank) of the values are used for non-parametric tests whereas the values themselves are used in parametric tests.

The two adhesion responses (CHT or SJT) in Table 4.2 and the numerical responses in Table 4.4 were experimentally determined. The ANOVA test was used to evaluate if the population means (of the data measured) were equal, so that the null hypothesis was  $H = \mu_1 = \mu_2 = \dots = \mu_k$ . It assumed the population variance was equal and that the data were normally distributed. Subsequently, an ANOVA F-test could give inaccurate results when the data were not normally distributed, therefore, the non-parametric Kruskal-Wallis test

was also used which is based on the ranks of the measurements and does not assume the data follows a normal distribution. However, it did assume population distributions of equal size and shape (skew in populations was not accounted for). The Kruskal-Wallis test ranks all the values from low to high, neglecting which group each value belonged to. The smallest number had a rank of 1 and the largest number had a rank of N, where N was the total number of values in all the groups. The null hypothesis of the Kruskal-Wallis test was that the samples were from identical populations.

The ANOVA F parameter was used to assess the variation within, and between groups, where a value of 1 indicated no variation, hence no adhesion effects. Values greater than one indicated increasing variance and deviation from the null hypothesis.

The Kruskal-Wallis P parameter was used to assess the variation between groups, where a low value indicated the populations had different distributions and was not due to random sampling, and a larger value indicated smaller effects.

Further details of how ANOVA and Kruskal-Wallis tests are performed and the parameters calculated can be found elsewhere.<sup>158</sup>

### **4.35.3 Rigorous Empirical Model Building using Stepwise Ordinary Least Squares (stepOLS) $y_j = g_j(x_i)$**

Stepwise ordinary least squares (stepOLS) is a method of regressing multiple variables while simultaneously removing those that aren't important.

Rigorous empirical model building using stepOLS, based on  $y_j = g_j(x_i)$ , was used to estimate and quantify the effect of predictors ( $x_i$ ) on the major responses: CHT and SJT.

Before the model was calculated, data with missing values were first omitted. StepOLS progressively calculates correlation coefficients, as demonstrated in Figure 4.15. For example, the cross-product terms are measuring the degree of interaction between two  $x_i$  variables, and the effect on the CHT / SJT result. The output of the models calculated for CHT and for SJT can be found in Appendix 10.O.

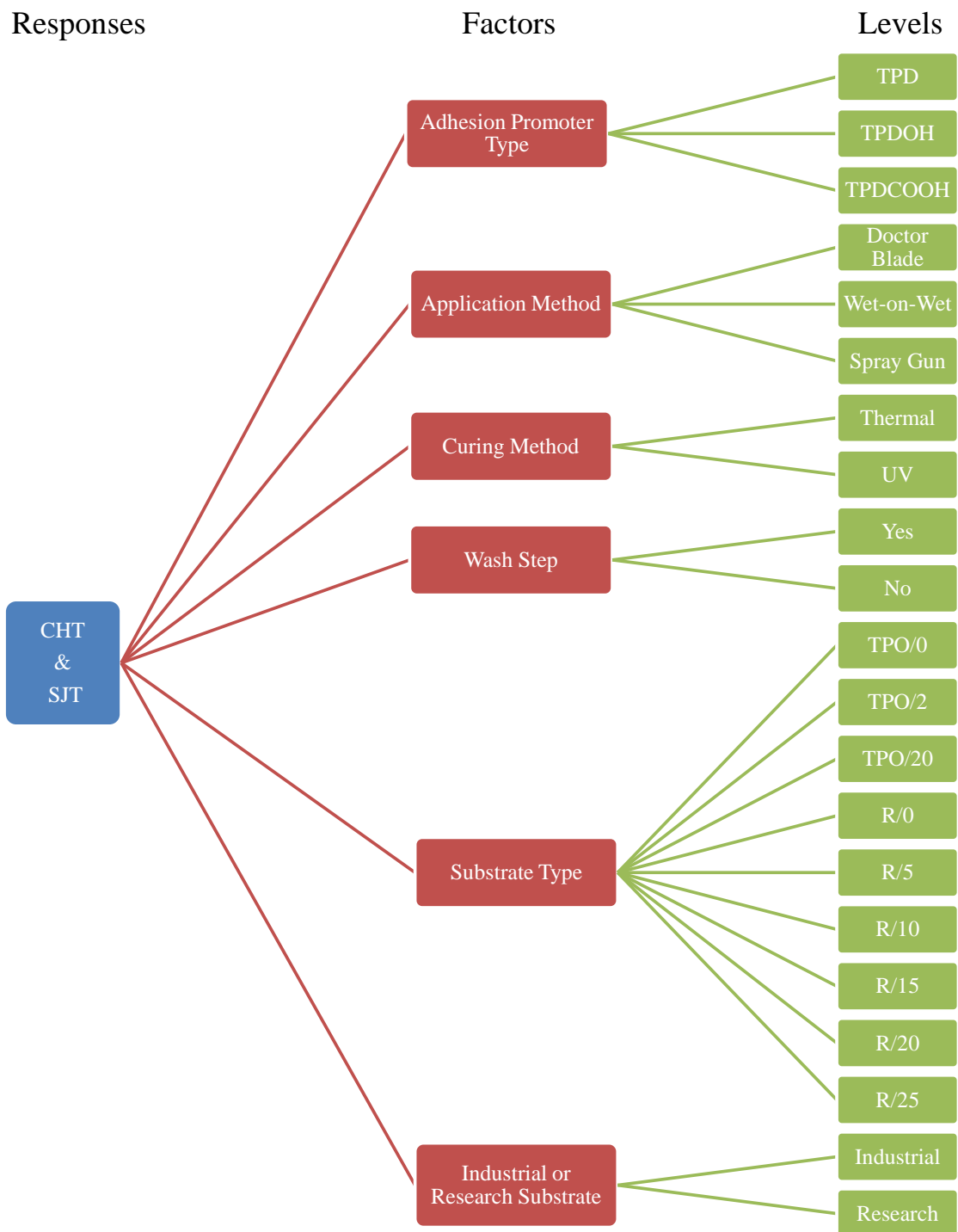


Figure 4.14: Hierarchical schematic diagram demonstrating the responses, factors and levels tested for categorical data.



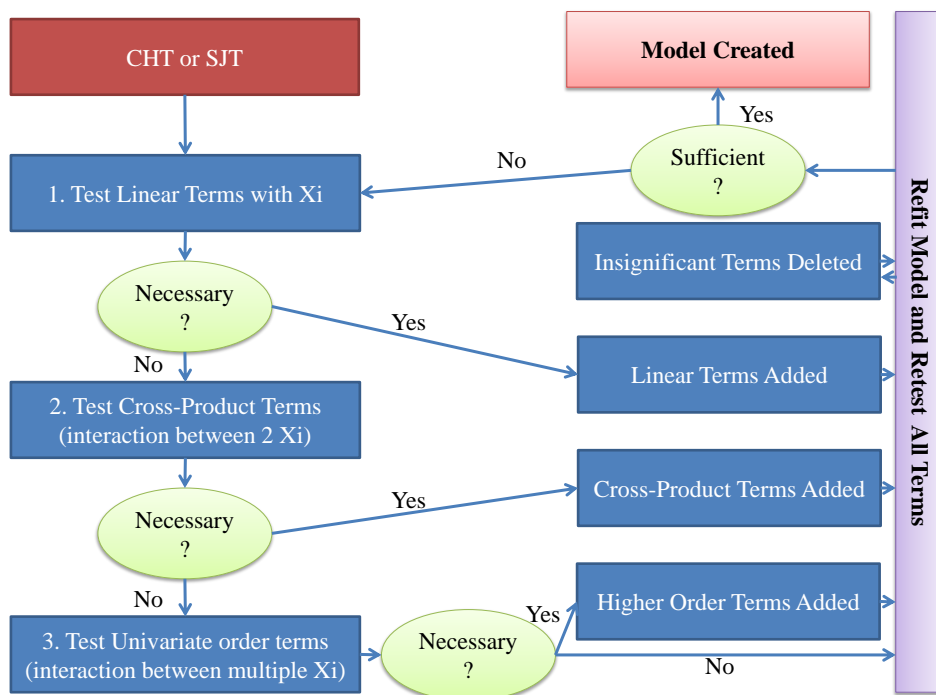


Figure 4.15: The stepwise Ordinary Least Squares (stepOLS) modelling process.

## Part III

# Results and Discussions

# Chapter 5

## SUBSTRATE CHARACTERISATION

### 5.1 Overview

An overview of this chapter to guide the reader through the results is shown in Figure 5.1. The main focus of this chapter was to predict the adhesive properties of various types of PP-based substrates, based on the characterisation of the surface and sub-surface properties (and the previous work of others discussed in Section 2.4). Additionally, the adhesive properties of flaming the substrates, and the use of a CPO AP were investigated, to be used as standards.

### 5.2 Introduction

Various research groups have linked surface and sub-surface properties of TPO substrates to the adhesion performance of applied coatings.<sup>3,67,68,72,73,73</sup> It is thought that the presence of an elastomer (such as EPDM) in a TPO substrate strongly influences the adhesive properties. Other surface properties such as chemical composition, surface roughness, surface free energy as well as the substrate hardness and Young's modulus, have all been previously linked to the paintability of TPO substrates, as discussed in Section 2.4.

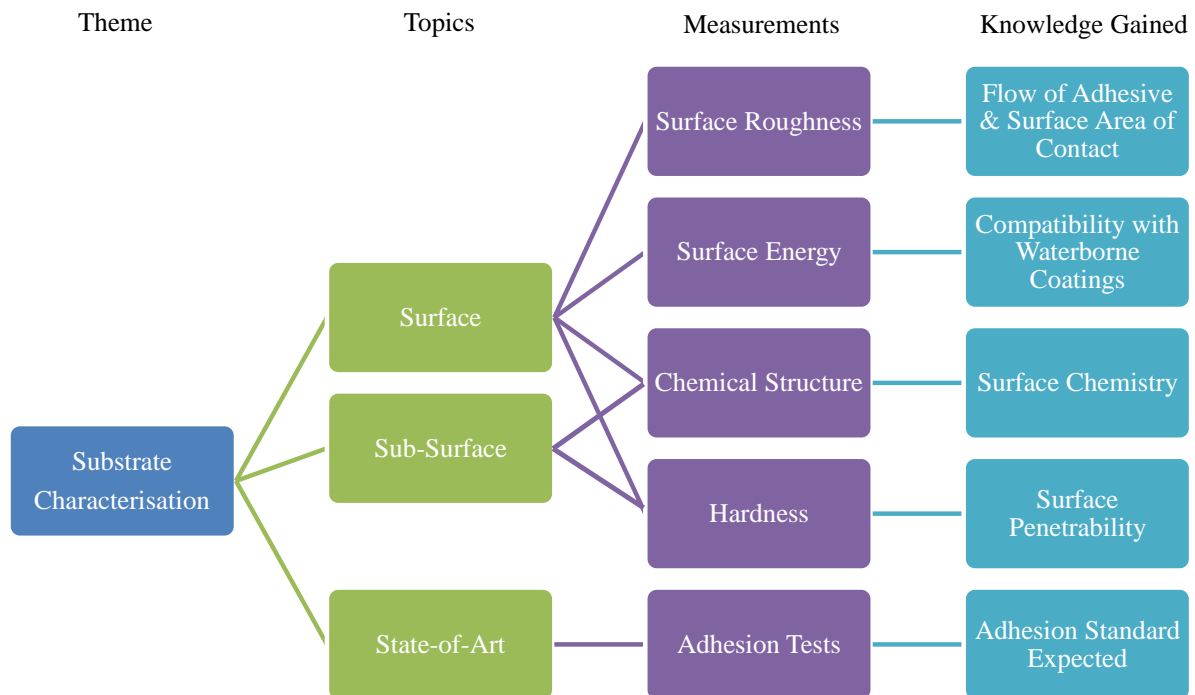


Figure 5.1: A summary of the substrate characterisation chapter.

## 5.3 Substrate Morphology

### 5.3.1 EPDM Mapping

#### 5.3.1.1 Untreated Substrates

As discussed in Section 2.4, literature suggests that EPDM effects the adhesion of polar coatings to TPO substrates. It is believed that CPO APs are able to anchor into the EPDM subsurface domains, which modifies the TPO surface, and increases the adhesion to waterborne coatings. Likewise, the flame pretreatment is more effective on TPO substrates containing EPDM. The double bonds within EPDM are broken by the flame, and the surface oxidises. Thus, the adhesion to waterborne coatings is improved. A method was therefore developed, to assess the microstructure of the substrates to locate the EPDM domains within the PP matrix. Based on these findings, hypotheses could be made predicting the adhesive behaviour of the substrates.

Literature suggests in co-extruded PP / EPDM injection moulded TPOs, the EPDM

often sits in domains in a sub-surface layer, having a significant effect on adhesion.<sup>45,64</sup> Therefore, to understand such adhesion mechanisms, the substrates used in this research project were fully characterised. Two dyes for staining EPDM, which have previously been used,<sup>104,105,108–110,159</sup> were tried and tested: OsO<sub>4</sub> and RuO<sub>4</sub>. Staining by OsO<sub>4</sub> is useful for TPO blends containing unsaturated elastomers because it reacts directly with double bonds (see Figure 5.2).<sup>109,160</sup> The reactions between polymers and RuO<sub>4</sub> are not as well understood. It is also an oxidising reaction but of a different mechanism. It is known that RuO<sub>4</sub> is capable of oxidising almost any hydrocarbon but it is able to penetrate and react with amorphous (lower density) regions at a faster rate than more crystalline, higher density areas. Therefore, higher electron density is generated at the sites of greatest oxidation rate (for example, amorphous EPDM regions), enabling a contrast in polymer blends to be observed in SEM and TEM.<sup>104</sup> Thus, EPDM is visible in the PP matrix of a PP / EPDM (TPO) polymer blend. Both methods were tried in this experiment (with correct safety procedures), however, a phase contrast was only observed with RuO<sub>4</sub>. This suggests the EPDM domains contained few double bonds, and was a saturated phase.

To analyse the distribution of EPDM, a series of four SEM measurements were taken for each substrate: the surface, and from the top of the cross-section down to the bottom.

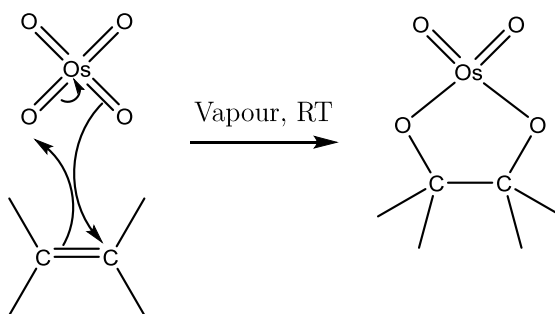


Figure 5.2: The oxidation reaction between osmium tetroxide and alkene double bonds, forming a five-membered ring: a cyclic osmate ester<sup>160</sup>

Figure 5.3 shows topographical micrographs of the  $\text{RuO}_4$  stained substrate cross-sections taken from the top part of the substrate cross-section, generated with SEM using back-scattered electrons to provide image contrast (areas of higher density, higher atomic number or smaller porosity appear brighter). An industrial TPO/0 substrate was used as a blank, and two industrial substrates were analysed: TPO/2 and TPO/20.

A description of the substrates can be found in Table 3.1. Globularly shaped EPDM domains were observed in both the TPO/2 and TPO/20 substrates, characterised by the presence of Ruthenium (Ru) from the dye, verified by EDX. They were found to have an interpenetration phase morphology structure (the EPDM interpenetrates with the PP).<sup>161–164</sup> The EPDM domains that were observed in SEM were not observed in the TEM micrographs collected.

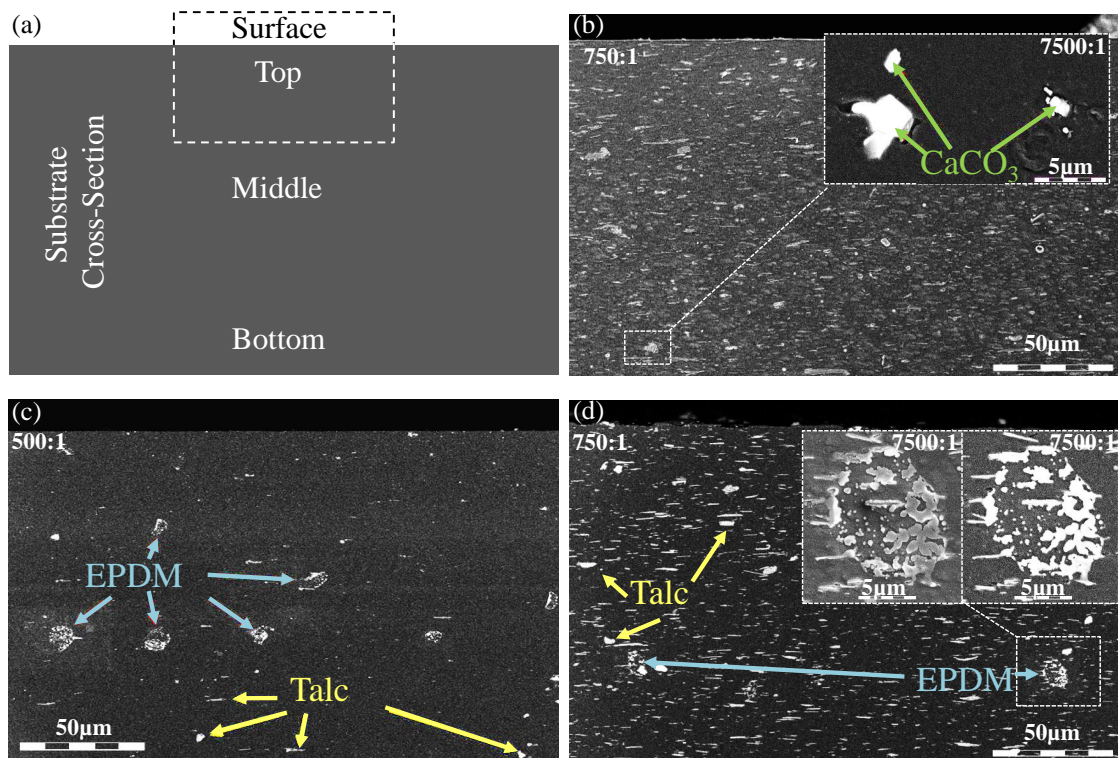


Figure 5.3: SEM micrographs of the top cross-section of ruthenium tetraoxide ( $\text{RuO}_4$ ) stained industrial substrates, schematically represented in (a), for (b) TPO/0, (c) TPO/2 and (d) TPO/20 (insert shows backscattered electrons on RHS) substrates.

The cross section of TPO/0 verified no EPDM domains were present. On the cross-section of the TPO/2, the EPDM domains were found to be inhomogeneously distributed, varying in size, with an average diameter of 10  $\mu\text{m}$ . Figure 5.3 (c) highlights five EPDM domains found at the top part of the cross-section. To calculate the approximate percentage (%) of EPDM coverage area, the SEM micrographs of TPO/2 were processed, as described in the Section 4.2. Figure 5.4 shows the traced outlines of EPDM regions and the approximate area coverage. The presence of the other additives in the TPO, which may contribute to the calculation makes verification of this prediction difficult, however, it could be observed that there was no significant accumulation of EPDM near the surface, contradicting the findings of Ryntz *et al.*<sup>29,30,45,64,66,67</sup> The distance between the EPDM domains varied between 50 - 100  $\mu\text{m}$ , explaining the reason why they were not observed in TEM (they were beyond the field of view). The presence of EPDM was also checked at the surface of the RuO<sub>4</sub> stained substrates but no evidence of EPDM on the surface was observed. Therefore, in the case of these industrial TPO substrates, it was expected that EPDM would have little effect on adhesion.

For the TPO/20 substrate (Figure 5.3 (d)), the EPDM domains were also found to be inhomogeneously distributed over the cross-section, with an average diameter of 1  $\mu\text{m}$ , smaller than that of TPO/2 (average diameter of 10  $\mu\text{m}$ ). Reasons for this are likely to be the large difference in EPDM content, or different processing conditions in which the substrates are manufactured and/or possibly the use of different grades of EPDM. It was unexpectedly found that compared to TPO/2, less EPDM was detected in TPO/20 and the EPDM distribution in the micrographs did not match the given composition. However, both samples contained a significant amount of calcium carbonate (CaCO<sub>3</sub>) and talc, which both also appear lighter in contrast to the PP matrix, and therefore likely hampered the interpretation of EPDM in the back-scattered micrographs. For this reason, the micrographs of TPO/20 were not processed to predict the % coverage area of EPDM. To eliminate the hindrance of other additives, substrates containing EPDM and only a mould releasing agent were analysed with SEM. The change of substrate morphology as

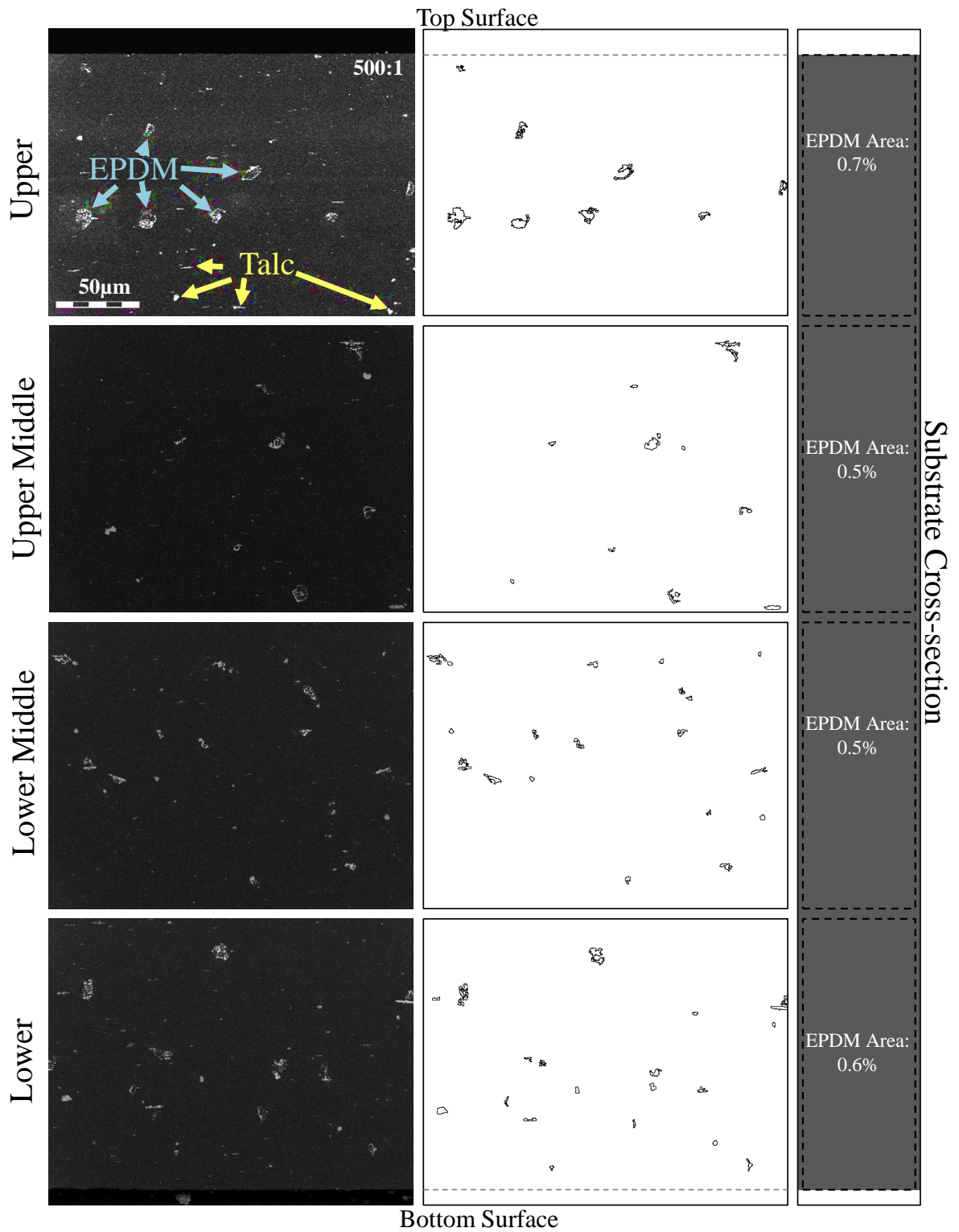


Figure 5.4: SEM micrographs (left) taken from the cross -section of a TPO/2 substrate and images showing the traced EPDM domains and % area coverage calculated (right).



the % of EPDM increased was investigated and checked against the structure previously described by Ryntz *et al.*<sup>29,30,45,64,66,67</sup>

The substrates in Figure 5.5 were manufactured for research purposes (they are not used in the automotive industry), to assess the influence of EPDM on adhesion. They contained varying percentages of EPDM (0 - 25 %) and were denoted as R/x, where x was the % of EPDM. The only extra additive used other than EPDM, was a mould-releasing agent needed for the production process. Again, RuO<sub>4</sub> was found to be the best staining method for the EPDM/PP contrast, and a combination of SEM and EDX was the best technique to view the topography and composition. All samples, with the exception of R/0 (blank), showed a clear visible phase separation between the PP matrix and the EPDM dispersed phase, which due to the RuO<sub>4</sub> staining, appeared bright in the image contrast (backscattered electron mode). EDX confirmed the lighter domains were the areas containing Ru from the dye. The blank substrate (R/0) verified the method.

Figure 5.5 shows that the EPDM was distributed inhomogeneously throughout the matrix of the substrates, whereas the bulk EPDM appeared more spherical. As the % of EPDM increased, elliptical shaped EPDM domains became more apparent towards the surface, due to the shear forces imposed during the injection mould process.<sup>45,64</sup> EPDM particle dimensions varied and were typically between 1 and 10  $\mu\text{m}$ , with some up to 50  $\mu\text{m}$ . No larger domains of EPDM could be seen in the cross-section of (R/25), suggesting a possible % of EPDM boundary at which only smaller domains were formed (however, further experiments are required to prove this).

The SEM micrographs were processed as described in Section 4.2, to calculate the approximate % area coverage of EPDM from the upper, middle and lower parts of the substrates. The SEM micrographs displayed in Figure 5.6 are from the upper part of the cross-section. The area of EPDM traced for calculation is displayed directly below each micrograph. The table in Figure 5.6 shows the % area of EPDM calculated for each part of the cross-section analysed. It was found that % area of EPDM calculated from each section of each substrate did not match that of the given composition. However, a clear

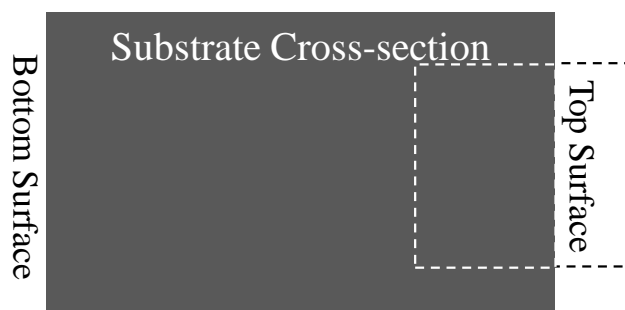
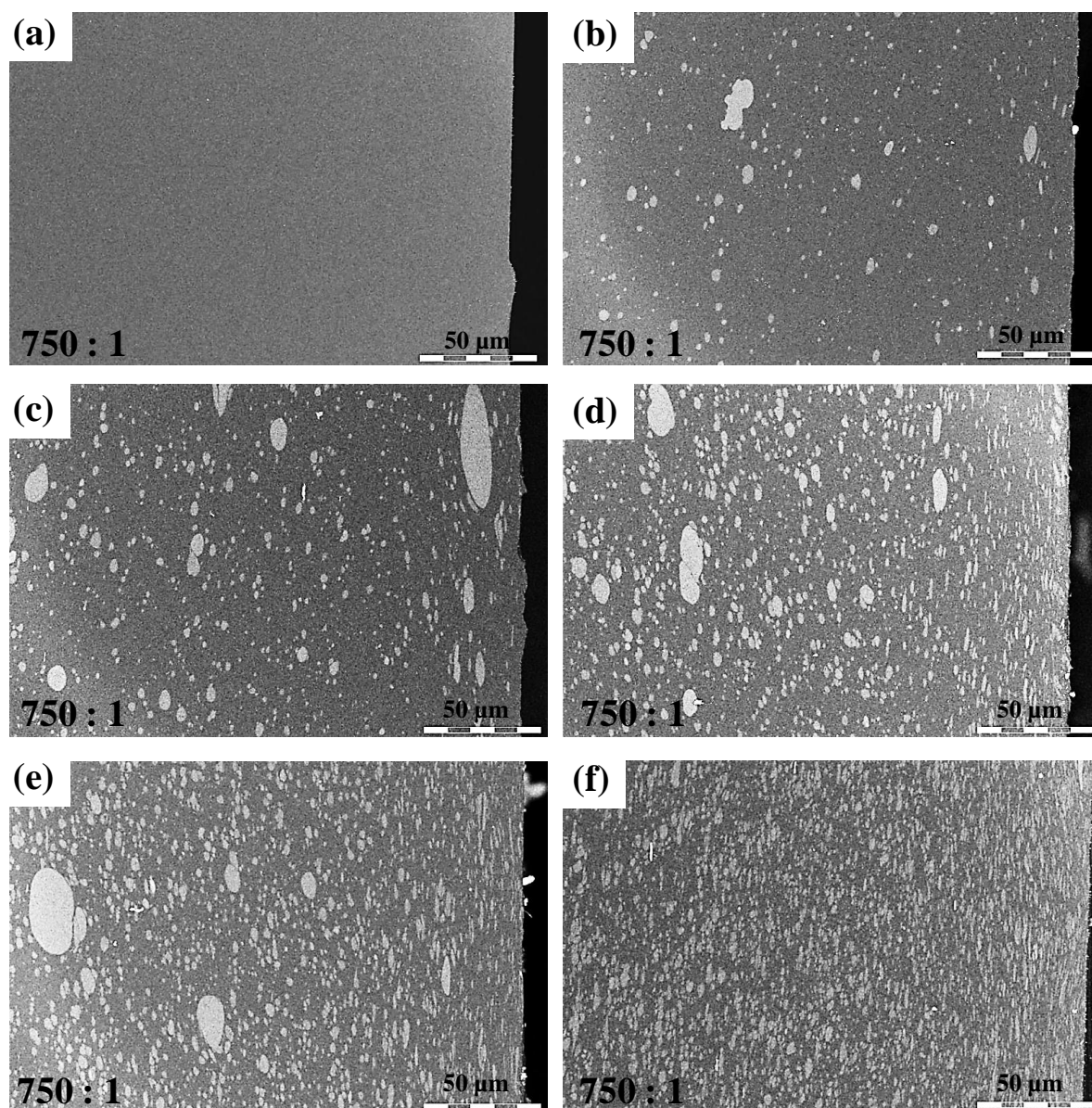


Figure 5.5: SEM micrographs of ruthenium tetroxide ( $\text{RuO}_4$ ) stained research PP substrates containing (a) R/0, (b) R/5, (c) R/10, (d) R/15, (e) R/20, (f) R/25, taken from the top part of the substrate cross section as shown in the schematic diagram.

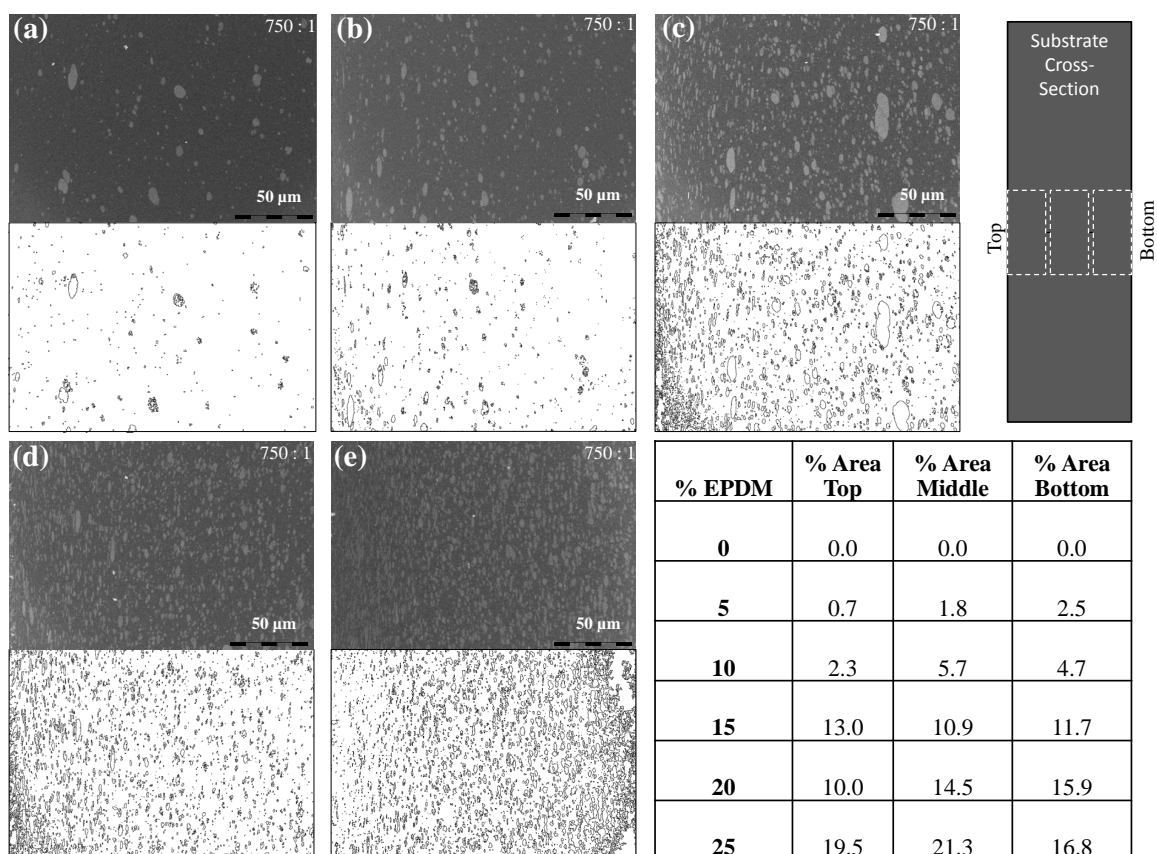


Figure 5.6: SEM micrographs of ruthenium tetroxide ( $\text{RuO}_4$ ) stained research PP substrates taken from the top cross-section, containing: (a) R/5, (b) R/10, (c) R/15, (d) R/20, (e) R/25 (top) and images of the subsequent traced EPDM domains (bottom). Table: % area coverage of EPDM for the top, middle and bottom cross-sectional areas as shown in the schematic diagram (top, right).

% area increase was observed as the given % of EPDM increased. Since EPDM is 3D in nature and these calculations are from a 2D image, the discrepancy in values could be due to the directional nature of EPDM. Perhaps in an alternative direction (*i.e.* a cross-section from an alternative plane), the % of EPDM would be greater. The irregularity of % areas calculated also confirmed the inhomogeneous nature of the substrates. As with the industrial TPOs, no significant accumulation of EPDM near the surface was observed, differing from the structures observed by Ryntz *et al.*<sup>29,30,45,64,66,67</sup> A difference between the injection moulding parameters used in this study and by Ryntz *et al.* could be a reason for the different morphologies observed.

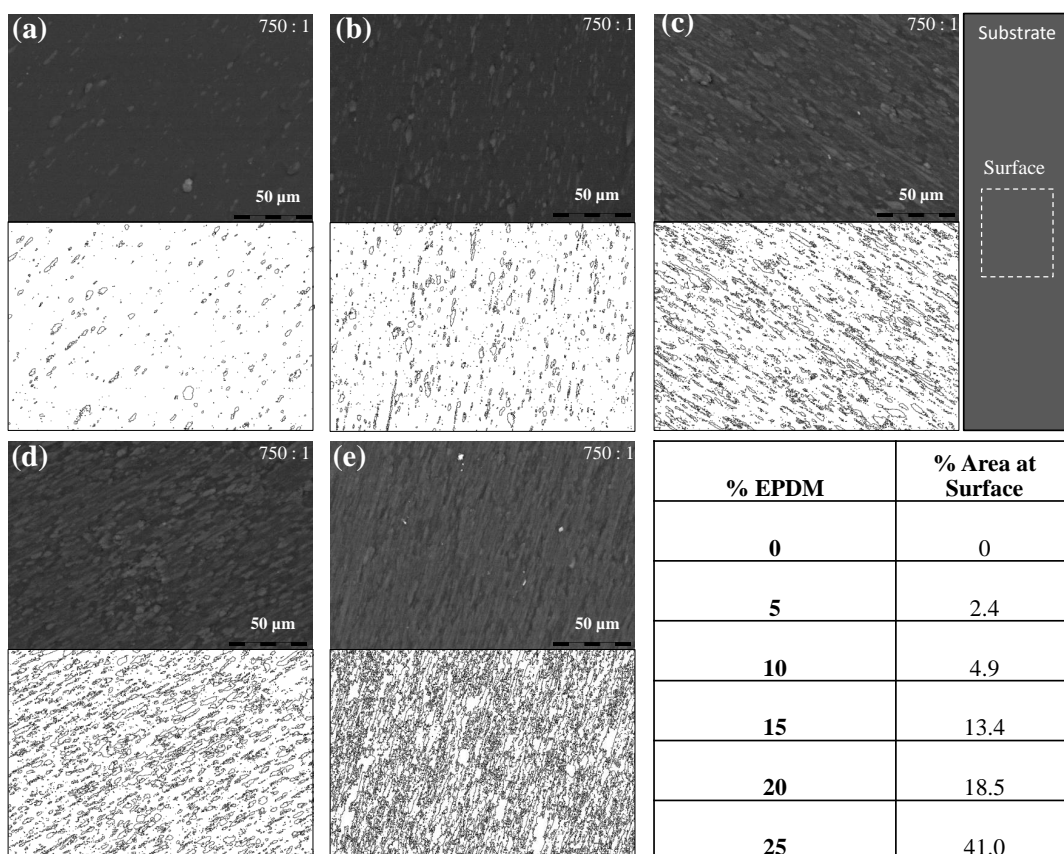


Figure 5.7: SEM micrographs of ruthenium tetraoxide stained research PP substrates taken from the surface, containing (a) R/5, (b) R/10, (c) R/15, (d) R/20, (e) R/25 (top) and images of the subsequent traced EPDM domains (bottom). Table: % area coverage of EPDM for the substrate surface, as shown in the schematic diagram (top, right).

Figure 5.7 shows the  $\text{RuO}_4$  stained SEM micrographs (top) and traced EPDM area coverage images (bottom) of each research substrate surface. Although not displayed, no image contrast was seen for the blank (R/0) substrate, verifying the method. No evidence of EPDM at or near the surface on the cross-section of the R/5 substrate could be seen in Figure 5.5(b), however, this was found not to be the case when looking at the stained surface of the substrate, as shown in Figure 5.7(a). A clear contrast between EPDM and the PP matrix was observed and the % of EPDM coverage was calculated to be 2.4 %.

All substrates were found to have EPDM domains at the surface (with the exception of R/0). As the given % of EPDM increased, the % area coverage of the substrate surface also increased. A clear difference in surface composition was seen between all substrates,

and from 10 - 25 % of EPDM, the direction of flow during the injection mould process became apparent as the EPDM domains were found to be directional and elliptical in nature (as previously described).

The calculation of the approximate area of EPDM coverage was found to be more problematic as the given % of EPDM increased due to the EPDM and PP phase becoming less distinguishable (may account for the large % of EPDM coverage area calculated for the 25 % EPDM substrate). However, the calculations indicate that adhesion was expected to increase with given % of EPDM, if the EPDM at the surface was a significant factor determining adhesion.

**Heat Treatment** It has previously been shown that heat treatment of a TPO substrate promotes EPDM migration.<sup>72,73</sup> This was important to analyse because the substrates were subjected to two heat treatments at 80 °C during the basecoat and clearcoat curing process (a ten minute treatment and a thirty minute treatment). When EPDM migrates towards the surface of the substrate, it may play a significant role in an adhesion mechanism. To test this theory, all three industrial substrates, and all six EPDM research substrates were subjected to a heat treatment at 80 °C for one hour, before being stained with RuO<sub>4</sub> and measured with SEM/EDX. No significant difference before and after treatment could be seen for all substrates, with the exception of the TPO/20. Before treatment, no EPDM was found at the surface, but Figure 5.8 shows that EPDM migration occurred during the heat treatment of the TPO/20 substrate. A large % of Ru (confirmed by EDX) was found at the white areas of the treated TPO/20 substrate, due to the stained EPDM domains. It was therefore hypothesised that if adhesion was significantly better for TPO/20 substrates compared to TPO/2 and TPO/0, it was likely that the heat treatment during the coating process caused EPDM migration, which played a role in the adhesion mechanism.

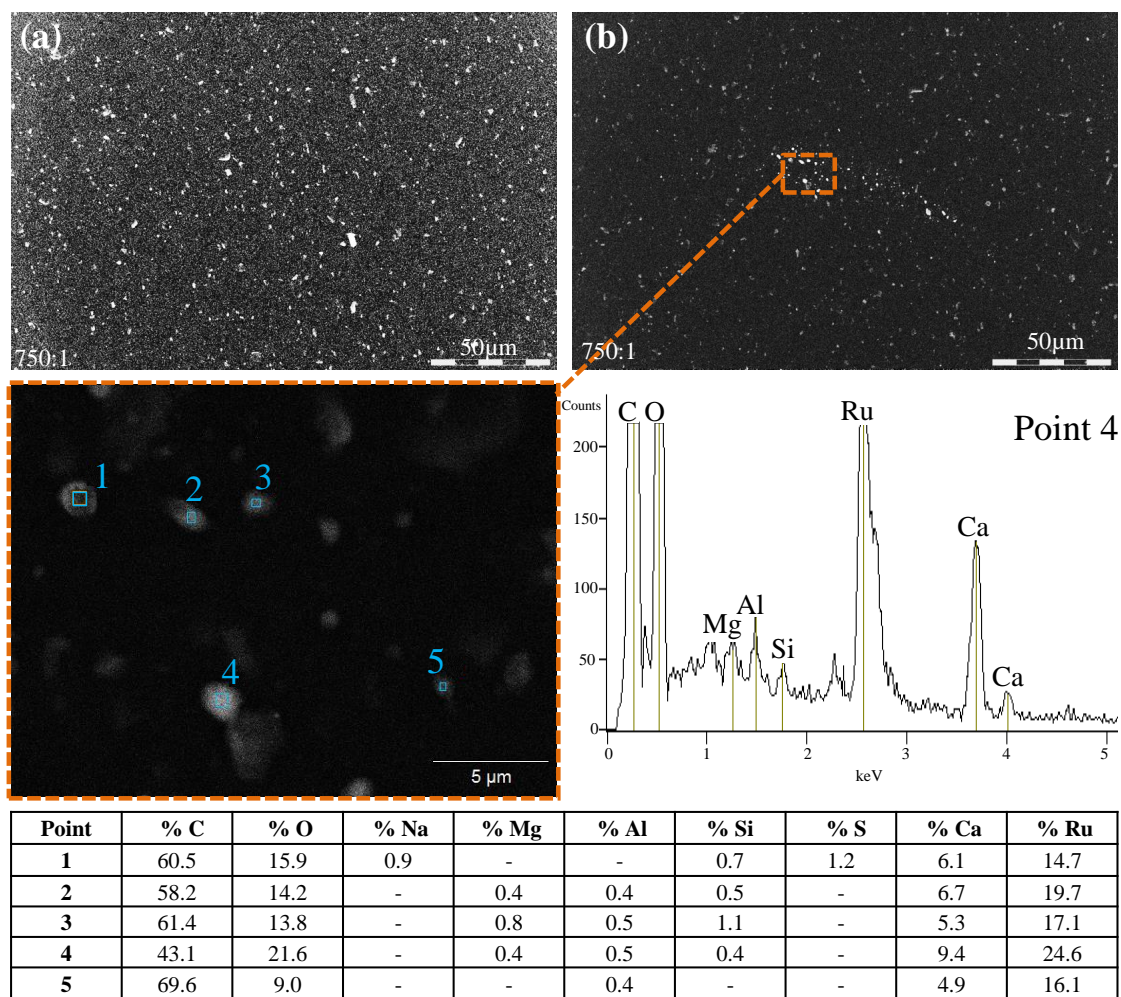


Figure 5.8: SEM micrographs of the surface of TPO/20 (a) before treatment and (b) after heat treatment at 80 °C for 1 hour. Inset: area of EPDM magnified. The EDX graph shows the chemical composition at point 4. The atomic % is displayed in the table (bottom) showing the presence of Ru (staining) on the areas appearing whiter in contrast, due to EPDM.

## 5.4 Physical Properties of Substrates

Further studies of the substrate properties can be found in Appendix 10.F. Hypotheses were made to predict the adhesion of a substrate based on the influence of the substrates surface roughness, chemical composition, mechanical properties (substrate hardness and Young's modulus) as well as the effect of abrasive and non-abrasive cleaning.

## 5.5 Thermodynamics: Surface Energy

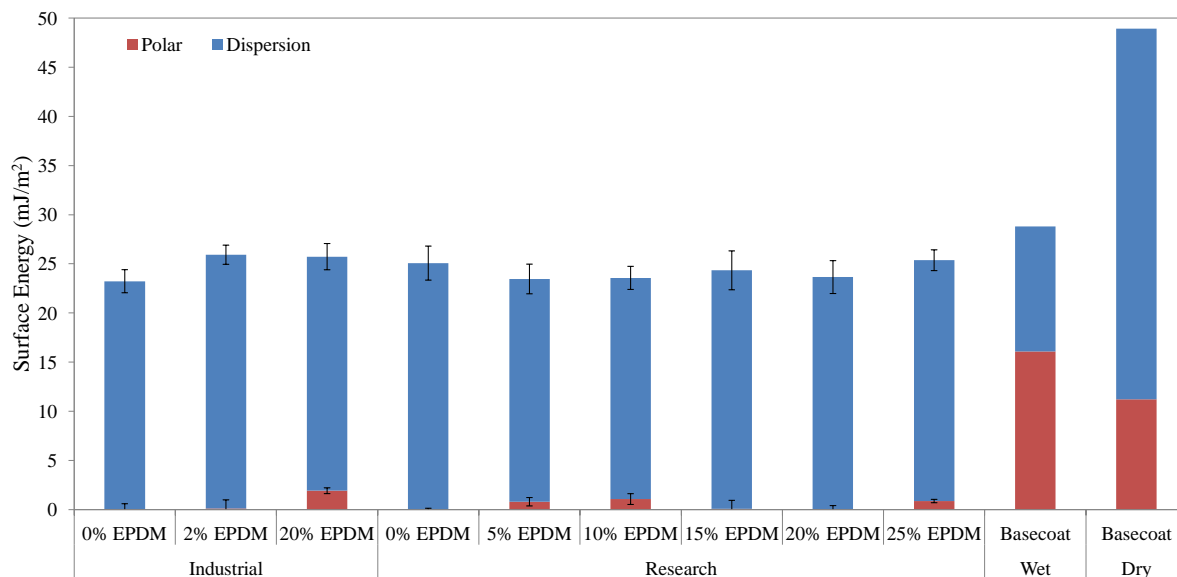


Figure 5.9: A bar graph representing the surface energy values of the labelled substrates and a waterborne basecoat before and after drying. All surface energy calculations were measured using the Owens-Wendt method, with the exception of the wet basecoat which was calculated using the Wu method.

The surface energy of a substrate depends on the chemical composition at the surface. As discussed in Section 1.1, the difference between the polar component of the surface energy of a substrate and a waterborne basecoat has been shown to be a significant factor determining the adhesion between the two surfaces. For example, a flame pre-treatment increases the polar component of a substrate, which then more closely matches to the polar component of the waterborne basecoat and good adhesion is obtained. The surface energy of each untreated substrate was therefore measured, to predict the adhesive properties of the surface and to investigate the influence of any additives present in the formulation.

The reliability of the surface energy measurements were confirmed with surface roughness parameters of the substrates, which were within the accepted range (it is difficult to measure the surface energy of a rough surface due to contact angle hysteresis).<sup>150,165–167</sup>

Figure 5.9 shows the surface energies of the industrial and research substrates alongside the surface energy of the wet and dry basecoat. The total surface energy did not differ

significantly between substrates within error. All substrates had a total surface energy of a value close to  $25 \text{ mJ m}^{-2}$ , which is a typical value for an inert, unreactive substrate.

The dispersive component (due to van der Waals forces) of the surface energy was found to be the main contributing component and all substrates had a low polar component. However, the industrial TPO/20 substrate, as well as the three research substrates R/5, R/10 and R/25, showed higher polar component values compared to the other substrates. The SEM micrographs (Section 5.3) of the substrate cross-sections, shown in Figure 5.3, showed more talc and  $\text{CaCO}_3$  present near the surface of the industrial TPO/20 substrate.

As discussed in Appendix 10.F.2, particles of talc have the shape of platelets due to the layered structure of the mineral. The basal surfaces are hydrophobic<sup>168,169</sup> and the edge surfaces are hydrophilic.<sup>170-173</sup> Therefore, the extra amount of talc observed in the TPO/20 substrate, could be a reason for the larger polar contribution observed compared to the other TPO substrates.

The  $\text{CaCO}_3$  particles are often coated with stearic acid<sup>174</sup> because they have a tendency to agglomerate in a TPO substrate (due to their large surface energy). This has the effect of lowering the surface energy of the particles. It was not known if the  $\text{CaCO}_3$  had been coated in the analysed substrates, however, the presence of uncoated  $\text{CaCO}_3$  at the surface of the TPO/20 substrate could also have been a reason for the higher polar component of the surface energy observed.

EPDM is reported to have a low surface energy of  $23 \text{ mJ m}^{-2}$  with a low polar component,<sup>175,176</sup> so it was unlikely that the EPDM contributed to the polar component of the substrate surface energy. Furthermore, Figure 5.7 showed an increase in % of EPDM at the surface of the substrates as the given % of EPDM of the substrates increased, but this trend was not observed for the polar component of the surface energy with increasing % of EPDM, also suggesting EPDM did not play a role in the increase of the polar component of the surface energy of the substrates.



Overall, the polar contribution from the untreated substrates was low when compared to the value of the waterborne basecoat (dry and wet). The surface energy difference was too large, thus the basecoat was not able to wet the surface of the substrates. This was found to be a main contributing factor which determined the poor adhesion observed between a waterborne basecoat and untreated substrate.

## **5.6 The State of the Art: Adhesion of Polar Coatings to Hydrophobic PP/EPDM (TPO) Substrates**

As discussed in Section 2.4, two state of the art techniques to improve adhesion of polar coatings to non-polar substrates are currently utilised in the automotive industry worldwide. One is a flaming pre-treatment that is used to oxidise the surface, increasing the interaction with subsequent applied coatings. The other is the use of liquid CPO APs, which are thought to mechanically interlock into the substrate surface, thus increase interactions with the subsequent coatings applied. They were discussed in greater detail in the literature review found in Section 2.4. Both of the state of the art techniques were tried and tested to find the correct parameters to obtain adhesion results that met industrial standards. These techniques were then used as adhesion test standards, to compare with newly developed APs.

### **5.6.1 Flaming Pre-treatment**

Flaming is the current state of the art technique used in the European automotive industry, as discussed in Section 2.3.1. It is used to physically modify the surface of the plastic via oxidation. Many oxygen-containing species on the surface are formed as a result of the flame. This makes the surface compatible with the waterborne basecoat, thus adhesion to an industrial standard TPO is significantly improved. The change in surface energy upon the flaming treatment, particularly of the polar component, has been shown to be a key contributing factor to the improvement of adhesion.

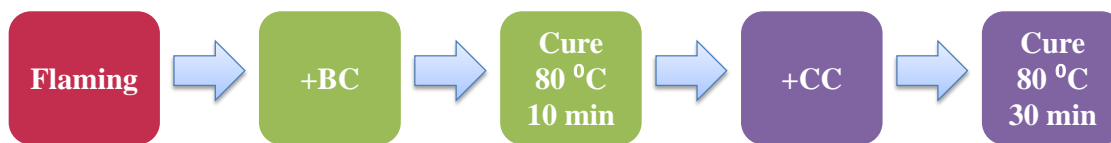


Figure 5.10: Steps of the coating application and curing process.

To predict the adhesion on a flamed substrate, and test the hypothesis of a higher polar component of the surface energy resulting in good adhesion, the surface energy was measured of all substrates before and after flaming. As a first test to assess the adhesion of the substrates before and after flaming, an ISO standard CHT was performed,<sup>85</sup> as described in Section 4.15. Before the adhesion test, all coatings were applied and cured, as shown in Figure 5.10 (no substrate cleaning procedures were used).

It was important to test the adhesion after all coatings had been applied and cured, because the adhesion was measured as a function of the whole system. For example, good adhesion between a treated substrate and a waterborne basecoat did not necessarily result in good adhesion after the top coat had been applied and cured. Furthermore, previous work by Ryntz *et al.* found that various topcoat attributes effected the adhesion of a CPO AP applied as a thin layer onto a TPO substrate.<sup>64</sup> However, it was not an individual property that affected the overall adhesion, but rather the whole *system* attributes.

The coatings were left to post-cure for 7 days after the final topcoat was applied, prior to the adhesion tests. Figure 5.11 shows the setup of the cross-hatch test (CHT). Tesa<sup>®</sup> tape was applied to a grid on the coated surface, created by a 8-bladed knife, and manually pulled away to assess the adhesion (number of squares delaminated), as described in Section 4.15. The % of squares remaining in the grid determined the grade of adhesion: 5 was the worst (0 % adhesion) and 0 was the best (100 % adhesion). When good adhesion was obtained with the CHT, a further SJT test with Daimler-Chrysler specifications was performed, as described in Section 4.16. When no delamination of the painted layer was visible, the paint adhesion was considered as sufficient, meeting the required industrial standards set by Daimler-Chrysler.

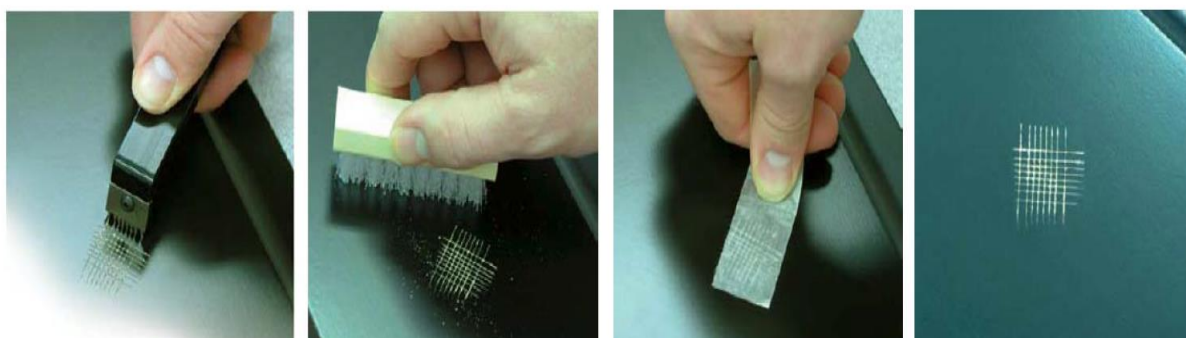


Figure 5.11: Photographs displaying the cross-hatch test (adhesion test) procedure. Reproduced with permission from BASF Coatings GmbH.

The surface energy measurements taken of the flamed and untreated substrates are shown in Figure 5.12. The flaming pre-treatment was carried out on all types of substrates using laboratory equipment with a setup shown in the schematic diagram in Figure 4.5. The errors were calculated using maximum and minimum contact angles of the three test liquids, as described in Section 4.5.1. As expected, it was found that the flaming treatment significantly increased the overall surface energy of the substrates compared to the untreated substrates. The increase in the polar component of the surface energy was the greatest contributing factor, caused by the new oxygen containing species that were created on the surface of the plastic substrate during the flaming treatment.

The results of the CHT and SJT from before and after flaming are displayed in Table 5.1. A correlation between the results of the CHT and the SJT was observed, and in general, a poor CHT usually resulted in a poor SJT for the same flaming conditions. The research substrates containing EPDM produced the best adhesion results compared to the industrial TPO substrates. The substrate that produced the best results out of all the substrates was the R/15 substrate, with a CHT score of 0 and a SJT score of 1 (for the grading of the CHT and SJT, see Section 4.15 and Section 4.16). It was evident from the surface energy result of the 15 % EPDM research substrate after flaming (shown in Figure 5.12), as to why the adhesion was greatly improved. The increase in polar component of the surface energy was the greatest compared to all other substrates, and the value was the closest match to the polar component of the wet basecoat. Therefore, when the

Table 5.1: Adhesion results before and after flaming pre-treatment. The basecoat and topcoat were dried at 80 °C for 10 minutes and 30 minutes respectively. All adhesion tests were performed after a 7 day post-cure period after the topcoat was applied.

| Substrate                   | % EPDM | CHT | SJT |
|-----------------------------|--------|-----|-----|
| <b>Industrial</b>           | 0      | 5   | 4   |
|                             | 2      | 5   | 4   |
|                             | 20     | 5   | 4   |
| <b>Research</b>             | 0      | 5   | 4   |
|                             | 5      | 1   | 1   |
|                             | 10     | 1   | 1   |
|                             | 15     | 0   | 1   |
|                             | 20     | 1   | 2   |
|                             | 25     | 1   | 1   |
| <b>Untreated Substrates</b> |        | 5   | 5   |

waterborne basecoat was applied to the flamed surface, it was able to wet the surface enabling the greatest interfacial contact between the substrate surface and the coating surface, thus maximising the interaction between the surfaces and optimising adhesion.

ToF-SIMS data shown in Figure 5.13, shows the relative intensities of oxygen ( $O^-$ ) and hydroxyl groups ( $OH^-$ ) found at the surface of the R/15 substrate before and after flaming, and 6 hours after the flaming treatment, to test any immediate ageing effects. Evidence of the oxygen containing species were found on the untreated substrate surface, showing that oxidation of the substrate had occurred. Polymer surfaces usually undergo this undesired oxidative effect which can occur during manufacturing (moulding), storage, processing, handling or exposure to UV light.<sup>48</sup> However, a significant increase in  $O^-$  and  $OH^-$  intensity occurred upon flaming. It is thought that hydrogen bonding between the waterborne basecoat and -OH groups at the flamed substrate surface was the main contributing interaction which improved the adhesion at the interface.<sup>53,54,102</sup> As previously reported,<sup>177</sup> no significant ageing effects were found.

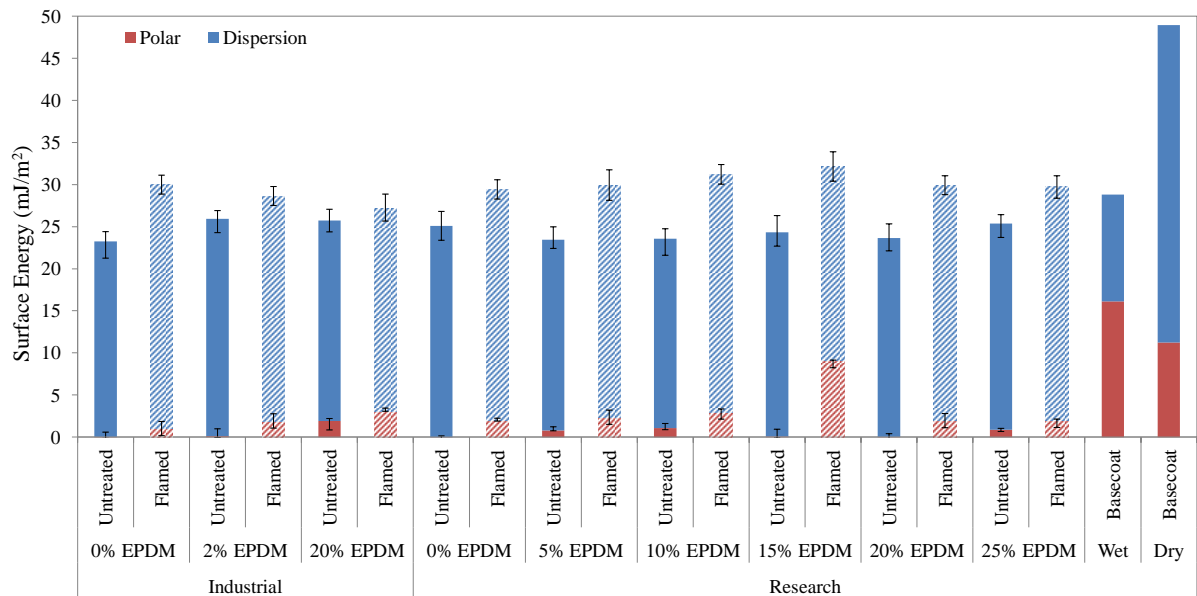


Figure 5.12: A bar graph representing the surface energy values of the labelled substrates before and after flaming and a waterborne basecoat before and after drying. All surface energy calculations were measured using the Owens-Wendt method, with the exception of the wet basecoat which was calculated using the Wu method.

It was not clear why the R/15 substrate gave the largest increase in polar component of the surface energy after flaming, because no significant difference between the microstructure of the R/15 and other research substrates was observed (the surface morphology, chemical composition, surface roughness, mechanical properties and surface energy before treatment were all analysed). Thus, no unique properties of R/15 had been found, so it was likely that a combination of properties determined the adhesion, rather than one single property.

One possible reason for the better adhesion results obtained for R/15, could have been that the substrate hardness and Young's modulus were optimum values. The adhesion tests on the softer substrates could have lead to cohesive failure within the substrates. The harder substrates (found to have a lower surface roughness) could have resulted in a lower depth of oxidation during flaming, or lower surface area of oxidation, resulting in a lower amount of hydroxyl groups (considered the main promoter of paint adhesion).<sup>102</sup>

Although the R/15 substrate gave the best adhesion results after flaming, evidence of a small delamination after the SJT was observed. Overall, none of the substrates produced

a non-damaged surface after the SJT. The Daimler-Chrysler SJT is a very tough adhesion test, designed to mimic a car wash applying steam and pressure to an already damaged coated surface, and it is difficult to achieve 100 % adhesion with this test.<sup>87</sup> Varying the flame parameters could have resulted in a greater SJT result, however, the flaming parameters that were selected (described in Section 4.7) are those typically used in the industry and were therefore chosen as a standard. Based on the results, the flamed R/15 substrate was selected to be the standard benchmark test, to compare with adhesion results from novel APs.

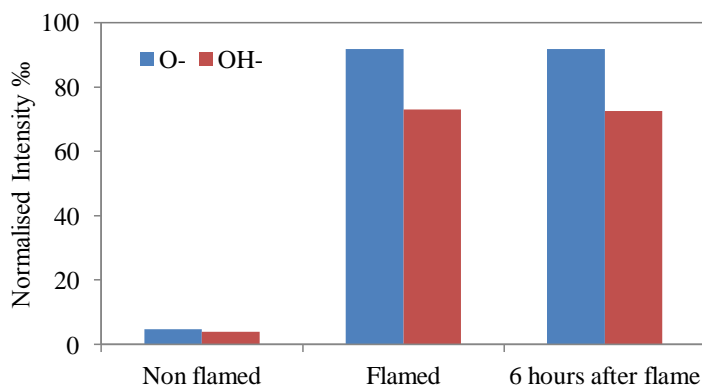


Figure 5.13: Normalised negative ToF-SIMS data taken from a R/15 research substrate before and after flaming, and 6 hours after the flaming treatment.

## 5.6.2 CPO Adhesion Promoters

A second state of the art used in the industry to improve the adhesion between TPO substrates and waterborne basecoats, is the use of CPO APs, as described in Section 2.3.2 (although, as previously mentioned, their use in Europe is limited due to the change in environmental laws<sup>6</sup>). One type of CPO, supplied by Eastman, was tried and tested to be used as a second standard benchmark ( in conjunction with a flamed substrate) to compare with the adhesion of novel APs. Many papers that focus on understanding the mechanism of adhesion with CPOs can be found.<sup>29,30,45,64,66–68</sup> The mechanism is a subject of speculation and is a complex topic. More details of the postulated mechanisms

can be found in the Literature review, Chapter 2.3.2.

Only one substrate type was tested (TPO/2, industrial and containing EPDM which may improve CPO adhesive properties<sup>3,45,64</sup> as discussed in Section 2.4.2) and research effort was focused on finding the correct curing conditions to achieve good adhesion with the CPO. It was reported that some types of CPO are able to penetrate into the substrate surface, enabling a physical-mechanical interlocking-type adhesion mechanism. A cross-sectional analysis of the cured substrate was performed using ToF-SIMS to analyse the adhesion characteristics and generate ideas for new APs based on the same mechanism.

Although CPO APs can be used as an additive for a coating formulation, the best results were obtained by applying the CPO directly to the substrate as a primer, followed by the subsequent basecoat and topcoat.<sup>178</sup> It was recommended in the CPO product specification<sup>178</sup> that the CPO worked best when prepared as a 8 - 10 % solid solution. However, 8 %, 9 % and 10 % solid solutions were tested, and no good adhesion was obtained. The application method was likely the reason for this, as preliminary tests were done using a Doctor blade to apply the coatings, whereas the spray gun application often yields the best results due to better controllability.

When the solution was applied as 40 wt.% solids in xylene, improved adhesion results were obtained. Several primer layer thicknesses and two curing conditions were tested: applying the CPO primer and allowing it to dry at 80 °C for ten minutes or applying the CPO and basecoat wet-on-wet (that is, the basecoat is applied without drying the CPO primer layer first). The results are shown in Table 5.2. Only the CHT was performed, however, this was sufficient for having a standard for preliminary tests. The optimum thickness for adhesion was found to be a 4  $\mu\text{m}$  wet thickness and the wet-on-wet application method was found to be the best curing condition, giving a CHT grade of 0. It was not unexpected for the thicker primer layers to have poor adhesion because cohesive failure occurred within the CPO primer layer itself.<sup>70</sup>

The cross-sectional image generated by ToF-SIMS of the TPO/CPO/basecoat/topcoat is displayed in Figure 5.14. An additional layer is present: an epoxy-glue on top of the

Table 5.2: CHT adhesion results from before and after CPO (40 % solids in xylene) primer application. The CPO was applied with varying thickness's and dried at 80 °C for 10 minutes or applied wet-on-wet with the basecoat. The basecoat and topcoat were dried at 80 °C for 10 minutes and 30 minutes respectively. All CHT tests were performed after a 7 day post-cure period after the topcoat was applied.

| CPO Primer Thickness ( $\mu\text{m}$ ) |            | CHT             |                    |
|--|------------|-----------------|--------------------|
| Wet                                    | Dry        | Applied & Dried | Applied Wet-on-Wet |
| 4                                      | 2.9 – 3.0  | 5               | 0                  |
| 6                                      | 5.2 – 6.3  | 5               | 1                  |
| 12                                     | 7.9 – 8.0  | 5               | 5                  |
| 24                                     | 9.2 – 12.2 | 5               | 5                  |
| Untreated Substrate                    |            | 5               |                    |

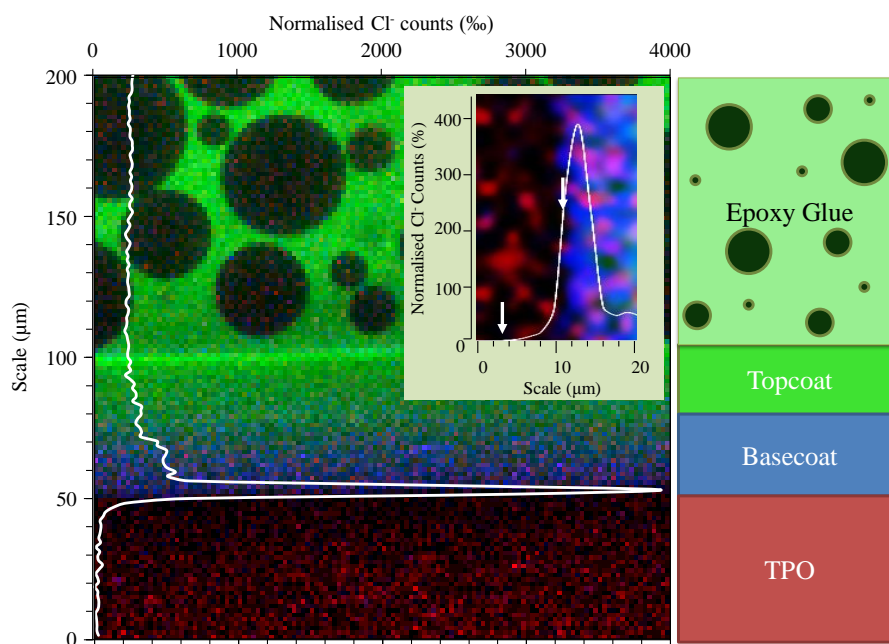


Figure 5.14: Left: Negative, high lateral resolution mode ToF-SIMS image of a  $200 \mu\text{m}^2$  area taken from a cross section of TPO/CPO/basecoat/topcoat/epoxy-glye substrate, cut with a cryo-microtome; Graph overlay: Line graph showing the chloride ( $\text{Cl}^-$ ) ion distribution across the coatings; Image overlay: Magnified cross-section showing the  $\text{Cl}^-$  diffusion into the TPO and basecoat. Right: Schematic diagram showing the positioning of the layered coatings. ToF-SIMS data were normalised to the total ion count. Image resolution is  $1.6 \mu\text{m}/\text{pixel}$ .



topcoat which was applied only for the microtome cutting process. Individual images and characterisations were made for each layer, and a characteristic, unique mass peak was identified in the ToF-SIMS spectrum to differentiate the topcoat, basecoat, CPO and TPO substrate. The image was generated by a 3-colour scheme which was implemented in the ToF-SIMS software, differentiating the TPO, basecoat and topcoat, as demonstrated in the schematic diagram. The CPO  $\text{Cl}^-$  ion intensity is shown as a line graph overlaying the image. The white arrows shown on the magnified image of the CPO distribution highlight the boundaries where the CPO may have penetrated into the TPO substrate.

Although, the  $1.6 \mu\text{m}/\text{pixel}$  resolution limits the information available, the results suggest CPO penetrated into the TPO by  $\sim 6 - 8 \mu\text{m}$ , similar to that found by Ryntz *et al.*<sup>28</sup> and others.<sup>179</sup> The penetration depth and diffusion rate of a CPO primer was previously found to be dependent on the CPO molecular weight and molecular weight distribution, as well as the degree of chlorination, maleation and crystallinity.<sup>28,67,180</sup> Comparing the experimental results with the literature results suggests there was no effect of the CPO layer thickness on the penetration depth as the thicknesses were different in each study:  $10 - 15 \mu\text{m}$ ,<sup>28</sup>  $50 \mu\text{m}$ <sup>179</sup> and  $4 \mu\text{m}$  in this study.

The mechanism of how the CPO APs improve adhesion has been speculated on over the last several years. Clemens *et al.*<sup>70</sup> also used ToF-SIMS as well as XPS and TEM analysis, to attempt to elucidate an adhesion mechanism. It was determined that CPO primers did not penetrate deeply into the PP and TPO substrates, and that adhesion was likely to be due to the improved wetting of the substrate allowing for sufficient dispersion interactions. However, several publications by Ryntz *et al.*<sup>28,45,64,69,71</sup> suggest penetration of CPO via solvent swelling and chain entanglement into the TPO substrate plays a key role in the adhesion mechanism. The results obtained in Figure 5.14 suggest a similar model, however, further work using an alternative method with higher lateral resolution to analyse the cross-section would be required to verify the data obtained (this was not the focus of this study).

## 5.7 Conclusions

One of the main influences on the adhesion of a TPO substrate cited in literature was the EPDM content. Therefore, this was the first investigation. The characterisation of the substrates to determine the EPDM content showed that the domains were inhomogeneously distributed and only little amounts were present in a subsurface layer, which differed to the model previously suggested by Ryntz *et al.* It was thought that a difference in the processing conditions used to produce the injection-moulded substrates was the main cause of the differences observed. Predicting the adhesion behaviour of a substrate based on the given % of EPDM was therefore challenging, due to the inhomogeneity of each substrate.

Based on the characterisation of the substrates used in this study (in addition, see Appendix 10.F), several hypotheses were made for determining the substrate characteristics that would lead to greater adhesion. Better adhesion results were expected for:

- Research substrates with EPDM present at the surface: the AP is able to penetrate into the EPDM domains causing polymer chain entanglement (mechanical adhesion mechanism)
- TPO/20 substrate during thermal curing: EPDM migrates to the substrate surface, allowing the AP to penetrate into the EPDM domains, causing polymer chain entanglement (mechanical adhesion mechanism)
- Substrates containing EPDM or additives: creates a higher surface roughness which allows for a higher contact area between the substrate and AP / basecoat, or substrates have a lower hardness and Young's modulus to allow an AP to penetrate into the substrate surface causing a polymer chain entanglement (mechanical adhesion mechanism)
- Substrates with CaCO<sub>3</sub> and talc present at the surface: chemical reactions or interactions with AP or basecoat (chemical adhesion mechanism)

- Substrates without the Irgafos 168 additive present at the surface → its hydrophobic and bulky nature causes steric hindrances with the AP or basecoat
- TPO substrates: they have a lower hardness and Young's modulus, which enables the AP, solvent or basecoat to penetrate into substrate surface allowing a higher contact area and greater interactions, or the anchoring of an AP into the substrate causing polymer chain entanglement (mechanical adhesion mechanism)
- Substrates cleaned with an abrasive method: creates a higher surface roughness allowing for a higher contact area between the substrate and the AP or basecoat

The next chapter will investigate the ability of a group of candidate APs to physically adhere to a substrate surface (swollen and non-swollen) via a polymer chain entanglement mechanism, based on the believed mechanism of the state of the art CPO AP.

# Chapter 6

## PHYSICAL ADHESION: SURFACE SWELLING AND INTERFACIAL POLYMER CHAIN ENTANGLEMENT

### 6.1 Overview

An overview of this chapter to guide the reader through the results is shown in Figure 6.1. The main focus of this chapter was to identify suitable solvents to swell the PP-based substrates, and test the ability of candidate APs to anchor into swollen or non-swollen substrates, facilitating adhesion via a molecular chain entanglement (between the substrate and AP polymer chains) mechanism. This adhesion mechanism was based on CPO state of the art APs.

### 6.2 Introduction

APs are often dissolved in a solvent to aid wettability and reduce viscosity when they are applied to the substrate surface. This increases the surface contact area and thus, adhesion. Some solvents are able to swell the substrate surface, which could allow an AP to penetrate into the substrate, enabling a mechanical interlocking adhesion mechanism.<sup>28–30</sup>

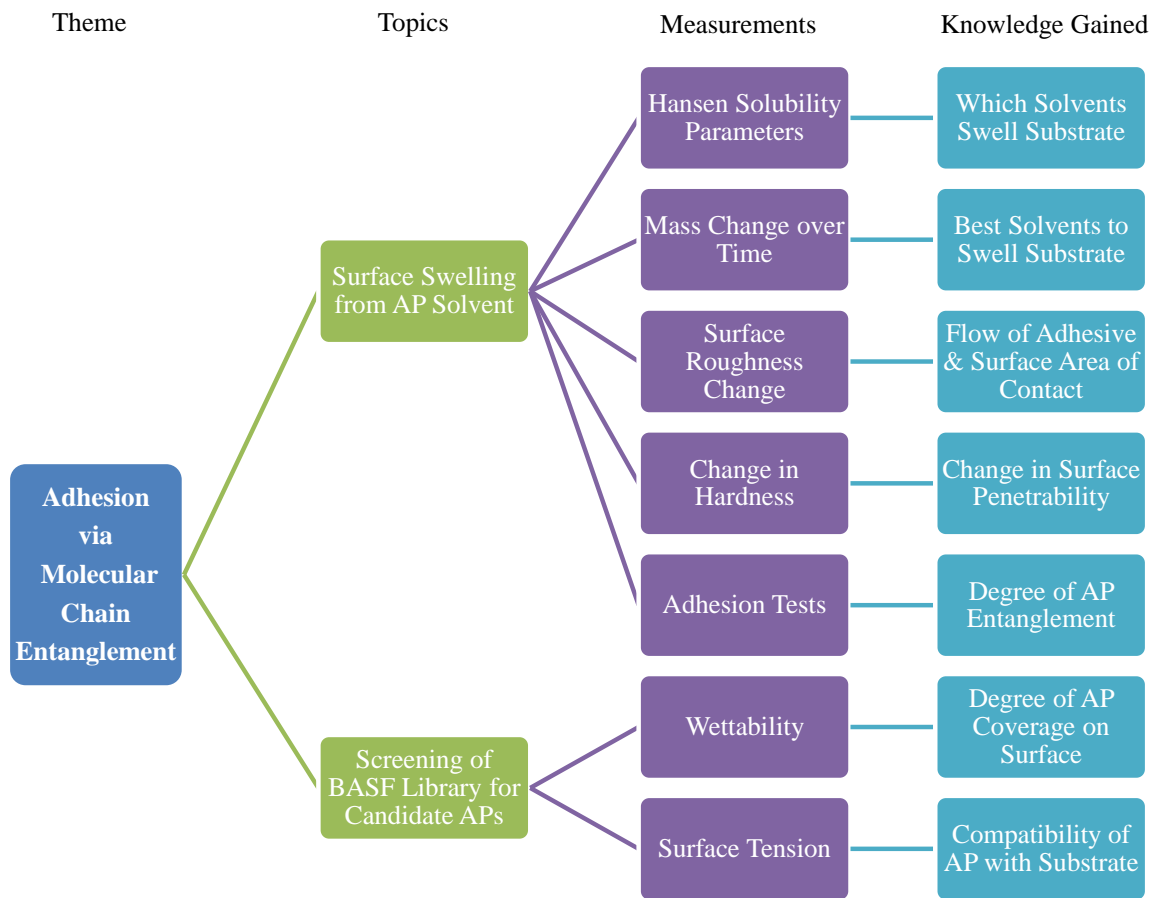


Figure 6.1: A summary of the physical adhesion chapter.

It is important that the chosen solvent system evaporates at a reasonable rate, so that the fully cured system is no longer swollen; if the substrate remained swollen, this could result in a possible cohesive failure within the substrate material.<sup>45,74</sup>

Ryntz *et al.*<sup>45,64</sup> demonstrated that adhesion to TPO is strongly influenced by the type and amount of solvent within a CPO primer, as well as the TPO surface morphology. It was suggested that the CPO is able to penetrate through a PP surface layer to the rubber EPDM domains in a subsurface layer, where entanglements between CPO and substrate polymer chains occur. An alternative perspective by Schuman *et al.*<sup>27</sup> suggests not only does the solvent need to swell the substrate, but it also needs to induce topographical changes at the surface for an improved adhesion.

Jaehnichen *et al.*<sup>88</sup> found that solvent swelling played a significant role in the improvement of adhesion via a flaming pre-treatment. It was discovered that not only was the

increase in polarity at the surface a necessary condition for improved adhesion, but the increase in polymer chain mobility upon solvent swelling (which occurred from the organic solvent component of the waterborne basecoat) was important to improve the miscibility between the waterborne basecoat components and the substrate polymer. This formed a type of inter-phase.

As well as solvents found in AP solutions, solvents from subsequent coatings applied, such as the topcoat, could also swell the substrate.<sup>45</sup> The system studied in this report used the same basecoat and topcoat, so it was assumed that the same solvent effect from these coatings occurred for all adhesion tests. The focus on this chapter was to identify possible solvents to be used for candidate AP solutions, with the aim to induce substrate swelling and create a physical entanglement adhesion with the substrate polymer chains (mimicking the adhesion mechanism of a CPO AP).

### 6.3 Substrate Swelling

HSPs<sup>151</sup> were used to predict the best solvents to swell PP, as described in Section 4.17. Initially, the relative mass change over time, was measured for one substrate type upon exposure to four different solvents (selected by their HSPs). Cyclohexane was then selected for further tests. To predict the adhesion behaviour on swollen substrates, the effect of surface roughness and surface hardness upon exposure to cyclohexane (inducing swelling of the substrates) was measured as a function of time. It should be noted that measurements were not used to assess the surface energy change after solvent swelling, due to the increased surface roughness upon exposure to the solvent which caused hysteresis in the contact angles measured, and impeded the surface energy values calculated on the hydrophobic surfaces.<sup>150, 165–167</sup>

As discussed in Appendix 10.F.3, the mechanical and physical properties of the substrate are likely to have an effect on solvent penetration of the substrate surface. When highly crystalline PP regions reside at the surface, the rate of penetration is likely to

be slower. When amorphous regions are present at the surface, such as EPDM rubber domains or semi-crystalline PP regions, the solvent penetration rate is likely to increase due to the lower density of the material. Measuring the effect of solvent swelling was important because initial adhesion to a TPO substrate is said to be a function of PP crystallinity at the surface, as it relates to the ability of a solvent and AP to permeate through and into the rubber layers beneath.<sup>28, 45, 64, 69, 181</sup>

### 6.3.1 Selecting Appropriate Solvent: Mass Change

The solvent selection process for swelling the PP-based substrates is described in Section 4.17. Out of the four solvents selected by HSP parameters, the best solvent was chosen by initial mass increase tests, upon exposure to solvent. A TPO/2 substrate was chosen to select the best solvent because it was a good representation for the materials used in industry and contained EPDM, which was predicted to increase the swelling rate. It was assumed that the solvent selected would swell all the other substrate types also. The effect of substrate type was then later tested with nano-indentation and surface roughness measurements (see below).

The effect of cyclohexane, Toluene, Solvesso 150 and Solvesso 200 exposure to TPO/2 substrates is shown in Figure 6.2. During substrate swelling, the mass increased with time as shown in Figure 6.2(a). Toluene was found to have the greatest swelling rate, cyclohexane and Solvesso 150 had a lower but similar swelling rate, and Solvesso 200 had the slowest swelling rate and was the least effective. Although the area and volume of solvent exposure to the substrate was controlled and kept constant, the data for each solvent did not follow a straight line (mass uptake plotted against the square root of time), which would be expected if the swelling effect of the solvent followed Fick's law of diffusion (where the larger the area and difference in concentration and the thinner the surface, the quicker the rate of diffusion). However, non-Fickian behaviour for the TPO/2 substrate would not be unexpected due to the heterogeneous nature and phase separation of the EPDM in the PP matrix as well as other additives (discussed in Chapter

5). For example, it was postulated that if the solvent initially penetrated into an area of the substrate lower in density, but then reached an area higher in density, the solvent swelling rate would decrease. This inhomogeneity in the substrate is therefore reflected in the changing swelling rates.

After the substrates were exposed to solvent for one hour, and subsequently air dried for one hour, their mass decreased with drying time as shown in Figure 6.2(b). This was explained by the evaporation of the solvent over time. Although toluene had the greatest swelling rate, cyclohexane was found to be the solvent that evaporated the fastest. However, it was observed that the substrates did not return to their original mass after the one hour drying period. The substrates swollen with Solvesso 200 and Solvesso 150 remained 18.6 mg and 28.1 mg heavier than before swelling. The substrates swollen with toluene and cyclohexane remained 48 mg and 15.6 mg heavier than before swelling. The inhomogeneity of the substrates was likely to be a reason for this, and it was thought that solvent molecules may have been trapped in different phases, such as the lower density EPDM within the substrate, and could not readily evaporate through the denser phases. As previously discussed in Section 2.4.2, a solvent that does not readily evaporate from the substrate after treatment could cause a cohesive failure at the surface. Therefore, cyclohexane was chosen as a good solvent for further tests due to its good swellability of the substrate and importantly, its fast rate of evaporation (which would be accelerated in any thermal curing processes of subsequent coatings applied). Environmental factors were also considered, where alternative solvents which were more environmentally friendly would better suit new industrial products. However, cyclohexane was used as a proof-of-concept with the scope that in the event of successful adhesion via swelling and molecular chain entanglement, the HSP solvent optimiser built into the HSPiP software<sup>151</sup> could be used to select more environmentally friendly solvents or a mixture of solvents with similar properties (HSP parameters) to cyclohexane.



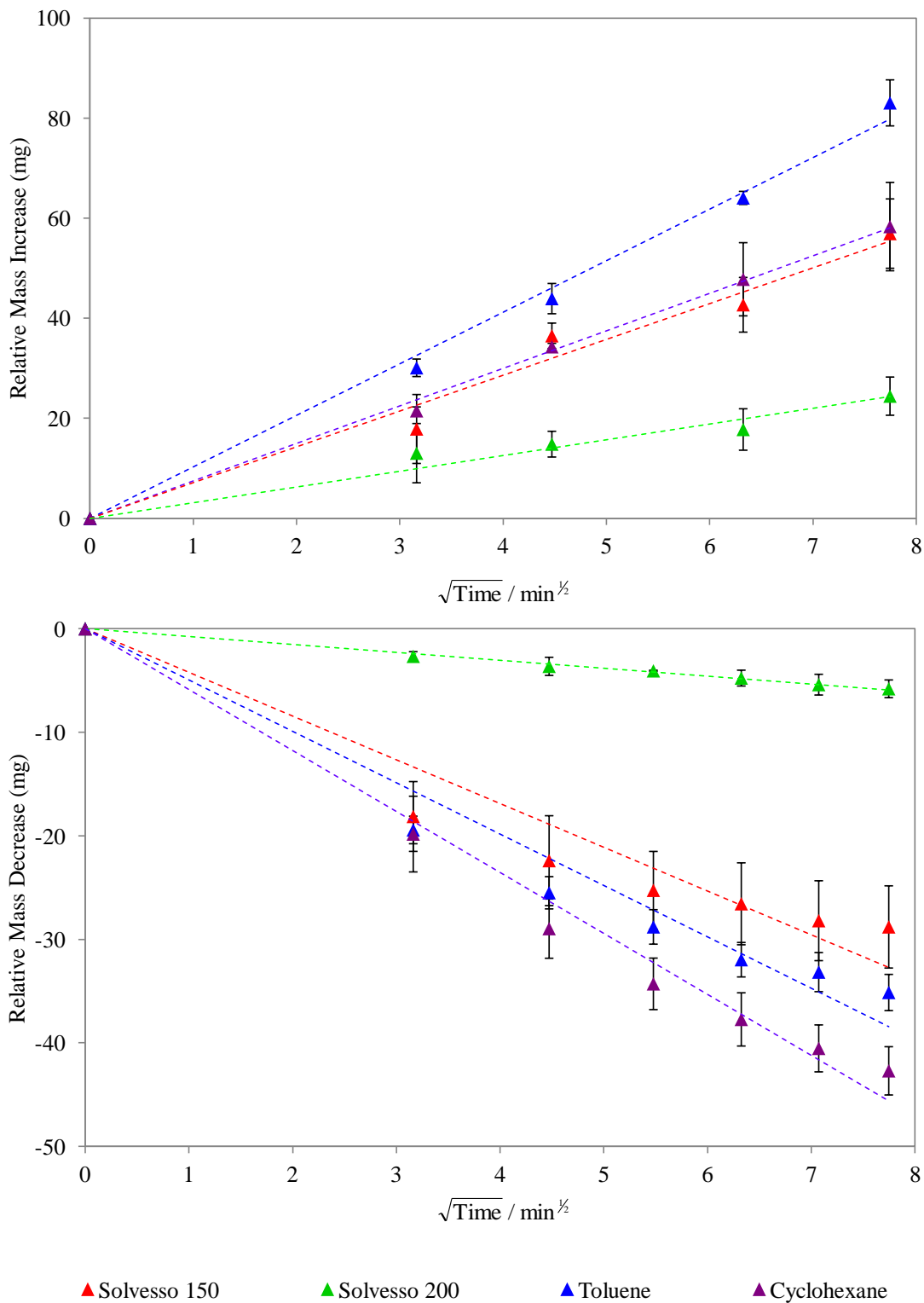


Figure 6.2: The mass change with the square root of time, after TPO/2 substrates were firstly (a) exposed to the four solvent types selected by HSP parameters for 1 hour, and (b) left to air dry for 1 hour. Presented data are averaged values taken from 3 different substrates. Lines of best fit are shown for deviations from Fick's Law.

### 6.3.2 Mechanical Properties: Substrate Hardness and Young's Modulus

Nanoindentation was used to assess the change in the substrate surface hardness and Young's modulus before and after substrate swelling with cyclohexane. As the indenter tip was pushed into the surface, the parameters were measured from 300 nm - 3000 nm below the surface. Figure 6.3 shows a schematic diagram of polymer chains before and after swelling (top right). The solvent molecules penetrate into the surface of the substrate and diffusion occurs (Fick's law), pushing the polymer chains apart. Consequently, the chains increase in mobility, and the force required for indenting the surface decreases. This analogy can also relate to an AP applied to the surface, where penetration into a softer, more mobile polymer phase would be more likely to occur than into a rigid (non swollen) substrate. Therefore, polymer chain entanglement between an AP and a swollen polymer surface is more likely to occur than with an unswollen surface.

This was the hypothesis in the first part of this research report, where candidate APs were screened and applied to swollen substrates, with the aim of modifying the substrate surface properties via a physical chain entanglement adhesion, mimicking the type of adhesion mechanism of a CPO AP. The vision was that hydrophilic functional groups attached to the AP (anchored into the substrate surface) would then interact with the hydrophilic basecoat and adhesion would be improved.

The hardness values of (a) TPO/0, (b) R/0, and (c) R/25 substrates were measured before and after swelling, as shown in Figure 6.3. These three substrates were selected to investigate the difference between substrates containing no EPDM (TPO/0 and R/0), the effect of EPDM (R/25), as well as the effect of other additives (TPO/0). The average Young's modulus values measured over the depth of 300 - 3000 nm are also displayed in Figure 6.3, overlaying the graph. The solvent treatment time was found to be unimportant as it didn't matter if the solvent treatment with cyclohexane was for one hour, ten minutes or one minute for the industrial TPO/0 substrate, as shown in Figure 6.3(a). The impact

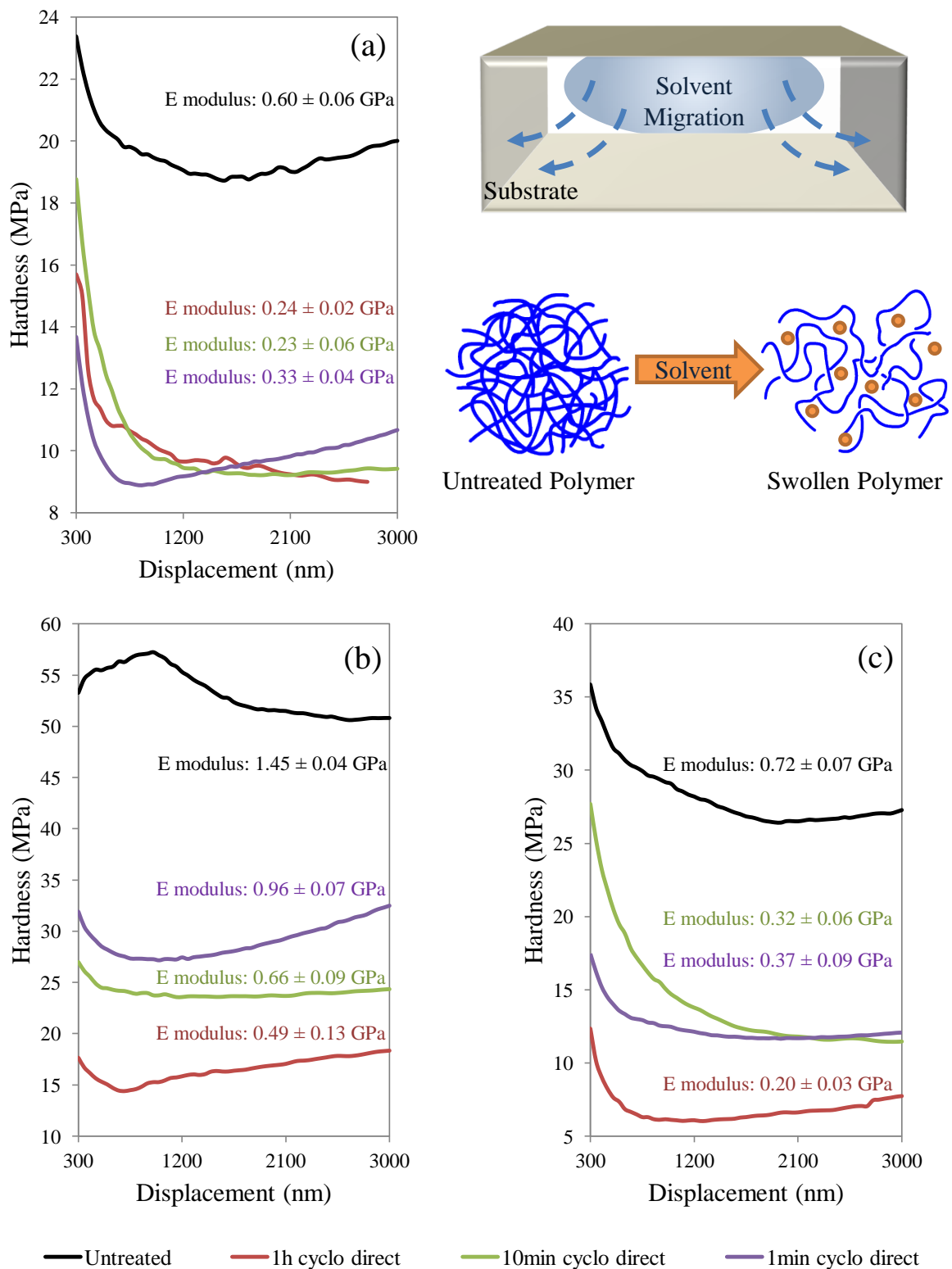


Figure 6.3: Surface hardness profile of a (a) TPO/0, (b) R/0 and a (c) R/25 substrate, before and after swelling for 1 hour, 10 minutes, and 1 minute. Top right: schematic diagram showing solvent migration into the surface of a substrate, with the solvent molecules (orange spheres) pushing apart the substrate polymer chains, increasing their mobility.

of solvent penetration on the surface hardness was apparent after just one minute. As expected, the substrate hardness decreased after exposure to cyclohexane (the solvent will have diffused into the substrate, pushing the polymer chains apart, increasing their mobility and hence making the substrate softer). After one minute swelling time, the TPO substrate hardness decreased by  $\sim 50\%$ , as did the Young's modulus.

As discussed in Appendix 10.F.3, the untreated R/0 substrate is significantly harder than the TPO/0 and R/25 substrate (see Figure 10.16). However, a swelling effect was observed. Also, a difference between the swelling times for the R/0 substrate was observed, shown in Figure 6.3(b). The longer the exposure time of the substrate to the solvent, the softer the substrate became as expected. After one minute of swelling of the R/0 substrate, the hardness value decreased by  $\sim 47\%$ , but was  $\sim 3$  times higher than the hardness value of the TPO/0 after one minute swelling and  $\sim 2.3$  times higher than the hardness value of R/25 substrate after one minute swelling. This suggested that the degree of crystallinity in the R/0 substrate remained higher than the other substrates (as discussed in Section 10.F.3). It was therefore expected that improved adhesion between an AP and a substrate would be observed for the TPO/0 and R/25 substrates, assuming that the adhesion was dependent on penetration ability of the AP into the surface of the substrate. Due to higher hardness values of R/0, an improvement in adhesion after solvent swelling was not expected. The same trends were observed for the Young's modulus results. Values of  $\sim 0.3$  GPa were expected to give improved adhesion if an AP functioned like that of a CPO,<sup>68</sup> as discussed in Appendix 10.F.3.2.

It was interestingly observed that the hardness depth profile of the R/0 substrate changed upon solvent exposure (Figure 6.3(b)). As discussed in Appendix 10.F, the initial increase in hardness with penetration depth into the surface of the untreated substrate, was suspected to be due to a higher degree of crystallinity in a subsurface layer. This effect was removed after solvent swelling, suggesting the structure changed in the initial surface layers, and the polymer chains rearranged, decreasing the degree of crystallinity. Therefore, the solvent used in an AP solution would be likely to have a large impact on

the adhesion to the substrate surface for the R/0 substrate (the swelling may allow for the penetration of an AP to entangle with the surface polymer chains of the substrate).

Although the substrate hardness significantly decreased after one hour swelling time of the R/25 substrate (by  $\sim 76\%$ ), as shown in Figure 6.3(c), little difference between the substrate hardness obtained after ten minutes and one minute swelling times occurred, and the hardness decreased by  $\sim 56\%$  compared to the untreated substrate.

Figure 6.4 shows the effect of drying times after swelling the substrate for one minute. The hardness profile changes after the (a) R/0 and the (b) R/25 substrates were swollen for one minute, and left to dry for six hours and for three days. As expected, the hardness values increased with increasing drying time (demonstrated in the schematic representation in Figure 6.4, left hand side), as the solvent evaporated out of the substrate surface and the polymer chain mobility within the substrate reduced.

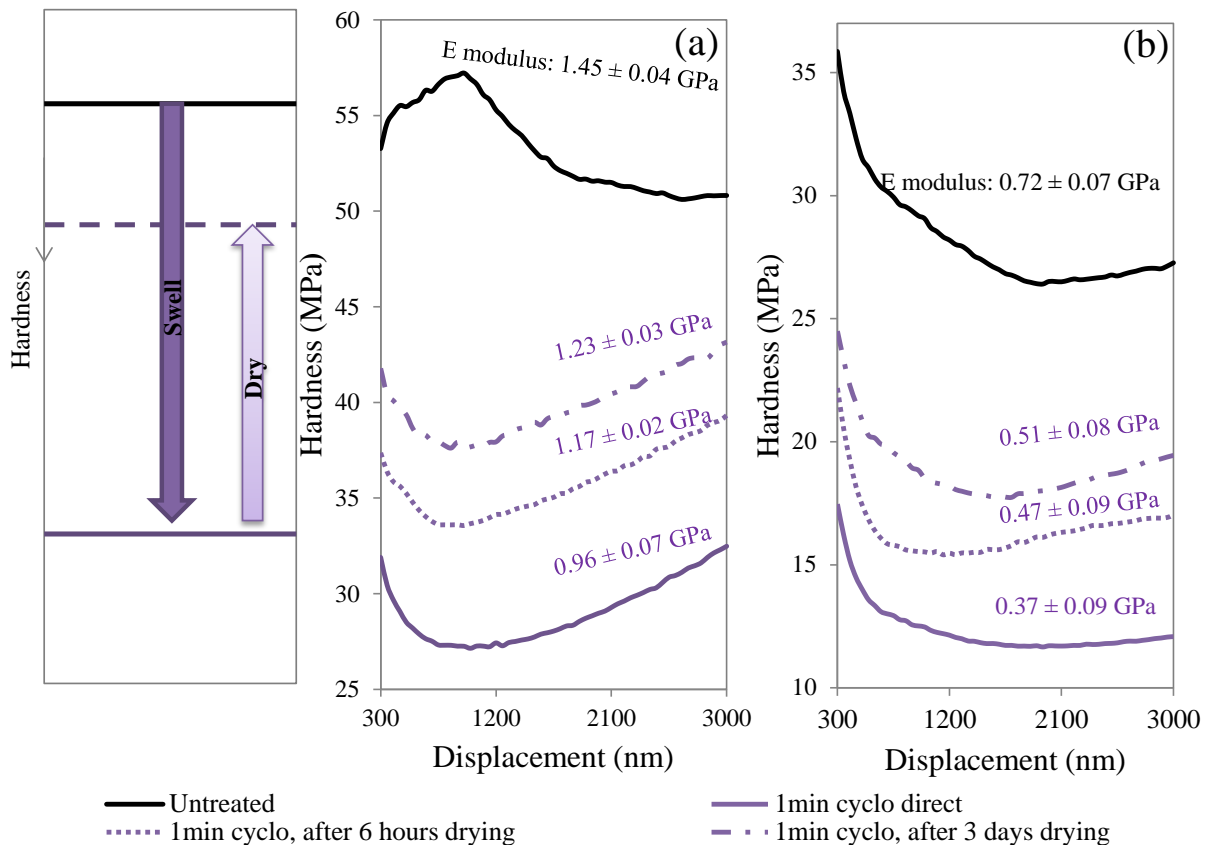


Figure 6.4: Surface hardness profile of a (a) R/0 and (b) R/25 substrate, before and after swelling for 1 minute, and drying for 6 hours and for 3 days.

After 3 days drying time, the hardness value of the R/0 substrate (Figure 6.4(a)) increased to  $\sim 73$  % of its original value before swelling (with the exception of the 300 - 1200 nm region, where the untreated substrate increased in hardness), and the R/25 substrate increased to  $\sim 66$  % of its original value before swelling. The hardness profile of the dried substrate remained the same shape as the swollen substrate, and in the case of the R/0 substrate (Figure 6.4(a)), it appeared solvent swelling had permanently changed the surface structure as no evidence to return to the initial profile (with an increase in hardness at the surface) was observed.

A summary of the hardness profiles of all tested substrates before and after swelling for one minute, and allowing the substrates to dry for six hours is shown in Figure 6.5. The bar graph displayed at the bottom of Figure 6.5 emphasises the higher hardness values for the R/0 substrate compared to the other substrates. Figure 6.5(a) shows that the change in hardness profile for the TPO/0 substrate is similar to that of the R/25 substrate, although the hardness value of TPO/0 increased at a greater rate after 6 hours of drying. As discussed in Chapter 5 and Appendix 10.F.2, additives are present in the TPO/0 (talc,  $\text{CaCO}_3$ , carbon black and irgafos 168) and R/25 substrates (EPDM), which is likely to be the reason why the hardness profiles have similar values compared to the R/0 substrate which contains no additives.

Assuming that the substrate hardness played a key role in the adhesion mechanism of AP solutions applied to a substrate, it was expected a greater adhesion would be observed between an AP and a TPO/0 substrate or R/25 substrate, compared to the R/0 substrate. This hypothesis assumes a higher % of EPDM or the presence of fillers and additives to lower the substrate hardness and Young's modulus was important for improving the mechanical properties of substrates which would lead to a greater degree of swelling, allowing for molecular chain entanglement with an AP.

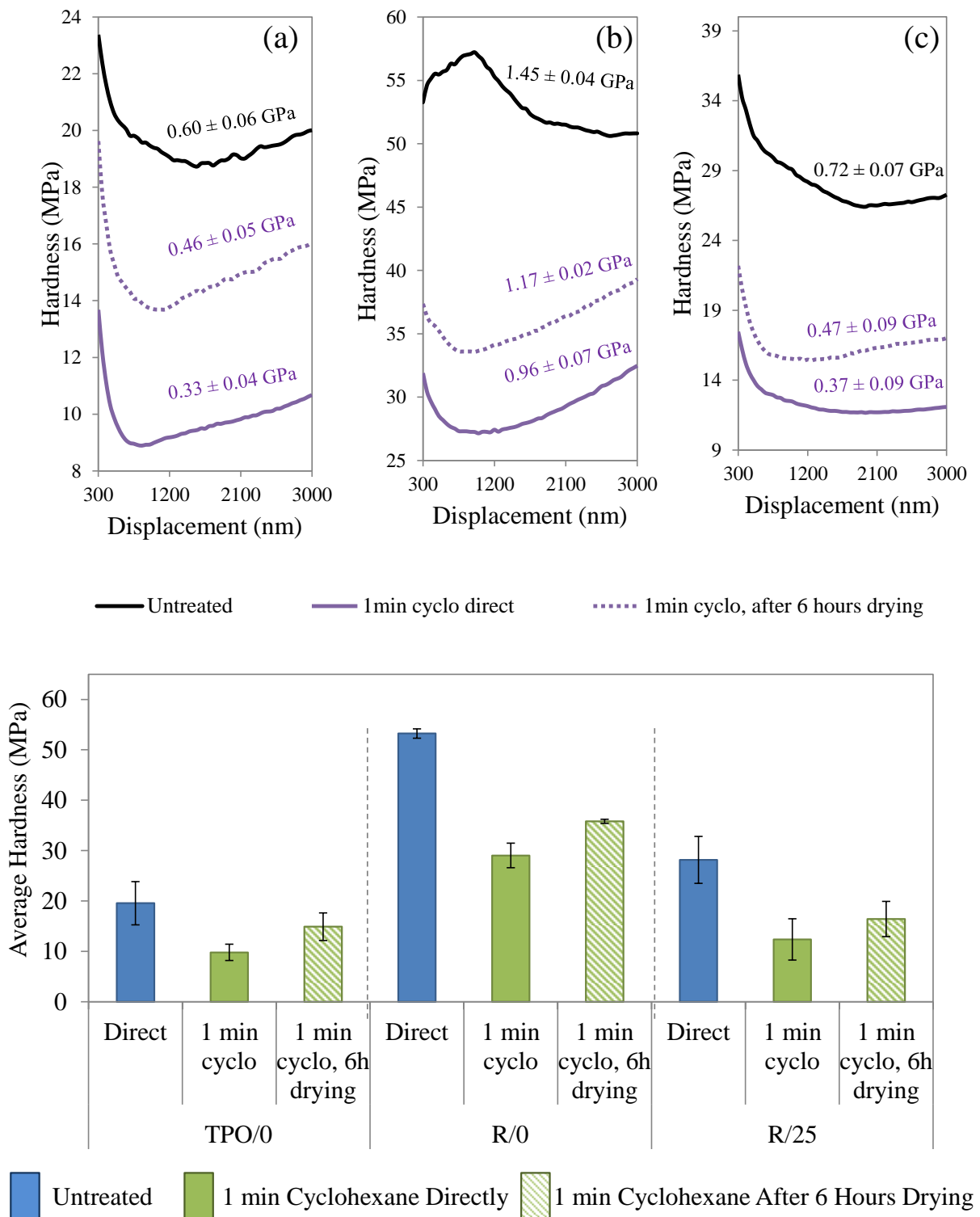


Figure 6.5: Summary of surface hardness profiles of a (a) TPO/0, (b) R/0 and (c) R/25 substrate, before and after swelling for 1 minute, and drying for 6 hours. Bottom: Average hardness change of TPO/0, R/0 and R/25 substrates before and after swelling for 1 minute and drying for 6 hours.

### 6.3.3 Surface Roughness

The change in surface topography upon exposure to solvents was thought to be an important contributing factor for achieving good adhesion, as discussed in Appendix 10.F.4. White light interferometry was used to assess the change in surface topography (*i.e.* surface roughness) during solvent swelling. The same three types of substrates (TPO/0, R/0 and R/25) that were used for assessing the change in surface hardness during solvent swelling were used to assess the change in surface roughness during swelling. These three substrates were selected to investigate the difference between substrates containing no EPDM (TPO/0 and R/0), the effect of EPDM (R/25), as well as the effect of other additives (TPO/0). Swelling times of one and ten minutes with five hours drying time were investigated. Two surface roughness parameters (described in Section 4.3), Ra and Rq, were used to assess the change in surface roughness. The bar chart in Figure 6.6 summarises the change in Rq (this parameter was chosen because it was more sensitive to substrates containing valleys).

Figure 6.6(e) shows Rq values for the different substrates tested, before and after swelling for ten minutes and for one minute, and after five hours drying time. The 2D and 3D images of the roughness profiles for the TPO/0 substrate after swelling, as well as the 2D and 3D roughness profiles of the R/0 and R/25 substrates after swelling for ten minutes can be found in Appendices 10.C - 10.E. The 2D and 3D roughness profiles of the untreated substrates are discussed in Appendix 10.F.

Before swelling, the TPO/0 substrate had roughness values of Ra = 258 nm and Rq = 329 nm. The substrate appeared to have areas with craters or valleys scattered across the surface, suspected to be due to the additives, as discussed in Appendix 10.F.1. After the substrate was immersed in cyclohexane for ten minutes, these craters no longer existed, but the surface roughness increased by  $\sim 50\%$  (Ra = 391 nm and Rq = 500 nm). A clear difference in surface topography was observed when looking at the 2D and 3D profiles.

The surface was re-measured after five hours of drying time. Just as the surface



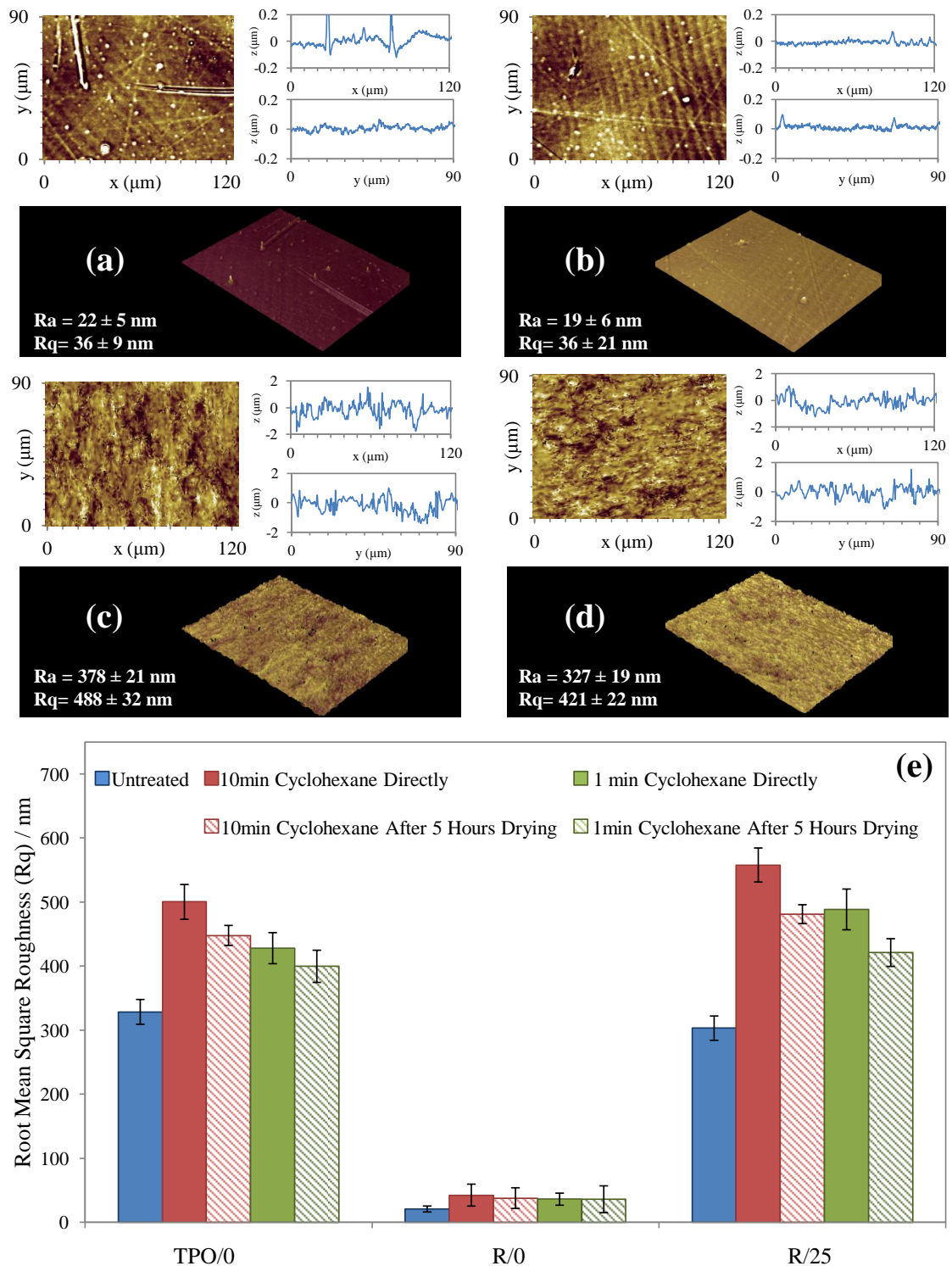


Figure 6.6: Top: 2D and 3D images of surface roughness and x and y profiles of R/0 after (a) 10 minute swelling time, (b) after it was left to dry for 5 hours and (c) R/25 after 1 minute swelling time, (d) after it was left to dry for 5 hours. Bottom: Average root mean square roughness ( $Rq$ ) of the TPO/0, R/0 and R/25 substrates before and after swelling for 10 minutes and drying for 5 hours, and after swelling for 1 minute and drying for 5 hours.

hardness did not return to the original values, the topography also did not return to the original state after drying for five hours, and visually appeared indifferent to the 2D and 3D profiles of the measurement directly after swelling. However, the surface roughness decreased with drying time by  $\sim 10\%$  ( $R_a = 352$  nm,  $R_q = 448$  nm). It was not tested if the surface would eventually return to its original state, as it was the immediate time at swelling that would have the greatest impact on adhesion. The large increase observed for  $R_a$  and  $R_q$ , and the change in surface topography observed, all suggested an improved adhesion would be observed upon cyclohexane swelling.

After only one minute of swelling the TPO/0 substrate, the surface topography had changed compared to the untreated substrate and the surface roughness increased by  $\sim 30\%$  ( $R_a = 334$  nm,  $R_q = 428$  nm). The significant change in the surface topography, also observed in the hardness profile and Young's modulus profiles of the substrate after just one minute swelling time, suggested cyclohexane would facilitate adhesion mechanisms at a fast time scale once in contact with the substrate surface. This was based on the assumption that the increase in surface roughness would lead to a greater contact area between an AP and the substrate surface, allowing a greater adhesive interaction. However, the substrate was found to dry at a slower rate compared to the substrate that was in cyclohexane for ten minutes (surface roughness decreased by  $\sim 7\%$ ,  $R_a = 311$  nm,  $R_q = 400$  nm), which could affect the cohesive integrity of the substrate surface, and could cause cohesive failure. It was again observed that the change in topography induced by swelling remained after five hours of drying time.

As discussed in Appendix 10.F, the untreated R/0 substrate was significantly smoother (by 10-fold) compared to the industrial TPO/0 and R/25 substrate. It was suggested that this was due to the absence of EPDM, and the higher degree of crystallinity suggested by the nanoindentation data (also found in Appendix 10.F). After ten minutes of immersion time in cyclohexane the surface roughness parameter  $R_a$  increased by  $\sim 56\%$  ( $R_a = 9$  nm) whilst  $R_q$  increased by  $\sim 100\%$  ( $R_q = 21$  nm). However, the values are 10 times lower than that of the TPO/0, which could result in a significant difference between adhesion

results of the two substrates. The difference between the R/0 substrate, and the TPO/0 and R/25 substrates, was further emphasised when comparing the 2D and 3D profiles. Unlike the TPO/0 and R/25 substrates, there appeared to be no significant difference after swelling. After five hours drying time, the surface roughness decreased by  $\sim 23\%$  ( $R_a = 21$  nm,  $R_q = 38$  nm), but as with the other substrates, it did not return to its original value.

The 2D and 3D surface roughness profiles for the R/0 substrate after one minute swelling time and five hours drying time, are shown in Figure 6.6 (a) and (b). Swelling the R/0 substrate for ten minutes and one minute had little effect on the surface roughness compared with the other substrates measured. As discussed in Appendix 10.F.1, the EPDM and additives in the other substrates were found to be the cause of the change in surface roughness when subjected to solvent, therefore, the lack of additives or EPDM in R/0 explained why the surface roughness did not significantly change. Furthermore, the hardness depth profiles shown in Figure 6.3 showed that all substrates changed to lower hardness values after solvent subjection, therefore, a difference in solvent penetration as being a reason for the difference in surface roughness was ruled out. Therefore, it was assumed that if the substrate hardness was the dominating factor of adhesion (penetration of an AP into the substrate surface), the R/0 substrate would have good adhesive properties, however if the surface topography change upon swelling was the dominating factor (increase in surface contact area between AP and surface), the R/0 substrate would not have improved adhesive properties, compared to TPO/0 and R/25.

Furthermore, the scratch resistance of the R/0 substrate appeared to decrease after solvent swelling, as many scratches were observed in the topography (likely to be caused from sample handling), suggesting the substrate became brittle in nature upon swelling. The effect of the scratches could be seen in the difference between  $R_a$  and  $R_q$ : the  $R_q$  value was higher because it was more sensitive to the valleys caused by the scratches at the surface, compared to  $R_a$ . This would have a detrimental effect on the efficacy of a car component. The higher Young's modulus values obtained for R/0 compared to the other

substrates, shown in Figure 6.5, also supported this claim.

The behaviour of the R/25 substrate after substrate swelling for ten minutes, one minute and drying for five hours was very similar to that observed from the TPO/0. After a swelling time of ten minutes, the surface roughness increased by  $\sim 85\%$  ( $R_a = 440$  nm,  $R_q = 558$  nm).  $R_q$  increased more than  $R_a$ , due to a greater deviation in peaks and valleys from the mean surface roughness. This could have been caused by the large amount of amorphous EPDM domains found at the surface of the substrate that was previously observed in SEM measurements (Section 5.3, Figure 5.7). They were likely to have swollen to a greater extent than the surrounding PP matrix, causing the large peaks and valleys at the surface. This hypothesis is represented schematically in Figure 6.7. As previously discussed, this significant change in topography is likely to improve adhesive properties to the surface,<sup>27</sup> by increasing the contact area between the substrate surface and the AP. After five hours drying time, the surface roughness decreased by  $\sim 14\%$  ( $R_a = 377$  nm and  $R_q = 481$  nm).

The 2D and 3D surface roughness profiles for the R/25 substrate after one minute swelling time and five hours drying time, are shown in Figure 6.6 (c) and (d). After one minute of swelling time, the surface roughness increased by  $\sim 61\%$  ( $R_a = 378$  nm,  $R_q = 488$  nm) and after five hours drying time it decreased by  $\sim 14\%$  ( $R_a = 327$  nm and  $R_q = 422$  nm).

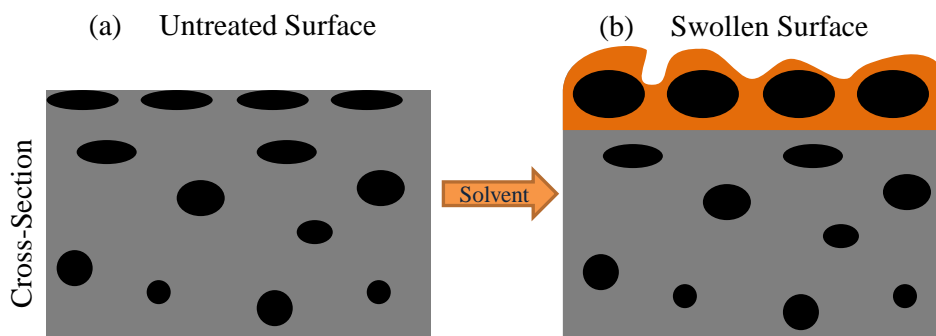


Figure 6.7: Schematic diagram demonstrating the hypothesis that the regions of EPDM found at the surface of a substrate could swell at a greater rate than the surrounding PP matrix, causing a greater deviation in peaks and valleys at the surface as demonstrated by the orange area (different parts of the surface will swell at different rates).

Although there was a difference between a swelling time of ten minutes and one minute for the TPO/0 and R/25 substrates, shown in the bar graph summary of the Rq change upon swelling (Figure 6.6), the Rq value significantly increased after a swelling time of just one minute. This suggested the adhesion of an AP/cyclohexane solution applied to a substrate would significantly improve on a fast time scale, assuming the topographical changes at the surface are a main contributing factor upon substrate swelling. A drying time of five hours decreased the Rq value, however, the substrates' roughness remained significantly higher compared to the untreated substrate. It was assumed that this did not cause a problem for the cohesive integrity of the substrates, because the subsequent coatings applied were thermally cured at 80 °C (see Figure 4.6) which should have accelerated the substrate drying process.

## 6.4 Candidate Adhesion Promoter Selection

A range of candidate AP molecules were selected from a list of functional molecules readily available from BASF. The business drive in this case was to screen molecules already in production from BASF, with the scope that the company would save time and money if the project was to be successful.

The molecules chosen were commonly used as surfactants and were amphiphilic in nature. Hence bi-functional molecules were chosen: a hydrophobic component for interaction with the hydrophobic substrate, and a hydrophilic component for interaction with the hydrophilic basecoat that would be applied. The hypothesis was that if cyclohexane was used to swell the substrates and increase the substrate polymer chain mobility, and subsequently apply an AP: the hydrophobic part of the candidate AP would entangle with the substrate polymer chains and anchor into the surface (like the mechanism postulated for CPO APs) and the hydrophilic part would interact/react with the hydrophilic basecoat. This matching of the interfacial properties with the candidate AP would then increase the adhesion between the applied coatings and the substrate. This hypothesis is

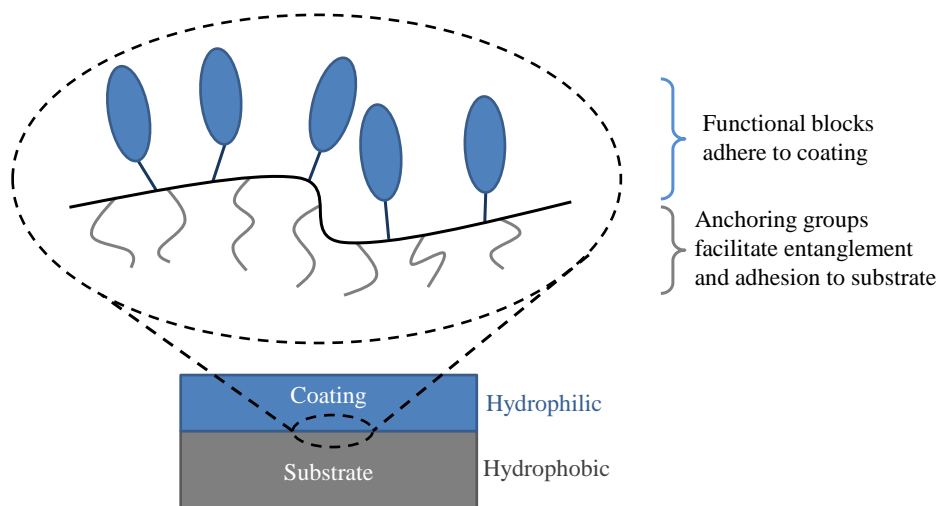


Figure 6.8: Schematic diagram demonstrating the hypothesis of achieving improved adhesion between a hydrophilic waterborne basecoat and a hydrophobic PP-based substrate, via molecular chain entanglement with a candidate AP and subsequent interactions between function groups of the AP and the basecoat.

demonstrated in Figure 6.8

A list of the commercial names of the candidate APs and their description is shown in Table 3.2. Due to confidentiality, the exact structure of each polymer is not disclosed, however, an idea of the functionalities is given in the description. The number added to the commercial name indicates chain length differences in the monomer units, for example Plurafac LF1300 contains larger monomer units than Plurafac LF223. The structures of each type of polymer varies as does the locality of the hydrophobic and hydrophilic functions. For example, the Pluronic polymers consist of EO/PO block copolymers, therefore, switch between hydrophilic and hydrophobic sections along the polymer backbone. To deduce which polymers were best for testing adhesion, the surface tension and the wettability of the polymers on a TPO/2 substrate were tested. A TPO/2 substrate was chosen as it represented an industrial sample containing all additives and EPDM which could influence the swelling and entanglement adhesive behaviour. The results are shown in Figure 6.9. To achieve surface coverage, the wettability of the AP on the substrate surface was important, and a lower contact angle represented a greater wetting of the substrate. The polymers with the best wettability characteristics tended to have lower surface ten-

sion values as expected (the forces holding the polymer droplets together were weaker enabling spreading at the surface of the substrate compared to the polymers with higher surface tension). Seven polymers were selected for adhesion tests, which are highlighted in Figure 6.9. Five were chosen because of their lower contact angles (higher wettability) and two were chosen because of their low surface tension values.

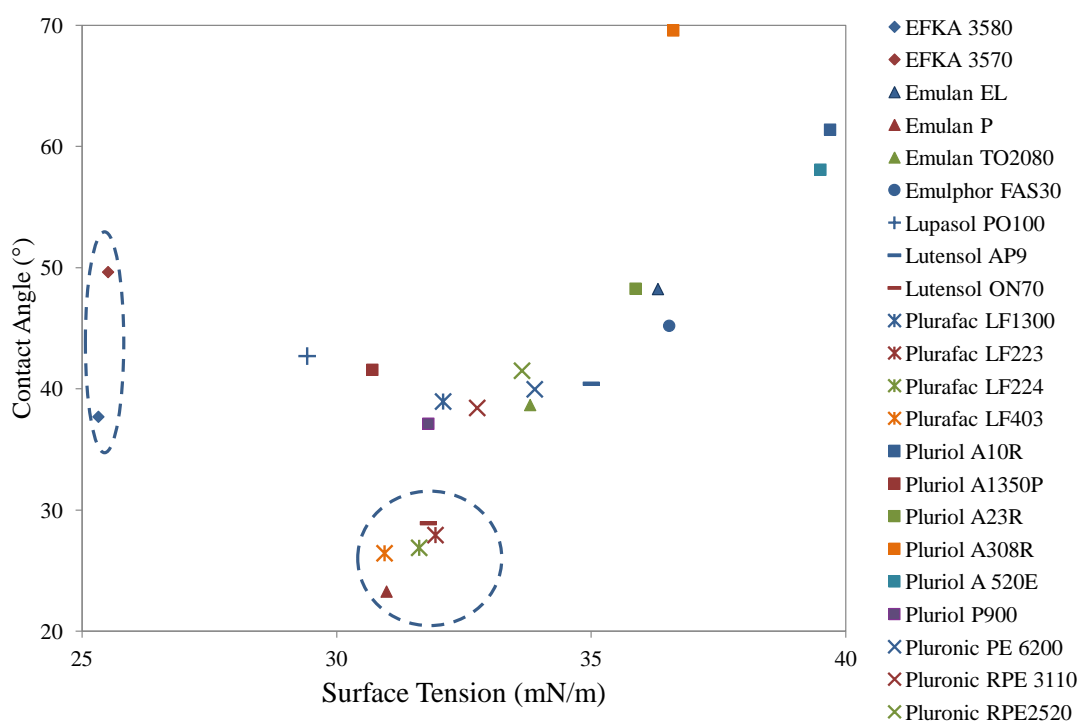


Figure 6.9: A scatter graph showing the surface tension (x-axis) and wettability (y-axis) of the candidate APs on a TPO/2 substrate. The polymers chosen for adhesion tests are highlighted with blue dashed circles.

### 6.4.1 Interaction of APs with PP

The modelling of the interaction of the candidate APs with PP substrates was attempted using a quartz crystal micro balance with dissipation (QCM-D). PP surfaces were made by spin coating gold quartz sensors, and the thickness was measured using ellipsometry. The sensors vibrated and the resonant frequencies were measured. The AP solution was

rinsed across the surface of the sensors and the frequency dampened upon contact with the solution. This damping effect indicated an increase of mass at the surface, however, it was not distinguished if it was due to the solvent and swelling, or the anchoring of an AP. An alternative problematic scenario was that the solvent or AP penetrated into the PP, but then was trapped between the sensor and the PP layer, in which case the interaction results would have been false. The solution concentrations were kept constant to test a qualitative comparison between the different APs. However, a second problem was encountered, which was that it could not be judged if the PP was dissolving into the cyclohexane and washing away, therefore, also having an effect on the dampening of the frequency, hence mass change. An idea to overcome this problem was to graft SAMs with hydrophobic tail ends to the gold sensor surface and then spin coat the PP to improve adhesion between the PP and the sensor. However, due to other experimental priorities, time did not permit this experiment and it remains as possible future work.

#### **6.4.2 Adhesion Tests**

Adhesion tests were performed for all seven selected polymers. For preliminary studies, a non-pigmented basecoat was used to minimise competing interfaces (previous work in BASF often found candidate APs to react at the pigment/basecoat interface, rather than the substrate/basecoat interface.) Adhesion tests were performed on industrial TPO/0 and research R/0 and R/25 substrates, to look at the effect of EPDM and other additives.

As a proof-of-concept, the APs were applied as primer layers to check for any improvements in adhesion at the substrate/basecoat interface. APs were applied in pure form and as 5 wt.% solutions in cyclohexane. They were tested 'wet-on-wet' with the basecoat (no intermediate drying step) and with a drying step (ten minutes, 80 °C) before the basecoat application. All these variables were performed on untreated substrates, and substrates that had been swollen in cyclohexane for one minute. The adhesion (CHT) was tested seven days post-cure time after the application of the clearcoat (all substrates were coated with both basecoat and topcoat and fully cured before adhesion tests were performed)



and compared to the two standards (flame and CPO), as well as a blank substrate which did not have any primer or pre-treatment.

The adhesion results are shown in Table 6.1. For all experimental variables, the CHT grade was 5 (65 - 100 % delamination). Although the effect of swelling was tested by both a pre-swelling step in cyclohexane for one minute, and by having the AP in a cyclohexane solution, no significant adhesion promotion was observed. It was also thought that the drying step after the primer layer application may have locked the anchored AP into the substrate surface. However, it appeared not to be the case, assuming that adhesive failure occurred and not cohesive failure within the substrate surface.

Table 6.1: CHT adhesion results after the candidate AP primer layer was applied to a dried substrate and to a substrate that was pre-swollen in cyclohexane for one minute. All adhesion tests were performed after a 7 day post-cure period after the topcoat was applied. No improvement in adhesion was observed for all variables tested.

| Adhesion Promoter          |       | CHT             |                    |
|----------------------------|-------|-----------------|--------------------|
| Name                       | Wt. % | Applied & Dried | Applied Wet-on-Wet |
| <b>EFKA 3580</b>           | 100   | 5               | 5                  |
|                            | 5     | 5               | 5                  |
| <b>EFKA 3570</b>           | 100   | 5               | 5                  |
|                            | 5     | 5               | 5                  |
| <b>Lutensol ON70</b>       | 100   | 5               | 5                  |
|                            | 5     | 5               | 5                  |
| <b>Plurafac LF223</b>      | 100   | 5               | 5                  |
|                            | 5     | 5               | 5                  |
| <b>Plurafac LF224</b>      | 100   | 5               | 5                  |
|                            | 5     | 5               | 5                  |
| <b>Plurafac LF403</b>      | 100   | 5               | 5                  |
|                            | 5     | 5               | 5                  |
| <b>Emulan P</b>            | 100   | 5               | 5                  |
|                            | 5     | 5               | 5                  |
| <b>Untreated Substrate</b> |       | 5               |                    |
| <b>Flame</b>               |       | 0               |                    |
| <b>CPO</b>                 |       | 0               |                    |

Due to the poor adhesion results, a decision was made to stop looking for adhesion improvement via molecular chain entanglement, and the failure mode of the coating was not measured. However, future work could be to use ToF-SIMS and XPS (surface sensitive techniques) to measure the two delaminated surfaces and compare the intensities of a signal characteristic of the AP, to conclude if adhesive failure or cohesive failure occurred.

## 6.5 Future Work

Future work to find a successful AP for physical adhesion, could be to tailor-make a molecule or polymer with the desired structure and properties. The surface energy and polar/dispersion components could be measured using the Wu method (how the wet basecoat was measured, see Section 4.5.3) to look for matching properties to the substrate and basecoat.

Future experiments were designed where model surfaces would be used to test the orientation and interaction of the candidate APs with AFM, based on similar experiments by Gourianova *et al.*<sup>92</sup> For example, a silicon wafer could be coated with PP and used as a hydrophobic surface, and the candidate AP applied. A hydrophilic functionalised AFM tip could then be used to measure the adhesive attractive forces across the surface, giving an indication if the AP is anchored into the PP surface and to what extent. However, the fundamental flaw with this experiment design was ensuring the AP remained at the hydrophobic wafer surface, otherwise if it would be pulled away by the AFM tip, the tip would be 'contaminated' and the remaining adhesive forces measured at the surface would be false. A possible solution could be to have the AP grafted to the AFM tip, and measure the adhesive attractive forces with a hydrophobic surface, however, this also required a lot of work to implement and test, and due to other experimental priorities, time did not permit these tests. A further idea could also be to freeze the substrate, trying to trap the AP in the substrate surface after swelling, as a proof-of-concept before testing the adhesion.

## 6.6 Conclusions

HSP parameters were successfully implemented to determine suitable solvents to swell the PP-based substrates. Evidence of surface swelling was determined through mass increase measurements as well monitoring the change of the substrate hardness, Young's modulus and surface roughness. The substrates containing additives or EPDM were found to have the lowest hardness and Young's modulus profiles before and after swelling. They were also found to have the greatest surface roughness increase after solvent swelling. Therefore, it was hypothesised that these two substrates, TPO/0 and R/25, would lead to greater adhesion than the R/0 substrate which contained no additives.

However, despite the identification of several bi-functional candidate APs based on their surface tensions and ability to wet the substrate surfaces, poor adhesion results were obtained after they were applied as a primer (100 wt.% or 5 wt.%) on swollen and non-swollen substrates.

Adhesion via polymer chain entanglement, based on the believed mechanism of CPO APs, was not successful. Therefore, the research was taken into a new direction to search for candidate APs that could graft to the substrate surface via covalent bonding, mimicking the adhesion mechanism of the flaming state of the art technique, as discussed in Chapter 7.

# Chapter 7

## CHEMICAL ADHESION: A PROOF- OF-CONCEPT GRAFTING STUDY

### 7.1 Overview

An overview of this chapter to guide the reader through the results is shown in Figure 7.1. The main focus of this chapter was to identify candidate APs, capable of forming covalent bonds with the PP-based substrates, for improved adhesion with a waterborne basecoat. The adhesion mechanism was inspired by the flame pre-treatment state of the art, in which oxygen-containing species are covalently bonded to the substrate surface. The APs were characterised, and their ability to graft to various substrates was tested, focusing on the adhesion at the substrate/AP interface.

### 7.2 Introduction

Alternative adhesion mechanisms were investigated after the adhesion of candidate APs to swollen and nonswollen substrates was unsuccessful in Chapter 6. Since a mechanism inspired by state of the art CPO APs was unsuccessful, a mechanism based on the flame pre-treatment was investigated, where hydrophilic reactive groups are covalently bonded (O and OH) to the substrate surface during treatment.

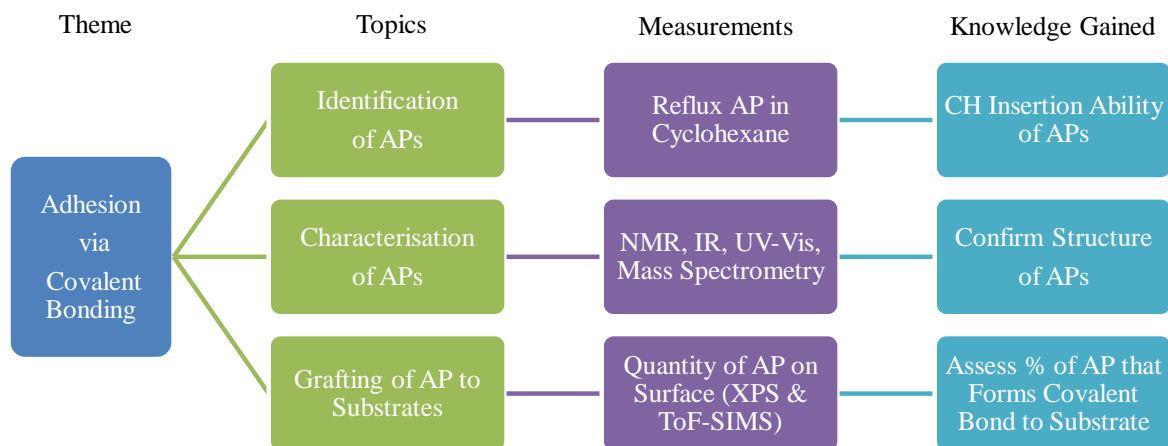


Figure 7.1: A summary of the chemical adhesion, a proof-of-concept chapter.

### 7.3 Identifying and Characterising Adhesion Promoters (AP's)

Carbenes are highly reactive species, as described in the Literature Review (Section 2.9). Diazirines are a group of carbene-generating species that can be relatively stable with the correct functional groups. The parent compound in this study, denoted as TPD (shown in Figure 3.1), contains an electron-withdrawing trifluoromethyl ( $\text{CF}_3$ ) group which is able to pull electron density from the carbene generated. It also contains a phenyl ring which is able to de-localise the electron density from the carbene generated. Both of these groups contribute towards the stability of the carbene, giving a lifetime that enables CH insertion reactions.<sup>135</sup> Therefore, TPD was thought to be an ideal candidate AP for potential CH insertion reactions into a PP-based substrate (creating a covalent bond). Furthermore, it could be readily functionalised on the phenyl ring to add hydrophilic groups, accounting for adhesion with the waterborne basecoat (for example, forming H-bonds with the basecoat like that of the flaming pre-treatment discussed in Section 5.6<sup>53,54,102</sup>). A full characterisation of the candidate APs can be found in Appendix 10.G.

The grafting ability (CH insertion into the substrate) of TPD to substrate surfaces was first tested, concentrating on the adhesion at the AP/substrate interface (via covalent

bonding). The next progression, once this was achieved, was to modify TPD with an OH and COOH functional group (shown in Figure 3.1). These molecules, denoted as TPDOH and TPDCOOH, were grafted to the substrate and the adhesion to the waterborne basecoat was tested, concentrating on the adhesion at the AP/basecoat interface.

### 7.3.1 CH Insertion Proof-of-Concept

Once the candidate APs were identified and characterised, their ability to generate carbenes and undergo CH insertion reactions was assessed. Brunner *et al.*<sup>135</sup> had previously performed this investigation with TPD, identifying successful insertion products from UV initiated reactions with cyclohexane and methanol. The procedure used here was adapted from this study, and used cyclohexane to test the ability of the TPD. Cyclohexane was the preferred choice of solvent for the reaction with TPD due to the limited number of CH insertion products possible (cyclohexane is a small simple molecule), which aided the subsequent analysis of the products formed. Furthermore, the boiling point is 81 °C, close to the curing temperature of the coatings used in this study (80 °C). For the carbene-precursors to be formulated into the coatings system, the carbene would have to be thermally active at this temperature. Therefore, the reflux reaction between TPD and cyclohexane was a good test for the suitability of TPD. As well as thermal activation, UV activation of the carbene in cyclohexane was also tested and compared.

Figure 7.2 schematically represents the CH insertion reaction between TPD and cyclohexane, and the expected insertion product (assuming multiple TPD molecules do not insert into each other, and assuming only one TPD molecule would react with one cyclohexane molecule). A trade-off was made between excess cyclohexane to decrease the competition between the TPD and cyclohexane molecules (competing reaction sites) and the concentration of TPD to ensure enough product was formed in the required concentration for successful analysis. The ratio was chosen to be seven cyclohexane molecules available per TPD molecule.

After an eight hour reflux, the reaction products were separated and their mass spec-

tra recorded using GC/MS. There were eight components identified with GC (GC chromatogram not shown); one component was cyclohexane as expected (present in excess) and all other components were a mixture of products. The mass spectrum of the component containing the desired CH insertion product is displayed in Figure 7.2 and shows the molecular ion peak from the expected CH insertion product at  $m/z = 242$  (10 % abundance). The base peak (greatest intensity, 100 % abundance) was due to cyclohexane ( $m/z = 83$ ) which had not been fully separated from the reaction mixture by GC. A peak due to the fragmented TPD moiety from the insertion product was also observed at  $m/z = 159$  (5 % abundance). It was therefore concluded that TPD was active at  $\sim 80^\circ\text{C}$  and was a suitable candidate AP for the coatings system studied.

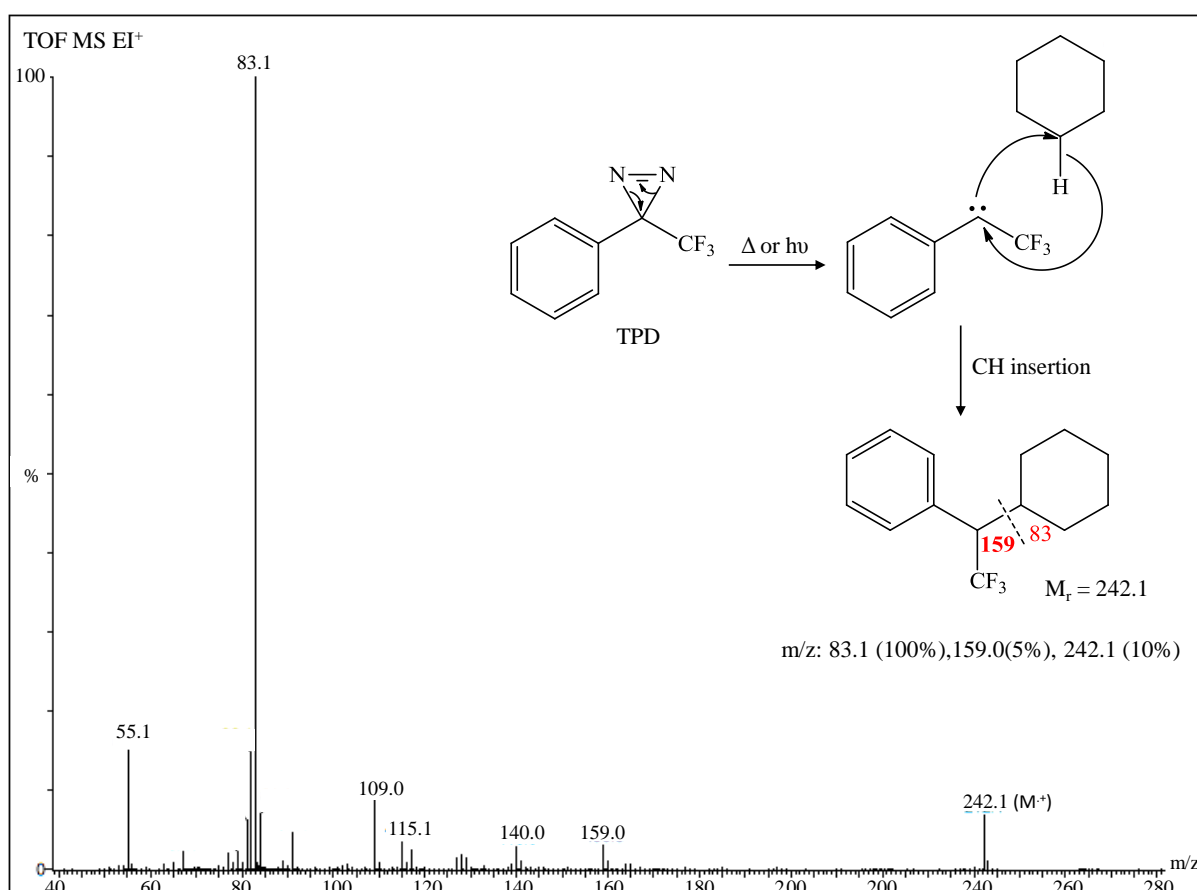


Figure 7.2: The mass spectrum of the reaction products after a highly concentrated solution of TPD in cyclohexane (1.3 M) was refluxed for 8h. Cyclohexane was in excess to TPD by 7:1.

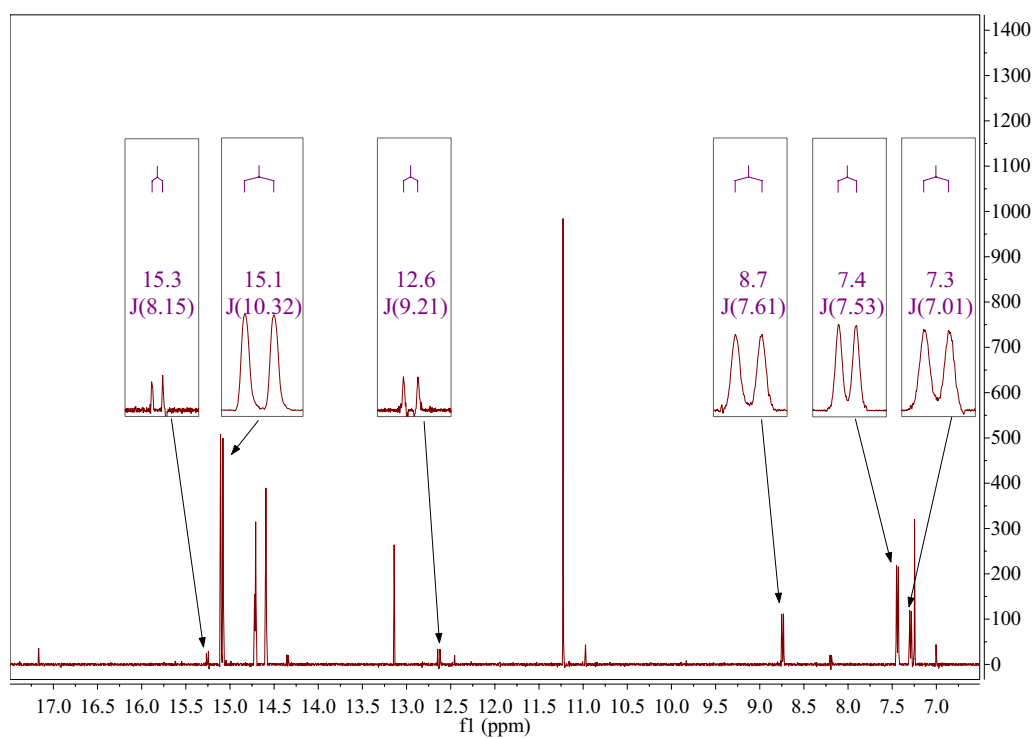
The reaction mixtures from an eight hour and two hour reflux and eight hour UV illumination (2.2 mW) were analysed by  $^{19}\text{F}$  NMR. The reactions were then repeated using deuterated ( $\text{D}_{12}$ ) cyclohexane and also analysed with  $^{19}\text{F}$  NMR. The results are displayed in Figure 7.3 (eight hour reflux) and Figure 7.4 (UV). As found by Brunner *et al.*,<sup>135</sup> the large number of peaks observed in the spectra reveal many components were present. Although not displayed, the spectra from the two hour reflux products were found to be the same. The doublets present in Figure 7.3(a) and Figure 7.4(a) indicate the insertion products in normal cyclohexane reactions. The coupling constants displayed from the doublets are in the range expected for vicinal fluorine-proton coupling.<sup>182</sup> Repeating the reactions in  $\text{D}_{12}$ -cyclohexane showed a loss of these doublets to singlets, as shown in Figure 7.3(b) and Figure 7.4(b). This was consistent with vicinal fluorine-deuterium coupling,<sup>135</sup> thus giving confidence that these resonance peaks were due to fluorine from the TPD coupling with vicinal protons from the cyclohexane, hence further proving insertion reactions had occurred. It should be noted that  $^1\text{H}$  NMR spectra were also measured, but many peaks were revealed indicating many products and making analysis difficult.

When comparing the spectra of the thermal reaction products shown in Figure 7.3 with the UV reaction products shown in Figure 7.4, interestingly they appear quite different. The UV products show prominent peaks at  $\sim 14$  ppm (suggested to be due to the parent TPD) and  $\sim 6$  ppm which were also observed by Brunner *et al.*<sup>135</sup> However, the spectrum also revealed a prominent peak at  $\sim 10$  ppm which had not been observed previously. Furthermore, the peak observed by Brunner *et al.* at  $\sim -2$  ppm was not observed in this study. Therefore, the reaction mixture appeared to be different than observed previously by Brunner *et al.*

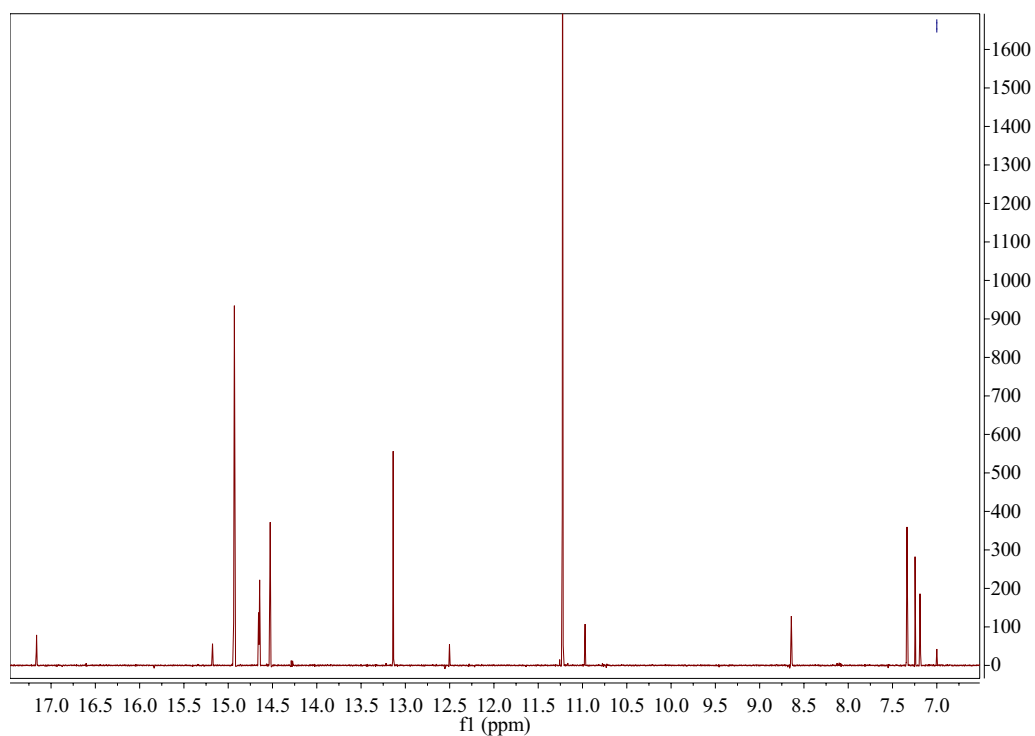
The spectra obtained from the thermal products appear significantly different, with chemical shifts on a different range compared to the products from the UV reaction. The most prominent peaks were observed at  $\sim 15$  ppm,  $\sim 13$  ppm and  $\sim 11$  ppm, suggesting different reaction products were formed depending on the activation method.

Despite the product mixtures appearing different in  $^{19}\text{F}$  NMR for thermal and UV



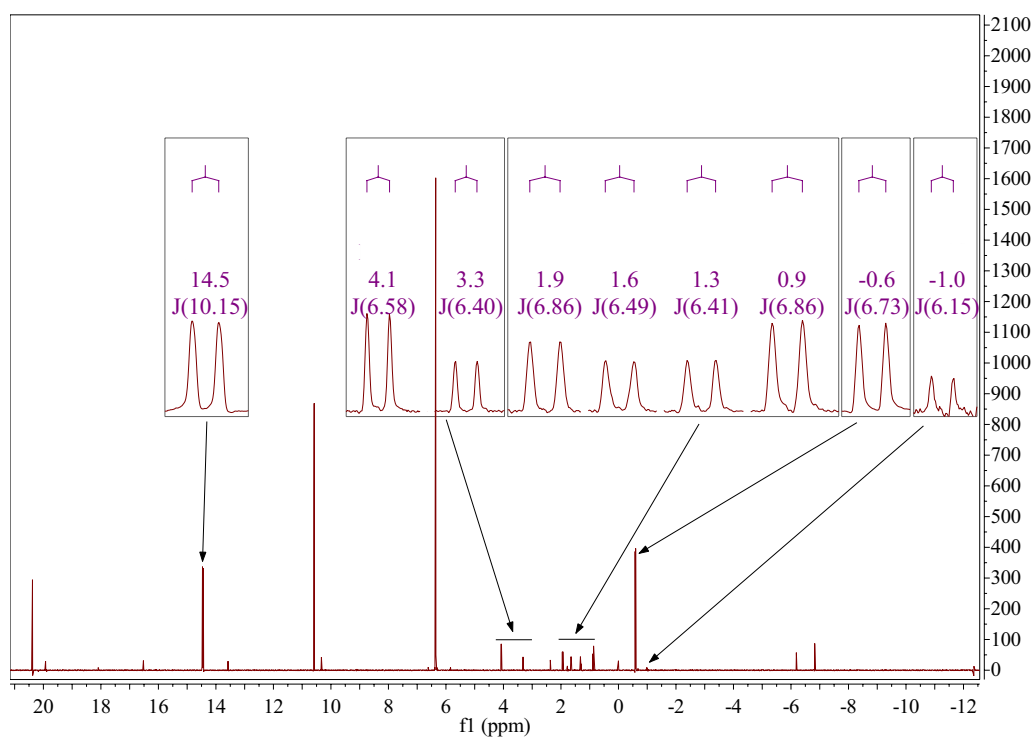


(a)

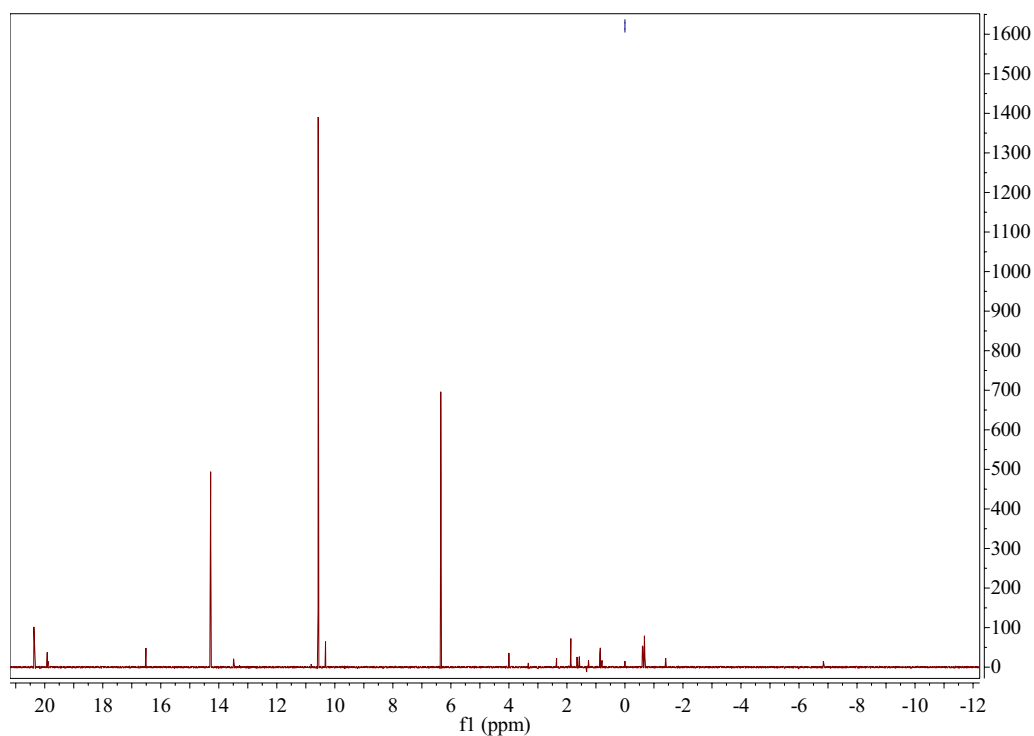


(b)

Figure 7.3:  $^{19}\text{F}$  NMR spectra of thermally reacted ( $80^\circ\text{C}$ , 8h) 3 mM TPD solutions in (a) cyclohexane and (b)  $\text{D}_{12}$ -cyclohexane. Inserts show magnified doublet peaks, labelled with chemical shift (ppm) and coupling constant,  $J$  (Hz). Chemical shifts were calculated relative to 100 %  $\text{CF}_3\text{COOH}$ .



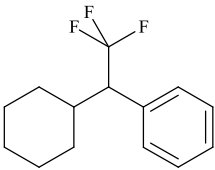
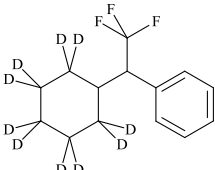
(a)



(b)

Figure 7.4:  $^{19}\text{F}$  NMR spectra of UV reacted (2.2 mW, 8h) 3 mM TPD solutions in (a) cyclohexane and (b)  $\text{D}_{12}$ -cyclohexane. Inserts show magnified doublet peaks, labelled with chemical shift (ppm) and coupling constant,  $J$  (Hz). Chemical shifts were calculated relative to 100 %  $\text{CF}_3\text{COOH}$

Table 7.1: GC relative peak-to-TPD ratios of CH insertion products. [\* indicates product in excess.]

| Solution                           | Reaction conditions             | Product  | Ratio Product : TPD |
|------------------------------------|---------------------------------|--|---------------------|
| Cyclohexane + TPD                  | Reflux 80°C, 2h                 |  | 0.48                |
|                                    | Reflux 80°C, 8h                 |  | 1.23*               |
|                                    | UV 2.2 mW cm <sup>-1</sup> , 8h |  | 1.04*               |
| D <sub>12</sub> -Cyclohexane + TPD | Reflux 80°C, 2h                 |  | 0.5                 |
|                                    | Reflux 80°C, 8h                 |  | 0.88                |
|                                    | UV 2.2 mW cm <sup>-1</sup> , 8h |  | 0.84                |

reactions, GC/MS revealed that the expected insertion product was a major fraction of the mixtures from both reactions. Table 7.1 displays the relative ratio of the insertion product : TPD, obtained from the GC peaks for two reflux reactions (two hours and eight hours), and for the UV initiated reaction at 2.2 mW for eight hours. As expected, the longer reflux time led to a greater proportion of the inserted product, indicating the reaction was incomplete after two hours. After the eight hour reflux in cyclohexane, the insertion product was found to be in excess of the TPD reactant. This was also observed for the eight hour UV reaction in cyclohexane. The D<sub>12</sub>-cyclohexane revealed a similar pattern with the eight hour reactions both containing a greater proportion of insertion product than the two hour reflux, however, not in excess of TPD.

These preliminary results successfully showed that TPD was able to generate a carbene and undergo CH insertion reactions. It was assumed that the modified TPDOH and TPDCOOH would also undergo CH insertions in the same manor. Following these findings, the CH insertion ability of TPD into solid surfaces, referred to as *grafting*, was assessed for the suitability of TPD as an AP for polar coatings onto plastic substrates.

## 7.4 Grafting to Substrates

A systematic approach was used to investigate the grafting ability of TPD to various substrates, as shown in Figure 7.5. The substrates became progressively more complex, starting with a model system (Figure 7.5(a)), which was designed to test the proof-of-concept of grafting TPD to simple alkane chains with no additives, then moving to a PP substrate (Figure 7.5(b)) closer in characteristics to that used in industry, but containing no additives, and finally using industrial PP based substrates containing all additives (Figure 7.5(c)).

The proof-of-concept study was conducted by comparing several different surfaces before and after TPD deposition, and after various washing steps, as shown in Figure 7.6, taken from the concept by Léonard *et al.*<sup>183-185</sup> Substrate A (before cleaning) was measured to check for any surface contamination and substrate B (A after cleaning) was measured to check the reduction of contaminations after a washing step at the surface. Substrate C (deposition of TPD without cure) was measured to assess the presence of the TPD, and substrate E (C after wash) was measured to verify the washing step and check the selected solvent, THF, washed all TPD away from the surface. Substrate D (C after cure) was used to assess the amount of TPD at the surface after the cure and substrate F (D after wash) was used to assess how much TPD remained at the surface after any ungrafted TPD was washed away (ability to graft to the surface only).

To test the grafting, three drops of pure TPD were deposited via a glass syringe onto the surface and cured. Initially, thermal curing was of great interest because both the waterborne basecoat and topcoat utilised in this study were thermally cured. Therefore, using the same curing method would reduce the number of steps in the coating production line; this being one of the goals of this research topic, as described in Section 1.2.

As a first test, a long curing time of 24 hours was selected, and the temperature was set to 80 °C (the same curing temperature as the basecoat and clearcoat). Secondly, a shorter realistic curing time of 30 minutes was tested and compared.

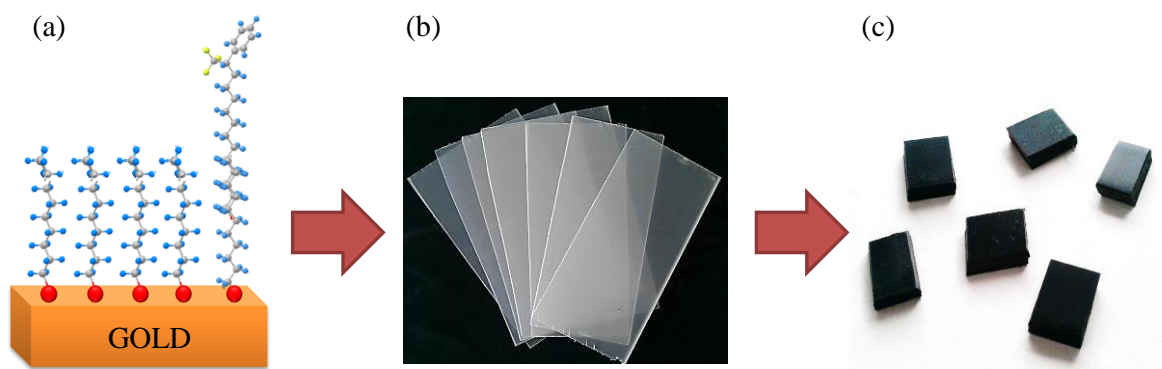


Figure 7.5: A systematic approach to testing the grafting ability of TPD to solid surfaces: (a) model alkane-thiol-gold self-assembled monolayer surface of differing chain lengths, (b) polypropylene sheet containing no pigment, (c) industrial TPO polypropylene substrate containing all additives including pigment.

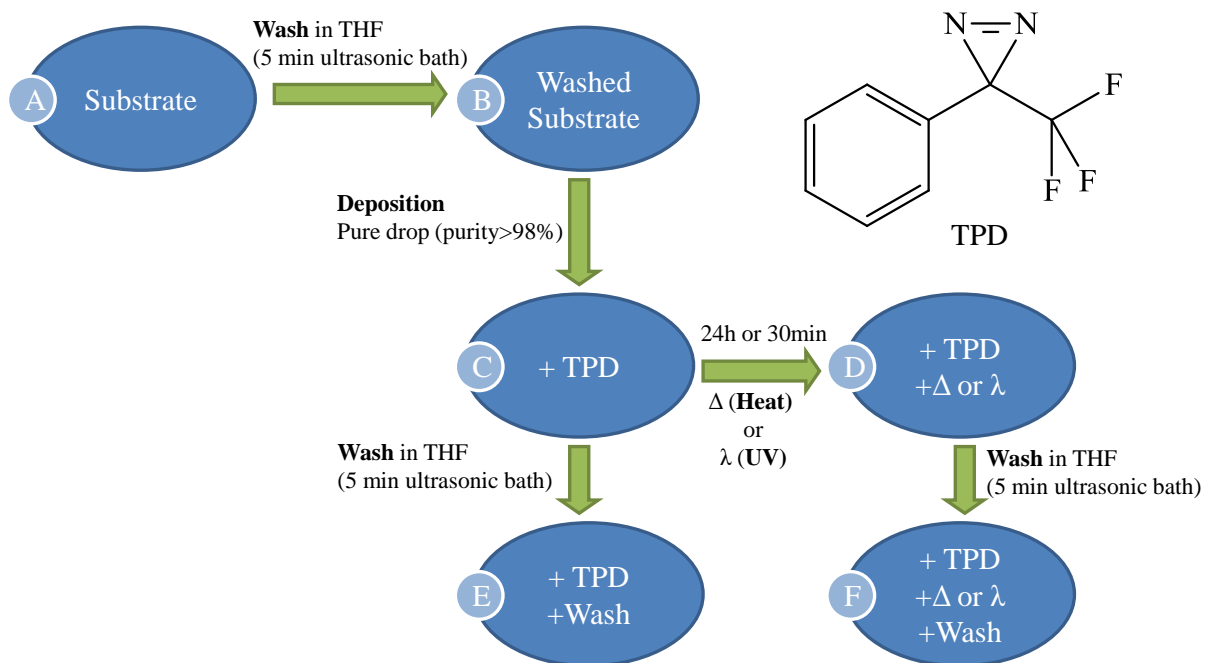


Figure 7.6: Experimental protocol for the grafting proof-of-concept experiment.

Two surface sensitive complementary techniques were used to compare the surfaces: ToF-SIMS which is qualitative, but extremely surface sensitive, measuring only the uppermost 1 - 2 atomic layers (approx. 10 Å), and XPS which is quantitative, but not as sensitive having a depth penetration of approx. 10 - 30 Å.<sup>95,186</sup>

The marker signal used to compare the surfaces was selected as fluorine (F) because it distinguished the TPD from the rest of the surface (*i.e.* the element was unique to TPD) and the substrate surfaces were found to only be lightly contaminated with F-containing substances, regarded as insignificant when compared to the grafted surfaces.

#### **7.4.1 Surface Grafting of TPD to the Model Self Assembled Monolayer (SAM) Surface**

After verifying the SAM had successfully formed on the gold surface to create the model (full details can be found in Appendix 10.H), the different surfaces A-F (Figure 7.6) were created and the ToF-SIMS and XPS spectra measured. The results are shown in Figure 7.7, where the F<sup>-</sup> intensity was measured using ToF-SIMS and normalised against the total ion count, so that a qualitative comparison could be performed. The F wt.% was measured using XPS, so that a quantitative comparison could be performed. The two techniques were compared to verify results. Figure 7.8 shows a magnified XPS spectra from substrate F after 24 hour curing at 80 °C. It demonstrates how the presence of TPD was identified through the use of modelling and matching binding energies which enabled the identification of the organic C-F<sub>3</sub> bond from the F 1s peak and the CF<sub>3</sub> bond from the C 1s peak, distinguishing it from any inorganic F-containing contaminants.

Firstly, the difference between the different substrates A-F were compared and discussed. It should be noted that the large error bars found in Figure 7.7(a) and (b) were due to surface inhomogeneity merely from the deposition method (glass syringe) not creating a uniform thickness of TPD on the surface (this was sufficient for a proof-of-concept study; however, film homogeneity becomes important when assessing adhesion in the later chapters).

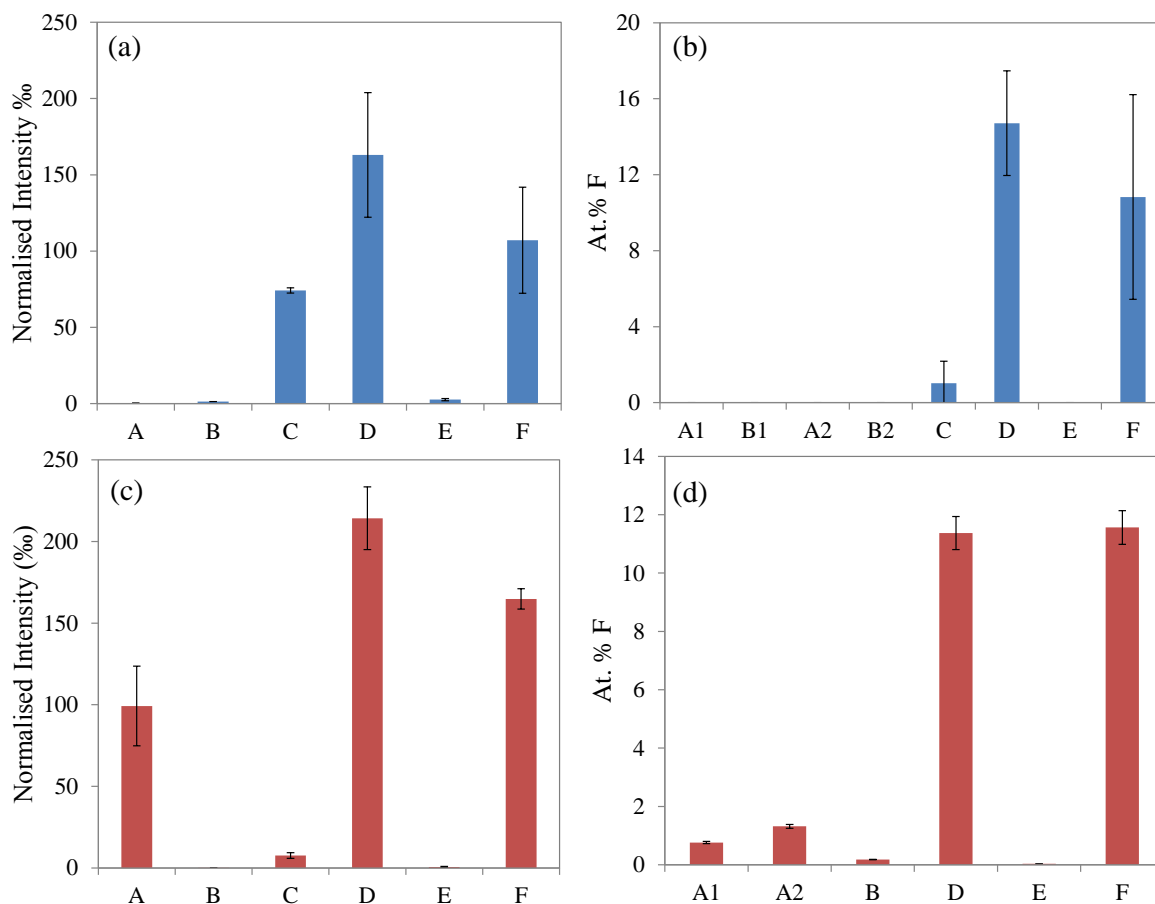


Figure 7.7: Thermal grafting of TPD at 80 °C on the model SAM surface. ToF-SIMS results show normalised F<sup>-</sup> intensity found at the surface and XPS results show F wt.% found at the surface: (a) normalised F<sup>-</sup> intensity, 24 h cure; (b) \*F wt.%, 24 h cure; (c) normalised F<sup>-</sup> intensity, 30 min cure; (d) \*F wt.%, 30 min cure: for surfaces A-F as represented in Figure 7.6 (substrate C was not measured in XPS (d) to avoid contamination). \*A1 represents the gold surface before plasma cleaning and SAM formation and A2 after plasma cleaning and SAM formation.

Initially, the untreated substrates were checked for fluorine contamination, which if present, would render the identification of TPD via fluorine intensity inaccurate. With the exception of the F<sup>-</sup> intensity shown in Figure 7.7(c), little fluorine contamination of the ungrafted, uncleaned substrate A was found. It was not known what caused the contamination of the surface during the ToF-SIMS measurement, however, washing the surface to give substrate B showed a significant effect and the contamination was successfully washed away. Two substrate A's were produced for XPS analysis when using SAM model surfaces, to compare the gold surface before plasma cleaning (A1) and after

plasma cleaning and SAM formation (A2). A small increase in F wt.% was observed after SAM formation, as shown in Figure 7.7(d) (cause of contamination unknown). However, washing the surface to give substrate B, showed a significant effect and the contamination was successfully washed away.

The stability of ungrafted TPD in the ultra-high vacuum conditions required for ToF-SIMS and XPS measurements was initially unknown, however, due to the high volatility of TPD, measurement of substrate C (ungrafted TPD deposited) caused some challenges. It was found to contaminate the vacuum chamber for XPS during the measurement of the 24 hour cure experiment, and so was no longer measured for the other XPS experiments. However, an increase in signal intensity from substrate B to substrate C was found for the 24 hour and the 30 minute cure, shown by the  $F^-$  intensity change in 7.7(a) and 7.7(c), and the F wt.% change in 7.7(b) indicating the presence of TPD.

As expected, a signal intensity increase was observed from substrate B to substrate D (addition of TPD and thermal curing), indicating the presence of TPD after grafting. The signal intensity also increased from substrate C to substrate D, further demonstrating the volatility of TPD. Thermal curing was thought to create covalent bonds between the TPD and the substrate surface, so that it could not readily evaporate as it could from substrate C, accounting for the greater signal intensity.

To confirm a C-C covalent bond had formed during the grafting of TPD, a peak from the fragmentation of a C-C bond past the newly formed C-C bond of the C-H inserted product was highlighted in the negative ToF-SIMS spectra, shown in Figure 7.9. Fragments of  $C_{17}H_{24}F_3S^-$  from an intact  $C_9$  SAM chain with one TPD molecule grafted were also evident at  $m/z = 317$ , proving the grafting theory had worked. This also demonstrated the TPD remained intact after the thermal curing at  $80^\circ C$  and no evidence of further decomposition, other than to the carbene intermediate, occurred. Although it was expected that grafting of TPD to the longer chain would be more likely to occur due to lower steric hindrances, there was no evidence of an intact  $C_{18}$  SAM with a TPD molecule (expected  $C_{26}H_{42}F_3S^-$  at  $m/z$  443). This was likely to be due to the lower fraction of



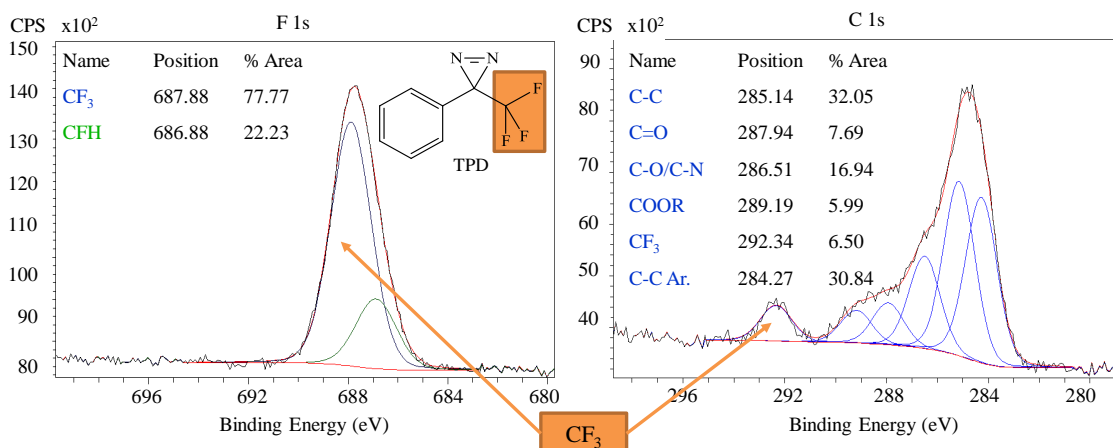


Figure 7.8: XPS peaks taken from the survey spectrum of a TPD-grafted SAM surface (80 °C, 24h) showing the F 1s peak (LHS), and the C1s peak (RHS), and the subsequent modelling highlighting the binding energies due to the C-F<sub>3</sub> bonding at 687.9 eV and 292.3 eV. This shows strong evidence that the TPD moiety can be distinguished from inorganic C-F surface contamination and other C bonding from the surface. For comparing the different surfaces, the F wt.% was taken from the F 1s peak (spectra were fitted by assuming a Gaussian/Lorentzian-Sum-Shape (90/10) for all components).

longer chains present compared to the smaller chains (making the fraction probability lower) and due to the vast excess of TPD molecules available to bond to all the chains present. It was further found that signal intensities of the fragments characteristic of the SAM decreased upon thermal grafting of TPD, indicating the TPD covered the top 1-3 atomic layers of the surface (sensitivity of measurement). The TPD also appeared to graft to oxygen found on the SAM surface (see Appendix 10.H), with a peak at  $m/z = 175$ , likely to be due to  $C_8H_6F_3O^-$ .

Substrate E represented substrate C after washing the ungrafted TPD away from the surface, significantly lowering the signal intensity. This verified the washing step and indicated the reliability of the results produced for substrate F, the washing of substrate D after TPD grafting.

Substrate F represented substrate D after a washing step, where it was expected that any ungrafted TPD on the surface would be washed away resulting in a reduced signal intensity (the TPD was applied as a pure liquid, therefore, it was highly likely that not all of the TPD would graft to the substrate surface).

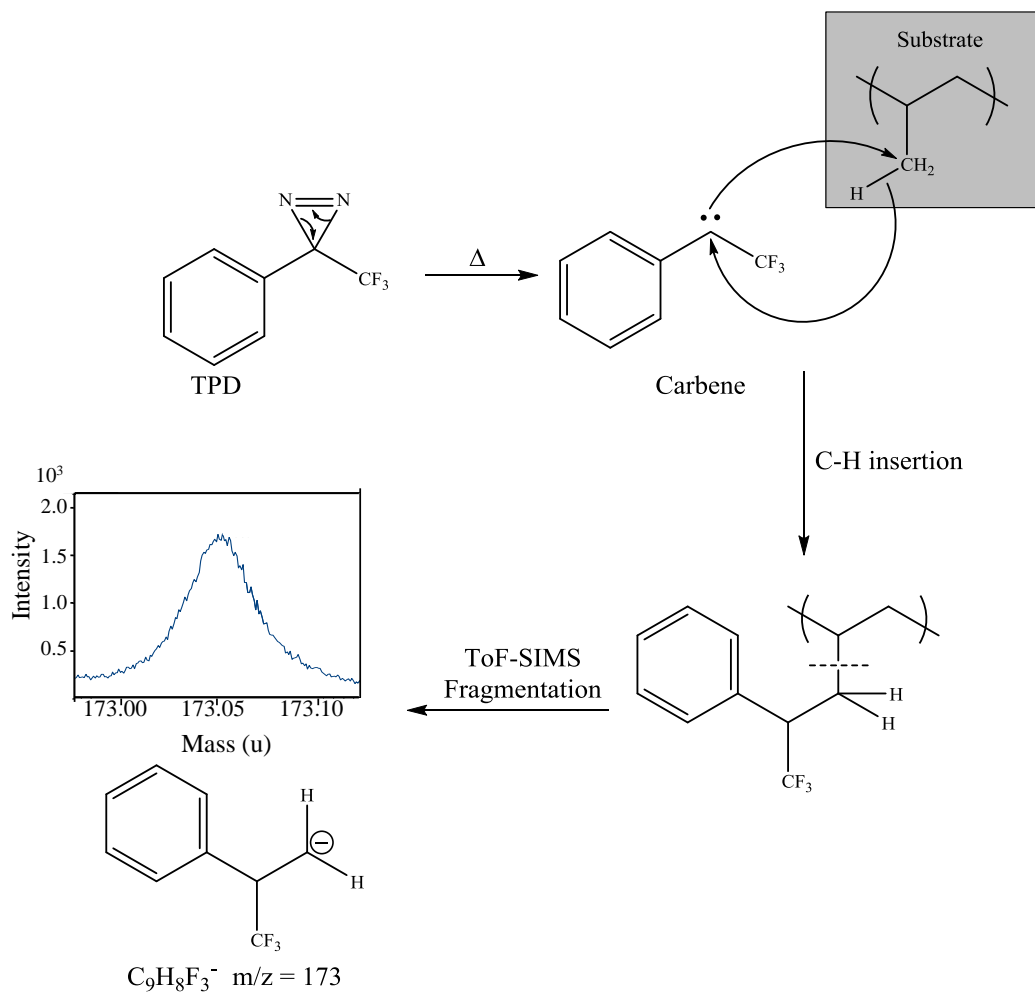


Figure 7.9: Top: the mechanism of carbene generation via thermal activation and the subsequent C-H insertion into the substrate surface, highlighting the fragmentation; bottom: negative ToF-SIMS peak at  $m/z = 173$  due to the fragmentation of the C-H insertion product past the newly formed C-C bond, proving a covalent bond is formed during the grafting process.

The only exception to this was found in the XPS spectrum for the 30 min cure shown in Figure 7.7(d), where the signal intensity of substrate F remained approximately the same as substrate D, implying no TPD was washed from the surface. Therefore, the TPD could have grafted to TPD layers already grafted to the substrate, forming a multi-layered structure which could not be washed away. Grafting between TPDOH molecules and between TPDCOOH molecules was observed in their mass spectra (see Appendix 10.G.1). However, this was not observed in the mass spectrum of TPD. It was found, however, that TPD was extremely sensitive and could only be detected using low energy ionisation

techniques. This grafting experiment suggests grafting between TPD molecules may have occurred, but were unable to be detected during mass spectrometry measurements.

Having compared the different substrates A-F to prove the grafting of TPD was possible, the difference in curing times displayed in Figure 7.7 were compared. The 24 hour curing time is shown in Figure 7.7(a)-(b) (in blue) and the 30 min curing time is shown in Figure 7.7(c)-(d) (in red). The difference between the F wt.% found on substrate D after 24 hour and 30 minute curing was approximately 3 %. The difference after the washing step on substrate F was nearer 0 %. The F<sup>-</sup> intensity change also showed little difference, suggesting no significant difference between the two curing times.

Overall, the XPS and ToF-SIMS data shown in Figure 7.7, complement each other and proved that TPD was able to graft to a model SAM surface via thermal curing at 80 °C. A curing time of greater than 30 minutes did not significantly improve the grafting efficiency.

#### **7.4.2 Surface Grafting of TPD to Polypropylene Substrates Containing No Additives**

The SAM model surface proved the ability of the TPD to thermally graft to the simple polymer brush-like surface. The next progression was to assess the grafting ability to a PP substrate closely related to substrates used in the industry, but containing no additives including pigments. The identification of the TPD grafting efficiency on progressively increasing complex substrates, enabled the assessment of any probable causes for a decrease in grafting efficiency. It was predicted that the grafting efficiency of TPD to the PP model surfaces would be less than the SAM model surface, due to a decrease in the order and possible higher density of polymer chains, hence, higher steric hinderances.

Figure 7.10 shows the F<sup>-</sup> intensity taken from ToF-SIMS data and the F wt.% taken from XPS data measured on the various surfaces A-F (experimental protocol shown in Figure 7.6). The thermally cured substrates D and F were cured at 80 °C for 24 hours and 30 minutes to be compared with the SAM model surface.

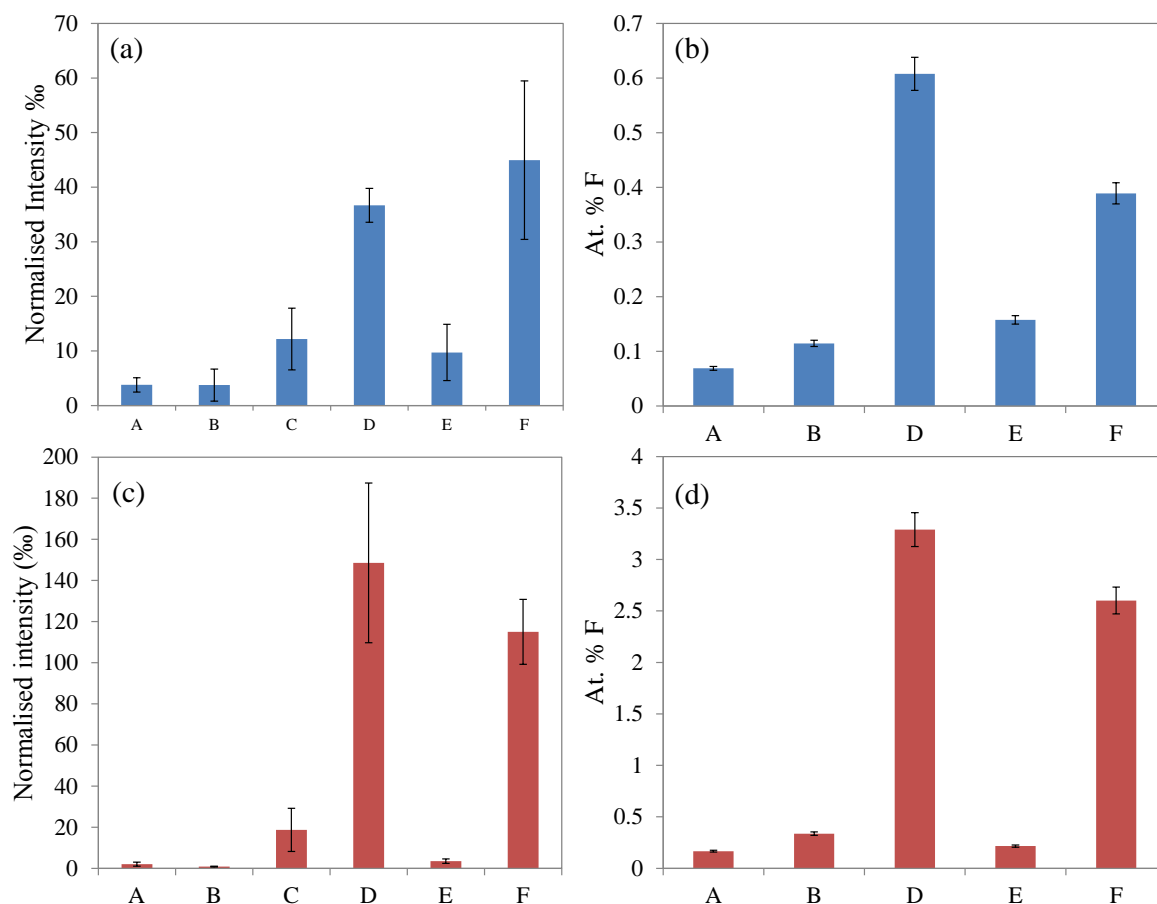


Figure 7.10: Thermal grafting of TPD at 80 °C on PP sheets containing no pigment. ToF-SIMS results show normalised F<sup>-</sup> intensity found at the surface and XPS results show F wt.% found at the surface: (a) normalised F<sup>-</sup> intensity , 24 h cure; (b) F wt.% , 24 h cure; (c) normalised F<sup>-</sup> intensity , 30 min cure; (d) F wt.%, 30 min cure: for surfaces A-F as represented in Figure 7.6 (substrate C was not measured in XPS to avoid contamination).

As expected, a similar trend to the SAM model surfaces was observed. Evidence of a low level of contamination from F-containing species was evident on substrates A and B (before and after cleaning), however, again once the TPD was deposited onto the PP surface in substrate C, there was a significant increase in signal intensity of F<sup>-</sup>. The volatility of TPD was again evident from the significant increase of the intensity after thermal curing for substrate D. Step E verified the washing step giving F<sup>-</sup> and F wt.% intensities on the scale of substrate B (before TPD deposition). For the 24 hour cure, the F<sup>-</sup> intensity of substrate F after a washing step of substrate D unexpectedly increased. However, analysis of the positive ToF-SIMS data revealed significant silicone contamination on the surface of substrate D (from an unknown source), which likely

hindered the signal. The F wt.% in the XPS data contradicts this and shows the expected pattern with substrate F having a lower intensity than substrate D, due to the washing away of any ungrafted TPD from the surface (and also the depth of analysis from XPS is larger than ToF-SIMS which may improve the F wt.% signal).

Interestingly when comparing the two curing times, the intensity of the data from the grafted substrates (D and F) of the 30 minute cure was significantly larger than the 24 hour cure. Comparing the ratios of the F<sup>-</sup> and F wt.% intensity from substrate D: substrate E and substrate F: substrate E, they were significantly larger for the 30 minute cure than the 24 hour cure, also showing that more TPD had grafted at the surfaces after 30 minutes. Analysis of the positive ToF-SIMS spectrum equivalent to Figure 7.10(a) revealed significant silicone-based contamination of the substrates D and F, being a likely explanation for the cause of the lower intensities after 24 hours (significant contamination was not present on substrates after 30 minute cure). However, it was not necessary to repeat the experiment because 24 hours would not be a plausible curing time in an industrial set-up, and the positive results shown after the 30 minute cure were of greater interest. It should also be noted that silicon-containing compounds were not of interest as APs because they cause the undesired effect of craters in the coating.<sup>87</sup>

When comparing the grafting results from the model SAM surface in Figure 7.7 and the PP surface with no additives in Figure 7.10, a clear intensity drop was evident moving to the PP surface. For example, the F wt.% of substrate F after a 30 minute cure was  $\sim 11\%$  on a SAM surface and  $\sim 2.5\%$  on the PP surface, a significant difference. As previously mentioned, this was likely to be due to an increased steric hindrance of the randomly orientated, well-packed polymer chains of the PP surface, making it difficult for a TPD molecule to graft to an exposed chain, compared to the less hindered, vertically orientated polymer chains of the SAM surface. Overall, TPD was successfully grafted to a PP surface containing no additives.

### **7.4.3 Surface Grafting of TPD to Industrial TPO/0 Substrates, Containing No EPDM**

The next natural progression was to assess the grafting of TPD to industrial substrates. Firstly, the ability of TPD to graft to a TPO substrate containing no EPDM (which could potentially influence grafting properties) was assessed. To compare the various substrates tested, the same curing times of 24 hours and 30 minutes were used.

Figure 7.11 shows the  $F^-$  intensity and  $F$  wt.% of the various substrates shown in Figure 7.6. Little evidence of surface contamination was found, and as expected the overall intensities of the substrates were larger for the 24 hour curing time than for the 30 minute curing time. Between the substrates A-F, the same pattern was found as for the SAM model surface and PP surface. Clear evidence of TPD grafting was found, when comparing the signal intensities of substrate F and substrate B for both the 24 hour cure and the 30 minute cure. There was a 0.7 wt.% difference between substrate F after 30 minutes curing time on the TPO/0 substrate in Figure 7.11 (d) and the PP substrate in Figure 7.10 (d), suggesting the addition of the additives to PP-based substrates hindered the grafting ability to an extent. However, successful thermal grafting was observed at 80 °C.

### **7.4.4 Surface Grafting of TPD to Industrial TPO/2 Substrates, Containing EPDM**

The addition of 2 % EPDM to a TPO substrate (TPO/2) was tested subsequently, as shown in Figure 7.12. A decrease in signal intensity of the substrates D and F after a 24 hour cure compared to the 30 minute cure were again observed, as was found with the PP surfaces. Analysis of the positive ToF-SIMS spectra of these surfaces suggested this was due to signal hindrance from silicone contamination at the surface. However, it was not necessary to reproduce since successful TPD grafting evidence was found after the 30 minute cure (closer to industrial time scales).

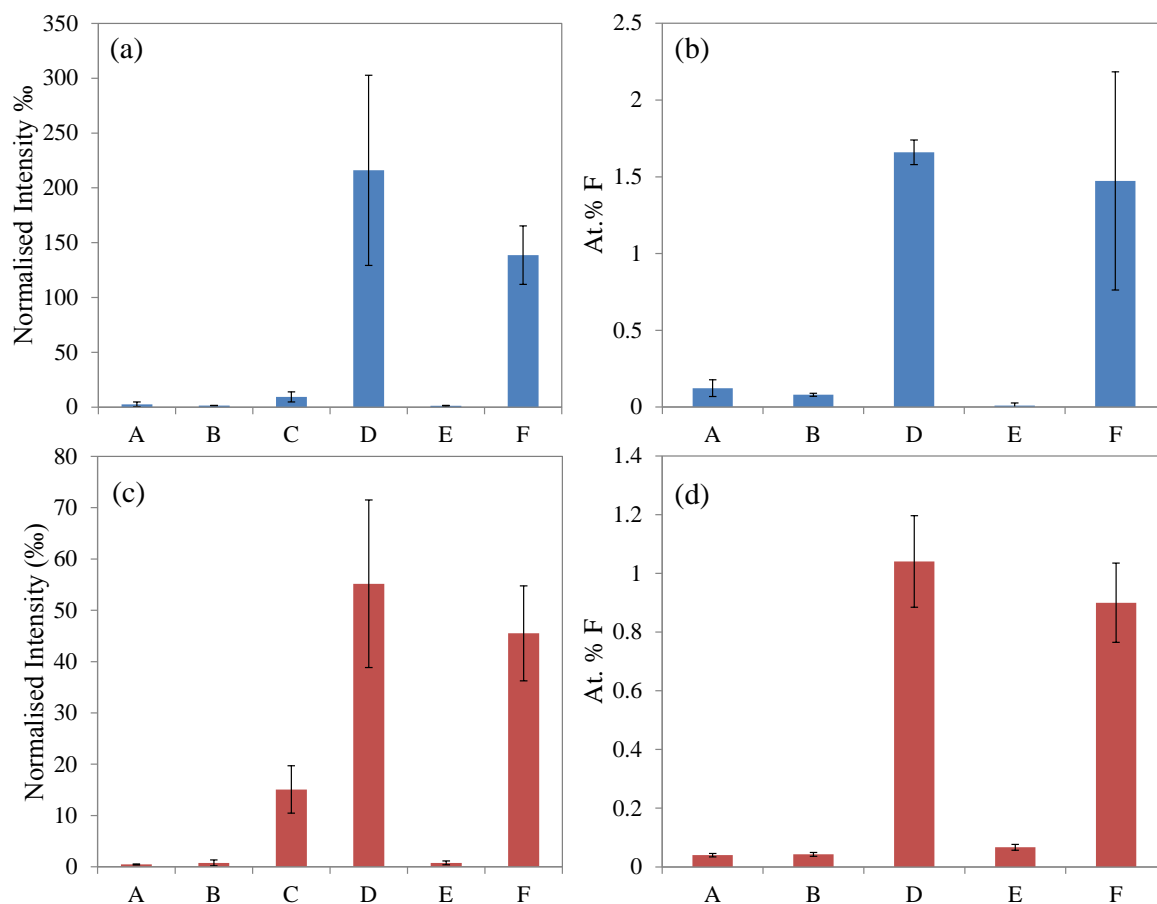


Figure 7.11: Thermal grafting of TPD at 80 °C on the industrial TPO/0 substrate. ToF-SIMS results show normalised F<sup>-</sup> intensity found at the surface and XPS results show F wt.% found at the surface: (a) normalised F<sup>-</sup> intensity , 24 h cure; (b) XPS , 24 h cure; (c) normalised F<sup>-</sup> intensity , 30 min cure; (d) F wt.%, 30 min cure: for surfaces A-F as represented in Figure 7.6 (substrate C was not measured in XPS to avoid contamination).

Despite taking precaution when handling the samples, often silicone surface contamination was present. This could have been due to a number of reasons, such as the contact with personal care products like hairspray or hand cream, however, it was not possible to identify the contamination source. The industrial laboratory limited the cleanliness that was possible when handling the samples, however, for the purpose of the study, the significance of the data was sufficient for all purposes.

A small difference in the signal intensity of the F wt.% of substrate F after a 30 minute cure on the TPO/2 surface ( $\sim 0.7\%$ ) and the TPO/0 surface ( $\sim 0.9\%$ ) was found, however when accounting for the low silicone contamination found at the surfaces, the significance of this difference is debatable. When comparing to the equivalent non-

pigmented PP surface (2.6 wt.%), the 0.2 wt.% difference between the TPO/0 and TPO/2 substrates can be considered as negligible. Therefore, future grafting experiments were carried out on the industrially relevant TPO/0 substrate.

Overall, TPD was successfully grafted to the industrial TPO/2 substrate at 80 °C.

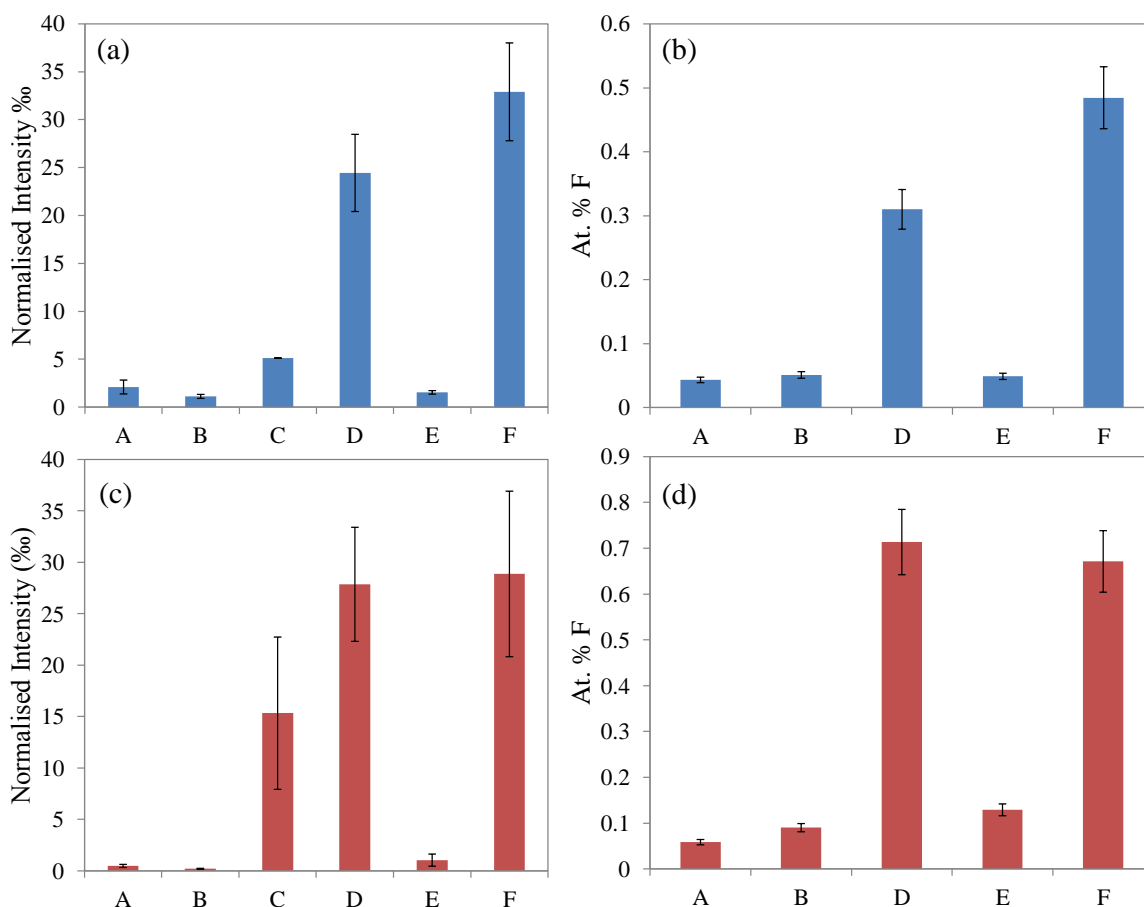


Figure 7.12: Thermal grafting of TPD at 80 °C on the industrial TPO/2 substrate (containing 2 % EPDM). ToF-SIMS results show normalised  $F^-$  intensity found at the surface and XPS results show F wt.% found at the surface: (a) normalised  $F^-$  intensity , 24 h cure; (b) F wt.%, 24 h cure; (c) normalised  $F^-$  intensity , 30 min cure; (d) F wt.%, 30 min cure: for surfaces A-F as represented in Figure 7.6 (substrate C was not measured in XPS to avoid contamination).



## 7.5 Modification of TPD, Tailoring for the Adhesion at the AP/Basecoat Interface

Having successfully grafted TPD to various substrates including industrially relevant substrates, the next step was taken to modify TPD with hydrophilic functional groups to account for adhesion between the newly grafted surface and the waterborne basecoat. Figure 7.13 shows the two structures that were chosen, denoted as TPDCOOH and TPDOH, which could potentially H-bond to other hydrophilic components found in the waterborne basecoat.

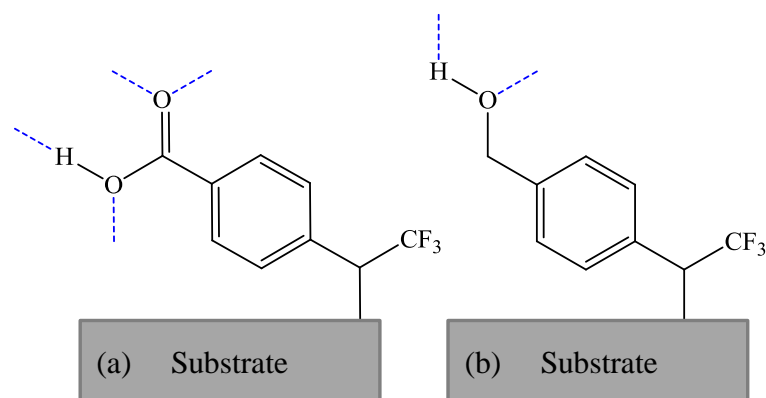


Figure 7.13: Modifying TPD with hydrophilic functional groups to allow for adhesion with the applied waterborne basecoat via hydrogen bonding, as shown schematically for (a) TPDCOOH and (b) TPDOH.

### 7.5.1 Surface Grafting of TPDOH to Industrial TPO/0 Substrates at 80 °C

As with TPD, TPDOH is a liquid, and can be easily applied in pure form or diluted with a solvent. To move the grafting conditions towards an industrial relevant protocol, TPDOH diluted with solvent was tested (more economical for industrial application), as well as TPDOH in its pure form for fundamental purposes.

The  $\text{F}^-$  and  $\text{F}$  wt.% intensities for pure TPDOH are shown in Figure 7.14(a)-(b), and for 0.5 M TPDOH in acetone are shown in Figure 7.14(c)-(d). Previous grafting

experiments with TPD showed that a grafting time of 30 minutes was sufficient to obtain significant results, therefore, this curing time was used for TPDOH and TPDCOOH tests.

Applying acetone solutions on a lab scale via syringe application for this proof-of-concept was not problematic, but it was known that in industrial practice, when applying acetone solutions (classified as highly flammable) to substrates using spray application systems, it can be dangerous and correct grounding (or earthing) and bonding (connection of two or more conductive objects by a conductor) procedures are very important. The solution passing through the nozzle of the spray gun would generate a static charge and the acetone would cause flammable vapours to evolve into the area where the spraying is conducted. This could cause a potential explosion. Thus, the spray gun must be bonded to the substrate and the substrate must be bonded to the ground (grounded) in order to prevent potential ignition of the flammable vapours generated by the acetone when using a spray application. Although it was known that acetone would not be a desirable solvent in an industrial application, a solvent with such a high volatility rate was desirable for the proof-of-concept, so that it would evaporate away from the surface leaving behind the TPDOH and eliminating the possible side reaction of TPDOH grafting with solvent molecules.

Figure 7.14(a) shows the  $F^-$  intensity for the substrates A-F, when the grafting ability of pure TPDOH was tested. Substrates A and B showed a minimal signal intensity, showing that very little fluorine-containing surface contamination was present before and after the substrate cleaning. The large signal intensity from substrate C, which was comparable in intensity to substrate D, showed that TPDOH was significantly less volatile than TPD, and a strong signal was measured when the TPDOH was deposited on the surface without grafting. A significantly larger signal intensity was present at surface D compared to surface B, after thermal curing. Substrate E again verified the washing step. Substrate F had a small intensity decrease compared to substrate D, due to any ungrafted TPDOH molecules being washed away, but had a significantly larger intensity than substrate B, demonstrating that TPDOH was able to thermally graft to TPO/0.

Interestingly, this pattern was not mimicked in the equivalent F wt.% results shown in Figure 7.14(b), where the intensity of substrate D dominated over the intensities of all the other substrates. One likely reason could be due to the low TPDOH volatility as previously mentioned. This could result in a high presence of ungrafted TPDOH at the surface of substrate D, before washing. Washing to give substrate F removed the large proportion of ungrafted TPDOH from the surface, so that only a small signal intensity remained (when comparing to substrate D of TPD, it could be that the signal intensities were lower because a proportion of the ungrafted TPD could readily evaporate).

When diluting the TPDOH to give 0.5 M solutions, the regular pattern of the substrates A-F was again observed. The F<sup>-</sup> intensity shown in Figure 7.14(c), again demonstrated the low volatility of TPDOH by substrate C giving a significantly high signal intensity (TPDOH deposited without grafting) compared to all other substrates. Substrates A and B showed minimal contamination, and substrate E verified the washing step. Substrate F showed a lower intensity than substrate D, but higher than substrate B and E, again showing some ungrafted TPDOH was washed away from the surface, but overall TPDOH was able to be thermally grafted to the TPO/0 substrate. The signal intensity of substrate F for the 0.5 M solution was about half of the signal intensity of the pure TPDOH, which would be expected for a lower concentration.

The F wt.% for the 0.5 M solutions, shown in Figure 7.14(d), showed a lower signal intensity for substrate D compared to the pure TPDOH in Figure 7.14(b), which was not unexpected due to the lower concentration used. The pattern of substrates A-F in Figure 7.14(d) was as expected. Small amounts of fluorine contamination was found on substrates A and B, where the washing step slightly reduced the contamination. The intensity significantly increased after TPDOH deposition and thermal curing for substrate D, and the intensity reduced slightly after ungrafted TPDOH was washed away on substrate F. Substrate E verified the washing step with an intensity comparable to substrate B. The intensity of substrate F for the 0.5 M solution was comparable to pure TPDOH (Figure 7.14 (b)), suggesting that the dilution of TPDOH did not affect the grafting efficiency.

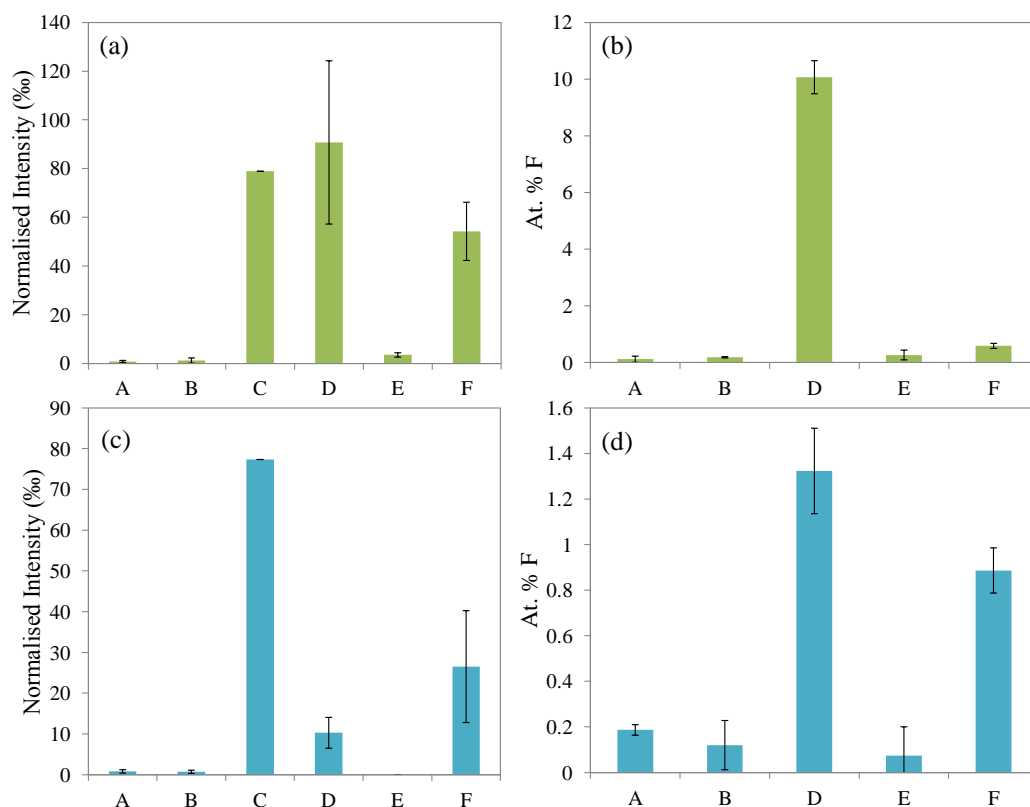


Figure 7.14: Thermal grafting of TPDOH at 80 °C for 30 min on the industrial TPO/0 substrate. ToF-SIMS results show normalised  $F^-$  intensity found at the surface and XPS results show F wt.% found at the surface: (a) normalised  $F^-$  intensity, TPDOH pure; (b) F wt.%, TPDOH pure; (c) normalised  $F^-$  intensity, 0.5 M TPDOH; (d) F wt.%, 0.5 M TPDOH: for surfaces A-F as represented in Figure 7.6 (substrate C was not measured in XPS to avoid contamination). Due to the lower volatility of TPDOH compared to TPD, the intensity of substrate C for TPDOH is larger.

This was expected since the acetone would readily evaporate, preventing possible side reactions with TPDOH (TPDOH would preferentially react with the mobile, less sterically hindered solvent molecules over the polymer substrate) as previously mentioned, and the amount of TPDOH molecules available to react at the surface was in large excess.

Overall, the grafting of TPDOH via thermal curing to an industrial TPO/0 substrate was possible after a 30 minute curing time at 80 °C, whilst the dilution with acetone did not significantly affect the grafting efficiency.

### **7.5.2 Surface Grafting of TPDCOOH to Industrial TPO/0 Substrates at 80 °C**

Unlike TPD and TPDOH, TPDCOOH is a solid white powder. Therefore, it was not applied in pure form and only a 0.5 M solution in acetone was tested. Once again the curing temperature remained 80 °C and the curing time was 30 minutes.

Figure 7.15 shows XPS andToF-SIMS spectra before and after the grafting of TPDCOOH. Figure 7.16 shows the F<sup>-</sup> and F wt.% intensity for the substrates A-F.

Minimal fluorine contamination was found on substrates A and B, and Figure 7.16(a) shows that a signal was detected after the TPDCOOH was deposited without curing on substrate C, because the TPDCOOH remained at the surface after the solvent evaporated (this was visually observed by the presence of a white layer). After thermal curing, a significant intensity was found on substrate D which was reduced after the washing step to give substrate F. However, the intensity of substrate F remained larger than substrate B or E, proving TPDCOOH was able to thermally graft to the industrial TPO/0 substrate. The intensity of substrate E was comparable to substrate B, verifying the washing step. Comparing substrate F in Figure 7.16(b) and 7.14(d) showed little difference between the grafting efficiency of 0.5 M TPDOH and 0.5 M TPDCOOH.

Overall, a solution of 0.5 M TPDCOOH in acetone is able to thermally graft at 80 °C for 30 minutes to an industrial TPO/0 substrate.

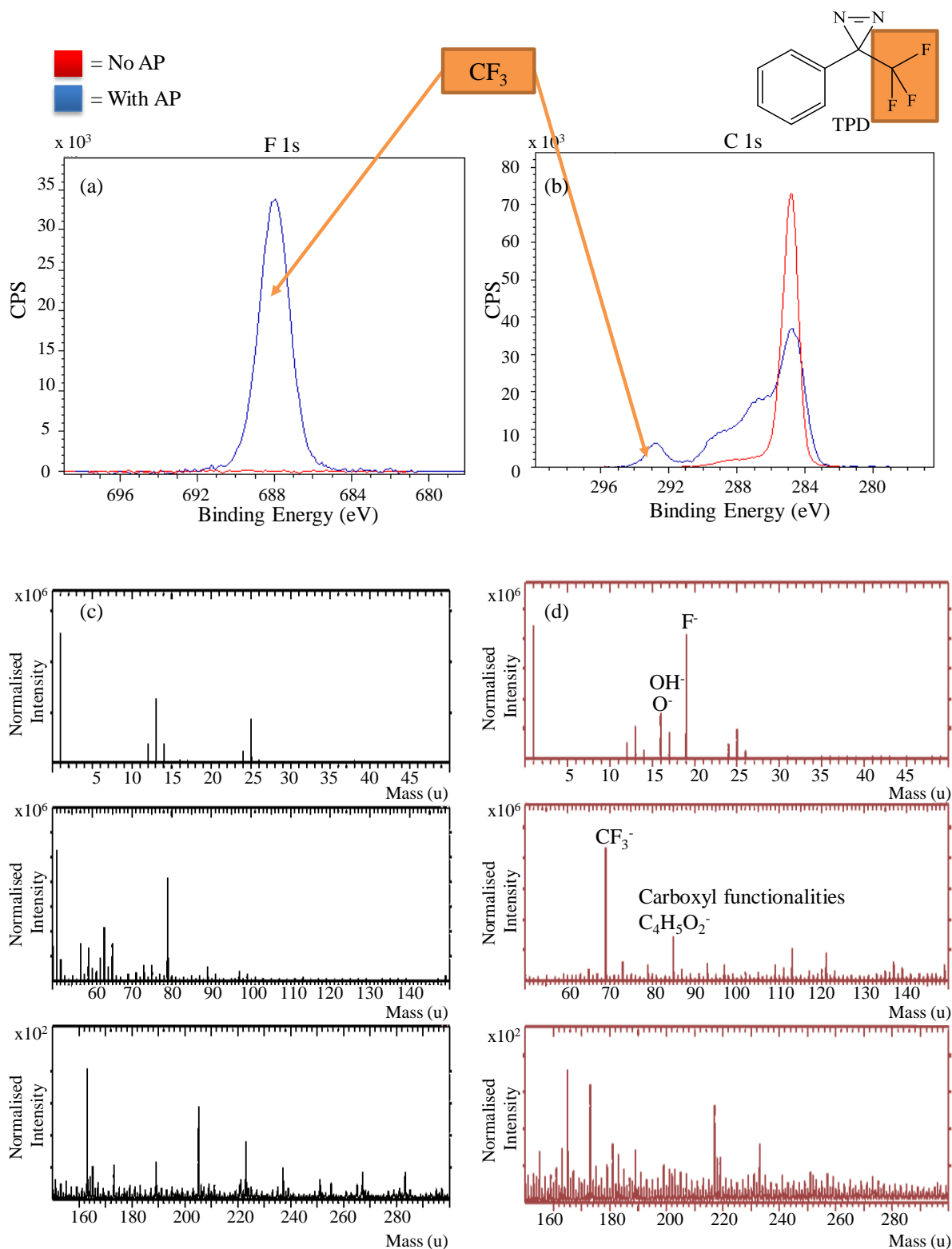


Figure 7.15: XPS narrow region scans of (a) F 1s peak and (b) C 1s peak, before and after TPDCOOH grafting, and ToF-SIMS spectra of (c) the TPO/0 substrate before and (d) after TPDCOOH grafting. The spectra show that F and O containing species are unique to TPDCOOH, (the C 1s spectrum shows a peak at 285 eV characteristic of C—C/C—H present in both TPO/0 and TPDCOOH.)

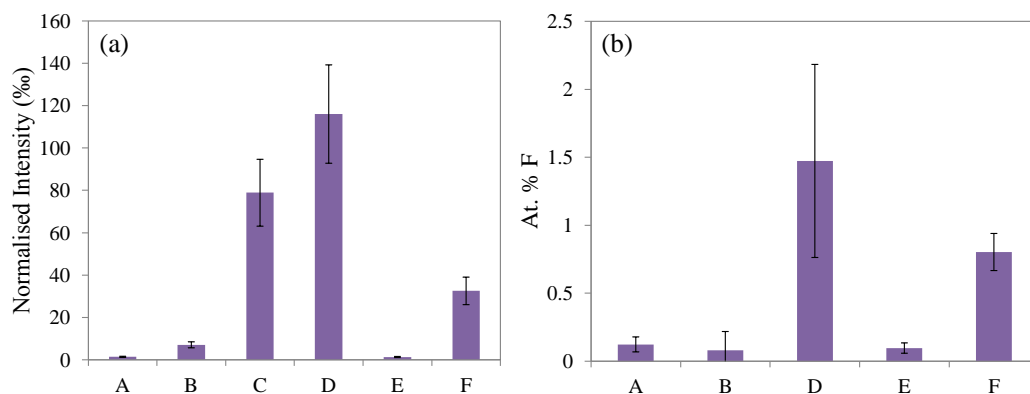


Figure 7.16: Thermal grafting of TPDCOOH at 80 °C for 30 min on the industrial TPO/0 substrate. ToF-SIMS results show normalised F<sup>-</sup> intensity found at the surface and XPS results show F wt.% found at the surface: (a) normalised F<sup>-</sup> intensity, 0.5 M TPDCOOH; (b) F wt.%, 0.5 M TPDCOOH: for surfaces A-F as represented in Figure 7.6 (substrate C was not measured in XPS to avoid contamination).

### 7.5.3 Surface Grafting of TPDOH to Industrial TPO/0 Substrates at 100 °C

Thus far, the grafting ability of TPD, TPDOH and TPDCOOH was tested at 80 °C. This temperature was the most relevant since the waterborne basecoat and topcoat, used later in this study, cure at this temperature. Therefore, the number of steps would be reduced in the production line if the AP could be formulated into the basecoat. However, to explore how the curing temperature would influence the grafting efficiency, the experiment using TPDOH and TPDCOOH was repeated at 100 °C.

The F<sup>-</sup> and F wt.% intensities for substrates A-F for pure TPDOH are shown in Figure 7.17(a)-(b), and for 0.5 M TPDOH are shown in Figure 7.17(c)-(d). The ratios of signal intensity for substrates A-F was as expected and as seen previously. The signal intensity for substrate F after the grafting of pure TPDOH was found to be higher at 100 °C (Figure 7.17 (b)) than at 80 °C (Figure 7.14 (b)) by ~ 6 wt.%, however the signal intensity for substrate F after the grafting of 0.5 M TPDOH at 100 °C (Figure 7.17 (b)) was slightly less than at 80 °C (Figure 7.14 (b)) by ~ 0.5 wt.% (a value close to the standard deviation) . Therefore, increasing the temperature by 20 °C only significantly

influenced the grafting efficiency of the pure TPDOH and not 0.5 M TPDOH.

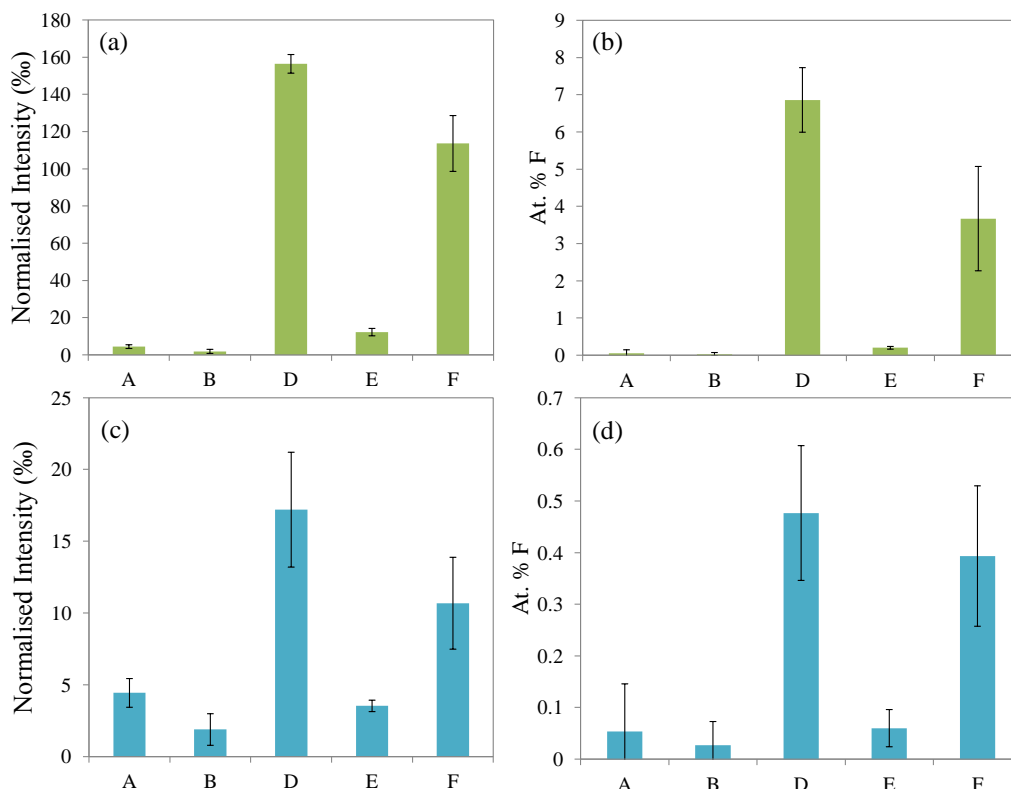


Figure 7.17: Thermal grafting of TPDOH at 100 °C for 30 min on the industrial TPO/0 substrate. ToF-SIMS results show normalised F<sup>-</sup> intensity found at the surface and XPS results show F wt.% found at the surface: (a) normalised F<sup>-</sup> intensity, TPDOH pure; (b) F wt.%, TPDOH pure; (c) normalised F<sup>-</sup> intensity, 0.5 M TPDOH; (d) F wt.%, 0.5 M TPDOH: for surfaces A-F as represented in Figure 7.6 (substrate C was not measured in XPS to avoid contamination).

#### 7.5.4 Surface Grafting of TPDCOOH to Industrial TPO/0 Substrates at 100 °C

The F<sup>-</sup> and F wt.% intensities when using 0.5 M TPDCOOH at 100 °C for substrates A-F are shown in Figure 7.18. The ratio of the intensities between the substrates A-F was as expected and evidence of grafting of TPDCOOH was shown as seen previously. The signal intensity for substrate F after the grafting of 0.5 M TPDCOOH was found to be higher at 100 °C (Figure 7.18 (b)) than at 80 °C (Figure 7.16 (b)) by ~ 2.5 wt.%. Also, the intensity of F wt.% found after the curing and washing of 0.5 M TPDCOOH on



substrate F was found to be  $\sim 3$  wt.% greater than for the substrate F after the curing and washing of 0.5 M TPDOH.

Overall, the curing temperature was shown to have a positive effect on the grafting efficiency of 0.5 M TPDCOOH, which was found to be better than 0.5 M TPDOH. It was therefore hypothesised that the adhesive effects of TPDCOOH would be greater than TPDOH, after thermal curing.

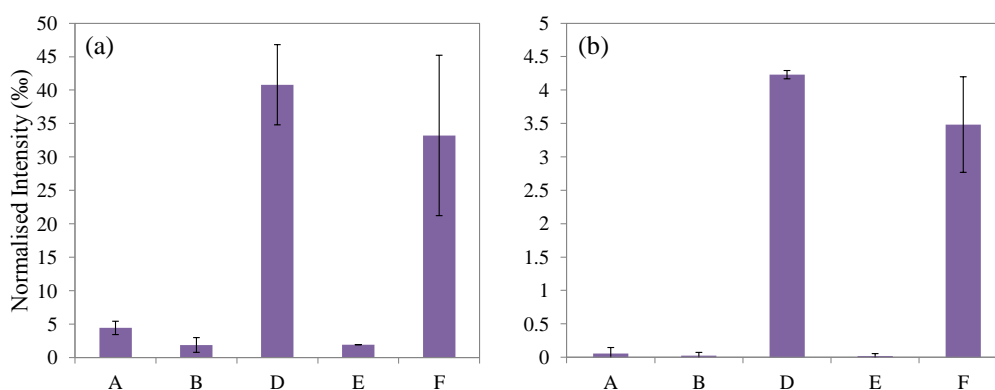


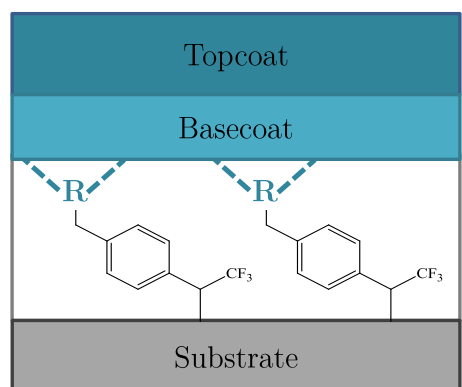
Figure 7.18: Thermal grafting of TPDCOOH at 100 °C for 30 min on the industrial TPO/0 substrate. ToF-SIMS results show normalised F<sup>-</sup> intensity found at the surface and XPS results show F wt.% found at the surface: (a) normalised F<sup>-</sup> intensity, 0.5 M TPDCOOH; (b) F wt.%, 0.5 M TPDCOOH: for surfaces A-F as represented in Figure 7.6 (substrate C was not measured in XPS to avoid contamination).

### 7.5.5 Prediction of TPD Solution Concentration to Create a Monolayer

The concentration of a TPD, TPDOH or TPDCOOH solution required to create a monolayer were predicted, as described in Section 4.21.1. This gave an estimation of the extent to which the TPD, TPDOH or TPDCOOH molecules were in excess in the solutions used during the grafting experiment.

The results are displayed in Figure 7.19. It was found that all three 0.5 M solutions that had been used in the grafting study were largely in excess, by  $\sim 60,000$  %. Assuming the film thickness formed was that of a 5  $\mu\text{m}$  doctor blade, and all molecules stacked on top of one another in the form of cuboids,  $\sim 4000$  layers of each molecule would be present.

This was a crude estimation, but it was useful to show that under the conditions used, the whole surface of the substrate would be expected to be covered by the TPD, TPDOH or TPDCOOH if the grafting efficiency at the set conditions was sufficient.



| AP      | Concentration for 1 monolayer (mol dm <sup>-3</sup> ) | % Excess compared to 0.5M solution | No. Layers in 5 μm thickness |
|---------|---|------------------------------------|------------------------------|
| TPD     | 9.43 x 10 <sup>-5</sup>                               | 53000                              | 4700                         |
| TPDOH   | 6.63 x 10 <sup>-5</sup>                               | 75000                              | 3900                         |
| TPDCOOH | 6.86 x 10 <sup>-5</sup>                               | 73000                              | 4000                         |

Figure 7.19: Theoretical calculations for the concentration required of each AP for one monolayer on the surface, the concentration % excess of the 0.5 M solutions used, and the number of layers that would be present in a 5 μm thickness. Calculations of the molecule diameter were calculated using Cosmo, assuming an energetically lower conformer is favoured in the gas phase. The volume occupied by one molecule of AP was modelled as a cube and rigidity of the AP molecules was assumed, so that layers of cubes stack on top of each other without collapsing. Calculations were based on a 5 μm layer thickness, and an area of 8 x 8 cm.

### 7.5.6 Surface Grafting of TPDOH and TPDCOOH to Industrial TPO/0 Substrates with UV Curing at a Radiance Exposure of 1900 mJ cm<sup>-2</sup>

So far, only thermal grafting of TPD, TPDOH or TPDCOOH had been considered because from an industrial point of view, having the curing method the same as the water-borne basecoat and topcoat (used in this study) would reduce the number of steps in the production line.

An alternative curing method sometimes used in the coatings industry is the use of UV light. It has the advantage that UV curing can be used in cool conditions so that substrates prone to deformation at high temperatures can be coated. However, a disadvantage is that it introduces an extra step into the production line (see Figure 1.4).

Positive UV initiated CH insertion reactions between TPD and cyclohexane had previously been observed in Section 7.3.1. As a last proof-of-concept in the grafting study, the grafting efficiency of 0.5 M TPDOH and 0.5 M TPDCOOH cured with UV at a radiance exposure of  $1900 \text{ mJ cm}^{-2}$  was tested and compared to the results of thermal curing at  $80^\circ\text{C}$  and  $100^\circ\text{C}$ .

The results are shown in Figure 7.20 for substrates A-F. Since UV light could generate oxygen radicals which could have a potential influence on the adhesive properties at the surface of the substrates,<sup>117</sup> an extra substrate, B(UV), was tested which was a washed substrate B that had been exposed to UV. Although only the  $\text{F}^-$  and F wt.% intensities are displayed in Figure 7.20, the oxygen content was also monitored at the surface via the  $\text{O}^-$  and O wt.% intensities, but no significant difference was found before and after UV treatment.

The ratio of the intensities of substrates A-F show the expected pattern previously observed. The significantly larger  $\text{F}^-$  and F wt.% intensities for substrate F compared to B and E showed that TPDOH and TPDCOOH successfully grafted to a TPO/0 substrate via UV curing.

The F wt.% (quantitative) of substrate F after 0.5 M TPDCOOH was cured (Figure 7.20(d)) is  $\sim 10$  times greater than for the 0.5 M TPDOH (Figure 7.20(b)). The  $\text{F}^-$  intensity (qualitative) of substrate F after 0.5 M TPDCOOH (Figure 7.20(c)) was cured is  $\sim 2$  times greater than the 0.5 M TPDOH (Figure 7.20(a)). Therefore, TPDCOOH showed a significantly greater grafting efficiency compared to TPDOH.

When comparing the F wt.% intensities between the different curing methods, the UV curing produced similar results found for thermal curing of TPDCOOH and TPDOH at  $100^\circ\text{C}$  (and greater intensities than thermal curing at  $80^\circ\text{C}$ ).

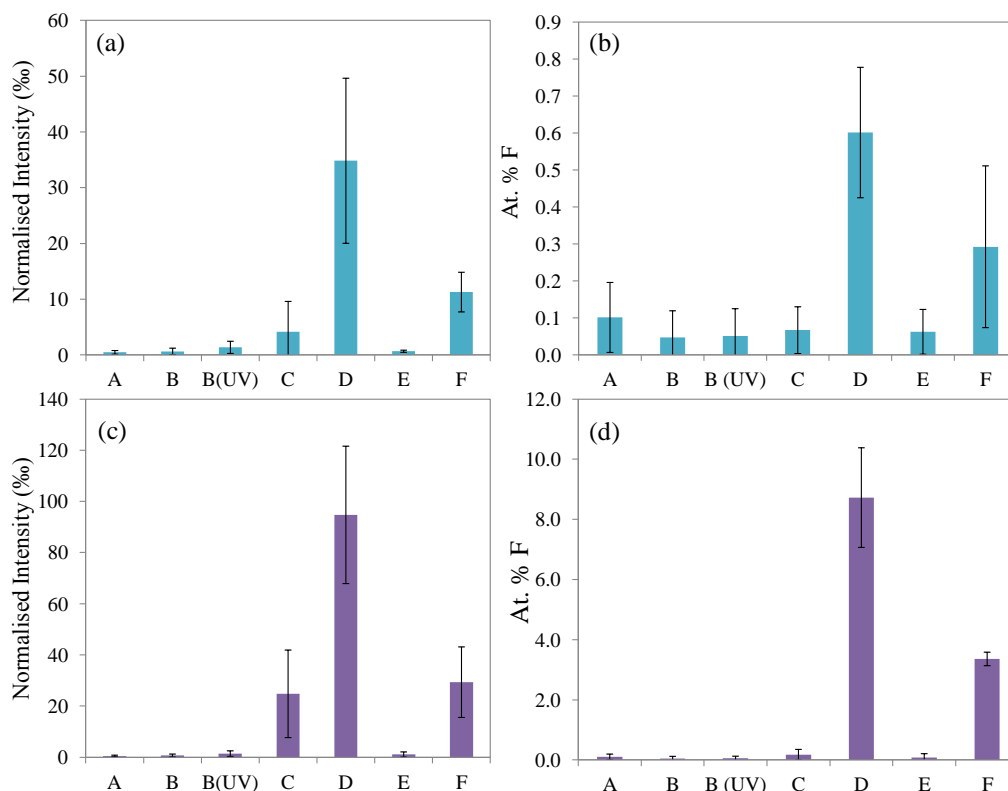


Figure 7.20: UV grafting of TPDOH and TPDCOOH at  $1900 \text{ mJ cm}^{-2}$  radiant exposure on the industrial TPO/0 substrate. ToF-SIMS results show normalised  $\text{F}^-$  intensity found at the surface and XPS results show F wt.% found at the surface: (a) normalised  $\text{F}^-$  intensity, 0.5 M TPDOH; (b) F wt.%, 0.5 M TPDOH; (c) normalised  $\text{F}^-$  intensity, 0.5 M TPDCOOH; (d) F wt.%, 0.5 M TPDCOOH: for surfaces A-F as represented in Figure 7.6 (substrate C was not measured in XPS to avoid contamination).

## 7.6 Summary

A direct comparison between the F wt.% and  $\text{F}^-$  intensities of substrate F for the different curing methods tested, is shown in Table 7.2. Overall, TPDCOOH had a greater grafting efficiency than TPDOH and TPD. Furthermore, the thermal curing at  $100^\circ\text{C}$  and UV curing at  $1900 \text{ mJ cm}^{-2}$  gave better yields than thermal curing at  $80^\circ\text{C}$ . Therefore, it was hypothesised that the adhesion of a waterborne basecoat would be greater to a TPDCOOH-modified substrate compared to TPDOH. Due to the lack of hydrophilic functional groups on TPD, it was expected that the adhesion of a waterborne basecoat would be poor to a TPD-modified substrate.

Table 7.2: Summary of the TPO/0 substrate surface after the grafting of TPD, TPDOH and TPDCOOH under the various conditions tested (thermal and UV exposure) and after washing with THF (= step F in Figure 7.6).

| AP              | F <sup>-</sup> Normalised Intensity |                  |                                | At.% F          |                  |                                |
|-----------------|-------------------------------------|------------------|--------------------------------|-----------------|------------------|--------------------------------|
|                 | 80 °C<br>30 min                     | 100 °C<br>30 min | 1900 mJ<br>cm <sup>-2</sup> UV | 80 °C<br>30 min | 100 °C<br>30 min | 1900 mJ<br>cm <sup>-2</sup> UV |
| Pure<br>TPDOH   | 54.20                               | 6.86             | -                              | 0.59            | 3.67             | -                              |
| TPDOH<br>0.5M   | 26.50                               | 10.68            | 11.28                          | 0.89            | 0.39             | 0.29                           |
| TPDCOOH<br>0.5M | 32.50                               | 33.22            | 29.32                          | 0.80            | 3.48             | 3.40                           |

## 7.7 Conclusions

The identification of diazirine molecules as candidate APs was a success. They are reactive carbene precursors that had been shown in literature to generate CH insertion reactions and were found in this study to be capable of inserting into the surface of industrial PP-based substrates. Before the grafting study commenced, the three types of diazirines, denoted as TPD, TPDOH and TPDCOOH, were successfully characterised to verify their chemical structure.

To assess the adhesion ability of TPD to bond to the surfaces, three different substrates were used during the grafting study in a sequence progressing from a simple model to the complex industrial substrates. Initially, grafting of TPD was proved to be successful to a model system, created by a SAM formation of mixed chain lengths on a gold surface. The next progression showed successful grafting of TPD to a PP substrate containing no additives, although the grafting efficiency was found to be less than the SAM substrate due to the increased steric hindrances from the densely packed PP polymer chains. Finally, TPD was shown to successfully graft to two types of industrial substrates, TPO/0 and TPO/2. However, the increased chemical complexity of the industrial substrates (such as

additives including pigments) compared to the other substrates caused a decrease in the grafting efficiency compared to the PP substrate containing no additives. Grafting for all three substrates was found to be successful with thermal and UV curing.

After the successful grafting of TPD was achieved, two modified versions with hydrophilic functional groups for adhesion with the basecoat were tested (TPDOH and TPDCOOH). Grafting was found to be successful on a TPO/0 substrate, however, UV curing at  $1900 \text{ mJ cm}^{-2}$  and curing at  $100 \text{ }^\circ\text{C}$  were the two conditions that gave the highest grafting efficiency from F wt.% data, and the TPDCOOH AP gave a higher grafting efficiency than TPDOH. Therefore, it was hypothesised that the grafting of TPDCOOH at  $100 \text{ }^\circ\text{C}$  for 30 minutes or  $1900 \text{ mJ cm}^{-2}$  UV would give the best adhesion performance with a waterborne basecoat. Also, the UV cure takes approximately 2 seconds, therefore, it would be the most efficient curing method in terms of time.

Furthermore, the calculation of the required AP concentration to produce one monolayer showed that the concentrations tested were in large excess. Therefore, it was expected that the AP would cover the substrate surface, assuming that grafting was effective.

# Chapter 8

## CHEMICAL ADHESION: CROSS-HATCH AND STEAM JET ADHESION TESTS

### 8.1 Overview

An overview of this chapter to guide the reader through the results is shown in Figure 8.1. The main focus of this chapter was to test the adhesion ability of the newly grafted TPDCOOH and TPDOH surfaces to a waterborne basecoat, focusing on the adhesion at the AP/basecoat interface. Two tests were used to assess the adhesion of substrates that were coated and cured in a range of different conditions.

### 8.2 Introduction

After the grafting ability of TPD, TPDOH and TPDCOOH was tested in Chapter 7, a waterborne basecoat and clearcoat were applied to freshly grafted substrates to test the adhesion properties. Two adhesion tests were performed: the CHT and the SJT. The CHT is often used in industry as a preliminary step to determine if adhesion has been improved. When the adhesion of the CHT gave a good result (=0), then a further more rigorous test, the SJT, was performed. This high-pressured steam test can give variable results, which was demonstrated by the reproducibility tests performed. Although all

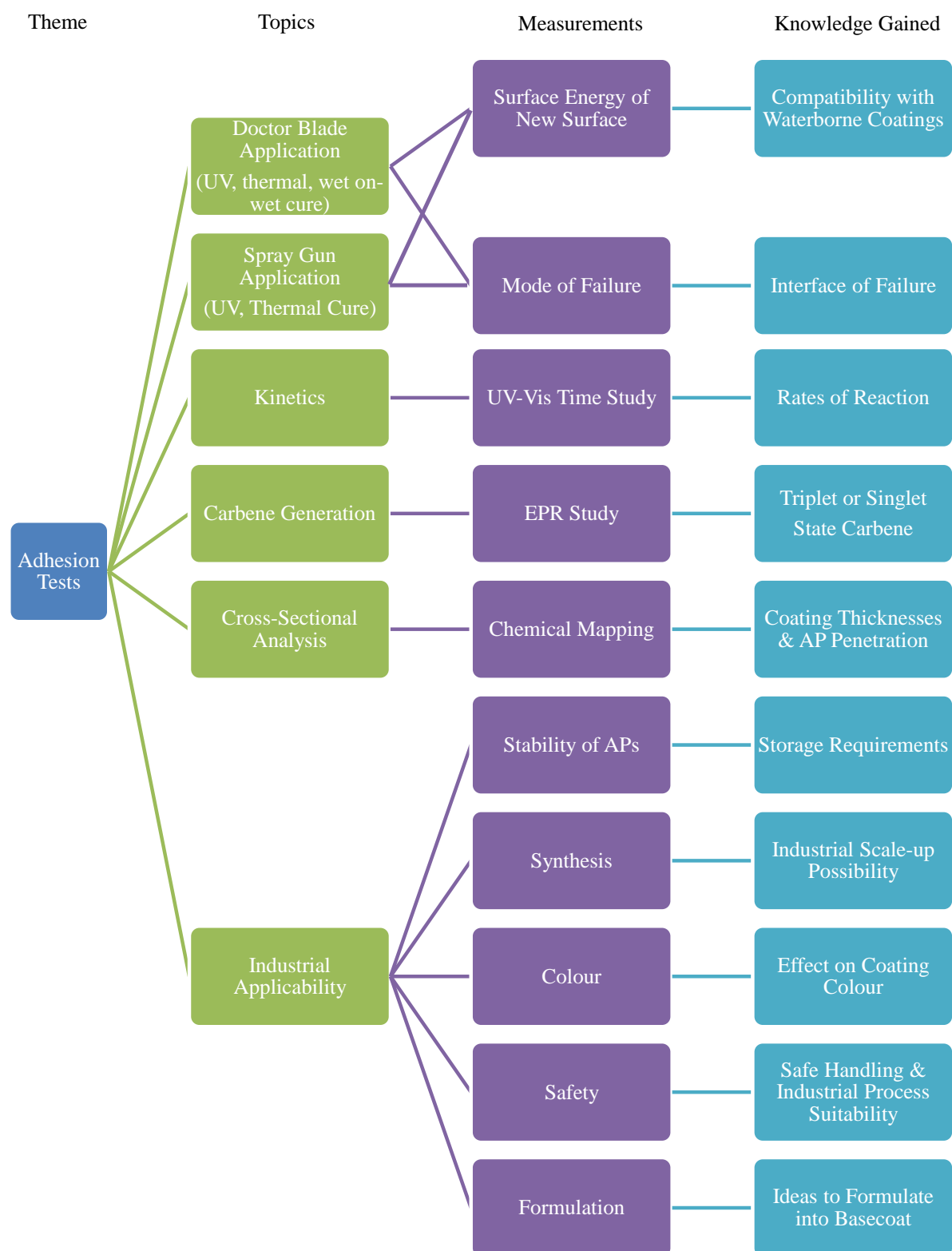


Figure 8.1: A summary of the chemical adhesion tests chapter.



CHT tests were reproducible, all SJT tests were reproducible within  $\pm 2$  gradings. Each condition tested was performed three times and the analysis below was performed on the coated substrates from the first CHT and SJT.

A schematic representation of the cross-section of a coated substrate is shown in Figure 8.2. As mentioned in Chapter 7, the first step was to apply the AP as a primer layer to test the adhesive ability at the substrate/AP interface and the AP/basecoat interface. The adhesion tests were therefore testing the AP's ability to function as a covalent bridge between a hydrophobic substrate and a hydrophilic basecoat. It was expected that grafting functional molecules to the substrate surface would improve the adhesion by the same mechanism as the state of the art flame pre-treatment. The polar functional groups introduced to the substrate surface would increase the polar component of the surface energy, to better match the polar surface energy component of the applied waterborne basecoat, thus adhesion is improved.

The application variables of the applied primer layer are displayed in Table 8.1. Firstly, the adhesion of TPD was tested as a proof-of-concept and the lack of hydrophilic group was hypothesised to lead to adhesive failure at the AP/basecoat interface. Next, TPDOH and TPDCOOH were tested which were hypothesised to give good adhesion through hydrogen bond interactions with the basecoat at the AP/basecoat interface, as shown in Figure 7.13.

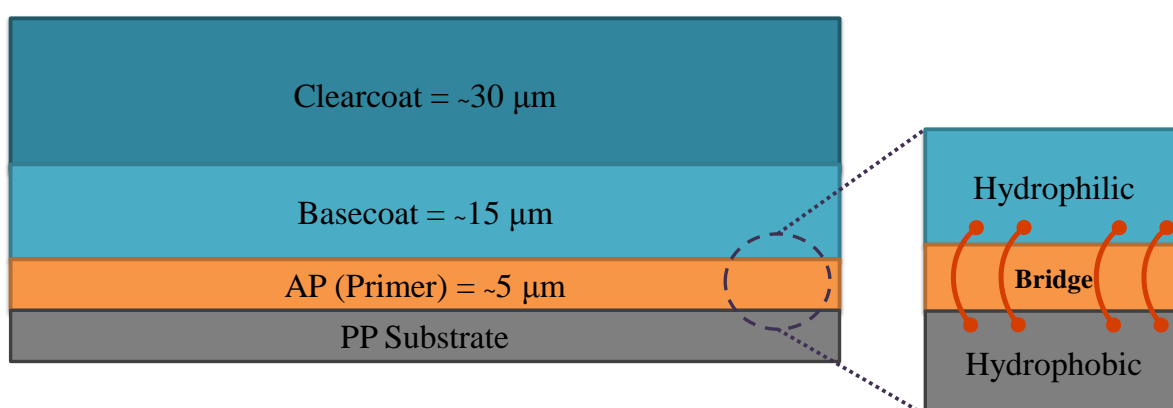


Figure 8.2: A schematic diagram showing the cross-section of a finished coated substrate, and the thicknesses of the wet coatings.

Table 8.1: The variables of the AP type, concentration, thickness and application method that were tested to investigate their affect on adhesion.

|  |  |
|--|--|
| <b>Adhesion Promoter Type</b>          | TPD                                      |
|  | TPDOH                                    |
|  | TPDCOOH                                  |
|  | Standards (Flamed substrate, CPO, Blank) |
| <b>Adhesion Promoter Concentration</b> | Pure (TPD and TPDOH only)                |
|  | 0.5 M                                    |
|  | 5 mM                                     |
| <b>Primer Layer Thickness</b>          | 5 $\mu\text{m}$                          |
| <b>Primer Application Method</b>       | Doctor Blade                             |
|  | Spray Gun                                |
|  | Wet-on-Wet                               |

The liquid APs were tested in pure form (TPD and TPDOH) and all three APs were diluted with solvent to test a relatively high concentration (0.5 M) and a lower concentration (5 mM).

The solvent chosen for the tests was MEK. There were several reasons for this choice:

1. It is a solvent that is used in the formulation of the basecoat, therefore, could be easily adapted to new basecoat formulations.
2. MEK was found to have the highest evaporation rate ( $= 3.3$  using DIN 53170, where ether  $=1$ ) out of all the solvents in the basecoat formulation, with the exception of Acetone ( $= 2.1$  using DIN 53170 where ether  $=1$ ), which was too dangerous to use in spray gun applications as mentioned in Section 7.5.1. (A solvent with a higher relative evaporation rate was desired to minimise possible side reactions of the AP with the solvent molecules.)
3. The surface tension of MEK ( $= 24.60$  mN/m) was found to be the closest matching value to a TPO/0 substrate (24.55 mN/m) out of all the solvents in the basecoat for-

mulation. Therefore, MEK had the best properties for wetting the TPO/0 substrate surface and spreading the AP homogeneously upon application.

4. HSPs predicted MEK to be the most likely solvent, out of all the solvents in the basecoat, to have a swelling effect on PP. (Future work could include investigating mixtures of solvents to maximise swellability and look at the effect on adhesion).

The AP primer was applied with two different application methods, including a doctor blade which was used for preliminary laboratory experiments, and a spray gun which replicated industrial application. The hierarchy of application methods is shown in Figure 8.3. Initially, the coatings were applied with a doctor blade and after curing, the CHT was measured. If the CHT gave good results, the next progression was the SJT. When good SJT results were obtained, the application method was changed to the spray gun, to replicate an industrial application process, and the adhesion tests performed in succession as before. The final step for substrates which had passed all stages in Figure 8.3, was to perform modelling tests to conclude the most influential parameters on the adhesion. It should be noted, however, that the spray gun application was also used for some tests that did not give good results with the doctor blade. This was to test if the difference in application method influenced the adhesion properties.

A third method was also tested, known as *wet-on-wet*, which indicated the basecoat was applied directly to the wet AP layer without a pre-curing step. For all methods, the approximate AP thickness was  $5 \mu\text{m}$ , and the effect of applying several layers of  $\sim 5 \mu\text{m}$  was tested during the spray gun application.

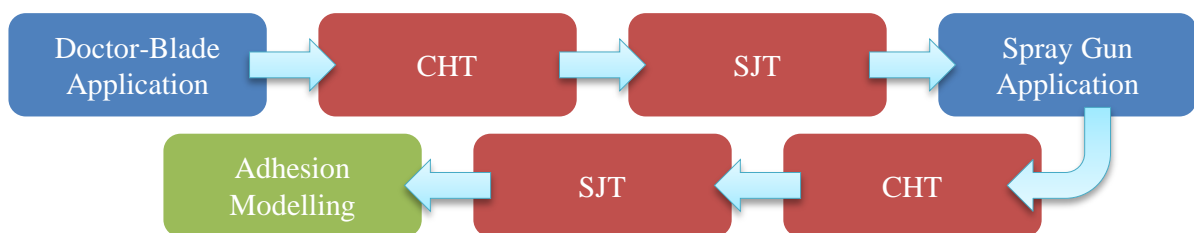


Figure 8.3: A flow diagram showing the progression of application methods and adhesion tests performed.

The two different curing methods that were tested in Chapter 7 were also tested in this chapter. The AP's were cured either thermally or with UV radiation, before applying and curing the basecoat and clearcoat for adhesion tests. The variables of thermal and UV curing that were tested are shown in Table 8.2.

Table 8.2: The variables of each curing method that were tested to investigate their affect on adhesion.

|                          |                |                   |                          |
|--------------------------|----------------|-------------------|--------------------------|
| <b>Curing Conditions</b> | Thermal Curing | Temperature       | 80 °C                    |
|                          |                |                   | 100 °C                   |
|                          |                | Time              | 24 hours                 |
|                          |                |                   | 30 minutes               |
|                          | UV Curing      | Exposure Radiance | 1900 mJ cm <sup>-2</sup> |
|                          |                |                   | 630 mJ cm <sup>-2</sup>  |
| 120 mJ cm <sup>-2</sup>  |                |                   |                          |

## 8.3 Doctor Blade Application of Coatings

To test the adhesion ability of TPD, TPDOH and TPDCOOH, a preliminary study was conducted using a doctor blade and TPO/0 substrates. This method was easy to implement in a laboratory and served well as a proof-of-concept to assess the adhesion before progressing to the spray gun application and testing other types of substrates.

### 8.3.1 Thermal Curing

Firstly, thermal curing was tested. The grafting study in Chapter 7 showed that thermal curing at 100 °C for 30 minutes gave results comparable to UV curing. Thermal curing was a desired method because both the basecoat and clearcoat used in this study were thermally cured, therefore, the AP system could be easily implemented into production.

The surface energy of each tested substrate after thermal curing at 80 °C and 100 °C for 30 minutes and 24 hours is shown in Figure 8.4. The hypothesis was that good adhesion would be obtained if the polar contribution of the surface energy from newly

grafted surfaces was comparable in magnitude to the polar contribution from the flamed substrate (used as a standard).

Substrates cured for 24 h at 80 °C, or 24 h / 30 min at 100 °C, showed the 0.5 M TPDCOOH primer to have the largest polar contribution of the surface energy after curing (the surfaces were not washed after AP application). However, the 80 °C, 30 minute cure showed pure TPDOH to have the largest polar contribution, which was the only result comparable in magnitude to the polar contribution of the flamed surface.

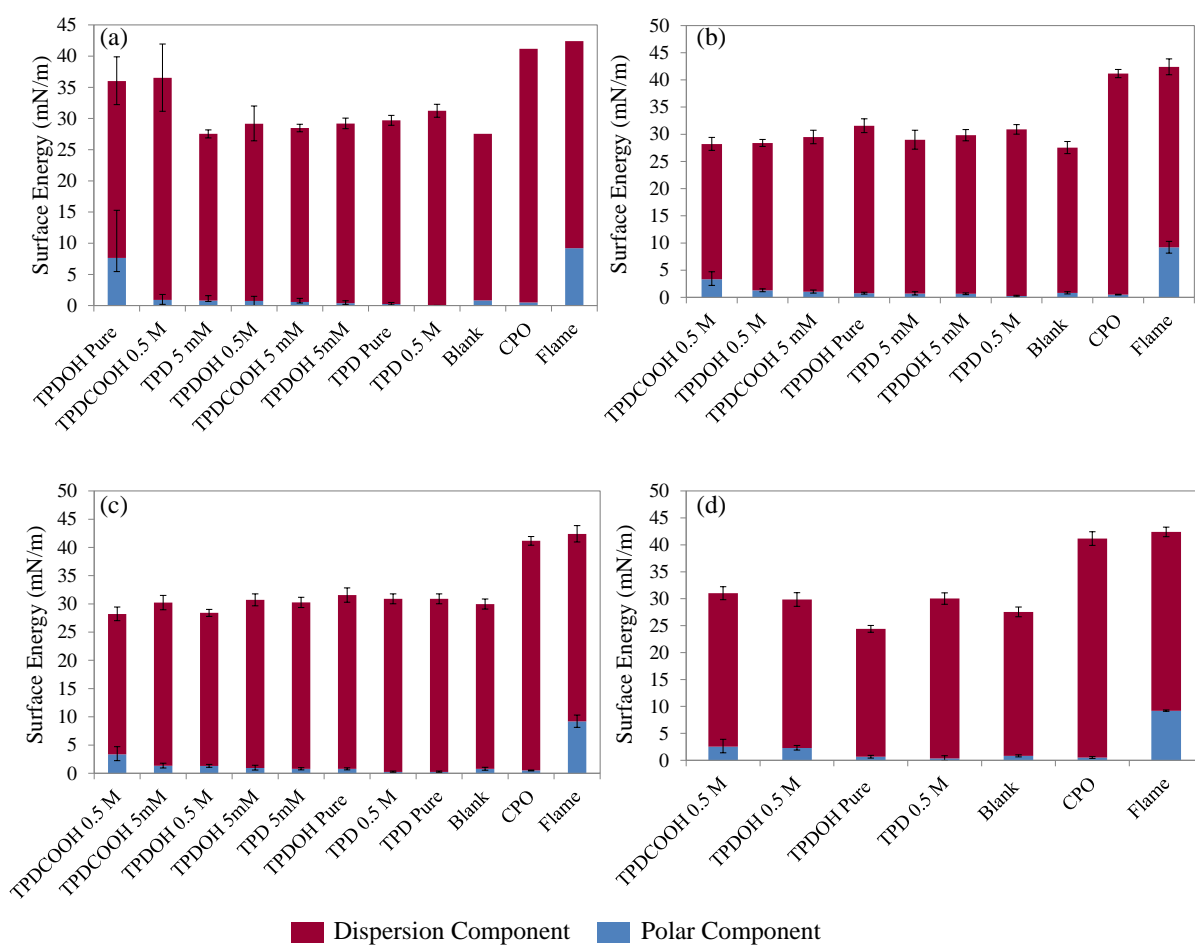


Figure 8.4: A bar graph showing the dispersion and polar components of the surface energy (together making the total surface energy) of a TPO/0 substrate surface after various AP's were applied with a doctor blade and cured at (a) 80 °C for 30 min (b) 80 °C for 24h (c) 100 °C for 30 min and (d) 100 °C for 24h. The results of each chart are displayed in descending order of AP polar contribution from the left-hand side of the chart, with the two state-of-arts displayed at the right-hand side of the chart.

Table 8.3: CHT results after various AP's were applied with a doctor blade and thermally cured before the basecoat and clearcoat were applied, cured and left for a 7 day post-cure.

| Adhesion Promoter   | Concentration | CHT            |              |                 |               |
|---------------------|---------------|----------------|--------------|-----------------|---------------|
|                     |               | 80 °C<br>30min | 80 °C<br>24h | 100 °C<br>30min | 100 °C<br>24h |
| TPD                 | Pure          | 5              | 5            | 5               | -             |
|                     | 0.5 M         | 5              | 5            | 5               | 5             |
|                     | 5 mM          | 5              | 5            | 5               | -             |
| TPDOH               | Pure          | 5              | 5            | 5               | 5             |
|                     | 0.5 M         | 5              | 5            | 5               | 5             |
|                     | 5 mM          | 5              | 5            | 5               | -             |
| TPDCOOH             | 0.5 M         | 5              | 5            | 5               | 5             |
|                     | 5 mM          | 5              | 5            | 5               | -             |
| Untreated Substrate | 5             |                |              |                 |               |
| Flame               | 0             |                |              |                 |               |
| CPO                 | 0             |                |              |                 |               |

However, a poor adhesion result was obtained for the coated sample, as shown in Table 8.3. The 80 °C 30 minute cure conditions were the lowest temperature and shortest time tested so it was expected that the rate of reaction would be the lowest. Furthermore, TPDOH pure was the purest and least volatile AP tested. Therefore, one plausible explanation for this result, which goes against the hypothesis, was that the TPDOH had not fully grafted to the surface due to the lack of reactivity/energy at 80 °C for 30 minutes, but some or all of it remained unbound at the surface causing the large polar contribution measured and it was easily removed from the surface.

Table 8.3 shows that only poor adhesion results were obtained for the thermally cured APs tested. The results were comparable to the blank substrate, which did not have an AP primer applied.

Several different types of delamination can occur during an adhesion test. Figure 8.5 shows a schematic diagram demonstrating good adhesion, cohesive failure, adhesive

failure at the AP/basecoat interface and adhesive failure at the substrate/AP interface.

During the application and curing of the AP primer layer, no washing step was implemented. This meant several layers of TPD or TPDOH or TPDCOOH APs were likely to be at the surface of the substrate. As discussed in Section 7.4.1, it was thought that the AP molecules grafted to one-another under the correct conditions, due to the high reactivity of the APs during the curing stage. This would result in a multilayer as shown in Figure 8.5(a). The APs in closest proximity to the substrate would covalently bond to the substrate, and the APs in closest proximity to the basecoat would bind by interactions such as hydrogen bonding to the basecoat. This model would result in optimum adhesion.

Figure 8.5(b) shows an example where insufficient interactions between the APs result in a breakage through the bulk region of the primer layer, resulting in a cohesive failure. It should be noted that cohesive failure could also occur in the bulk of the basecoat, clearcoat or substrate. However, these systems have previously been optimised for performance and so were assumed to remain intact during the adhesion tests.

Figure 8.5(c) shows an example of adhesive failure at the AP/basecoat interface where the AP is covalently bonded to the substrate, but insufficient interactions occur between the AP and the basecoat, causing delamination. In contrast, Figure 8.5(d) shows an example of adhesive failure at the substrate/AP interface where the AP binds to the basecoat, but is not covalently bonded to the substrate and delamination occurs.

To test the type of failure that had occurred during the adhesion test, an adapted method of Clemens *et al.*<sup>70</sup> was implemented. ToF-SIMS was used to measure the signal intensity of F<sup>-</sup> from the top side of the substrate and the underside of the coating after delamination. These measurements were done soon after the adhesion test, to minimise contamination at the sample surfaces. As a control, a substrate that had been coated with the basecoat and clearcoat without the addition of an AP primer layer was also tested to verify the results and check the F<sup>-</sup> was due to the CF<sub>3</sub> group from TPD and not from contamination.

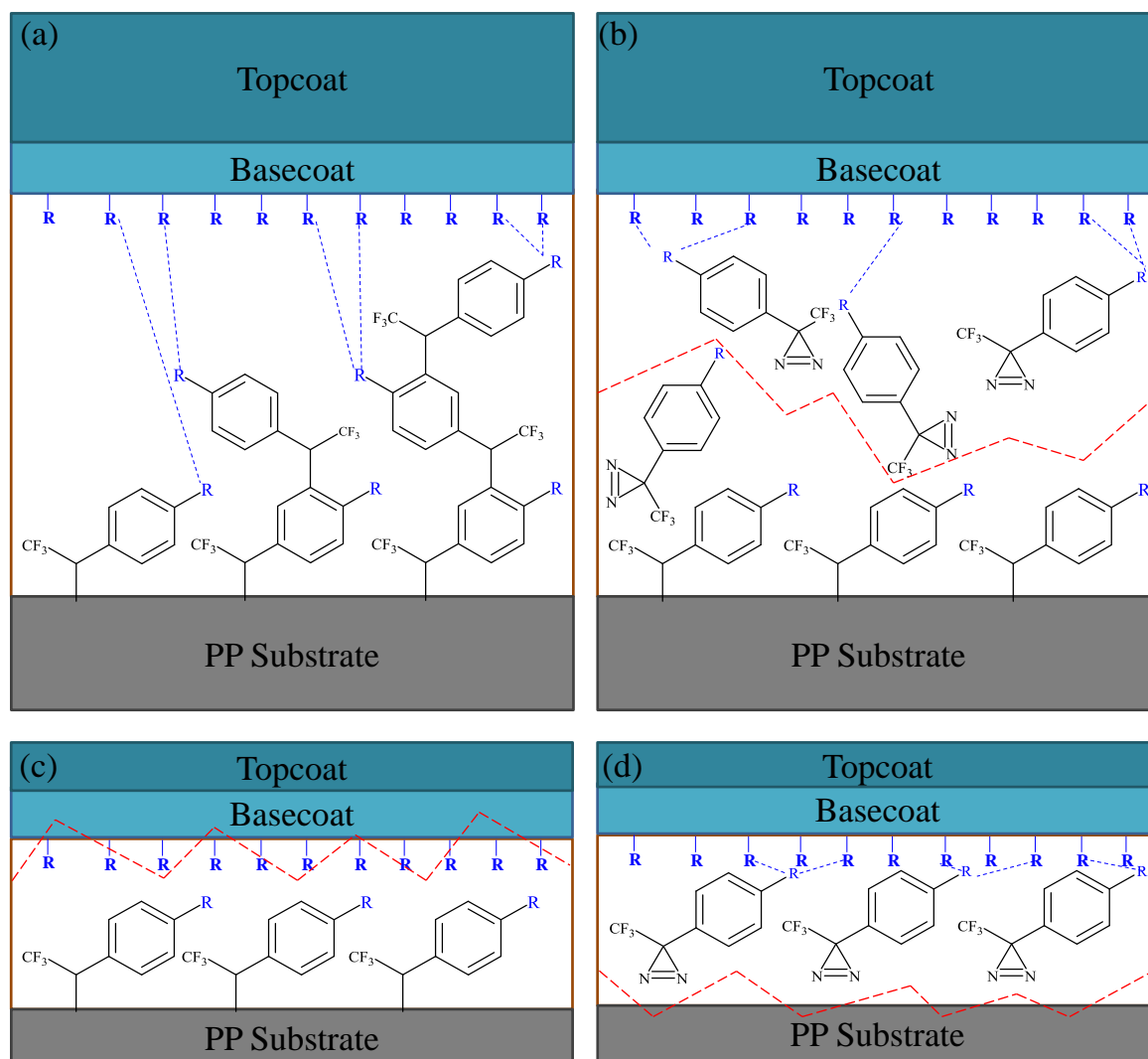


Figure 8.5: Schematic diagram demonstrating (a) good adhesion, (b) cohesive failure, and adhesive failure at the (c) AP/basecoat interface and (d) substrate/AP interface.

The terms *adhesive* and *cohesive* are somewhat ambiguous. However, in this study adhesive failure was defined as a significant difference between the  $F^-$  signal intensity of the delaminated surfaces, and cohesive failure was defined as comparable intensities of  $F^-$  on the delaminated surfaces. The type of failure was not concluded when the intensities of both of the surfaces measured were comparable to the blank (where no primer was applied). This was because it was not possible to say if the measured intensity was from the AP or from surface contamination.

Figure 8.6 shows the  $F^-$  signal intensity from the delaminated surfaces of the thermally cured samples, which resulted in poor adhesion. Table 8.4 summarises the mode of failure



concluded for each sample. The coating was easily removed from the surface of the substrate, therefore, no forced removing was necessary which may have resulted in false modes of failures.

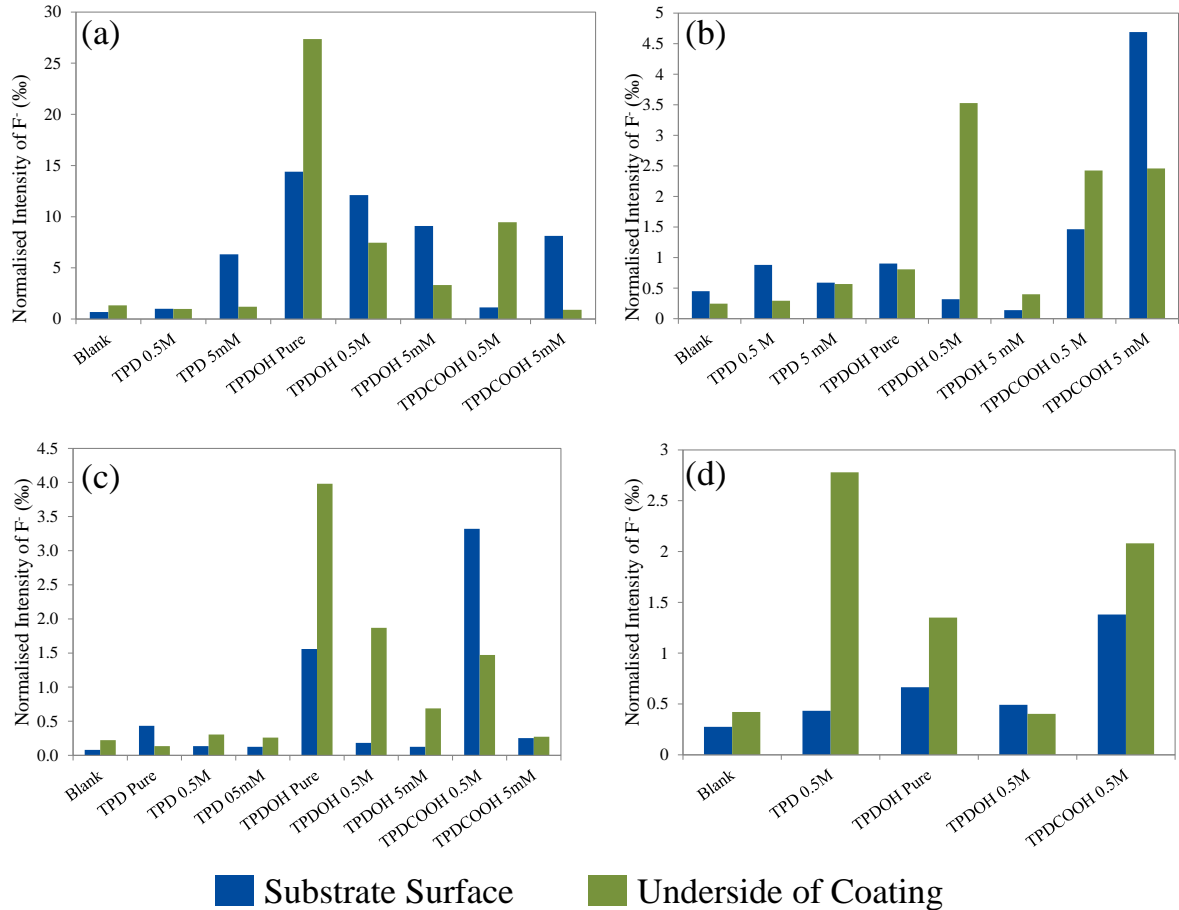


Figure 8.6: The F<sup>-</sup> intensities measured from the delaminated surfaces of the substrate and basecoat after the AP primer layer was cured thermally at (a) 80 °C for 30 mins, (b) 80 °C for 24h, (c) 100 °C for 30 minutes and (d) 100 °C for 24h, before the basecoat and clearcoat were applied, cured and left for a 7 day post-cure.

Several samples showed signal intensities that were comparable to the magnitudes of the blank and therefore were concluded negligible. Across all the thermal curing conditions tested, TPD was found to have the lowest signal intensities. This was likely to be due to the high volatility of TPD compared to the other APs, resulting in the evaporation of TPD from the substrate surface at a higher rate than the rate of grafting. As expected, adhesive failure at the AP/BC interface occurred in the cases where sufficient intensities

Table 8.4: Summary of the modes of failure observed for each tested sample, after the coated surface had delaminated from the substrate during the adhesion test. The AP primer was applied with a doctor blade and thermally cured before the basecoat and clearcoat were applied and cured, and left for a 7 day post-cure.

| Adhesion Promoter | Concentration | Mode of Failure     |                     |                     |                    |
|-------------------|---------------|---------------------|---------------------|---------------------|--------------------|
|                   |               | 80 °C<br>30 min     | 80 °C<br>24h        | 100 °C<br>30 min    | 100 °C<br>24h      |
| TPD               | 0.5 M         | Negligible          | Adhesive<br>(BC: P) | Negligible          | Adhesive<br>(S: P) |
|                   | 5 mM          | Adhesive<br>(BC: P) | Negligible          | Negligible          | -                  |
| TPDOH             | Pure          | Cohesive            | Cohesive            | Adhesive<br>(S: P)  | Adhesive<br>(S: P) |
|                   | 0.5 M         | Adhesive<br>(BC: P) | Adhesive<br>(S: P)  | Adhesive<br>(S: P)  | Adhesive<br>(S: P) |
|                   | 5 mM          | Adhesive<br>(BC: P) | Negligible          | Adhesive<br>(S: P)  | -                  |
| TPDCOOH           | 0.5 M         | Adhesive<br>(S: P)  | Adhesive<br>(S: P)  | Adhesive<br>(BC: P) | Adhesive<br>(S: P) |
|                   | 5 mM          | Adhesive<br>(BC: P) | Adhesive<br>(BC: P) | Negligible          | -                  |

were measured for TPD. The lack of a hydrophilic functional group present in TPD, resulting in no interactions with the basecoat, caused this type of failure.

After the AP primer was cured at 80 °C for 30 minutes, the majority of the samples showed an adhesive failure at the AP/basecoat interface. This indicated insufficient binding between the AP and the basecoat. Furthermore, the magnitudes of signal intensities measured were relatively low and comparable to the results from the grafting proof-of-concept in Chapter 7. Therefore, it was likely that the grafting efficiency was inadequate with not enough TPDOH/TPDCOOH molecules grafted at the surface for good adhesive interactions with the basecoat.

After the TPDOH pure primer was cured at 80 °C for 30 minutes, a significant intensity on both the substrate and coating surface after delamination was observed, suggesting a cohesive failure within the primer bulk. The results in Section 7.3.1 revealed that car-

benes were generated at 80 °C, therefore, it was thought that a low rate of thermal energy transfer was insufficient to induce any reactions/interactions between the high concentration of the bulk TPDOH molecules within the primer. This resulted in a breakage through the primer leaving a layer of TPDOH on the basecoat and substrate surfaces. The interactions between the TPDOH and the basecoat/substrate were therefore greater than the interactions between the TPDOH molecules within the primer.

The 0.5 M TPDCOOH primer cured at 80 °C for 30 minutes showed an adhesive failure at the substrate/AP interface. The higher concentration of the primer solution was likely to be the reason for this result. The rate of thermal energy transferred to the concentrated layer to induce grafting at the substrate surface was insufficient and the interaction between TPDCOOH and the basecoat was greater than with the substrate. In contrast, the 5 mM TPDCOOH primer had a lower density of molecules, allowing a faster rate of thermal energy transfer and grafting to occur. The interaction between the substrate and TPDCOOH was greater than the TPDCOOH and the basecoat, thus resulting in adhesive failure at the AP/basecoat interface.

The modes of failure observed after the AP primer was cured at 80 °C for 24 h were the same as the cure for 30 minutes, with the exception of 5 M and 5 mM TPDOH. In this case, adhesive failure was observed at the AP/substrate interface. This mode of failure was also observed for the TPDOH substrates that had been cured at 100 °C for 30 minutes, and all substrates that had been cured at 100 °C for 24 h. (The higher concentration AP solutions cured for 24 h at 100 °C, which caused delamination, were measured to be compared with the other curing conditions.) The reasons why this failure occurred were not known. However, one plausible reason could be that contamination of the primer surface occurred over the long period of time in the conventional oven, causing delamination (which could occur in an industrial process). Furthermore, the hydrophilic functional groups present at the primer surface would attract a greater amount of contamination than the bare substrate surface, therefore, the TPDCOOH and TPDOH grafted surfaces were likely to attract dirt during the curing time.

Although the modes of failure for TPDCOOH for each curing condition were not consistent, the majority of TPDOH cases showed adhesive failure at the substrate/AP interface. This indicated that TPDCOOH had a greater grafting efficiency than TPDOH.

The inhomogeneity of the applied primer layer using the doctor blade application was found to be another contributing factor which caused the poor adhesion observed when the primer layer was thermally cured. This was discovered by creating 2D chemical maps of the delaminated surfaces using ToF-SIMS. Figure 8.7 shows four examples of delaminated surfaces, in which segregated areas of higher  $F^-$  intensity were observed. An inhomogeneous primer layer would decrease the interaction between the two interfaces (low contact area) and create areas of no interaction, which could potentially propagate under stress and cause delamination in the areas of interaction. Therefore, homogeneous layers were desired, which would maximise the interactions between the interfaces.

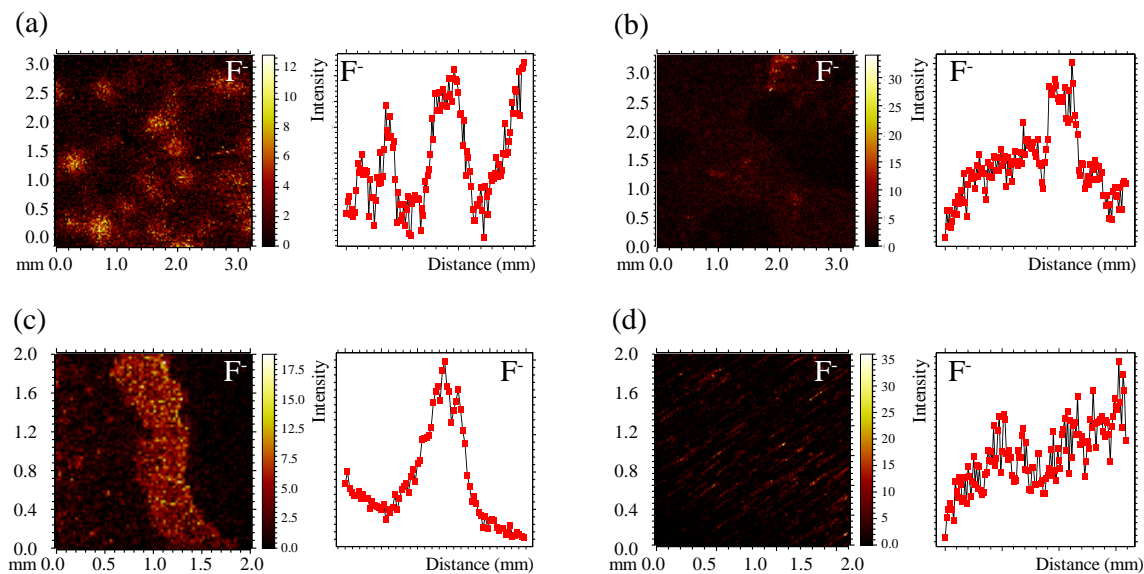


Figure 8.7: 2D chemical maps showing the normalised  $F^-$  intensity measured from the delaminated side of the basecoat from the samples: (a) 0.5 M TPDOH cured at 80 °C for 24 h, (b) 0.5 M TPDCOOH cured at 80 °C for 24 h, (c) 0.5 M TPDOH cured at 80 °C for 30 min and (d) 5 mM TPDCOOH cured at 80 °C for 30 min. The line scans represent a sum of the line scans in the x-direction (pixel by pixel).

### 8.3.2 UV Curing

UV curing was found to be to be significantly more effective than thermal curing at 80 °C in the grafting study in Chapter 7. Therefore, adhesion tests were performed on samples that contained UV-cured primers. The adhesive properties were then investigated.

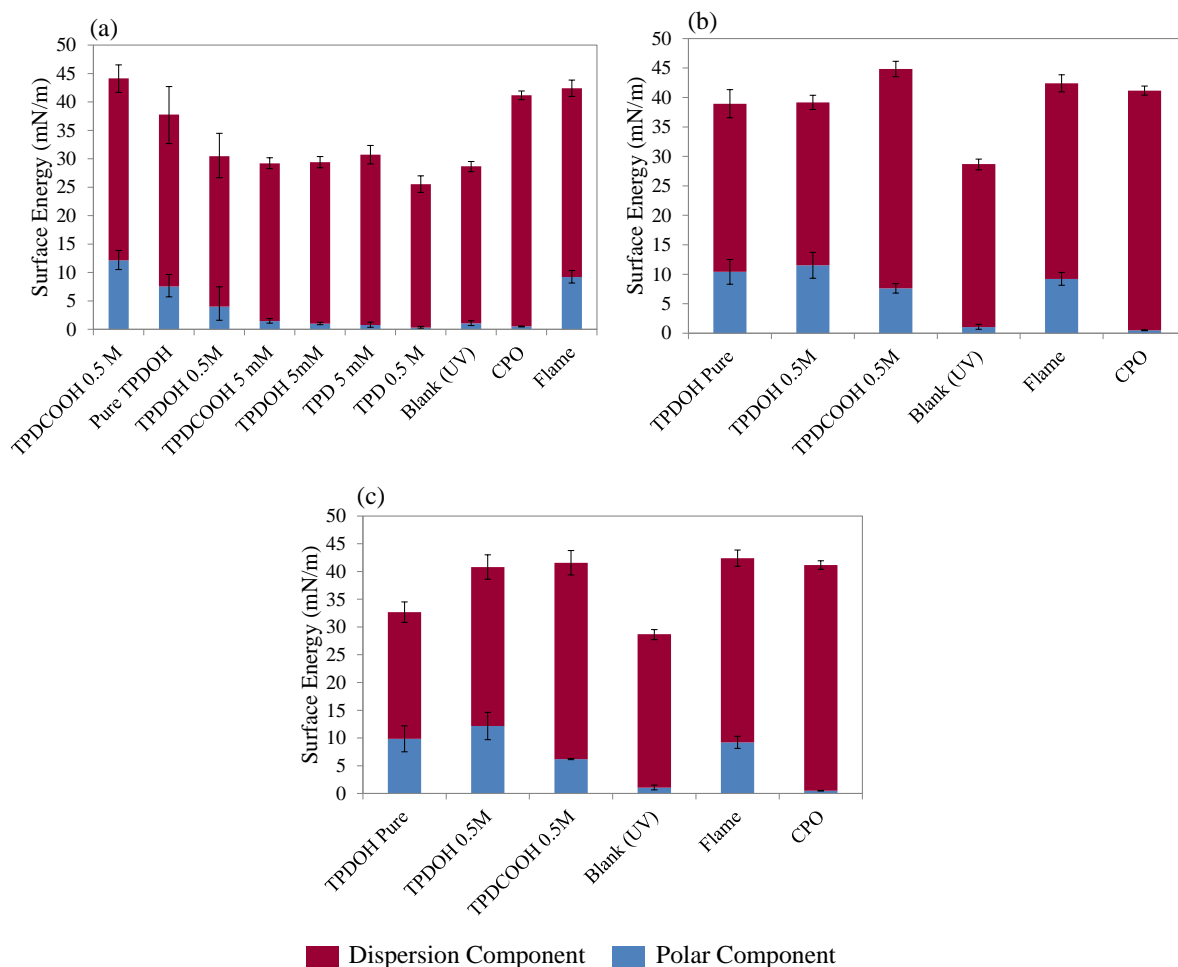


Figure 8.8: A bar graph showing the dispersion and polar components of the surface energy (together making the total surface energy) of a TPO/0 substrate surface after various AP's were applied with a doctor blade and cured at (a) 1900 mJ cm<sup>-2</sup> (b) 630 mJ cm<sup>-2</sup> and (c) 122 mJ cm<sup>-2</sup>. The results of each chart are displayed in descending order of AP polar contribution from the left-hand side of the chart, with the two state-of-arts displayed at the right-hand side of the chart.

Figure 8.8 shows the surface energy of each tested substrate after UV curing at 1900, 630 and 122 mJ cm<sup>-2</sup>. The hypothesis was that if the polar contribution from the surface

energy of the newly grafted surface was comparable to the polar contribution from the flamed substrate (standard), good adhesion would be obtained.

It was clearly observed that the polar component of surface energies from the UV grafted surfaces were significantly higher than the polar contributions from the thermal grafted surfaces (shown in Figure 8.4). Furthermore, several samples had polar component contributions on the same order of magnitude as the flamed substrate.

The primers with higher concentrations of APs cured at  $1900 \text{ mJ cm}^{-2}$  gave the greatest polar components of surface energy. Therefore, only pure and 0.5 M AP primers were cured at 630 and  $122 \text{ mJ cm}^{-2}$ , to investigate the dependence of UV radiant exposure. It was hypothesised that the pure TPDOH, 0.5 M TPDOH and the 0.5 M TPDCOOH would give good adhesion results due to their high polar component of surface energy.

Initially, the tests were performed using a non-pigmented basecoat to minimise possible side reactions of the AP with pigments found within the basecoat. The adhesion results were found to be good at  $1900 \text{ mJ cm}^{-2}$ , therefore, the test was repeated with a black pigmented basecoat which gave the CHT results shown in Table 8.5. As expected, TPD at both concentrations (0.5 M and 5 mM) gave poor adhesion results due to the lack of a hydrophilic functional group for interaction with the basecoat. Furthermore, it was clear that UV curing of TPDOH/TPDCOOH gave significantly better adhesion results than that of thermal curing.

It was observed that the higher UV radiant exposure ( $1900 \text{ mJ cm}^{-2}$ ) gave the best adhesion results, and the adhesive properties decreased with decreasing UV radiant exposure. This can be explained in terms of activation energy. The larger UV radiant exposure provided a greater energy to the AP molecules which overcame the energy barriers for a reaction. This induced the decomposition of the diazirine group to allow for CH insertion/grafting to take place. The UV radiant exposure at  $630 \text{ mJ cm}^{-2}$  provided a lower energy so that less AP molecules were able to overcome the energy barrier in the given time, hence the adhesion was not as good. The poor adhesion observed at  $122 \text{ mJ cm}^{-2}$  indicated the energy was too low for any grafting reaction to occur.

Table 8.5: CHT results after various AP's were applied with a doctor blade and cured with UV before the basecoat and clearcoat were applied, cured and left for a 7 day post-cure.

| Adhesion Promoter          | Concentration | Wash | CHT                         |                            |                            |
|----------------------------|---------------|------|-----------------------------|----------------------------|----------------------------|
|                            |               |      | 1900<br>mJ cm <sup>-2</sup> | 630<br>mJ cm <sup>-2</sup> | 120<br>mJ cm <sup>-2</sup> |
| TPD                        | 0.5 M         | N    | 5                           | -                          | -                          |
|                            | 5 mM          | N    | 5                           | -                          | -                          |
| TPDOH                      | Pure          | N    | 0                           | 1                          | 5                          |
|                            |               | Y    | -                           | 4                          | 5                          |
|                            | 0.5 M         | N    | 0                           | 0                          | 5                          |
|                            |               | Y    | -                           | 0/1                        | 5                          |
|                            | 5 mM          | N    | 4                           | -                          | -                          |
| TPDCOOH                    | 0.5 M         | N    | 0                           | 0                          | 5                          |
|                            |               | Y    | -                           | 0/3                        | 5                          |
|                            | 5 mM          | N    | 1                           | -                          | -                          |
| <b>Untreated Substrate</b> |               |      | 5                           |                            |                            |
| <b>Flame</b>               |               |      | 0                           |                            |                            |
| <b>CPO</b>                 |               |      | 0                           |                            |                            |

A decrease in the AP concentration also correlated with a decrease in adhesion results, due to the smaller amount of molecules available to graft to the surface and interact with the basecoat.

A second application step was introduced when looking at UV radiant exposures of 630 and 122 mJ cm<sup>-2</sup>. This was a washing step after the cure of the primer layer but before the application of the basecoat/clearcoat. It was thought that washing away any ungrafted APs from the substrate surface (which may have hindered adhesion) may improve the adhesive properties. However, it was found that the washing step decreased the adhesive properties as shown in Table 8.5. Therefore, the solvent molecules may have remained/adhered to the newly grafted surface rather than washed or evaporated away from the surface, causing a type of contamination which caused delamination of the coatings. The mode of failure results shown in Table 8.9 also suggest this, showing AP/BC

adhesive failures for all washed samples.

The delaminated surfaces of the samples that had poor adhesion were again analysed using ToF-SIMS. The results are shown in Figure 8.9 and a summary of the modes of failures can be found in Table 8.6. It was found that the majority of the 5 mM TPDCOOH sample had good adhesion and the results shown were obtained from only a small part of the sample that had delaminated. The results suggest there was an area with a lower proportion of APs which resulted with insufficient adhesion to the basecoat, causing the delamination.

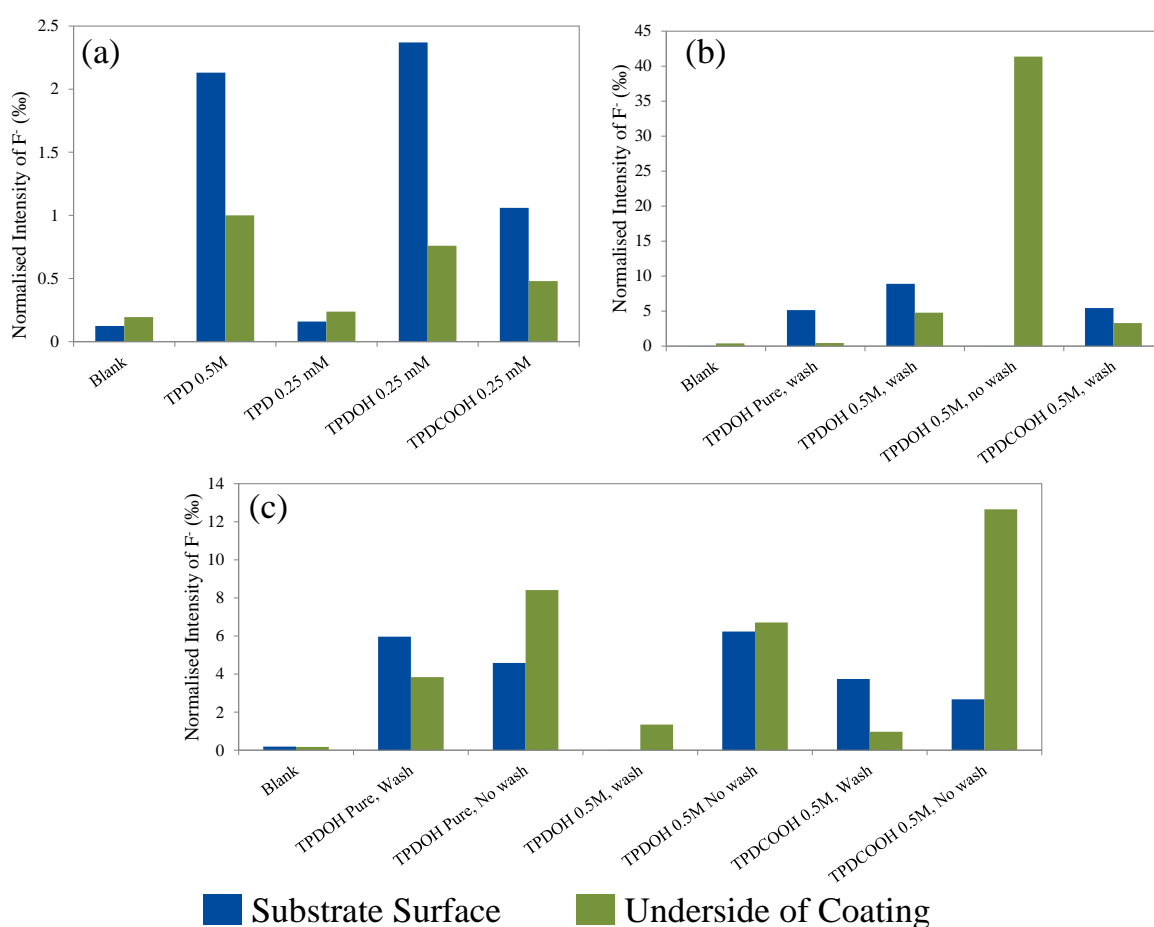


Figure 8.9: The  $F^-$  intensities measured from the delaminated surfaces of the substrate and basecoat after the AP primer layer was UV cured at (a)  $1900 \text{ mJ cm}^{-2}$ , (b)  $630 \text{ mJ cm}^{-2}$  and (c)  $122 \text{ mJ cm}^{-2}$ , before the basecoat and clearcoat were applied, cured thermally and left for a 7 day post-cure.



TPD showed evidence of AP/BC adhesive failure which was expected as previously mentioned. The remaining samples were a mixture of modes of failure, with no obvious correlation. However, it was concluded that the higher UV radiant exposure gave the best adhesion results. Also, the CHT results suggest TPDCOOH had better adhesive properties than TPDOH.

Although at a low rate, thermal curing of the APs had previously shown evidence of grafting.

Table 8.6: Summary of the modes of failure observed for each tested sample after the coated surface had delaminated from the substrate during the adhesion test. The AP primer was applied with a doctor blade and UV cured before the basecoat and clearcoat were applied and cured, and left for a 7 day post-cure.

| Adhesion Promoter | Concentration | Wash | Mode of Failure          |                         |                         |
|-------------------|---------------|------|--------------------------|-------------------------|-------------------------|
|                   |               |      | 1900 mJ cm <sup>-2</sup> | 630 mJ cm <sup>-2</sup> | 120 mJ cm <sup>-2</sup> |
| TPD               | 0.5 M         | N    | Adhesive (BC: P)         | -                       | -                       |
|                   | 5 mM          | N    | Negligible               | -                       | -                       |
| TPDOH             | Pure          | N    | Good Adhesion            | Good Adhesion           | Adhesive (S: P)         |
|                   |               | Y    | -                        | Adhesive (BC: P)        | Adhesive (BC: P)        |
|                   | 0.5 M         | N    | Good Adhesion            | Adhesive (S: P)         | Cohesive                |
|                   |               | Y    | -                        | Adhesive (BC: P)        | Adhesive (S: P)         |
|                   | 5 mM          | N    | Adhesive (BC: P)         | -                       | -                       |
| TPDCOOH           | 0.5 M         | N    | Good Adhesion            | Good Adhesion           | Adhesive (S: P)         |
|                   |               | Y    | -                        | Adhesive (BC: P)        | Adhesive (BC: P)        |
|                   | 5 mM          | N    | Adhesive (BC: P)         | -                       | -                       |
|                   |               | Y    | -                        | -                       | -                       |

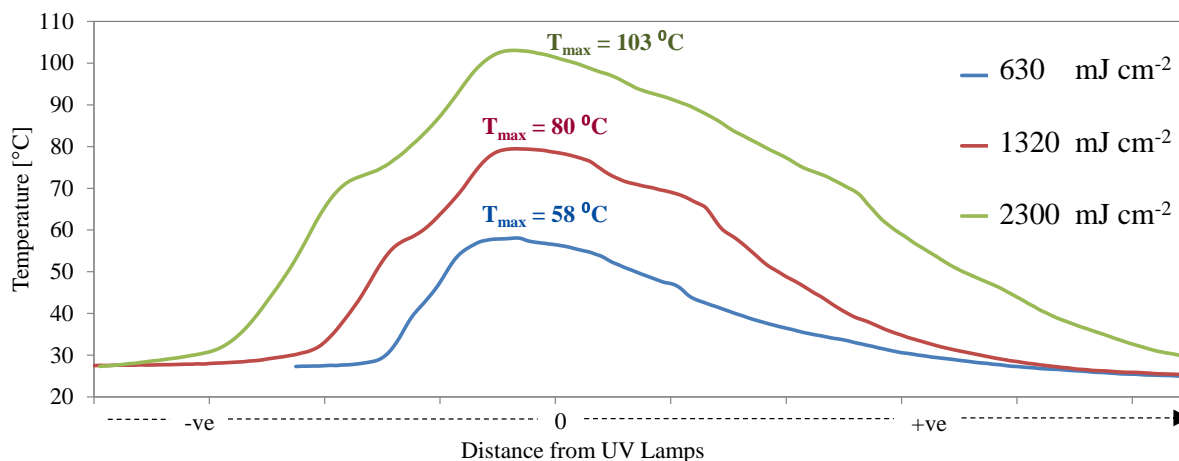


Figure 8.10: The temperature generated during UV curing at the various radiant exposures measured. The cure at  $2300 \text{ mJ cm}^{-2}$  took  $\sim 2$  seconds.

Therefore, to test for any thermal contributions from the UV lamps during the curing step which may have influenced the grafting of APs, the temperature was measured at each UV radiant exposure. The results are shown in Figure 8.10. It was found that the temperature increased as the radiant exposure increased, which was expected due to the increasing UV exposure times. The heat generated was from infrared radiation emitted from the UV lamps. It had previously been shown that poor adhesion occurred at  $100 \text{ }^\circ\text{C}$ , which was the temperature reached at  $1900 \text{ mJ cm}^{-2}$ . Therefore, the temperature influence during UV curing was regarded as negligible.

Another contributing factor of the poor adhesion obtained by some of the samples, was found to be inhomogeneity of the AP primer layer, which was previously observed for the thermal cure using the doctor blade application method. Figure 8.11 shows four delaminated surface examples of varying homogeneity. Although the use of the doctor blade had served its purpose for a proof-of-concept for coatings application in a laboratory environment, the production of a homogeneous layer was found to be difficult. The method did allow, however, the production of the encouraging positive results obtained by UV curing. Before alternative application methods were explored to improve homogeneity, a wet-on-wet application method was tested (which was also used for the state-of-the-art CPO AP).

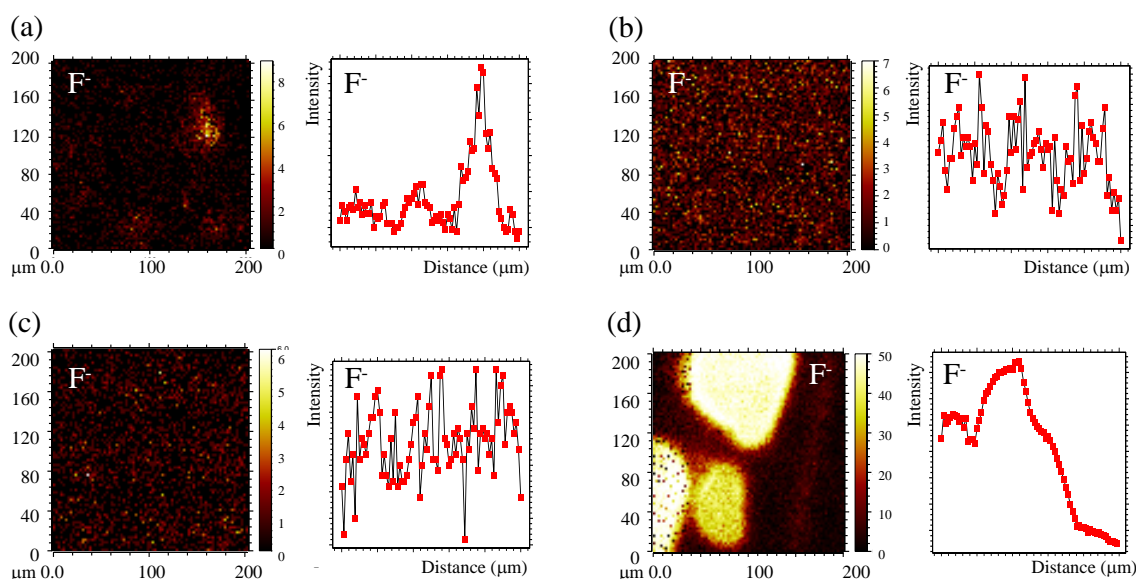


Figure 8.11: 2D chemical maps showing the normalised  $F^-$  intensity measured from the delaminated side of the substrate from (a) 5 mM TPDCOOH cured at  $1900 \text{ mJ cm}^{-2}$  and (b) 5 mM TPDOH cured at  $1900 \text{ mJ cm}^{-2}$ , and from the delaminated side of the basecoat from the samples: (c) 5 mM TPDOH cured at  $1900 \text{ mJ cm}^{-2}$  and (d) 0.5 M TPDOH cured at  $1900 \text{ mJ cm}^{-2}$ . The line scans represent a sum of the line scans in the x-direction (pixel by pixel).

### 8.3.3 Wet-on-Wet

As previously shown in Section 5.6, the state-of-the-art CPO was found to give the best adhesion results when applied using a wet-on-wet method with a doctor blade. This method is when the basecoat is applied directly to the primer layer without any pre-curing of the primer layer.

It was not possible to measure accurate surface energies (using the OW method) of the wet primer layers to predict the adhesion, due to uneven surfaces and the possibility of interactions between the test solutions of known surface tension and the wet surface.

The CHT adhesion results are shown in Table 8.7. As a first test, only higher concentrations were tested using TPDOH and TPDCOOH. However, the adhesion results obtained were poor and comparable to the blank substrate which contained no AP primer layer. Therefore, no further tests were done using this method of application.

Table 8.7: CHT results after various AP's were applied with a doctor blade wet-on-wet with the basecoat, which was cured before the clearcoat was applied, cured and left for a 7 day post-cure.

| Adhesion Promoter   | Concentration | CHT Wet-on-Wet |
|---------------------|---------------|----------------|
| TPDOH               | Pure          | 5              |
|                     | 0.5 M         | 5              |
| TPDCOOH             | 0.5 M         | 5              |
| Untreated Substrate | 5             |                |
| Flame               | 0             |                |
| CPO                 | 0             |                |

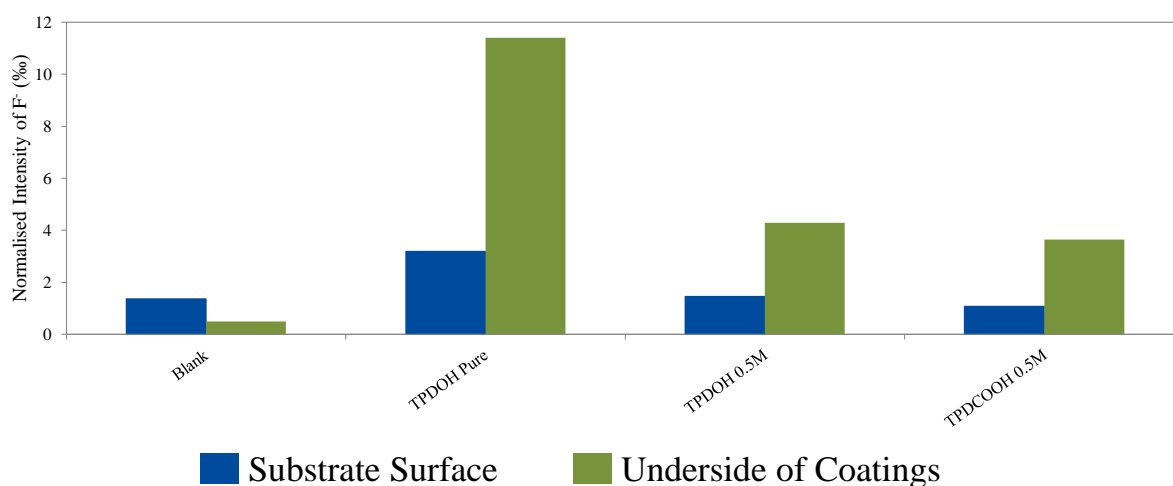


Figure 8.12: The F<sup>-</sup> intensities measured from the delaminated surfaces of the substrate and basecoat after the AP primer layer was applied wet-on-wet with basecoat and cured before the application and curing of the clearcoat, which was left for a 7 day post-cure.

The F<sup>-</sup> signal intensities measured from the delaminated surfaces are shown in Figure 8.12. A summary of the mode of failures are shown in Table 8.8. All three samples tested showed adhesive failure at the substrate/AP interface, showing the AP was unable to graft to the substrate. This was not unexpected as the basecoat was applied in liquid form which would be more favourable for a reaction with the AP than the sterically hindered, rigid, solid substrate surface.

Table 8.8: Summary of the modes of failure observed for each tested sample after the coated surface had delaminated from the substrate during the adhesion test. The AP primer was applied with a doctor blade and applied wet-on-wet with the basecoat before applying the clearcoat which was cured and left for a 7 day post-cure.

| <b>Adhesion Promoter</b> | <b>Concentration</b> | <b>Mode of Failure</b> |
|--------------------------|----------------------|------------------------|
| TPDOH                    | Pure                 | Adhesive (S: P)        |
|                          | 0.5 M                | Adhesive (S: P)        |
| TPDCOOH                  | 0.5 M                | Adhesive (S: P)        |

## 8.4 Spray Gun Application of Coatings

The spray gun application method is used to apply automotive coatings in the industry. It allows a better control of the coatings applied. Primers of TPDOH and TPDCOOH were spray applied and cured, before subsequent coatings were applied and the adhesion tested. The different research substrates containing 0 - 25 % EPDM, as well as the 3 industrial TPO substrates (TPO/0, TPO/2 and TPO/20) were used to look for correlations between the adhesion and the substrate properties that were calculated in Chapter 5.

### 8.4.1 Thermal Curing

Although thermal curing of the AP primer with the doctor blade application gave poor adhesion results, it was decided to repeat the experiment using a spray gun to test if the adhesive properties could be improved. Greater control of the applied coating was achieved using a spray gun rather than a doctor blade. The coatings generated had improved consistency and homogeneity. Thinner, more uniform layers are also obtained.

TPDOH and TPDCOOH solutions were tested with the spray gun. TPD had previously shown bad adhesion properties with the doctor blade, due to the lack of a hydrophilic group for interaction with the basecoat. Therefore, TPD was not tested with the spray gun.

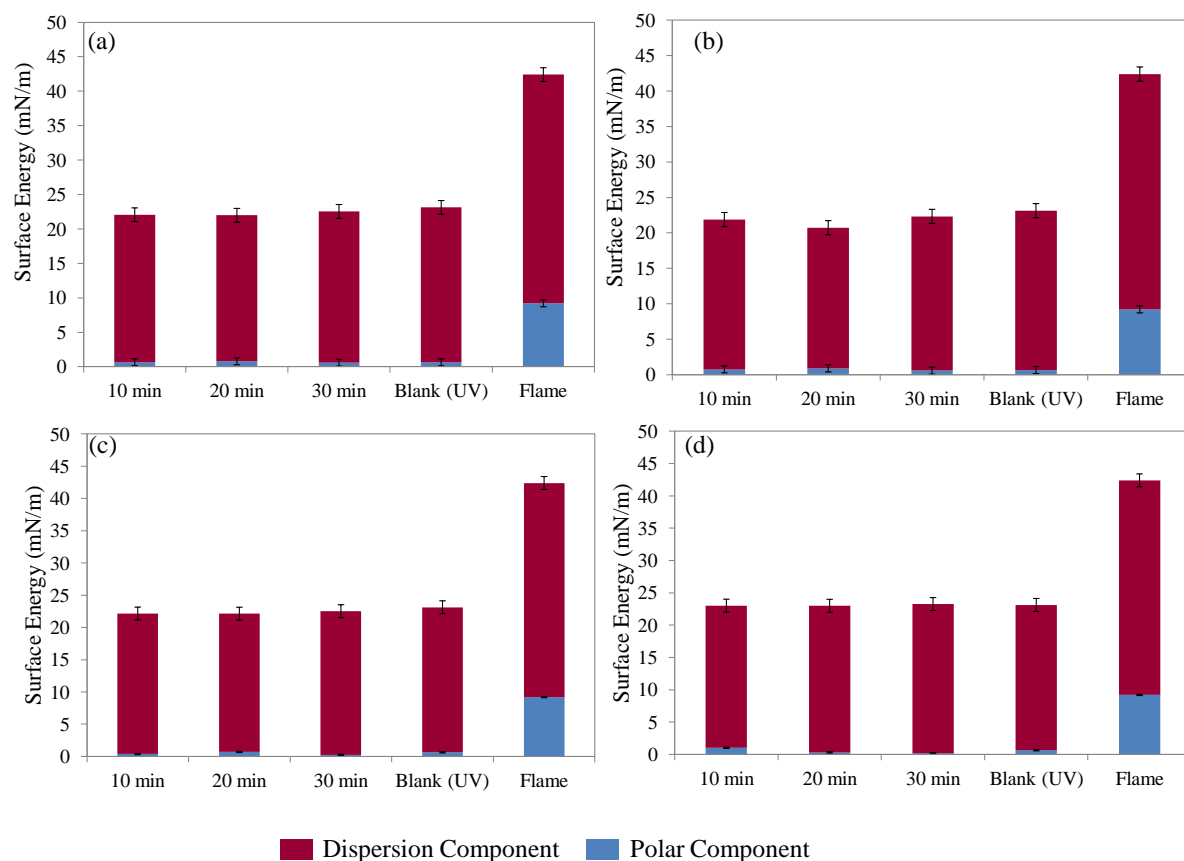


Figure 8.13: A bar graph showing the dispersion and polar components of the surface energy (together making the total surface energy) of a TPO/0 substrate surface after (a) 5 mM TPDCOOH and (b) 5 mM TPDOH was applied with a spray gun and cured at 80 °C, and (c) 5 mM TPDCOOH and (d) 5 mM TPDOH was applied with a spray gun and cured at 100 °C. The two state-of-arts are displayed at the right-hand side of the chart.

IR spectroscopy verified that the AP solutions were not destroyed during high pressure release from spray gun application (the N=N functional group remained intact).

Figure 8.13 displays the surface energy of the TPO/0 substrate surfaces after the APs were applied and thermally cured. Only the TPO/0 substrates were measured, but the results were sufficient to observe the effect of the AP on the polar component of the surface energy. The results show that using a spray gun application method did not improve the polar component of the surface energies, and the values were not comparable to the flame standard. It was therefore predicted that poor adhesion would be obtained, which was confirmed as shown in Table 8.9. It was concluded that the temperatures and time scales tested for thermal curing of TPDOH and TPDCOOH did not yield sufficient grafting to

Table 8.9: CHT results after various AP's were applied with a spray gun and thermally cured before the basecoat and clearcoat were applied, cured and left for a 7 day post-cure.

| Adhesion Promoter          | Concentration | CHT                              |    |    |                                   |    |    |
|----------------------------|---------------|----------------------------------|----|----|-----------------------------------|----|----|
|                            |               | Curing Time at 80 °C<br>/minutes |    |    | Curing Time at 100 °C<br>/minutes |    |    |
|                            |               | 10                               | 20 | 30 | 10                                | 20 | 30 |
| TPDOH                      | 5 mM          | 5                                | 5  | 5  | 5                                 | 5  | 5  |
| TPDCOOH                    | 5 mM          | 5                                | 5  | 5  | 5                                 | 5  | 5  |
| <b>Untreated Substrate</b> |               | 5                                |    |    |                                   |    |    |
| <b>Flame</b>               |               | 0                                |    |    |                                   |    |    |
| <b>CPO</b>                 |               | 0                                |    |    |                                   |    |    |

improve adhesive properties of the coatings applied to the substrate.

The  $F^-$  intensity was measured on the substrate and underside of the basecoat of the delaminated surfaces cured for 10 and 30 minutes. The intensities measured on the majority of the surfaces, shown in Figure 8.14(a), were comparable to the blank measured, suggesting a little amount of the AP remained at the surface. The mode of failure did not depend on the substrate types that contained additives, although when comparing Figure 8.14(b)-(d), the R/0 substrates were distinguishable from the other substrates with larger  $F^-$  intensities and an adhesive mode of failure at the AP/BC interface. Previously, the physical properties of the substrates were compared in Chapter 5 and one property which particularly distinguished R/0 from the other substrates was the significantly large hardness. This could result in the AP not being able to penetrate into the surface, which could be a controlling factor determining the delamination behaviour.

The only other substrate which showed a significant intensity on a delaminated surface was R/20 with the TPDOH 5 mM primer after an 80 °C cure for 30 min. The results suggest adhesive failure at the AP/substrate interface. The reason for this anomaly is not known and could have been caused by contamination. The intensities measured from the

other delaminated substrates of the 80 and 100 °C cure for TPDOH and TPDCOOH 5 mM showed little significance when compared to the blank. Overall, the low magnitude of signal intensities obtained suggested the low grafting efficiency from thermal curing was the dominating factor for poor adhesion. Although not displayed, the chemical mapping of F<sup>-</sup> intensity from the delaminated surfaces revealed that the primer was homogeneous, an improvement from the doctor blade application.

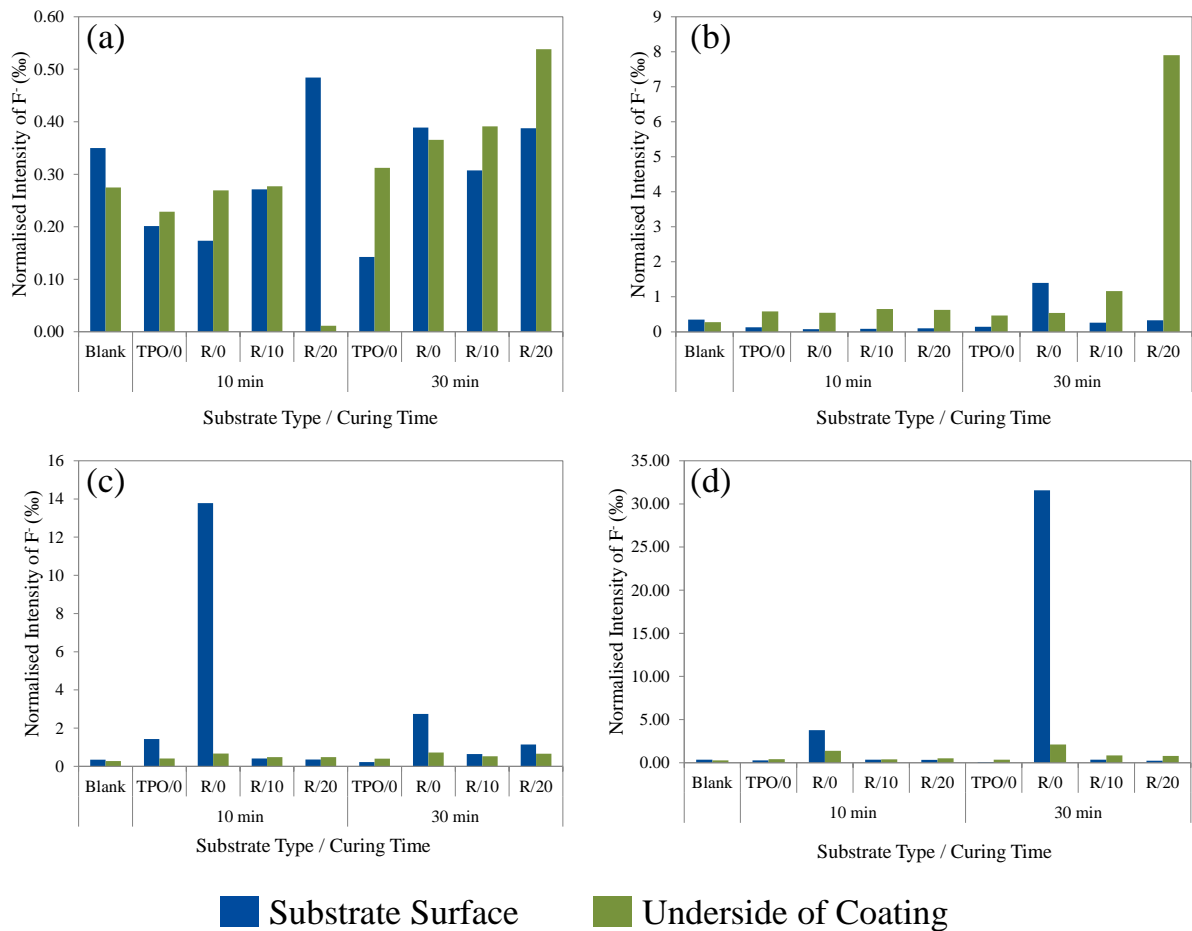


Figure 8.14: The F<sup>-</sup> intensities measured from the delaminated surfaces of the substrate and basecoat after (a) 5 mM TPDCOOH was cured thermally at 80 °C for 10 and 30 mins, (b) 5 mM TPDOH was cured thermally at 80 °C for 10 and 30 mins, (c) 5 mM TPDCOOH was cured thermally at 100 °C for 10 and 30 mins and (d) 5 mM TPDOH was cured thermally at 100 °C for 10 and 30 mins, before the basecoat and clearcoat were applied, cured and left for a 7 day post-cure.



## 8.4.2 UV Curing

Previous results with the doctor blade application method showed that UV curing of the AP primer was successful at improving the adhesive properties of the applied coatings to the modified substrates. The reproducibility of these results was tested using the spray gun application method. It was expected that better the quality of coatings produced by the spray gun would improve the adhesion.

### 8.4.2.1 Dependence of the Substrate Type and UV Radiant Exposure on the Adhesion

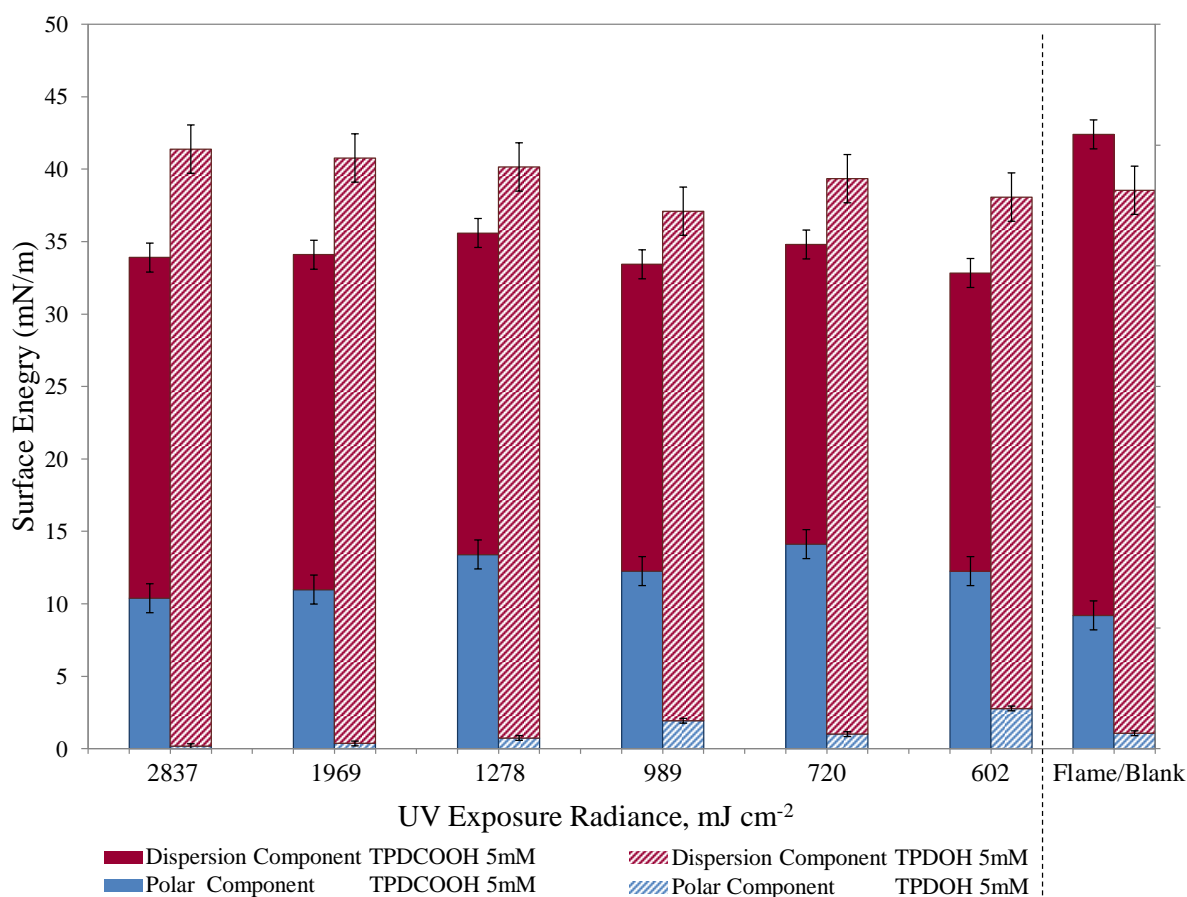


Figure 8.15: A bar graph comparing the dispersion and polar components of the surface energy (together making the total surface energy) of a TPO/0 substrate after 5 mM TPDCOOH and 5 mM TPDOH were applied with a spray gun and UV cured at different radiance exposures. The two state-of-arts are displayed at the right-hand side of the chart.

Table 8.10: CHT results after 5 mM TPDCOOH and 5 mM TPDOH were applied with a spray gun and cured with UV before the basecoat and clearcoat were applied, cured and left for a 7 day post-cure. These CHT results were obtained for all tested substrates: TPO/0, TPO/2, TPO/20, R/0, R/5, R/10, R/15, R/20, R/25 (no CHT variance occurred).

| Adhesion Promoter   | Concentration | CHT                                     |      |      |     |     |     |
|---------------------|---------------|---|------|------|-----|-----|-----|
|                     |               | UV Radiant Exposure/mJ cm <sup>-2</sup> |      |      |     |     |     |
|                     |               | 2387                                    | 1969 | 1278 | 989 | 720 | 602 |
| TPDOH               | 5 mM          | 5                                       | 5    | 5    | 5   | 5   | 5   |
| TPDCOOH             | 5 mM          | 0                                       | 0    | 0    | 0   | 0   | 0   |
| Untreated Substrate |               | 5                                       |      |      |     |     |     |
| Flame               |               | 0                                       |      |      |     |     |     |
| CPO                 |               | 0                                       |      |      |     |     |     |

Initially, the TPDCOOH and TPDOH primers were applied to different types of substrates and cured at varying UV radiant exposures. Positive adhesion results were obtained in Section 8.3.2 using a concentration of 5 mM, therefore, this was the chosen concentration for these tests. Furthermore, high concentrations were undesirable for industrial use (greater costs), therefore, the lower concentrations were desired.

Figure 8.15 shows the surface energies of the TPO/0 substrate after the primers were applied and cured. The polar components of the surface energies from the TPDCOOH on TPO/0 substrates were comparable in magnitude to the flamed standard for all radiant exposures, 2937 - 602 mJ cm<sup>-2</sup>. Therefore, good adhesion was predicted for these substrates and not for TPDOH on TPO/0 substrates.

The CHT results from the different substrate types with varying radiant exposures used for curing the 5 mM TPDCOOH and 5 mM TPDOH primers are displayed in Table 8.10. The results from the doctor blade application indicated that TPDCOOH had a higher grafting efficiency than TPDOH. The CHT results from the spray gun application further confirmed this, with good adhesion results found for all substrates with a 5 mM TPDCOOH primer, but poor adhesion results found for the 5 mM TPDOH primer.

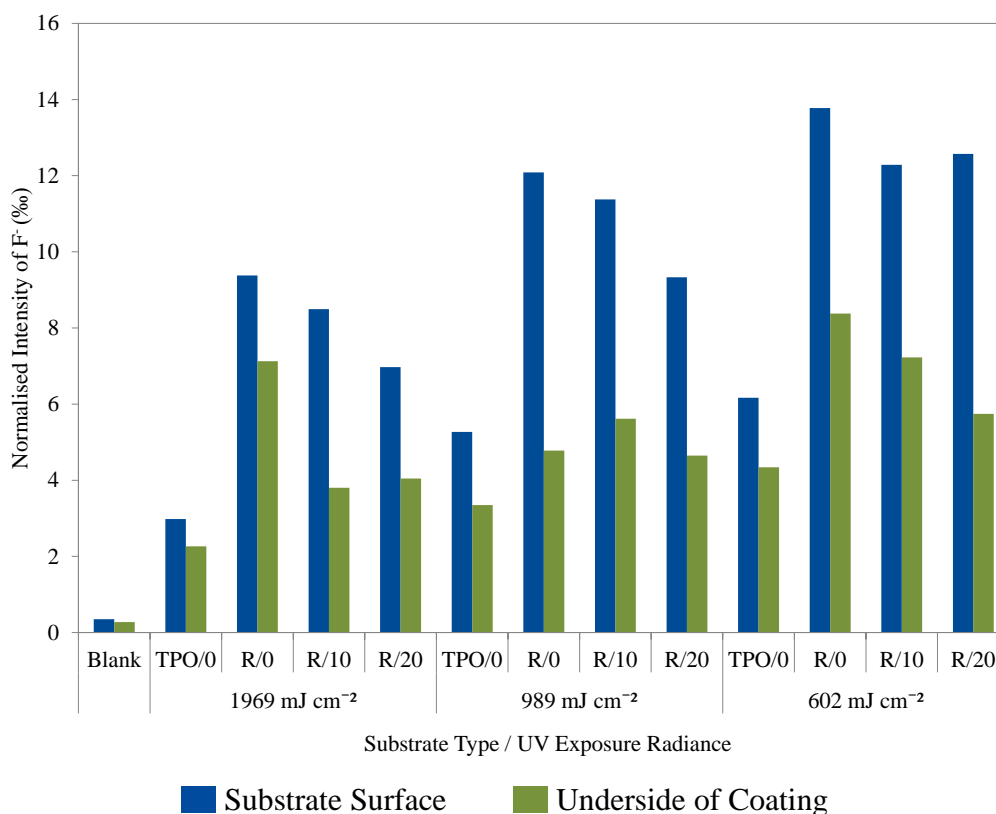


Figure 8.16: The  $F^-$  intensities measured from the delaminated surfaces of the substrate and basecoat after 5 mM TPDOH was applied as a primer and UV cured, before the basecoat and clearcoat were applied, cured thermally and left for a 7 day post-cure.

The  $F^-$  intensity of the 5 mMTPDOH delaminated surfaces were measured to investigate the mode of failure. Due to the high volume of samples, only four surfaces from different substrate types and three UV radiant exposures were measured. The results are shown in Figure 8.16. In all cases, the intensity measured was larger than the blank, proving that TPDOH was present at the surface. Furthermore, all substrates showed evidence of adhesive failure at the AP/basecoat interface. This suggested either the grafting efficiency of TPDOH was lower than TPDCOOH (which had good adhesion) and insufficient interactions with the basecoat occurred, or the grafting efficiency of TPDOH was comparable to TPDCOOH, but the interaction between a TPDOH and the basecoat was lower than that of TPDCOOH and the basecoat. Inhomogeneity of the primer was ruled out as a possible cause of poor adhesion, because chemical mapping of the surface showed the primer to be homogeneous.

Table 8.11: SJT results after 5 mM TPDCOOH was applied with a spray gun to various types of substrates, and cured with UV before the basecoat and clearcoat were applied, cured and left for a 7 day post-cure.

| Substrate Type             | Concentration | SJT                                     |      |      |     |     |     |
|----------------------------|---------------|---|------|------|-----|-----|-----|
|                            |               | UV Radiant Exposure/mJ cm <sup>-2</sup> |      |      |     |     |     |
|                            |               | 2387                                    | 1969 | 1278 | 989 | 720 | 602 |
| TPO/0                      | 5 mM          | 4                                       | 4    | 4    | 4   | 5   | 5   |
| TPO/2                      | 5 mM          | 3                                       | 2    | 4    | 5   | 5   | 4   |
| R/0                        | 5 mM          | 5                                       | 5    | 5    | 5   | 5   | 5   |
| R/5                        | 5 mM          | 4                                       | 3    | 5    | 5   | 5   | 5   |
| R/10                       | 5 mM          | 5                                       | 5    | 5    | 5   | 5   | 5   |
| R/15                       | 5 mM          | 5                                       | 5    | 5    | 3   | 3   | 5   |
| R/20                       | 5 mM          | 0                                       | 4    | 4    | 5   | 5   | 5   |
| R/25                       | 5 mM          | 5                                       | 5    | 5    | 5   | 5   | 5   |
| <b>Untreated Substrate</b> |               | 5                                       |      |      |     |     |     |
| <b>Flame</b>               |               | 0                                       |      |      |     |     |     |
| <b>CPO</b>                 |               | 0                                       |      |      |     |     |     |

Due to the poor adhesion results from the 5 mM TPDOH primer, further adhesion tests were performed only with TPDCOOH primers.

Since a CHT result of 0 (the best possible grade) was achieved for all the tested substrates with a 5 mM TPDCOOH primer, the next test, a harsher SJT was performed. The results are displayed in Table 8.11.

The best SJT result obtained was on a R/20 substrate after the primer was cured with the largest UV radiant exposure tested, 2387 mJ cm<sup>-2</sup>. However, as previously mentioned, the SJT did not yield reproducible results. Two further tests for each substrate were performed which gave results within  $\pm 2$  gradings. The steam jet parameters were set to one of the harshest standards known in the automotive industry, so it was not surprising to see such variations. In the reproducibility tests, a SJT grading of 2 was achieved for the R/20 substrate, cured at 2387 mJ cm<sup>-2</sup>. Better and worse adhesion compared to the

first SJT test was observed. Nevertheless, a significant improvement in the adhesion of the applied coatings to the grafted substrates was evident.

#### **8.4.2.2 Dependence of the TPDCOOH Concentration, Substrate Type and UV Radiant Exposure on the Adhesion**

A second experiment was performed to investigate the influence of concentration of TPDCOOH on the adhesion of the coatings to the grafted substrate. Two different ways of varying the concentration were tested: increasing the molar concentration of the solution from 5 mM to 10 mM, and increasing the number of primer layers applied. To compare the adhesion performance with radiant exposure, a radiant exposure which gave the best adhesion results in the previous experiment,  $2837 \text{ mJ cm}^{-2}$  and a lower one,  $1278 \text{ mJ cm}^{-2}$ , were tested. To reduce the sample volume, three substrate types were selected, and to make the experiment industrially relevant, TPO types were chosen that are currently used in the automotive industry.

The surface energy measured on the TPO/0 substrates is shown in Figure 8.17. The polar component of the surface energy from all the substrates tested was found to be larger than the flamed standard, indicating good adhesion could be obtained. The CHT results were all found to be a grading of 0 (100 % adhesion). Therefore, a SJT was performed. Table 8.12 shows the SJT results from the substrates with primers cured at  $2837 \text{ mJ cm}^{-2}$ . It was found that the higher molar concentration, 10 mM, and the higher number of primer layers applied, improved the adhesion. The type of substrate did not appear to have a significant influence on the results. Reproducibility SJT tests produced results within  $\pm 2$  gradings.

Table 8.13 shows the SJT results from the substrates with primers cured at  $1278 \text{ mJ cm}^{-2}$ . As observed in the previous experiment, the lower UV radiant exposure resulted in poorer adhesion results. The higher molar concentration, 10 mM, again showed improved adhesion results compared to 5 mM. However, it was found that the lower number of primer layers, 2, gave the best adhesion result for the  $1278 \text{ mJ cm}^{-2}$  cure, whereas a

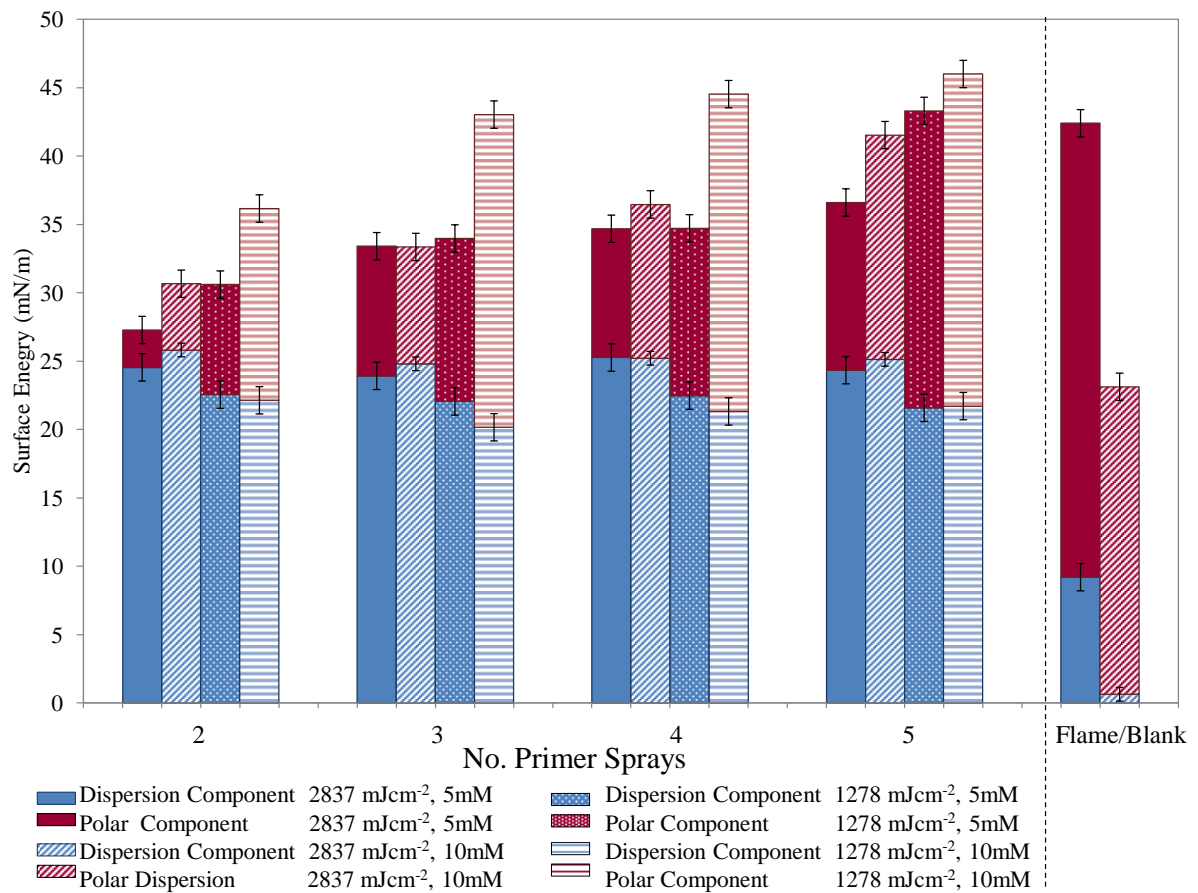


Figure 8.17: A bar graph comparing the dispersion and polar components of the surface energy (together making the total surface energy) of a TPO/0 substrate after 5 mM TPDCOOH was applied at different concentrations with a spray gun and UV cured at different radiant exposures. The two state-of-arts are displayed at the right-hand side of the chart.

higher number of primer layers gave the best adhesion results for substrates cured at 2837 mJ cm<sup>-2</sup>. Therefore, optimum adhesion was achieved with the correct balance of the number of primer layers and UV radiant exposure. The same trends were observed in the reproducibility tests, in which the results agreed within  $\pm 2$  gradings. One reason for this observation could be that the lower UV radiant exposure was able to better penetrate the smaller AP primer thickness (from the low number of primer applications) to induce significant grafting and adhesion. The larger number of primer layers applied would result in a thicker layer through which the UV may not have been able to penetrate and hence activate the APs. On the contrary, the higher radiant exposure of 2837 mJ cm<sup>-2</sup> may have been sufficient to penetrate the thicker primer layers to allow for better adhesion.

Table 8.12: SJT results after 5 mM TPDCOOH was applied with a spray gun to various types of substrates, and cured with UV at  $2837 \text{ mJ cm}^{-2}$ , before the basecoat and clearcoat were applied, cured and left for a 7 day post-cure.

| Substrate Type             | Concentration | SJT       |           |           |           |
|----------------------------|---------------|-----------|-----------|-----------|-----------|
|                            |               | 2 x spray | 3 x spray | 4 x spray | 5 x spray |
| TPO/0                      | 5 mM          | 5         | 5         | 1         | 3         |
| TPO/2                      | 5 mM          | 5         | 5         | 5         | 3         |
| TPO/20                     | 5 mM          | 5         | 3         | 5         | 3         |
| TPO/0                      | 10 mM         | 4         | 3         | 0         | 5         |
| TPO/2                      | 10 mM         | 5         | 5         | 1         | 0         |
| TPO/20                     | 10 mM         | 4         | 0         | 5         | 0         |
| <b>Untreated Substrate</b> | 5             |           |           |           |           |
| <b>Flame</b>               | 0             |           |           |           |           |
| <b>CPO</b>                 | 0             |           |           |           |           |

Table 8.13: SJT results after 5 mM TPDCOOH was applied with a spray gun to various types of substrates, and cured with UV at  $1278 \text{ mJ cm}^{-2}$ , before the basecoat and clearcoat were applied, cured and left for a 7 day post-cure.

| Substrate Type             | Concentration | SJT       |           |           |           |
|----------------------------|---------------|-----------|-----------|-----------|-----------|
|                            |               | 2 x spray | 3 x spray | 4 x spray | 5 x spray |
| TPO/0                      | 5 mM          | 5         | 5         | 5         | 5         |
| TPO/2                      | 5 mM          | 5         | 5         | 5         | 4         |
| TPO/20                     | 5 mM          | 5         | 5         | 5         | 5         |
| TPO/0                      | 10 mM         | 1         | 2         | 5         | 4         |
| TPO/2                      | 10 mM         | 1         | 5         | 5         | 5         |
| TPO/20                     | 10 mM         | 4         | 5         | 5         | 5         |
| <b>Untreated Substrate</b> | 5             |           |           |           |           |
| <b>Flame</b>               | 0             |           |           |           |           |
| <b>CPO</b>                 | 0             |           |           |           |           |

The modes of failure from the substrates which gave poor SJT results were not able to be measured. This was because the coating and substrate had to be forced apart, which could have resulted in a false interpretation of the mode of failure. For example, the high force used to manually pull the coatings away from the substrate surface was different to the high pressure steam in SJT which caused delamination, so the methods were not comparable.

### 8.4.3 UV Curing vs. Thermal Curing

#### 8.4.3.1 Surface Elemental Composition

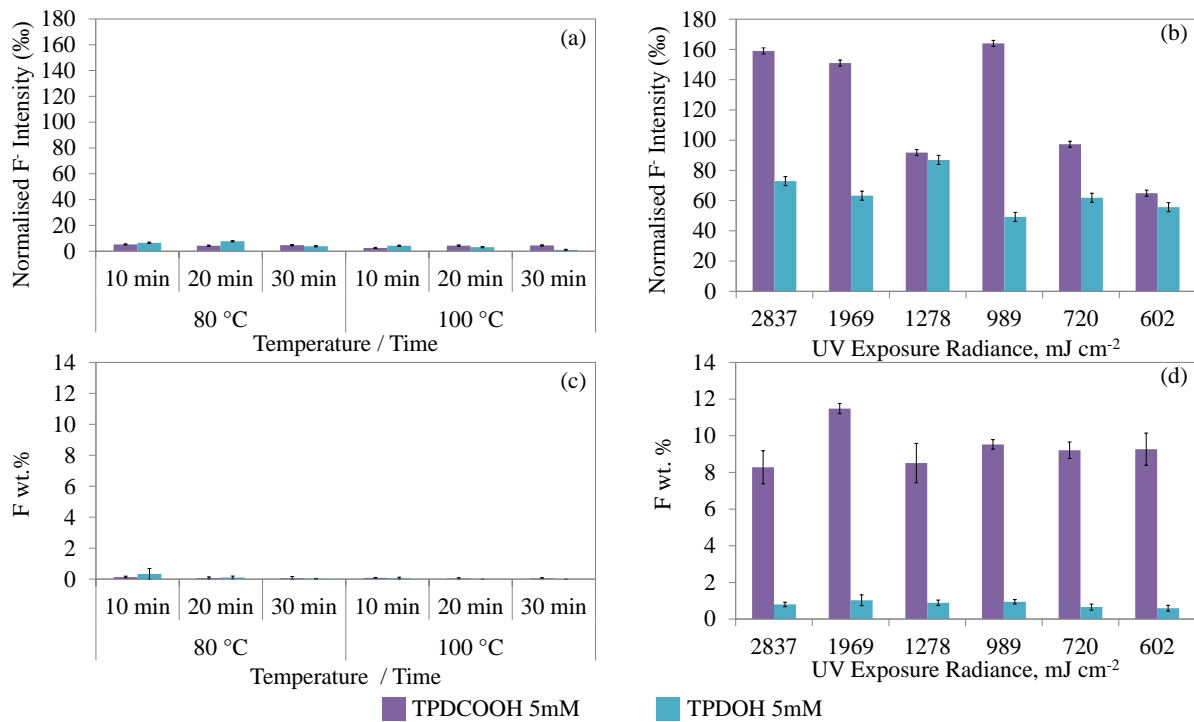


Figure 8.18: Bar graphs displaying the F<sup>-</sup> intensity on a TPO/0 substrate from (a) thermally cured substrates and (b) UV cured substrates, and the F wt.% on a TPO/0 substrate from (c) thermally cured substrates and (d) UV cured substrates. Both 5 mM TPDOH and 5 mM TPDCOOH AP primers were tested.

Figure 8.18 compares the F<sup>-</sup> intensity and the F wt.% from thermally cured and UV cured TPO/0 substrates after 5 mM TPDOH and 5 mM TPDCOOH were applied as primers. These measurements were taken directly after the primers were cured (no



other coatings had been applied). The y-axes have the same scale, enabling a direct comparison between the curing methods. It was immediately apparent that the signal intensities from the UV cured samples were significantly larger than the thermally cured samples. The F wt.% after UV curing is on the order of 10 times higher than the thermal curing. Therefore, it can be concluded with confidence that UV grafting yields a better efficiency (grafted molecule per area over time) than thermal grafting, in the conditions tested. Furthermore, TPDCOOH showed higher F<sup>-</sup> and F wt.% intensities after UV curing, compared to TPDOH, as previously observed. No obvious trend between the F<sup>-</sup> intensity / F wt.% and the UV radiant exposure was observed. Surface contamination from silicone or dust particles found in the laboratory atmosphere is a likely reason for the lack of trend.

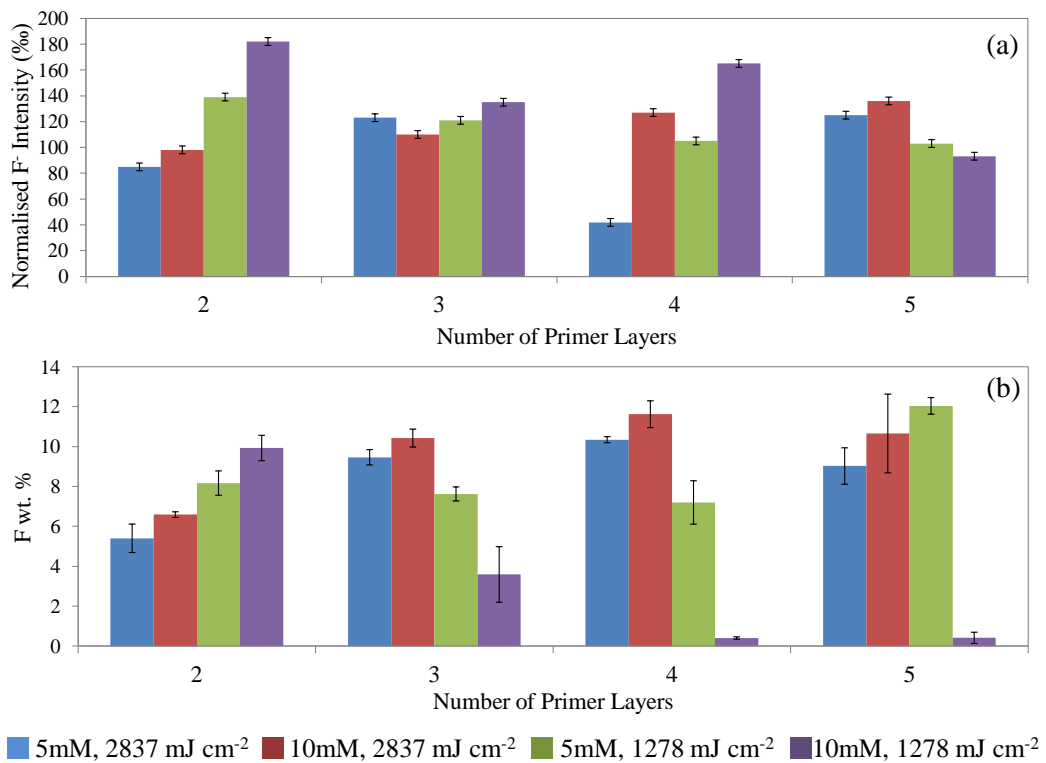


Figure 8.19: Bar graphs displaying the (a) F<sup>-</sup> intensity and (b) F wt.% after a 5 mM TPDCOOH AP primer was applied at varying concentrations and cured with two different UV radiant exposures.

Figure 8.19 shows the F<sup>-</sup> intensity and the F wt.% from UV cured TPO/0 substrates after 5 mM TPDCOOH was applied at different concentrations as the primer. Again, no

obvious trend was observed between the numbers of sprays and the molar concentration of TPDCOOH, likely to be due to low levels of surface contamination.

#### 8.4.3.2 UV-Vis Kinetics Study

To further investigate why UV curing gave greater grafting efficiencies than thermal curing, a UV-Vis kinetic study was performed to calculate the rates of reaction at the various curing conditions. To investigate thermal curing, the AP solutions were heated up in the UV-Vis chamber and the absorbance spectrum was measured over time, monitoring the decrease of the absorbance due to the N=N chromophore (as discussed in Appendix 10.G.1). Figure 8.20 shows the results measured at 80 °C and Figure 8.21 shows the results measured at 100 °C. Calibration curves were used to calculate the concentration change over time, to monitor the loss of the diazirine functional group as a carbene was generated.

It should be noted that in all measurements, the product generated from the loss of the diazirine group (-N<sub>2</sub>) appeared to absorb by a low level at the maximum wavelength characteristic of the diazirine (N=N). Kinetic studies were, however, calculated at the maximum wavelength. Therefore, the time scales presented in Table 8.14 are for a rule of thumb only, and cannot be relied upon for accuracy.

To investigate the UV reaction kinetics, a UV LED chamber was used. The sample was measured over time to measure the change in UV-Vis absorbance, for powers of 0.1, 0.3, 0.5, 0.7, 0.9 and 2 mW cm<sup>-2</sup>. Figure 8.22 shows the absorbance spectra change over time with a UV power of 2 mW cm<sup>-2</sup>. Calibration curves were used to calculate the change in concentration over time. The relationship between the rate of decomposition and UV power was then calculated, as shown in Figure 8.22. All the decomposition reactions were found to be first order, as expected for a uni-molecular process.

In the region of 400 - 600 nm (not displayed on the Figure) during the UV kinetics study, small absorptions (all below 0.1) due to the diazo isomer of the diazirine were observed.<sup>135</sup> The UV reaction of the TPD-based molecules to the diazo compound was a

competing process, as shown in Figure 8.23. This may have reduced the carbene generation efficiency, because in a previous study by Brunner *et al.*,<sup>135</sup> it was found that the diazo isomer converted to the carbene but at a slower rate than the diazirine. Using a 450 W mercury lamp at a 4 cm distance, the half life of diazirine was found to be 25 seconds, whilst the half life of the diazo compound was 22 minutes (UV cure lasted approximately 2 seconds). These absorptions due to the diazo isomer were only observed during UV reactions and not the thermal reactions, suggesting different reaction pathways for each method.

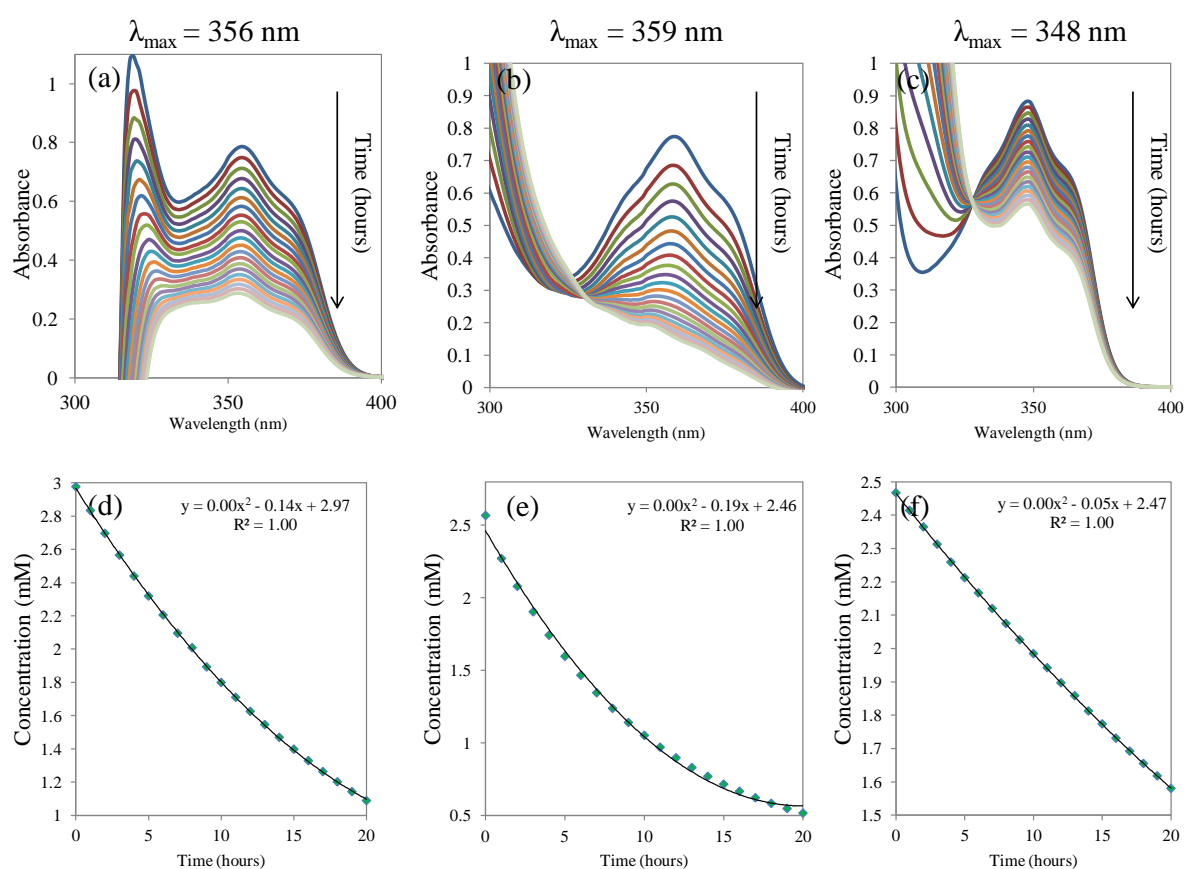


Figure 8.20: Top: UV-Vis spectra taken at 80 °C of the -N=N- chromophore, from (a) TPD in Toluene, (b) TPDOH in Toluene, (c) TPDCOOH in Toluene. Bottom: Concentration vs. time curves at 80 °C for (d) TPD, (e) TPDOH and (f) TPDCOOH. All reactions are first order: rate of reaction is directly proportional to the concentration of TPD/OH/COOH. The decomposition of TPD is a unimolecular process.

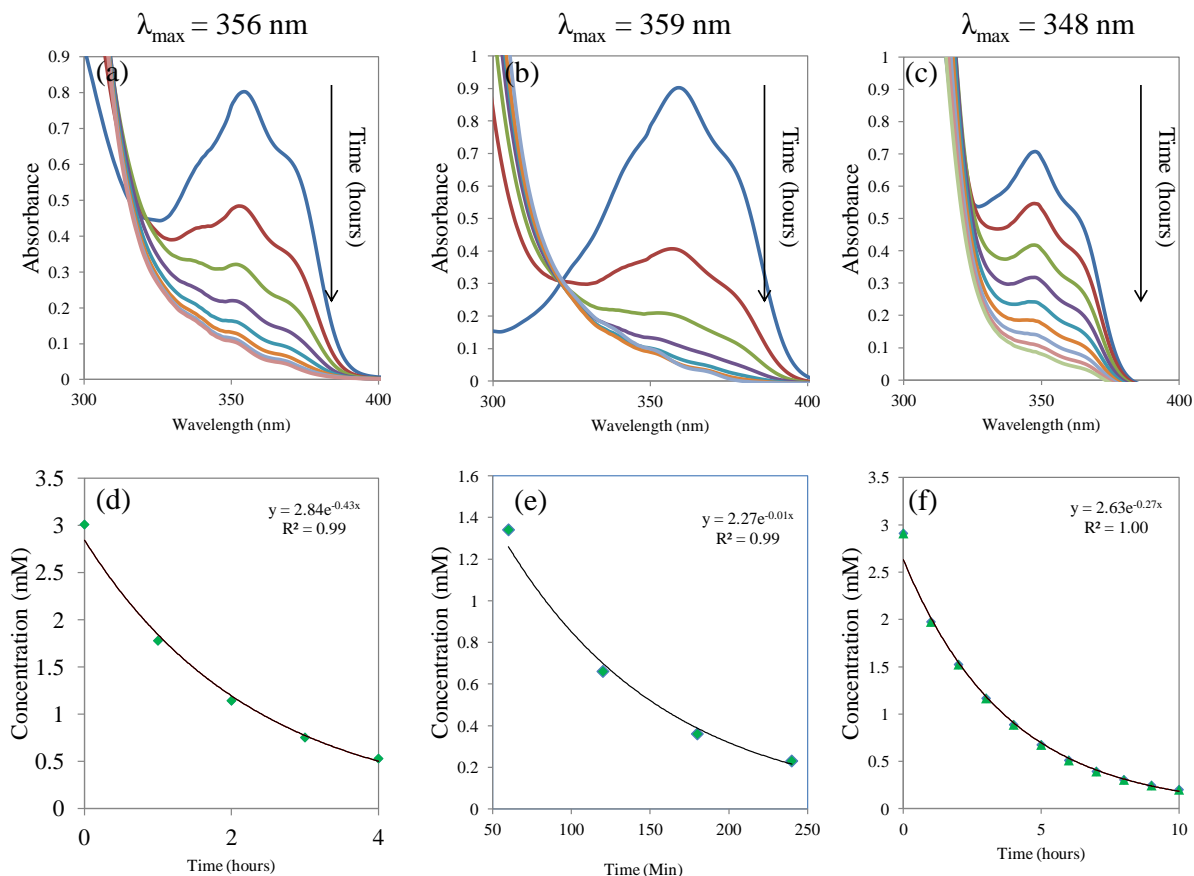


Figure 8.21: Top: UV-Vis spectra taken at 100 °C of the -N=N- chromophore, from (a) TPD in Toluene, (b) TPDOH in Toluene, (c) TPDCOOH in Toluene. Bottom: Concentration vs. time curves at 100 °C for (d) TPD , (e) TPDOH and (f) TPDCOOH. All reactions are first order: rate of reaction is directly proportional to the concentration of TPD/OH/COOH. The decomposition of TPD is a unimolecular process.

A summary of thermal vs. UV curing kinetics is found in Table 8.14. A power of 400 mW cm<sup>-2</sup> was calculated to be the equivalent of 1900 mJ cm<sup>-2</sup>, which was used during the adhesion tests. The results highlight the significantly faster UV kinetics compared to the thermal kinetics. UV curing was found to be on the order of 10<sup>5</sup> times faster than thermal curing. This therefore explained the higher grafting efficiency and better adhesion results found for UV curing compared to thermal curing during the adhesion tests.

It was found that TPDOH reacted faster than TPD, which reacted faster than TPDCOOH. This was not the expected order since the best adhesion results had been obtained with TPDCOOH. However, it was thought that the higher volatility of TPDOH compared

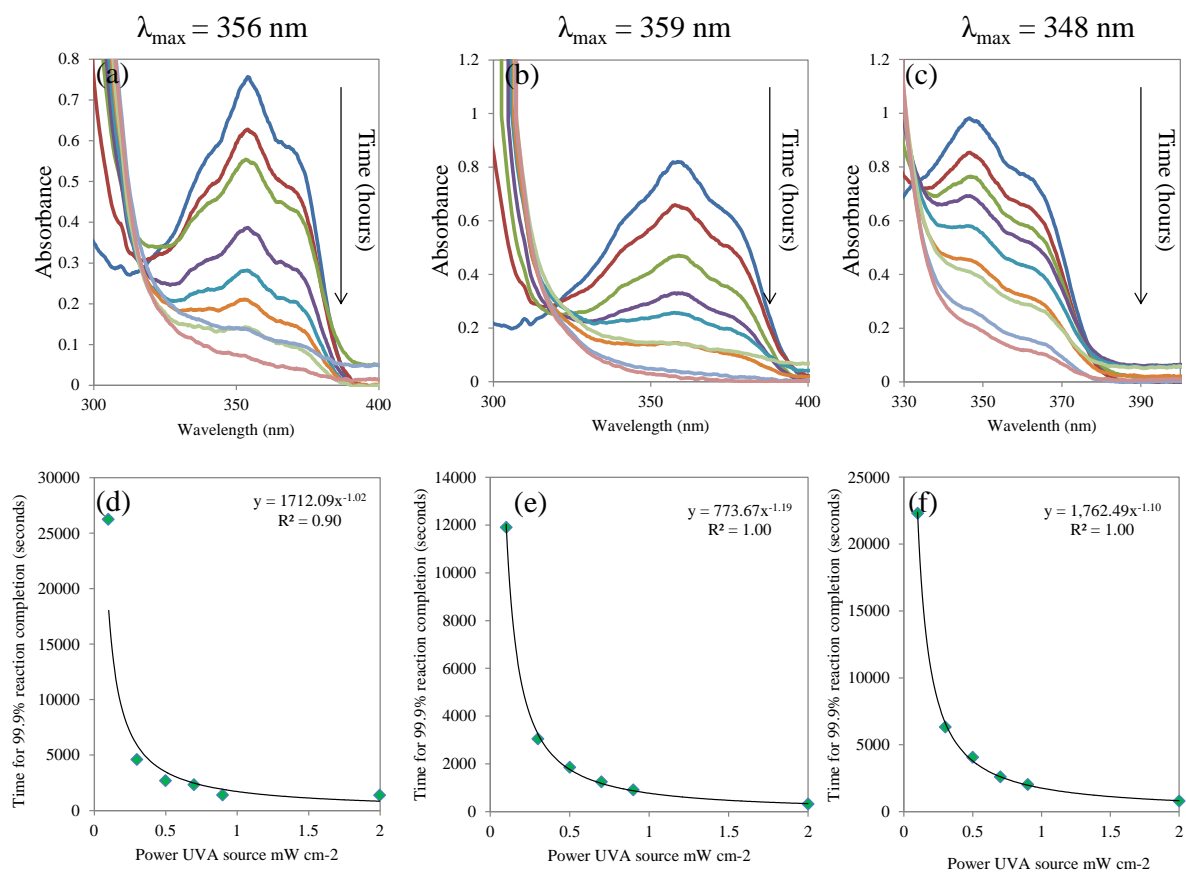


Figure 8.22: Top: UV-Vis spectra of the  $-N=N-$  chromophore, taken at  $2 \text{ mW cm}^{-2}$  from (a) TPD in Toluene, (b) TPDOH in Toluene, (c) TPDCOOH in Toluene. Bottom: Time for 99 % reaction completion vs. power of UV source in  $\text{mW cm}^{-2}$  for (d) TPD, (e) TPDOH and (f) TPDCOOH. All reactions are first order: rate of reaction is directly proportional to the concentration of TPD/OH/COOH. The decomposition of TPD is a unimolecular process.

Table 8.14: Summary of the kinetic study from thermal and UV reactions of TPD, TPDOH and TPDCOOH.

| Active Molecule | Time for 99.9% conversion |        |                         | Reaction rate increase |                                    |
|-----------------|---------------------------|--------|-------------------------|------------------------|------------------------------------|
|                 | 80 °C                     | 100 °C | 400 $\text{mW cm}^{-2}$ | 80 °C<br>→ 100°C       | 100°C<br>→ 400 $\text{mW cm}^{-2}$ |
| TPD             | 139h                      | 16h    | 3.7s                    | x 8.7                  | x $1.4 \times 10^5$                |
| TPDOH           | 91h                       | 11h    | 0.6s                    | x 8.3                  | x $5.5 \times 10^5$                |
| TPDCOOH         | 306h                      | 26h    | 2.4s                    | x 11.8                 | x $4.6 \times 10^5$                |

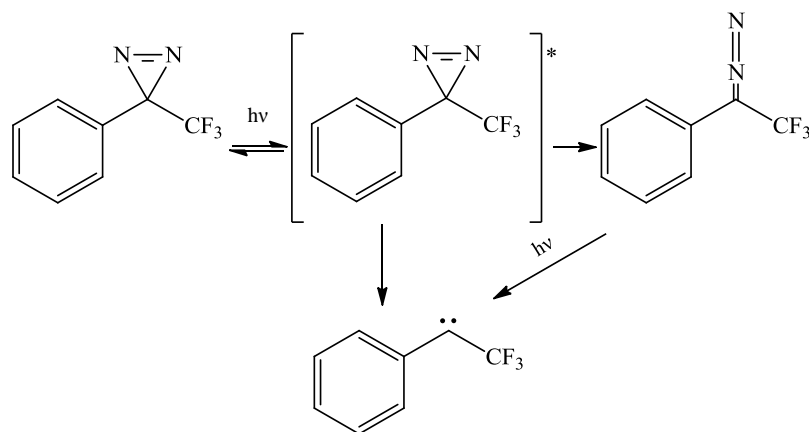


Figure 8.23: The UV reaction scheme for TPD showing the formation of the diazo isomer and subsequent indirect formation of the carbene. Adapted from Brunner *et al.*<sup>135</sup>

to TPDCOOH could have been a reason for the differences in adhesion, or the TPDOH may have reacted on a time scale that was too fast to allow for CH insertion reactions with the substrate to occur.

To test if further decomposition of the AP's had occurred during the reaction with toluene, the products from the kinetic study (3 mM AP in toluene) which were cured at 100 °C for eight hours under reflux (thermal) and 2 mW for 180s (UV) were analysed with GC/MS. A cool-on-column technique (described in Section 4.26.1) was used for the prevention of thermal decomposition of the samples during the analysis process, although a temperature ramp and a heated interface between the gas chromatograph and mass spectrometer could not be avoided.

The expected target compounds were identified without decomposition, as shown in Figure 8.24. Therefore, the UV-Vis absorptions were confirmed to be from the N=N chromophore of the diazirine functional group, and not any decomposition side products. The AP's were found to have undergone regioselective CH insertion reactions with the methyl group of toluene only (Figure 8.24 (b), (e) and (g)) and no evidence of CH insertion into the phenyl ring was observed.

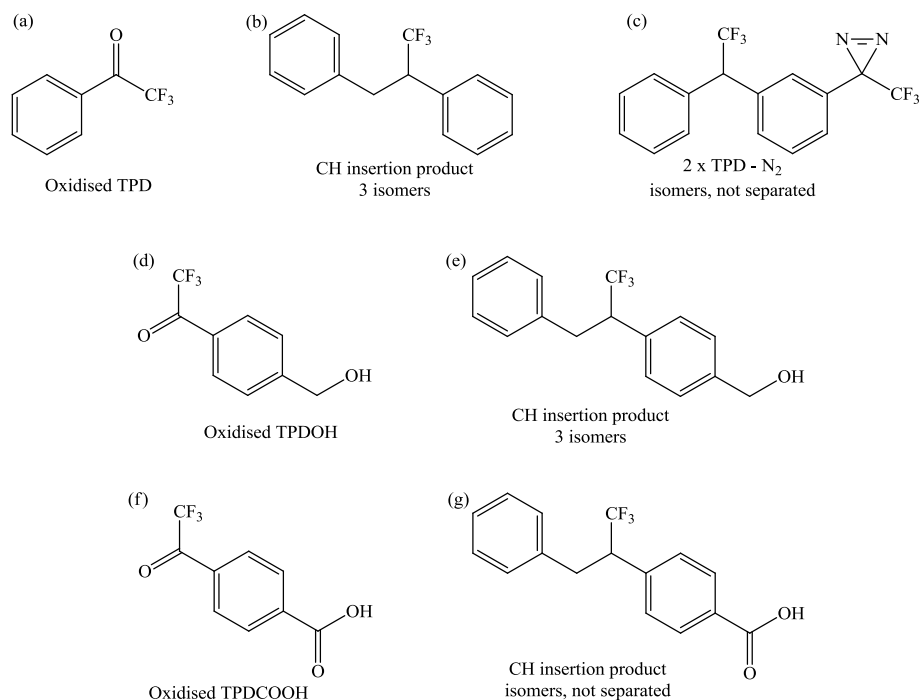


Figure 8.24: Structures of the products identified with GC-MS from the thermal and UV activated reactions of 3 mM solutions of TPD (a-c), TPDOH (d-e) and TPDCOOH (f-g) in toluene.

This regioselectivity has also been observed from different carbenes reacting with toluene in previous studies.<sup>187</sup> The reaction is selective because the methyl group of toluene is the most sterically accessible group for the TPD to react with. Evidence of oxidation reactions from all AP's were also observed, which generated ketone derivatives as shown in Figure 8.24 (a), (d) and (f). TPD was also found to have CH inserted into another TPD molecule generating the structure with Mr = 344 (Figure 8.24 (c)). No differences between thermal or UV activated reaction products were observed.

#### 8.4.3.3 EPR Spectrometry Study

To take the investigation further, EPR spectroscopy measurements were performed to see if reactive triplet carbene species could be detected upon thermal and UV activation of TPDCOOH. Although computational calculations (described in Section 4.21.3) predicted all three APs to form triplet carbenes, it was thought that the electronic state of the carbene may vary depending on the curing method used to generate the carbene. EPR

does not detect singlet carbenes, therefore, the difference (if any) between the carbene ground state generated, depending on whether the reaction was thermally or UV activated, could be tested. Any observable differences in the ground states of carbenes formed, determined by the signal generated in EPR, would aid the understanding of why UV initiated reactions had such significantly faster time scales than thermal reactions.

Few cases exist in the literature where both UV and thermal activation have been used to generate a carbene and the reaction mechanisms compared. However, previous investigations show striking differences in the products produced, depending on whether the carbenes were generated thermally or by UV. Various carbene precursors have been found to have mixed singlet and triplet carbene processes during CH insertion reactions.<sup>188-190</sup> Furthermore, significant differences in the insertion products and the distribution of isomers formed upon UV and thermal reactions of TPDs have been observed.<sup>191,192</sup> This was also observed during the proof of concept experiment in Section 7.3.1, where the <sup>19</sup>F NMR spectra of the products from the thermal or UV reaction between cyclohexane and TPD were significantly different. It has been postulated that the higher reactivity of the carbenes generated by UV activation compared to thermal activation is due to vibrationally excited carbenes (hot radicals) generated by UV irradiation.<sup>188</sup>

**UV degradation** Two scans were recorded before and after TPDCOOH was subjected to the UV LED. The first (red line, as shown in Figure 8.25) was recorded with no irradiation, whereas the second (black line in Figure 8.25) was run after five minutes of irradiation using a 365 nm LED, guided by fibre-optic cable into the sample tube. This was maintained whilst running the spectrum. In Figure 8.25, these two data sets are offset on the y-axis for clarity (these being otherwise overlapping), which represents intensity in arbitrary units.

The similarity of the two measurements in Figure 8.25 suggested either a singlet (diamagnetic/spin paired) species was being formed which wouldn't be detected in EPR, or potentially a carbene species wasn't being formed in the reaction conditions. However,



it was previously suggested by Brunner *et al.*,<sup>135</sup> that the formation of a triplet carbene by UV activation of TPD was unlikely since no evidence of oxygen quenching of triplet carbenes was found during reactions performed in air, and OH insertion reactions were formed in very high yields ( $\sim 95\%$ ).

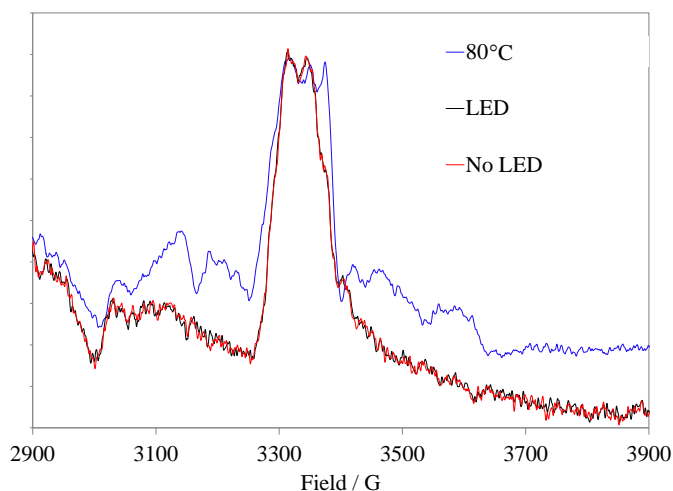


Figure 8.25: X-band EPR spectra recorded at 293 K (experimental conditions: frequency was 9.87 GHz; power was 20 mW) for a non-irradiated (red), irradiated with UV LED (black) and thermally activated at 80 °C (blue) sample.

**Thermal degradation** Figure 8.25 displays a sample that was measured at 80 °C under the same measurement conditions as the sample before and after LED exposure. Although the signals measured were relatively weak, it appeared as if the portion at 3400 - 3700 G on the thermal sample was changing significantly and acquiring extra features. This implied that *something* was occurring chemically, although it wasn't possible to confirm with confidence that it was due to a triplet carbene formation. If it was due to a triplet carbene formation, or a difference in the energetics of the ground state carbene formed, this could help to explain the lower CH insertion yield obtained from thermal activation. Further experiment repeats would be needed to gain confidence with this measurement but due to instrument time restrictions, this was not possible in the duration of this project.

Although it was difficult to interpret the EPR spectra with confidence, the difference

measured between thermal and UV curing, as shown in Figure 8.25, suggested a difference in the energetics of the carbenes or reactive species formed during the reaction which could have been a reason for the difference in adhesion observed, with UV curing generating the best results.

Future experiments to further understand the electronic states of the carbenes generated in different conditions, could include determining the yield of a thermal or UV reaction in methanol under an air atmosphere, which would help to determine if any triplet species were formed because oxygen quenching by triplets would result in a lower yield than expected.<sup>135</sup> IR spectroscopy has also been used to characterise the electronic state of TPD molecules, using flash pyrolysis as the activation method. Future work could use the predicted spectra for a singlet and triplet carbene to compare with the measured IR spectra, as investigated by Fischer *et al.*<sup>193</sup>

#### 8.4.4 Chemical Mapping of Coated Cross-Sections

To assess the adhesion mechanisms of the AP primers applied at the substrate/basecoat interface, ToF-SIMS was used to measure the  $F^-$  intensity of a defined area from cross-sections of coated and cured substrates that showed good CHT or SJT results. Characteristic ions of the basecoat, clearcoat and substrate were chosen.  $NCO^-$  was found in polyisocyanates from the clearcoat,  $C_2N_3^-$  was found in the basecoat formulation, and  $C_{28}H_{42}PO_4^-$  was from the Irgafos 168 additive in the substrate (Appendix 10.F.2).

Initially, a spray gun was used to coat a blank substrate (no AP) with a basecoat and clearcoat, which were cured using the standard procedure. A small sectioned piece of the delaminated coating was then set in a resin to be held in place for cutting with a microtome. By careful handling of the sample, a cross-section was cut and immediately placed into the ultra high vacuum (UHV) chamber for ToF-SIMS analysis. It was important to measure the cross-sectioned surfaces on the same day to avoid contamination at the surface. However, an argon cluster ion gun was used to etch the surface clean before analysis as a precaution, to remove any contamination that reached the surface in the

short transfer time.

#### 8.4.4.1 Basecoat and Clearcoat on an Untreated Substrate

It was important to measure a delaminated basecoat and clearcoat to check if a significant  $F^-$  intensity could be detected, which could have hindered any signals from the AP primer.

The results are shown in Figure 8.26. The basecoat was clearly identified with the  $C_2N_3^-$  ion, and the clearcoat was clearly identified using the  $CNO^-$  ion. All intensities were normalised against the total ion counts. The overlay of the  $F^-$  intensity in Figure 8.26(b) shows a low signal. This was then compared with the coated substrates containing a primer layer.

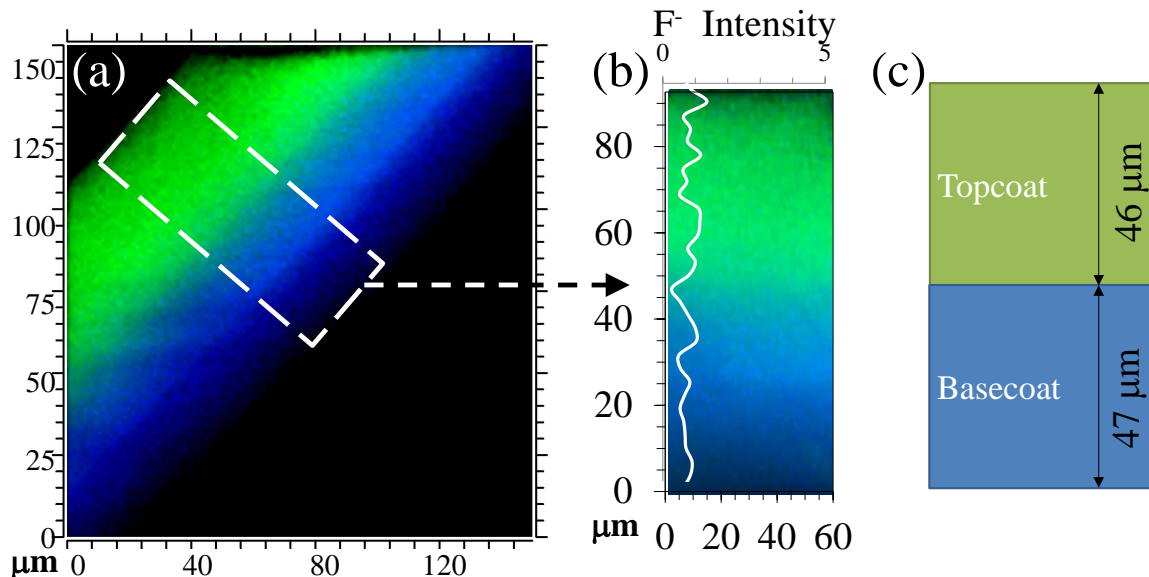


Figure 8.26: (a) ToF-SIMS image showing the clearcoat from the  $NCO^-$  ion ( $m/z = 42$ ) and the basecoat from the  $C_2N_3^-$  ion ( $m/z = 66$ ), normalised against total ion counts, (b) image: magnified area of basecoat/clearcoat; overlay: line graph of  $F^-$  ( $m/z = 19$ ) normalised intensity, and (c) schematic diagram of basecoat/clearcoat with estimated coating thicknesses.

An estimation of the coating thickness was measured using Ion-ToF software. However, the basecoat and clearcoat mixed during the thermal curing stage, therefore, no clear interface existed between the layers. The total thickness of the coatings was almost double than the expected thickness. The low accuracy of a hand held spray gun (human

error) may have caused this.

#### 8.4.4.2 Comparing TPDOH and TPDCOOH

The  $F^-$  intensity images shown in Figure 8.27 show a clear difference between the grafting abilities of TPDOH and TPDCOOH. The TPDCOOH primer was applied with a concentration 100 times lower than the TPDOH, and the signal intensity from  $F^-$  of the TPDCOOH was found to be significantly higher than TPDOH. Furthermore, the  $F^-$  intensity found on the primer coated substrates was between 100 times (TPDOH) or 500 times (TPDCOOH) larger than the blank coatings shown in Figure 8.26. This proved that the  $F^-$  intensity was from the AP and not any components in the coatings.

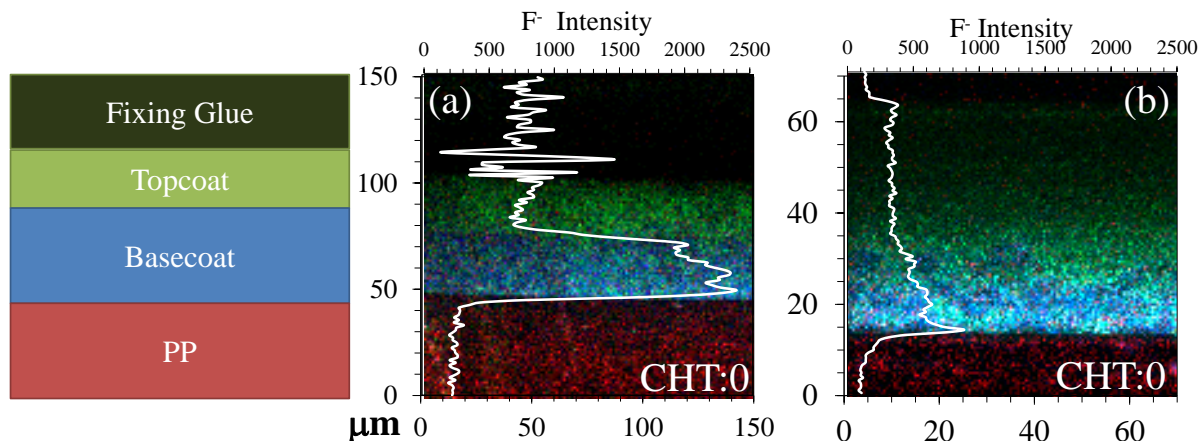


Figure 8.27: ToF-SIMS images showing the clearcoat from the  $NCO^-$  ion ( $m/z = 42$ ), the basecoat from the  $C_2N_3^-$  ion ( $m/z = 66$ ), and the TPO substrate from the  $C_{28}H_{42}PO_4^-$  ion ( $m/z = 473$ ), with an overlay of the  $F^-$  ( $m/z = 19$ ) for a UV cured ( $1900 \text{ mJ cm}^{-2}$ ) (a) 5 mM TPDCOOH and (b) 0.5 M TPDOH primer layer, applied with a doctor blade. All intensities were normalised against total ion count.

#### 8.4.4.3 Comparing the Doctor Blade and Spray Methods of Application

Two substrates, one which had coatings applied with a doctor blade and the other with a spray gun, were cross-sectioned and imaged to compare the two application methods. The results are shown in Figure 8.28. The  $F^-$  axis was set to the same scale for both measurements, so that a direct comparison between the application methods could be

made.

A distinct difference in the maximum intensities was observed, with the doctor blade giving an  $F^-$  intensity on the order of 200 times larger than the spray applied substrate. This was not unexpected due to the difficulty of controlling the applied primer with a doctor blade, often resulting in much thicker layers than desired, which would increase  $F^-$  intensity.

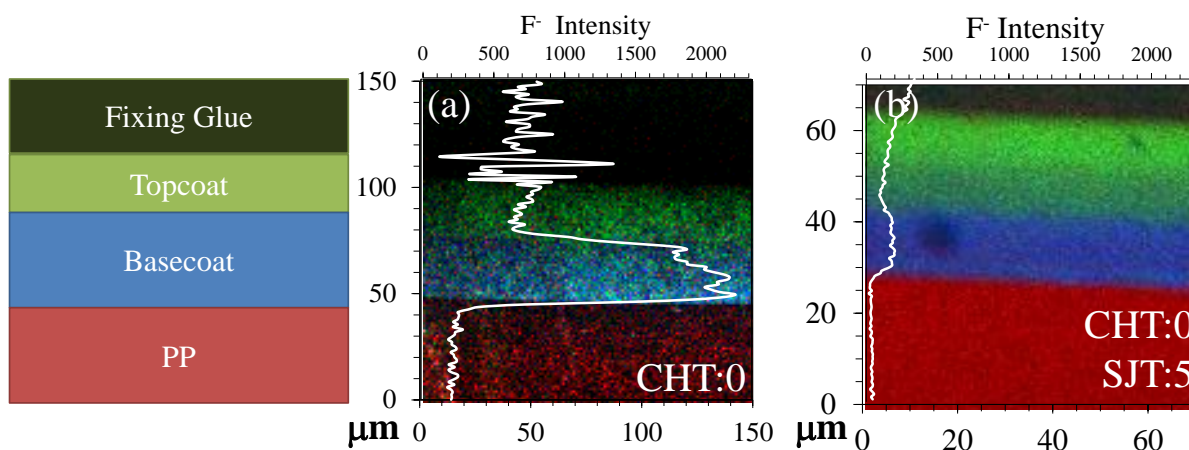


Figure 8.28: ToF-SIMS images showing the clearcoat from the  $NCO^-$  ion ( $m/z = 42$ ), the basecoat from the  $C_2N_3^-$  ion ( $m/z = 66$ ), and the TPO substrate from the  $C_{28}H_{42}PO_4^-$  ion ( $m/z = 473$ ), with an overlay of the  $F^-$  ( $m/z = 19$ ) for a primer of 5 mM TPDCOOH which was cured by UV at  $1900 \text{ mJ cm}^{-2}$  and applied with a (a) doctor blade and (b) spray gun. All intensities were normalised against total ion count.

The spray application gave a finer finish and better controllability, which was preferential from an industrial perspective. Furthermore, the thinner AP layer achieved with the spray gun gave a CHT result comparable to the thicker layer from the doctor blade. The thinner layer was formed using less AP, therefore, the use of the spray gun was more economical and less wasteful to produce the same adhesion result, which would be more industrially applicable from a financial point of view.

It was also learnt from Figure 8.28 that the AP did not remain only at the substrate/basecoat interface, but leached into the basecoat as shown by the wide peak of high intensity due to  $F^-$ . This was different from what was observed in the image formed from the CPO state of the art coated substrate, shown in Section 5.6, Figure 5.14, where the

$\text{Cl}^-$  had a sharp intensity increase at the interface. When considering the estimated concentration for a monolayer of TPDCOOH at the substrate surface (calculated in Section 4.21.1, shown in Table 7.19), this result was not unexpected due to the high concentration of molecules at the surface. Either single unbound molecules leached into the basecoat or the excess molecules grafted to one-another, forming a brush-like structure that was grafted to the substrate surface. If this structure was mobile once the basecoat was applied, it could have set in the coating during the curing stage, increasing the adhesion by locking the two layers together. The kinetics study indicated that it would take in the order of 2.4 s for 99.9 % conversion of TPDCOOH to the active carbene. Therefore, the APs are very likely to have reacted and the brush like structure is quite possible. Furthermore, the mass spectra results discussed in Section 7.4.1 also support the multilayer model suggested.

#### 8.4.4.4 Comparing Substrate Type

Further analysis was done to look for any differences between the types of substrates used. Figure 8.29 compares a R/0, R/10 and R/20 substrate. All the substrates had given a CHT result of 0 (the best), however, only the R/20 substrate gave the highest result possible from the SJT (100 % adhesion). It could not be seen why the R/20 substrate gave the best adhesion results when comparing the  $\text{F}^-$  intensity, which was of a similar magnitude for all substrates. Therefore, the improved adhesion was likely to be due to the physical properties of the R/20 substrate that distinguished it from the other substrates.

The physical properties of the substrates, (see Appendix 10.F), revealed that the R/20 was significantly softer than the other substrates. This could have resulted in the penetration of the TPDCOOH into the surface of the substrate during the application/curing process, allowing a type of mechanical adhesion as well as forming a covalent bond at the surface. The basecoat could have also penetrated into the substrate, allowing a better interaction with the grafted surface compared to the other substrates. The resolution of the images and the deviations of the coating interfaces from a straight line limited ToF-SIMS

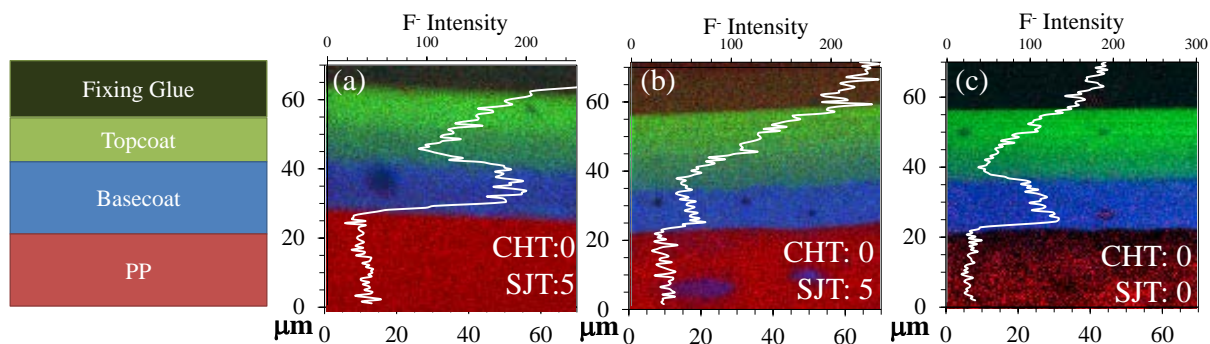


Figure 8.29: ToF-SIMS images showing the clearcoat from the  $\text{NCO}^-$  ion ( $m/z = 42$ ), the basecoat from the  $\text{C}_2\text{N}_3^-$  ion ( $m/z = 66$ ), and the TPO substrate from the  $\text{C}_{28}\text{H}_{42}\text{PO}_4^-$  ion ( $m/z = 473$ ), with an overlay of the  $\text{F}^-$  ( $m/z = 19$ ) for a primer of 5 mM TPDCOOH which was cured by UV at  $1900 \text{ mJ cm}^{-2}$  and spray applied to the following substrates: (a) R/0, (b) R/10 and (c) R/20. All intensities were normalised against the total ion count.

as a measurement technique for detecting penetration of the AP or basecoat. Future experiments could include measuring the cross-sections at a higher lateral resolution using ToF-SIMS (accredited for its high spacial resolution abilities<sup>194</sup>).

#### 8.4.4.5 Comparing Number of Primer Layers

The concentration of the primer applied was varied in two ways: by changing the solution concentration and by applying multiple primer layers (number of sprays). Cross-sections of TPO/0 substrates containing varying numbers of 5 mM TPDCOOH primer layers were prepared and measured. The results are shown in Figure 8.30. A clear difference was observed and the  $\text{F}^-$  intensity increased with the number of sprays, as expected. Although a significantly low AP intensity was detected for the substrate containing two primer layers (shown in Figure 8.30(a)), a CHT grading of 0 was achieved, suggesting it wasn't only the  $\text{F}^-$  that determined the adhesion results. It appeared that the AP had leached into the basecoat and clearcoat during the coatings application, which could have enhanced the adhesion by locking the layers together, as discussed previously.

A higher AP intensity was detected for the substrate containing three primer layers (shown in Figure 8.30(b)), and the AP had leached into the basecoat as observed before, yet the same adhesion results were obtained as the substrate with two primer layers.

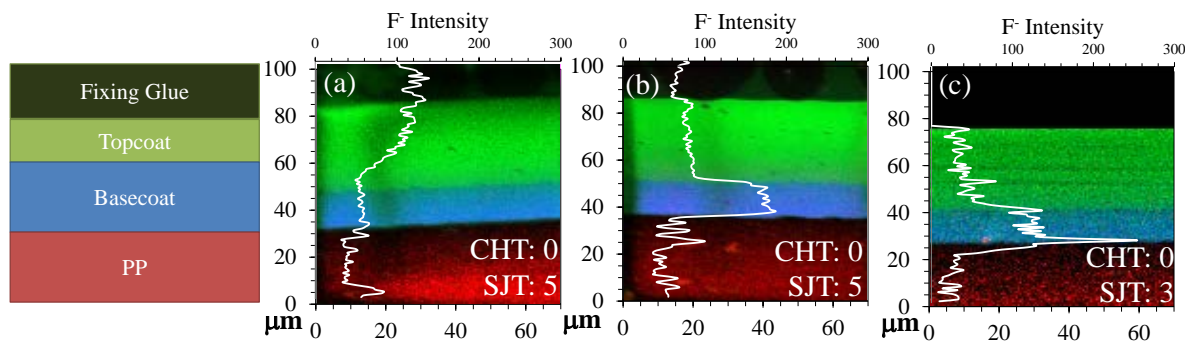


Figure 8.30: ToF-SIMS images showing the clearcoat from the  $\text{NCO}^-$  ion ( $m/z = 42$ ), the basecoat from the  $\text{C}_2\text{N}_3^-$  ion ( $m/z = 66$ ), and the TPO substrate from the  $\text{C}_{28}\text{H}_{42}\text{PO}_4^-$  ion ( $m/z = 473$ ), with an overlay of the  $\text{F}^-$  ( $m/z = 19$ ) for a primer of 5 mM TPDCOOH which was spray applied (a) 2 x, (b) 3 x, and (c) 5 x, to a TPO/0 substrate and cured by UV at  $1900 \text{ mJ cm}^{-2}$ . All intensities were normalised against the total ion count.

However, a significant improvement in adhesion was noted when five primer layers were applied (shown in Figure 8.30(c)). This substrate was distinguishable from the others by a sharp  $\text{F}^-$  intensity at the substrate/basecoat interface, similar to that previously observed for CPO (shown in Figure 5.14). This indicated a greater % grafting of the AP at the substrate surface, of which less migrated into the basecoat. Therefore, it was proposed that the greater adhesion was caused by a brush-like structure of grafted AP existing at the substrate surface which was able to extend into the basecoat and enhance adhesion, as well as a higher intensity of the AP at the substrate/basecoat interface for greater interactions.

#### 8.4.4.6 Comparing the TPDCOOH Solution Concentration

Figure 8.31 compares the two solution concentrations of TPDCOOH: 5 mM and 10 mM. Unlike the 5 primer layered substrate in Figure 8.30, no sharp  $\text{F}^-$  intensity at the interface was observed and the intensity appeared broad due to the leaching of the AP into the basecoat. No significant difference between the cross-sections from the two solutions was observed and the increase in TPDCOOH concentration did not improve the SJT result (5 for both substrates).



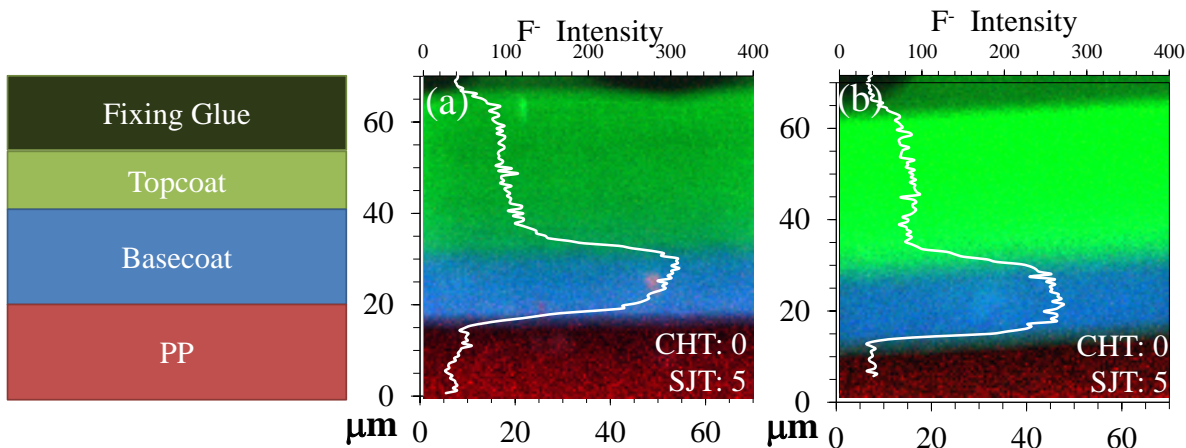


Figure 8.31: ToF-SIMS images showing the clearcoat from the  $\text{NCO}^-$  ion ( $m/z = 42$ ), the basecoat from the  $\text{C}_2\text{N}_3^-$  ion ( $m/z = 66$ ), and the TPO substrate from the  $\text{C}_{28}\text{H}_{42}\text{PO}_4^-$  ion ( $m/z = 473$ ), with an overlay of the  $\text{F}^-$  ( $m/z = 19$ ) for a primer of (a) 5 mM TPDCOOH and (b) 10 mM TPDCOOH which was spray applied and UV cured at  $1900 \text{ mJ cm}^{-2}$ . All intensities were normalised against the total ion count.

## 8.5 Industrial Applicability

### 8.5.1 Stability of TPD's

#### 8.5.1.1 Storage Stability

To assess the stability of the APs over time when stored in a refrigerator or in day light, 3 mM solutions in toluene were stored and measured with UV-Vis over a six month period. As shown in Figure 8.32, the solutions stored on the windowsill at room temperature decomposed at a significantly higher rate than the solutions stored in the dark refrigerator at  $3^\circ\text{C}$ , due to exposure to the higher temperature and the daylight. Furthermore, TPD showed a greater decomposition in the refrigerator than TPDOH and TPDCOOH, which both showed minimal decomposition over the 6 month period. The storage of APs in a refrigerator is a costly process in industry. Therefore, further storage tests at room temperature would be performed. However, TPDCOOH was the most stable at room temperature in daylight and therefore is the most suitable for industrial application in this study.

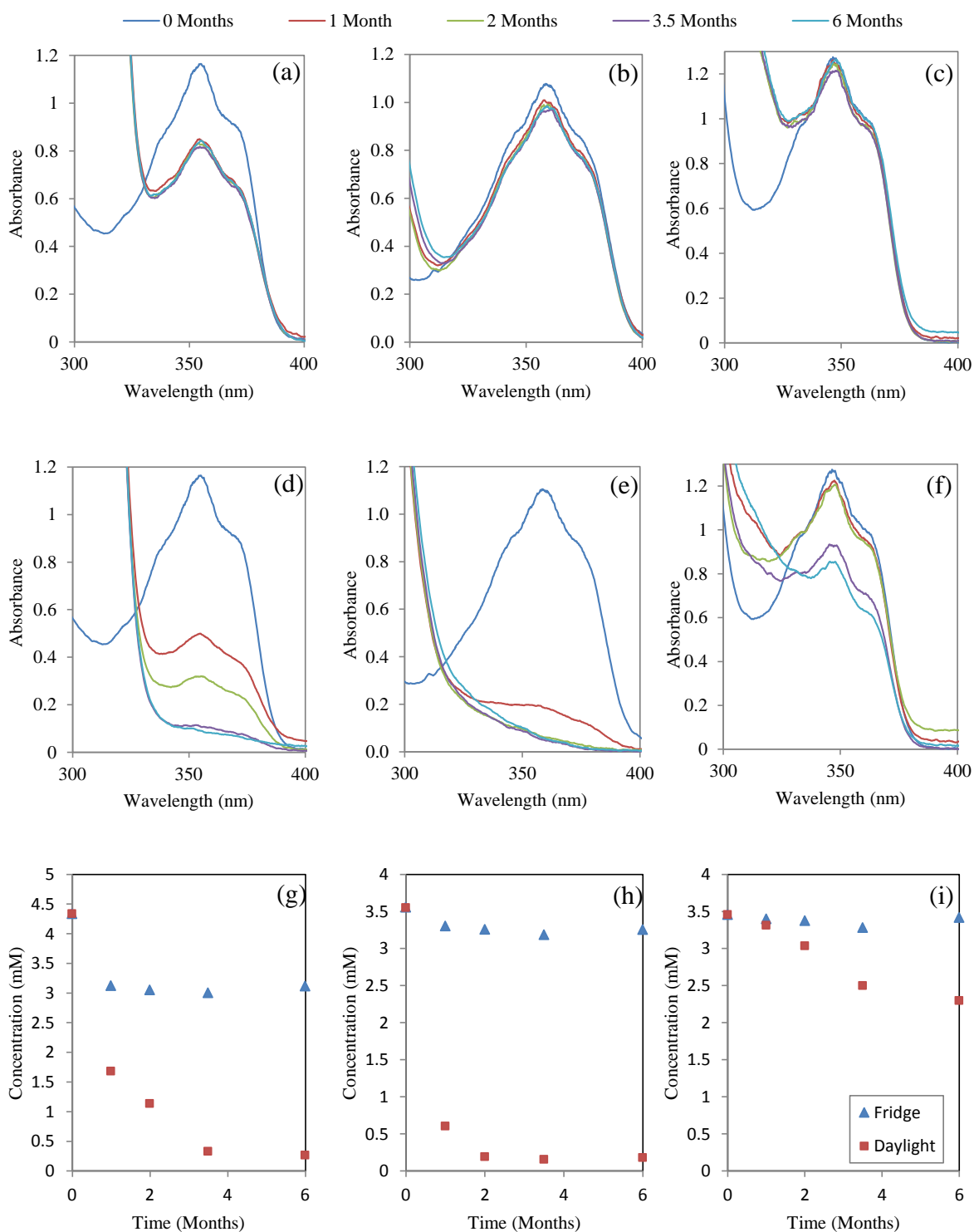


Figure 8.32: Stability study measuring UV-Vis spectra of 3 mM solutions in toluene, over a six month period, for solutions of (a) TPD, (b) TPDOH and (c) TPDCOOH stored in the refrigerator at 3 °C, and solutions of (d) TPD, (e) TPDOH and (f) TPDCOOH stored in transparent glass vials on a windowsill at room temperature.

### 8.5.1.2 Ageing Effect

Corona discharge and plasma treatments have been demonstrated to have an ageing effect, where the wettability of the functionalised surface decreases over time.<sup>49,195</sup> This has an industrial impact as the treated substrates cannot be stored for long and must be coated within a particular time period. Therefore, to test the industrial applicability of the TPDCOOH functionalised surface, an ageing test was performed where the TPDCOOH was applied with a doctor blade, cured with UV at  $1900 \text{ mJ cm}^{-2}$ , and stored at room temperature in a closed Petri dish for 7 days, before the basecoat and topcoat were applied and cured. The adhesion was tested with the CHT, and a grading of 0 was achieved (100 % adhesion). Therefore, these preliminary tests suggested the ageing of a TPDCOOH graft would not cause any potential problems.

## 8.5.2 Evaluation of Synthesis

The synthesis of TPD is described in Appendix 10.M. It was performed for an understanding of the synthesis process and its industrial applicability. TPD was successfully synthesised and characterised, producing a yield of 2.7 g ( $\sim 90\%$ ). Table 8.15 shows the amount of material required for each step (described in Appendix 10.M) to generate 2.7 g of TPD and an estimation of the cost based on the initial starting material from step 1 and the silver oxide required to generate TPD (the two materials assumed to be the most costly for the synthesis), summing to a total of £20.87. This results in a cost of £7.73 per gram of TPD. Assuming MEK was the solvent that would be used for a coating solution, which cost £90.90 per 2.5 L (Signal Aldrich), it would cost £22.05 for a 500 ml 5 mM TPD solution (based on the solution that gave the best adhesion results). The amount of substrate that could be sprayed with this volume was tested, and the cost of solution per  $\text{m}^2$  was found to be £12.25 (£0.18 per 12 x 12 cm square substrate).

Table 8.15: (a) Working backwards, the 1:1 mole ratios for each step were used to calculate the mass required of each step for synthesising the 2.7 g TPD that was produced [\*Assuming £1,870 per 1 kg (AnalR Normapur, VWR, as of January 2014), \*\*Assuming £112.00 per 100 g (ALFA (AESAR), VWR, as of January 2014)], (b) Estimating the cost on the basis of the starting material (1) and the silver oxide required to generate TPD. It is assumed in mass production that the solvent costs and other chemicals used would be minimal.

| (a) | Product           | Amount needed for 2.7 g TPD |  |
|-----|-------------------|-----------------------------|--|
|     | Ag <sub>2</sub> O | 9.55                        |  |
|     | 4                 | 3.00                        |  |
|     | 3                 | 5.47                        |  |
|     | 2                 | 3.01                        |  |

| (b) | Product           | Cost (£) per g | Amount needed for 2.7 g of TPD | Cost (£) |
|-----|-------------------|----------------|--------------------------------|----------|
|     | Ag <sub>2</sub> O | 1.87*          | 9.55                           | 17.85    |
|     | 1                 | 1.12**         | 2.70                           | 3.02     |

### 8.5.3 Colour of APs after CH Insertion

Colorimetry was used to assess the colour of the AP solutions after reflux and UV initiated reactions. The results shown in Table 8.16 were measured using a so-called Hazen-Farbzahl (DIN 53 409) method, which is commonly used in the industry to measure the degree of yellowness in coatings.

Some degree of yellowness from the unreacted solutions was initially observed before the reactions (compared to water). This increased after both reactions. The UV reaction gave a greater yellowing than the thermal reaction. Out of three APs, the TPD gave the lowest yellowing in the thermal reaction, whereas the TPDCOOH gave the lowest

Table 8.16: Calorimeter results using Hazen-Farbzahl method (calibrated against H<sub>2</sub>O = 0) for 3 mM TPD, TPDOH, and TPDCOOH in toluene after 1h reflux and 1h UV (1 mW cm<sup>-2</sup>). Scale = 1 – 1000.

| Adhesion Promoter | Before Reaction | 1h reflux, 120 °C | 1h UV, 1 mW cm <sup>-2</sup> |
|-------------------|-----------------|-------------------|------------------------------|
| TPD               | 19              | 16                | 248                          |
| TPDOH             | 24              | 63                | 169                          |
| TPDCOOH           | 17              | 21                | 117                          |

yellowing in the UV reaction. This was encouraging because TPDCOOH gave the best adhesion results with UV curing. Furthermore, the scale ranged from 0 - 1000, therefore, the degree of yellowness of the AP solutions was relatively low (water = 0).

The difference between the intensities that were measured for both of the curing methods were further indicative that different reactions had proceeded, as previously discussed in Section 8.4.3.3.

Future work could include the consideration of the colour and if it would affect the pigments in the coatings, affecting the refinish of vehicles.

#### 8.5.4 Differential Scanning Calorimetry (DSC) and Simultaneous Differential Scanning Calorimetry-Thermogravimetry (DSC-TG)

DSC was used as a rapid screening test to detect any potentially hazardous reactions and for identifying the temperatures at which these reactions occur. DSC-TG was used to look at the gas evolution rate at the peak temperatures observed in DSC.

These measurements were not only crucial for learning how to safely handle the substances, but also for learning how such substances could be used in an industrial process.

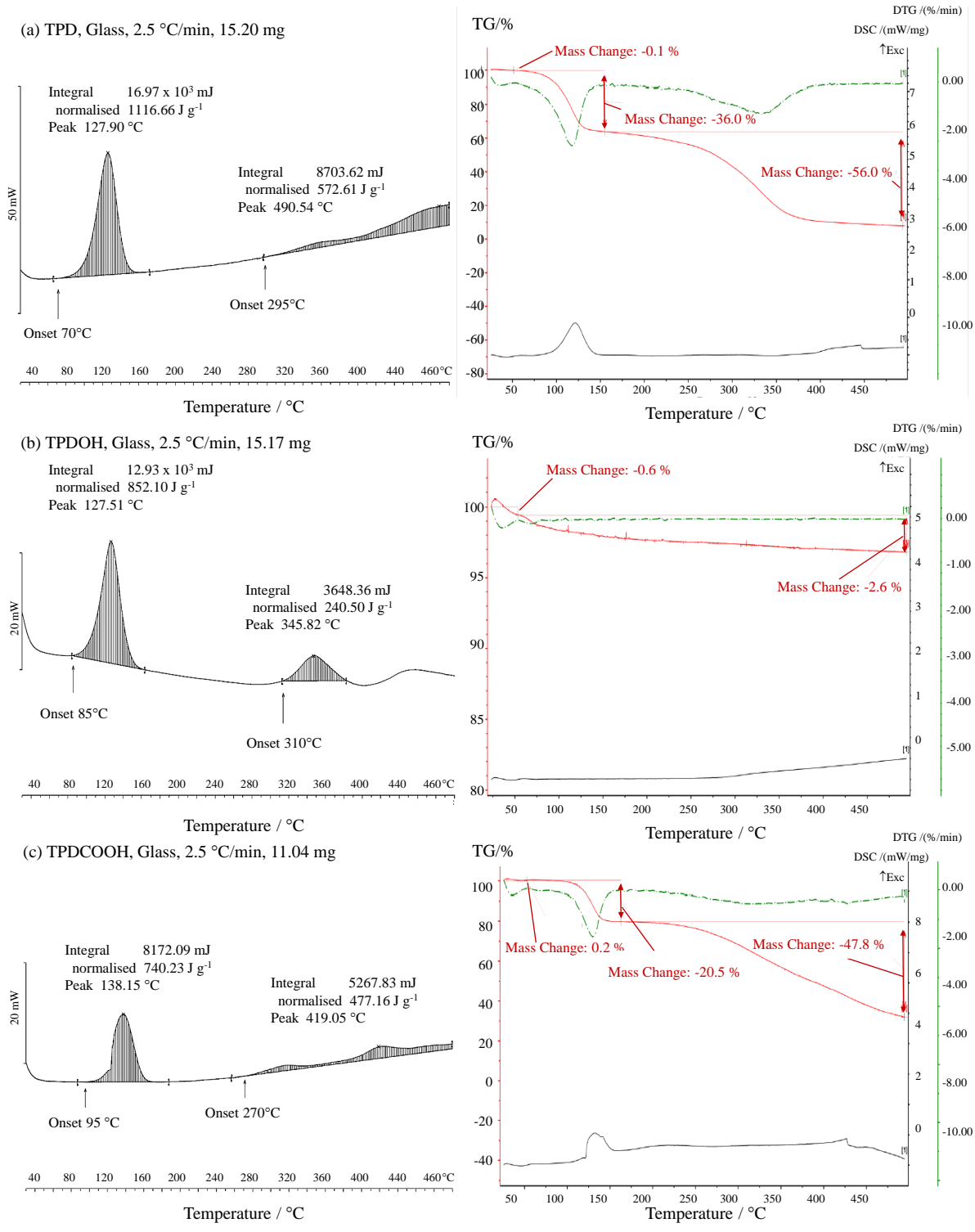


Figure 8.33: LHS: DSC results, RHS: simultaneous DSC-TGA for (a) TPD, (b) TPDOH and (c) TPDCOOH.

#### 8.5.4.1 Reaction Processes Occurring

Figure 8.33 shows the DSC plots recorded for the three APs (TPD, TPDOH and TPDCOOH). For all three plots, two exothermic reactions can be observed: one at a lower temperature and one at a higher temperature. It is likely, and in line with literature,<sup>196–198</sup> that the lower temperature exothermic peak occurring at an onset between 70 - 85 °C was due to the N<sub>2</sub> loss from the diazirine moiety during carbene formation.

Han *et al.* studied the temperature effect ( $\sim 100 - 400$  °C) of annealing carbon-based fluorinated films. The thermal release from the breaking of C-F bonds increased as the annealing temperature increased. Thus it was plausible that the second exothermic reactions observed in DSC analysis from the APs could be due to the C-F bonds breaking from the CF<sub>3</sub> functional group. Furthermore, it was unlikely that any thermal decomposition of benzene occurred at temperatures lower than 500 °C,<sup>199</sup> as oxidation of benzene derivatives can occur at temperatures as high as 1300 °C without any phenyl ring decomposition.<sup>200</sup> Therefore, it was unlikely that the phenyl ring of the APs was affected during the DSC measurement.

The data obtained from the DSC-TGA for TPD, shown in Figure 8.33(a), was found to be inconclusive, due to the evaporative loss of the sample preventing the establishment of a stable baseline at the start of the experiment. This led to discrepancies in the recorded mass losses (See Table 8.17).

However, clearer DSC-TGA plots were obtained for TPDOH and TPDCOOH, although the quantitative data was not as expected. The expected mass losses are displayed in Table 8.17. The mass change observed for the first exothermic reaction of TPDOH was significantly less than expected for the N<sub>2</sub> loss, suggesting it was not reactive. However, the mass change of the first exothermic reaction from TPDCOOH was  $\sim 2$  times larger than expected. Alternative reactions could have occurred or be a result of the loss of the material by evaporation. For TPDCOOH, the melting point (125 °C quoted by TCI chemicals materials data sheet) occurs at the same temperature of the first reaction observed in DSC, and so in its molten state it could have evaporated.

Table 8.17: Expected mass losses from the APs

| Adhesion Promoter | % Mass Loss Expected |       |                  |                  |                                |
|-------------------|----------------------|-------|------------------|------------------|--------------------------------|
|                   | -N <sub>2</sub>      | -CF   | -CF <sub>2</sub> | -CF <sub>3</sub> | -C <sub>6</sub> H <sub>5</sub> |
| TPD               | 15.05                | 16.66 | 26.87            | 37.07            | 41.37                          |
| TPDOH             | 12.96                | 14.35 | 23.14            | 31.93            | 35.62                          |
| TPDCOOH           | 12.17                | 13.47 | 21.73            | 29.98            | 33.46                          |

Interestingly, an endothermic event due to melting was not observed in the DSC and could have been masked by the first exothermic reaction.

The mass changes at the second exothermic reactions from both TPDOH and TPDCOOH were also larger than expected. When comparing with predicted values in Table 8.17, the mass losses were more closely matched the loss of the phenyl ring, however, due to the relatively low temperatures this was unlikely as previously mentioned.

#### 8.5.4.2 Safety of Substances

For all three AP's tested, two reactions were observed, all of which were exothermic and showed *self-accelerating* behaviour. For non-self-accelerating reactions, the material can be considered as safe if the difference between the onset and peak temperature is greater than 100 °C. However, higher safety measures were needed as the reaction was found to be self-accelerating (reaction proceeded at constant temperature).

According to TRAS 410 (German guideline for plant safety), an exotherm of less than 100 J g<sup>-1</sup>, which is equivalent to an adiabatic temperature rise of about 50 °C, presents no safety problems. As a general rule (from previous unpublished in-house experiments), reactions with an energy content of less than 200 J g<sup>-1</sup> may be considered as safe. However, all exothermic reactions from the AP's, shown in Figure 8.33, had an energy content of greater than 200 J g<sup>-1</sup>, as shown in Table 8.18. Therefore, careful safety considerations had to be taken.



Table 8.18: Summary of DSC results.

| Adhesion Promoter | 1 <sup>st</sup> Reaction |                                      |                                     |  |                        |
|-------------------|--------------------------|--------------------------------------|-------------------------------------|--|------------------------|
|                   | Process                  | (1a)<br>Onset<br>Temperature<br>(°C) | (2a)<br>Peak<br>Temperature<br>(°C) | Released<br>Heat<br>(J g <sup>-1</sup> ) | Self-<br>Accelerating? |
| TPD               | Exothermic               | 85                                   | 128                                 | 850                                      | Y                      |
| TPDOH             | Exothermic               | 70                                   | 128                                 | 1120                                     | Y                      |
| TPDCOOH           | Exothermic               | 95                                   | 138                                 | 740                                      | Y                      |
| Adhesion Promoter | 2 <sup>nd</sup> Reaction |                                      |                                     |  |                        |
|                   | Process                  | (1b)<br>Onset<br>Temperature<br>(°C) | (2b)<br>Peak<br>Temperature<br>(°C) | Released<br>Heat<br>(J g <sup>-1</sup> ) | Self-<br>Accelerating? |
| TPD               | Exothermic               | 310                                  | 346                                 | 240                                      | Y                      |
| TPDOH             | Exothermic               | 295                                  | 419                                 | 570                                      | Y                      |
| TPDCOOH           | Exothermic               | 270                                  | 419                                 | 480                                      | Y                      |

For handling regulations, the second reactions of TPD and TPDCOOH were less than 500 J g<sup>-1</sup> and would be considered safe. However, the first reactions of TPD and TPDCOOH, as well as both reactions observed from TPDOH, had decomposition energies above 500 J g<sup>-1</sup> and would be considered unsafe and would need further investigation.

Therefore, safety of these molecules is a key factor in determining the industrial applicability of the APs. Further work to investigate the safety of the AP's in diluted forms would be recommended and a thorough investigation into how the safety could be improved for a plausible industrial coatings process to be achievable.

### 8.5.5 Impact Sensitivity

A drop-weight was used to assess what effect the impact would have on the APs. The results are shown in Table 8.19. TPD was found to be the most dangerous AP, with explosive properties (bang and/or inflammation) observed from as little as 2 J of impact energy. TPDOH was the second most dangerous AP with an explosive effect observed from impact energies of 7.5 J and higher. Both TPD and TPDOH were concluded to be dangerous and cautious handling care was needed. TPDCOOH, the AP which showed the best adhesive results, showed no impact sensitivity at the energies tested. Therefore, in accordance with this test, further tests and formulations containing TPDCOOH would be recommended (when used as pure molecules). However, it should be noted that the impact sensitivity may be different once the AP is grafted to a surface.

Table 8.19: The impact sensitivity results from each AP.

| AP      | Impact Energy (J) | Explosive decomposition? |
|---------|-------------------|--------------------------|
| TPD     | 40                | Yes                      |
|         | 7.5               | Yes                      |
|         | 2                 | Yes                      |
| TPDOH   | 40                | Yes                      |
|         | 7.5               | Yes                      |
|         | 2                 | No                       |
| TPDCOOH | 40                | No                       |
|         | 7.5               | No                       |
|         | 2                 | No                       |

### 8.5.6 Formulation into Coatings

Further work was begun to investigate possible TPD modifications that could be used in the waterborne basecoat formulation. Trimeric isocyanates are often found in automotive coatings as a cross-linker. Therefore, an idea of reacting three equivalent TPDOH

molecules with one equivalent of trimeric isocyanate to form the structure shown in Figure 8.34 was formed (a known reaction between an isocyanate and an alcohol to form a urethane bond), with the future scope of formulating the structure into the basecoat.

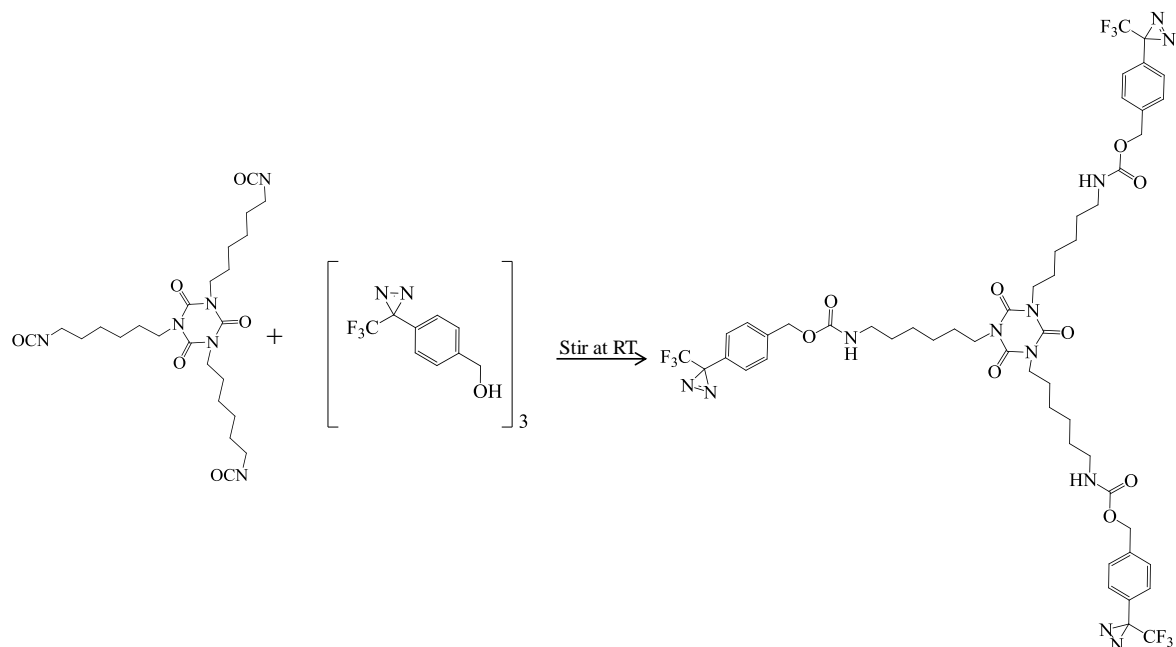


Figure 8.34: The reaction of trimeric isocyanate with three equivalents of TPDOH.

IR spectroscopy was used to monitor the reaction using characteristic bands which were monitored over time. Bands due to the urethane bond (-NH-COO-) that was formed between the OH of TPDOH and the C=O of NCO increased over time, and bands due to the NCO decreased over time as the reaction progressed, as shown in Figure 8.35. After 96 h of stirring the reaction at room temperature, the IR spectrum showed evidence of the desired structure, although the reaction had not gone to completion. The structure was further verified with  $^1\text{H}$  NMR (400 Mz,  $\text{CDCl}_3$ ):  $\delta$  7.51 (1H, d), 7.26 (1H, d), 6.38 (1H, s), 5.10 (2H, s), 3.85 (2H, t), 3.38 (2H, t), 1.63 (4H, m), 1.41 (4H, t), which contained the extra features due to the addition of TPDOH compared to the  $^1\text{H}$  NMR of the starting trimeric isocyanate:  $\delta$  3.84 (2H, t), 3.37 (3H, t), 1.64 (4H, m), 1.40 (4H, m). Mass spectrometry was not measured but it could be in future work to further verify the structure that had been formed and confirm that it wasn't two separate molecules of TPDOH and trimeric isocyanate that were being measured.

The resulting solution after 96 h was applied as a primer layer to a TPO/0 substrate using a doctor blade for a provisional adhesion test. The primer was then cured with UV at  $1900 \text{ mJ cm}^{-2}$  before the subsequent basecoat and clearcoat were applied and thermally cured. After 7 days, a CHT was performed on 5 areas of the coated substrate, which all gave a grading of 0, comparable to that of the flame and CPO standard. This was a very positive result, being the last adhesion test performed in the duration of this project, and providing a future pathway for integrating a TPD structure into the basecoat formulation. Further work would be to check reproducibility of this test, optimise the reaction rate between trimeric isocyanate and TPDOH, and to test the formulation with a spray gun application and a SJT, firstly as a primer, and secondly after formulating it into the basecoat. It would first be tested as a direct additive in the basecoat, but in the event that it would react with the basecoat before reaching the substrate interface causing bad adhesion, encapsulation mechanisms would be investigated to prevent this.

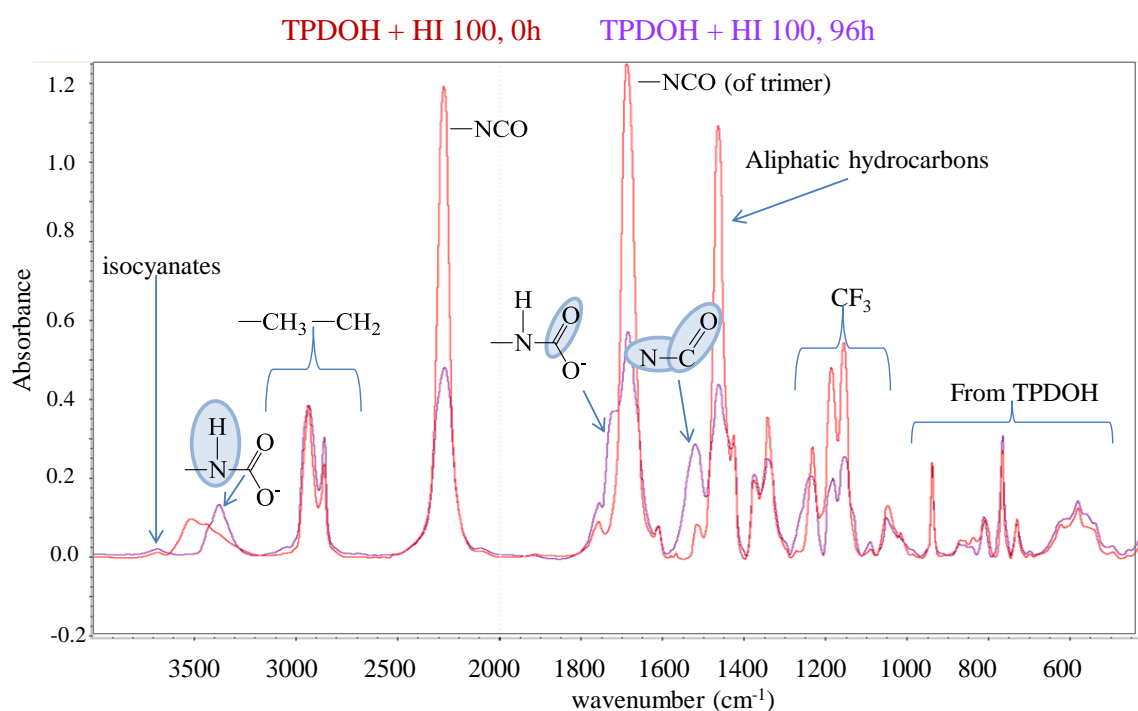


Figure 8.35: The reaction of HDI trimeric isocyanate with three equivalents of TPDOH, monitored by IR spectroscopy at 0h and after 96h of stirring at room temperature.

## 8.6 Conclusions

It was hypothesised in Chapter 7 that two curing conditions, 100 °C for 30 minutes and 1900 mJ cm<sup>-2</sup> of UV, would give the best adhesion results due to their higher grafting efficiency, compared to the other conditions tested. However, for both the doctor blade and spray gun application methods, poor adhesion was obtained for thermal curing. The best adhesion results were obtained for UV curing, particularly at higher intensities when using the doctor blade.

The hypothesis of a higher polar contribution of surface energy from a grafted surface, comparable to the waterborne basecoat, leading to improved adhesion was found to be false. It was found in some cases that ungrafted AP at the surface of a substrate caused a high polar component of the surface energy to be measured, however, adhesive failure at the substrate/AP primer interface occurred due to the lack of bonding.

It was also hypothesised in Chapter 7 that TPDCOOH would give greater adhesion results than TPD or TPDOH, due to the higher grafting efficiency observed. Although the doctor blade application could not distinguish so well between TPDCOOH and TPDOH, the spray gun application method showed that TPDCOOH gave significantly better adhesion results than TPDOH. This was not expected from the UV-Vis kinetics study which revealed TPDOH reacted on a faster time scale than TPDCOOH. However, it was thought that either the higher volatility of TPDOH caused evaporation during the grafting stage which lead to a decreased adhesion, or the reaction rate was too fast for CH insertion reactions to occur with the substrates.

A difference in optimal AP concentration was observed when using the doctor blade, which showed that a higher concentration of TPDCOOH lead to greater adhesion. However, a greater adhesion was obtained at lower UV intensities and lower AP concentrations for the spray gun compared to the doctor blade application method. It was thought that this was due to the improved coatings quality generated by the spray gun method, which lead to homogeneous layers.

The wet-on-wet application method with the basecoat, as well as the introduction of a washing step after curing of the AP primer, were also tested but were found to give poor adhesion results.

TPD gave poor adhesion results in all cases due to the lack of hydrophilic functional group available to H-bond to the waterborne basecoat.

The industrial applicability study revealed that TPDCOOH was the safest AP to handle and it decomposed the least when stored in solution, making it the ideal AP out of TPDOH and TPD. However, TPDOH was successfully modified with a trimer isocyanate to give a new AP as a possible additive (based on already used additives) to go into a basecoat formulation, which gave promising CHT results. Synthesis of TPD was successful, however it would have to be further optimised for successful industrial scale-up and to make it more cost-effective than a flame pre-treatment or CPO state of the art alternative.

# Chapter 9

## MODELLING ADHESION RESULTS

### 9.1 Overview

An overview of this chapter to guide the reader through the results is shown in Figure 9.1. The main focus of this chapter was to test hypotheses claimed in Chapter 5. A statistical study was performed to assess the effect of different variables on the adhesion results obtained from the newly grafted TPDCOOH and TPDOH surfaces after a waterborne basecoat and clearcoat had been applied and cured.

### 9.2 Introduction

A statistical study was made to investigate the effect of various parameters on the adhesion of the basecoat/clearcoat to the TPDCOOH or TPDOH-grafted substrates. Based on the hypotheses stated in Chapter 5, conclusions could be made stating the most influential parameters that affected the adhesion measured.

### 9.3 Exploratory Data Analysis

Exploratory data analysis (EDA) was used to look at relationships between numerical data and categorical data, shown in Tables 4.3 - 4.5 (described in Appendix 10.N).

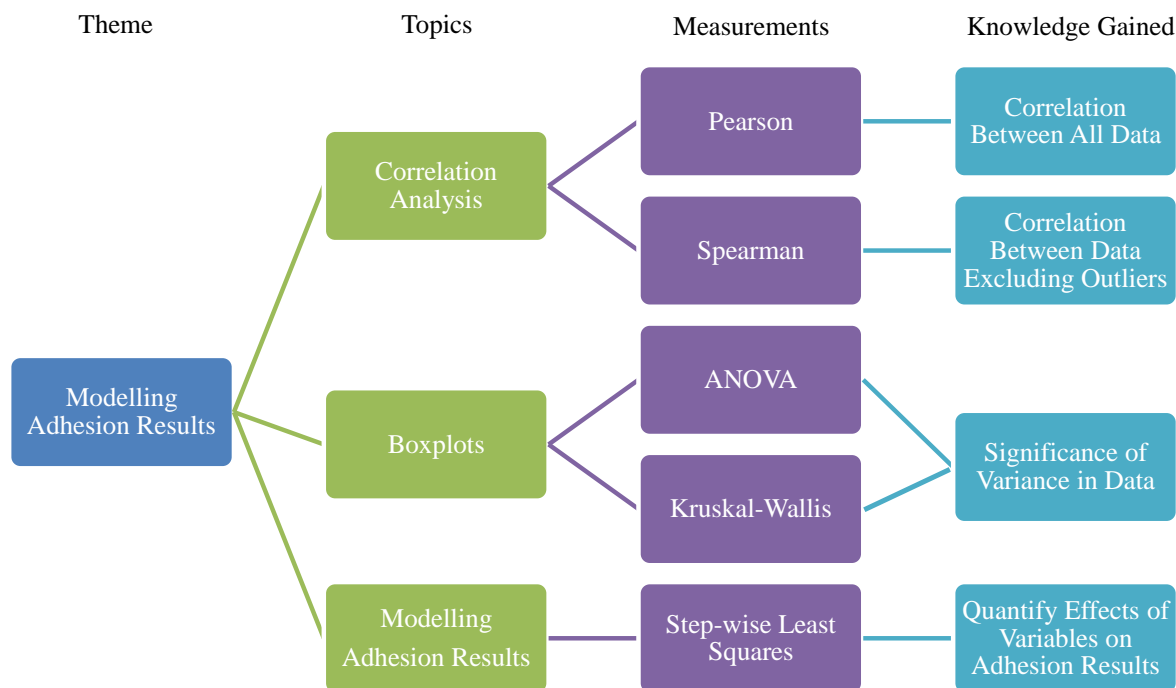


Figure 9.1: A summary of the chemical adhesion tests chapter.

Firstly, to understand the mutual dependencies of all numerical variables, Pearson and Spearman correlation analysis was used, in which no hypothesis or assumptions were made, only pure data analysis to look for the greatest contributing factors. Secondly, the correlation between the numerical variables measured and the adhesion results from both the CHT and the SJT were analysed.

ANOVA and Kruskal-Wallis tests were also performed, to explore and understand the relationship between lead responses and potential categorical factors (text based)  $x_i$  using boxplots.

### 9.3.1 Pearson and Spearman Correlation Analysis

Pearson correlation took into account all data including possible outliers and produced a line of best fit for all the data present, whereas the Spearman correlation didn't take into account outliers. No large differences between the regression coefficients from both methods were calculated.



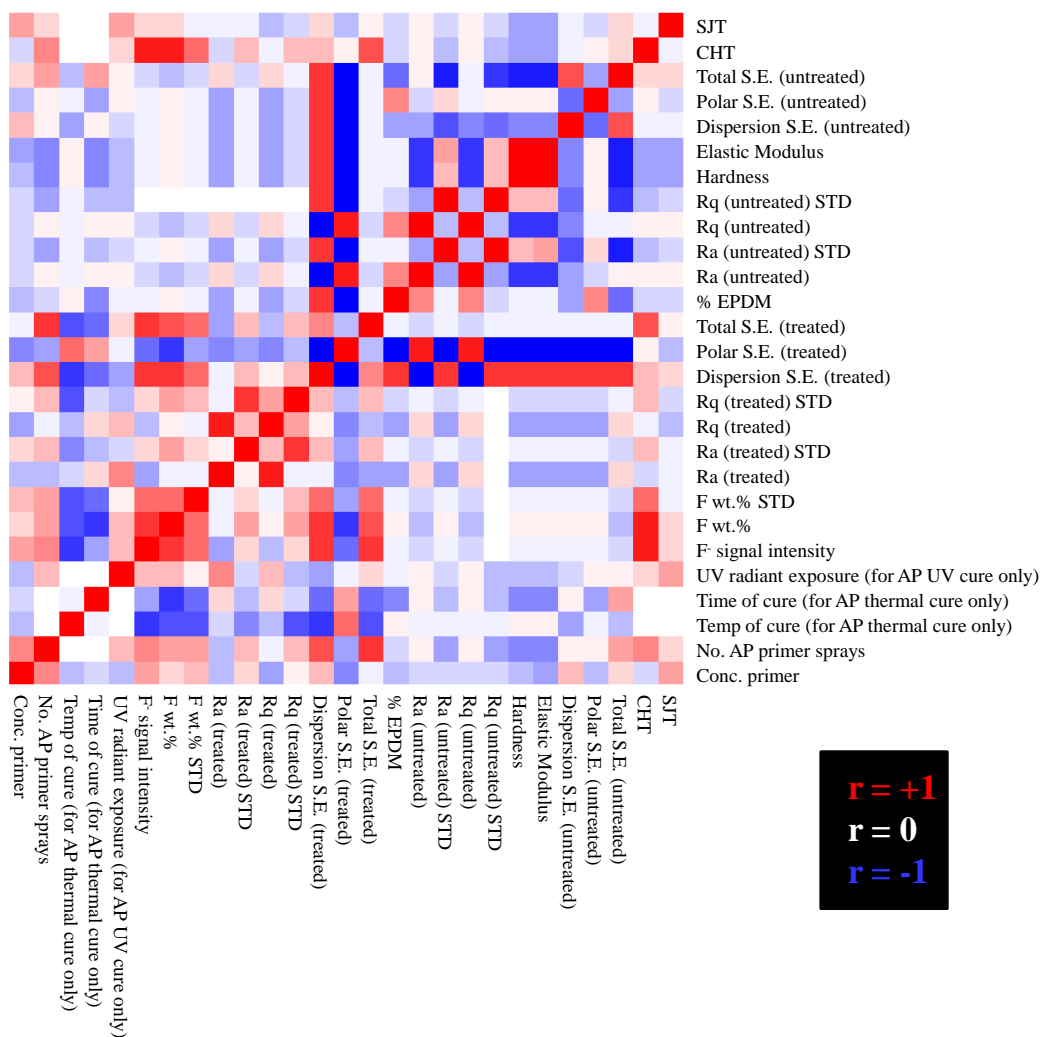


Figure 9.2: Pearson correlation heat-map,  $r = \pm 1$  is perfect correlation ;  $r = 0$  is no correlation.

The two methods correlated well with each other, therefore, the results were concluded to be reliable with no outliers (a significant difference would have indicated a large amount of outliers and/or problems with the data analysis).

Heat graph representations of the Pearson correlation coefficients ( $r$ ) (for all numerical variables that were tested) can be found in Figure 9.2 and the Spearman correlation coefficients ( $r$ ) can be found in Figure 9.3, where  $r = \pm 1$  was the best correlation (red), and  $r = 0$  indicated no correlation (blue).

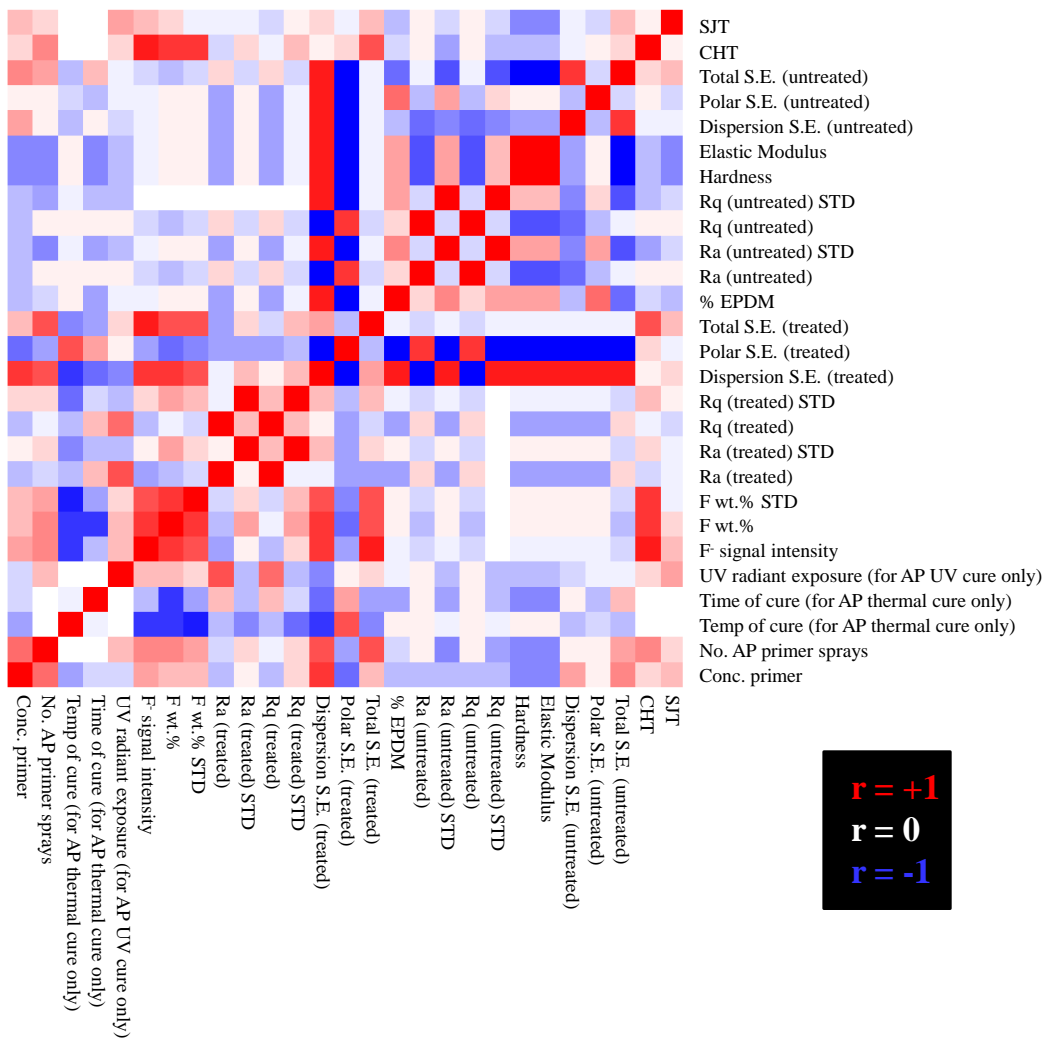


Figure 9.3: Spearman correlation heat-map,  $r = \pm 1$  is perfect correlation ;  $r = 0$  is no correlation.

For some of the variables, the standard deviation (STD) was also included in the analysis. It was hypothesised that a correlation between the adhesion results and the variation of a variable across the substrate would indicate significance. For example, the substrate roughness was measured on an area of  $120 \times 90 \mu\text{m}$ , 10 times on different areas of the surface. The standard deviation of the 10 measurements would therefore indicate if there was greater deviance of the roughness over the whole substrate, which could have influenced the adhesion (where an AP could penetrate into some areas of the substrate at a greater rate than other areas).

The list of the top ten variables with the greatest Pearson and Spearman correlation coefficient values, indicating the greatest influence on the CHT and SJT results, can be found in Appendix 10.L. The highest correlation coefficients from the Spearman and Pearson analysis for correlation between the variables and the CHT results are shown in the radar graph in Figure 9.4.

It was found that the CHT results correlated the best with the F wt.% from the XPS data (Spearman  $r = 0.849$ , Pearson  $r = 0.875$ ) and the  $F^-$  intensity from the ToF-SIMS data (Spearman  $r = 0.810$ , Pearson  $r = 0.875$ ). Both these measurements represent the amount of TPD/TPDOH/TPDCOOH grafted onto the substrate surface. Therefore, transitivity occurred, meaning the F wt.% and the  $F^-$  intensity correlated with each other. This can be seen in the area of red squares where these variables crossover in Figure 9.2 and Figure 9.3, representing this correlation.

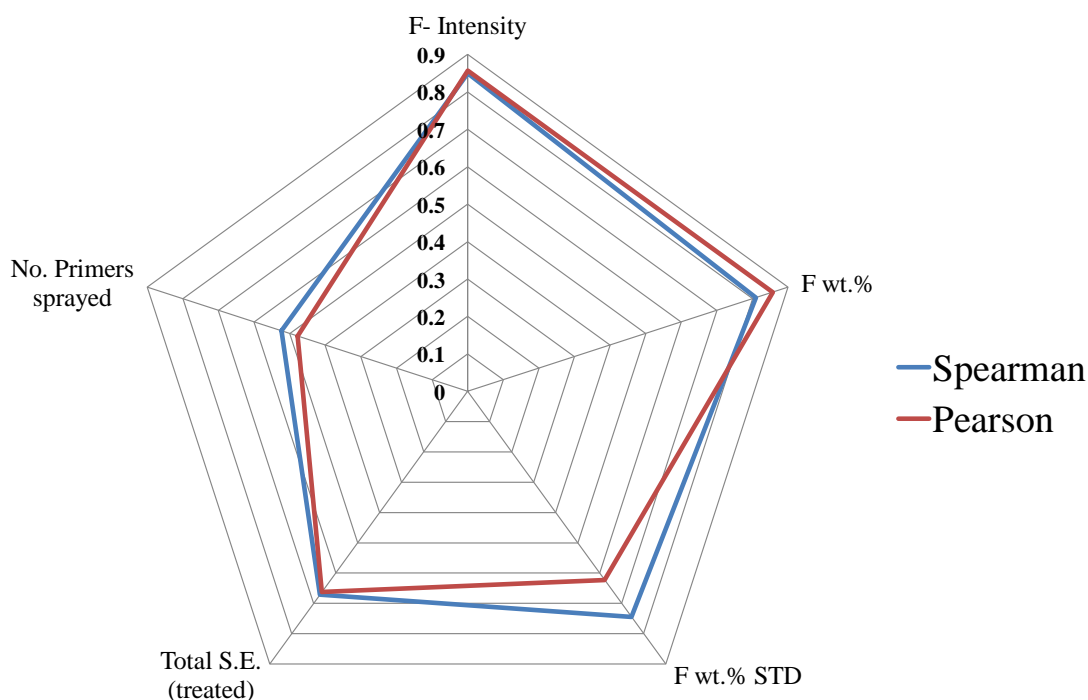


Figure 9.4: Radar graph showing greatest Spearman and Pearson correlation coefficients for the CHT, where  $r = \pm 1$  is perfect correlation ;  $r = 0$  is no correlation.

Another variable with a correlation coefficient greater than 0.5 included the STD of the F wt.%. The greater CHT results were achieved for homogeneously covered surfaces (represented by a lower STD) whereas the lower CHT results were obtained from inhomogeneous surfaces (represented a higher STD) due to the areas of non-interaction (where no was AP present) which resulted in delamination. The total surface energy after the AP application (greater adhesion observed for a greater surface energy) and number of AP primer spray applications (the thicker the AP primers had greater CHT results) were also found to significantly correlate with the CHT results.

Another variable in the top 10 correlation coefficients for the CHT was called the observation number. As part of the analysis, this number was included automatically. It was simply a number assigned in ascending order (starting at one) to each of the variables in the given data for analysis. Therefore, it represented a type of time scale which usually would allow for identification of experimental errors over time (for example, if the efficiency of a spectrometer depreciates with time, it would be identified from a correlation between the observation number and the spectrometer output). However, due to a slicing of data, the observation number was not useful in this study because the experimental variables were decreased with time as the conditions found to give poor adhesion were eliminated. Therefore, an increase of the CHT results was automatically correlated to the observation number. Future work could be to measure the variables for all of the data, to make the observation number a useful parameter and allow for identification of such errors on a time scale.

The top correlation coefficients from the Spearman and Pearson analysis looking at the SJT results are shown in the radar graph in Figure 9.5. The correlation coefficients from both the Spearman and Pearson analysis were less than 0.5, lower than that of the analysis of the CHT results. This was not unexpected for the SJT results, which were known for difficult reproducibility (the reproducibility tests in Chapter 8 gave values within  $\pm 2$  gradings), particularly at high pressures.<sup>87</sup> However, there was some evidence of correlation. The UV radiant exposure gave the best correlation (Spearman  $r = 0.395$ ,

Pearson  $r = 0.398$ ) between the SJT results and the variables measured. In general, a larger radiant exposure gave better adhesion results due to a greater grafting efficiency of the AP to the surface which resulted in greater adhesion to the waterborne basecoat.

The AP concentration and  $F^-$  intensity (from ToF-SIMS data) were found to give correlation coefficients of  $\sim 0.3$ . The higher AP concentration lead to a greater  $F^-$  intensity, which then lead to greater adhesion due to the higher interactions between the AP grafted to the surface and the waterborne basecoat. The Young's modulus and substrate hardness gave negative correlation coefficients of  $\sim -0.3$ , because a lower Young's modulus and a lower substrate hardness gave greater adhesion results. Therefore, the hypothesis stated in Chapter 5, claiming a substrate of lower hardness and Young's modulus values was predicted to improve adhesion, was correct. This was also discussed in Appendix 10.F.3, where it was suggested an AP could penetrate into substrates of lower hardness and Young's modulus values (corresponding to a lower crystallinity) at a faster rate than a harder and higher modulus substrate. Therefore, the AP could have improved adhesion via a physical entanglement mechanism with the substrate polymers, or the penetration of the AP into the surface could have increased the contact area between the AP and the waterborne basecoat, improving the adhesion by a greater number of chemical bonds to the surface via covalent bonding, thus increasing the reactions or interactions with the basecoat.

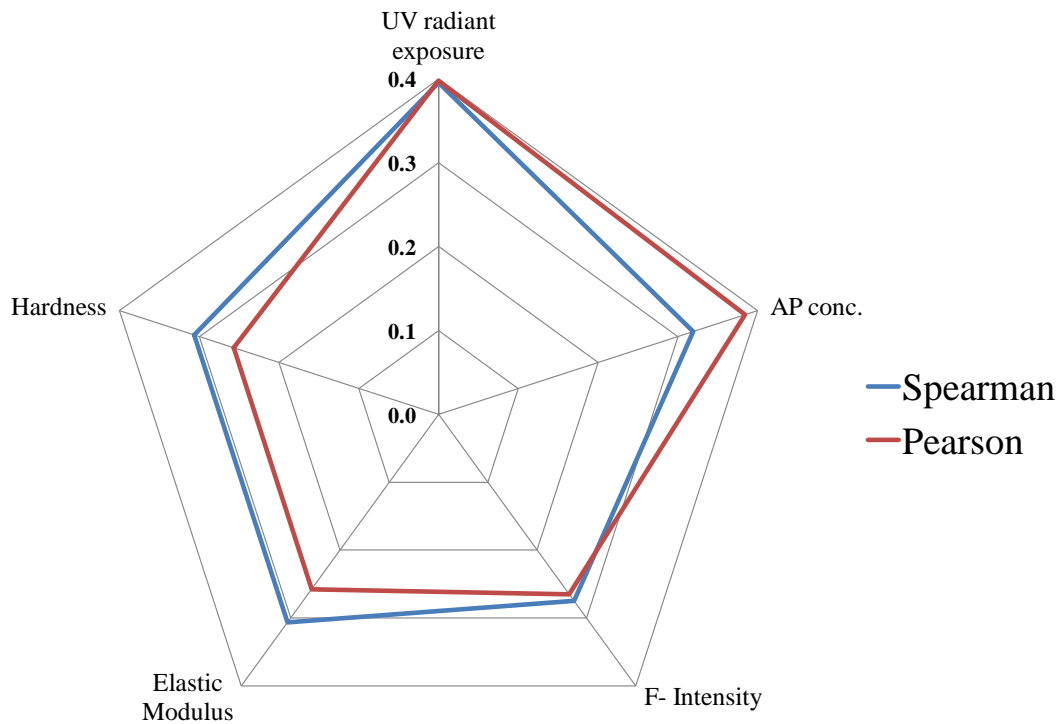


Figure 9.5: Radar graph showing greatest Spearman and Pearson correlation coefficients for the SJT, where  $r = \pm 1$  is perfect correlation ;  $r = 0$  is no correlation. Note: Elastic Modulus and Hardness are negative correlation coefficients.

### 9.3.2 Boxplots: Understanding and Exploring the Relationship between Lead Responses and Potential Categorical Factors $X_i$

As described in Section 4.35.2, two analysis methods were used to perform a statistical analysis on categorical data (text): ANOVA where the ANOVA.F parameter was measured and the Kruskal-Wallis test where the kruskal.p parameter was measured, to assess the effect of  $x_i$  (categorical factors) on  $y_j$  (lead responses, CHT and SJT results) and determine which levels varied the most significantly between the factors (the levels and factors are described in Figure 4.14).

Table 9.1: ANOVA.F and p.kruskal values sorted list in order of decreasing discrimination (=relevance of  $x_i$ )

| # | $y_j$ | $x_i$                        | ANOVA.F | p.kruskal |
|---|-------|------------------------------|---------|-----------|
| 1 | CHT   | Curing Method                | 100.08  | 0.00      |
| 2 | CHT   | AP Type                      | 83.74   | 0.00      |
| 3 | CHT   | Industrial or Research<br>PP | 21.31   | 0.00      |
| 4 | SJT   | Industrial or Research<br>PP | 7.01    | 0.00      |
| 5 | CHT   | Application Method           | 3.92    | 0.07      |
| 6 | CHT   | Washing Step (Y/N)           | 0.12    | 0.89      |

Larger ANOVA.F parameters or smaller kruskal.p parameters indicated a larger effect / discriminatory power. For some of the variables, the F and p values could not be estimated due to missing data or a low number of levels (no distinguishable variation). This was particularly apparent for the SJT results, which were sparsely populated (due to slicing of the data over time, as previously discussed). Future work could be to increase the data set measured for the different variables that were missing, to further investigate their effect on the SJT results.

A summary of the results is shown in Table 9.1, sorted in order of decreasing discrimination (relevance of  $x_i$ ). The corresponding box plots showing the lower quartile, median, and upper quartile range (outliers are marked as individual points) are shown in Figure 9.6. The bigger the difference between the spread of the box plots from each level within a factor, the greater the influence the factor had on the adhesion test result (CHT or SJT).

It should be noted that the washing step boxplot is not shown in Figure 9.6 due to the lack of variance between the factors and the lack of data (it was an individual experiment with a small data set used only to investigate the adhesive effect of washing any ungrafted AP away from the substrate before applying the waterborne basecoat).

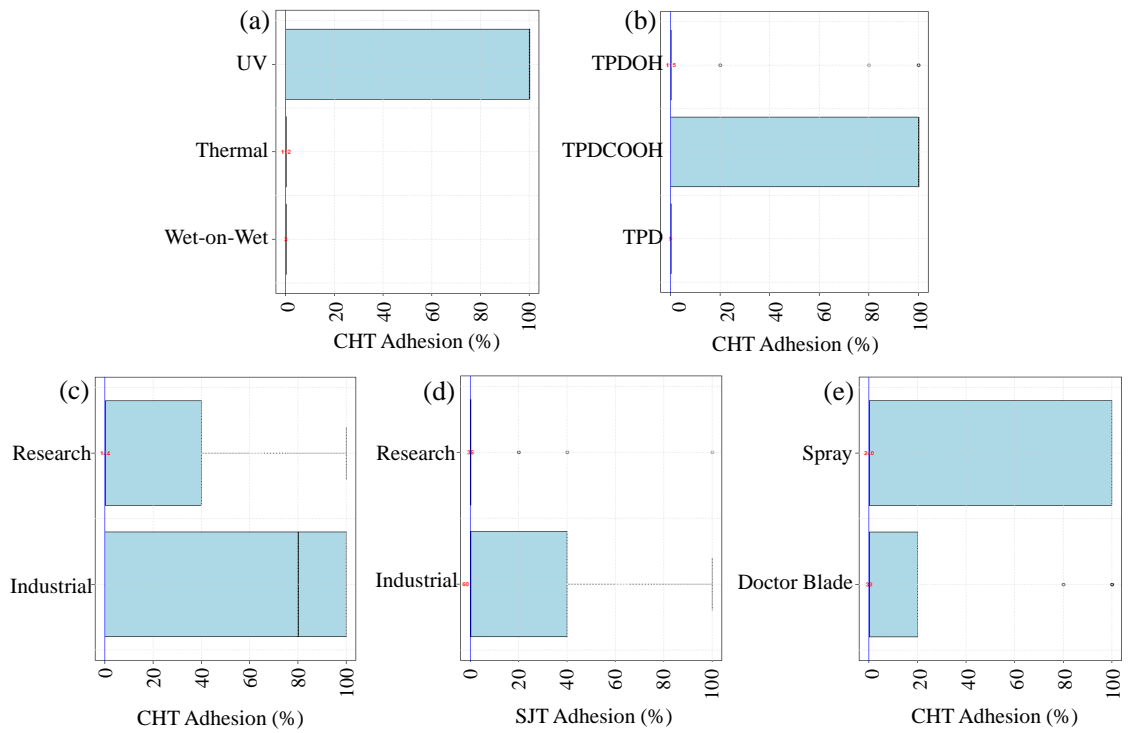


Figure 9.6: Boxplots of (a) CHT vs Cure Method [ANOVA.F = 100.0835, p.kruskal = 0], (b) CHT vs AP Type [ANOVA.F = 83.7393, p.kruskal = 0], (c) CHT vs Substrate Type [ANOVA.F = 21.3075, p.kruskal = 0], (d) SJT vs Substrate Type [ANOVA.F = 7.0076, p.kruskal = 0.003] and (e) CHT vs AP Application Method [ANOVA.F = 3.9211, p.kruskal = 0.889].

The AP type and curing method were found to have the greatest influence on the CHT results out of the five factors shown in Figure 9.6. In order of decreasing CHT results (decreasing adhesion), where  $n$  = sample size:

- AP Type: TPDCOOH (Sample size,  $n=155$ )  $\gg$  TPDOH( $n=115$ )  $\approx$  TPD( $n=9$ )
- Curing Method: UV( $n=164$ )  $\gg$  Thermal( $n=112$ )  $\approx$  Wet-on-Wet( $n=3$ )

Although slicing of data resulted in samples of different sizes for each level, the variance was observable. The difference between the curing methods was visually evident during the adhesion testing, when it was observed that thermal curing and applying wet-on-wet were unsuccessful compared to UV curing, which the statistical analysis further confirmed. The analysis also confirmed that the TPDCOOH AP produced better adhesion results than TPDOH and TPD (although poor adhesion was expected for TPD due to



the lack of polar sites for hydrogen bonding to the waterborne basecoat). The difference between TPDOH and TPDCOOH could be explained by the difference in the number of sites available for hydrogen bonding to the waterborne basecoat, as shown in Figure 9.7. TPDOH has just one donor site (H) and one acceptor site (O) whereas TPDCOOH has one donor site (H) and three acceptor sites (C=O x2 and O). Therefore, TPDCOOH could potentially have double the interaction of TPDOH with the waterborne basecoat, thus better adhesion.

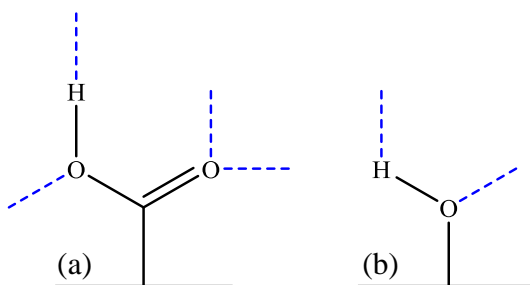


Figure 9.7: Schematic diagram highlighting the donor and acceptor sites for H-bonding for (a) carboxylic acids and (b) alcohols.

## 9.4 Stepwise Ordinary Least Squares (stepOLS)

StepOLS was used to estimate and quantify the effects of the potential predictors  $x_i$  on the major responses: the CHT and SJT results, based on  $y_j = g_j(x_i)$ . All x variables with missing data were omitted and the software automatically removed parameters that had no correlation. The x variables were tested for their individual influence on CHT and SJT results, as well as the combined influence with other x variables to test their interaction. All data was standardised by subtracting the mean value and dividing by the standard deviation.

### 9.4.1 CHT

The curing method, the AP type and the combined interaction of both together, were found to be the sole predictors for the CHT result, as shown in Figure 9.8 where the predicted and observed response show a high correlation ( $r^2 = 0.981$ ). As shown in Figure 9.9, combining TPDCOOH with UV curing gave the best CHT results, explaining 98 % variance of the data. The extreme outlier present at 0 % adhesion was due to the low UV radiant exposure tested ( $120 \text{ mJ cm}^{-2}$ ) in Section 8.4.2, which did not have a high enough intensity to produce sufficient grafting of TPDCOOH, thus poor adhesion was observed.

As a result of the combination of TPDCOOH and UV being unique at maximising the CHT results (in accordance to stepOLS analysis), they were then used for stepOLS analysis of the SJT results (other AP types and curing methods were not tested) to test the effect of the other  $x_i$  variables (potential predictors).

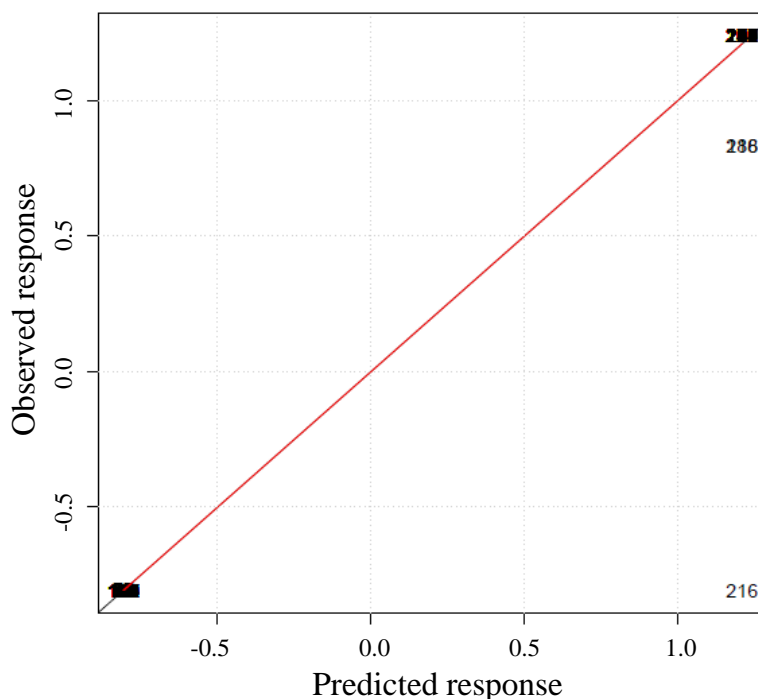


Figure 9.8: StepOLS results on standardised data for  $\text{CHT} = f(x_i)$ .  $R^2 = 0.981$ .

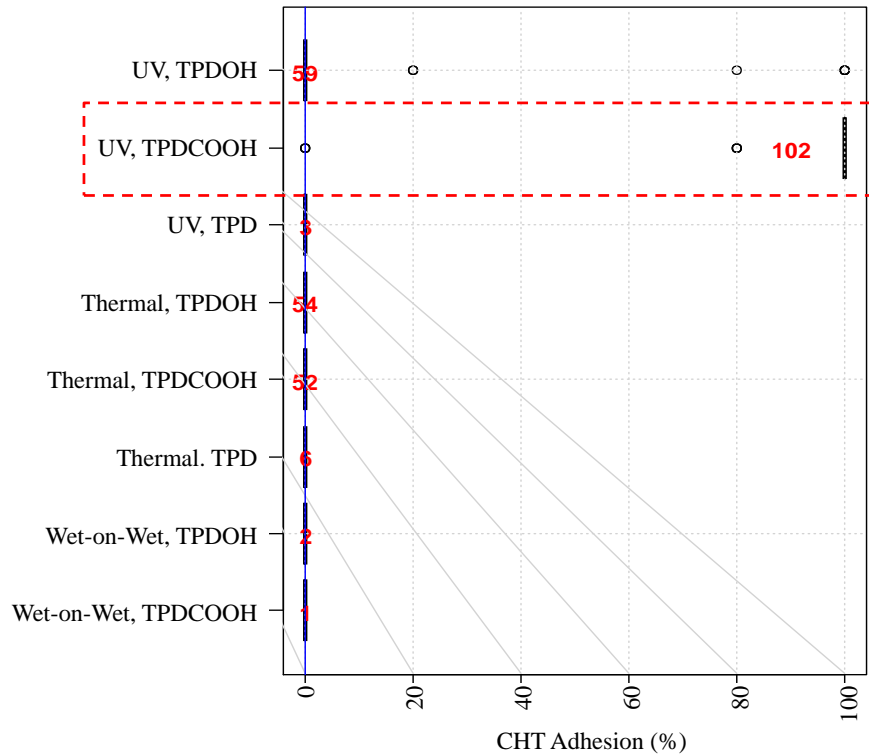


Figure 9.9: Boxplot of CHT vs the combined interaction between the cure method and the AP type [ANOVA.F = 303.7315, p.kruskal = 0]. The combination of TPDCOOH and UV was unique at maximising the CHT result in accordance with stepOLS analysis. The red numbers display the number of results for each variable.

## 9.4.2 SJT

The x variables that contained only one level or had missing data were omitted (due to the lack of variance). The modelling of the SJT results was not as successful as the CHT results, explaining only 34 % variance in the data. It was thought that it was due to the lack of data and/or the unreliable nature of the SJT (difficult reproducibility). Another plausible reason for the difference could be due to the adhesion mechanism. The CHT measures adhesive forces whereas the SJT measures energy dissipation. The AP concentration, the number of AP layers applied, the UV radiant exposure, as well as the interaction between the number of AP layers applied and the UV radiant exposure, were found to show some significance and a non-linear trend, as shown in Figure 9.10.

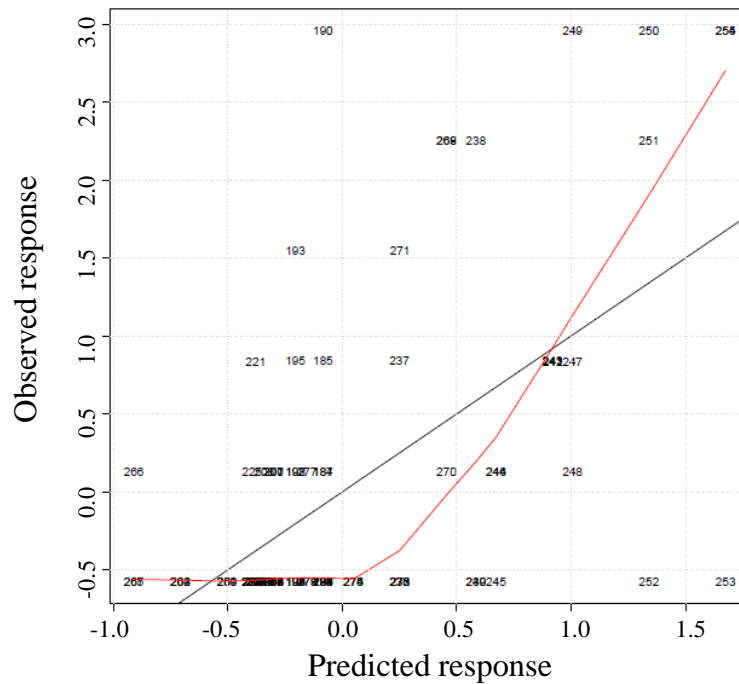


Figure 9.10: stepOLS results on standardised data for  $SJT=f(x_i)$ .  $R^2 = 0.34$  (non-linear).

The interaction can be explained in terms of UV intensity, where a higher UV intensity (radiant exposure) would be able to penetrate a thicker AP layer and induce more reactions of the AP to the substrate surface, hence improving adhesion. Whereas a lower intensity would not be able to penetrate an AP layer of the same thickness at the same rate, thus the rate of reaction would be slower (poorer adhesion). Therefore, it was suggested that the ability of the UV to penetrate the AP layer was an influencing factor determining the adhesion results obtained.

Figure 9.11 shows a trellis plot that shows the interaction between the SJT results, the number of AP layers applied, the UV radiant exposure as well as the AP concentration. A high SJT was achieved by applying a high number of AP primer sprays and using a high UV radiant exposure. The third plot (RHS) shows that the maximum SJT was achieved at the highest concentration of the AP tested.

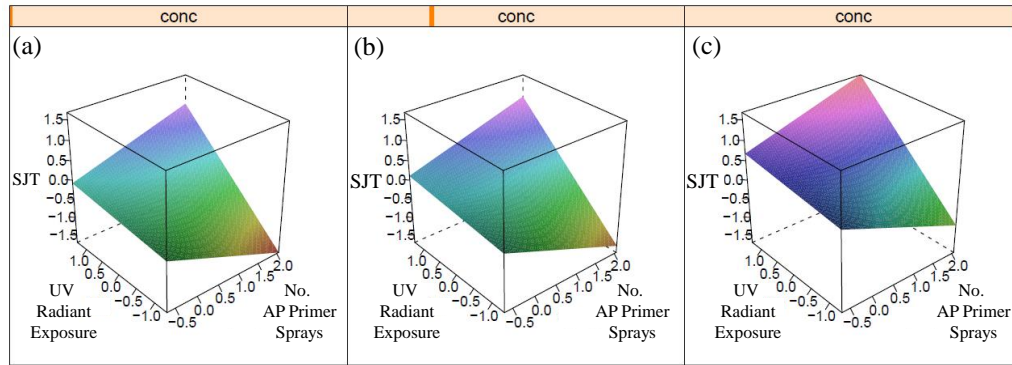


Figure 9.11: A trellis plot showing standardised correlation between the SJT results and the UV radiant exposure, number of primer sprays for varying concentration: (a) Low concentration, (b) middle concentration and (c) high concentration.

## 9.5 Conclusions

Statistical modelling was successfully implemented to learn the main contributing factors that affected the adhesion results obtained.

Several hypotheses were made in Chapter 5 to predict the adhesion properties of the studied substrates based on their characterisation. The statistical modelling enabled the following conclusions of each stated hypothesis:

- Research substrates with EPDM present at the surface: the AP is able to penetrate into the EPDM domains causing polymer chain entanglement (mechanical adhesion mechanism)
- ✘ The industrial substrates were found to give greater adhesion results than the research substrates, therefore, the EPDM at the surface of a substrate did not seem to have a significant effect on the adhesion.
- TPO/20 substrate during thermal curing: EPDM migrates to the substrate surface, allowing the AP to penetrate into the EPDM domains, causing polymer chain entanglement (mechanical adhesion mechanism)
- ✘ The % EPDM did not come up as a main factor affecting the adhesion results, and furthermore the thermal curing did not produce any positive adhesion results. Therefore, it was assumed that EPDM migration did not significantly influence the

adhesion.

- Substrates containing EPDM or additives: creates a higher surface roughness which allows for a higher contact area between the substrate and AP / basecoat, or substrates have a lower hardness and Young's modulus to allow an AP to penetrate into the substrate surface causing a polymer chain entanglement (mechanical adhesion mechanism)
  - ✓ The surface roughness was found not be a significant contributing factor. However, the softness and low modulus caused by the EPDM and other additives in the substrates were found to play a significant role in the improvement of adhesion.
- Substrates with  $\text{CaCO}_3$  and talc present at the surface: chemical reactions or interactions with the AP or basecoat (chemical adhesion mechanism)
  - ✗ A distinct difference between the industrial substrates was not made when exploring the correlation of properties with the adhesion results, therefore, it was assumed no chemical reactions occurred with the additives.
- Substrates without the Irgafos 168 additive present at the surface: its hydrophobic and bulky nature causes steric hindrances with the AP or basecoat
  - ✗ The irgafos 168 additive did not appear to have an effect since it was observed that adhesion was improved on the industrial substrates compared to the research substrates.
- TPO substrates: they have a lower hardness and Young's modulus, which enables the AP, solvent or basecoat to penetrate into substrate surface allowing a higher contact area and greater interactions, or the anchoring of an AP into the substrate causing polymer chain entanglement (mechanical adhesion mechanism)
  - ✓ Industrial TPO substrates were found to have better adhesion results than the research substrates. It was assumed that the significantly softer and low modulus properties of these substrates resulted in the penetration and perhaps anchoring of the AP, which generated greater interactions with the basecoat.

- Substrates cleaned with an abrasive method: creates a higher surface roughness allowing for a higher contact area between the substrate and the AP or basecoat
- ✘ All washings steps that were implemented caused delamination of the coatings. It was thought to be due to contamination of the solvent, which would hinder any effects of an increase in surface roughness.

Based on the hypotheses above, the physical properties of the substrates appeared to have the greatest influence on the adhesion results obtained, such as substrate roughness, hardness and modulus. One can draw the conclusion that the EPDM content of the substrate only appeared to influence the adhesion by increasing the surface roughness along with other additives present. Therefore, a molecular chain entanglement theory, suggested by Ryntz *et al*<sup>28,45,64,67,69,74</sup> for the adhesion of a CPO, did not seem to be a main contributing factor in this study.

The modelling of the CHT results was more successful than the SJT results. The AP type and curing method were found to be the sole predictors for the CHT results, explaining 98 % of the data. The concentration of the AP, the number of AP primers applied and the UV radiant exposure were found to be the greatest influence on the SJT results, explaining only 34 % of the data. Other experimental measurements which were found to have an effect the adhesion results were:

- F<sup>-</sup> intensity (from ToF-SIMS data)
- F wt.% (from XPS data)
- F wt.% STD (from XPS data)
- Total surface energy (from OW theory)
- Substrate Young's modulus (from nano-indentation data)
- Substrate hardness (from nano-indentation data)

## **Part IV**

# **Final Conclusions and Future Work**



This project achieved its goal of identifying novel candidate APs for improving the adhesion of a waterborne basecoat to an untreated PP-based substrate. A summary of the results chapters can be found in Figure 9.12. The first stage of the overall objective was achieved, as shown by stages 1 - 3 in Figure 9.13.

In a previous study by Hintze-Brüning *et al.*,<sup>107</sup> it had been found that nitrogen analogues to carbenes, known as nitrenes, formed from linear azido functional groups were unsuccessful at promoting adhesion via CH-insertion reactions. However, the APs identified in this study were diazirine-based carbene precursors (three-membered ring functional groups) which were able to C-H insert into the substrate surface under the correct curing conditions. Therefore, this study proved that adhesion promotion was possible via C-H insertion.

The main contributing factors found to influence the adhesion results obtained, were the AP type, the curing method used, the UV intensity (when UV curing was used) and the concentration of the AP, both in terms of the solution concentration or the number of primer layers applied.

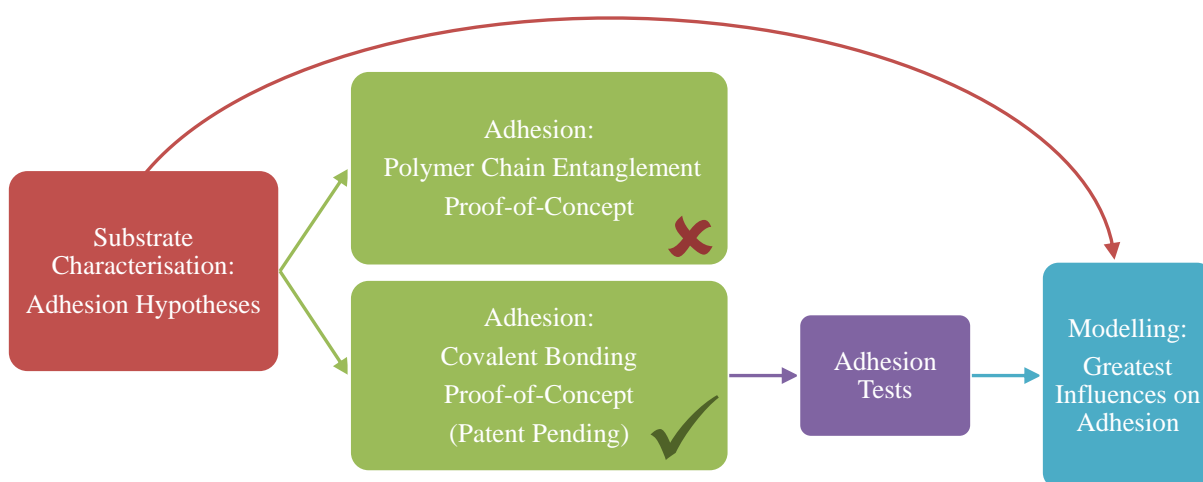


Figure 9.12: A summary of the results chapters, highlighting the flow of the work and the interactions between the chapters.

The best adhesion results were obtained with UV curing, which caused diazirine carbene precursors to covalently bond to the substrate surface, and adhere to the waterborne basecoat through H-bonding between hydrophilic functional groups on the AP as well as the basecoat. The best AP was found to be TPDCOOH, which also demonstrated the best industrial applicability properties.

To better implement TPDCOOH into the industrial coating production line, future work could be to test alternative basecoats and topcoats which are cured via UV rather than thermally. This would then reduce the number of curing steps in the production line, as shown in Figure 1.4.

Alternatively, future work could include optimising TPDCOOH, or other candidate APs, for thermal curing. The AP could then be implemented into the production step currently studied without the need for the extra UV curing step. This work would include optimising the molecular structure of the AP, so that it is reactive enough at 80 °C, but stable enough to store and use safely. The possibility of higher curing temperatures to increase the reactivity of the AP could also be explored, however, the range to which one could increase the temperature would be limited due to the melting point of the substrates, which would deform at too high temperatures.

Other future work includes the formulation of the AP into the basecoat, as shown by step 4 of the overall objective in Figure 9.13. During the last months of this project, work began to investigate the ability of creating TPD-based structures using additives already present in the coatings formulation. The trimeric molecule developed in Section 8.5.6 showed a very promising future, producing a CHT results of 0 (100 % adhesion). Future work would be to perform a SJT (the next level of more rigorous adhesion testing) to see if the coating could withstand the harsher conditions, and to apply the primer and coatings using a spray gun application method rather than a doctor blade, for improved control and homogeneity of the coatings.

The formulation of the TPD-based APs into the basecoat without any protective layering, could result in unwanted reactions with the pigments and other additives in the

basecoat, rather than the substrate surface. Therefore, encapsulation of the APs would also be a suggested future exploration. The idea would be to have the AP encapsulated, and the curing step would trigger the release of the AP. Therefore, a time scale would have to be accounted for to allow the release and the reaction of the AP, and the movement of the encapsulated AP would have to be accounted for to ensure that the AP is released at the correct coating/substrate interface (a challenge). For example, a denser encapsulated AP (compared to the rest of the coating) could migrate to the substrate interface by gravitational forces, which could be encouraged by higher temperatures which would decrease the viscosity of the coating and increase the mobility of the AP. Then once a particular temperature was reached, the thermal release of the AP could be triggered. Previous work by Overbeek,<sup>124</sup> discussed in Section 2.6.2, showed that tailoring polymeric systems such as using block copolymers, can result in the correct properties and kinetics to release an AP for successful adhesion. Encapsulation of the TPD based APs could be developed based on a similar block copolymer system.

An alternative idea is to formulate the basecoat with the AP so that it would self-stratify without the need for encapsulation. This is when two incompatible polymers are mixed, and upon an external trigger, they phase separate. In this case, the development of a coating in which the AP would separate to the substrate/coating interface could be explored.<sup>201,202</sup>

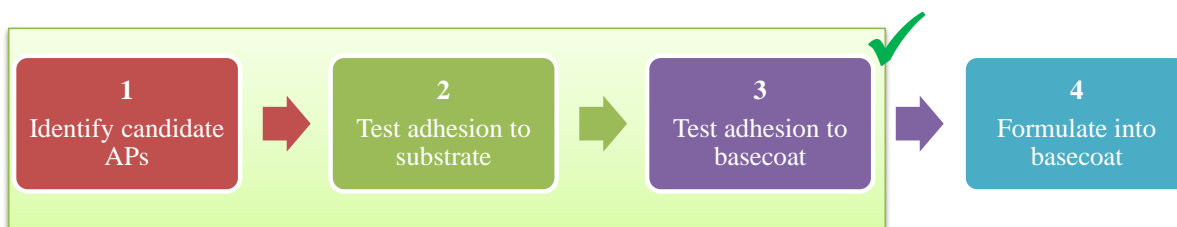


Figure 9.13: The overall objective of the project, highlighting the goals achieved during this study. The technology is patent pending.

It should be noted that future work would be likely to concentrate on the development of APs to be formulated into the basecoat, rather than looking at ways to improve the adhesion by modifying the substrate formulation. This is due to the industrial nature of the project, where the company would benefit from a competitive coatings formulation in the market, and not from a change in the substrate formulation which was manufactured elsewhere.

The successful adhesion improvement with UV curing could also be implemented into alternative industries, which often use UV curing. For example, the packaging industry, which often utilises UV curing,<sup>203</sup> had already shown interest in this work and had planned to do some testing using the results obtained in this study. Therefore, a promising future was not limited only to the automotive industry.

It was found that the adhesive properties of candidate APs applied to swollen or non-swollen substrates was poor. It was therefore concluded that under the conditions tested, adhesion via polymer chain entanglement was unsuccessful.

The results from this study have resulted in a pending patent application, for the use of TPD derivatives as APs. This signifies the importance and success of this work and its industrial applicability.

# Part V

## Appendices

# Chapter 10

## SUPPLEMENTARY MATERIAL

## Appendix 10.A Standard Used for Nanoindentation

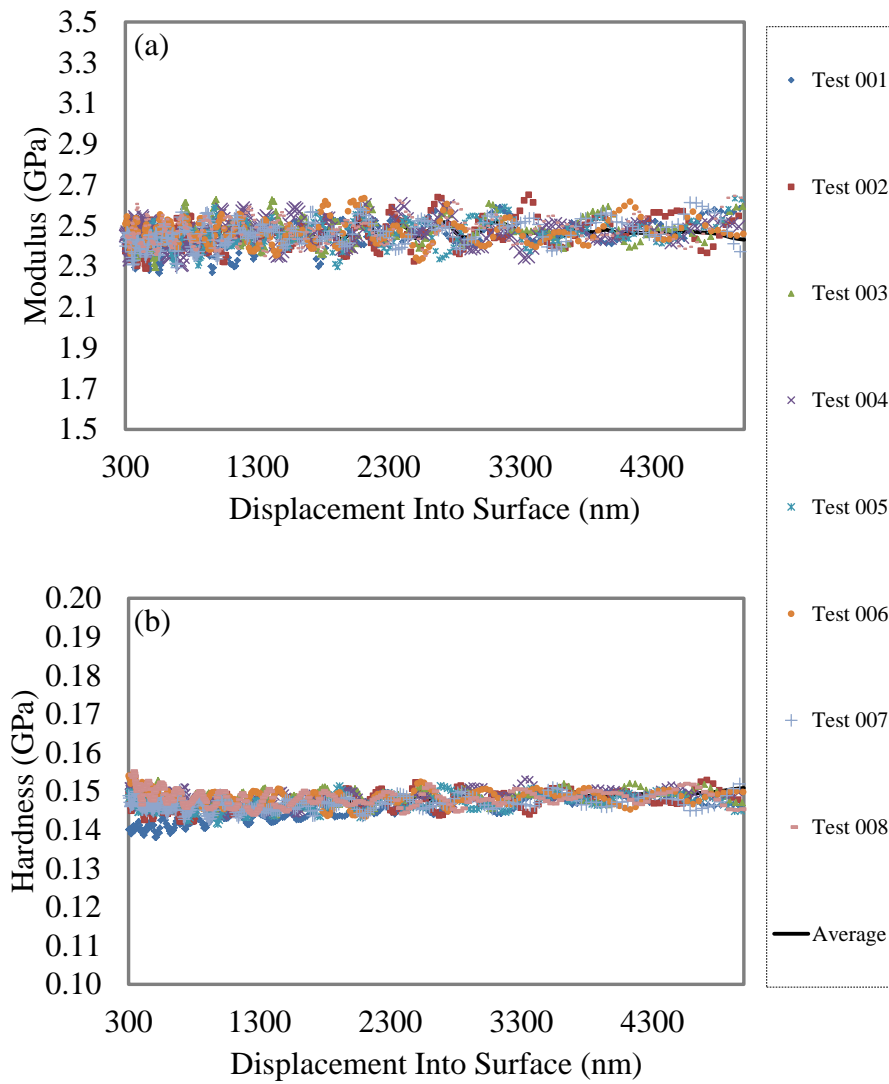


Figure 10.1: Graphs of (a) the Young's modulus profile and (b) the hardness profile of the reference material, polycarbonate, over a displacement of  $5 \mu\text{m}$  from the substrate surface.

## Appendix 10.B Data Interpolation

**Data interpolation** was performed in Microsoft Excel.<sup>139</sup> Interpolation was used to calculate to the average of the modulus and hardness measurements (experimentally determined in Section 4.4) for a defined displacement range (the displacement range varied for each measurement, therefore, a defined displacement range was needed to calculate an average).

The following formula was used in Excel:

```
=FORECAST(NewX,OFFSET(KnownY,MATCH(NewX,KnownXa,1)-1,0,2),  
OFFSET(KnownXb,MATCH(NewX,KnownXa,1)-1,0,2))
```

Where the NewX was replaced with the cell reference containing the displacement to interpolate, the KnownX<sup>a</sup> was replaced with the cell range of experimentally measured modulus or hardness values, the KnownX<sup>b</sup> was replaced with the cell reference containing the first experimentally measured modulus or hardness value and the KnownY was replaced with the cell reference containing the first experimentally measured displacement value. Modulus or hardness values were calculated for a displacement range of 0.3 - 3  $\mu\text{m}$ , every 50 nm, for 10 measurements from each substrate. Average and standard deviations were then calculated, and the average modulus and hardness profiles were plotted against displacement.



## Appendix 10.C Surface Roughness of Swollen TPO/0

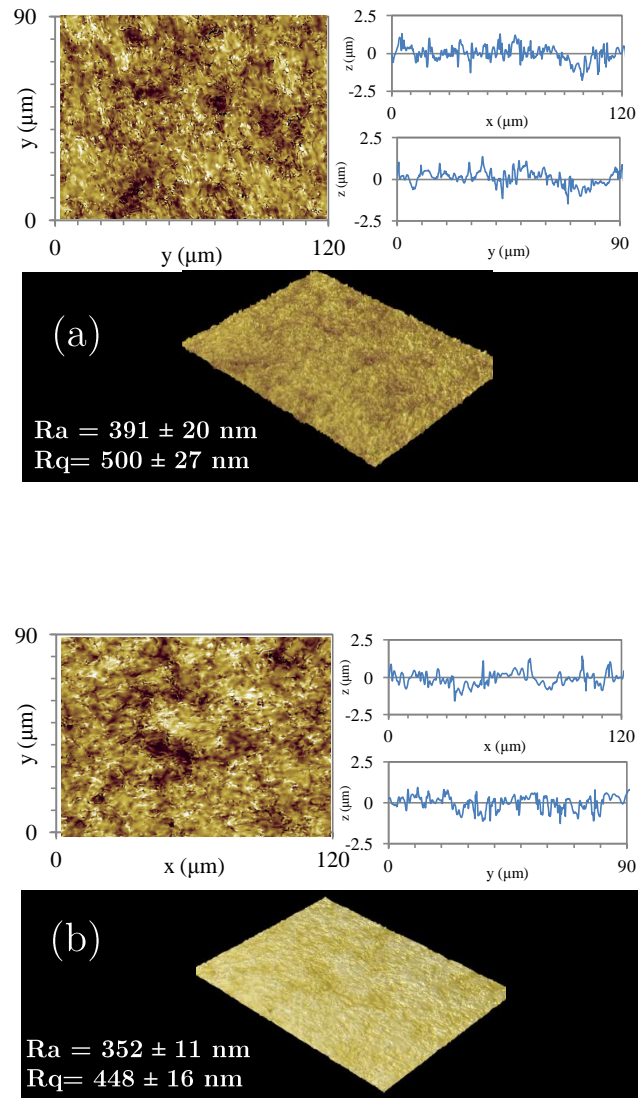


Figure 10.2: 2D and 3D images of surface roughness and x and y profiles of TPO/0 after (a) 10 minute swelling time and (b) after it was left to dry for 5 hours.

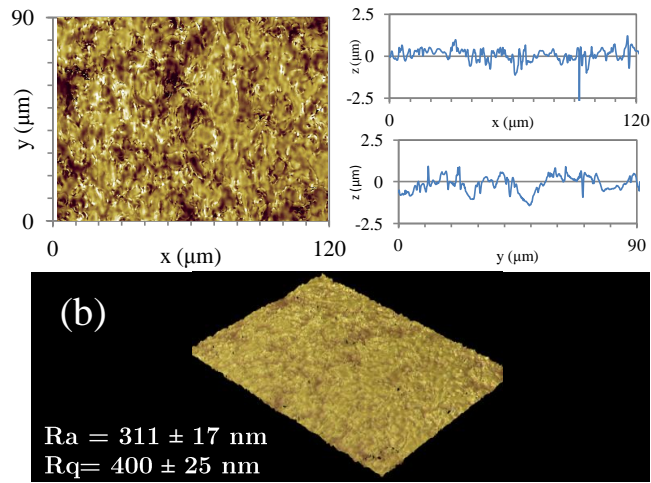
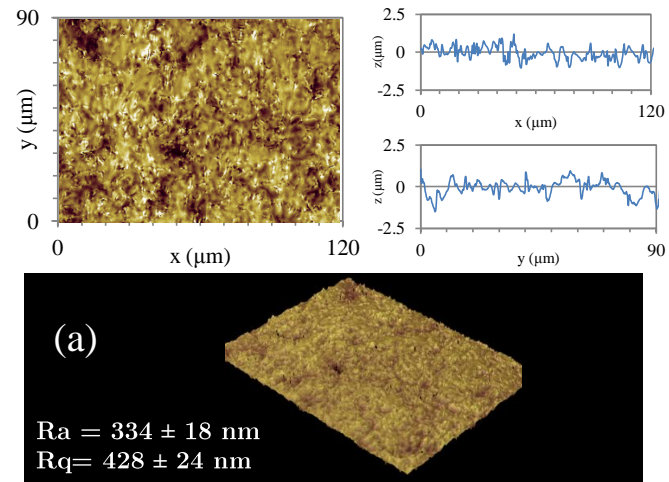


Figure 10.3: 2D and 3D images of surface roughness and x and y profiles of TPO/0 after (a) 1 minute swelling time and (b) after it was left to dry for 5 hours.

## Appendix 10.D Surface Roughness of Swollen R/0

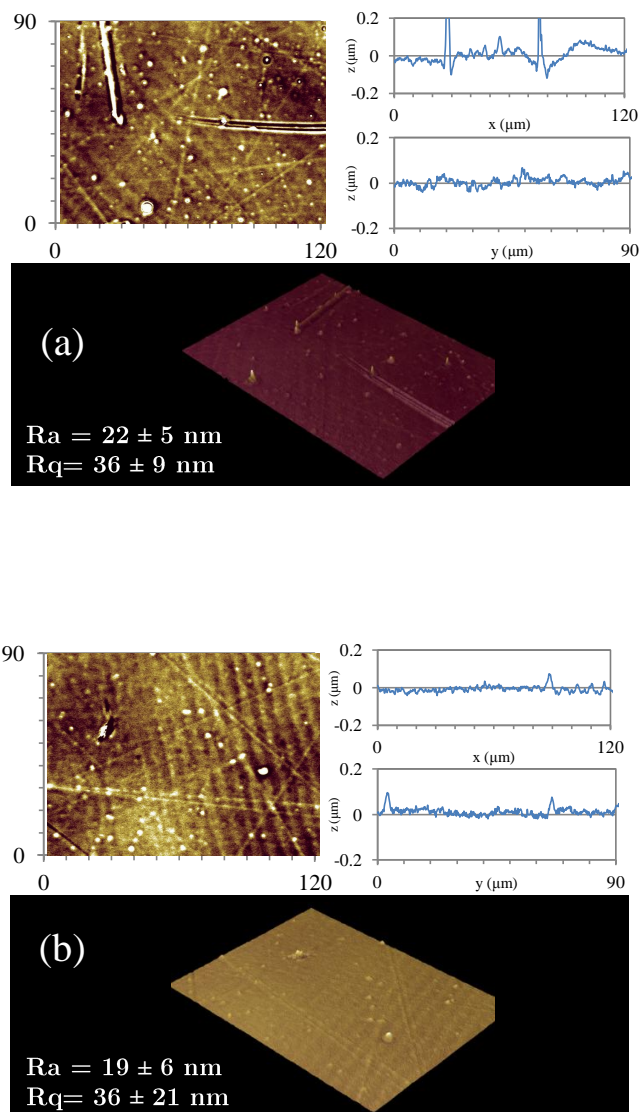


Figure 10.4: 2D and 3D images of surface roughness and x and y profiles of R/0 after (a) 1 minute swelling time and (b) after it was left to dry for 5 hours.

## Appendix 10.E Surface Roughness of Swollen R/25

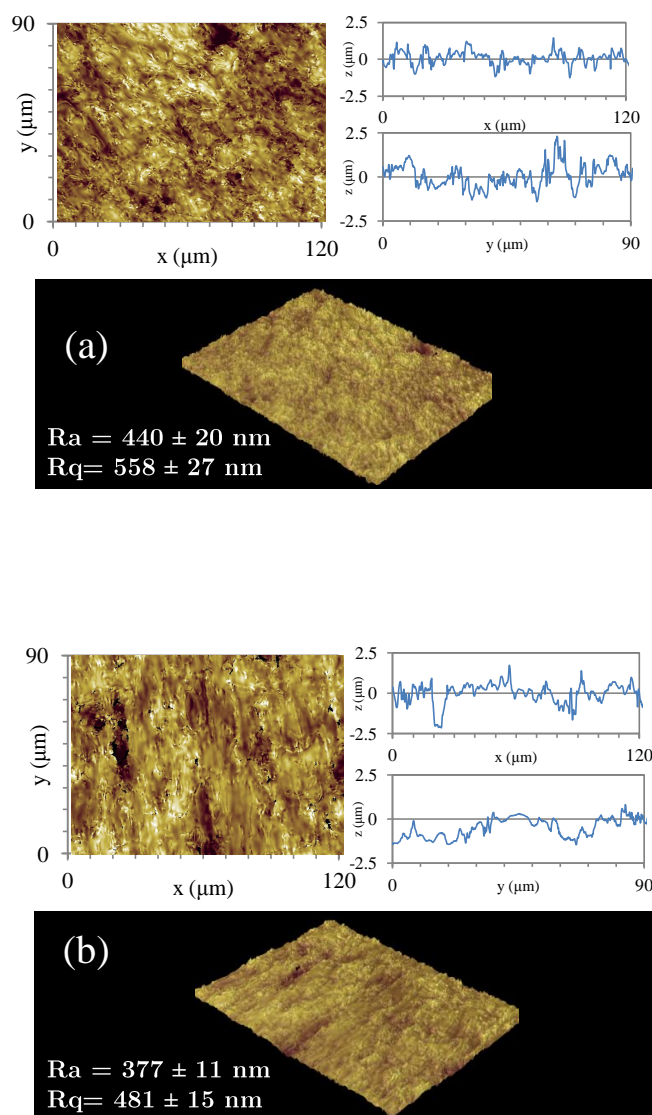


Figure 10.5: 2D and 3D images of surface roughness and x and y profiles of R/25 after (a) 10 minute swelling time and (b) after it was left to dry for 5 hours.

## Appendix 10.F Substrate Characterisation

### 10.F.1 Surface Roughness

As discussed in Section 2.4, the surface roughness of a substrate has been shown to influence the adhesion of coatings to the substrate surface. A rougher surface has a greater surface area, thus greater contact between the surface and a coating is achieved maximising the adhesion interactions.

Figures 10.6 - 10.8 displays the 2D and 3D images of the surface roughness profiles of all the untreated substrates (both industrial and research). The x and y profiles were taken from midway across the substrate in both x and y directions. The scale of the x and y profiles are alike so direct comparisons can be made.

The different surface roughness parameters that were measured are described in Section 4.3. The bar graph in Figure 10.9 shows the average Rq values of the different substrates. The Rq parameter was used for comparing the substrates, because it was more sensitive to peaks and valleys observed at the surface (due to the squaring of the amplitude in its calculation), compared to the average roughness (Ra). The results provide evidence that the surface roughness of a substrate had a strong dependence on its composition.

The smoothest substrate was the R/0, containing PP and no additives other than a mould releasing agent. The x and y profiles were relatively straight, and the 3D image looked smooth apart from one peak which may have been caused during the mould release process. The 2D image showed a mesh-like pattern which may have also been caused from the mould used.

A clear difference between the surface roughness profile of the R/0 substrate and the other substrates could be seen. The profile for TPO/0 (Figure 10.6(a)) had a similar profile to R/20 (Figure 10.8(h)), showing that it was not only the presence of EPDM that influenced the surface roughness, but also the other additives present in a TPO substrate.

This was further verified by the fact that the Ra and Rq values of the TPO/0 substrate were higher than the TPO/2 and TPO/20.

However, a clear difference in the surface roughness profile was observed as the % of EPDM increased in the research substrates (Figure 10.7(d)-(f) and 10.8(g)-(i)). The EPDM caused valleys in the substrate surface which became more frequent as the given % of EPDM increased, causing an increase in Ra and Rq values. This suggested it was solely the EPDM that caused the valleys, contrary to findings previously published,<sup>66</sup> where it was suggested that the removal of the substrates from the mould in the injection mould process caused the increase in surface roughness (as the substrates were torn, creating the craters). Therefore, the EPDM that was identified at the substrate surfaces in the SEM measurements (Section 5.3), was found to have a significant impact on the surface roughness. This was likely to be a significant contributing factor to the adhesion properties of the substrates.

It was hypothesised that substrates containing a higher content of EPDM or additives, which results in a higher surface roughness, would enable a greater contact area between the substrate surface and a waterborne coating or AP, resulting in higher adhesive interactions compared to a smoother substrate. Therefore, greater adhesion was expected for the TPO substrates and higher % EPDM research substrates. Poor adhesion was expected for the R/0 substrate, which was significantly smoother than the other substrates.

## **10.F.2 Chemical Composition**

### **10.F.2.1 Microscopy**

The chemical nature of each substrate surface will determine the surface energy, as well any reactions or interactions with the applied basecoat. Therefore, techniques were used to assess the chemical nature of the substrate surfaces (other than EPDM which was characterised in Section 5.3) and predict any influences on the adhesive properties.

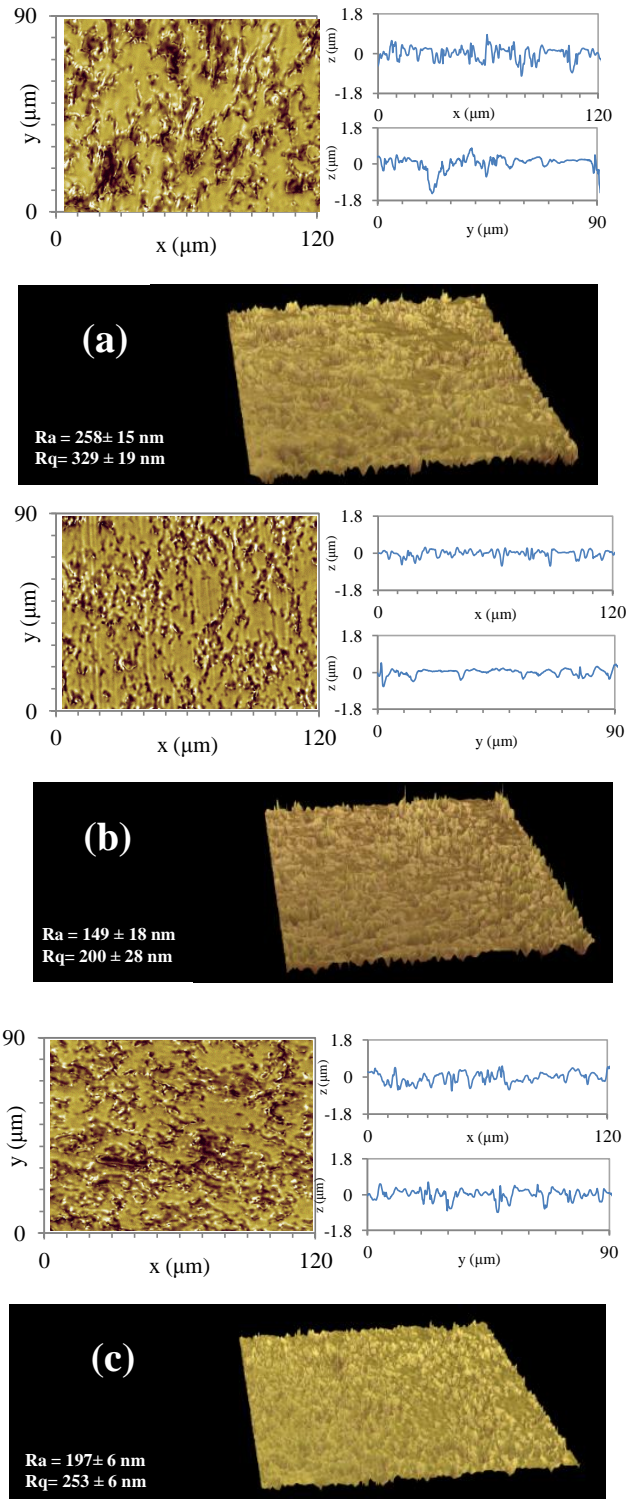


Figure 10.6: 2D and 3D images of the surface roughness and x and y profiles of (a) TPO/0, (b) TPO/2 and (c) TPO/20 substrates.

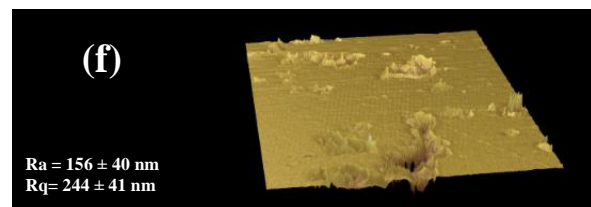
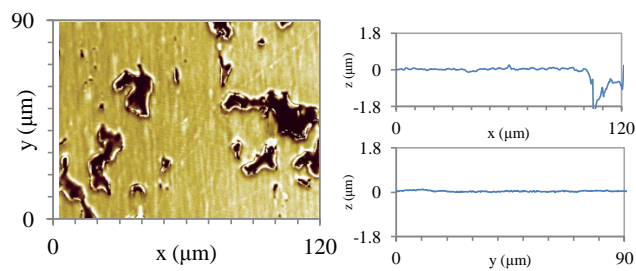
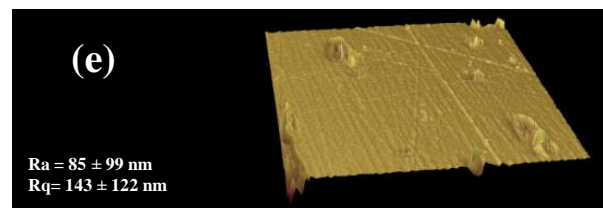
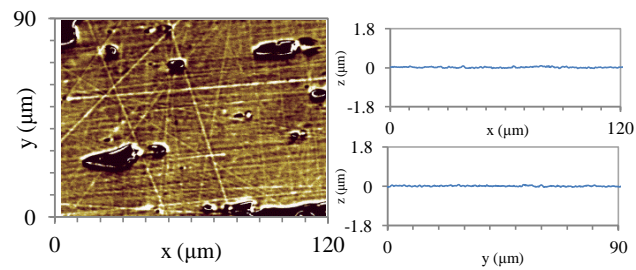
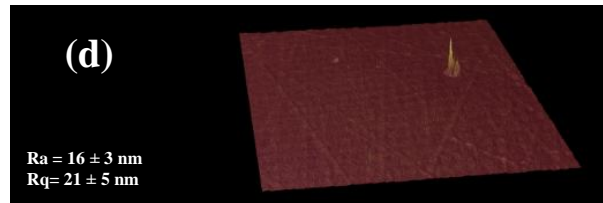
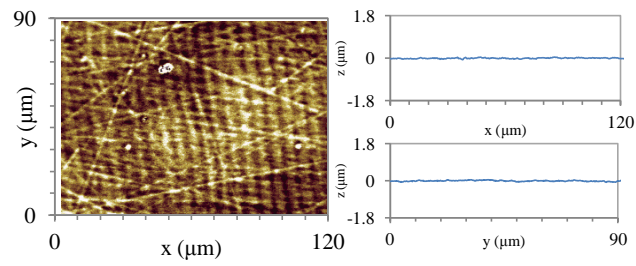


Figure 10.7: 2D and 3D images of the surface roughness and x and y profiles of (d) R/0, (e) R/5 and (f) R/10 substrates.



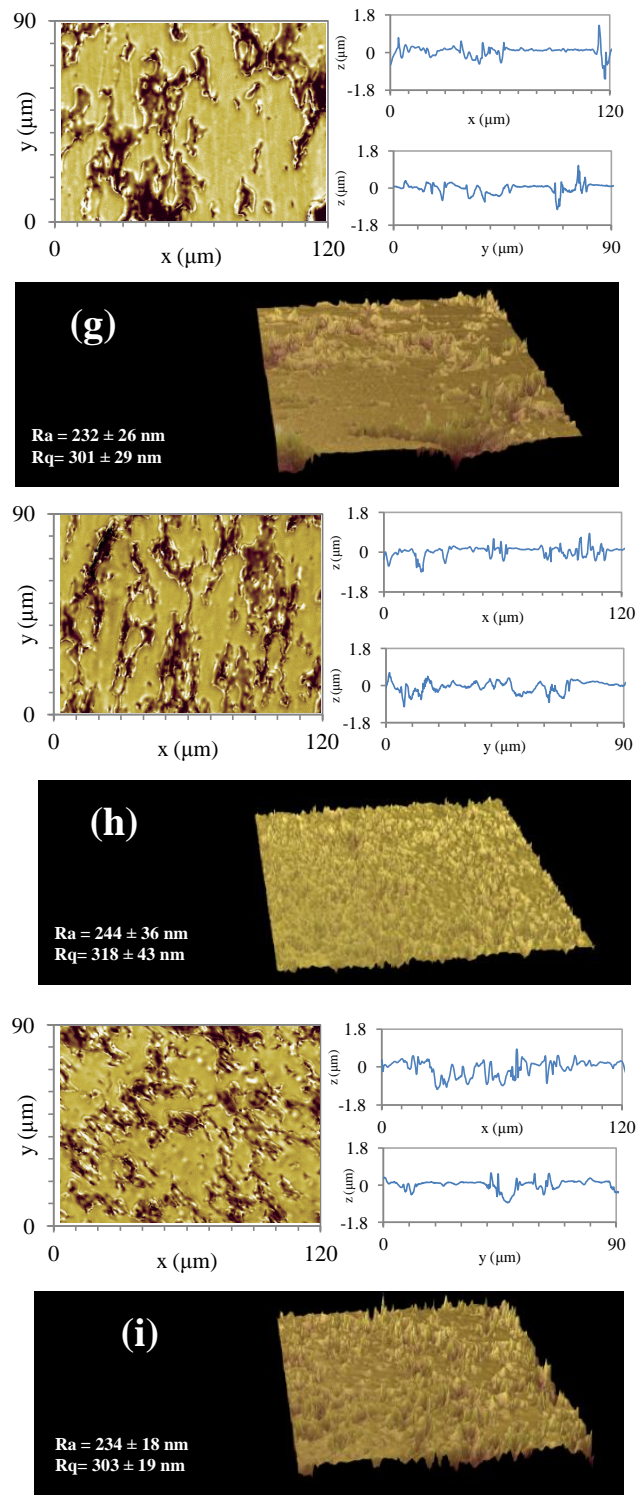


Figure 10.8: 2D and 3D images of the surface roughness and x and y profiles of (g) R/15, (h) R/20 and (i) R/25 substrates.

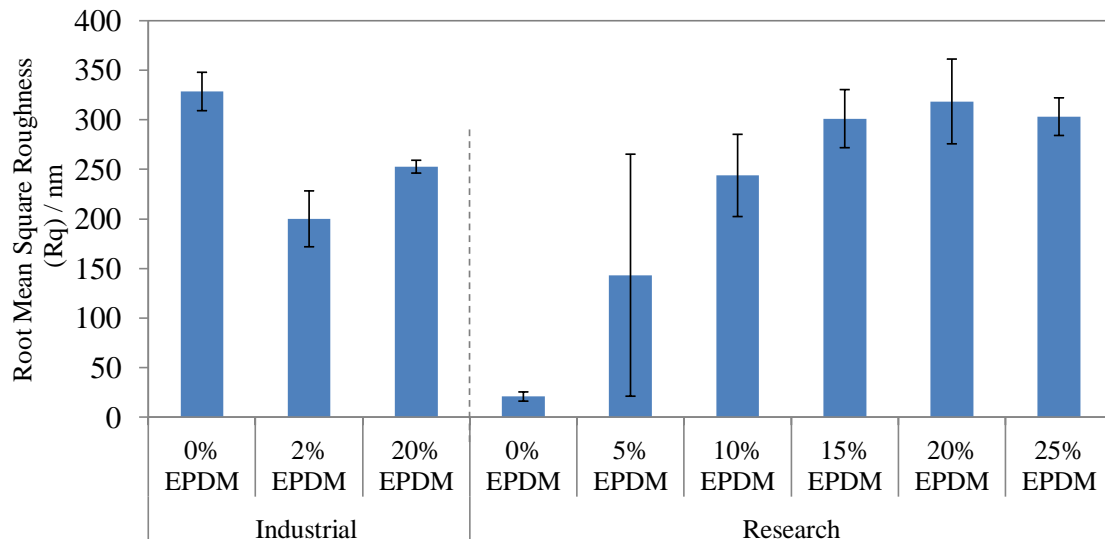


Figure 10.9: Average root mean square roughness (Rq) of the different polymer substrates

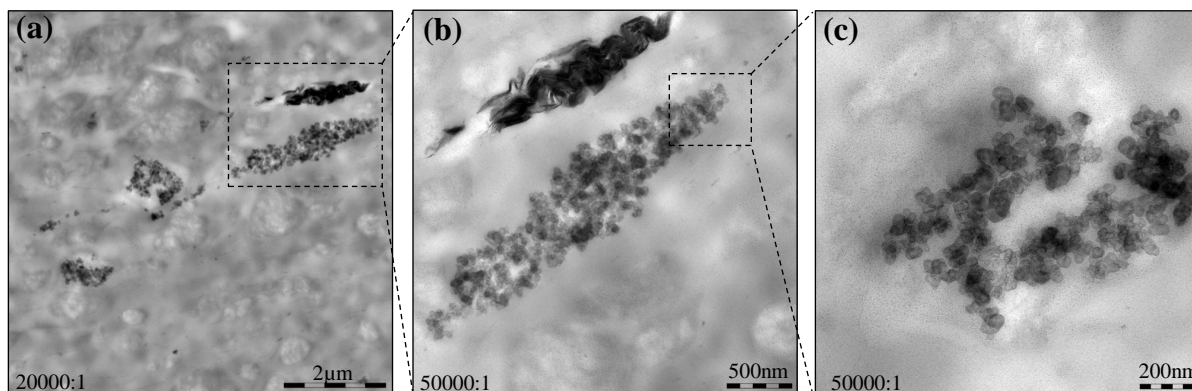


Figure 10.10: TEM micrographs taken from a stained  $\text{RuO}_4$  ultra-thin section (cross-section) of a TPO/2 substrate, (a) showing talc (top) and carbon black (bottom), at 20,000 x magnification, (b) the same but 50,000 x magnification, (c) carbon black spherical particles, 50,000 x magnification

Although TEM was not successful to analyse EPDM in Section 5.3, it was useful to identify other additives in the composition of the TPO substrates. An ultrathin section (cross-section of the substrate) was prepared, stained with  $\text{RuO}_4$  and imaged with TEM. Figure 10.10(a)-(c) shows a series of TEM micrographs from a TPO/2 substrate. Figure 10.10(b)-(c) are magnified micrographs from Figure 10.10(a). Two components were identified: carbon black, and talc.

Carbon black is a form of amorphous carbon which was identified by its characteristic colloidal suspension, showing carbon agglomerates<sup>204</sup> of spheric particles fused together (Figure 10.10(c)), schematically represented in Figure 10.11(a). It is added to TPO substrates for increased resistance to UV light (which usually degrades the PP over time) and it also acts a pigment, giving the substrate its dark colour.<sup>205</sup> The surface chemistry of carbon black varies, and is dependent on the particle size, the structure, and the number of functional groups found at the surface. Carbon blacks are produced from hydrocarbons, and the dangling bonds at the edges of the carbon layers are saturated mostly by hydrogen. Other elements are also found in the carbon black. The most important of these is oxygen. Whereas sulfur and nitrogen originate from the oil precursor, oxygen can also be taken up during carbon black formation or storage.<sup>206</sup> Therefore, it is likely the addition of carbon black to a TPO substrate creates a small number of hydroxyl groups present on the surface of the TPO. Carbon black could therefore enhance adhesion mechanisms of the substrate to the polar coatings applied.

Talc is a mineral filler composed of hydrated magnesium silicate (Figure 10.11(c)). It is darker in contrast because it contains silicon (Si) and magnesium (Mg) which have a higher atomic number compared to the carbon (C) in the PP matrix. It is added to the PP for higher stiffness and rigidity. It also reduces shrinkage, lowers the thermal expansion and controls the morphology (important for painting) and a better flow of parts during moulding.<sup>174,207</sup> It has also been shown that talc acts as a nucleating agent in crystalline polymers and the addition of talc to PP increases the crystallinity of the polymer.<sup>208</sup> This influences the swellability of the substrate, which may therefore have an influence on the

adhesive nature of the polymer to the coatings.

Also, the surface chemistry of talc present at the substrate surface may influence adhesive properties. Particles of talc have the shape of platelets due to the layered structure of the mineral. The basal surfaces are hydrophobic, while the edge surfaces are hydrophilic.<sup>168,169</sup> The hydrophobicity of the basal surfaces arises from the fact that the atoms exposed on the surface are linked together by siloxane (Si-O-Si) bonds and hence, do not form strong hydrogen bonds with water.<sup>168,209</sup> The edge surfaces are composed of hydroxyl ions, magnesium, silicon and substituted cations, all of which undergo hydrolysis. As a result, the edges are hydrophilic, and upon surface fracture, can form strong hydrogen bonds with water molecules and polar substances.<sup>170–173,208,210</sup> Therefore, it is possible that chemical reactions or interactions between hydrophilic coatings and a TPO substrate with exposed talc surfaces could improve adhesion.

Although the properties of cohesion within a TPO substrate (adhesion between the mineral fillers and PP matrix) has been extensively studied,<sup>211,212</sup> no previous reports were found on the topic of adhesion of polar coatings to the talc and carbon black component of a TPO surface. If such reactions are possible, it would be a significant contributing factor to the understanding of the adhesion mechanism between a PP-based substrate, an AP and a polar coating.

Calcium carbonate ( $\text{CaCO}_3$ ) was another additive identified in the SEM images taken from the industrial TPO substrates (see Figure 5.3(c)). A schematic 3D representation is shown in Figure 10.11(b). It is one of the most popular mineral fillers in the plastics industry, and it is typically added to a TPO substrate. It provides opacity and surface gloss, which improves surface finish. When the particle size is carefully controlled,  $\text{CaCO}_3$  also increases both impact strength and flexural modulus (stiffness) of a TPO substrate. Although it is hydrophilic in nature,<sup>210</sup> which would be beneficial to adhesion mechanisms to polar coatings at the TPO surface, it is usually treated with stearic acid to reduce the surface energy and prevent particle agglomeration, hence improve compatibility with the hydrophobic PP in a TPO substrate.<sup>174</sup> In the SEM/TEM with EDX measurements, it

was not possible to know to what extent the  $\text{CaCO}_3$  had been treated, thus what effect it was likely to have on adhesion. For a better understanding of whether the additives have an effect on the surface energy of the substrates, the polar and dispersion components of the surface energy were measured in Section 5.5.

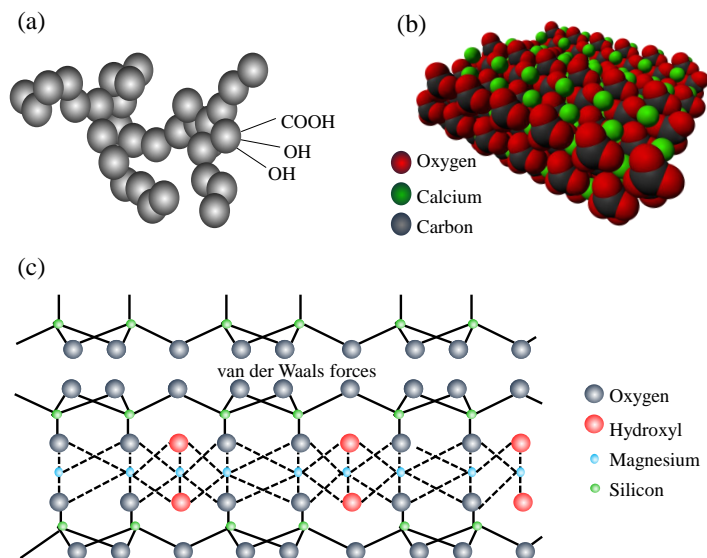


Figure 10.11: Typical fillers found in TPO plastics: (a) Schematic representation of carbon black spherical particles, with hydrophilic functional groups at the surface, (b) a 3D lattice of  $\text{CaCO}_3$  and (c) a 2D representation of talc and the different interactions between the layered structure<sup>171</sup>

### 10.F.2.2 Time of Flight Secondary Ion Mass Spectrometry (ToF-SIMS)

For further surface characterisation of the industrial PP substrates, ToF-SIMS was used to identify additives not previously identified with alternative techniques. Figure 10.12 and Figure 10.13 show the positive and negative ion spectra for the industrial TPO/0 substrate. Both spectra show typical fragments of the antioxidant additive Irgafos 168,<sup>213</sup> shown in Figure 10.14. It was found to be present in all three industrial TPO substrates. Irgafos 168 is an organophosphite of low volatility which is resistant to hydrolysis. It is an anti-oxidant and is used to protect polymers which are prone to oxidation during processing steps (compounding/pelleting, fabrication and recycling), molecular weight change (e.g. chain scission/cross-linking) and it also prevents discolouration.<sup>214</sup> ToF-

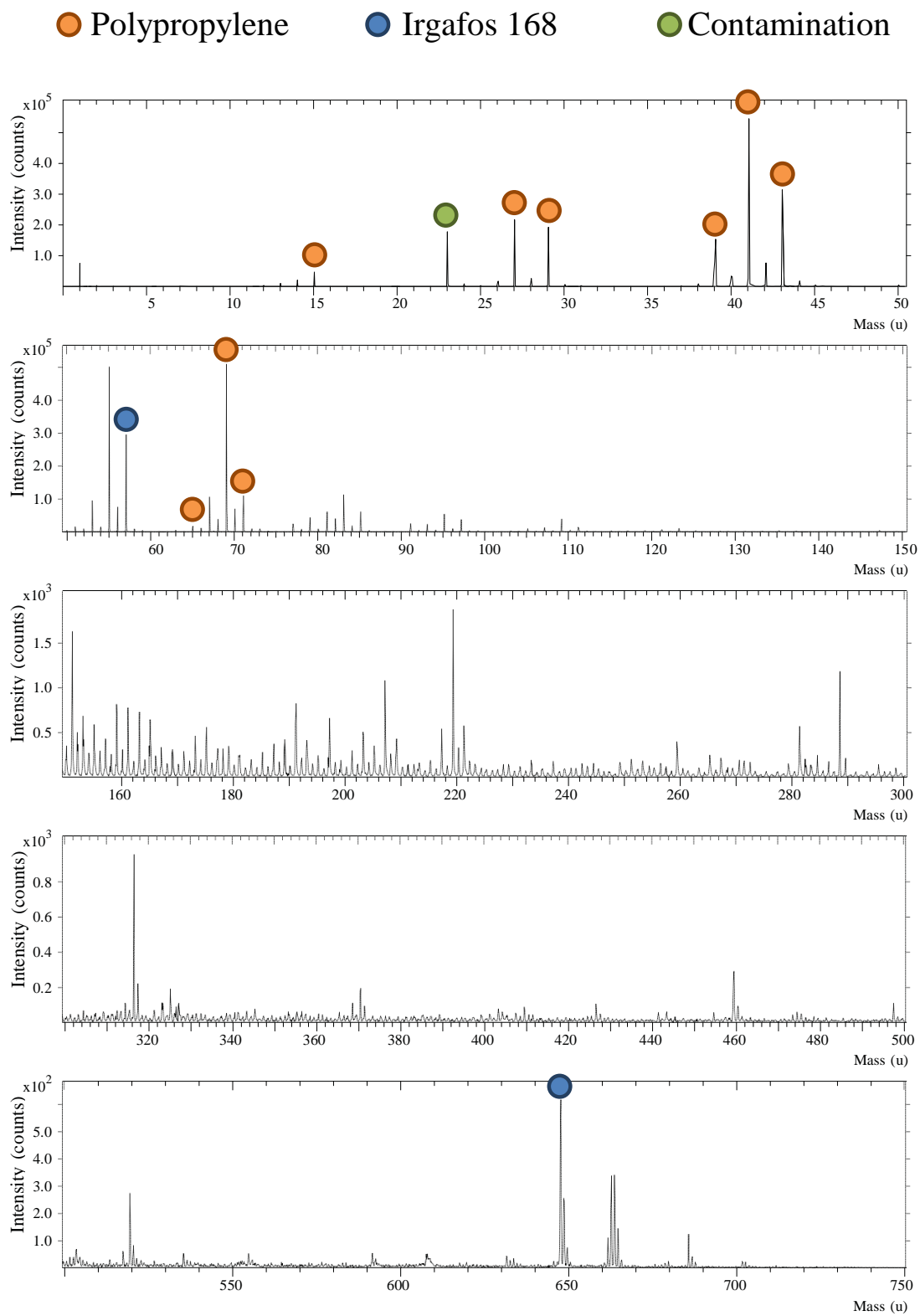


Figure 10.12: The positive ion ToF-SIMS spectrum of the TPO/0 substrate surface

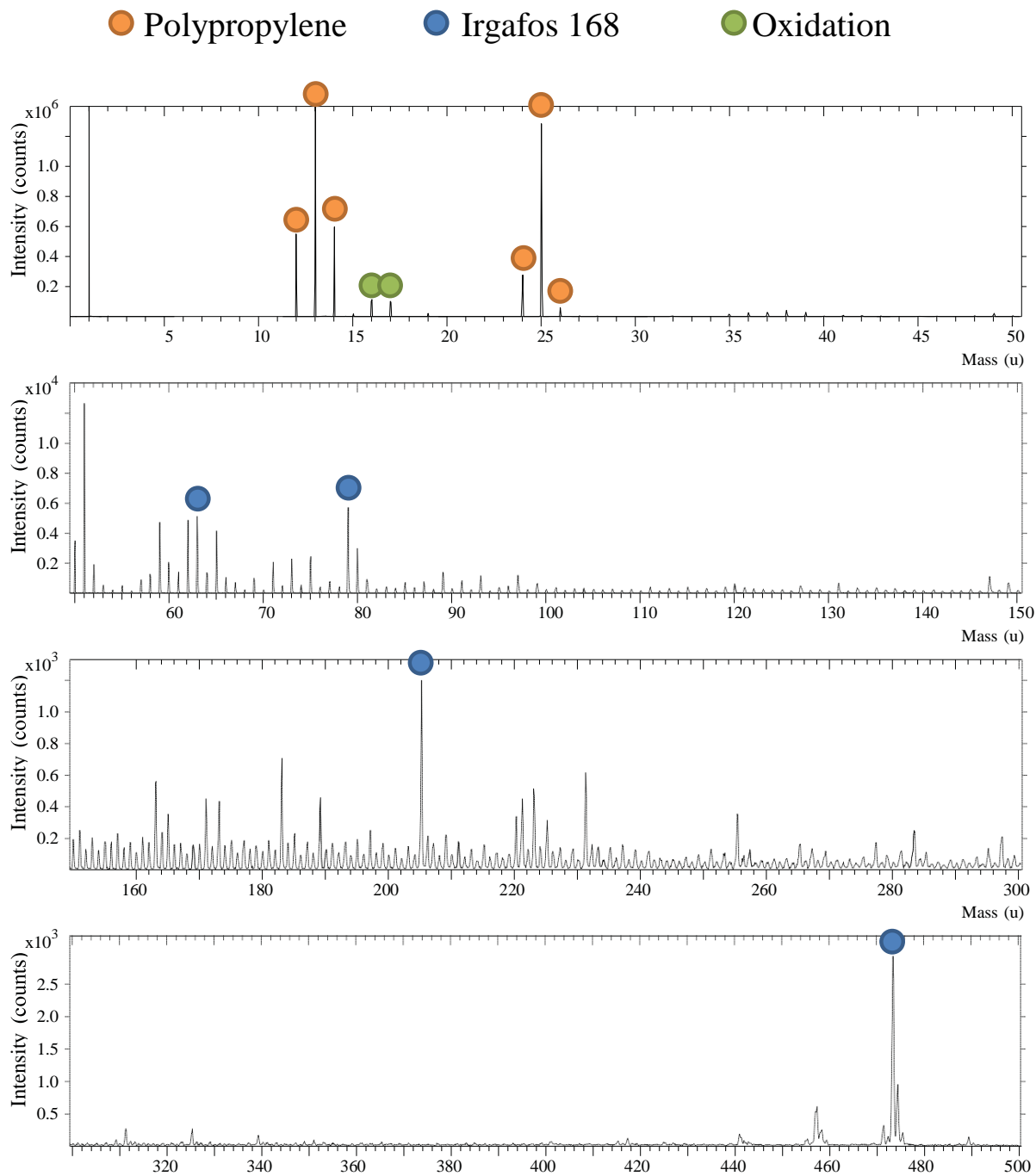


Figure 10.13: The negative ion ToF-SIMS spectrum of the TPO/0 substrate surface

SIMS is a very surface sensitive technique (first few atomic layers) and so it was assumed that the additive would come into direct contact with any applied AP.

A previous AFM study with functionalised tips studied force distance curves of PP substrates containing additives such as Irgafos 168.<sup>215</sup> It was found to be relatively hydrophobic in nature. This behaviour is likely to be due to the many *t*-butyl groups present at the surface of Irgafos 168, which are bulky in nature and are likely to mask the rest of the molecule. Due to the steric hinderance, its reactivity towards other compounds (not small) is reduced. Therefore, it is unlikely that Irgafos 168 will have any significant chemical interactions with an applied AP.

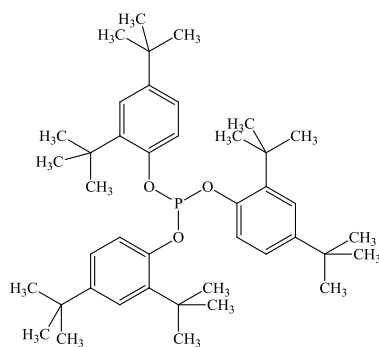


Figure 10.14: Irgafos 168

As previously reported,<sup>216</sup> the positive ion spectrum shown in Figure 10.12 reflects essentially the hydrocarbon fragmentation of the PP. The peak at  $m/z = 15$  is due to the methyl cation, and those at  $m/z = 27$  and  $29$  are due to the fragments with two carbon atoms ( $C_2H_3^+$  and  $C_2H_5^+$ ). Fragments with three carbon atoms produce peaks at  $m/z = 39$ ,  $41$ , and  $43$ , fragments with four carbon atoms produce peaks at  $m/z = 53$ ,  $55$ ,  $57$  and fragments with five carbon atoms produce peaks at  $m/z = 65$ ,  $69$ ,  $71$ . It has previously been reported that the peak at  $m/z = 69$  is very characteristic of PP (due to the methyl pendant groups), and it is attributed to either the dimethylcyclopropylium<sup>217,218</sup> or more likely an allyl ion,<sup>219</sup> which is particularly stable because of resonance and induction effects.<sup>220</sup>

The peak at  $m/z = 23$  is due to  $Na^+$  and suggests surface contamination. Surface contamination was very important to monitor when testing adhesion at the surface, as



such cations could potentially hinder any adhesion mechanism by separating the interfaces and interfering with chemical reactions/interactions. Polydimethylsiloxane (PDMS) was also a typical surface contaminant often found in ToF-SIMS spectra when samples had not been cleaned or handled correctly.<sup>94</sup> Day to day toiletries such as hand cream, hand soap and hairspray are known to cause such contamination. Some spectra showed evidence of PDMS fragments on untreated substrates, however, after a cleaning step with isopropanol the peak intensities were greatly reduced or eliminated. However, it must not be forgotten that solvent cleaning induces other surface changes (reported in Appendix 10.F.4) such as surface roughness, which could also potentially have an effect on adhesion.

The negative ion spectrum shown in Figure 10.13 is also dominated by hydrocarbon fragmentation from the PP. Peaks at  $m/z = 12, 13, 14$  are due to  $C^-$ ,  $CH^-$ ,  $CH_2^-$  fragments and the peaks at  $m/z = 24, 25, 26$  are due to  $C_2^-$ ,  $C_2H^-$ ,  $C_2H_2^-$  fragments. Peaks from  $m/z = 36$  onwards are due to the fragments with three carbon atoms, the peaks from  $m/z = 48$  onwards are due to fragments with four carbon atoms and the peaks from  $m/z = 60$  onwards are due to fragments with five carbon atoms. The peaks at  $m/z = 16$  and  $17$  in the negative spectra are due to  $O^-$  and  $OH^-$ . The presence of oxygen containing species in PP is well known,<sup>221</sup> as the injection moulding process sometimes causes oxidation at the surface (as previously mentioned, Irgafos 168 is often added to prevent oxidation).

## 10.F.3 Mechanical Properties: Substrate and Young's Modulus

### 10.F.3.1 Substrate Hardness

Crystallinity has been shown to influence the adhesive properties of TPO substrates when using CPO APs, as discussed in Section 2.4. The degree of crystallinity at the substrate surface determines the penetrability of the CPO, which subsequently determines the adhesion performance.<sup>64,67</sup> Therefore, the mechanical properties of the substrates were

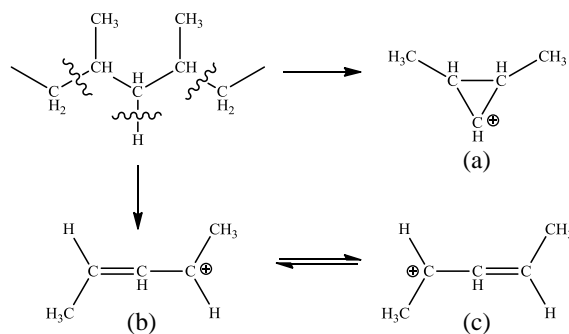


Figure 10.15: Schematic diagram showing the generation of the  $m/z = 69$  fragment characteristic of PP: (a) dimethylcyclopropyl cation or (b) and (c) allyl cation, which are stabilised through the inductive effective of the methyl groups or by resonance stabilisation.

characterised to hypothesise the adhesion performance expected based on the findings.

Although the crystallinity of the substrates has not been directly measured in this study as it has been in previous studies,<sup>64,67</sup> the substrate hardness that was measured gave a good indication of the variation of the crystallinity with penetration depth into the substrate surface. It was previously shown that crystallinity is directly proportional to hardness of the material, and that the surface hardness increases as the degree of crystallinity increases.<sup>67</sup> It is often cited<sup>64</sup> that the ability of a solvent to penetrate the substrate surface is determined by the surface PP crystallinity, which consequently influences the adhesion and the ability of an AP to penetrate into the surface. Thick highly crystalline boundaries of PP will tend to retard diffusion and therefore result in poor adhesion.

**0 % EPDM Research Substrate** Previous studies<sup>45</sup> have shown the surface morphology to consist of a PP transcrySTALLINE surface layer followed by a layer consisting of larger crystal PP spherulites, as discussed in Section 2.4 and shown in Figure 2.4. It was expected that the surface hardness would initially be lower in the transcrySTALLINE region and would increase with penetration depth towards the higher crystalline regions, where the increase in hardness is related to the better orientation of the PP chains, resulting in a more dense chain packing.

However, Figure 10.16(a) shows this result only to be true during the first region of

the surface hardness profile of the R/0 substrate. Three distinct regions were identified for this substrate. The first region, between 300 - 850 nm from the surface, increased in hardness by  $\sim 3$  MPa, which was thought to be due to an increase in crystallinity with penetration depth. This would be caused by the decrease in cooling rate from the surface of the substrate, as it entered the mould during the injection moulding process. The second region, between 850 - 2600 nm from the surface, showed a decrease in hardness with penetration depth by about 6.5 MPa, suggesting a layer of a second softer phase that formed as a subsurface layer during the injection mould process. This differs from the morphology described in previous studies.<sup>45,64</sup>

Without doing further investigation of the injection mould apparatus used (to which no access was possible), it was not possible to conclude the reason why this second region exists, although it was likely to be due to the thermal gradients present in the mould as the rotating screw was used to drive the TPO into the mould during the injection process. As described in Section 2.4, the substrate microstructure heavily depends on the moulding conditions in which the plastic part is made.

Hardness values of  $\sim 50$  MPa for the R/0 research substrate indicated isotactic PP in a semi-crystalline phase (hardness values for crystalline  $\alpha$ -iPP (monoclinic) = 111 MPa; crystalline  $\beta$ -iPP (hexagonal) = 90 MPa; amorphous iPP =  $\sim 30$ MPa<sup>222</sup>), however, further investigation such as determining the melting points in the different regions and DSC analysis would further determine the crystallinity of the different regions. In this study, it was sufficient to determine the effect of substrate hardness variation with substrate composition, to better understand adhesion mechanisms.

The substrate hardness varied very little from 2600 - 500 nm below the surface in the third region identified, as it tended to a relatively stable value between 50.7 - 52.7 MPa, in which the temperature was likely to be relatively consistent in the moulding process (representing the bulk of the polymer).

**5 % - 25 % EPDM Research Substrates** The effect of EPDM in the other research substrates, shown in Figure 10.16(a), was apparent when comparing the hardness profiles with the blank substrate (R/0). All 5 substrates (5 - 25 % of EPDM) showed a clear decrease in hardness, which did not support the structure suggested by Ryntz *et al.*<sup>29,30,45,64,66,67</sup> (an initial increase in hardness was expected, corresponding to an increase in crystallinity). Furthermore, contrary to the previous findings, the steady decrease in hardness suggested no skin was present at the substrate surface within the depths measured. However, it was not known if the postulated microstructure in Figure 2.4 was within the depth scale measured. Therefore, this could have been the reason for the mismatch in TPO models, or it could be due to a difference in the process parameters of the injection moulding process (as discussed in Chapter 2.4).

For all 5 research substrates containing EPDM, there was an initial decrease of hardness, before levelling at a relatively steady value in the bulk material. The hardness values were less than the blank R/0 substrate, showing that EPDM had a significant effect. Between 1800 - 5000 nm, assumed to be the bulk below the surface, the hardness values decreased as the % of EPDM increased, for all substrates with the exception of R/15 and R/20, where the hardness value for both substrates was  $\sim 34$  MPa. The amorphous rubber EPDM component is added to TPOs for improved impact strength, so a decrease of substrate hardness with increasing % of EPDM was expected. However, the position of the EPDM domains relative to the surface had a large influence on the hardness values recorded. The lack of trend observed between the hardness and the % of EPDM in the substrate, further demonstrated the inhomogeneous nature of the substrates that was previously seen in the SEM measurements (Section 5.3). Assuming that the substrate hardness correlated to the amount of EPDM at the point of measurement, the hardness depth profiles in Figure 10.16 suggest the amount of EPDM at different points in the cross-section of the substrate relative to the surface, varied for each substrate.

In conclusion, the R/20 and R/25 research substrates were expected to have the greatest adhesive properties, due to a solvent or AP being able to penetrate into the substrates

at a greater degree compared to the other harder research substrates (influencing the amount of contact between the EPDM domains and the AP). The hardest substrate, R/0, was expected to have the worst adhesive properties. Furthermore, the adhesive properties were not able to be predicted based on the given % of EPDM in a substrate, due to the lack of trend observed with the hardness values obtained.

**Industrial Substrates** As measured in Appendix 10.F.2, many components were present in the PP matrix of the industrial substrates, including talc, carbon black, calcium carbonate and Irgafos 168, as well as the EPDM rubber. The influence of these components on the substrate hardness was clearly observed, as shown in Figure 5.7. When comparing the industrial substrates TPO/0, TPO/2 and TPO/20 with the research substrates (0 - 25 % of EPDM). The hardness profiles of all three industrial substrates were lower than all research substrates, by  $\sim 10$  MPa in the near surface region and  $\sim 6$  MPa in the bulk region, when compared to the softest research substrate (R/25). When comparing the R/0 and TPO/0 substrates, it was clear that the additives (other than EPDM) within the PP matrix in the industrial substrate had a great influence on the substrate hardness, decreasing the value from  $\sim 55$  to  $\sim 20$  MPa.

The hardness profile of the industrial TPO/0 substrate followed the same depth profile shape as all the other substrates containing EPDM: an initial decrease in hardness, differing from the research R/0 substrate. This showed that the EPDM alone did not have a significant effect on hardness when other additives were present in the matrix, but rather the collective presence of additives determined a substrates hardness. Furthermore, all three industrial substrates had relatively similar values of hardness, showing that the % of EPDM did not have such a significant effect.

The TPO substrates had lower hardness values compared to the research substrates, therefore, it was expected that a solvent or AP would be able to better penetrate TPO substrates resulting in greater adhesive effects.

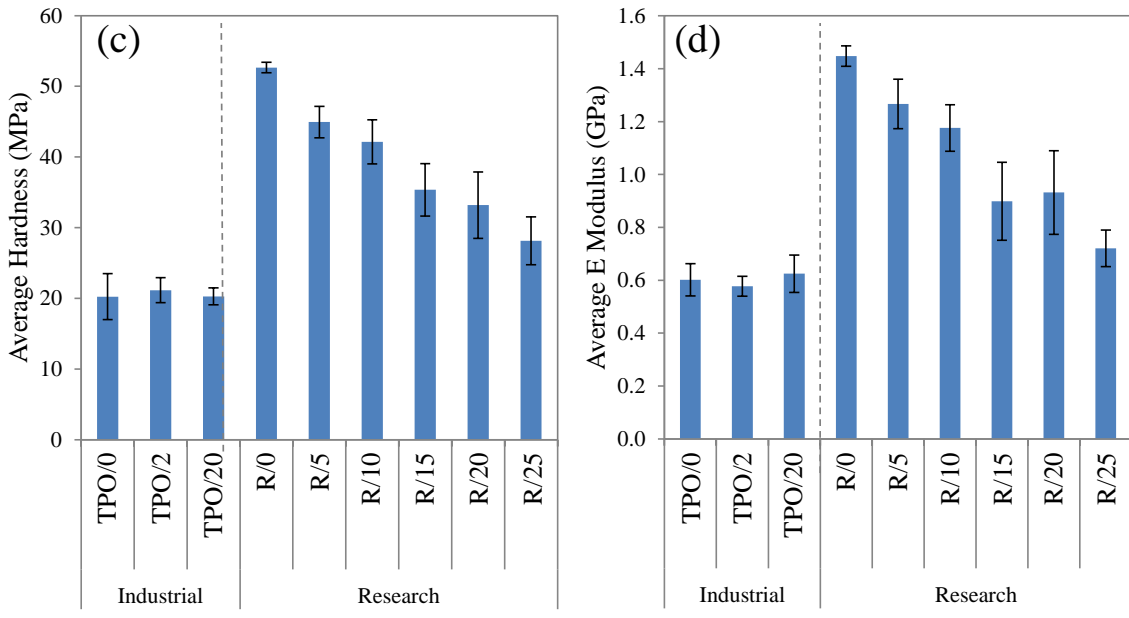
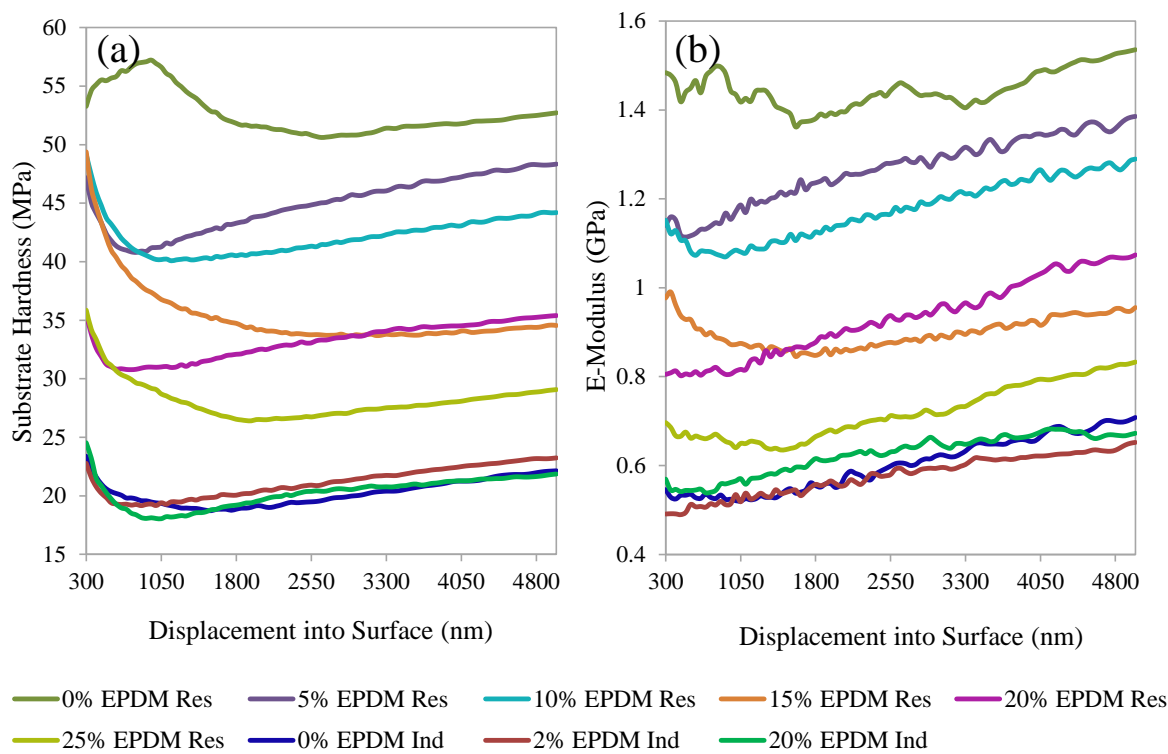


Figure 10.16: Top: (a) Surface hardness profile of all substrates and (b) Young's modulus profile of all substrates, measured using nano-indentation. Bottom: (c) Average hardness for all substrates and (d) average Young's modulus for all substrates.

### 10.F.3.2 Substrate Young's Modulus

A previous study concluded that increasing the amount of rubber, such as EPDM, in a TPO leads to a layer of higher elasticity within the substrate. Thus, a higher cohesive energy was attained before reaching its yield stress and delamination occurred.<sup>45,64</sup> It was also found that lower modulus (higher rubber content) TPO materials exhibited better adhesion than those with a higher modulus.<sup>68</sup> TPO substrates with a modulus value of 1.2 GPa were found to give poor adhesion using a CPO primer layer, whereas TPO substrates with a modulus of 0.3 GPa gave good adhesion (independent of the two types of clear coats tested). Hence, the selection of the TPO modulus in determining the ability to accommodate for external stresses was important when assessing adhesion.

Figure 10.16(d) shows the Young's modulus of the substrates. As expected, the modulus decreased as the % of EPDM increased, for all research substrates with the exception of R/20. When assessing the trend, the R/15 substrate had a lower modulus than expected, whilst the R/20 substrate had a higher modulus than expected. As was found for the hardness measurements, Figure 10.16(b) shows that the modulus depth profiles highly depended on the point of penetration and whether EPDM was present or not at that particular point. Initially, the modulus of R/20 was lower than that of R/15 as expected. However, at 1300 nm into the substrate, the modulus exceeded that of R/15, further supporting the heterogeneous nature of the EPDM distribution in the injection moulded substrates.

The modulus did not vary linearly as expected with the given EPDM compositions of the substrates. For example, the TPO/20 industrial substrate contained 10 times more EPDM than the TPO/2 substrate, yet the modulus measured was larger for TPO/2. As it was found with the substrate hardness values, additives in the TPO formulation of the substrates were found to have a large influence on the Young's modulus. Furthermore, the modulus values for the industrial substrates containing all additives were lower than that of the research substrates containing only EPDM.

The substrates studied almost covered the range of modulus values studied by Ryntz *et*

*al.*,<sup>68</sup> although no substrate reached a value as low as 0.3 GPa which was previously shown to give good adhesion. However, the values did go below 1.2 GPa at which previously poor adhesion was observed, therefore, assuming the adhesion mechanisms functioned in the same way as the CPO, an improved adhesion was expected for the substrates with lower modulus values (the industrial TPO substrates had the lowest modulus range).

## **10.F.4 Effect of Solvent Cleaning on the Substrate Morphology**

### **10.F.4.1 Surface Roughness**

It is common practice in industrial laboratories to prepare TPO substrates by wiping them clean with solvent-soaked clothes before they are coated. This is to prevent contamination of dirt particles and/or mould-releasing agents at the surface of the substrate, which may hinder adhesion. However, solvent wiping/rinsing is not a viable step in the production line of a vehicle due to the added costs and environmental impact. For research purposes, however, implementing a washing step was helpful to establish if contamination was causing delamination (assuming the solvent was clean and did not contaminate the surface itself).

It was previously found that such cleaning procedures have an impact on the adhesion properties at the surface of the substrate. Firstly, solvent wiping removes contaminants such as oil and grease which can form weak boundary layers at the surface, causing poor adhesion.<sup>94,223</sup> Secondly, it was found that some solvents can introduce hydroxyl groups to the surface which were thought to facilitate adhesion via an acid-base interaction.<sup>71</sup> A third important impact of solvent cleaning, which was previously reported, was the change in surface roughness of TPO substrates. Solvent wiping significantly increased the surface roughness of the TPO substrate measured, which influenced the penetration of a CPO AP.<sup>66</sup> It was found from model experiments that the pure PP was relatively unaffected by solvent wiping, whereas the surface roughness change of the elastomer (such as EPDM) had a similar value to that of the TPO (PP and EPDM). Therefore, it was



concluded that the surface roughness change of the elastomers caused the overall TPO surface roughness change.

To assess the effects of solvent cleaning on the substrates used in this study, the surface roughness was measured before and after solvent wiping and solvent rinsing with isopropanol. The experiments were carried out on three different types of substrate: an industrial TPO/0, and two research substrates looking at the effect of EPDM: R/0 and R/25. One set of substrates were wiped once with a fabric soaked in isopropanol, and another set of substrates were rinsed with isopropanol, preventing any abrasive contact to the surface. Uncleaned surfaces were also examined for comparison. All samples were immediately measured after cleaning.

For each sample, images were obtained from 10 different areas on the surface. Values for Ra and Rq were taken from the combined data of all 10 measurements, and the average values were calculated, shown in Figure 10.17 - 10.19.

The 2D average surface roughness profiles and 3D surface images of each substrate without a cleaning procedure are shown in Figure 10.17(a)-(c). In both the 2D and 3D images, peaks and valleys on the substrate were observed. (Although the surface roughness initially appears severe in the images of Figure 10.17(a) and (c), the z-axis is highly magnified). The Ra and Rq values indicated the roughness was on a fine scale. For comparison, a standard Aluminium-Oxide 100 sand paper (typically used to sand bare wood) has an Ra value of  $35.83 \mu\text{m}$  and Rq value of  $49.89 \mu\text{m}$ ,<sup>224</sup> an order of magnitude greater than the studied substrates.

A clear difference was observed between the industrial TPO (Figure 10.17(a)), R/0 (Figure 10.17(b)) and R/25 (Figure 10.17(c)). As discussed in Appendix 10.F.1, the R/0 substrate is significantly less rough (smoother) than the other two substrates, indicating the effect of additives which increase the substrate roughness. The industrial TPO and R/25 substrates had surface roughness parameters on a similar scale, whereas the R/0 substrate had surface roughness parameters over 10 times lower.

This difference was also emphasised in the 2D images: R/0 showed a relatively smooth

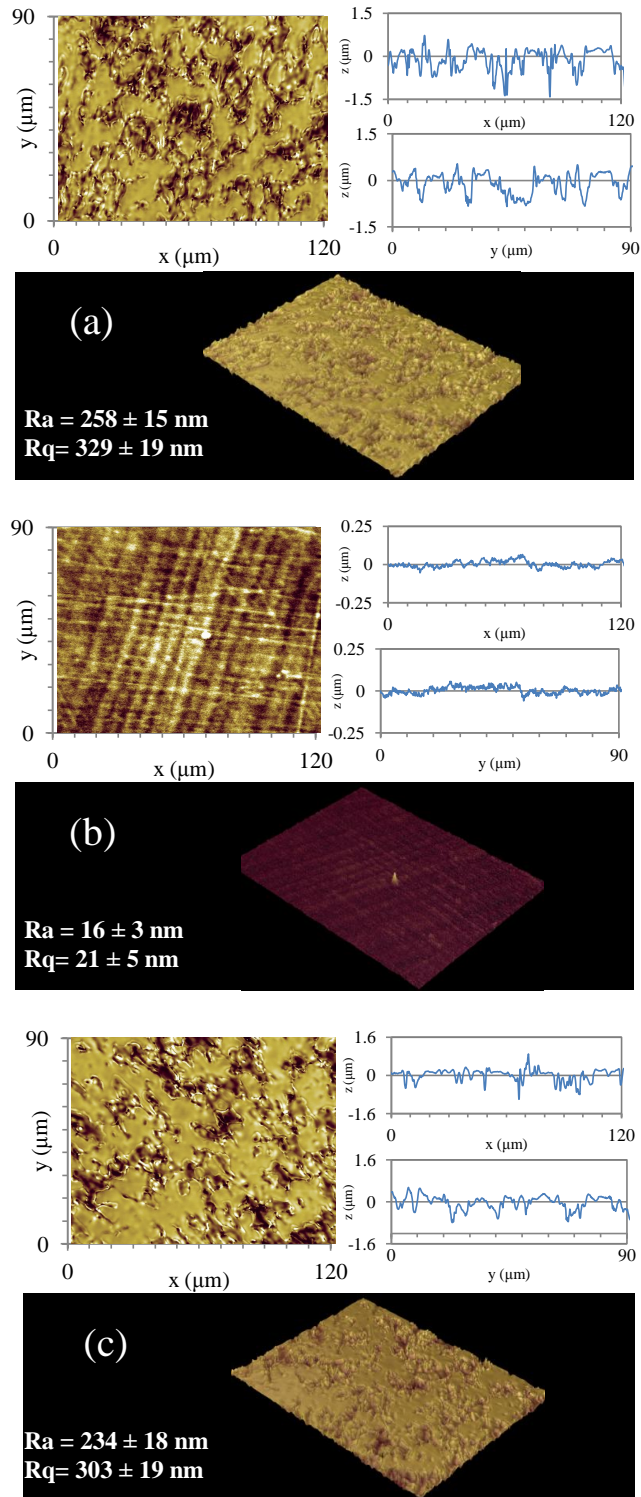


Figure 10.17: 2D and 3D images of the surface roughness and x and y profiles of untreated (a) TPO/0, (b) R/0 and (c) R/25 substrates.

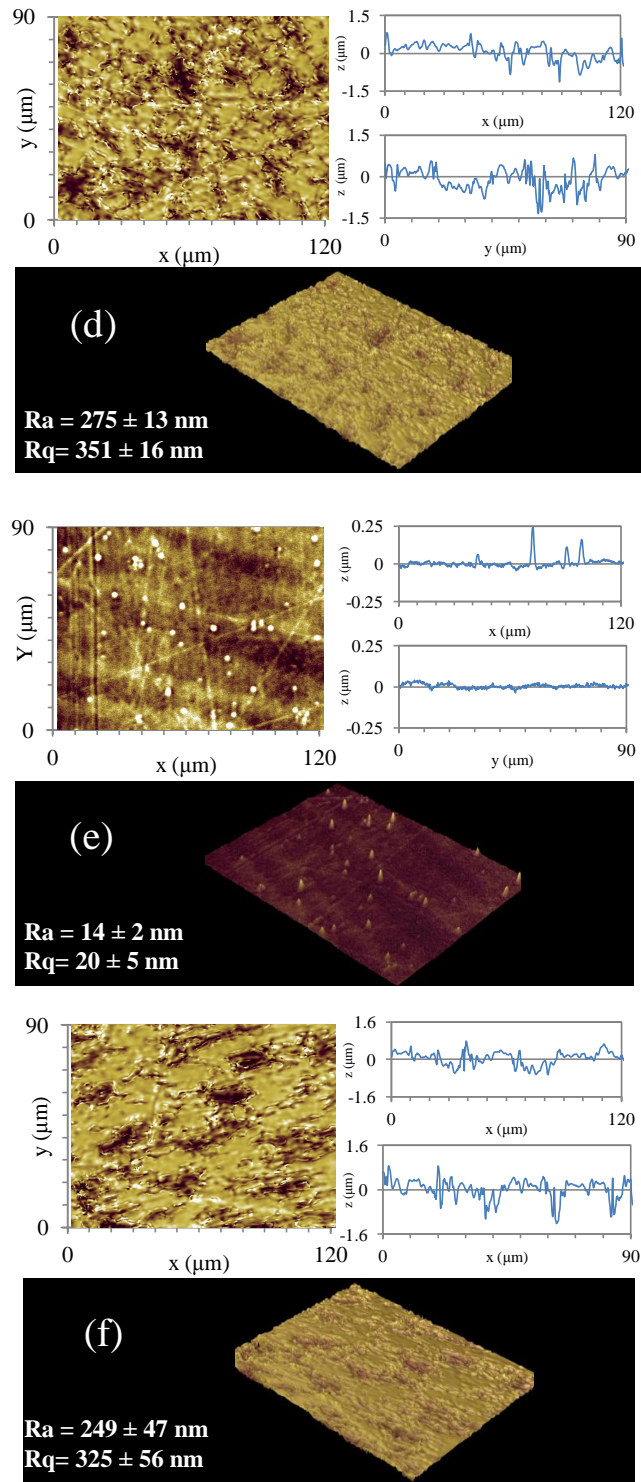


Figure 10.18: 2D and 3D images of the surface roughness and x and y profiles of solvent wiped (c) TPO/0, (d) R/0 and (e) R/25 substrates.

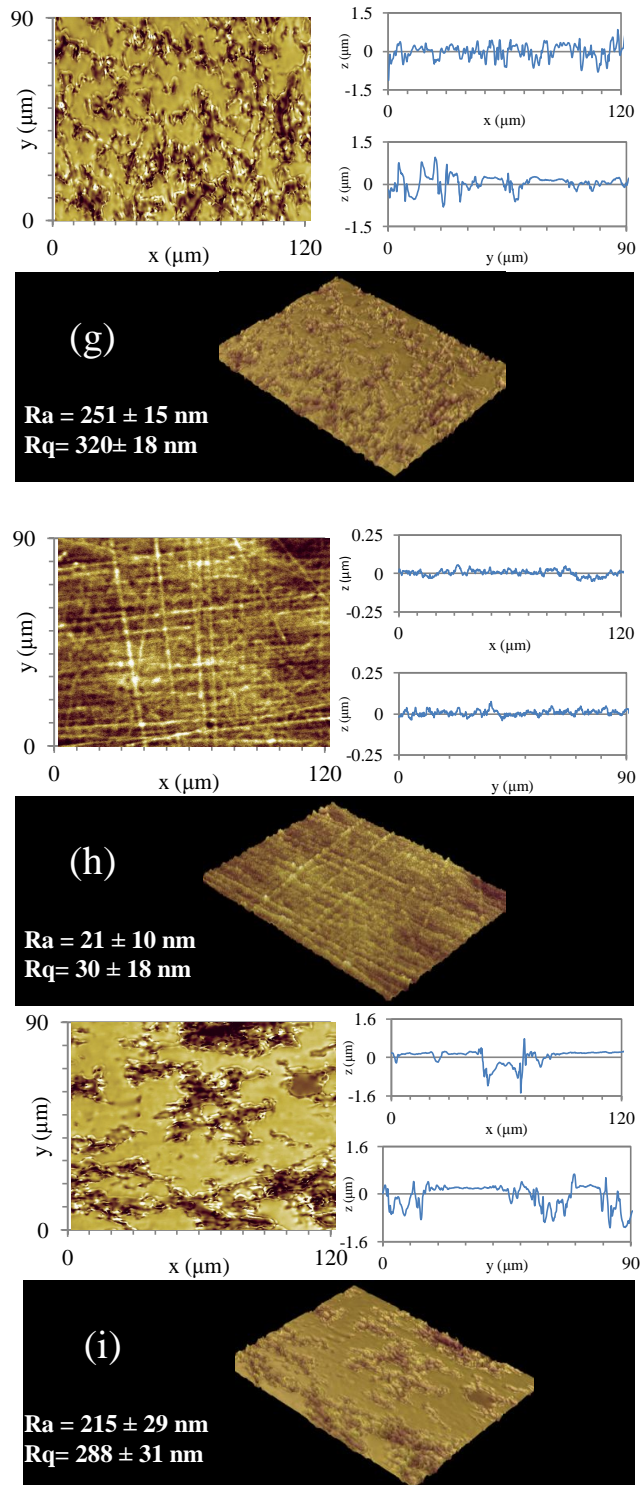


Figure 10.19: 2D and 3D images of the surface roughness and x and y profiles of non-abrasive solvent cleaned (c) TPO/0, (d) R/0 and (e) R/25 substrates.

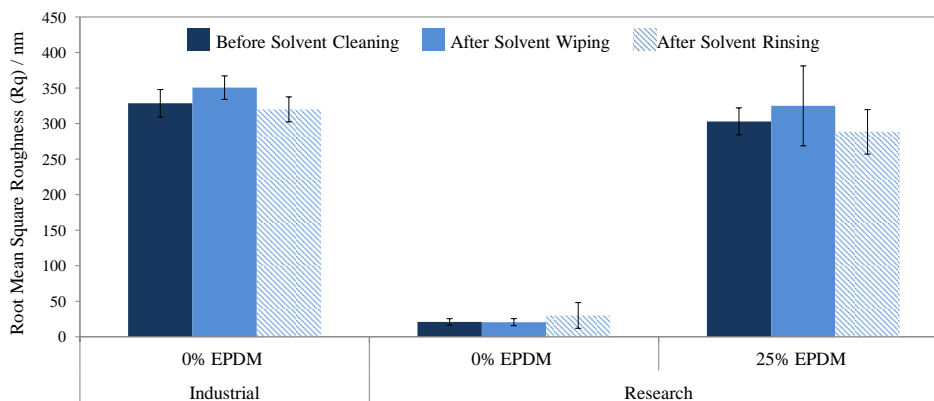


Figure 10.20: The effect of substrate cleaning on the Rq surface roughness parameter.

profile with a linear pattern on the surface (could be due the injection moulding direction of flow), whereas the TPO/0 and R/25 showed a rough crater-like surface profile. There was no indication that the crater-like features formed in the pattern of the injection mould direction, as they appeared uniform in both x and y directions. The increase in surface roughness with increased % of EPDM was likely to have a contributing factor to the adhesion mechanisms at the surface, by creating a greater contact area between the substrate and a waterborne basecoat or AP, as discussed in Appendix 10.F.1.

The surface roughness profiles of the substrates after the abrasive cleaning method, solvent wiping, are shown in Figure 10.18(d)-(f). There was no significant visual difference between the substrates before and after the wiping procedure for the TPO and the R/25 substrates. However, the R/0 substrate showed several peaks on the surface, possibly due to dirt that had been transferred during the wiping process.

The bar graph summarising Rq shown in Figure 10.20, reveals that for the TPO/0 and R/25 substrates, solvent wiping resulted in an average increase of Rq by 22 nm. However, the solvent wiping did not affect Rq (= 20 nm) of the R/0 substrate.

The SEM micrographs in Section 5.3 revealed that EPDM was present at the surface of R/25, therefore, the roughness results fitted well with the previous study, suggesting PP itself was not affected but it was the elastomer (EPDM) that induced a change in the surface roughness.<sup>66</sup> This was likely to be because of the density difference between EPDM and PP. The substrate hardness results in Appendix 10.F.3.1 revealed that EPDM had a

softening effect of the substrates. Therefore, it was likely that the solvent would penetrate into the EPDM more readily than the PP, inducing the change of the roughness. Also, the mechanical nature of the cleaning procedure could have induced physical changes of the softer EPDM domains present at the substrate surface.

It was expected that a similar scenario occurred for TPO/0, where it was not EPDM that induced the surface roughness change after solvent wiping, but the other additives that were present (described in Section 5.3).

As expected, the less abrasive technique of rinsing the TPO and R/25 substrates with solvent to avoid physical contact with the surface, lead to a smaller difference in Rq values from before and after cleaning, as shown in Figure 10.19(g) and (i). However, interestingly the Rq of R/0 increased after non-abrasive cleaning, which was likely to have resulted from partial contamination suggested by the large error bar shown in Figure 10.19(h). Nevertheless, the Rq of R/0 remained significantly lower than the Rq of TPO and R/25. Counter to the previous increase in the Rq value upon abrasive solvent wiping, a small decrease of Rq by 5 and 9 nm was observed for the TPO and R/25 substrates after non-abrasive cleaning. This was explained by the solvent rinsing step removing any dirt contamination from the surface, and the EPDM at the surface remaining unchanged due to the non abrasive nature of this cleaning step. Therefore, it was concluded that the mechanical changes induced by solvent wiping were the dominating factor for the changes observed for additive-containing substrates.

Based on the results, solvent wiping of the TPO and R/25 substrates was hypothesised to improve adhesion to waterborne coatings or APs, by increasing the surface roughness which increased the contact area, maximising reactions or interactions. However, non-abrasive solvent cleaning was expected to have no effect on the adhesive properties of the substrates due to the lack of change in surface roughness. Furthermore, neither cleaning method was expected to effect the adhesive properties of the R/0 substrate which did not change after cleaning.

## Appendix 10.G Candidate Adhesion Promoter Characterisation

### 10.G.1 Carbene Precursors

The three candidate APs used in this study (TPD, TPDOH and TPDCOOH) were purchased from TCI chemicals, as described in Section 3.4. To verify their purity and structure, analysis was performed with NMR, IR and UV-Vis spectroscopy as well as mass spectrometry.

Figure 10.21 shows the  $^1\text{H}$  and  $^{13}\text{C}$  NMR spectra for all three AP's. These spectroscopic techniques were used to clarify the AP structures by identifying the carbon-hydrogen framework. In the case of  $^1\text{H}$  NMR analysis, the presence of the aromatic protons was confirmed for all three AP's. The OH proton was also visible for TPDOH, however the signal was too weak to be detected for the TPDCOOH. Furthermore, the spectra measured suggested TPD and TPDCOOH had a purity  $>95\%$ , however, the spectra from TPDOH suggest the purity was lower at  $\sim 90 - 95\%$ . The  $^{13}\text{C}$  NMR spectra further confirmed the structures of the three AP's with successful assignments of all C atoms in each structure at the expected chemical shifts. Evidence of C-F coupling was observed from the carbon in the  $\text{CF}_3$  group, also assisting the assignment of the spectra.

To further clarify the AP's structure, IR spectra were measured as shown in Figure 10.22. Figure 10.22(a) shows the measured IR spectrum for the parent compound, TPD. The red overlay stick spectra shows the predicted IR spectrum, which helped to assign the absorptions specific to TPD. The Sadtler handbook<sup>225</sup> was also used to clarify the regions expected for the various functional groups.

Four regions of the spectrum identified the mono-substituted phenyl group: between  $2997 - 3146\text{ cm}^{-1}$ , CH stretching characteristic of a benzene ring was observed; weak overtones from the mono-substituted benzene were shown between  $1673 - 1978\text{ cm}^{-1}$ ; four characteristic absorptions highlighted as 1-4 in the insert in Figure 10.22(a) due to

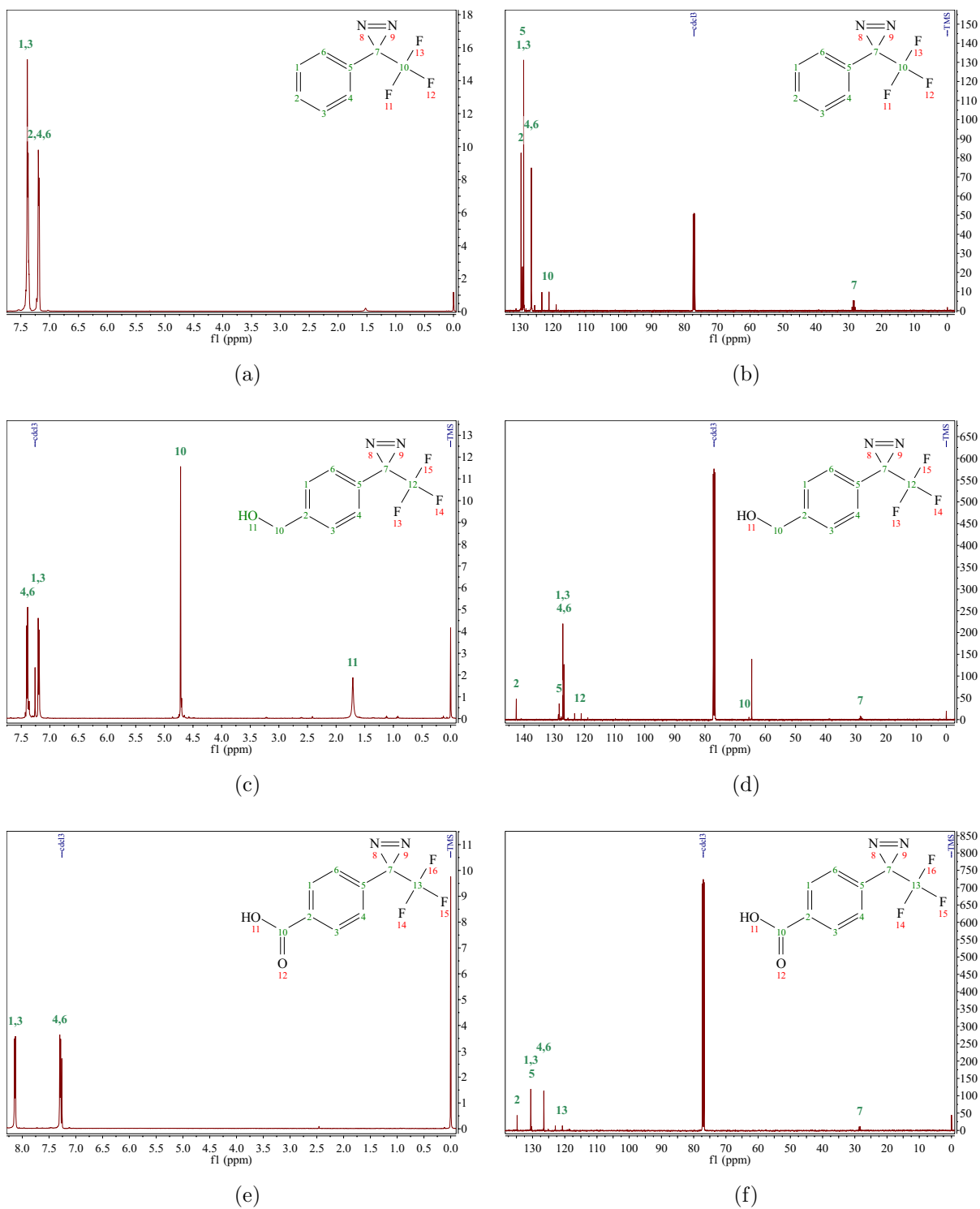


Figure 10.21: Plots of (a)  $^1\text{H}$  NMR of TP, (b)  $^{13}\text{C}$  NMR of TP, (c)  $^1\text{H}$  NMR of TPDOH, (d)  $^{13}\text{C}$  NMR of TPDOH, (e)  $^1\text{H}$  NMR of TPDCOOH and (f)  $^{13}\text{C}$  NMR of TPDCOOH.



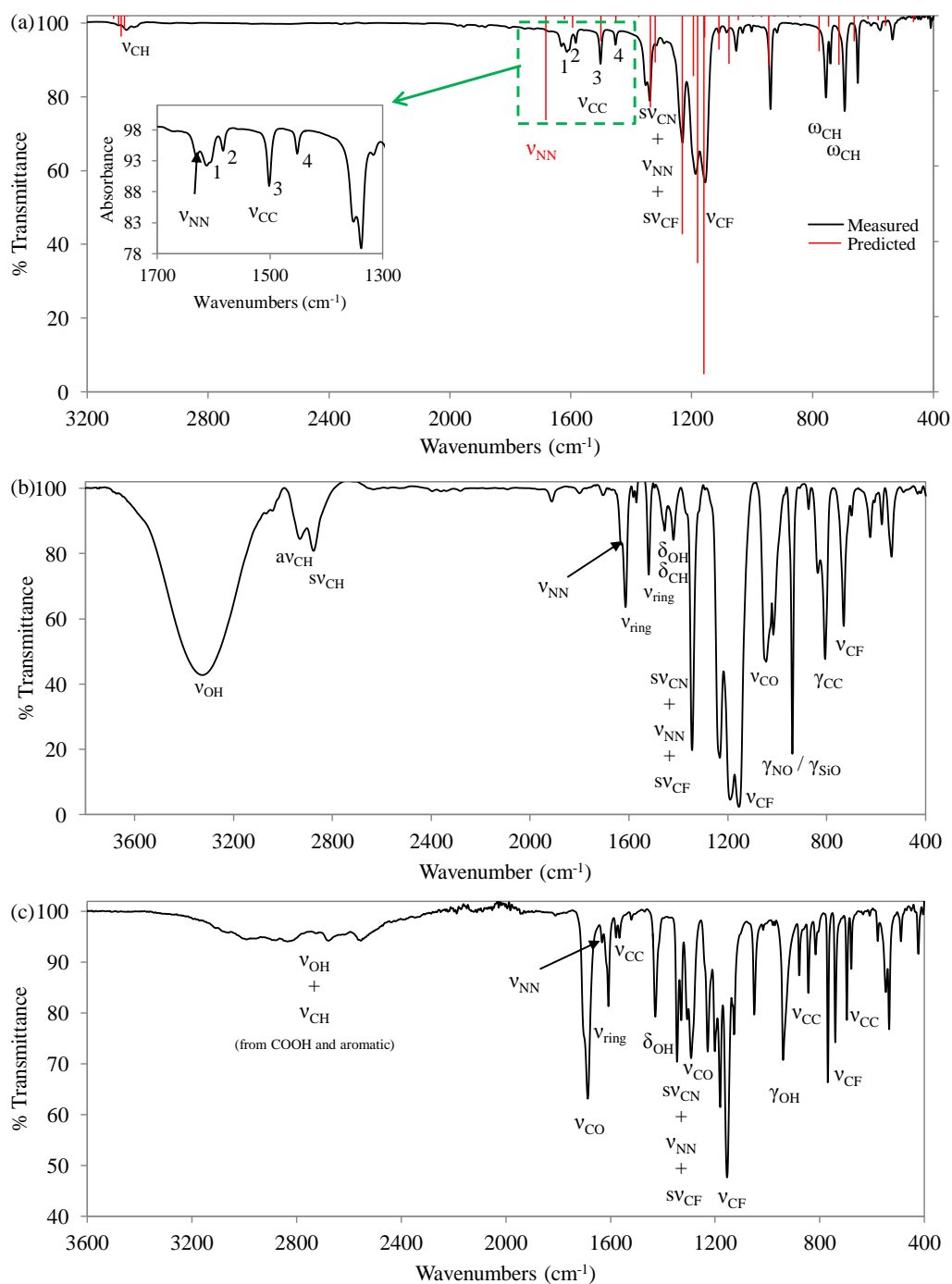


Figure 10.22: The IR spectra of (a) TPD, (b) TPDOH and (c) TPDCOOH. For TPD, the measured spectrum is shown in black, and the red overlay stick spectra shows the predicted IR spectrum. IR symbols: between 2 atoms:  $\nu$  = stretch; between 3 atoms:  $\delta$  = symmetric bending, a = anti-symmetric bending,  $\omega$  = out of plane bending/wagging,  $\rho$  = rocking; between 4 or more atoms:  $\tau$  = torque,  $\delta$  = in plane deformation and  $\gamma$  = out of plane deformation.

C=C in-plane vibrations were observed between 1449 - 1611  $\text{cm}^{-1}$ ; two absorptions at 693 and 755  $\text{cm}^{-1}$  were observed due to CH out-of-plane bending from the mono-substituted benzene.

TPDOH and TPDCOOH contain ortho-disubstituted benzene rings, changing the absorption of the overtones compared to TPD, and more noticeably the absorption of the out-of-plane CH bending. A characteristic peak for an ortho-disubstituted benzene ring was found at 805  $\text{cm}^{-1}$  for TPDOH and at 843  $\text{cm}^{-1}$  for TPDCOOH.

The presence of the OH group in TPDOH was confirmed with IR by the broad characteristic absorption due to the OH stretch at 3327  $\text{cm}^{-1}$ . Although still present, the OH absorption was found to be not as strong for TPDCOOH, and also interfered with CH stretching from the aromatic ring.

The N=N stretching frequency did not show at the absorption position expected from the predicted spectra. One plausible reason could be that the prediction did not take into account interactions with other TPD molecules and was made assuming one TPD molecule was present in vacuum. For comparison, an IR spectrum was measured of the diaziridine TPD parent compound, containing an HN-NH three-membered ring with C, which is oxidised to give the N=N three-membered ring in TPD. The absorption at 1631  $\text{cm}^{-1}$ , shown in the insert in Figure 10.22(a), was found to be the absorption that distinguished TPD from its parent molecule. Therefore, the absorption at 1631  $\text{cm}^{-1}$  was assigned to the N=N stretch, in agreement with the Infrared Characteristic Group Frequencies book.<sup>226</sup> The N=N stretch was found at 1632  $\text{cm}^{-1}$  for both TPDOH and TPDCOOH.

There was a strong unassigned absorption at 936  $\text{cm}^{-1}$  found in the TPDOH spectrum, shown in Figure 10.22(b). It was thought to be evidence of an oxime present (C=N-OH) from characteristic absorptions at 1616  $\text{cm}^{-1}$  due to C=N stretching, 936  $\text{cm}^{-1}$  due to N-O stretching and a broad OH band at  $\sim 3325$   $\text{cm}^{-1}$ , or evidence of silicone contamination due to Si-O stretching at 963  $\text{cm}^{-1}$ . The NMR spectra of TPDOH previously showed  $\sim 95$  % purity, therefore, these stretches could be due to small amounts of decomposed

TPDOH or silicone-containing contamination which was often found to be present during ToS-SIMS studies (discussed in Section 4.19).

The presence of the diazirine N=N group in the three AP's was further verified by UV-Vis spectroscopy. Several papers report UV-Vis as a good method to measure the presence of the N=N chromophore.<sup>135,227-229</sup> The results shown in Figure 10.23, verify this strong absorption observed at  $\sim 350 - 360$  nm.

A limited number of contradicting studies can be found on the electronic structure of diazirine molecules, particularly of TPD and its derivatives. Several papers studying various types of diazirines in the 1960's reported the transition observed in the UV-Vis spectrum from the N=N chromophore to be due to an n- $\pi^*$  transition, which was close in energy to a  $\pi$ - $\pi^*$  state,<sup>230-233</sup> although a recent 2009 paper by Blencowe *et al.*<sup>234</sup> contradict this and suggest the absorption from TPD derivatives was from the  $\pi$ - $\pi^*$  transition. A theoretical paper by Han *et al.*<sup>235</sup> in 1999 suggest the n- $\pi^*$  transition to be from the first excited state of a singlet carbene generated where as the  $\pi$ - $\pi^*$  transition is from the first excited state of a triplet carbene. To get an idea of the transition occurring, the electronic excited state of the carbenes generated from TPD, TPDOH and TPDCOOH were computationally calculated as described in Section 4.21.3. The results can be found in Appendix 10.L, and all three APs were predicted to generate triplet carbenes. Therefore, based on the theory by Han *et al.*,<sup>235</sup> a  $\pi$ - $\pi^*$  transition would occur during UV-Vis measurements.

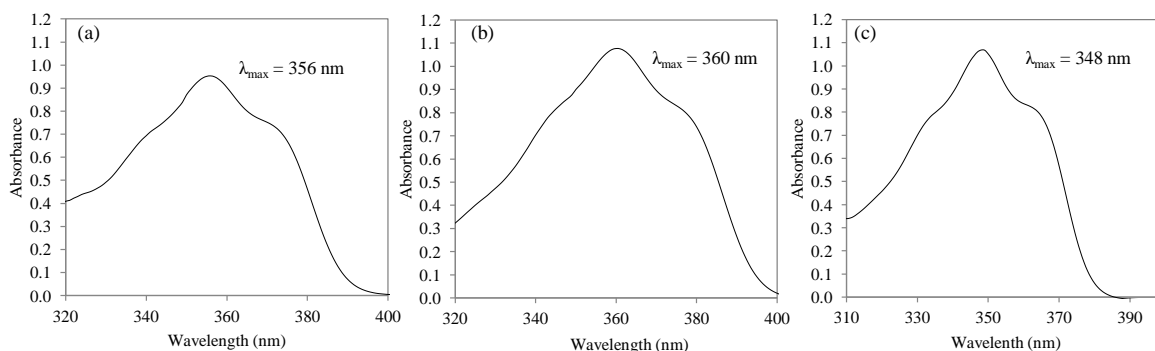


Figure 10.23: The UV-Vis spectra of 3 mM solutions of (a) TPD, (b) TPDOH and (c) TPDCOOH in toluene, measured at 25 °C.

The three AP's were distinguishable in UV-Vis by their maximum absorptions: TPD  $\lambda_{max} = 356$  nm; TPDOH  $\lambda_{max} = 360$  nm; TPDCOOH  $\lambda_{max} = 348$  nm.

Mass spectrometry was the final technique used to verify the structure of the three APs. Due to the high reactivity of the TPD molecules, a low ionisation technique was used for the prevention of decay or any side reactions, other than fragmentation. However, it was not possible to prevent heat generation during the measurement, which could have resulted in the decomposition of TPD. Nevertheless, the mass spectra shown in Figure 10.24 provided evidence of the intact-AP molecules, showing the molecular ion peaks for all three AP's (TPDCOOH also appeared protonated at  $m/z = 231$ ). Evidence of decomposition was also observed with the loss of  $N_2$  observed for all AP's. An isomer of TPD at  $m/z = 344$  was observed and a suggested structure is shown in Figure 10.24(a). The corresponding isomers were not observed for TPDOH and TPDCOOH. However, evidence of TPDOH and TPDCOOH clusters were observed in their spectra, with fragments up to three times the molecular ion mass observed for TPDOH and two times the molecular ion mass for TPDCOOH. Decomposition of the carboxylic acid in TPDCOOH with the loss of  $H_2O$  was also found.

All four characterisation techniques verified the structure of the three APs purchased. Therefore, further experiments were performed with the certainty of their structures.

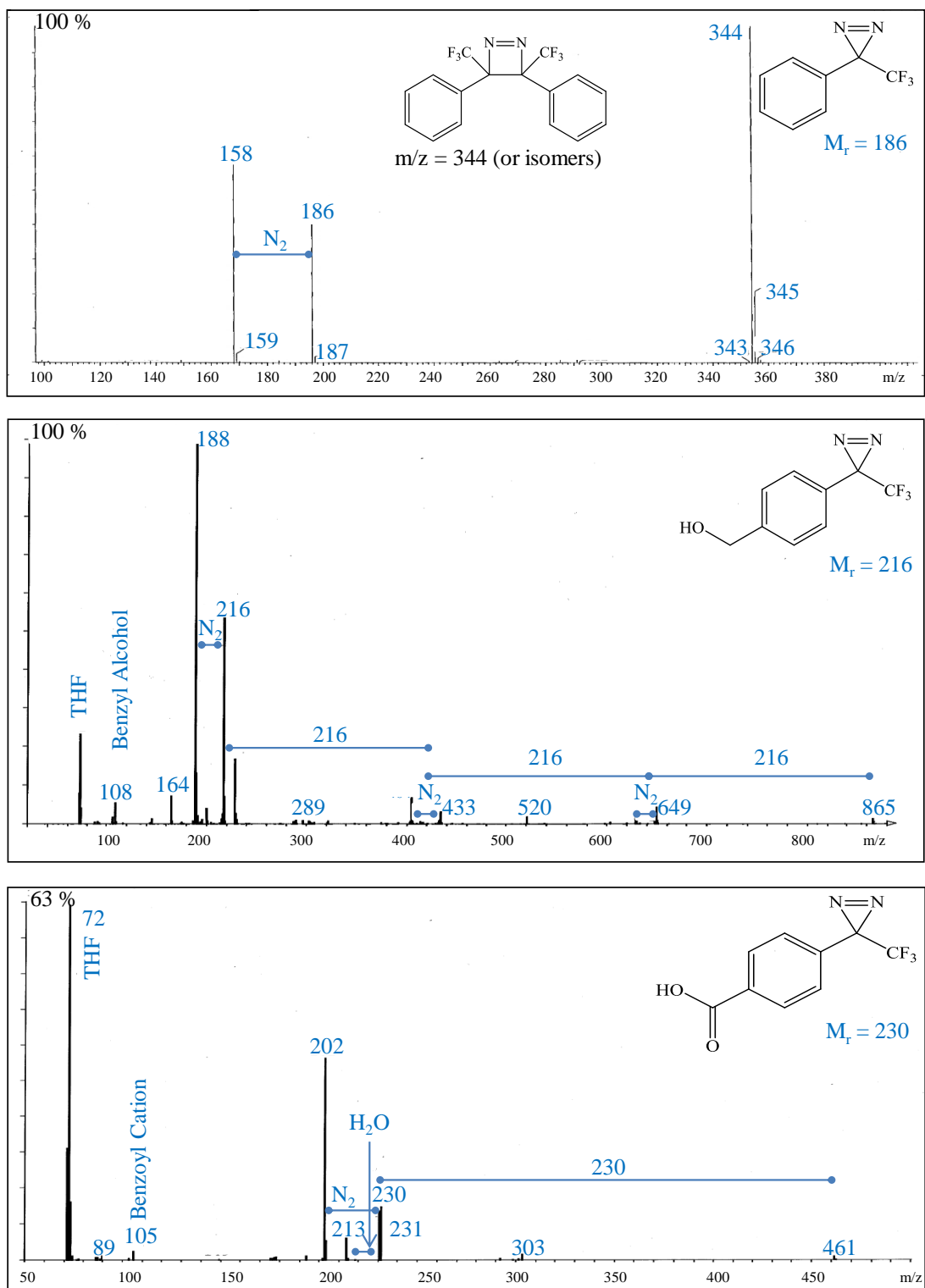


Figure 10.24: The mass spectra measured of (a) TPD, (b) TPDOH and (c) TPDCOOH.

## Appendix 10.H Self Assembled Monolayers (SAMs) on Gold Surfaces as Model Systems

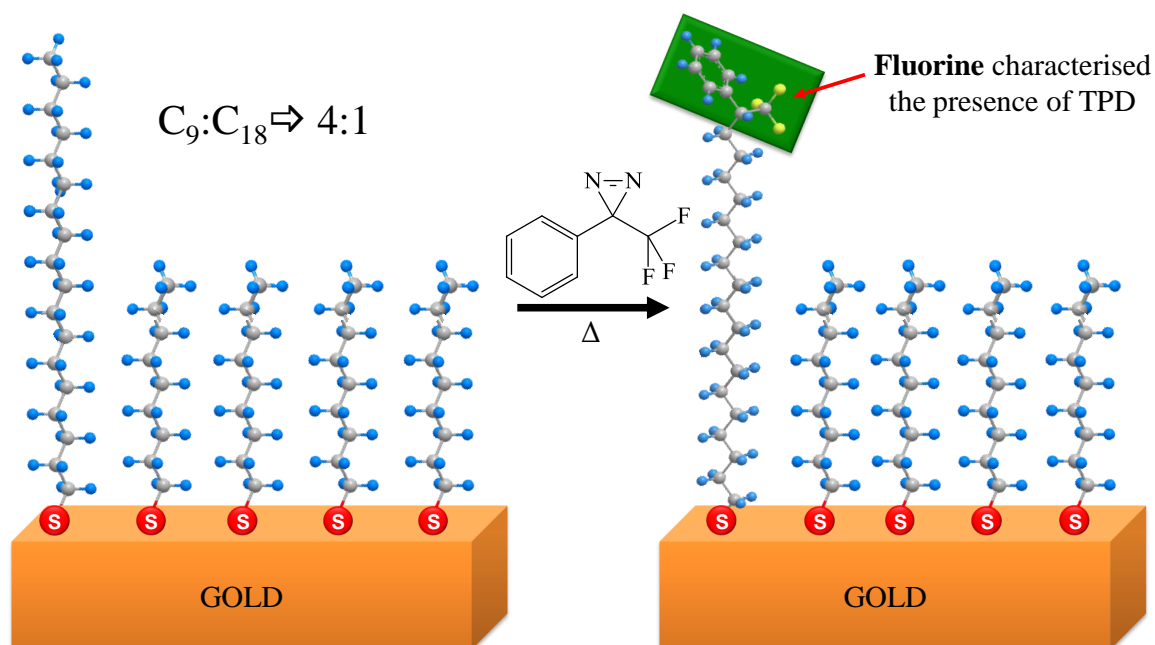


Figure 10.25: A schematic diagram showing a self assembled monolayer (SAM) covalently bonded to a gold surface (left). A mixture of alkyl thiols,  $C_9$  and  $C_{18}$ , in a ratio of 4:1 were used to form the SAM. After the TPD was thermally reacted with the SAM surface it was likely to graft to the exposed top part of the  $C_{18}$  chain due to less steric hindrances (right). The fluorine atoms of the  $CF_3$  group on the TPD moiety, chemically distinguished the TPD from the rest of the surface, and was used in ToF-SIMS and XPS to characterise the grafting efficiency.

Initially, a simple system using SAMs on a gold surface was used as a model to mimic a polyolefin surface, as shown in Figure 10.25. For a proof-of-concept study, the TPD candidate AP was grafted to the model surface. A mixture of alkyl thiols,  $C_9H_{20}S$  and  $C_{18}H_{38}S$ , in a ratio of 4:1 were used to form a SAM on a gold-coated silicon wafer, to be used as the model surface. The long alkyl chains were to mimic hydrophobic polymer chains found in PP-based substrates. The ratio was chosen so that upon SAM formation, the smaller proportion of  $C_{18}$  alkyl thiols would distribute across the gold surface amongst the larger proportion of  $C_9$  alkyl thiols (see Figure 10.26(b)) and provide an area of less steric hindrance where the upper part of the longer chains are exposed and more

susceptible to grafting with the TPD (by covalent bonding via C-H insertion).

However, it was shown in previous studies of mixed thiol SAMs that often the solution composition doesn't match the final SAM composition on the surface. The degree of order of the SAM composition and the degree of homogeneity can also vary, as demonstrated in Figure 10.26. This can be due to preferential adsorbance of a particular chain length due to lower solubility in the solution, a difference in diffusion time scales between the different chain lengths, and/or greater interactions between longer chains causing domains to form (larger dispersion forces between longer chains).<sup>236,237</sup> It was also demonstrated that a greater difference between the chain lengths lead to preferential adsorbance of the longer chain length,<sup>236</sup> therefore, the proportion of long chains in this study was kept small.

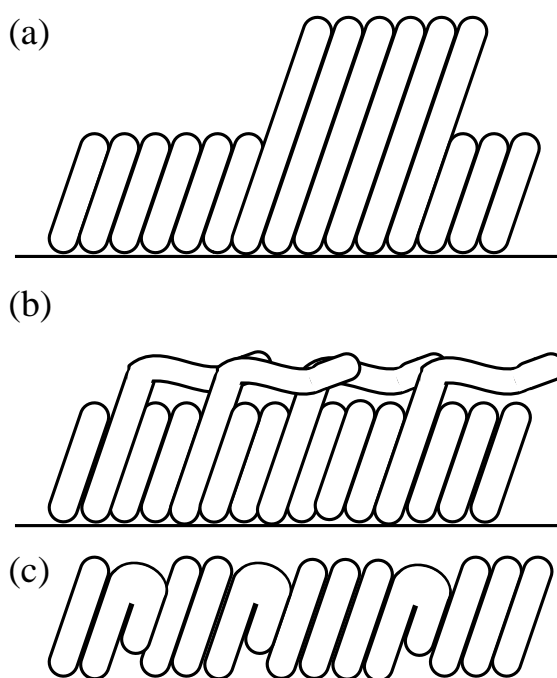


Figure 10.26: A schematic diagram showing three ways in which mixed chain length SAMs can form: (a) ordered, highly packed domains of alike chain lengths, (b) highly packed ordered chains at the surface and lower ordering diffuse chains at the outer surface with mixing of the two chain lengths and (c) a less packed, disordered surface where longer chains fold.

Furthermore, the so called "odd-even" effect was also taken into account, as it was previously shown that there is a difference between the tilt angle of SAMs formed from an odd or even number of CH<sub>2</sub> groups.<sup>238</sup> Therefore, a mixture of odd and even chain lengths were used in this study to influence the packing of the chains, the effect of which is to create a more diffuse surface due to the difference in tilt angles of C<sub>9</sub> (odd) and C<sub>18</sub> (even) chains which could aid the grafting of TPD (less steric hindrances at the surface, allowing better access for TPD to graft).

The SAMs formed were assumed to be well mixed, with a higher order of packing of the chains closer to the gold surface and a lower degree of order at the outer surface, where the extra chain length of the longer chains were assumed to be diffuse, as in Figure 10.26 (b). For the purpose of this study, it was sufficient to measure the average film thickness using ellipsometry, which gave a value of  $1.27 \pm 0.30$  nm. This value is between the film thickness formed by single C<sub>9</sub> (1.1 nm) SAM and a single a C<sub>18</sub> (2.0 nm) SAM, previously reported in literature,<sup>239</sup> concluding both the short and longer chains were present.

To verify the SAM formation, ToF-SIMS spectra of the gold substrate before and after SAM formation were measured. Both positive and negative spectra were measured, however, the negative spectra gave the most useful information. This was because the electronegativity of sulphur (from the SAM) favoured negative ion formation. The negative spectra of the surface after SAM formation is shown in Figure 10.27, highlighting several characteristic peaks.<sup>240</sup>

In the low mass region of the negative spectrum, small fragmentations of CH<sup>-</sup> ( $m/z = 13$ ), C<sub>2</sub>H<sup>-</sup> ( $m/z = 25$ ), S<sup>-</sup> ( $m/z = 32$ ) and SH<sup>-</sup> ( $m/z = 33$ ) were enhanced after the SAM formation. The small intensity of these peaks on the plasma cleaned gold surface indicated a low hydrocarbon and sulphur contamination, often found on cleaned gold surfaces once they are exposed to a laboratory atmosphere. However, the enhancement of the these peaks after the SAM formation indicated the presence of the organosulphur molecules from the SAM. The positive spectra also indicated the presence of the SAM through the enhancement of hydrocarbon fragmentation peaks (C<sub>x</sub>H<sub>y</sub><sup>+</sup>), particularly of CH<sub>3</sub><sup>+</sup> ( $m/z =$



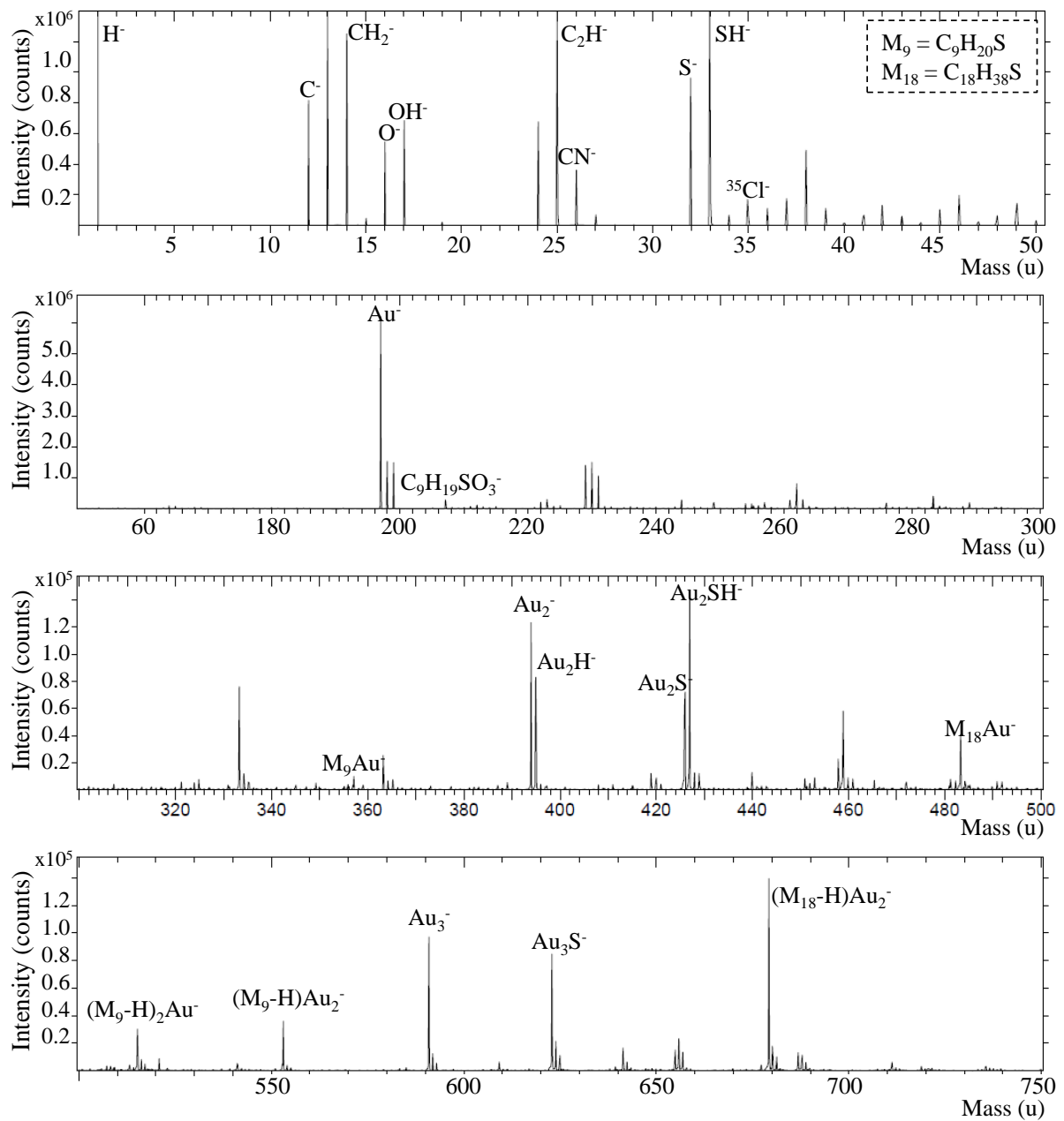


Figure 10.27: Regions of the negative ion ToF-SIMS spectrum of the mixed thiol ( $C_9:C_{18} \rightarrow 4:1$ ) SAM on a gold surface, after 24 hours of adsorption, highlighting the characteristic peaks.

15) due to the methyl terminating groups at the surface from the alkanethiols of the SAM. In the negative spectra in Figure 10.27, the strong peak due to gold was still observed after the SAM formation at  $m/z = 197$ , as well as gold clusters ( $\text{Au}_2^-$  and  $\text{Au}_3^-$  at  $m/z = 394$  and  $591$ ) and several gold-sulphur fragments such as  $\text{Au}_2\text{S}^-$  ( $m/z = 426$ ) and  $\text{Au}_2\text{SH}^-$  ( $m/z = 427$ ).

The smaller fragments merely indicated the presence of the alkanethiols, but it was the larger peaks at higher  $m/z$  values due to fragmentations of the intact thiol molecules that proved the SAM formation (alkanethiols covalently bonded to the gold surface) and the presence of both chain lengths, as shown in Figure 10.27. The fragment  $\text{M}_9\text{Au}^-$ , (denoting  $\text{M}_9$  as  $\text{C}_9\text{H}_{20}\text{S}$ ) is shown at  $m/z = 357$ , due to the intact smaller chain bonded to gold, and likewise the fragment  $\text{M}_{18}\text{Au}^-$ , (denoting  $\text{M}_{18}$  as  $\text{C}_{18}\text{H}_{38}\text{S}$ ) is shown at  $m/z = 483$ , due to the intact larger chain bonded to gold. The smaller chain clusters with gold,  $(\text{M}_9\text{-H})\text{Au}_2^-$  and the larger chain clusters with gold,  $(\text{M}_{18}\text{-H})\text{Au}_2^-$  were also found at  $m/z = 553$  and  $679$  respectively, as was the smaller chain dimer,  $(\text{M}_9\text{-H})_2\text{Au}^-$  at  $m/z = 515$ . This proves not only were the thiols covalently bonded to the gold, but also that both chain lengths were present in the SAM formed. The intensity of the dimer suggests the surface is almost fully covered with a packed SAM with the chains in a vertical orientation, as described in a previous study by Houssiau *et al.*<sup>240</sup> The mass spectral range was not measured high enough to see evidence of the longer chain dimer, however, the intensity would likely be lower due to the smaller amount of longer chains present in the SAM. At higher mass ranges, trimers formed with gold could also be possible, further demonstrating the packing of the SAM.<sup>240</sup>

SAM oxidation was also evident, indicated by the presence of the fragment  $\text{C}_9\text{H}_{19}\text{SO}_3^-$  at  $m/z = 207$  (the Au-S bond is attacked by oxygen atoms<sup>241</sup>) and the large intensity of  $\text{O}^-$  and  $\text{OH}^-$  at  $m/z = 16$  and  $17$  respectively.

## Appendix 10.I Lowest Energy Conformers of Diaziridine and Diazirine (TPD)

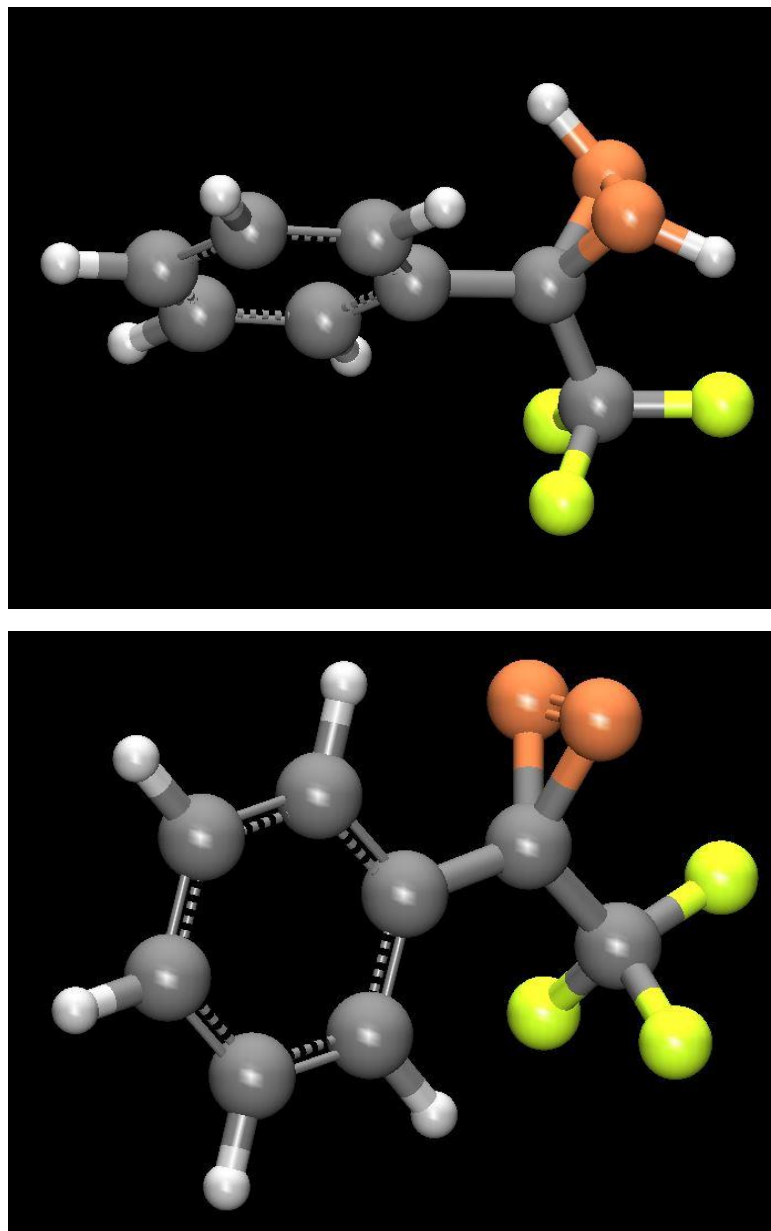


Figure 10.28: Optimised lowest energy conformers of diaziridine (top) and diazirine (=TPD) (bottom), used to calculate the predicted IR spectra.

## Appendix 10.J Predicted IR Sprectra of Diaziridine

| Mode | Symmetry | Wave Number cm <sup>-1</sup> | Intensity | Mode | Symmetry | Wave Number, cm <sup>-1</sup> | Intensity |
|------|----------|------------------------------|-----------|------|----------|-------------------------------|-----------|
| 1    | 0        | 0                            | -         | 31   | a        | 933.31                        | 22.84497  |
| 2    | 0        | 0                            | -         | 32   | a        | 966.15                        | 0.48498   |
| 3    | 0        | 0                            | -         | 33   | a        | 986.04                        | 0.31049   |
| 4    | 0        | 0                            | -         | 34   | a        | 986.83                        | 0.26203   |
| 5    | 0        | 0                            | -         | 35   | a        | 1027                          | 7.62908   |
| 6    | 0        | 0                            | -         | 36   | a        | 1073.63                       | 6.49057   |
| 7    | a        | 23.95                        | 0.06543   | 37   | a        | 1106.08                       | 94.26706  |
| 8    | a        | 58.64                        | 0.03708   | 38   | a        | 1135.76                       | 157.50703 |
| 9    | a        | 103.28                       | 0.20502   | 39   | a        | 1141.65                       | 13.21429  |
| 10   | a        | 170.55                       | 0.31125   | 40   | a        | 1151.87                       | 180.15728 |
| 11   | a        | 217.41                       | 1.35438   | 41   | a        | 1157.94                       | 141.55443 |
| 12   | a        | 262.85                       | 1.23431   | 42   | a        | 1166.17                       | 46.05562  |
| 13   | a        | 292.88                       | 0.96494   | 43   | a        | 1177.28                       | 38.78034  |
| 14   | a        | 314.83                       | 0.72774   | 44   | a        | 1199.38                       | 141.1364  |
| 15   | a        | 362.23                       | 5.53319   | 45   | a        | 1286.08                       | 28.19098  |
| 16   | a        | 404.74                       | 0.17067   | 46   | a        | 1317.9                        | 16.15407  |
| 17   | a        | 411.86                       | 0.29064   | 47   | a        | 1364.8                        | 6.23181   |
| 18   | a        | 472.31                       | 1.8509    | 48   | a        | 1378.46                       | 20.09229  |
| 19   | a        | 519.03                       | 6.7056    | 49   | a        | 1398.54                       | 13.5927   |
| 20   | a        | 557.01                       | 6.01291   | 50   | a        | 1444.52                       | 5.082     |
| 21   | a        | 604.38                       | 2.01059   | 51   | a        | 1491.17                       | 7.88882   |
| 22   | a        | 613.09                       | 1.24986   | 52   | a        | 1595.59                       | 0.82953   |
| 23   | a        | 634.2                        | 20.06218  | 53   | a        | 1618.91                       | 0.66102   |
| 24   | a        | 700.39                       | 34.34527  | 54   | a        | 3091.46                       | 0.09873   |
| 25   | a        | 715.16                       | 10.67562  | 55   | a        | 3102.02                       | 11.62715  |
| 26   | a        | 759.96                       | 16.67937  | 56   | a        | 3113.15                       | 15.29509  |
| 27   | a        | 812.95                       | 2.09763   | 57   | a        | 3126.59                       | 3.95369   |
| 28   | a        | 840.72                       | 0.41982   | 58   | a        | 3130.79                       | 2.83232   |
| 29   | a        | 862.21                       | 17.61979  | 59   | a        | 3277.46                       | 1.07786   |
| 30   | a        | 917.57                       | 15.25767  | 60   | a        | 3306.31                       | 7.10149   |

Figure 10.29: IR vibrational spectrum output from control file of Diaziridine

## Appendix 10.K Predicted IR Sprectra of Diazirine (TPD )

| Mode | Symmetry | Wave Number cm <sup>-1</sup> | Intensity | Mode | Symmetry | Wave Number cm <sup>-1</sup> | Intensity |
|------|----------|------------------------------|-----------|------|----------|------------------------------|-----------|
| 1    | 0        | 0                            | -         | 28   | a        | 864.16                       | 0.40827   |
| 2    | 0        | 0                            | -         | 29   | a        | 910.8                        | 0.11312   |
| 3    | 0        | 0                            | -         | 30   | a        | 929.66                       | 32.91528  |
| 4    | 0        | 0                            | -         | 31   | a        | 953.69                       | 0.44715   |
| 5    | 0        | 0                            | -         | 32   | a        | 983.14                       | 0.14576   |
| 6    | 0        | 0                            | -         | 33   | a        | 983.23                       | 0.03399   |
| 7    | a        | 12.4                         | 0.01893   | 34   | a        | 1032.4                       | 2.46951   |
| 8    | a        | 60.8                         | 0.12007   | 35   | a        | 1063.86                      | 31.46868  |
| 9    | a        | 123.43                       | 0.09125   | 36   | a        | 1097.75                      | 22.02153  |
| 10   | a        | 133.92                       | 0.62525   | 37   | a        | 1145.9                       | 14.0319   |
| 11   | a        | 227.56                       | 1.07858   | 38   | a        | 1148.55                      | 237.84775 |
| 12   | a        | 253.32                       | 1.08038   | 39   | a        | 1169.87                      | 163.98502 |
| 13   | a        | 313.21                       | 0.54211   | 40   | a        | 1184                         | 39.65147  |
| 14   | a        | 326.14                       | 0.48139   | 41   | a        | 1221.27                      | 144.82524 |
| 15   | a        | 365.21                       | 0.54212   | 42   | a        | 1313.16                      | 30.58312  |
| 16   | a        | 398.85                       | 0.01041   | 43   | a        | 1329.27                      | 60.54378  |
| 17   | a        | 435.28                       | 0.8971    | 44   | a        | 1368.66                      | 0.50716   |
| 18   | a        | 440.82                       | 3.7604    | 45   | a        | 1445.86                      | 3.15285   |
| 19   | a        | 535.06                       | 6.30241   | 46   | a        | 1496.29                      | 16.52787  |
| 20   | a        | 559.93                       | 2.60523   | 47   | a        | 1591.83                      | 7.49672   |
| 21   | a        | 594.6                        | 1.77371   | 48   | a        | 1619.32                      | 2.08003   |
| 22   | a        | 611.55                       | 0.02023   | 49   | a        | 1682.14                      | 68.97216  |
| 23   | a        | 641.01                       | 16.59432  | 50   | a        | 3095.66                      | 0.05604   |
| 24   | a        | 692.57                       | 32.10916  | 51   | a        | 3105.29                      | 8.60974   |
| 25   | a        | 727.44                       | 6.77702   | 52   | a        | 3116.27                      | 13.40557  |
| 26   | a        | 759.48                       | 23.18838  | 53   | a        | 3124.98                      | 5.75669   |
| 27   | a        | 823.7                        | 0.46838   | 54   | a        | 3141.89                      | 1.58023   |

Figure 10.30: IR vibrational spectrum output from control file of Diazirine

## Appendix 10.L Predicted Excited States of TPD, TP- DOH and TPDCOOH

| Molecule | Geometry Optimization - both individually [atomic units (au)] |             | T-S [kJ mol <sup>-1</sup> ] | MSSCF (frozen 11, closed 37 (total occupied: 40)) | MSSCF (frozen 11, closed 37 (total occupied: 40)) | T-S [kJ mol <sup>-1</sup> ] |
|----------|---|-------------|-----------------------------|---|---|-----------------------------|
|          | Singlet (S)   | Triplet (T) |                             | Singlet (S)                                       | T-S [kJ mol <sup>-1</sup> ]                       |                             |
| TPD      | -606.833  | -606.848    | -38.2                       | -603.685  | -603.696  | -27.0                       |
| TPDOH    | -721.273  | -721.285    | -32.2                       | -717.490  | -717.496  | -15.3                       |
| TPDCOOH  | -795.282  | -795.300    | -47.1                       | -791.156  | -791.168  | -32.4                       |

Figure 10.31: Predicted electronic excited states of TPD, TPDOH and TPDCOOH. The energy of the optimised states is given in atomic units (au). The difference between the excited states was converted from the atomic unit of energy, called Hartree: 1 Hartree = 2625.5 kJ/mol. Geometry optimisation method = BP86/def2-SV(P).

## Appendix 10.M Adhesion Promoter Synthesis

### 10.M.1 Synthesis of 3-phenyl-3-(trifluoromethyl)-3H-diazirine (or TPD)

Figure 10.32 shows the synthesis steps for the synthesis of 3-phenyl-3-(trifluoromethyl)-3H-diazirine (TPD). Each step is described below.

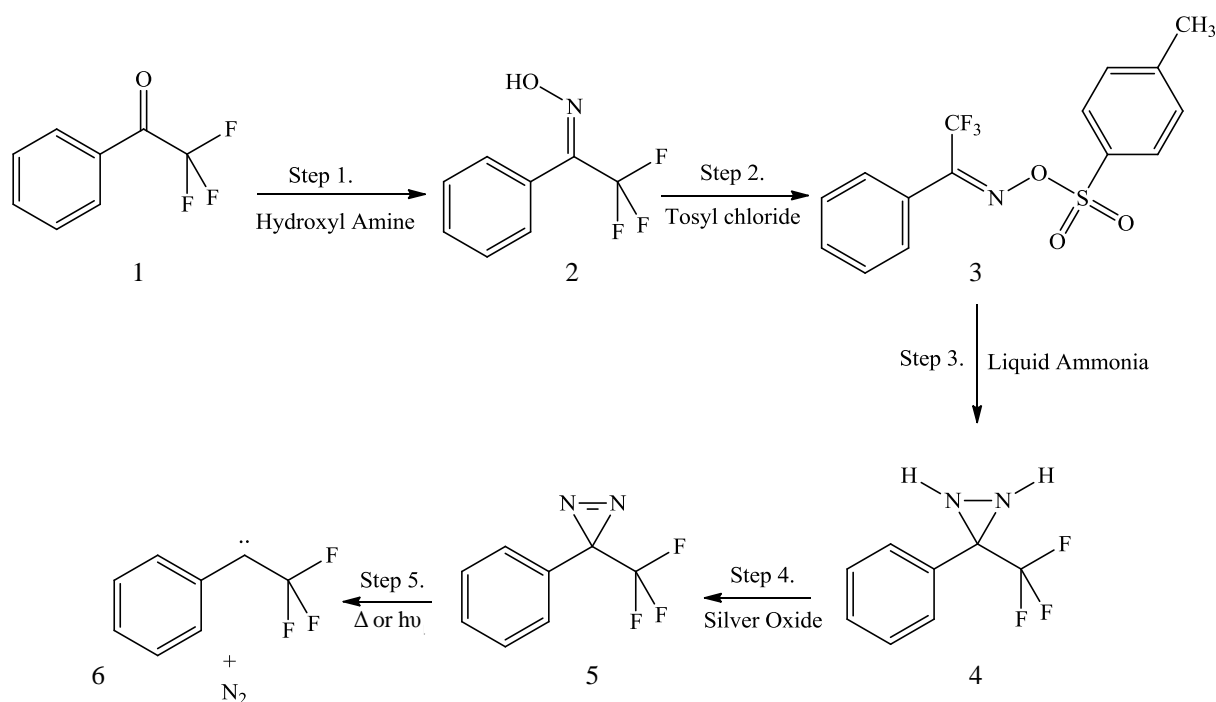


Figure 10.32: Reaction scheme for synthesis of 3-phenyl-3-(trifluoromethyl)-3H-diazirine (or TPD)

#### 10.M.1.1 Step 1: 2,2,2-trifluoro-1-phenylethanone oxime (2) from 2,2,2-trifluoro-1-phenylethanone (1)

2,2,2-trifluoro-1-phenylethanone (1) (ALFA AESAR, VWR) (20.9 g, 0.12 mol) and 9.17 g (0.13 mol) of hydroxyl ammonium chloride were dissolved in 120 ml ethanol. The pH was continuously adjusted to 5 with a 4 M NaOH solution whilst refluxing the mixture for 5 hours. Precipitated sodium chloride was removed by filtration, washed with 10 ml

of ethanol and the filtrates evaporated to dryness. The residue was dissolved in 400 ml ethyl acetate and extracted 3 times with water (400 ml) before being dried with Na<sub>2</sub>SO<sub>4</sub>. Evaporation of the solvent yielded the crude 2,2,2-trifluoro-1-phenylethanone oxime (2) in 86 % yield, <sup>1</sup>H NMR (CDCl<sub>3</sub>): 2.1 (OH), 7.5-7.6 (aromatic). Chemical analysis calculated for C<sub>8</sub>H<sub>6</sub>F<sub>3</sub>NO (%): C (50.8); H(3.2); N (7.4); F (30.1); O (8.5) and chemical analysis measured (%):C (50.6); H(3.4); N (7.5); F (30.0); O (8.4).

#### 10.M.1.2 Step 2: 2,2,2-trifluoro-1-phenylethanone O-tosyl oxime (3) from (2)

Oxime (2) (19.5 g, 0.10 mol) and 23.11 g (0.12 mol) p-toluenesulphonylchloride were dissolved in 200 ml pyridine and refluxed for 6 hours. The solvent was removed at reduced pressure, and the remaining solid was dissolved in 300 ml ethyl acetate to give pH = 5. The solution was extracted with water (1x 100 ml) to give pH = 3, 0.1 M HCl (2 x 50 ml) to give pH = 1 and a concentrated solution of NaHCO<sub>3</sub> (2 x 50 ml) to give pH = 10. The organic layer was dried over Na<sub>2</sub>SO<sub>4</sub>. Evaporation of the solvent yielded the crude tosylate (3). To purify the oxime, 3 g (9 mmol) of crude tosylate (3) was dissolved in 45 ml toluene and lightly stirred in a water bath at 58 °C. 50 ml of cyclohexane was added to the solution dropwise to afford the recrystallised product precipitate from the solution. Yield: 75 % based oxime (26.5 g); <sup>1</sup>H NMR (CDCl<sub>3</sub>): 2.4 (CH<sub>3</sub>), 7.2-7.8 (aromatic). Chemical analysis calculated for C<sub>15</sub>H<sub>12</sub>NO<sub>3</sub>F<sub>3</sub>S (%): C (52.5); H(3.5); N (4.1); O (14.0); F (17.1); S (9.3) and chemical analysis measured (%):C (52.7); H(3.6); N (4.0); O (14.0); F (17.1); S (9.5).

#### 10.M.1.3 Step 3: 3-phenyl-3-(trifluoromethyl)diaziridine (4) from (3)

2,2,2-trifluoro-1-phenylethanone O-tosyl oxime (3) (14.0 g, 0.04 mol) was dissolved in 80 ml THF and cooled to -78 °C using dry ice. The apparatus used for the addition of liquid ammonia is shown in Figure 10.33. Approximately 6 ml of liquid ammonia was added and the mixture stirred in the flask at room temperature for 12 hours, allowing the gas to be leave through the pressure release system built. The crystallised p-toluenesulfonylamide



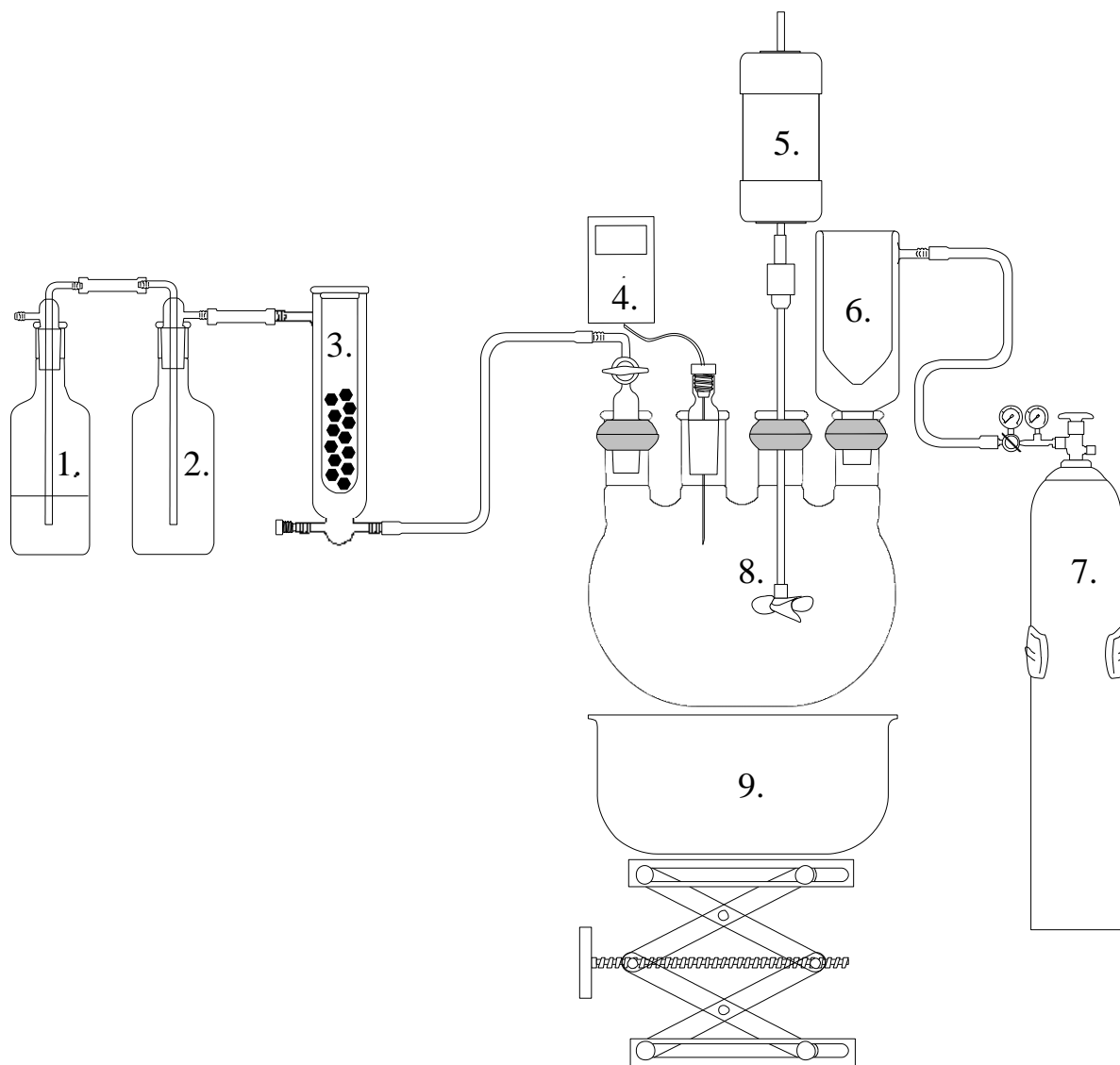


Figure 10.33: Reaction set-up for addition of liquid ammonia to reaction mixture: 1. Gas release bottle containing acetic acid (50 % in water); 2. Empty safety pressure release (in case acid jumps from other bottle under pressure); 3. Over pressure release (containing metal balls to maintain pressure); 4. Thermometer; 5. Mechanical stirrer; 6. Cold finger (containing dry ice,  $-78.5\text{ }^{\circ}\text{C}$ ); 7. Ammonia gas cylinder; 8. 4-necked round bottomed flask containing reaction dispersion; 9. Dish filled with dry ice & acetone to maintain cold reaction dispersion and keep ammonia in its liquid phase as long as possible.

was removed by filtration and washed with THF. The remaining solution was dissolved in 100 ml ethyl acetate, and the organic phase was extracted twice with water (2 x 50 ml) and dried over Na<sub>2</sub>SO<sub>4</sub>. Evaporation of the solvent yielded a red/orange oil (4), which crystallised overnight at room temperature. To purify the crude product, it was dissolved in a minimum amount of cyclohexane using a water bath at 45 °C (mp is 30 – 33 °C, therefore, product was melted) and then the solution was allowed to cool to room temperature, allowing clean crystal formation. The crystals were filtered and dried. Crude yield = 9.08 g (containing starting material and product, 118 %), recrystallised product (purified) = 4.92 g (64 %); <sup>1</sup>H NMR (CDCl<sub>3</sub>): 4.03 and 4.14 (AB-system, J=8 Hz, 2H), 7.4-7.6 (multiplet, 5H). Chemical analysis calculated for C<sub>8</sub>H<sub>7</sub>N<sub>2</sub>F<sub>3</sub>(%): C (51.1); H(3.8); N (14.9); F (30.3) and chemical analysis measured (%):C (51.3); H(4.0); N (14.3); F (30.1) [evidence of O (<0.5 %) was also observed].

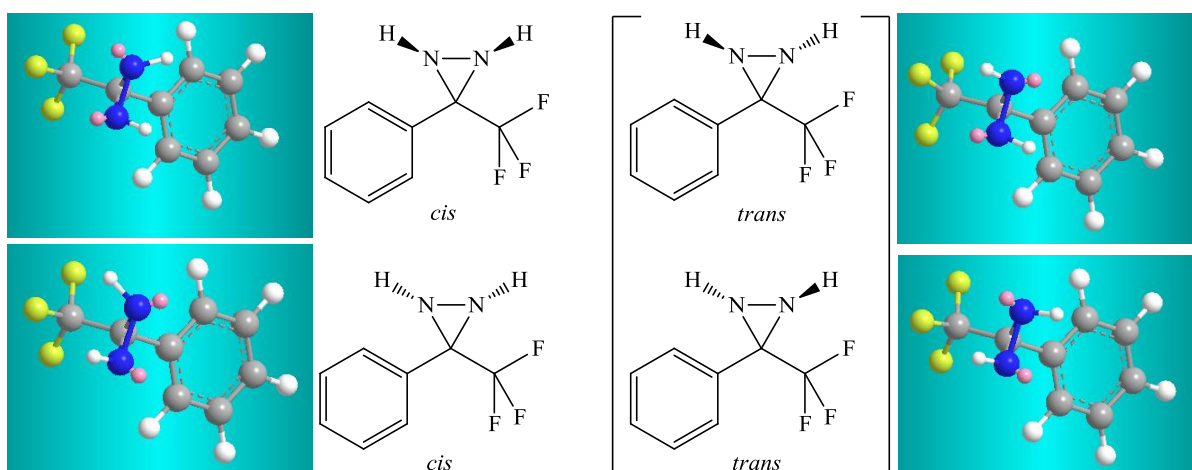


Figure 10.34: Possible stereoisomers of 2,2,2-Trifluoromethyl-3-phenyldiaziridine. 3D images: energy minimisation ran through chemBio3D version 12.0, using implemented MM2 energy minimise option (pink sphere = lone pair of electrons, yellow = fluorine, blue = nitrogen, white = hydrogen, grey = carbon).

#### 10.M.1.4 AB System

The AB quartet system observed from the NH protons was found to be due to a *trans* stereoisomer shown in Figure 10.34. Figure 10.35 shows the <sup>1</sup>H NMR, highlighting the NH protons, which were confirmed by a D<sub>2</sub>O shake (in which the NH protons were substituted

by deuterium, resulting in the loss of the NH resonance signals). The coupling between the HH protons and the aromatic protons was confirmed with 2D COSY, whilst the 2D NOSEY spectrum assessed the stereo information of the diaziridine and showed a strong nuclear overhauser effect (NOE) signal between an *ortho* (*o*-) aromatic H and only 1 NH proton. Therefore, this NH and *o*-H were within a 5 Å proximity (limit for an NOE detection) and the distance between the other NH proton and aromatic protons was greater, suggesting a *trans* isomer as shown in the 3D diagrams in Figure 10.34.

AB quartet systems are often observed when two protons couple to one-another, and the difference in coupling constant ( $J_{AB}$ ) is negligible compared to the difference in chemical shift ( $d_{AB}$ ). The AB quartet is described by second order arithmetic and  $J_{AB}$  was calculated to be 8.18 Hz (average). Coalescence, defined as the temperature at which the appearance of the spectrum changes from that of two separate peaks to a single peak, was not observed at temperatures up to 120 °C. Two well resolved doublets were observed due the angular strain within the three-membered ring of the diaziridine functional group, which hindered the change of the bond angle to 120 ° for the transition state required for nitrogen inversion (energy too high).

#### 10.M.1.5 Step 4: 3-phenyl-3-(trifluoromethyl)-3H-diazirine (or TPD)(5) from (4)

Silver oxide was made by boiling a solution of silver nitrate (AnalaR Normapur, VWR) (17.0 g, 0.1 mol) in 50 ml water and adding 100 ml NaOH slowly, dropwise. The silver oxide was filtered on sintered glass and washed thoroughly with water, acetone and THF. Silver oxide (7.0 g, 0.03 mol) was added to a solution of 3.0 g (16 mmol) diaziridine (4) in 65 ml THF, and the dispersion stirred at room temperature for 5 hours. Although the vessel was covered in foil to avoid light decomposition, it was later found this was not necessary. Progress of the reaction was followed by TLC (cyclohexane: methylene chloride: methanol, 19:2:1,  $R_f$ (diazirine)=0.7,  $R_f$ (diaziridine)=0.3), and measured by the UV-Vis absorbance at 356 nm ( $\mathcal{E}_{\lambda=356nm}$  (diaziridine) = 0;  $\mathcal{E}_{\lambda=356nm}$  (diazirine) = 263.5

$M^{-1}cm^{-1}$ ). Yield based on  $\lambda_{356nm} = 90 - 95 \%$  ( $\sim 2.7$  g). Silver oxide was removed by filtration and washed with THF. The combined filtrates were dried over  $Na_2SO_4$  and the solvent was evaporated under reduced pressure at room temperature to approximately 50 wt.%. The yellow liquid was separated by column chromatography and monitored with TLC (eluent = cyclohexane: methylene chloride: methanol, 19:2:1 as mentioned above). The product was stored in the dark at  $3^\circ C$ .  $^1H$  NMR ( $CDCl_3$ ): 7.2-7.6 (aromatic),  $\lambda_{max}$  (toluene) = 356 nm,  $\mathcal{E}_{\lambda=356nm} = 263.5 M^{-1}cm^{-1}$ . Chemical analysis calculated for  $C_8H_5F_3N_2$  (%): C (51.6); H(2.7); N (15.1); F (30.6) and chemical analysis measured (%): C (51.5); H (2.8); N (15.1); F (30.4).

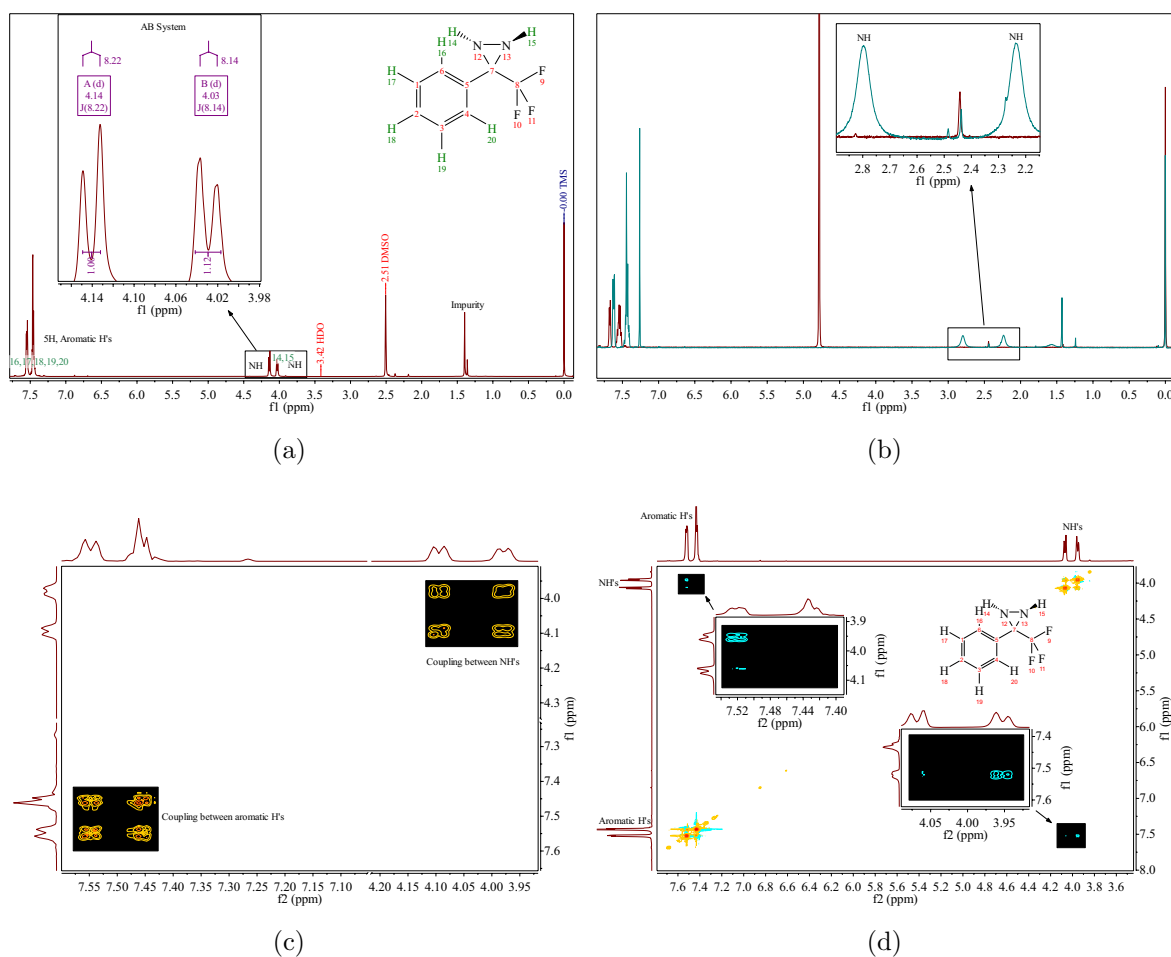


Figure 10.35: NMR spectra of diaziridine, 4: (a)  $^1H$  NMR spectrum (insert of NH protons, AB system), (b)  $^1H$  NMR spectrum before and after  $D_2O$  shake up, (c) 2D COSY  $^1H$  NMR spectrum and (d) 2D NOSEY spectrum.

## Appendix 10.N Statistical Modelling Data

| #  | Var    | Type      | label1                                     | label2                                | label3                                    | N         | Mean       | Median  | Stddev | Min    | Max     |
|----|--------|-----------|--|---------------------------------------|---|-----------|------------|---------|--------|--------|---------|
| 1  | obsnr  | integer   |  |                                       |   | 279       | 140.00     | 140.00  | 80.68  | 1.00   | 279.00  |
| 2  | cht    | integer   | Adhesion Tests                             |                                       | CHT (% Adhesion)                          | 279       | 37.13      | 0.00    | 48.04  | 0.00   | 100.00  |
| 3  | sjt    | integer   |  |                                       | SJT (% Adhesion)                          | 96        | 16.25      | 0.00    | 28.33  | 0.00   | 100.00  |
| 4  | prom   | character |  |                                       | Adhesion Promoter Type                    | 279       | nlevels=4  | ---     | ---    | ---    | ---     |
| 5  | conc   | numeric   | Adhesion Promoter Application              |                                       | Concentration (M)                         | 279       | 0.31       | 0.01    | 1.36   | 0.01   | 7.00    |
| 6  | meth   | character |  |                                       | Application method                        | 279       | nlevels=2  | ---     | ---    | ---    | ---     |
| 7  | cure   | character |  |                                       | Curing Method                             | 279       | nlevels=3  | ---     | ---    | ---    | ---     |
| 8  | spray  | integer   |  |                                       | No. Sprays                                | 240       | 2.30       | 2.00    | 0.78   | 2.00   | 5.00    |
| 9  | temp   | integer   |  |                                       | Temperature (°C)                          | 112       | 88.57      | 80.00   | 9.94   | 80.00  | 100.00  |
| 10 | time   | numeric   |  |                                       | Time (hours)                              | 112       | 12.46      | 10.00   | 7.11   | 0.50   | 30.00   |
| 11 | uv     | integer   |  |                                       | UV Radiant exposure (mJ/cm <sup>2</sup> ) | 164       | 1541.34    | 1278.00 | 860.79 | 120.00 | 2837.00 |
| 12 | intens | numeric   |  |                                       | Normalised ToF SIMS F Intensity           | 40        | 80.12      | 89.50   | 59.41  | 0.99   | 182.00  |
| 13 | xps    | numeric   |  |                                       | XPS F wt.%                                | 40        | 4.62       | 2.31    | 4.59   | 0.00   | 12.00   |
| 14 | xps.sd | numeric   |  |                                       | ±   | 40        | 0.40       | 0.27    | 0.44   | 0.00   | 1.98    |
| 15 | ra     | numeric   | Surface Roughness After Primer Application | Ra                                    | 40  | 234.65    | 236.41     | 15.30   | 205.67 | 267.28 |         |
| 16 | ra.sd  | numeric   |  | ±                                     | 40  | 13.47     | 13.12      | 6.71    | 2.44   | 28.38  |         |
| 17 | rq     | numeric   |  | Rq                                    | 40  | 294.56    | 296.66     | 25.47   | 223.93 | 352.72 |         |
| 18 | rq.sd  | numeric   |  | ±                                     | 40  | 23.21     | 18.55      | 17.97   | 4.08   | 92.98  |         |
| 19 | wash   | character |  | Wash Step?                            | 12  | nlevels=3 | ---        | ---     | ---    | ---    | ---     |
| 20 | disp   | numeric   | Surface Energy After Primer Application    | S.E. (disp)                           | 74  | 20.70     | 25.00      | 13.25   | 0.10   | 44.84  |         |
| 21 | polar  | numeric   |  | S.E. (polar)                          | 74  | 11.57     | 10.83      | 9.22    | 0.01   | 24.73  |         |
| 22 | total  | numeric   |  | S.E. (total)                          | 74  | 30.12     | 29.54      | 5.93    | 20.72  | 46.00  |         |
| 23 | type   | character | Substrate                                  |                                       | Substrate Type                            | 279       | nlevels=10 | ---     | ---    | ---    | ---     |
| 24 | epdm   | integer   |  |                                       | %EPDM                                     | 279       | 8.16       | 2.00    | 8.72   | 0.00   | 25.00   |
| 25 | pp     | character |  |                                       | Industrial or Research PP                 | 279       | nlevels=2  | ---     | ---    | ---    | ---     |
| 26 | ra2    | integer   |  | Surface Roughness Untreated Substrate | Ra  | 279       | 173.66     | 156.00  | 71.51  | 16.00  | 258.00  |
| 27 | ra2.sd | integer   |  |                                       | ±   | 279       | 26.69      | 18.00   | 24.39  | 3.00   | 99.00   |
| 28 | rq2    | integer   |  |                                       | Rq  | 279       | 232.72     | 244.00  | 87.72  | 21.00  | 329.00  |
| 29 | rq2.sd | integer   |  |                                       | ±   | 279       | 33.28      | 28.00   | 29.35  | 5.00   | 122.00  |
| 30 | hard   | numeric   |  |                                       | Substrate Hardness (Gpa) at 800 nm        | 279       | 0.03       | 0.02    | 0.01   | 0.01   | 0.06    |
| 31 | modul  | numeric   |  |                                       | Substrate E modulus (Gpa) at 800 nm       | 279       | 0.74       | 0.58    | 0.36   | 0.41   | 1.46    |
| 32 | disp2  | numeric   |  | Surface Energy of Untreated Substrate | S.E. (disp)                               | 279       | 24.27      | 24.26   | 1.20   | 22.51  | 25.81   |
| 33 | polar2 | numeric   | S.E. (polar)                               |                                       | 279                                       | 0.39      | 0.12       | 0.52    | 0.00   | 1.91   |         |
| 34 | total2 | numeric   | S.E. (total)                               |                                       | 279                                       | 25.04     | 25.36      | 0.98    | 23.46  | 25.93  |         |

Responses  $Y_j$

Factors  $X_i$  potentially affecting  $Y_j$

Figure 10.36: A list of the numerical, catagorical data. Red = lead responses  $y_j$ . Blue = factors  $x_i$  (that were controlled), potentially affecting  $y_j$ . Black = variables measured.

|           | <b>Cure</b>       |                |           |
|-----------|-------------------|----------------|-----------|
| <b>AP</b> | <b>Wet-on-Wet</b> | <b>Thermal</b> | <b>UV</b> |
| TPD       | 0                 | 6              | 3         |
| TPDCOOH   | 1                 | 52             | 102       |
| TPDOH     | 2                 | 54             | 59        |

Figure 10.37: The number of samples measured from the adhesion tests, demonstrating the slicing of data that occurred.

# Appendix 10.O Stepwise Ordinary Least Squares Analysis

**stepOLS results on standardized data,  $cht=f(X_i)$**

**Start model; Type III ANOVA;  $y=cht$**

$cht \sim prom:cure + prom + conc + cure + spray + type + epdm + pp$

[1] "N.complete.cases=240"

Anova Table (Type III tests)

Response: cht

| Sum                | Sq      | Df  | F      | value  | Pr(>F) |
|--------------------|---------|-----|--------|--------|--------|
| <b>(Intercept)</b> | 31.274  | 1   | 1661   | <2e-16 | ***    |
| <b>prom</b>        | 0       | 1   | 0      | 1      |        |
| <b>cure</b>        | 130.309 | 1   | 6921   | <2e-16 | ***    |
| <b>prom:cure</b>   | 55.847  | 1   | 2966.1 | <2e-16 | ***    |
| <b>Residuals</b>   | 4.443   | 236 |        |        |        |

Call:

$lm(formula = cht \sim prom + cure + prom:cure, data = z, x = T,$

$y = T)$

Residuals:

Min 1Q Median 3Q Max

-2.01796 0.00000 0.00000 0.02986 0.02986

Coefficients:

Estimate Std. Error t value Pr(>|t|)

(Intercept) -8.072e-01 1.981e-02 -40.76 <2e-16 \*\*\*

promTPDOH 1.597e-14 2.801e-02 0.00 1

cureUV 2.018e+00 2.426e-02 83.19 <2e-16 \*\*\*

promTPDOH:cureUV -2.018e+00 3.705e-02 -54.46 <2e-16 \*\*\*

Signif. codes: 0 '\*\*\*' 0.001 '\*\*' 0.01 '\*' 0.05 '.' 0.1 ' ' 1

Residual standard error: 0.1372 on 236 degrees of freedom

Multiple R-squared: 0.9814, Adjusted R-squared: 0.9812

F-statistic: 4153 on 3 and 236 DF, p-value: < 2.2e-16

kappa=7.780456

Figure 10.38: Rigorous empirical model building using stepwise Ordinary Least Squares (stepOLS)  $Y_j = CHT(x_i)$

**stepOLS results on standardized data,  $sjt=f(X_i)$**

**Start model; Type III ANOVA;  $y=sjt$**

$sjt \sim (conc + spray + uv + type + epdm + pp)^2 + I(conc * conc) + I(spray * spray) + I(uv * uv) + I(epdm * epdm)$

[1] "N.complete.cases=96"  
Anova Table (Type III tests)  
Response: sjt

| Sum                | Sq    | Df | F       | value    | Pr(>F) |
|--------------------|-------|----|---------|----------|--------|
| <b>(Intercept)</b> | 0.643 | 1  | 0.9335  | 0.336525 |        |
| <b>conc</b>        | 8.448 | 1  | 12.2606 | 0.000719 | ***    |
| <b>spray</b>       | 0.201 | 1  | 0.2923  | 0.590094 |        |
| <b>uv</b>          | 9.904 | 1  | 14.3744 | 0.000269 | ***    |
| <b>spray:uv</b>    | 8.518 | 1  | 12.3629 | 0.000685 | ***    |
| <b>Residuals</b>   | 62.7  | 91 |         |          |        |

Call:  
lm(formula = sjt ~ conc + spray + uv + spray:uv, data = z, x = T,  
y = T)  
Residuals:  
Min 1Q Median 3Q Max  
-2.2481 -0.3814 -0.1956 0.3370 3.0404  
Coefficients:  
Estimate Std. Error t value Pr(>|t|)  
(Intercept) -0.08513 0.08811 -0.966 0.336525  
conc 0.32913 0.09400 3.502 0.000719 \*\*\*  
spray -0.05269 0.09747 -0.541 0.590094  
uv 0.33854 0.08929 3.791 0.000269 \*\*\*  
spray:uv 0.32179 0.09152 3.516 0.000685 \*\*\*  
---  
Signif. codes: 0 '\*\*\*' 0.001 '\*\*' 0.01 '\*' 0.05 '.' 0.1 ' ' 1  
Residual standard error: 0.8301 on 91 degrees of freedom  
Multiple R-squared: 0.34, Adjusted R-squared: 0.311  
F-statistic: 11.72 on 4 and 91 DF, p-value: 1.014e-07  
kappa=1.76137  
**sjt**

Figure 10.39: Rigorous empirical model building using stepwise Ordinary Least Squares (stepOLS)  $Y_j=SJT(x_i)$



| Pearson |          |       |          |        |
|---------|----------|-------|----------|--------|
|         | Variable | CHT   | Variable | SJT    |
| 1       | xps      | 0.857 | uv       | 0.398  |
| 2       | intens   | 0.857 | conc     | 0.384  |
| 3       | obsnr    | 0.710 | intens   | 0.265  |
| 4       | total    | 0.662 | modul    | -0.258 |
| 5       | xps.sd   | 0.622 | hard     | -0.257 |
| 6       | spray    | 0.478 | disp     | 0.254  |
| 7       | rq.sd    | 0.331 | spray    | 0.234  |
| 8       | ra.sd    | 0.280 | xps      | 0.210  |
| 9       | disp     | 0.276 | total2   | 0.190  |
| 10      | uv       | 0.232 | ra2      | 0.143  |

| Spearman |          |        |          |        |
|----------|----------|--------|----------|--------|
|          | Variable | CHT    | Variable | SJT    |
| 1        | intens   | 0.849  | uv       | 0.395  |
| 2        | xps      | 0.810  | conc     | 0.319  |
| 3        | xps.sd   | 0.745  | hard     | -0.307 |
| 4        | obsnr    | 0.704  | modul    | -0.307 |
| 5        | total    | 0.671  | intens   | 0.275  |
| 6        | spray    | 0.523  | total    | 0.274  |
| 7        | rq.sd    | 0.270  | total2   | 0.259  |
| 8        | uv       | 0.245  | xps      | 0.240  |
| 9        | ra.sd    | 0.235  | disp     | 0.213  |
| 10       | ra2.sd   | -0.208 | spray    | 0.175  |

| Key    |  |
|--------|--|
| obsnr  | Observation Number   |
| cht    | Cross hatch test   |
| SJT    | Steam jet test   |
| conc   | Concentration of adhesion promoter                           |
| spray  | No. of primer layers spray applied                           |
| temp   | Cure temperature (for thermal cured substrates)              |
| time   | Cure Time (for thermal cured substrates)                     |
| uv     | UV intensity (for UV cured substrates only)                  |
| intens | F- Intensity (measured after AP applied, using ToF-SIMS)     |
| xps    | F wt.% (measured after AP applied, using XPS)                |
| xps.sd | F wt.% STD   |
| ra     | Ra before AP application                                     |
| ra.sd  | Ra STD before AP application                                 |
| rq     | Rq before AP application                                     |
| rq.sd  | Rq STD before AP application                                 |
| disp   | Dispersion component of surface energy before AP application |
| polar  | Polar component of surface energy before AP application      |
| total  | Total surface energy before AP application                   |
| epdm   | % EPDM in substrate  |
| ra2.sd | Ra after AP application                                      |
| rq2.sd | Rq after AP application                                      |
| hard   | Substrate Hardness   |
| modul  | Substrate Young's Modulus                                    |
| disp   | Dispersion component of surface energy after AP application  |
| polar  | Polar component of surface energy after AP application       |
| total  | Total surface energy after AP application                    |

Figure 10.40: Top 10 variables that were found to have the greatest influence on the CHT and SJT results, based on standard linear regression.

## Appendix 10.P Patent Search

### Patent Search 2012 Summary of Findings

Criteria:

*Functionalized photo- or thermoreactive (carbene) precursors as adhesion promoters for coatings which can be coupled to nonpolar polymer surfaces (especially PP or polyethylene (PE))*

1. \*Thermal or Unspecified Curing\*, carbene generating species, on non-reactive surfaces (e.g. Plastics) [see Figures 10.42 - 10.43 for patent number references]
  - (a) Patent no. 55 (DERWENT database) Production of substrate having adhesive surface for wide variety of substrate with carbene precursor, generating carbene reactive intermediate and converting precursor; Carbene precursor compound (specific compounds include diazo compounds); substrates can be polyolefins, rubbers etc (covers PP and PP with EPDM); Curing of carbene not stated
  - (b) Patent no. 41 (PATBASE search) Process for surface functionalisation of polymeric substrates using diaryl carbenes as reactive intermediates; solid surface is not specific; photolytic or thermolytic
  - (c) Patent no. 16 (CA database) Method for modifying a surface of plastic contact lenses during molding; methylene derivative carbene; modifying surface; hydrophilic coatings; plastics; does not specify curing conditions of carbene but it is put in to the mold of the lens
  - (d) Patent no. 36 (PATBASE search) Functional Surface Coatings; various solid substrates; preparing functional thin films or coatings; provides surface coatings that specifically recognises target proteins, many carbene generating species listed incl. Diazirines
  - (e) Patent no. 49 (DERWENT search) New functionalised compound useful e.g. as an agent for producing a chemically-bound three-dimensional network on or

within a substrate; carbene reactive intermediates; disposing a coating formulation onto the surface of a substrate; diazo carbenes listed; BUT PP is not in long list of polymers but thermoplastic elastomer is listed

- (f) Patent no. 64 (DERWENT search) Formation of electrically conductive impregnated fibres for radio-frequency shielded plastic articles involves feeding electrically conductive fibres into bath containing organic wetting agent and applying thermoplastic or thermoset sheath; Sheath can be PP or elastomer; coupling agent can be carbene
- (g) Patent no. 71 (DERWENT search) Modifying substrate with covalently bonded polymer by coating with polymer containing latent reactive group, then activating, useful for implants in humans; Active forms include carbene; stimulation is by heating or electromagnetic radiation incl. UV, Visible and IR; wide variety of substrates; latent group is covalently bonded to polymer molecules of substrate

**MAYBE OF INTEREST for the EPDM containing substrates:**

- (h) Patent No. 76 (DERWENT search) Adhesives for bonding natural or synthetic rubber to solid supports; Halo or dichlorocarbene is the preferred carbene; the rubbers contain double bonds but it is the nitroso compounds added that improve the adhesion (Nitroso compounds are a class of organic compounds containing the nitroso functional group,  $\text{RN}=\text{O}$ )

2. \*UV Curing or other\*, Carbene generating species, on non-reactive surfaces (e.g. Plastics)

- (a) Patent no. 14 (CA search) Photocurable coating compositions with good adhesion and scratch resistance for Plastics; BUT substrate is described in abstract as a polycarbonate (not as inert as PP? - contains O); good adhesion of coating; No mention of PP; metal halide lamp irradiation; Diazonium compounds

- (b) Patent no. 6 (Web of Science search) Oriented and covalent immobilization of target molecules to solid supports synthesis and application of a light-activatable and thiol-reactive cross-linking reagent; covalent bond; Diazirine; light activation; coupling of carbene to inert support; carbene-mediated insertion into the surface materials; Glass and Polystyrene as substrates (polystyrene is hydrophobic);; inert surfaces
- (c) Patent no. 11 (CA search) Methods for modification of surfaces with nanoparticles; UV irradiation grafting of nanoparticles; mentions phenyl diazirine as linking agent for nanoparticles and polystyrene substrate (hydrophobic substrate); nanoparticles are spin-coated onto polystyrene substrate
- (d) Patent no. 12 (CA search) Novel photoreactive copolymers for surface modification for increasing hydrophilicity, reducing adsorption and providing substance-immobilizing sites; UV radiation; photoreactive group is described by diazirine; coating of surface; Biological adhesion is mentioned but the inhibition of surface adhesion!
- (e) Patent no. 15 (CA search) Photocoupling of medical polymers with good surface lubricity by photocoupling optically active group-containing copolymers; e.g. of medical polymer is polyethylene (hydrophobic); UV light coupling of copolymer to medical polymer; PP also listed; Azido (N<sub>3</sub> functional group) photoactive group- can it form carbenes?
- (f) POI: Patent no. 3 (Web of Science search) Activation of bifunctional coupling agents in fiberglass/polyethylene composites by electron beam; Diazo compounds; Adhesion is a key word; BUT its for coupling between fiberglass and plastic phases

### 3. Grey Area:

- (a) Carbene generating species, any type of curing (UV and thermal), on unreactive solid surfaces (not specific), \*adhesion promoter for coatings\*

(b) Carbene generating species, any type of curing (UV and thermal), on unreactive surfaces (e.g. Plastics), \*adhesion promoter for coatings\*

| Web of Science | Result(HITS/Perhaps of Interest) | Reactive species   | Adhesion ? | Curing method                        | coating mentioned? | Photoaffinity labeling? | Surface?                                     | PP? | Journal/Patent | Automotive? |
|----------------|----------------------------------|--|------------|--------------------------------------|--------------------|-------------------------|--|-----|----------------|-------------|
| 1              | 1H                               | Dioxazolone compounds                                    | N          | Photocrosslinking                    | N                  | N                       | Metal  | N   | J              | N           |
| 2              | 3H                               | Diazonium compound                                       | N          | Electron beam and heat treatment     | N                  | N                       | Alkyl  | N   | J              | N           |
| 3              | 4H                               | Diazirine  | N          | UV                                   | N                  | N                       | Nucleic acid                                 | N   | J              | N           |
| 4              | 4H                               | Diazirine  | N          | UV                                   | N                  | N                       | Polyethylene terephthalate                   | N   | J              | N           |
| 5              | 6H                               | Diazirine  | N          | Light                                | N                  | N                       | HW-1 adhesive emulsions                      | N   | J              | N           |
| 6              | 6H                               | Diazirine  | N          | UV                                   | N                  | N                       | Chloro and Polyurethane                      | N   | J              | N           |
| 7              | 7 Ed                             | Diazirine  | N          | UV                                   | N                  | N                       | Jou says substrate!                          | N   | J              | N           |
| 8              | 8H                               | Diazomethane   | Y          | UV                                   | Y                  | N                       | Cross linking                                | N   | P              | N           |
| 9              | 9H                               | Carbene (methylene derivatives, nitrenes, azides)        | N          | Decrease say                         | N                  | N                       | Polypropylene                                | N   | P              | N           |
| 10             | 11H                              | Diazirine  | N          | UV                                   | Y                  | N                       | Polypropylene                                | N   | P              | N           |
| 11             | 11H                              | Diazirine  | N          | UV                                   | Y                  | N                       | Polypropylene                                | N   | P              | N           |
| 12             | 12H                              | Diazirine  | N          | UV                                   | Y                  | N                       | N (solid surface)                            | N   | P              | N           |
| 13             | 12H                              | Diazirine  | N          | UV                                   | Y                  | N                       | N (solid surface)                            | N   | P              | N           |
| 14             | 14H                              | Diazomethane   | Y          | UV                                   | Y                  | N                       | Plastics                                     | N   | P              | N           |
| 15             | 14H                              | Diazomethane   | Y          | UV                                   | Y                  | N                       | Plastics                                     | N   | P              | N           |
| 16             | 15H                              | 3-azidolysine  | N          | UV                                   | Y                  | N                       | Medical polymers                             | N   | P              | N           |
| 17             | 16H                              | Carbene (methylene derivatives)                          | N          | Does not say                         | N                  | N                       | Plastic surface films                        | Y   | P              | N           |
| 18             | 17H                              | Peroxide is mentioned                                    | Y          | radical grafting                     | Y                  | N                       | Polyethylene Polypropylene                   | Y   | P              | N           |
| 19             | 18H                              | Diazomethane   | Y          | Added in polymer melt                | Y                  | N                       | Provide materials (implants etc)             | Y   | J              | N           |
| 20             | 19H                              | Carbene (methylene derivatives, azide, diazo compounds)  | N          | UV                                   | Y                  | N                       | Mixed in polyolefins (monomers polyethylene) | N   | P              | N           |
| 21             | 21H                              | Diazirine  | N          | UV                                   | Y                  | N                       | UV   | N   | P              | N           |
| 22             | 21H                              | Diazirine  | N          | UV                                   | Y                  | N                       | UV   | N   | P              | N           |
| 23             | 22H                              | Carbene (or Nitrene)                                     | N          | Not mentioned                        | N                  | N                       | UV   | N   | P              | N           |
| 24             | 24H                              | Diazirine  | N          | UV                                   | Y                  | N                       | UV   | N   | P              | N           |
| 25             | 25H                              | Diazirine  | N          | UV                                   | Y                  | N                       | UV   | N   | P              | N           |
| 26             | 25H                              | Diazirine  | N          | UV                                   | Y                  | N                       | UV   | N   | P              | N           |
| 27             | 27H                              | CPO  | Y          | UV                                   | Y                  | N                       | UV   | N   | P              | N           |
| 28             | 28H                              | Diazirine  | Y          | UV                                   | Y                  | N                       | UV   | N   | P              | N           |
| 29             | 28H                              | Diazirine  | Y          | UV                                   | Y                  | N                       | UV   | N   | P              | N           |
| 30             | 30H                              | Carbene  | N          | Thermal                              | N                  | N                       | UV   | N   | P              | N           |
| 31             | 31H                              | Diazomethane   | Y          | Not mentioned                        | N                  | N                       | UV   | N   | P              | N           |
| 32             | 33H                              | Carbene (keto derivatives)                               | Y          | Only Primer                          | Y                  | N                       | UV   | N   | P              | N           |
| 33             | 34H                              | Diazirine  | N          | Photocrosslinking                    | Y                  | N                       | UV   | N   | P              | N           |
| 34             | 34H                              | Diazirine  | N          | Photocrosslinking                    | Y                  | N                       | UV   | N   | P              | N           |
| 35             | 35H                              | Diazirine  | N          | Electromagnetic discharge or UV lamp | Y                  | N                       | UV   | N   | P              | N           |
| 36             | 36H                              | Diazirine, azides etc                                    | Y          | Decrease say                         | Y                  | N                       | UV   | N   | P              | N           |
| 37             | 37H                              | Azides   | N          | Photocrosslinking                    | Y                  | N                       | UV   | N   | P              | N           |
| 38             | 38H                              | Diazirine  | N          | Photo active                         | N                  | N                       | UV   | N   | P              | N           |
| 39             | 39H                              | Carbenes   | N          | Photoactive                          | N                  | N                       | UV   | N   | P              | N           |
| 40             | 40H                              | Carbenes   | N          | Photoactive                          | N                  | N                       | UV   | N   | P              | N           |
| 41             | 41H                              | Carbenes   | N          | Photoactive                          | N                  | N                       | UV   | N   | P              | N           |
| 42             | 42H                              | Carbenes   | N          | Photoactive                          | N                  | N                       | UV   | N   | P              | N           |
| 43             | 43H                              | Carbenes   | N          | Photoactive                          | N                  | N                       | UV   | N   | P              | N           |
| 44             | 44H                              | Carbenes   | N          | Photoactive                          | N                  | N                       | UV   | N   | P              | N           |
| 45             | 45H                              | Carbenes   | N          | Photoactive                          | N                  | N                       | UV   | N   | P              | N           |
| 46             | 45H                              | Carbenes   | N          | Photoactive                          | N                  | N                       | UV   | N   | P              | N           |
| 47             | 47H                              | Diazonium (radical treatment) but with washing treatment | Y          | Does not say                         | Y                  | N                       | UV   | N   | P              | N           |
| 48             | 48H                              | Monoradicals   | Y          | Does not say                         | Y                  | N                       | UV   | N   | P              | N           |
| 49             | 49H                              | Carbene (Diazirine)                                      | N          | Decrease say                         | Y                  | N                       | UV   | N   | P              | N           |
| 50             | 50H                              | Diaziridine, Diazomethane                                | N          | UV                                   | Y                  | N                       | UV   | N   | P              | N           |
| 51             | 51H                              | Diazirine, diazoalkyl                                    | N          | Decrease say                         | Y                  | N                       | UV   | N   | P              | N           |
| 52             | 52H                              | Diazirine, diazoalkyl                                    | N          | Decrease say                         | Y                  | N                       | UV   | N   | P              | N           |
| 53             | 53H                              | Diazirine, diazoalkyl                                    | N          | Decrease say                         | Y                  | N                       | UV   | N   | P              | N           |
| 54             | 54H                              | Diazirine  | N          | Decrease say                         | Y                  | N                       | UV   | N   | P              | N           |
| 55             | 55H                              | Diazo  | Y          | Does not say                         | N                  | N                       | UV   | N   | P              | N           |
| 56             | 56H                              | Carbene (nitrene, diazomium)                             | N          | Decrease say                         | N                  | N                       | UV   | N   | P              | N           |
| 57             | 57H                              | Diazirine  | N          | UV                                   | Y                  | N                       | UV   | N   | P              | N           |
| 58             | 58H                              | Diazirine  | N          | UV                                   | Y                  | N                       | UV   | N   | P              | N           |
| 59             | 59H                              | Diazirine  | N          | UV                                   | Y                  | N                       | UV   | N   | P              | N           |
| 60             | 60H                              | Diazirine  | N          | UV                                   | Y                  | N                       | UV   | N   | P              | N           |
| 61             | 61H                              | Diazirine  | N          | UV                                   | Y                  | N                       | UV   | N   | P              | N           |
| 62             | 62H                              | Diazirine  | N          | UV                                   | Y                  | N                       | UV   | N   | P              | N           |
| 63             | 63H                              | Carbenes   | N          | Photocrosslinking                    | Y                  | N                       | UV   | N   | P              | N           |
| 64             | 64H                              | Carbenes   | N          | Photocrosslinking                    | Y                  | N                       | UV   | N   | P              | N           |
| 65             | 65H                              | Carbenes   | N          | Photocrosslinking                    | Y                  | N                       | UV   | N   | P              | N           |
| 66             | 66H                              | Carbenes (Diazirine)                                     | N          | Blue light irradiation               | Y                  | N                       | UV   | N   | P              | N           |
| 67             | 67H                              | Diazirine  | N          | UV                                   | Y                  | N                       | UV   | N   | P              | N           |
| 68             | 68H                              | Diazirine  | N          | UV                                   | Y                  | N                       | UV   | N   | P              | N           |
| 69             | 69H                              | Carbene (radicals)                                       | N          | Does not say                         | N                  | N                       | UV   | N   | P              | N           |
| 70             | 70H                              | Diazomethane   | N          | Photocrosslinking                    | Y                  | N                       | UV   | N   | P              | N           |
| 71             | 71H                              | Carbenes   | N          | UV and IR                            | Y                  | N                       | UV   | N   | P              | N           |
| 72             | 72H                              | Diaziridine  | Y          | Irradiation of stable or UV rays     | Y                  | N                       | UV   | N   | P              | N           |
| 73             | 73H                              | Diaziridine  | Y          | Irradiation of stable or UV rays     | Y                  | N                       | UV   | N   | P              | N           |
| 74             | 74H                              | Azide or Diazo compound (nitrene or carbene)             | N          | Does not say                         | N                  | N                       | UV   | N   | P              | N           |
| 75             | 75H                              | Carbene (nitrene or carbene)                             | N          | Does not say                         | N                  | N                       | UV   | N   | P              | N           |
| 76             | 76H                              | Carbene (nitrene or carbene)                             | N          | Does not say                         | N                  | N                       | UV   | N   | P              | N           |

Figure 10.41: Patent search summary part 1. Available on CD for magnified view.

| Other Searches | Result (HITS/Patent of Interest) | Reactive species | Adhesive 7    | Curing method     | coating mentioned? | Prosoffinity labeling? | Surface?                             | PP7? | Journal/Patent | Automotive? |
|----------------|----------------------------------|------------------|---------------|-------------------|--------------------|------------------------|--------------------------------------|------|----------------|-------------|
| 77 F01         | NO carbones                      |                  | Resistance to |                   |                    |                        |                                      |      |                |             |
| 78 F01         | Phenacetyl                       |                  | Grating       | light irradiation |                    |                        | silicon, silicon nitride and diamond |      | J              | N           |
| 79 F01         | Phenacetyl                       |                  | Grating       | light irradiation |                    |                        | diamond                              |      | J              | N           |
| 80 F01         | Phenacetyl                       |                  | Grating       | light irradiation |                    |                        | Polypyrrole (to immobilize proteins) |      | J              | N           |
| 81 F01         | Phenacetyl                       |                  | Grating       | light irradiation |                    |                        |                                      |      | J              | N           |
| 82 F01         | Phenacetyl                       |                  | Grating       | light irradiation |                    |                        |                                      |      | J              | N           |
| 83 F01         | Phenacetyl                       |                  | Grating       | light irradiation |                    |                        |                                      |      | J              | N           |
| 84 F01         | Phenacetyl                       |                  | Grating       | light irradiation |                    |                        |                                      |      | J              | N           |
| 85 F01         | Phenacetyl                       |                  | Grating       | light irradiation |                    |                        |                                      |      | J              | N           |
| 86 F01         | Phenacetyl                       |                  | Grating       | light irradiation |                    |                        |                                      |      | J              | N           |
| 87 F01         | Phenacetyl                       |                  | Grating       | light irradiation |                    |                        |                                      |      | J              | N           |
| 88 F01         | Phenacetyl                       |                  | Grating       | light irradiation |                    |                        |                                      |      | J              | N           |
| 89 F01         | Phenacetyl                       |                  | Grating       | light irradiation |                    |                        |                                      |      | J              | N           |
| 90 F01         | Phenacetyl                       |                  | Grating       | light irradiation |                    |                        |                                      |      | J              | N           |
| 91 F01         | Phenacetyl                       |                  | Grating       | light irradiation |                    |                        |                                      |      | J              | N           |
| 92 F01         | Phenacetyl                       |                  | Grating       | light irradiation |                    |                        |                                      |      | J              | N           |
| 93 F01         | Phenacetyl                       |                  | Grating       | light irradiation |                    |                        |                                      |      | J              | N           |
| 94 F01         | Phenacetyl                       |                  | Grating       | light irradiation |                    |                        |                                      |      | J              | N           |
| 95 F01         | Phenacetyl                       |                  | Grating       | light irradiation |                    |                        |                                      |      | J              | N           |
| 96 F01         | Phenacetyl                       |                  | Grating       | light irradiation |                    |                        |                                      |      | J              | N           |
| 97 F01         | Phenacetyl                       |                  | Grating       | light irradiation |                    |                        |                                      |      | J              | N           |
| 98 F01         | Phenacetyl                       |                  | Grating       | light irradiation |                    |                        |                                      |      | J              | N           |
| 99 F01         | Phenacetyl                       |                  | Grating       | light irradiation |                    |                        |                                      |      | J              | N           |
| 100 F01        | Phenacetyl                       |                  | Grating       | light irradiation |                    |                        |                                      |      | J              | N           |
| 101 F01        | Phenacetyl                       |                  | Grating       | light irradiation |                    |                        |                                      |      | J              | N           |
| 102 F01        | Phenacetyl                       |                  | Grating       | light irradiation |                    |                        |                                      |      | J              | N           |
| 103 F01        | Phenacetyl                       |                  | Grating       | light irradiation |                    |                        |                                      |      | J              | N           |
| 104 F01        | Phenacetyl                       |                  | Grating       | light irradiation |                    |                        |                                      |      | J              | N           |
| 105 F01        | Phenacetyl                       |                  | Grating       | light irradiation |                    |                        |                                      |      | J              | N           |
| 106 F01        | Phenacetyl                       |                  | Grating       | light irradiation |                    |                        |                                      |      | J              | N           |
| 107 F01        | Phenacetyl                       |                  | Grating       | light irradiation |                    |                        |                                      |      | J              | N           |
| 108 F01        | Phenacetyl                       |                  | Grating       | light irradiation |                    |                        |                                      |      | J              | N           |
| 109 F01        | Phenacetyl                       |                  | Grating       | light irradiation |                    |                        |                                      |      | J              | N           |
| 110 F01        | Phenacetyl                       |                  | Grating       | light irradiation |                    |                        |                                      |      | J              | N           |
| 111 F01        | Phenacetyl                       |                  | Grating       | light irradiation |                    |                        |                                      |      | J              | N           |
| 112 F01        | Phenacetyl                       |                  | Grating       | light irradiation |                    |                        |                                      |      | J              | N           |
| 113 F01        | Phenacetyl                       |                  | Grating       | light irradiation |                    |                        |                                      |      | J              | N           |
| 114 F01        | Phenacetyl                       |                  | Grating       | light irradiation |                    |                        |                                      |      | J              | N           |
| 115 F01        | Phenacetyl                       |                  | Grating       | light irradiation |                    |                        |                                      |      | J              | N           |
| 116 F01        | Phenacetyl                       |                  | Grating       | light irradiation |                    |                        |                                      |      | J              | N           |
| 117 F01        | Phenacetyl                       |                  | Grating       | light irradiation |                    |                        |                                      |      | J              | N           |
| 118 F01        | Phenacetyl                       |                  | Grating       | light irradiation |                    |                        |                                      |      | J              | N           |
| 119 F01        | Phenacetyl                       |                  | Grating       | light irradiation |                    |                        |                                      |      | J              | N           |
| 120 F01        | Phenacetyl                       |                  | Grating       | light irradiation |                    |                        |                                      |      | J              | N           |
| 121 F01        | Phenacetyl                       |                  | Grating       | light irradiation |                    |                        |                                      |      | J              | N           |
| 122 F01        | Phenacetyl                       |                  | Grating       | light irradiation |                    |                        |                                      |      | J              | N           |
| 123 F01        | Phenacetyl                       |                  | Grating       | light irradiation |                    |                        |                                      |      | J              | N           |
| 124 F01        | Phenacetyl                       |                  | Grating       | light irradiation |                    |                        |                                      |      | J              | N           |
| 125 F01        | Phenacetyl                       |                  | Grating       | light irradiation |                    |                        |                                      |      | J              | N           |
| 126 F01        | Phenacetyl                       |                  | Grating       | light irradiation |                    |                        |                                      |      | J              | N           |
| 127 F01        | Phenacetyl                       |                  | Grating       | light irradiation |                    |                        |                                      |      | J              | N           |
| 128 F01        | Phenacetyl                       |                  | Grating       | light irradiation |                    |                        |                                      |      | J              | N           |
| 129 F01        | Phenacetyl                       |                  | Grating       | light irradiation |                    |                        |                                      |      | J              | N           |
| 130 F01        | Phenacetyl                       |                  | Grating       | light irradiation |                    |                        |                                      |      | J              | N           |
| 131 F01        | Phenacetyl                       |                  | Grating       | light irradiation |                    |                        |                                      |      | J              | N           |
| 132 F01        | Phenacetyl                       |                  | Grating       | light irradiation |                    |                        |                                      |      | J              | N           |
| 133 F01        | Phenacetyl                       |                  | Grating       | light irradiation |                    |                        |                                      |      | J              | N           |
| 134 F01        | Phenacetyl                       |                  | Grating       | light irradiation |                    |                        |                                      |      | J              | N           |
| 135 F01        | Phenacetyl                       |                  | Grating       | light irradiation |                    |                        |                                      |      | J              | N           |
| 136 F01        | Phenacetyl                       |                  | Grating       | light irradiation |                    |                        |                                      |      | J              | N           |
| 137 F01        | Phenacetyl                       |                  | Grating       | light irradiation |                    |                        |                                      |      | J              | N           |
| 138 F01        | Phenacetyl                       |                  | Grating       | light irradiation |                    |                        |                                      |      | J              | N           |
| 139 F01        | Phenacetyl                       |                  | Grating       | light irradiation |                    |                        |                                      |      | J              | N           |
| 140 F01        | Phenacetyl                       |                  | Grating       | light irradiation |                    |                        |                                      |      | J              | N           |
| 141 F01        | Phenacetyl                       |                  | Grating       | light irradiation |                    |                        |                                      |      | J              | N           |
| 142 F01        | Phenacetyl                       |                  | Grating       | light irradiation |                    |                        |                                      |      | J              | N           |
| 143 F01        | Phenacetyl                       |                  | Grating       | light irradiation |                    |                        |                                      |      | J              | N           |
| 144 F01        | Phenacetyl                       |                  | Grating       | light irradiation |                    |                        |                                      |      | J              | N           |
| 145 F01        | Phenacetyl                       |                  | Grating       | light irradiation |                    |                        |                                      |      | J              | N           |
| 146 F01        | Phenacetyl                       |                  | Grating       | light irradiation |                    |                        |                                      |      | J              | N           |
| 147 F01        | Phenacetyl                       |                  | Grating       | light irradiation |                    |                        |                                      |      | J              | N           |
| 148 F01        | Phenacetyl                       |                  | Grating       | light irradiation |                    |                        |                                      |      | J              | N           |
| 149 F01        | Phenacetyl                       |                  | Grating       | light irradiation |                    |                        |                                      |      | J              | N           |
| 150 F01        | Phenacetyl                       |                  | Grating       | light irradiation |                    |                        |                                      |      | J              | N           |
| 151 F01        | Phenacetyl                       |                  | Grating       | light irradiation |                    |                        |                                      |      | J              | N           |
| 152 F01        | Phenacetyl                       |                  | Grating       | light irradiation |                    |                        |                                      |      | J              | N           |
| 153 F01        | Phenacetyl                       |                  | Grating       | light irradiation |                    |                        |                                      |      | J              | N           |
| 154 F01        | Phenacetyl                       |                  | Grating       | light irradiation |                    |                        |                                      |      | J              | N           |
| 155 F01        | Phenacetyl                       |                  | Grating       | light irradiation |                    |                        |                                      |      | J              | N           |
| 156 F01        | Phenacetyl                       |                  | Grating       | light irradiation |                    |                        |                                      |      | J              | N           |
| 157 F01        | Phenacetyl                       |                  | Grating       | light irradiation |                    |                        |                                      |      | J              | N           |
| 158 F01        | Phenacetyl                       |                  | Grating       | light irradiation |                    |                        |                                      |      | J              | N           |
| 159 F01        | Phenacetyl                       |                  | Grating       | light irradiation |                    |                        |                                      |      | J              | N           |
| 160 F01        | Phenacetyl                       |                  | Grating       | light irradiation |                    |                        |                                      |      | J              | N           |
| 161 F01        | Phenacetyl                       |                  | Grating       | light irradiation |                    |                        |                                      |      | J              | N           |
| 162 F01        | Phenacetyl                       |                  | Grating       | light irradiation |                    |                        |                                      |      | J              | N           |
| 163 F01        | Phenacetyl                       |                  | Grating       | light irradiation |                    |                        |                                      |      | J              | N           |
| 164 F01        | Phenacetyl                       |                  | Grating       | light irradiation |                    |                        |                                      |      | J              | N           |
| 165 F01        | Phenacetyl                       |                  | Grating       | light irradiation |                    |                        |                                      |      | J              | N           |
| 166 F01        | Phenacetyl                       |                  | Grating       | light irradiation |                    |                        |                                      |      | J              | N           |
| 167 F01        | Phenacetyl                       |                  | Grating       | light irradiation |                    |                        |                                      |      | J              | N           |
| 168 F01        | Phenacetyl                       |                  | Grating       | light irradiation |                    |                        |                                      |      | J              | N           |
| 169 F01        | Phenacetyl                       |                  | Grating       | light irradiation |                    |                        |                                      |      | J              | N           |
| 170 F01        | Phenacetyl                       |                  | Grating       | light irradiation |                    |                        |                                      |      | J              | N           |

Figure 10.42: Patent search summary part 2. Available on CD for magnified view.







## References

- [1] Marketsandmarkets, “Automotive Plastics Market for Passenger Cars: Global Trends and Forecasts to 2016 - By Types and Geography,” April 18, 2012. Marketing study.
- [2] M. Kamieth, “Presentation: BASF’s Coatings Division: Focusing on Growth and Value,” September 5th, 2012.
- [3] J. E. Lawniczak, K. A. Williams, and L. T. Germinario, “Characterisation of Adhesion Performance of Topcoats and Adhesion Promoters on TPO Substrates,” *Journal of Coatings Technology and Research*, vol. 2, no. 5, pp. 399–405, 2005.
- [4] Markets and Markets, “Automotive Plastics Market for Passenger Cars by Type, Application & Geography- Trends & Forecasts to 2018,” June 2013. Global Marketing Study.
- [5] R. A. Ryntz, “Coating Adhesion to Low Surface Free Energy Substrates,” *Progress in Organic Coatings*, vol. 25, pp. 73–83, 1994.
- [6] “The Council of the European Union.” Council Regulation (EU) No 1344/2011, December 2011. (Non-legislative acts).
- [7] R.-Y. Qin and H. Schreiber, “Adhesion at Partially Restructured Polymer Surfaces,” *Colloids and Surfaces*, vol. 156, pp. 85–93, 1999.
- [8] H. Brown, “Polymer Adhesion,” *Materials Forum*, vol. 24, pp. 49–58, 2000.
- [9] N. M. Bikales, *Adhesion and Bonding*. Wiley-Interscience, 1971.

- [10] W. Wake, *Adhesion and the Formulation of Adhesives*. Applied Science Publishers, 2nd ed., (1982).
- [11] Y. Lipatov, *Polymer Reinforcement*. ChemTec Publishing, 1995.
- [12] D. Myers, *Surfaces, Interfaces, and Colloids: Principles and Applications*. VCH, Weinheim, 1991.
- [13] M. C. an der Leeden and G. Frens, “Surface Properties of Plastic Materials in Relation to their Adhering Performance,” *Advanced Engineering Materials*, vol. 4, no. 5, pp. 280–289, 2002.
- [14] C. G. Morris, *Academic Press Dictionary of Science and Technology*. Academic Press Inc., 1992.
- [15] A. Dupre, *Théorie Mécanique de la Chaleur*. Gauthier-Villars, 1869.
- [16] K. L. Mittal, “Adhesion Measurement of Thin Films,” *Electrocomponent Science and Technology*, vol. 3, pp. 21–42, 1976.
- [17] K. L. Mittal, *Adhesion Measurement of Thin Films, Thick Films and Bulk Coatings*. ASTM International, 1978.
- [18] K. L. Mittal, *Adhesion Measurement of Films and Coatings*, vol. 2. VSP, 2001.
- [19] A. V. Pocius, *Adhesion and Adhesives Technology: An Introduction*. Hanser, 2002.
- [20] N. K. Adam and G. Jessop, “Angles of Contact and Polarity of Solid Surfaces,” *Journal of the Chemical Society*, vol. 127, pp. 1863–1868, 1925.
- [21] D. H. Bangham and R. I. Razouk, “Adsorption and the Wettability of Solid Surfaces,” *Transactions of the Faraday Society*, vol. 33, no. 2, pp. 1459–1462, 1937.
- [22] M. E. Schrader, “Young–Dupre Revisited,” *Langmuir*, vol. 11, pp. 3585–3589, 1995.

- [23] J. Rouquerol, F. Rouquerol, P. Llewellyn, G. Maurin, and K. S. Sing, *Adsorption by Powders and Porous Solids: Principles, Methodology and Applications*. Academic Press, Google eBook, 2013.
- [24] M. Berins, *Plastics Engineering Handbook of the Society of the Plastics Industry*. Springer, 1991.
- [25] D. M. Brewis and I. Mathieson, *Adhesion and Bonding to Polyolefins*, vol. 12. iSmithers Rapra Publishing, 2002.
- [26] R. Förch, H. Schönherr, and A. T. A. Jenkins, *Surface Design: Applications in Bioscience and Nanotechnology*. John Wiley and Sons, 2009.
- [27] T. Schuhman and S. F. Thames, “Coating Solvent Effects Producing Adhesion to Molded Plastic Parts,” *Journal of Adhesion Science and Technology*, vol. 19, no. 13–14, pp. 1207–1235, 2005.
- [28] R. A. Ryntz, “Attaining Durable Painted Plastic Components,” *Journal of Coatings Technology and Research*, vol. 2, no. 5, pp. 351–360, 2005.
- [29] H. R. Morris, B. Munroe, R. A. Ryntz, and P. J. Treado, “Fluorescence and Raman Chemical Imaging of Thermoplastic Olefin (TPO) Adhesion Promotion,” *Langmuir*, vol. 14, pp. 2426–2434, 1998.
- [30] H. R. Morris, J. F. Turner, B. Munroe, R. A. Ryntz, and P. J. Treado, “Chemical Imaging of Thermoplastic Olefin (TPO) Surface Architecture,” *Langmuir*, vol. 15, pp. 2961–2972, 1999.
- [31] A. J. Kinloch, *Adhesion and Adhesives: Science and Technology*. Springer, 1987.
- [32] S. Mirabedini, H. Arabi, A. Salem, and S. Asiaban, “Effect of Low-Pressure O<sub>2</sub> and Ar Plasma Treatments on the Wettability and Morphology of Biaxial-Oriented Polypropylene (BOPP) Film,” *Progress in Organic Coatings*, vol. 60, pp. 105–111, 2007.

- [33] K. Autumn and A. M. Peattie, “Mechanisms of Adhesion in Geckos,” *Integrative and Comparative Biology*, vol. 42, no. 6, pp. 1081–1090, 2002.
- [34] M. Zhou, N. Pesika, H. Zeng, Y. Tian, and J. Israelachvili, “Recent Advances in Gecko Adhesion and Friction Mechanisms and Development of Gecko-Inspired Dry Adhesive Surfaces,” *Friction*, vol. 1, no. 2, pp. 114–129, 2013.
- [35] M. D. Bartlett, A. B. Croll, D. R. King, B. M. Paret, D. J. Irschick, and A. J. Crosby, “Looking Beyond Fibrillar Features to Scale Gecko-Like Adhesion,” *Advanced Materials*, vol. 24, pp. 1078–1083, 2012.
- [36] M. Bartlett, D. Irschick, and A. Crosby, eds., *Scaling Reversible Adhesion in Synthetic and Natural Adhesive Systems*, 3 - 6th March, 2013.
- [37] D. King, M. D. Bartlett, D. Irschick, and A. Crosby, eds., *Comparing the Performance of Draping Adhesives to Geckos on Various Surfaces*, 3 - 6th March, 2013.
- [38] A. Drane, “Sticking to Science, Geckskin™ Revolutionizes the Field of Adhesion,” *Feature Stories, University of Massachusetts Amherst*, 2012.
- [39] Oil and C. C. Association, *Surface Coatings: Volume 1 Raw Materials and their Usage*. Springer, 1993.
- [40] B. LU and T. C. CHUNG, “Synthesis of Maleic Anhydride Grafted Polyethylene and Polypropylene, with Controlled Molecular Structures,” *Journal of Polymer Science: Part A: Polymer Chemistry*, vol. 38, pp. 1337–1343, 2000.
- [41] H. Morgan, *Electrostatics 2003. Proceedings of the Institute of Physics Conference Edinburgh, 23 - 27 March 2003*. CRC Press, 2003.
- [42] K. Bellman and A. Khare, “European Response to Issues in Recycling Car Plastics,” *Technovation*, vol. 19, pp. 721–734, 1999.
- [43] R. R. Tiwari and D. R. Paul, “Polypropylene-Elastomer (TPO) Nanocomposites: 1. Morphology,” *Polymer*, vol. 52, pp. 4955–4969, 2011.

- [44] K. Deng, N. Felorzabihi, M. A. Winnik, Z. Jiang, Z. Yin, Y. Liu, P. V. Yaneff, and R. A. Ryntz, "Influence of Position and Composition on Adhesion to Injection-Molded TPO Plaques as Model Automotive Parts," *Polymer*, vol. 50, pp. 5084–5093, 2009.
- [45] R. A. Ryntz, "The Effects of Thermoplastic Poly(olefin) (TPO) Morphology on Subsequent Paintability and Thermal Shock Performance," *Progress in Organic Coatings*, vol. 27, pp. 241–254, 1996.
- [46] J. Maxwell, *Plastics in the Automotive Industry*. Woodhead Publishings, 1994.
- [47] Y. S. Lin and H. K. Yasuda, "Low-Temperature Cascade Arc Torch Treatments for Enhanced Adhesion of Primer to Thermoplastic Olefins," *Journal of Applied Polymer Science*, vol. 67, no. 5, pp. 855–863, 1998.
- [48] A. P. Pijpers and R. J. Meier, "Adhesion Behaviour of Polypropylenes after Flame Treatment Determined by XPS(ESCA) Spectral Analysis," *Journal of Electron Spectroscopy and Related Phenomena*, vol. 121, pp. 299–313, 2001.
- [49] M. Strobel, M. C. Branch, M. Ulsh, R. S. Kapaun, S. Kirk, and C. S. Lyons, "Flame Surface Modification of Polypropylene Film," *Journal of Adhesion Science and Technology*, vol. 20, no. 6, pp. 515–539, 1996.
- [50] S. Farris, S. Pazzoli, P. Biagioni, L. Duo, S. Mancinelli, and L. Piergiovanni, "The Fundamentals of Flame Treatment for the Surface Activation of Polyolefin Polymers - A Review," *Polymer*, vol. 51, pp. 3591–3605, 2010.
- [51] D. K. Owens, "Mechanism of Corona-Induced Self-Adhesion of Polyethylene Film," *Journal OF Applied Polymer Science*, vol. 19, no. 1, pp. 265–271, 1975.
- [52] D. Briggs and C. R. Kendall, "Derivatization of Discharge-Treated LDPE: an Extension of XPS Analysis and a Probe of Specific Interactions in Adhesion," *International Journal of Adhesion and Adhesives*, vol. 2, no. 1, pp. 13–17, 1982.

- [53] D. Briggs and C. R. Kendall, "Chemical Basis of Adhesion to Electrical Discharge Treated Polyethylene," *Polymer*, vol. 20, pp. 1053–1054, 1979.
- [54] D. Briggs and C. R. Kendall, "Electrical Discharge Treatment of Polypropylene Film," *Polymer*, vol. 24, pp. 47–52, 1983.
- [55] D. Briggs, "New Developments in Polymer Surface-Analysis," *POLYMER*, vol. 25, no. 10, pp. 1379–1391, 1984.
- [56] J. A. Lanauze and D. L. Myers, "Ink Adhesion on Corona-Treated Polyethylene Studied by Chemical Derivatization of Surface Functional-Groups," *Journal of Applied Polymer Science*, vol. 40, no. 3–4, pp. 595–611, 1990.
- [57] E. Sheng, I. Sutherland, and D. M. Brewis, "Effects of Flame Treatment on Propylene Ethylene Copolymer Surfaces," *Surface and Interface Analysis*, vol. 19, no. 1–2, pp. 151–156, 1992.
- [58] E. Sheng, I. Sutherland, and D. M. Brewis, "An X-ray Photoelectron-Spectroscopy Study of Flame Treatment of Polypropylene," *Applied Surface Science*, vol. 78, no. 3, pp. 249–254, 1994.
- [59] Y. D. Puydt, D. Leonard, P. Bertrand, and K. L. Mittal, *Metallized Plastics 3: Fundamental and Applied Aspects*. Plenum Press, 1992.
- [60] E. Papirer, D. Y. Wu, and J. Schultz, "Adhesion of Flame-Treated Polyolefins to Styrene-Butadiene Rubber," *Journal OF Adhesion Science and Technology*, vol. 7, no. 4, pp. 343–362, 1993.
- [61] E. Tomasetti, D. Daoust, R. Legras, P. Bertrand, and P. G. Rouxhet, "Diffusion of Adhesion Promoter (CPO) into Polypropylene/EthylenePropylene (PP/EP) Copolymer Blends: Mechanism," *Journal of Adhesion Science and Technology*, vol. 15, no. 13, pp. 1589–1600, 2001.

- [62] H. Tang and D. C. Martin, "Microstructural Studies of Interfacial Deformation in Painted Thermoplastic Polyolefins (TPOs)," *Journal of Material Science*, vol. 37, pp. 4783–4791, 2002.
- [63] D. Choi, T. S. December, T. Glogovsky, G. Menovcik, W. Merritt, and B. T. Nguyen, *The Effects of TPO Composition an Adhesion and Proposed Chemical Mechanism, Paintings and Coatings Industry (PCI)*. 2008.
- [64] R. A. Ryntz, Q. Xie, and A. C. Ramamurthy, "Effects of Coating Solvents on the Morphology of Thermoplastic Polyolefins (tpo)," *Journal of Coatings Technology*, vol. 67, no. 843, pp. 45–55, 1995.
- [65] T. S. December, B. Nguyen, G. G. Menovcik, and W. H. Merritt, "Coatings and Methods for Improved Adhesion to Plasticc," 2009. Patent No. 20090258252, BASF Corporation.
- [66] Y. Ma and M. A. Winnik, "Surface and Interface Characterization of Chlorinated Polyolefin Coated Thermoplastic Polyolefin," *Journal of Coatings Technology*, vol. 2, no. 5, pp. 407–416, 2005.
- [67] R. A. Ryntz, "The Influence of Compositional Variations in Compounded Thermoplastic (TPOs) on the Physical and Mechanical Attributes of Injection Molded Plaques," *Journal of Vinyl and Additive Technology*, vol. 3, no. 4, pp. 295–300, 1997.
- [68] R. A. Ryntz and B. Buzdon, "The Realtionship between Clearcoat Permeability and Adhesion Promoter Penetration to the Gasoline Resistance of Painted TPO Substrates," *Progress in Organic Coatings*, vol. 32, pp. 167–172, 1997.
- [69] R. A. Ryntz, "Bring Back the Steel? The Growth of Plastics in Automotive Applications," *Journal of Coatings Technology and Research*, vol. 3, no. 1, pp. 3–14, 2006.



- [70] R. J. Clemens, G. N. Batts, J. E. Lawniczak, K. P. Middleton, and C. Sass, “How do Chlorinated Poly(olefins) Promote Adhesion of Coatings to Poly(propylene)?,” *Progress in Organic Coatings*, vol. 24, pp. 43–54, 1994.
- [71] S. Waddington and D. Briggs, “Adhesion Mechanisms between Polymer-Coatings and Polypropylene Studies by XPS and SIMS,” *Polymer Communications*, vol. 32, no. 16, pp. 506–508, 1991.
- [72] F. M. Mirabella, N. Dioh, and C. G. Zimba, “Theoretical Analysis and Experimental Characterization of the TPO/Adhesion Promoter/Paint Interface of Painted Thermoplastic Polyolefins (TPO),” *Polymer Engineering and Science*, vol. 40, no. 9, pp. 2000–2006, 2000.
- [73] A. M. Forster, C. A. Michaels, L. Sung, and J. Lucas, “Modulus and Chemical Mapping of Multilayer Coatings,” *Applied Materials and Interfaces*, vol. 1, no. 3, pp. 597–603, 2009.
- [74] R. A. Ryntz, D. Britz, D. M. Mihora, and R. Pierce, “Measuring Adhesion to Poly(olefins): The Role of Adhesion Promoter and Substrate,” *Journal of Coatings Technology and Research*, vol. 73, no. 921, pp. 107–115, 2001.
- [75] A. Andersen, “Adhesion of Coatings: An Interfacial Challenge.” Improvement of Adhesion with Increasing Levels of EPDM in PP, 10th Coatings Science International 2011, Hotels van Oranje Noordwijk , the Netherlands, June 2011.
- [76] A. Vasconcellos, J. Oliveira, and R. Baumhardt-Neto, “Adhesion of Polypropylene Treated with Nitric and Sulfuric Acid,” *European Polymer Journal*, vol. 33, no. 10–12, pp. 1731–1734, 1997.
- [77] T. Ebeling, A. Hiltner, and E. Baer, “Effect of Peel Rate and Temperature on Delamination Toughness of PC-SAN Microlayers,” *Polymer*, vol. 40, no. 6, pp. 1525–1536, 1999.

- [78] C. Poon, S. Chum, A. Hiltner, and E. Baer, "Adhesion of Polyethylene Blends to Polypropylene," *Polymer*, vol. 45, no. 3, pp. 893–903, 2004.
- [79] N. V. Bhat and D. J. Upadhyay, "Plasma-Induced Surface Modification and Adhesion Enhancement of Polypropylene Surface," *Journal of Applied Polymer Science*, vol. 86, no. 4, pp. 925–936, 2002.
- [80] R. Mahlberg, H. Niemi, F. Denes, and R. Rowell, "Application of AFM on the Adhesion Studies of Oxygen-Plasma-Treated Polypropylene and Lignocellulosics," *Langmuir*, vol. 15, no. 8, pp. 2985–2992, 1999.
- [81] L. Carrino and W. P. G. Moroni, "Cold Plasma Treatment of Polypropylene Surface: A Study on Wettability and Adhesion," *Journal of Materials Processing Technology*, vol. 121, no. 2–3, pp. 373–382, 2002.
- [82] C. Boullanger, J. Chapel, L. Danel, and J. Fournier, "Adhesion Mechanisms of EnamelVarnishes on Copper: Adhesion Promoter versus Corrosion Inhibitor," *Journal of Applied Polymer Science*, vol. 89, no. 4, pp. 952–958, 2003.
- [83] D. E. Packham, *Handbook of Adhesion*. John Wiley and Sons, 2006.
- [84] R. Lacombe, *Adhesion Measurement Methods: Theory and Practice*. CRC Press, 2006.
- [85] DIN, "Paints and Varnishes - Cross-Cut Test (ISO 2409:2007)," tech. rep., DIN Deutsches Institut für Normung e.V., Berlin, 2007.
- [86] A. J. Goldschmidt and H.-J. Streitbege, *BASF Handbook on Basics of Coating Technology*. BASF, 2003.
- [87] H.-J. Streitberger and K.-F. Dössel, *Automotive Paints and Coatings*. Wiley-VCH, 2008.

- [88] K. Jaehnichen, J. Frank, D. Pleul, and F. Simon, "A Study of Paint Adhesion to Polymeric Substrates," *Journal of Adhesion Science and Technology*, vol. 17, no. 12, pp. 1635–1654, 2003.
- [89] J. H. Clint, "Adhesion and Components of Solid Surface Energies," *Current Opinion in Colloid and Interface Science*, vol. 6, no. 1, pp. 28–33, 2001.
- [90] G. Grundmeier and M. Stratmann, "Adhesion and De-adhesion Mechanisms at Polymer/Metal Interfaces: Mechanistic Understanding Based on In Situ Studies of Buried Interfaces," *Annual Review of Materials Research*, vol. 35, pp. 571–615, 2005.
- [91] R. Jones, H. M. Pollock, J. A. S. Cleaver, and C. S. Hodges, "Adhesion Forces between Glass and Silicon Surfaces in Air Studied by AFM: Effects of Relative Humidity, Particle Size, Roughness, and Surface Treatment," *Langmuir*, vol. 18, no. 21, pp. 8045–8055, 2002.
- [92] S. Gourianova, N. Willenbacher, , and M. Kutschera, "Chemical Force Microscopy Study of Adhesive Properties of Polypropylene Films: Influence of Surface Polarity and Medium," *Langmuir*, vol. 21, pp. 5429–5438, 2005.
- [93] G. Tao, A. Gong, J. Lu, H.-J. Sue, and D. E. Bergbreiter, "Surface Functionalized Polypropylene: Synthesis, Characterization, and Adhesion Properties," *Macromolecules*, vol. 34, pp. 7672–7679, 2001.
- [94] J. C. Vickerman and D. Briggs, *ToF-SIMS Surface Analysis by Mass Spectrometry*. IM Publications, 2001.
- [95] E. D. F. A. Society, *Microelectronic Failure Analysis: Desk Reference : 2002 Supplement*. ASM International, 2002.
- [96] N. Fairley, *CasaXPS Manual 2.3.15 Introduction to XPS and AES*. Casa Software Ltd., 2009.

- [97] S. J. Hinder, C. Lowe, J. T. Maxted, and J. F. Watts, "A ToF-SIMS Investigation of a Buried Polymer/Polymer Interface Exposed by Ultra-Low-Angle Microtomy," *Surface and Interface Analysis*, vol. 36, pp. 1575–1581, 2004.
- [98] S. J. Davis and J. F. Watts, "Interfacial Chemistry of Adhesive Joint Failure: an Investigation by Small Area XPS, Imaging XPS and ToF-SIMS," *Journal of Materials Chemistry*, vol. 6, no. 3, pp. 479–493, 1996.
- [99] A. Rattana, M.-L. Abel, and J. F. Watts, "ToF-SIMS Studies of the Adsorption of Epoxy Resin Molecules on Organosilane-Treated Aluminium: Adsorption Kinetics and Adsorption Isotherms," *International Journal of Adhesion and Adhesives*, vol. 26, pp. 28–39, 2006.
- [100] K. Shimizu, C. Phanopoulos, R. Loenders, M.-L. Abela, and J. F. Watts, "The Characterization of the Interfacial Interaction between Polymeric methylene Diphenyl Diisocyanate and Aluminum: A ToF-SIMS and XPS Study," *Surface Interface Analysis*, vol. 42, pp. 1432–1444, 2010.
- [101] M.-L. Abel, J. F. Watts, and R. P. Digby, "The Adsorption of Alkoxysilanes on Oxidised Aluminium Substrates," *International Journal of Adhesion and Adhesives*, vol. 18, pp. 179–192, 1998.
- [102] F. Garbassi, E. Occhiello, F. Polato, and A. Brown, "Surface Effect of Flame Treatments on Polypropylene, Part 2," *Journal of Materials Science*, vol. 22, pp. 1450–1456, 1987.
- [103] F. Garbassi, E. Occhiello, and F. Polato, "Surface Effect of Flame Treatments on Polypropylene, Part 1," *Journal of Materials Science*, vol. 22, pp. 207–212, 1987.
- [104] D. Montezinos, B. G. Wells, and J. L. Burns, "The use of Ruthenium in Hypochlorite as a Stain for Polymeric Materials," *Journal of Polymer Science: Polymer Letters Edition*, vol. 23, no. 8, pp. 421–425, 1985.

- [105] J. S. Trent, J. I. Scheinbeim, and P. R. Couchman, "Ruthenium Tetraoxide Staining of Polymers for Electron Microscopy," *Macromolecules*, vol. 16, pp. 589–598, 1983.
- [106] J. S. Trent, "Rhuthenium Tetraoxide Staining of Polymers: New Preparative Methods for Electron Microscopy," *Macromolecules*, vol. 17, pp. 2930–2931, 1984.
- [107] H. Hintze-Brüning and H. Borgholte, "Coating of Untreated Polypropylene with Halogen Free Aqueous Materials," *Progress in Organic Coatings*, vol. 40, pp. 49–54, 2000.
- [108] G. M. Brown and J. H. Butler, "New Method for the Characterisation of Domain Morphology of Polymer Blends using Ruthenium Tetraoxide Staining and Low Voltage Scanning Electron Microscopy (LVSEM)," *Polymer*, vol. 38, no. 15, pp. 3937–3945, 1997.
- [109] L. L. Ban and K. S. Campo, "Determining the Polymer Domain Structure of Thermoplastic Elastomer Blends by Microscopy Techniques," *Rubber World*, vol. 207, no. 4, pp. 20–22, 1993.
- [110] R. M. A. l'Abee, A. M. J. T. Vissers, J. G. P. Goosens, A. B. Spoelstra, and M. van Duin, "Characterization of the Morphology of Co-Extruded, Thermoplastic/Rubber Multi-Layer Tapes," *Analytica Chimica Acta*, vol. 654, pp. 11–19, 2009.
- [111] Z. Yin, J. Yang, N. Coombs, M. A. Winnik, R. A. Ryntz, and P. V. Yaneff, "Quantitative Probing the Interfacial Structure of TPO/CPO Blends by Transmission Electron Microscopy via EDX," *Polymer*, vol. 48, pp. 1297–1305, 2007.
- [112] N. Meédard, C. Poleunis, X. V. Eynde, and P. Bertrand, "Characterization of Additives at Polymer Surfaces by ToF-SIMS," *Surface and Interface Analysis*, vol. 34, pp. 565–569, 2002.

- [113] M. Haunschmidt, C. W. Klampfl, W. Buchberger, and R. Hertsens, “Rapid Indentification of Stabilisers in Polypropylene using Time-of-Flight Mass Spectroscopy and DART as Ion Source,” *Analyst*, vol. 135, pp. 80–85, 2010.
- [114] U. D. Cakmak and T. Schöberl, “Nanoindentation of Polymers,” *Meccanica*, vol. 47, pp. 707–718, 2012.
- [115] I. Sutherland, D. M. Brewis, R. J. Heath, and E. Sheng, “Modification of Polypropylene Surfaces by Flame Treatment,” *Surface and Interface Analysis*, vol. 17, pp. 507–510, 1991.
- [116] Y. S. Lin and H. K. Yasuda, “Surface Modification on Thermoplastic Olefins by Low-Temperature Cascade Arc Discharge-Air Plasmas for Enhanced Adhesion with Primer,” *Journal of Polymer Science Part B-Polymer*, vol. 40, no. 7, pp. 623–637, 2002.
- [117] S. Wu, *Polymer Interface and Adhesion*. CRC Press, 1982.
- [118] F. Garbassi, M. Morra, and E. Occhiello, *Polymer Surfaces: From Physics to Technology*. Wiley, 1994.
- [119] J. Meister, *Polymer Modification: Principles, Techniques, and Applications*. Marcel Dekker, 2000.
- [120] E. Kiss, J. Samu, and A. Toth, “Novel Ways of Covalent Attachment of Poly(ethylene oxide) onto Polyethylene: Surface Modification and Characterization by XPS and Contact Angle Measurements,” *Langmuir*, vol. 12, no. 6, pp. 1651–1657, 1996.
- [121] L. G. Beholz, C. L. Aronson, and A. Zand, “Adhesion Modification of Polyolefin Surfaces with Sodium Hypochlorite in Acidic Media,” *Polymer*, vol. 46, no. 13, pp. 4604–4613, 2005.

- [122] L. W. McKee, *Fluorinated Coatings and Finishes Handbook: The Definitive User's Guide*. William Andrew, 2006.
- [123] M. J. Walzak, S. Flynn, R. Foerch, J. M. Hill, E. Karbasheski, A. Lin, and M. Strobel, "UV and Ozone Treatment of Polypropylene and Poly(ethylene Terephthalate)," *Journal of Adhesion Science and Technology*, vol. 9, no. 9, pp. 1229–1248, 1995.
- [124] A. Overbeek, "Polymer Heterogeneity in Waterborne Coatings," *Journal of Coatings Technology and Research*, vol. 7, no. 1, pp. 1–21, 2010.
- [125] M. A. J. Schellekens, G. C. Overbeek, T. Nabuurs, and J. Geurts, "Adhesion to Plastic with Block Copolymers obtained using RAFT," *PCT/EP2009/053891*, October 8th, 2009.
- [126] C.-W. Lin and W.-L. Lee, "An Investigation on the Modification of Polypropylene by Grafting of Maleic Anhydride Based on the Aspect of Adhesion," *Journal of Applied Polymer Science*, vol. 70, pp. 383–387, 1998.
- [127] D. L. Malotky, S. Hofmann, C. F. Diehl, M. D. Read, A. Batistini, H. C. Silvis, and C. Bette, "Adhesion Promoter System, and Method of Producing the Same," April 20th, 2011. Patent EP20110717141, Dow Global Technologies LLC.
- [128] D. M. Brewis and D. Briggs, "Adhesion to Polyethylene and Polypropylene," *Polymer*, vol. 22, no. 7–16, 1981.
- [129] Y. Komatsu, J. Kamimura, O. Aoki, D. B. Chung, and M. S. Wiseman, "New TPO and Coating Technology for Bumper without 1.1.1-Trichloroethane," Tech. Rep. Paper 940187, SAE Technical Papers, 1994.
- [130] K. Manabe, Y. Sato, and R. Muroi, "Process for the Pretreatment of a Polyolefin Product Before Coating," August 14th 1984. Patent No. 4465715, Toyoda Gosei Co Ltd.

- [131] H. Harada, Y. Ikezawa, S. Kanzaki, H. Shinonaga, and S. Sogabe, "Polypropylene Resin Composititon," April 29th 1997. Patent No. 5624991, Sumitomo Chemical Company Limited.
- [132] F. Awaja, M. Gilbert, G. Kelly, B. Fox, R. Brynolf, and P. Pigram, "Surface Properties of Polypropylene following a Novel Industrial Surface-Treatment Process," *Surface Interface Analysis*, vol. 40, pp. 1454–1462, 2008.
- [133] S. Hofmann, C. F. Diehl, and D. L. Malotky, "Adhesion Promoter System, and Method of Producing the Same," 7th March, 2013. Patent No. 20130059149, Dow Global Technologies.
- [134] J. W. Power and M. Thompson, "Waterborne Coating Composition Useful for Promoting Adhesion to Plastic Surfaces," August 15th, 2013. Patent US20130209792 A1, W.M. Barr & Company.
- [135] J. Brunner, H. Senn, and F. M. Richards, "3-Trifluoromethyl-3-phenyldiazirine," *The Journal of Biological Chemistry*, vol. 255, no. 8, pp. 3313–3318, 1980.
- [136] E. V. Anslyn, *Modern Physical Organic Chemistry*. University Science Books, Wilsted and Taylor Publishing Services, 2006.
- [137] M. Akay, *Introduction to Polymer Science and Technology*. Mustafa Akay and Ventus Publishing ApS, 2012.
- [138] W. Rasband, "Research Services Branch, National Institute of Mental Health, Bethesda, Maryland, USA.." Source code freely available. Accessed July 2013. <http://rsbweb.nih.gov/ij/index.html>.
- [139] Microsoft®, "Office Excel." 2007.
- [140] V. Bellitto, *Atomic Force Microscopy - Imaging, Measuring and Manipulating Surfaces at the Atomic Scale*. InTech, 2012.



- [141] Agilent Technologies, “Agilent Continuous Stiffness Measurement (CSM) Option Data Sheet,” tech. rep., Agilent Technologies, Inc. 2011, <http://cp.literature.agilent.com/litweb/pdf/5990-4183EN.pdf>, 2011.
- [142] W. Oliver and G. Pharr, “Measurement of Hardness and Elastic Modulus by Instrumented Indentation: Advances in Understanding and Refinements to Methodology,” *Journal of Materials Research*, vol. 19, no. 1, pp. 3–20, 2004.
- [143] W. C. Oliver and G. M. Pharr, “An Improved Technique for Determining Hardness and Elastic Modulus using Load and Displacement Sensing Indentation Experiments,” *Journal of Materials Research*, vol. 7, no. 6, pp. 1594–1583, 1992.
- [144] A. Rudawska and E. Jacniacka, “Analysis for Determining Surface Free Energy Uncertainty by the OwenWendt Method,” *International Journal of Adhesion & Adhesives*, vol. 29, pp. 451–457, 2009.
- [145] S. Wu, “Calculation of Interfacial Tension in Polymer Systems,” *Journal of Polymer Science Part C: Polymer Symposia*, vol. 34, no. 1, pp. 19–30, 1971.
- [146] Sigma-Aldrich, “Preparing Self-Assembled Monolayers (SAMs) A Step-by-Step Guide for Solution-Based Self-Assembly,” tech. rep., Technical Bulletin AL-266, Accessed 2013.
- [147] H. H. Telle, A. G. Urena, and R. J. Donovan, *Laser Chemistry: Spectroscopy, Dynamics and Applications*, ch. Chapter 10: Reflection, Refraction and Diffraction, p. 152. John Wiley and Sons, 2007.
- [148] H. Fujiwara, *Spectroscopic Ellipsometry: Principles and Applications*. John Wiley and Sons, 2007.
- [149] M. Prato, R. Moroni, F. Bisio, R. Rolandi, L. Mattera, O. Cavalleri, and M. Canepa, “Optical Characterization of Thiolate Self-Assembled Monolayers on Au(111),” *The Journal of Physical Chemistry*, vol. 112, pp. 3899–3906, 2008.

- [150] G. Bracco and B. Holst, *Surface Science Techniques*. 663, Springer, xxiii ed., 2013. ISBN 978-3-642-34242-4.
- [151] S. Abbott, C. M. Hansen, H. Yamamoto, and R. S. V. III, *Hansen Solubility Parameters in Practice: Software, Datasets, eBook*. Hansen-Solubility.com, 2008-2010. ISBN 978-0-9551220-2-6.
- [152] H. J. Vandenburg, A. A. Clifford, K. D. Bartle, and S. A. Zhu, “Factors Affecting High-Pressure Solvent Extraction (Accelerated Solvent Extraction) of Additives from Polymers,” *Analytical Chemistry*, vol. 70, pp. 1943–1948, 1998.
- [153] H. J. Vandenburg, A. A. Clifford, K. D. Bartle, R. E. Carlson, J. Carroll, and I. D. Newton, “A Simple Solvent Selection Method for Accelerated Solvent Extraction of Additives from Polymers,” *The Analyst*, vol. 124, pp. 1707–1710, 1999.
- [154] R. N. S. Sodhi, “Time-of-Flight Secondary Ion Mass Spectrometry (TOF-SIMS): Versatility in Chemical and Imaging Surface Analysis,” *The Analyst*, pp. 483–487, 2004.
- [155] N. Yamamoto, F. Bernardi, A. Bottoni, M. Olivucci, M. A. Robb, and S. Wilsey, “Mechanism of Carbene Formation from the Excited States of Diazirine and Diazomethane: An MC-SCF Study,” *Journal of the American Chemical Society*, vol. 116, no. 5, pp. 2064–2074, 1994.
- [156] G. Das, “Multiconfiguration Selfconsistent Field (MCSCF) Theory for Excited States,” *The Journal of Chemical Physics*, vol. 58, no. 11, pp. 5104–5110, 1973.
- [157] L. CMS, “www.fdms.de,” tech. rep., official website of Linden CMS, Accessed January 2013.
- [158] R. G. Lomax and D. L. Hahs-Vaughn, *An Introduction to Statistical Concepts*. Tailor and Francis Group, LLC, Third Edition ed., 2012.

- [159] Y. Jinghua, Z. Enle, J. Guiping, J. Feng, and H. Boatong, “Morphology of Vulcanized EPDM/PP Blend Thermoplastic Elastomers,” *Scientia Sinica (Series B)*, vol. XXIX, no. 12, pp. 1233–1238, 1986.
- [160] J. Maitland Jones, *Organic Chemistry*. New York & London: W. W. Norton & Company, 3rd ed., 2005. Page 472.
- [161] T. Nedvok and F. Lednický, “Morphologies of Polyethylene-Ethylene/Propylene/Diene Monomer Particles in Polypropylene-Rich Polyolefin Blends: Flake Structure,” *Journal of Applied Polymer Science*, vol. 90, pp. 3087–3092, 2003.
- [162] N. Holz, G. S. Goizueta, and N. J. Capiati, “Linear Low Density Polyethylene Addition to Polypropylene/Elastomer Blends: Phase Structure and Impact Properties,” *Polymer Engineering and Science*, vol. 36, no. 22, pp. 2765–2770, 1996.
- [163] W.-J. Ho and R. Salovey, “Processing of Polyolefin Blends,” *Polymer Engineering and Science*, vol. 21, no. 13, pp. 839–843, 1981.
- [164] F. C. Strehling, T. Huff, C. S. Speed, and G. Wissler, “Structure and Properties of Rubber-Modified Polypropylene Impact Blends,” *Journal of Applied Polymer Science*, vol. 26, pp. 2693–2711, 1981.
- [165] R. N. Wenzel, “Resistance of Solid Surfaces to Wetting by Water,” *Industrial and Engineering Chemistry*, vol. 28, no. 8, pp. 988–994, 1936.
- [166] A. B. D. Cassie and S. Baxter, “Wettability of Porous Surfaces,” *Transactions of the Faraday Society*, vol. 40, pp. 546–551, 1944.
- [167] M. C. Hsieh, J. P. Youngblood, W. Chen, and T. J. McCarthy, “Ultrahydrophobic Polymeric Surfaces Prepared using Plasma Chemistry,” vol. 2, pp. 77–90, 2000. ISBN 9067643270.

- [168] S. Yariv, M. E. Schrader, and G. I. Loeb, *Modern Approaches to Wettability*. Plenum Press, New York, 1992. pp. 279–326.
- [169] S. Chander, J. M. Wie, and D. W. Fuerstenau, “Advances in Interfacial Phenomena of Particulate/Solution/Gas Systems: Application to Flotation Research,” *AIChE Symposium Series 150*, pp. 183–188, 1975.
- [170] M. C. Fuerstenau, A. Lopez-Valdiviezo, and D. W. Fuerstenau, “Role of Hydrolyzed Cations in the Natural Hydrophobicity of Talc,” *International Journal of Mineral Processing*, vol. 23, pp. 161–170, 1988.
- [171] J. H. Rayner and G. Brown, “Crystal Structure of Talc,” *Clays and Clay Minerals*, vol. 21, no. 2, pp. 103–114, 1973.
- [172] P. A. Ciullo, *Minerals and their Uses – A Handbook and Formulary*. New Jersey, 1996.
- [173] B. Pukansky, *Polypropylene: Structure, Blends and Composites*, vol. 3. Chapman and Hall, London, 1995.
- [174] P. Durfton, *Functional Additives for the Plastics Industry: Trends in Use and Technology*. Rapra Technology Limited, 1998.
- [175] D. M. Brewis, ed., *Pretreatments of Polymers to Enhance Adhesion in Transport Applications*, (Brussels, Belgium), Polymers in Mass Transit Conference 2001, Rapra Technology, 2001.
- [176] N. P. Cheremisinoff, *Handbook of Engineering Polymeric Materials*. Marcel Dekker Inc., 1997.
- [177] M. Strobel, V. Jones, C. S. Lyons, M. Ulsh, M. J. Kushner, R. Dorai, and M. C. Branch, “A Comparison of Corona-Treated and Flame-Treated Polypropylene Films,” *Plasmas and Polymers*, vol. 8, no. 1, pp. 61–95, 2003.

- [178] Eastman, *How to Use Eastman CPOs As Adhesion Promoters*. North America, publication GN-408B ed., September 1998.
- [179] J. C. Rivière and S. Myhra, *Handbook of Surface and Interface Analysis*. CRC Press, 2nd ed., 2009.
- [180] F. Fujimoto, "Properties and Applications of Chlorinated Polypropylene," *Paint & Resin*, pp. 36–40, 1986.
- [181] S. Paul, "Painting of Plastics: New Challenges and Possibilities," *Surface Coatings International Part B: Coatings Transactions*, vol. 85, no. B2, pp. 79–168, 2002.
- [182] O. Zerbe and S. Jurt, *Applied NMR Spectroscopy for Chemists and Life Scientists*. John Wiley and Sons, 2013.
- [183] D. Léonard, Y. Chevolut, O. Bucher, H. Sigrist, and H. J. Mathieu, "ToF-SIMS and XPS Study of Photoactivatable Reagents Designed for Surface Glycoengineering, Part i. *N*-(*m*-(3-(Trifluoromethyl)diazirine-3-yl)phenyl)-4-maleimido-butylamide (MAD) on Silicon, Silicon Nitride and Diamond," *Surface and Interface Analysis*, vol. 26, pp. 783–792, 1998.
- [184] D. Léonard, Y. Chevolut, O. Bucher, W. Haenni, H. Sigrist, and H. J. Mathieu, "ToF-SIMS and XPS Study of Photoactivatable Reagents Designed for Surface Glycoengineering, Part II. *N*-[*m*-(3-(Trifluoromethyl)diazirine-3-yl)phenyl]-4-(3-thio(1-d-galactopyranosyl)-maleimidyl)butylamide (MAD-Gal) on Diamond," *Surface and Interface Analysis*, vol. 26, pp. 793–799, 1998.
- [185] D. Léonard, Y. Chevolut, F. Heger, J. Martins, D. H. G. Crout, H. Sigrist, and H. J. Mathieu, "ToF-SIMS and XPS Study of Photoactivatable Reagents Designed for Surface Glycoengineering, Part III. 5-Carboxamidopentyl-*N*-[*m*-(3-(Trifluoromethyl)diazirine-3-yl)phenyl]- $\beta$ -d-galactopyranosyl-(1->4)-1-thio- $\beta$ -d-glucopyranoside (lactose aryl diazirine) on Diamond," *Surface and Interface Analysis*, vol. 31, pp. 457–464, 2001.

- [186] S. Ebnesajjad and C. Ebnesajjad, *Surface Treatment of Materials for Adhesion Bonding*. William Andrew Incorporated, 2006.
- [187] G. C. Lloyd-Jones, R. W. Alder, and G. J. J. Owen-Smith, “Intermolecular Insertion of an N,N-Heterocyclic Carbene into a Nonacidic C-H Bond: Kinetics, Mechanism and Catalysis by (K-HMDS)<sub>2</sub> (HMDS = Hexamethyldisilazide),” *Chemistry - A European Journal*, vol. 12, pp. 5361–5375, 2006.
- [188] K. T. Chang and H. Shechter, “Roles of Multiplicity and Electronic Excitation on Intramolecular Reactions of Alkylcarbenes in Condensed Phases,” *Journal of the American Chemical Society*, vol. 101, no. 17, pp. 5082–5084, 1979.
- [189] A. Mansoor and I. D. R. Stevens, “Hot Radical Effects in Carbene Reactions,” *Tetrahedron Letters*, vol. 7, no. 16, pp. 1733–1737, 1966.
- [190] J. J. Havel, “Carbene Multiplicity in Decompositions of 2-Methyl-2-phenyldiazopropane,” *Journal of Organic Chemistry*, vol. 41, no. 8, pp. 1464–1465, 1976.
- [191] J. F. Arenas, I. López-Toc'on, J. C. Otero, and J. Soto, “Carbene Formation in its Lower Singlet State from Photoexcited 3H-Diazirine or Diazomethane. A Combined CASPT2 and ab Initio Direct Dynamics Trajectory Study,” *Journal of the American Chemical Society*, vol. 124, no. 8, pp. 1728–1735, 2002.
- [192] J. M. Figuera, J. M. Pérez, and A. Tobar, “Energy Distribution and Mechanism in 3-Chloro-3-methyldiazirine Photolysis,” *Journal of the Chemical Society, Faraday Transactions 1: Physical Chemistry in Condensed Phases*, vol. 74, pp. 809–817, 1978.
- [193] K. H. Fischer, P. Hemberger, I. Fischer, and A. M. Rijs, “Infrared Spectra of Reactive Species Generated by Flash Pyrolysis in a Free Jet,” *ChemPhysChem*, vol. 11, pp. 3228–3230, 2010.

- [194] K. Adamsons, "Chemical Surface Characterization and Depth Profiling of Automotive Coating Systems," *Progress in Polymer Science*, vol. 25, pp. 1363–1409, 2000.
- [195] L. Carrino, W. Polini, and L. Sorrentino, "Ageing Time of Wettability on Polypropylene Surfaces Processed by Cold Plasma," *Journal of Materials Processing Technology*, vol. 153–154, pp. 519–525, 2004.
- [196] A. Y. Vainer, K. M. Dyumaev, S. A. Mareeva, R. M. Dragunskaya, N. V. Efimova, and Z. A. Slyusarenko, "Synthesis and Thermo and Photochemical Reactions of Unsaturated Fluorene Containing Poly(arylene ether)s with Pendant Trifluoromethyl-diazirine Groups," *Doklady Physical Chemistry*, vol. 445, pp. 123–127, 2012.
- [197] C. N. Sanrame, C. P. Suhrada, H. Dang, and M. A. Garcia-Garibay, "Photochemistry of Crystalline Chlorodiazirines: The Influence of Conformational Disorder and Intermolecular Cl—N=N Interactions on the Solid-State Reactivity of Singlet Chlorocarbenes," *The Journal of Physical Chemistry A*, vol. 107, pp. 3287–3294, 2003.
- [198] G. Wagner, W. Knoll, M. M. Bobek, L. Brecker, H. W. G. van Herwijnen, and U. H. Brinker, "Structure–Reactivity Relationships: Reactions of a 5-Substituted Aziadamantane in a Resorcin[4]arene-based Cavitand," *Organic Letters*, vol. 12, no. 2, pp. 332–335, 2010.
- [199] J. E. Zanetti and G. Eglopf, "The Thermal Decomposition of Benzene," *The Journal of Industrial and Engineering Chemistry*, vol. 9, no. 4, pp. 350–356, 1917.
- [200] C.-Y. Lin and M. C. Lin, "Thermal Decomposition of Methyl Phenyl Ether in Shock Waves: The Kinetics of Phenoxy Radical Reactions," *Journal of Physical Chemistry*, vol. 90, pp. 425–431, 1986.
- [201] A. Toussaint, "Self-Stratifying Coatings for Plastic Substrates," *Progress in Organic Coatings*, vol. 28, pp. 183–195, 1996.

- [202] V. Verkholtantsev, "Self-Stratifying Coatings for Industrial Applications," *Pigment and Resin Technology*, vol. 32, no. 5, pp. 300–306, 2003.
- [203] G. L. Robertson, *Food Packaging: Principles and Practice*. CRC Press, Third Edition ed., 2012.
- [204] E. Hu, X. Hu, T. Liu, Y. Liu, R. Song, and Y. Chen, "Investigation of Morphology, Structure and Composition of Biomass-oil Soot Particles," *Applied Surface Science*, vol. 270, pp. 596–603, 2013.
- [205] M. A. Chinelatto and J. A. M. Agnelli, "Effect of the Chemical Stabilization System on the Photooxidation of Polypropylene containing Talc and Carbon Black," *Polymer Degradation and Stability*, vol. 50, pp. 13–19, 1995.
- [206] H. P. Boehm, "Some Aspects of the Surface Chemistry of Carbon Blacks and Other Carbons," *Carbon*, vol. 32, no. 5, pp. 759–769, 1994.
- [207] J. Brydson, *Plastics Materials*. Butterworth-Heinemann, A member of the Reed Elsevier plc group, 7th ed., 1999.
- [208] H. G. Karian, *Handbook of Polypropylene and Polypropylene Composites*. Taylor & Francis, 2nd, revised and expanded ed., 2009.
- [209] M. E. Schrader and S. Yariv, "Wettability of Clay Minerals," *Journal of Colloid and Interface Science*, vol. 136, no. 1, pp. 85–94, 1990.
- [210] M. Xanthos, *Functional Fillers for Plastics*. Wiley-VCH, 2nd, updated and enlarged edition ed., 2010.
- [211] Y.-C. Ou, T.-T. Guo, X.-P. Fang, and Z.-Z. Yu, "Toughening and Reinforcing Polypropylene with Core-Shell Structured Fillers," *Journal of Applied Polymer Science*, vol. 74, no. 10, pp. 2397–2403, 1999.
- [212] Y. U. Long and R. A. Shanks, "PP/Elastomer/Filler Hybrids. II. Morphologies and Fracture," *Journal of Applied Polymer Science*, vol. 62, no. 4, pp. 639–646, 1996.



- [213] B. SE, “ToF-SIMS Database.” Polymer Additive ToF SIMS Spectra, 2013.
- [214] Ciba, “Ciba IRGAFOS 168 Datasheet,” tech. rep., Ciba Inc, 2009.
- [215] D. Möbius and R. Miller, *Novel Methods to Study Interfacial Layers*. Elsevier, 2001.
- [216] W. L. Baun, “Ion Beam Methods for the Surface Characterisation of Polymers,” *Pure and Applied Chemistry*, vol. 54, no. 2, pp. 323–336, 1982.
- [217] D. Briggs, “Analysis of Polymer Surfaces by SIMS,” *Surface and Interface Analysis*, vol. 4, no. 4, pp. 151–155, 1982.
- [218] W. J. van Ooij and R. H. G. Brinkhuis, “Interpretation of the Fragmentation Patterns in Static SIMS Analysis of Polymers. Part I. Simple Aliphatic Hydrocarbons,” *Surface and Interface Analysis*, vol. 11, pp. 430–440, 1988.
- [219] D. Briggs, “Analysis of Polymer Surfaces by SIMS. Part 14. Aliphatic Hydrocarbons Revisited,” *Surface and Interface Analysis*, vol. 15, pp. 734–738, 1990.
- [220] L. Lianos, C. Quet, and T. M. Duc, “Surface Structural Studies of Polyethylene, Polypropylene and their Copolymers with ToF SIMS,” *Surface and Interface Analysis*, vol. 21, pp. 14–22, 1994.
- [221] Y. Kato, D. J. Carlsson, and D. M. Wiles, “The Photo-Oxidation of Polypropylene: Some Effects of Molecular Order,” *Journal of Applied Polymer Science*, vol. 13, no. 7, pp. 1447–1458, 1969.
- [222] A. M. Cunha and S. Fakirov, *Structure Development During Polymer Processing*. Springer; Softcover reprint of the original 1st ed. 2000 edition, 2000.
- [223] R. D. Adams, *Adhesive Bonding: Science, Technology and Applications*. Woodhead Publishing Limited, 2005.

- [224] A. T. Asbeck, S. Kim, M. R. Cutkosky, W. R. Provancher, and M. Lanzetta, "Scaling Hard Vertical Surfaces with Compliant Microspine Arrays," *The International Journal of Robotics Research*, vol. 25, pp. 1165–1179, 2006.
- [225] "Sadtlter handbook of infrared spectra." Sadtlter Research Laboratories, as implemented in KnowItAll software 9.0 by Bio-rad Laboratories 2001-2012.
- [226] G. Socrates, "Infrared Characteristic Group Frequencies." Wiley, 1980.
- [227] B. Latli, E. Wood, and J. E. Casida, "Insecticidal Quinazoline Derivatives with (Trifluoromethyl)diaziriny and Azido Substituents as NADH:Ubiquinone Oxidoreductase Inhibitors and Candidate Photoaffinity Probes," *Chemical Research in Toxicology*, vol. 9, no. 2, pp. 445–450, 1996.
- [228] T. Weber and J. Brunner, "2-(Tributylstannyl)-4- [ 3-(trifluoromethyl)-3h-diazirin-3-yl] Benzyl Alcohol: A Building Block for Photolabeling and Cross-Linking Reagents of Very High Specific Radioactivity," *Journal of the American Chemical Society*, vol. 117, no. 11, pp. 3084–3095, 1995.
- [229] M. Yamada, K. Harada, Y. Maeda, and T. Hasegawa, "A Versatile Approach to Functionalisation of [60]Fullerene using 3-Trifluoromethyl-3-phenyldiazirine Derivatives as Photolabelling Reagents," *New Journal of Chemistry*, vol. 37, pp. 3762–3769, 2013.
- [230] L. C. Robertson and J. A. Maerritt, "The Electronic Absorption Spectra of n-Diazirine, N<sub>1</sub><sup>15</sup>-Diazirine, d<sub>1</sub>-Diazirine and d<sub>2</sub>-Diazirine," *Journal of Molecular Spectroscopy*, vol. 19, pp. 372–388, 1966.
- [231] L. C. Robertson and J. A. Maerritt, "The Electronic Absorption Spectra of Bromomethyldiazirine and Chloromethyldiazirine," *Journal of Molecular Spectroscopy*, vol. 24, pp. 44–61, 1967.

- [232] L. C. Robertson and J. A. Maeritt, "Electronic Absorption Spectra of 3-Methyldiazirine and 3-Methyl-d<sub>3</sub>-Diazirine," *The Journal of Chemical Physics*, vol. 57, no. 2, pp. 941–947, 1972.
- [233] L. C. Robertson and J. A. Maeritt, "Electronic Absorption Spectra of 3,3'-Dimethyldiazirine," *The Journal of Chemical Physics*, vol. 56, no. 6, pp. 2919–2924, 1972.
- [234] A. Blencowe, K. Cosstick, and W. Hayes, "Surface Modification of Nylon 6,6 using a Carbene Insertion Approach," *New Journal of Chemistry*, vol. 30, pp. 53–58, 2006.
- [235] M. S. Han, H.-G. Cho, and B.-S. Cheong, "Theoretical Studies of the Low-Lying Electronic States of Diazirine and 3,3'-Dimethyldiazirine," *The Korean Chemical Society*, vol. 20, no. 11, pp. 1281–1287, 1999.
- [236] C. D. Bain and G. M. Whitesides, "Formation of Monolayers by the Coadsorption of Thiols on Gold: Variation in the Length of the Alkyl Chain," *Journal of the American Chemical Society*, vol. 111, no. 18, pp. 7164–7175, 1989.
- [237] J. P. Folkers, P. E. Laibinis, and G. M. Whitesides, "Self-Assembled Monolayers of Alkanethiols on Gold: Comparisons of Monolayers Containing Mixtures of Short- and Long-chain Constituents with CH<sub>3</sub> and CH<sub>2</sub>OH Terminal Groups," *Langmuir*, vol. 8, pp. 1330–1341, 1992.
- [238] Z. G. Hu, P. Prunici, P. Patzner, and P. Hess, "Infrared Spectroscopic Ellipsometry of n-Alkylthiol (C<sub>5</sub>-C<sub>18</sub>) Self-Assembled Monolayers on Gold," *The Journal of Physical Chemistry B*, vol. 110, pp. 14824–14831, 2006.
- [239] L. V. Protsailo and W. R. Fawcett, "Studies of Electron Transfer through Self-Assembled Monolayers using Impedance Spectroscopy," *Electrochimica Acta*, vol. 45, pp. 3497–3505, 2000.

- [240] L. Houssiau and P. Bertrand, "ToF-SIMS Study of Alkanethiol Adsorption and Ordering on Gold," *Applied Surface Science*, vol. 175-176, pp. 399–406, 2001.
- [241] D. A. Hutt and G. J. L. E. Cooper, "Structure and Mechanism of Photooxidation of Self-Assembled Monolayers of Alkylthiols on Silver Studied by XPS and Static SIMS," *The Journal of Physical Chemistry. B*, vol. 102, pp. 174–184, 1998.